

# TABLE OF CONTENTS

<b>ABSTRACT</b>	<b>i</b>
<b>ACKNOWLEDGEMENT</b>	<b>iii</b>
<b>TABLE OF CONTENTS</b>	<b>iv</b>
<b>LIST OF FIGURES</b>	<b>vii</b>
<b>LIST OF TABLES</b>	<b>xv</b>
<b>NOTATIONS</b>	<b>xvii</b>
<b>Chapter 1 INTRODUCTION</b>	<b>1</b>
1.1 Rocking Motion and Aseismic Structural Design	2
1.2 Research Objective and Motivation	6
1.3 Thesis Outline / Organisation	7
1.4 Reference Frames and Co-ordinate systems	8
<b>Chapter 2 LITERATURE REVIEW</b>	<b>13</b>
2.1 The Development of Rocking Science	13
2.2 Housner's Simple Rocking Model	14
2.3 Other Rocking Block Models	19
2.4 Rocking Structural Systems	22
2.4.1 Rigid interface solutions	23
2.4.2 Two-spring foundation solutions	25
2.4.3 Tensionless Winkler foundation solution	27
2.5 Rocking Systems as Nonlinear Dynamic Systems	29
2.5.1 Free standing block subjected to harmonic ground motion	29
2.6 Dirac- $\delta$ Representation of the Rocking Impact	39
2.7 Controlled Rocking Motion	46
2.8 Conclusion	54
<b>Chapter 3 FREE ROCKING OBJECTS</b>	<b>57</b>
3.1 Experimental Setup	57
3.2 Results and Analysis	59
3.2.1 Comparing experimental results against Housner's SRM model	60
3.2.2 Energy content during a rocking cycle	63
3.2.3 Support and impact forces of a rocking rigid block	67
3.2.4 Energy dissipation due to impacts	74
3.3 Summary of Findings	80
<b>Chapter 4 CONTROLLED ROCKING SYSTEMS</b>	<b>83</b>
4.1 Introduction	83
4.2 Experiment Details	85
4.3 Instrumentation and Data Acquisition	87
4.4 Shake Table Motion Selection	88
4.5 Experiment Results	91

4.5.1	Free vibration response (Test run 5)	92
4.6	Modelling the tendon extension	102
4.7	Developing the force-displacement relationship of a controlled rocking wall	105
4.7.1	Summary of findings from the free vibration response	118
4.8	Predicting the Free Vibration Time-history	119
4.8.1	Nonlinearly elastic equivalent sdof approximation	120
4.8.2	Modified Housner - Substitute Gravity approach	126
4.8.3	Sensitivity of the MHSG method to input parameters	136
4.9	PCM Wall Response Subjected to Base Excitation	140
4.9.1	Shake table tests with 75 kN initial tendon force	140
4.9.1.1	Wall uplifts and tendon force increases	151
4.9.1.2	Location of rotation centre	153
4.9.1.3	Predicting the time-history response to base excitation	159
4.9.1.4	Attempts to improve the equivalent SDOF procedure	163
4.9.1.5	Sensitivity of controlled rocking system	167
4.9.2	Shake table tests with 110 kN initial tendon force	171
4.9.2.1	Predicting the time-history response subjected to base excitation	176
4.10	Conclusion	177
<b>Chapter 5</b>	<b>SIMPLIFIED ROCKING STRUCTURAL SYSTEMS</b>	<b>181</b>
5.1	Introduction	181
5.2	Experimental Validation Data	182
5.2.1	Free rocking decays (FRD) – Solid Feet	185
5.2.2	Free rocking decays (FRD) – Soft Rubber Pad	190
5.2.3	Shake table tests	195
5.3	Theoretical models of rocking structural systems	197
5.3.1	Rigid lumped-mass structure rocking about fixed pivots on a rigid foundation	197
5.3.1.1	Validating the analytical model	202
5.3.2	Rigid lumped-mass rocking structure resting on two compression-only springs	206
5.3.2.1	Validating the analytical model	214
5.3.3	Elastic 2 DOF structure rocking about fixed pivots on a rigid foundation	219
5.3.3.1	Validating the analytical model	221
5.4	Conclusion	231
<b>Chapter 6</b>	<b>CONCLUSIONS AND FUTURE WORK</b>	<b>233</b>
6.1	Behaviour of Rigid, Rocking Blocks	234
6.2	Dynamics of Controlled Rocking Systems	235
6.3	Simplified Rocking Systems	236
6.4	Future Work	237
	<b>REFERENCES</b>	<b>239</b>
<b>Appendix A</b>	<b>DETAILED RESULTS FOR THE ANALYSES OF CONTROLLED ROCKING SYSTEMS</b>	<b>245</b>

<b>Appendix B</b>	<b>DERIVATION OF THE INDIVIDUAL ENERGY COMPONENTS OF A PCM WALL .....</b>	<b>252</b>
B.1	Gravitational potential energy .....	252
B.2	Kinetic energy .....	254
B.3	Elastic potential energy .....	255
<b>Appendix C</b>	<b>SIMULATED TIME-HISTORIES OF THE SHAKE TABLE TESTS .....</b>	<b>257</b>
<b>Appendix D</b>	<b>MATHEMATICAL DESCRIPTION OF THE FLEXIBLE ROCKING STRUCTURE ON RIGID GROUND.....</b>	<b>274</b>

# LIST OF FIGURES

Figure 1-1 – Illustration of a simple rocking motion; a) a stable object at rest, b&c) a restoring force self centres the object and the object rotates about its pivots .....	2
Figure 1-2 – a) The South Rangitikei Viaduct, b) a close up of rocking hinge at the pier base.....	5
Figure 1-3 – Force-displacement characteristic of typical rocking systems.....	5
Figure 1-4 – Reference frame for models with rigid block on rigid ground.....	8
Figure 1-5 – Reference frame for models with rigid block on bed of springs.....	9
Figure 1-6 – Reference frame for simple structural models rocking on a) rigid ground, b) Two-spring foundation and c) Tensionless-Winkler spring foundation.....	10
Figure 1-7 – Reference frame for the controlled rocking wall models.....	11
Figure 2-1 – The Housner Rocking Block.....	15
Figure 2-2 – Theoretical prediction of coefficient of restitution of blocks of different aspect ratio compared with experimentally established values.....	18
Figure 2-3 – Key parameters for an impacting rigid body.....	21
Figure 2-4 – Rocking block on tensionless, visco-elastic Winkler foundation .....	21
Figure 2-5 – Three categories of rocking interface assumption .....	22
Figure 2-6 – Free vibration time-history of a SDOF rocking system ( $H/B = 1/0.3$ m, $\omega = 56.10$ $\text{rads}^{-1}$ , $f = 8.9$ Hz, $\xi = 0.03$ , $\frac{\theta_0}{\theta_{\text{crit}}} = 0.05$ ).....	24
Figure 2-7 – Free rocking decay history of a SDOF rocking system ( $H/B = 1000/300$ mm) (Source: McManus 1980) .....	25
Figure 2-8 – The effective moment-rotation characteristics for unbounded foundation mats with three rocking interface constraint assumptions .....	28
Figure 2-9 – Phase Portrait of a free rocking rigid block without energy dissipation.....	32
Figure 2-10 – Phase Portrait of a free rocking rigid block with $r = 0.9$ .....	32
Figure 2-11 – Examples of symmetric and asymmetric steady state orbits of a rocking block subjected to sinusoidal base excitation.....	33
Figure 2-12 – Bifurcation diagram for a free rocking block with $\alpha = 0.464$ , $r = 0.5$ , $\omega = \frac{2}{3}\pi$ and $\beta$ from 3 to 3.26 .....	35
Figure 2-13 – Time-history responses of a free rocking rigid block subjected to a single sine pulse increasing in peak acceleration ( $\alpha = 7.12^\circ$ , $r = 0.954$ ) .....	36
Figure 2-14 – Time-history responses of 4 freestanding rigid blocks subjected to an identical single sine pulse ( $\ddot{u}_{g\text{max}} = 0.3$ g, $T_{\text{pulse}} = 2$ s, $r$ is as per Equation 2-6).....	37
Figure 2-15 – The effect of varying $n$ on the Dirac- $\delta$ distribution approximation .....	41

Figure 2-16 – Time-history response of a 1:3 freestanding rigid block released from an initial rotation of $x_0 = 0.4$ ( $r = 0.7225$ , $n = 10^{-3}$ , $\Delta\tau = 0.5 \times 10^{-3}$ ) ....	44
Figure 2-17 – Time-history response of a 1:3 freestanding rigid block released from an initial rotation of $x_0 = 0.4$ ( $r = 0.7225$ , $\Delta\tau = 0.5 \times 10^{-3}$ ).....	45
Figure 2-18 – Typical schematic of an unbonded post-tensioned rocking wall .....	46
Figure 2-19 – Idealised nonlinear static force-displacement response (Blue arrows indicate the loading path and red arrows indicate the unloading path) 47	
Figure 2-20 – Illustrative non-dimensionalised Moment-Rotation plots for controlled rocking systems with added energy dissipating devices, i) Elastic-plastic, ii) Friction & iii) Viscous (Palermo et al. 2005).....	48
Figure 2-21 – Three typical hysteretic material models .....	50
Figure 2-22 – Equivalent hysteretic damping against displacement ductility .....	51
Figure 2-23 – Equivalent hysteretic damping corrections as a function of Effective Period .....	53
Figure 3-1 – Rigid Rocking Block Experiment Setup .....	58
Figure 3-2 – Schematic of the Steel Mechanism in action .....	58
Figure 3-3 – Typical angular rotation time-history of the concrete block released from an initial rotation .....	59
Figure 3-4 – Illustration of the peak finding algorithm .....	59
Figure 3-5 – Quarter periods versus normalised initial rotation .....	61
Figure 3-6 – Typical experimental and numerically simulated results.....	61
Figure 3-7 – Phase diagram of the experimental and simulated time-history .....	62
Figure 3-8 – Idealised energy content during a rocking cycle.....	63
Figure 3-9 – Energy content of a rocking block during an experimental test run .....	65
Figure 3-10 – Energy content of a rocking block including a hypothetical rotational spring.....	67
Figure 3-11 – Accelerations and forces acting on a rigid rocking block; and the vector diagram of the centroidal accelerations.....	68
Figure 3-12 – Support forces of a rocking block during an experimental test run .....	69
Figure 3-13 – Support forces of a simulated Housner rocking block .....	70
Figure 3-14 – Theoretical support forces just before and after an impact versus approaching angular speed .....	72
Figure 3-15 – Experimental support forces just prior and after an impact versus approaching angular speed .....	73
Figure 3-16 – Magnitude and direction of the impact force versus approaching angular speed.....	74
Figure 3-17 – Effects of energy correction for four experimental test runs .....	75
Figure 3-18 – Coefficient of restitution versus peak rotation before impact a) with all data points b) with small rotation data points omitted .....	76

Figure 3-19 – Frequency distribution of the coefficient of restitution.....	77
Figure 3-20 – Cumulative frequency distribution of the coefficient of restitution.....	77
Figure 3-21 – Experimental coefficient of restitution against impact speed .....	78
Figure 3-22 – Absolute change in energy content against angular impact speed .....	79
Figure 3-23 – Change in energy content against magnitude of the impact force .....	80
Figure 4-1 – A typical PCM wall construction.....	84
Figure 4-2 – a) An uplifting PCM wall, b) Distinctive force-displacement characteristics of a PCM wall.....	85
Figure 4-3 – a) Typical single PCM wall specimen and b) PCM structure on the shake table (Source: Wight 2006) .....	86
Figure 4-4 – Geometry of the PCM wall specimen .....	86
Figure 4-5 – Instrumentation plan for the shake table test (Source: Wight 2006).....	88
Figure 4-6 – A comparison of obtained and intended shake table motion for Run 2 (El Centro-A1-T1).....	89
Figure 4-7 – Response spectra of the shake table tests.....	90
Figure 4-8 – Wall response and table motion during the free vibration test.....	93
Figure 4-9 – Mounting of an edge uplift potentiometer (Source: Wight 2006).....	93
Figure 4-10 – Linear rotation profile assumption .....	94
Figure 4-11 – Corrected wall response and table motion for run 5 .....	95
Figure 4-12 – Free vibration decay with peaks and zero crossings highlighted.....	96
Figure 4-13 – Quarter periods of PCM wall versus peak ToW displacement.....	97
Figure 4-14 – a) Wall uplifts and b) tendon force versus ToW displacements .....	97
Figure 4-15 – a) Wall uplifts and b) tendon force versus ToW displacements .....	98
Figure 4-16 – The effect of a shifting centre of rotation on uplift.....	99
Figure 4-17 – Distance between the rotation centre and wall edge versus wall lateral displacement.....	100
Figure 4-18 – a) Wall uplifts versus ToW displacements, b) close up of the origin .	102
Figure 4-19 – Key variables controlling the tendon extension .....	103
Figure 4-20 – a) Tendon force versus ToW displacements, b) close up of the origin .....	104
Figure 4-21 – Two experiments where axial load is simulated through post-tensioning (Source: a)Elwood and Moehle 2003; b)Rahman and Restrepo 2000) .....	106
Figure 4-22 – a) Key parameters for dynamic properties calculation, b) $I_o/R$ versus the centre of rotation location .....	107
Figure 4-23 – Finite element model of the fixed based wall .....	107
Figure 4-24 – Quarter period predictions (Equation 4-17) against the test data.....	109

Figure 4-25 – Free vibration decay displayed in a phase diagram .....	110
Figure 4-26 – ToW speed versus ToW displacement.....	111
Figure 4-27 – Region of energy dissipation in the modified phase diagram.....	112
Figure 4-28 – Energy content during the first three cycles of the FVD .....	113
Figure 4-29 – Total energy content at displacement peaks.....	114
Figure 4-30 – Experimental coefficient of restitution versus Peak ToW displacement before impact and ToW velocity at impact .....	115
Figure 4-31 – Close up of Figure 4-30 with a focus on a range of realistic $r$ values.	115
Figure 4-32 – Experimental and conservative phase diagram trajectories .....	116
Figure 4-33 – Time-history response by integrating the theoretical phase diagram trajectories .....	117
Figure 4-34 – Empirical versus conjectural energy dissipation boundary.....	118
Figure 4-35 – Theoretical nonlinear restoring force-displacement relationship.....	121
Figure 4-36 – Preliminary numerical simulation results with a range of $r$ values.....	122
Figure 4-37 – Final numerical simulation against experimental result.....	124
Figure 4-38 – Comparison of simulated response with small deviations in $r$ value..	125
Figure 4-39 – Simplified, MHSg simulation results with a range of $r$ values .....	127
Figure 4-40 – $r$ values for each cycle for an accurate time-history simulation .....	128
Figure 4-41 – Moving average of ideal $r$ values for accurate time-history simulation against empirical expression for $r$ .....	129
Figure 4-42 – Simplified MHSg simulation with $r$ calculated using Equation 4-31	130
Figure 4-43 – Simplified MHSg simulation with $r$ calculated using Equation 4-36	131
Figure 4-44 – a) Parameters affected by the new assumption, b) centre of rotation migration relationship .....	133
Figure 4-45 – MHSg simulation with $r$ calculated using Equation 4-38 .....	135
Figure 4-46 – Effects of a variation in rotation centre migration rate ( $n$ ).....	136
Figure 4-47 – Comparison of simulated response with small deviations in $n$ value .	137
Figure 4-48 – Comparison of simulated response with small deviations in $r$ value..	138
Figure 4-49 – Shake table tests with 75 kN initial tendon prestressing force.....	141
Figure 4-50 (cont.) – Summary of the moving window transfer function analysis...	144
Figure 4-51 – Moving window transfer function analysis for the FV decay.....	146
Figure 4-52 – Transfer function variation for shake table test 1 (El Centro – A0.5 – T1.0) .....	148
Figure 4-53 – Transfer function variation for shake table test 2 (El Centro – A1.0 – T1.0) .....	148
Figure 4-54 – Transfer function variation for shake table test 3 (Tabas – A1.0 – T0.38) .....	149

Figure 4-55 – Transfer function variation for shake table test 4 (Northridge – A1.0 – T0.6) .....	149
Figure 4-56 – Transfer function variation for shake table test 6 (Valparaiso – A1.0 – T1.0) .....	150
Figure 4-57 – a) Wall uplifts versus ToW displacements, b) close up of the origin .	151
Figure 4-58 – a) Tendon force versus ToW displacements, b) close up of the origin .....	152
Figure 4-59 – a) Tendon force versus ToW displacements for test run 2 and 3 .....	152
Figure 4-60 – Distance between the rotation centre and wall edge versus wall lateral displacement for the 75 kN shake table tests .....	153
Figure 4-61 – Negative rotation centre distances and PCM wall in free flight .....	154
Figure 4-62 – Distance between the rotation centre and wall edge versus ToW displacement for the 75 kN shake table tests plotted individually .....	155
Figure 4-63 – The migration of rotation centre from rest to rocking.....	156
Figure 4-64 – The migration of rotation centre during developed rocking .....	157
Figure 4-65 – The migration of rotation centre during developed rocking .....	158
Figure 4-66 – Simulated and actual time-histories (Run 2 – El Centro – A1.0 – T1.0) .....	160
Figure 4-67 – Simulated and actual time-histories (Run 4 – Northridge – A1.0 – T0.6) .....	161
Figure 4-68 – A close up comparison of simulated time-history during rocking.....	162
Figure 4-69 – Theoretical pushover characteristics versus dynamic data .....	164
Figure 4-70 – A time-history simulation using a constant $r$ value ( $r = 0.852$ ).....	166
Figure 4-71 – a) Simulated peak ToW displacements versus the $r$ value, b) probability of a time-history analysis resulting in a conservative estimate.....	167
Figure 4-72 – A typical time-history simulation expressed on a phase diagram ( $P_e(t) = 5.88 \sin(16\pi t)$ ).....	168
Figure 4-73 – Bifurcation diagram of controlled rocking wall response subjected varying sinusoidal base excitation.....	169
Figure 4-74 – Displacement time-histories from two identical shake table tests .....	170
Figure 4-75 – Distance between the rotation centre and wall edge versus wall lateral displacement for the 110 kN shake table tests .....	172
Figure 4-76 – Wall uplifts versus ToW displacements for tests with 110 kN tendon prestress .....	174
Figure 4-77 – Tendon force versus ToW displacements for 110 kN prestress.....	175
Figure 4-78 – Theoretical pushover characteristics versus dynamic data .....	175
Figure 4-79 – Typical time-history simulation using a constant $r$ value ( $r = 0.852$ ). .....	176
Figure 5-1 – Two rocking interface assumptions examined in this chapter .....	182

Figure 5-2 – Geometry of the steel column specimen .....	183
Figure 5-3 – Photographs of the experimental rig (Source: McManus 1980) .....	183
Figure 5-4 – Stress-strain property of the soft rubber pad (Source: McManus 1980) .....	184
Figure 5-5 – Measurement location (dimensions shown in mm) .....	186
Figure 5-6 – Displacement time-history of run 1, FRD – solid feet .....	186
Figure 5-7 – Quarter periods versus norm. peak rotation (run 1, FRD – solid feet)..	187
Figure 5-8 – The equivalent lumped mass model of the system.....	187
Figure 5-9 – a) coefficient of restitution versus $\theta_{peak}/\alpha_e$ , b) A close up of a) with data points from small vibrations removed.....	189
Figure 5-10 – Displacement time-history of run 2, FRD – soft rubber pad.....	190
Figure 5-11 – Relationship between uplifts and centre of rotation.....	190
Figure 5-12 – Location of rotation centre versus time (run 2, FRD – rubber pad)....	191
Figure 5-13 – Location of rotation centre versus horizontal displacement .....	192
Figure 5-14 – Quarter periods versus rotation peak (run 2, FRD – rubber pad).....	193
Figure 5-15 – Horizontal accelerations versus time (run 2, FRD – rubber pad) .....	193
Figure 5-16 – Equivalent viscous damping ratio versus peak displacement .....	194
Figure 5-17 – Displacement time-history of test run 3 (El Centro NS – Solid feet) .	195
Figure 5-18 – Displacement time-history of test run 4 (Pacoima Dam N76°W –rubber pad).....	196
Figure 5-19 – Idealised rigid lumped-mass structure rocking about fixed pivots .....	198
Figure 5-20 – Free body diagram of the rocking rigid lumped-mass structure .....	199
Figure 5-21 – Velocity diagram of the lumped-mass model before and after impact	200
Figure 5-22 – Simulated versus actual displacement time-history of run 1 ( $r_{sim}=0.74$ ) .....	203
Figure 5-23 – Simulated versus actual displacement time-history of run 1 ( $r_{sim}=0.81$ ) .....	204
Figure 5-24 – Simulated versus actual displacement time-history of run 3 ( $r_{sim}=0.74$ ) .....	205
Figure 5-25 – Simulated versus actual displacement time-history of run 3 ( $r_{sim}=0.81$ ) .....	205
Figure 5-26 – Rigid lumped-mass rocking structure on two compression only springs .....	207
Figure 5-27 – The idealised SDOF mass cart .....	207
Figure 5-28 – Force diagrams of the rocking structure subjected to increasing displacement.....	209
Figure 5-29 – Simplified restoring force-displacement characteristic of a rigid rocking structure on two compression only springs .....	212

Figure 5-30 – Annotated screenshot of the Working Model analysis .....	213
Figure 5-31 – Force-displacement characteristics from Working Model simulation and the approximation formulae .....	213
Figure 5-32 – Simulated versus actual displacement time-history of run 2 ( $r_{sim}=0.74$ ) .....	215
Figure 5-33 – Displacement from FRD simulations with different $k_f$ values .....	216
Figure 5-34 – Simulated versus actual displacement time-history of run 4 ( $r_{sim}=0.74$ , $k_f=550$ kN/m) .....	217
Figure 5-35 – Simulated versus actual displacement time-history of run 4 ( $r_{sim}=0.74$ , $k_f=10$ MN/m) .....	218
Figure 5-36 – Simulated time-history of run 4 assuming a rigid foundation adopting Model A from Section 5.3.1 ( $r_{sim}=0.74$ ) .....	218
Figure 5-37 – Flexible 2 DOF rocking structure on rigid ground .....	220
Figure 5-38 – Simulated versus actual displacement time-history of run 1 ( $r_{sim}=0.74$ ) .....	222
Figure 5-39 – Individual simulated response time-histories for run 1 ( $r_{sim}=0.74$ ) .....	223
Figure 5-40 – Experimental time-history traces from run 1 (Source: McManus 1980) .....	224
Figure 5-41 – Simulated versus actual displacement time-history of run 1 ( $r_{sim}=0.81$ ) .....	225
Figure 5-42 – Simulated time-history traces of the FVD with two different $r$ values .....	226
Figure 5-43 – Simulated versus actual displacement time-history of run 3 ( $r_{sim}=0.74$ ) .....	227
Figure 5-44 – Individual simulated response time-histories for run 3 ( $r_{sim}=0.74$ ) .....	228
Figure 5-45 – Rocking system response versus fixed base response ( $r_{sim}=0.74$ , $k = 571.8$ kN/m and $c = 502.4$ Ns/m) .....	229
Figure 5-46 – Simulated response time-histories with a range of $k$ values ( $c = 502.4$ Ns/m) .....	230
Figure 5-47 – Simulated response time-histories with a range of $c$ values ( $k = 571.8$ kN/m) .....	231
Figure A-1 – Acceleration and Displacement traces of Run 1 (El Centro-A0.5-T1) .....	246
Figure A-2 – Response spectrum of Run 2 (El Centro-A0.5-T1), (5% damping) .....	246
Figure A-3 – Acceleration and Displacement traces of Run 2 (El Centro-A1-T1) .....	247
Figure A-4 – Response spectrum of Run 2 (El Centro-A1-T1), (5% damping) .....	247
Figure A-5 – Acceleration and Displacement traces of Run 3 (Tabas-A1-T0.38) .....	248
Figure A-6 – Response spectrum of Run 3 (Tabas-A1-T0.38), (5% damping) .....	248
Figure A-7 – Acceleration and Displacement traces of Run 4 (Sylmer-A1-T0.6) .....	249
Figure A-8 – Response spectrum of Run 4 (Sylmer-A1-T0.6), (5% damping) .....	249

Figure A-9 – Acceleration and Displacement traces of Run 6 (Valparaiso-A1-T1) .	250
Figure A-10 – Response spectrum of Run 6 (Valparaiso-A1-T1), (5% damping)....	250
Figure B-1 – Geometric relationships of a rotating PCM wall.....	253
Figure C-1 – Simulation Results using the unmodified nonlinearly elastic equivalent SDOF approach (Run 1 – El Centro A-0.5 T-1.0) .....	258
Figure C-2 – Simulated results using the unmodified nonlinearly elastic equivalent SDOF approach (Run 2 – El Centro A-1.0 T-1.0) .....	259
Figure C-3 – Simulated results using the unmodified nonlinearly elastic equivalent SDOF approach (Run 3 – Tabas A-1.0 T-0.38) .....	260
Figure C-4 – Simulated results using the unmodified nonlinearly elastic equivalent SDOF approach (Run 4 – Northridge A-1.0 T-0.6) .....	261
Figure C-5 – Simulated results using the unmodified nonlinearly elastic equivalent SDOF approach (Run 6 – Valparaiso A-1.0 T-1.0) .....	262
Figure C-6– Simulated results using the MHSG approach from free vibration analysis (Run 1 – El Centro A-0.5 T-1.0) .....	263
Figure C-7– Simulated results using the MHSG approach from free vibration analysis (Run 2 – El Centro A-1.0 T-1.0) .....	264
Figure C-8 – Simulated results using the MHSG approach from free vibration analysis (Run 3 – Tabas A-1.0 T-0.38) .....	265
Figure C-9 – Simulated results using the MHSG approach from free vibration analysis (Run 4 – Northridge A-1.0 T-0.6) .....	266
Figure C-10 – Simulated results using the MHSG approach from free vibration analysis (Run 6 – Valparaiso A-1.0 T-1.0) .....	267
Figure C-11 – Simulated results using the SDOF approach with a constant $r = 0.835$ (Run 7 – El Centro A-1.0 T-1.0, 110kN prestress) .....	268
Figure C-12 – Simulated results using the SDOF approach with a constant $r = 0.835$ (Run 8 Tabas A-1.0 T-0.38, 110kN prestress) .....	269
Figure C-13 – Simulated results using the SDOF approach with a constant $r = 0.835$ (Run 9 Northridge A-1.0 T-0.6, 110kN prestress) .....	270
Figure C-14 – Simulated results using the SDOF approach $r$ from FV analysis (Run 7 – El Centro A-1.0 T-1.0, 110kN prestress) .....	271
Figure C-15 – Simulated results using the SDOF approach $r$ from FV analysis (Run 8 Tabas A-1.0 T-0.38, 110kN prestress) .....	272
Figure C-16 – Simulated results using the SDOF approach $r$ from FV analysis (Run 9 Northridge A-1.0 T-0.6, 110kN prestress) .....	273
Figure D-1 – Displacement and velocity diagram of the flexible rocking structure (Positive Rotation).....	275
Figure D-2 – D’Alembert forces as a result of a base excitation ( $\ddot{u}_g$ ).....	277
Figure D-3 – Displacement and velocity diagram of the flexible rocking structure (Negative Rotation) .....	279

# LIST OF TABLES

Table 2-1 – Comparison of experimental and theoretical apparent c.o.r. values.....	18
Table 2-2 – Spring-damper element parameters for a rocking circular and rectangular rigid foundation .....	27
Table 2-3 – Equivalent viscous damping ratios determined from free vibration tests of unbonded post-tensioned concrete masonry wall.....	49
Table 2-4 – Parameters for Equation 2-33 (Grant et al. 2005) .....	52
Table 2-5 – Parameters for “design” expression, Equation 2-35.....	52
Table 3-1 – Experimental and theoretical support forces for a typical test run.....	71
Table 4-1 – Summary of input motions .....	89
Table 4-2 – Summary of wall response .....	91
Table 4-3 – Summary of simulation results .....	162
Table 4-4 – Shake table tests results with 75kN and 110kN prestress .....	171
Table 4-5 – Summary of simulation results .....	177
Table 5-1 – Summary of dynamic test data .....	184
Table A-1 – Wall response at peak displacements and zero crossings.....	251



# NOTATIONS

## Chapter 2

$a_{peak}$	=	Peak acceleration of a sinusoidal ground acceleration pulse
$c$	=	Viscous damping value of an equivalent SDOF structure
$c_f$	=	Viscous damping value of a two-spring rocking foundation
$c_w$	=	Viscous damping value per unit width of a Winkler foundation
$f$	=	Natural frequency of the superstructure in Hertz. (See Figure 2-5a)
$f_p$	=	Post-tensioning force in a controlled rocking wall
$g$	=	Gravitational acceleration = $9.81 \text{ ms}^{-2}$
$k$	=	Elastic stiffness of an equivalent SDOF structure
$k_f$	=	Spring stiffness of two-spring rocking foundation
$k_i, k_p$	=	Initial and post yield stiffness in various hysteretic material models
$k_w$	=	Spring stiffness per unit width of a Winkler foundation
$m$	=	Total mass of the system
$n$	=	Penalty parameter for the Dirac- $\delta$ function
$p$	=	A dimensional constant for the rocking rigid block
$q_c$	=	Bearing capacity of the supporting soil
$r$	=	Apparent coefficient of restitution
$t$	=	Time or the non-dimensional time ordinate in Section 2.4
$\ddot{u}_{g,peak}$	=	Peak ground acceleration
$u_g, \ddot{u}_g$	=	Ground displacement and ground acceleration

$u, \dot{u}, \ddot{u}$	=	Structural deformation, velocity and acceleration of superstructure. See Figure 2-5
$u_c$	=	The critical structural deformation at the onset of rocking
$\tilde{v}_G^+, \tilde{v}_G^-$	=	Velocity vector of the a rocking rigid block's mass centroid approaching and exiting an impact
$x, \dot{x}, \ddot{x}$	=	Non-dimensional rotation, angular velocity and angular acceleration of a generalised rocking block
$\dot{x}_0, \dot{x}_f$	=	Non-dimensional angular speed of a generalised rigid rocking block approaching and exiting an impact
$y$	=	Non-dimensional angular speed of a generalised rigid rocking block
$B$	=	Half-breadth of a rectangular block (Rigid blocks), or Half the horizontal distance between the two rocking pivots (Rocking SDOF structure)
$B_f$	=	Width of a rectangular rigid rocking foundation
$C^+, C^-$	=	Centre of rotation immediately before and after an impact
$C_z$	=	Vertical damping value of a rigid foundation based on a elastic half-space solution
$F_\delta$	=	Dirac- $\delta$ impulse force which emulates the effects of a rocking impact
$G_s$	=	Shear modulus of the supporting soil
$H$	=	Half-height of a rectangular block (Rigid blocks), or height from the rocking pivot to the centre of mass (Rocking SDOF structure)
$I_o$	=	Moment of inertia about point $O$
$K_z$	=	Vertical stiffness of a rigid foundation based on a elastic half-space solution
$L_f$	=	Length of a rectangular rigid rocking foundation

$M$	=	Restoring moment of a rocking system
$M_c$	=	Restoring moment of a rocking system situated over a two-spring foundation, when one of the spring is about to detach
$M_{AE}, M_N, M_{ED}$	=	Moment contributions from the added restoring element, axial load and additional energy dissipaters in a controlled rocking system
$M_{up}$	=	Restoring moment of a rocking system situated over a Winkler foundation, when one edge is about to detach
$O, O'$	=	Location of rocking pivots
$P$	=	The lateral resisting force from a structural specimen when it is loaded and unloaded in a pseudo-static manner. This can be derived from a nonlinear static pushover simulation or an actual physical test
$R$	=	Distance from the rocking edge to the centre of mass
$R_f$	=	Radius of a circular rigid rocking foundation
$S_a$	=	Spectral acceleration
$T$	=	Free rocking period
$T_e$	=	Effective natural period of an equivalent SDOF system in displacement based design procedures, this is calculated based on the secant stiffness
$T_i$	=	Rocking period estimate in the $i$ -th iteration in FEMA 365 procedures for modelling rocking system
$W$	=	Weight force
$\alpha$	=	Angle between the vertical and a line through the rocking pivot and the mass centroid, when the wall is at rest. (See Figure 2-1)
$\alpha_T$	=	Unloading stiffness degradation parameter in the Takeda hysteresis model
$\beta$	=	Non-dimensional amplitude of the sinusoidal base excitation

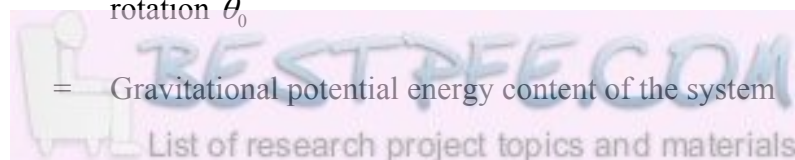
$\beta_{FS}$	=	Flag area parameter in the flag shape hysteresis model
$\beta_z$	=	Shape factor for the vertical stiffness of a rectangular rigid foundation. A graphical plot of this is available in Richart et al. (1970)
$\delta_i$	=	Peak displacement estimate in the $i$ -th iteration in FEMA 365 procedures for modelling rocking system
$\delta(x)$	=	A Dirac- $\delta$ function as a function of $x$
$\lambda$	=	Parameter describing the self-centering capability of a controlled rocking system
$\lambda_r$	=	Natural frequency of the rocking mode of motion. (See Figure 2-5a)
$\mu$	=	Displacement ductility factor
$\nu_s$	=	Poisson ratio of the supporting soil
$\theta, \dot{\theta}, \ddot{\theta}$	=	Angular displacement, velocity and acceleration
$\dot{\theta}^+, \dot{\theta}^-$	=	Angular speed of a rocking rigid block approaching and exiting an impact
$\theta_0$	=	Initial rotation
$\theta_c$	=	Angular rotation of a rocking system situated over a two-spring foundation, when one of the spring is about to detach
$\theta_{crit}$	=	The rotation of a rocking system which leads to overturning under zero external forcing
$\theta_i$	=	Peak rotation estimate in the $i$ -th iteration in FEMA 365 procedures for modelling rocking system
$\theta_{up}$	=	Angular rotation of a rocking system situated over a Winkler foundation, when one edge is about to detach
$\rho_s$	=	Density of the supporting soil
$\tau$	=	Natural time in Section 2.4

- $\omega$  = Natural frequency of the superstructure in  $\text{rads}^{-1}$ . (See Figure 2-5a) In Section 2.4, this is the frequency of the sinusoidal excitation in non-dimensional time ordinates
- $\xi$  = Equivalent viscous damping ratio of the superstructure. (See Figure 2-5a)
- $\xi_{el}, \xi_v$  = Elastic component of the viscous damping ratio of an equivalent SDOF oscillator
- $\xi_{eq}$  = Viscous damping ratio of an equivalent single degree of freedom oscillator
- $\xi_{hyst}$  = Hysteretic component of the viscous damping ratio of an equivalent SDOF oscillator
- $\zeta_r$  = Damping ratio of the rocking mode of motion. (See Figure 2-5a)
- $\Delta$  = Horizontal displacement at the top of a wall during a nonlinear static pushover simulation or a physical test
- $\Omega$  = Frequency of the sinusoidal excitation in natural time for Section 2.4

### **Chapter 3**

- $a_n$  = Normal acceleration of the centroid with respect to the centre of rotation  $O$  or  $O'$
- $a_t$  = Tangential acceleration of the centroid with respect to the centre of rotation  $O$  or  $O'$
- $g$  = Gravitational acceleration =  $9.81 \text{ ms}^{-2}$
- $k_{rot}$  = Rotational stiffness of a hypothetical rotation spring
- $m$  = Total mass of the system
- $r$  = Apparent coefficient of restitution. (Equation 2-4)

$r_{\text{Housner}}$	=	Coefficient of restitution predicted by Housner's equation, Equation 2-6
$\ddot{u}_c$	=	Acceleration of the centroid
$\ddot{u}_{cx}$	=	Horizontal acceleration of the centroid
$\ddot{u}_{cy}$	=	Vertical acceleration of the centroid
$\ddot{u}_{c/g}$	=	Acceleration of the centroid with respect to the centre of rotation $O$ or $O'$
$\ddot{u}_g$	=	Ground acceleration
$\ddot{u}_{gx}$	=	Horizontal component of the ground acceleration
$E_k$	=	Kinetic energy content of the system
$E_k^i$	=	Kinetic energy content just before the $i$ -th impact (B in Figure 3-8)
$E_k^{i+1}$	=	Kinetic energy content just after the $i$ -th impact (C in Figure 3-8)
$F_H$	=	Horizontal reaction force of a rigid rocking block
$F_V$	=	Vertical reaction force of a rigid rocking block
$I_o$	=	Moment of inertia about point $O$
$R$	=	Distance from the rocking edge to centre of mass. (See Figure 3-11)
$\bar{R}$	=	Resultant reaction force from an impact
$T$	=	Free rocking period
$T_0$	=	Free rocking period of the first cycle of motion. This is based on the initial rotation of the system, $\theta_0$
$U^0$	=	Initial gravitational energy content of the system at initial rotation $\theta_0$
$U$	=	Gravitational potential energy content of the system



- $U^i$  = Gravitational potential energy content at the time of peak rotation in the cycle preceding the  $i$ -th impact,  $(\theta_{peak}^i)$  (A in Figure 3-8)
- $U^{i+1}$  = Gravitational potential energy content at the time of peak rotation attained in the cycle following the  $i$ -th impact,  $(\theta_{peak}^{i+1})$  (D in Figure 3-8)
- $U_{rot}$  = Instantaneous potential energy stored in the hypothetical rotation spring
- $\alpha$  = Angle between the vertical and a line through the rocking pivot and the mass centroid, when the wall is at rest. (See Figure 3-11)
- $\gamma$  = Angle between the line of action of  $R$  and the vertical
- $\theta, \dot{\theta}, \ddot{\theta}$  = Angular displacement, velocity and acceleration
- $\theta_0$  = Initial rotation
- $\dot{\theta}_{max, impact}$  = Maximum impact angular velocity predicted by the SRM
- $\theta_{peak}^i$  = Peak rotation in the cycle preceding the  $i$ -th impact
- $\theta_{peak}^{i+1}$  = Peak rotation in the cycle following the  $i$ -th impact

Subscript *impact* denotes the value of the preceding variable at the instant of an impact

Operator  $\Delta$  denotes a change in the following variable

#### **Chapter 4**

- $a_{max}$  = Peak ground acceleration
- $b'$  = Effective half-width of the rocking wall or the horizontal distance between the mass centroid and the rotation centre,  $O$

$d$	=	Length of the detached wall base
$d_{max}$	=	Peak ground displacement
$d_T$	=	Distance from the rotation centre to the prestressing tendon. (See Figure 4-19)
$f_{pu}$	=	Specific rupture strength of the steel prestressing tendon
$f_{py}$	=	Yield strength of the steel prestressing tendon
$m_T$	=	Total mass of the PCM wall specimen
$n$	=	Penalty parameter for the Dirac- $\delta$ function
$r$	=	Apparent coefficient of restitution
$r_{Housner}$	=	Coefficient of restitution predicted by Housner's equation, Equation 2-6
$t$	=	Time
$u_L$	=	Uplift recorded by the left uplift gauge
$u_L'$	=	Uplift at the left wall edge
$u_R$	=	Uplift recorded by the right uplift gauge
$u_R'$	=	Uplift at the right wall edge
$u'$	=	Uplift at the wall edge
$u'_T$	=	Uplift at the tendon location
$\ddot{u}_g$	=	Ground acceleration
$x$	=	Distance from the centre of rotation to the left uplift gauge
$x'$	=	Distance from the centre of rotation to the left wall edge
$x_1$	=	Tendon extension at initial post-tensioning state
$x_2$	=	Tendon extension when the wall displacement is $\Delta$
$y$	=	Distance from the centre of rotation to the right uplift gauge
$y'$	=	Distance from the centre of rotation to the right wall edge
$B$	=	Half-width of the wall panel

$C_1, C_2$	=	Constant in rotation centre fitting equation (Equation 4-8)
$E$	=	Young's modulus
$E_k$	=	Kinetic energy content of the system
$F_{Damp}$	=	Dirac- $\delta$ damping force of the equivalent SDOF system
$F_k$	=	Nonlinear elastic restoring force of the equivalent SDOF system
$H$	=	Height of the wall panel
$H_c$	=	Vertical distance from the base to the centroid of wall system
$I_G$	=	Moment of inertia about the centroid
$I_o$	=	Moment of inertia about the a wall corner, $O$
$L_T$	=	Current length of the prestressing tendon
$L_{T0}$	=	Original length of the prestressing tendon
$M_e$	=	Effective mass of the equivalent SDOF system
$O$	=	Location of the rotation centre
$P_e(t)$	=	Effective driving force of the equivalent SDOF system
$PS_v$	=	Pseudospectral velocity
$P_{Tendon}$	=	Current axial force of the prestressing tendon
$P_{Tendon}^0$	=	Initial post-tension force of the prestressing tendon
$R$	=	Distance from the rotation centre to centre of mass. (See Figure 4-22)
$S_a$	=	Spectral acceleration
$T$	=	Free rocking period
$T_{Fixed Base}$	=	Fundamental natural period of a fixed base wall
$U$	=	Gravitational potential energy content of the system
$U_E$	=	Elastic potential energy content of the system
$U_{Total}$	=	Total energy content of the system

$Z$	=	Amplitude of sinusoidal acceleration in Section 4.7.1.4
$\alpha$	=	Angle between the vertical and a line through the rocking pivot and the mass centroid, when the wall is at rest. (See Figure 4-44)
$\varepsilon$	=	Empirical penalty parameter for the Dirac- $\delta$ function
$\theta, \dot{\theta}, \ddot{\theta}$	=	Angular displacement, velocity and acceleration of the wall panel
$\theta_0$	=	Initial rotation
$\rho$	=	Density
$\Delta, \dot{\Delta}, \ddot{\Delta}$	=	Top of wall displacement, velocity and acceleration
$\Delta_{limit}$	=	The top of wall displacement which defines the energy dissipation boundary
$\dot{\Delta}_{limit}$	=	The top of wall velocity which corresponds with $\Delta_{limit}$
$\Delta_{Peak}$	=	Peak top of wall displacement
$\Delta_0$	=	Initial top of wall displacement
$\Delta L_T$	=	Tendon extension = $L_T - L_{T0}$

Operator  $\delta$  denotes to an incremental change in the following variable

Operator  $\Delta$  denotes to a change in the following variable

## **Chapter 5**

$a_{max}$	=	Peak ground acceleration
$c$	=	Viscous damping value of a simple SDOF structure
$c_f$	=	Viscous damping value of a two-spring rocking foundation
$f_L$	=	Reaction force from the left spring foundation
$f_R$	=	Reaction force from the right spring foundation

$g$	=	Gravitational acceleration = $9.81 \text{ ms}^{-2}$
$\underline{i}, \underline{j}$	=	Versors in the horizontal and vertical direction respectively
$k$	=	Elastic stiffness of a simple SDOF structure
$k_f$	=	Spring stiffness of a two-spring rocking foundation
$m$	=	Mass of a simple SDOF structure
$m_b$	=	Effective lumped-mass representing the base structure
$m_e$	=	Effective lumped-mass representing the flexible steel column
$m_T$	=	Total mass of the steel column specimen including the base structure
$r$	=	Apparent coefficient of restitution
$r^i$	=	Apparent coefficient of restitution from the $i$ -th impact
$r_{\text{sim}}$	=	Coefficient of restitution used in the simulation
$r_{\text{theory}}$	=	Theoretical coefficient of restitution predicted by equation, Equation 5-14
$t$	=	Time
$u, \dot{u}, \ddot{u}$	=	Structural deformation, velocity and acceleration of superstructure. When the superstructure is rigid, these describe the rigid body motion
$u_{\text{crit}}$	=	The horizontal displacement of the rocking system measured at the height of $m_e$ corresponding to $\theta_{\text{crit}}$
$\ddot{u}_g$	=	Ground acceleration
$u_{\text{overturn}}$	=	The horizontal displacement of the rocking system measured at the height of $m_e$ , which causes the system to overturn when there are no external forces on the system
$v_L$	=	Uplift at the left edge of the base plate
$v_R$	=	Uplift at the right edge of the base plate

$x$	=	Horizontal distance from the left edge of the base plate to the rotation centre, $O$ . (See Figure 5-11)
$y$	=	Horizontal distance from the right edge of the base plate to the rotation centre, $O$ . (See Figure 5-11)
$B$	=	Half the horizontal distance between the two rocking pivots
$B'$	=	Effective half-width of the rocking system
$E_k$	=	Kinetic energy content of the system
$E_k^i$	=	Kinetic energy content of the system just before the $i$ -th impact
$E_k^{i+1}$	=	Kinetic energy content of the system just after the $i$ -th impact
$H$	=	Height from the rocking pivot to the mass centroid in the idealised SDOF system. (See Figure 5-1)
$H'$	=	Height from the rocking pivot to the centre of the additional masses
$H_b$	=	Height from the rocking pivot to the lumped-mass of the base structure ( $m_b$ ). (See Figure 5-19)
$H_c$	=	Height from the rocking pivot to the centroid of the two lumped-mass system. (See Figure 5-26)
$H_e$	=	Height from the rocking pivot to the lumped-mass of the flexible steel column ( $m_e$ ). (See Figure 5-19)
$I_{b,g}$	=	Moment of inertia of the base structure about its centroid
$I_{e,g}$	=	Moment of inertia of the flexible steel column about its centroid
$I_G$	=	Moment of Inertia of the rocking system about the mass centroid
$I_O$	=	Moment of inertia of the rocking system about $O$
$L_{O',\text{after}}$	=	Total angular momentum about $O'$ after an impact
$L_{O',\text{before}}$	=	Total angular momentum about $O'$ before an impact

$L_{orbital,b}$	=	The orbital component of angular momentum from lumped-mass $m_b$ about $O'$
$L_{orbital,e}$	=	The orbital component of angular momentum from lumped-mass $m_e$ about $O'$
$L_{spin,b}$	=	The spin component of angular momentum from lumped-mass $m_b$ about $O'$
$L_{spin,e}$	=	The spin component of angular momentum from lumped-mass $m_e$ about $O'$
$O$	=	Location of the rotation centre
$P$	=	Pseudo-static pushover force
$P_{crit}$	=	Pseudo-static pushover force to cause one of the springs in the two-spring foundation to detach
$P_{crit2}$	=	Pseudo-static pushover force required to keep the rocking system stationary when one of the springs in a two-spring foundation is just detached
$R'$	=	$\sqrt{B'^2 + H'^2}$
$R_b$	=	Distance from the rocking pivot to the lumped-mass of the base structure ( $m_b$ ). (See Figure 5-8)
$R_c$	=	Distance from the rocking pivot to the centroid of the two lumped-mass system. (See Figure 5-26)
$R_e$	=	Distance from the rocking pivot to the lumped-mass of the flexible steel column ( $m_e$ ). (See Figure 5-8)
$T$	=	Free rocking period, or kinetic energy of the system in Appendix D
$T_{fixed}$	=	Fundamental natural period of the fixed base steel column specimen
$U_{Grav}$	=	Gravitational potential energy content of the system

$U^i$  = Potential energy content at the time of peak rotation before the  $i$ -th impact

$U^{i+1}$  = Potential energy content at the time of peak rotation after the  $i$ -th impact

$W$  = Weight force of the structural model

$\alpha$  = Angle between the vertical and a line through the rocking pivot and the mass centroid

$\alpha'$  =  $\tan^{-1}\left(\frac{B'}{H'}\right)$

$\alpha_b$  = Angle between the vertical and a line through the rocking pivot and the lumped-mass of the base structure ( $m_b$ ). (See Figure 5-8)

$\alpha_c$  = Angle between the vertical and a line through the rocking pivot and the centroid of the two lumped-mass system. (See Figure 5-26)

$\alpha_e$  = Angle between the vertical and a line through the rocking pivot and the lumped-mass of the flexible steel column ( $m_e$ ). (See Figure 5-8)

$\delta_0$  = Initial settlement of the structural model on a two-spring foundation

$\varepsilon$  = Strain

$\theta, \dot{\theta}, \ddot{\theta}$  = Angular displacement, velocity and acceleration

$\dot{\theta}_1, \dot{\theta}_2$  = Angular velocity before and after an impact

$\theta_{crit}$  = The rotation of the rocking system at which one of the springs in the two-spring foundation is about to detach

$\theta_{peak}^i$  = Peak rotation in the cycle preceding the  $i$ -th impact

$\theta_{peak}^{i+1}$  = Peak rotation in the cycle following the  $i$ -th impact

$\sigma_{direct}$	=	Direct stress
$\xi^i$	=	Equivalent viscous damping ratio of the $i$ -th vibration cycle estimated by the logarithmic decay formula
$\Delta$	=	Horizontal displacement measured at the centre of the additional masses
$\Delta^i$	=	Peak horizontal displacement for the $i$ -th vibration cycle
$\Delta\delta$	=	Change in settlement of the two-spring foundation
$\Phi$	=	Normalised peak rotation
$\Sigma M_o$	=	Sum of moments about $O$

### **Appendix A**

Refer to symbols listed previously under Chapter 4

### **Appendix D**

In additional to symbols listed previously under Chapter 5:

$\underline{f}_b$	=	D'Alembert forces from ground acceleration ( $\ddot{u}_g$ ), on the lumped-mass representing the base structure ( $m_b$ )
$\underline{f}_e$	=	D'Alembert forces from ground acceleration ( $\ddot{u}_g$ ), on the lumped-mass representing the flexible column ( $m_e$ )
$q_i$	=	Generalised coordinate ( $i = \theta$ or $u$ )
$\underline{r}_b$	=	Position vector of lumped-mass representing the base structure ( $m_b$ )
$\underline{r}_e$	=	Position vector of lumped-mass representing the flexible column ( $m_e$ )
$\underline{v}_b$	=	Velocity vector of lumped-mass representing the base structure ( $m_b$ )

- $v_e$  = Velocity vector of lumped-mass representing the flexible column ( $m_e$ )
- $y_1 \dots y_4$  = Numerical integration variables
- $F_{nc}$  = Velocity dependent non-conservative generalised forces
- $Q_i$  = Displacement and velocity independent generalised forces in generalised coordinate  $q_i$ , where  $i = \theta$  or  $u$
- $T_b$  = Kinetic energy of the lumped-mass representing the base structure ( $m_b$ )
- $T_e$  = Kinetic energy of the lumped-mass representing the flexible column ( $m_e$ )
- $V$  = Potential energy of the system
- $\mathcal{L}$  = The Lagrangian = T – V

Operator  $\dot{\phantom{x}}$  denotes derivative with respect to time

Operator  $\ddot{\phantom{x}}$  denotes double derivative with respect to time

# Chapter 1

---

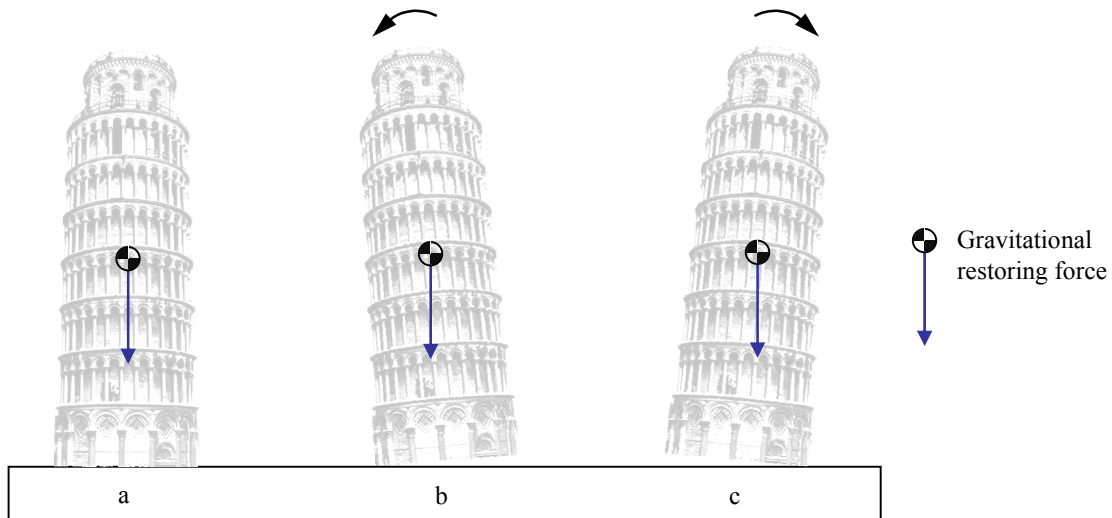
## INTRODUCTION

---

The dynamics of a rocking object has fascinated the wider scientific community for many years, partly because it is a phenomenon that is commonly observed. For instance, a package on a production line set in motion after it is released from a conveyor belt or a precious art statue set in motion by a bystander. Rocking motion typically occurs with slender objects unrestrained at their base. If the object is disturbed from its equilibrium position, it tends to rotate about one of its edges or corners. Providing overturning does not take place, the gravitational restoring force will return the object back towards its equilibrium or upright position. The object would typically arrive back at the upright position with a residual angular velocity and as a result causing it to overshoot the equilibrium position and continue to rotate about a new rocking pivot. This is repeated cyclically until the impacts that occur when the object passes through the upright position eventually dissipate all the potential energy from the initial rotation ending the oscillatory response. This sequence of events, for the purpose of this dissertation, is defined as rocking motion and is illustrated graphically in Figure 1-1.

Despite the familiar, intuitive nature of rocking motion, it is in fact a nonlinear process that is highly complex and sensitive to initial conditions. It has been widely studied, and understanding the mechanics behind the process remains the key to fully comprehending a wide range of mechanical system exhibiting this phenomenon. The

focus of the current study is on the applications of rocking motion to aseismic structural design.



**Figure 1-1 – Illustration of a simple rocking motion; a) a stable object at rest, b&c) a restoring force self centres the object and the object rotates about its pivots**

## 1.1 ROCKING MOTION AND ASEISMIC STRUCTURAL DESIGN

The prevalent philosophy around the world for aseismic structural design is “Capacity Design”, a concept developed in New Zealand some 30 years ago (Park and Paulay 1975). Capacity design has the primary objective of preserving life safety, and this is achieved by deliberately allowing damage to specific part of a structure in the event of a large earthquake, meanwhile ensuring a secure path for gravity loads to reach the ground. This ensures a survivable ductile structural response. However with this design approach, buildings may be left with extensive damage after an earthquake and the damages to the buildings are often difficult to repair. Consequently, substantial repair cost and interim loss of building operation are unavoidable. Recent earthquakes in urban environments, such as the 1994 Northridge and 1995 Kobe earthquakes, have illustrated that this level of damage is crippling to society and prompted a rethink of the design objectives of the current philosophy. As a result, more recently in the research community, there has been an increased focus on developing solutions that ensure either structural damage is isolated and repairable, or solutions which result in zero residual damage with the aim of maintaining post-earthquake serviceability.

With the above objectives in mind, engineers began to take a greater interest in the mechanics of rocking motion. It can be shown that by allowing rocking motion to take place in a structure, the resulting accelerations and hence forces can be significantly reduced. This approach when applied correctly can effectively act as a complementary *isolation*<sup>1</sup> mechanism for structures against severe ground motion (Beck and Skinner 1974). The outcome is a credible design solution as demonstrated by examples later in this section. A rocking solution yields little increase or often a decrease in construction cost, while substantially enhancing the seismic resistance of structures with an assured post-earthquake serviceability.

Evidence suggests the interest in the behaviour of a rocking object may have begun as early as ancient times. Well documented scholarly studies on the mechanics of rocking objects can be traced back to the late 19<sup>th</sup> Century, when scientists in Japan used the overturning of freestanding blocks to estimate the magnitudes of seismic events (Milne and Omori 1893; Omori 1900; 1902). This later became the prevalent way of describing earthquake magnitudes for the first half of the 20<sup>th</sup> Century until the emergence of readily available seismographs (Davison 1921). Then approximately from the 1960s, the potential of applying a rocking mechanism for seismic protection of structures was brought to the attention of earthquake engineering researchers, through the observations of seemingly unstable structures surviving devastating earthquakes (Cloud 1963; Hanson 1973). Earthquake engineers on reconnaissance visits suggested that the survival of many of these structures was attributable to the structures lifting off their bases and exhibiting a rocking motion. These postulated explanations were echoed by the survival of Greek and Roman free standing monuments and more recent Islamic minarets, from the many destructive earthquakes in the Eastern Mediterranean and Middle Eastern regions (Yim et al. 1980). Modern researchers suggested that the ancient Greeks may have deliberately designed their

---

<sup>1</sup> The term *isolation* in this thesis is to be interpreted in the context of seismic isolation. Seismic isolation is the practice of altering the dynamic characteristics of a structure to minimise the transmissibility of earthquake ground motion. This is typically achieved through the addition of special mechanical devices. A notable example of seismic isolation, is the implementation of lead-rubber bearing (LRB) isolators to buildings. LRB isolators introduces a laterally flexible layer beneath the superstructure, which leads to the creation of a much lower first-mode frequency. This ensures the deformation of the structure subjected to ground motion is predominantly contained in this flexible layer, and minimises the response of the superstructure by deflecting seismic energy in the higher frequency range. It should be noted that the effectiveness of base isolation is frequency dependent rather than what the literary definition of "isolation" would suggest. A comprehensive introduction into the topic can be found in a paper by Kelly (1986).

columns to rock in strong ground motions contributing to the survival of many ancient structures (Pampanin 2006; Psycharis et al. 2000).

It was not until the 1980s that New Zealand engineers constructed the first modern structures specifically designed to rock for seismic protection. The South Rangitikei Viaduct in Mangaweka (completed in 1981) and a reinforced concrete chimney at Christchurch International Airport are two of the few structures in the world to date, deliberately designed to rock (Beck and Skinner 1974; McConnel 1970; Sharpe and Skinner 1983). In both of these examples, hysteretic dampers were installed to provide additional damping to the rocking systems.

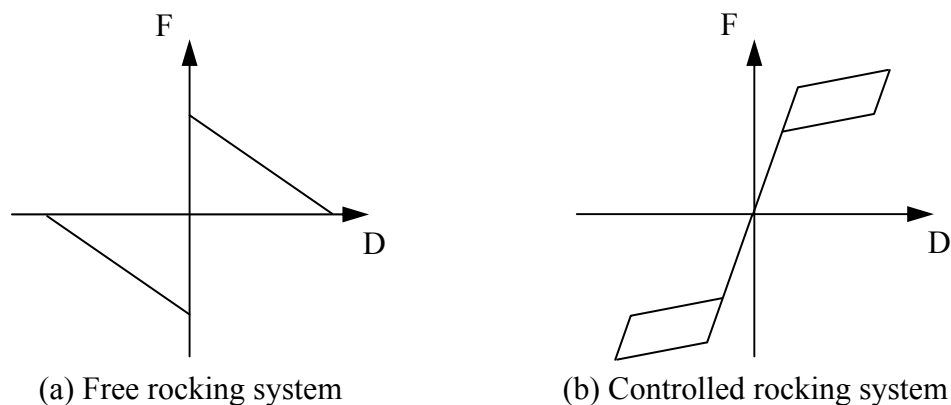
Since then, the adoption of rocking mechanisms for aseismic structural design has remained slow with only a handful of bridge type structures implementing rocking as a seismic retrofit solution. A prevalent sentiment amongst practitioners is that although the philosophy behind rocking as a seismic isolation solution is logical, it is prudent not to implement it for high seismic areas until the system performance has been tested by an actual major earthquake (Arze 1993).

A notable example of a recent implementation of rocking for seismic retrofit is the Lions Gate bridge retrofit program in Vancouver, Canada. (Klohn Crippen 2002). In this application, the bases of the bridge piers were detached from their supports, hysteretic devices were installed to control the rocking displacements and selective strengthening took place to withstand the additional axial load from the rocking motion. This use of rocking for retrofit has been gaining traction, as it is often more economical when compared to a conventional retrofit through strengthening alone.

Another popular adaptation of a rocking solution for seismic protection originated in 1991. A solution of a self centering rocking wall was developed within a ten year joint United States and Japan research programme, investigating solutions to improve the seismic performance of precast/prestressed concrete buildings (Englekirk 1990; Priestley 1991).



**Figure 1-2 – a) The South Rangitikei Viaduct, b) a close up of rocking hinge at the pier base**



**Figure 1-3 – Force-displacement characteristic of typical rocking systems**

In this programme, a jointed rocking wall was designed and constructed as part of a 60% scaled five-storey test building, commonly known as the Precast Seismic Structural Systems (PRESSSS) building. The PRESSSS building was tested pseudo-dynamically and the jointed rocking wall system was validated as a very successful lateral load resisting system. The testing yielded a residual drift of only 0.06%, following a peak drift of 1.8% under 1.5 times the design level earthquake (Priestley et al. 1999). These rocking walls, unlike typical shear walls, were designed to be weakly connected to their bases and they lifted off and rocked elastically about their wall corners under large lateral loads. Unbonded post-tensioned steel bars in vertical ducts within the wall provided restoring forces in addition to the gravity loads

and ensured the walls self-centred with minimum damage. U-shaped hysteretic energy dissipators were added to provide additional damping.

The above represents the two main engineering rocking systems for seismic protection that exist at the present time; namely, weakly restrained or free rocking structures; and *controlled rocking* structures (Palermo et al. 2005). A free rocking structure is characterised by its distinctive weakening force-displacement (F-D) behaviour, as presented in Figure 1-3a. Self-centering structures with additional hysteretic damping are characterised by a nonlinear force-displacement behaviour commonly known as a “flag-shaped” response as shown in Figure 1-3b.

## **1.2 RESEARCH OBJECTIVE AND MOTIVATION**

The main motivation for the current study is that whilst the benefit of a rocking system for aseismic structural design is evident, there has been a slow adoption to this technology. It is in the nature of structural engineers to be conservative, and it has not been helpful that the mechanics of rocking objects are complex and depart from conventional structural design theories. Studies have shown that traditional structural analysis methodologies cannot and should not be readily applied to rocking structures, and there is still a lack of reliable methods that are verified by dynamic testing, to assess the dynamic performance of rocking structures. A particularly controversial topic that remains is the treatment of the energy dissipation in a rocking system. In many of the current implementations, additional viscous damping devices are added as a failsafe measure as there are no accurate ways to represent the damping properties due to radiation damping when impacts occur. Energy losses due to the impacts are often assumed insignificant and subsequently ignored or approximated to viscous damping without any verification.

A principal objective of this research was to make a contribution to the current understanding of the behaviour of rocking objects subjected to base excitation. The research will systematically examine available experimental dynamic data on rocking systems, and provide example case studies on predicting the time-history response of these systems. For the purpose of this study, the prediction of time-history response is regarded as the quintessence of understanding the system behaviour.

### 1.3 THESIS OUTLINE / ORGANISATION

A comprehensive review of the published literature on the development of rocking science is presented in Chapter 2. This covers the development of the fundamental theory on the mechanics of a single rigid rocking block to the more advanced analyses addressing a rocking system as a nonlinear dynamic system. An overview of the current modelling procedures and design recommendations for the implementation of aseismic rocking systems is also presented.

Chapter 3 presents an investigation into the rocking behaviour of a freestanding slender rigid block. The study collated the time-history results from over 430 free vibration tests on a concrete block cast on a steel mechanism. The concrete block was released from a range of initial rotations and the results are compared against current prevalent analytical models.

Chapter 4 presents a thorough investigation of the dynamics of controlled rocking systems. The investigation utilised experimental data from a series of shake table tests on unbonded post-tensioned concrete masonry walls, conducted at North Carolina State University, U.S.A. (Wight et al. 2004). A new approach with a single unifying assumption is proposed to predict the time-history response of controlled rocking walls. Moreover, interesting behavioural traits resulted from the sensitivity of controlled rocking systems are also highlighted.

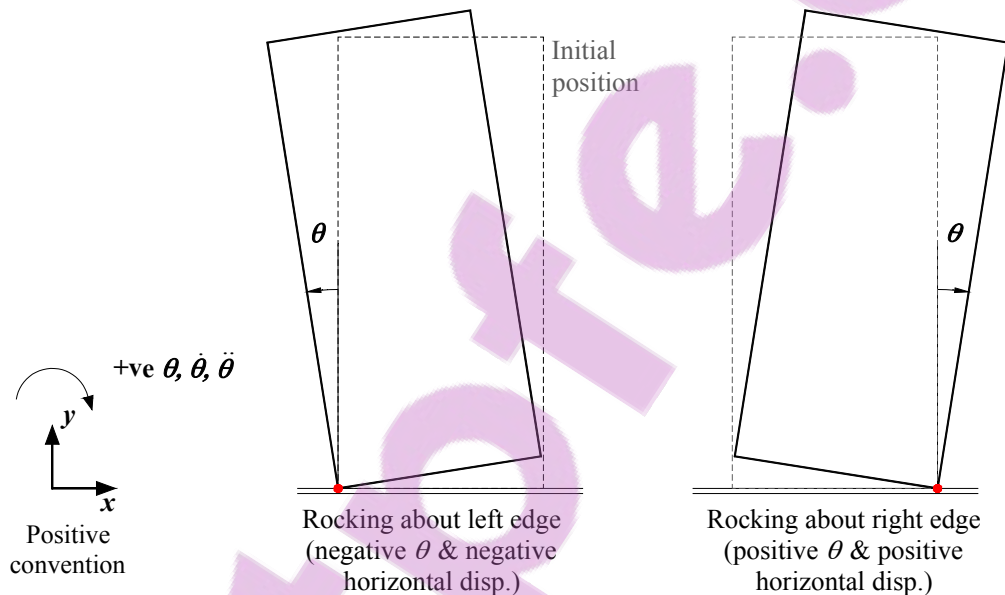
Chapter 5 describes the development of mathematical models for three simple, idealised structural systems permitted to rock when subjected to base excitations. These models were developed from first principles and contained as few assumptions as practical. The models were later validated by predicting the time-history response of published shake table tests conducted at the University of Canterbury, Christchurch (McManus 1980). A highlight of this section is a mathematical model for a flexible structure rocking on rigid ground. This enabled quantitative assessment of the benefits of implementing a rocking isolation solution.

Finally, chapter 6 summarises the main conclusions from the thesis and provides recommendations for future research.

## 1.4 REFERENCE FRAMES AND CO-ORDINATE SYSTEMS

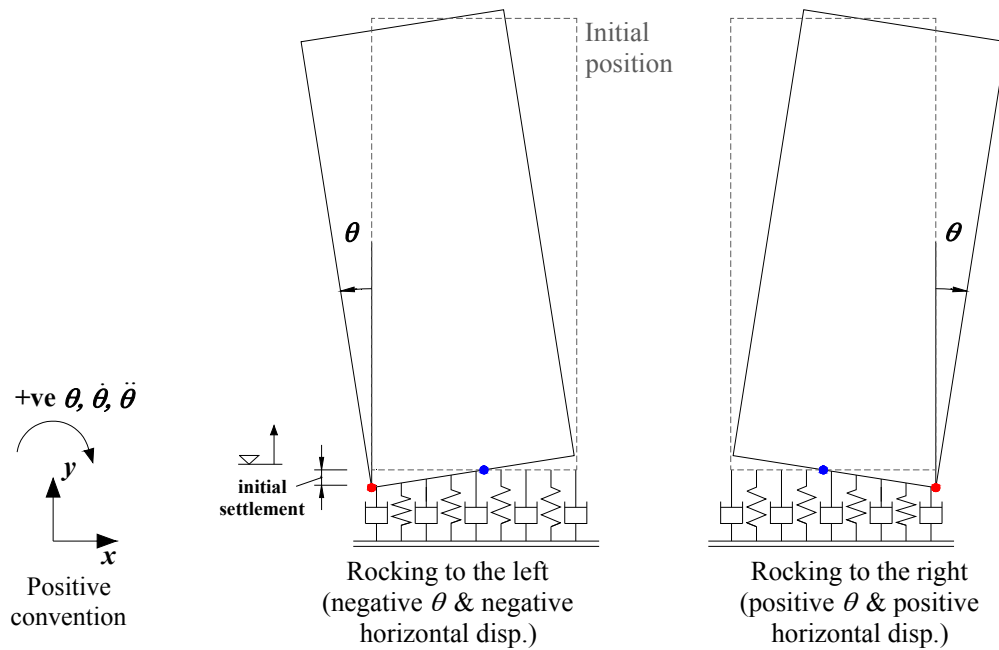
A number of reference frames and co-ordinate systems are adopted in the development of the different rocking models in this thesis. The definitions of the variables in each of the models are described in the notations section. They are also typically shown in a diagram that precedes the development of each model.

The majority of the models considered in this thesis assumed rigid bodies. This permitted the systems to be adequately represented by a single degree of freedom, typically the rotation about the rocking pivot. As rocking systems switch from rocking about one pivot to another, so too does the reference frame used for angular measurements. This is illustrated in Figure 1-4 below for a rigid block model.



**Figure 1-4 – Reference frame for models with rigid block on rigid ground**

This relative reference frame system is also extended for models where the rigid rocking block is situated over springs. In these cases, rotations are measured about the extreme rocking edges of the rigid body rather than the physical rocking centre. The physical rocking centre is the point on the block-ground interface at which lift off begins. The reference frame for these models is illustrated in Figure 1-5, and the blue dot in this figure denotes the physical rocking centre.



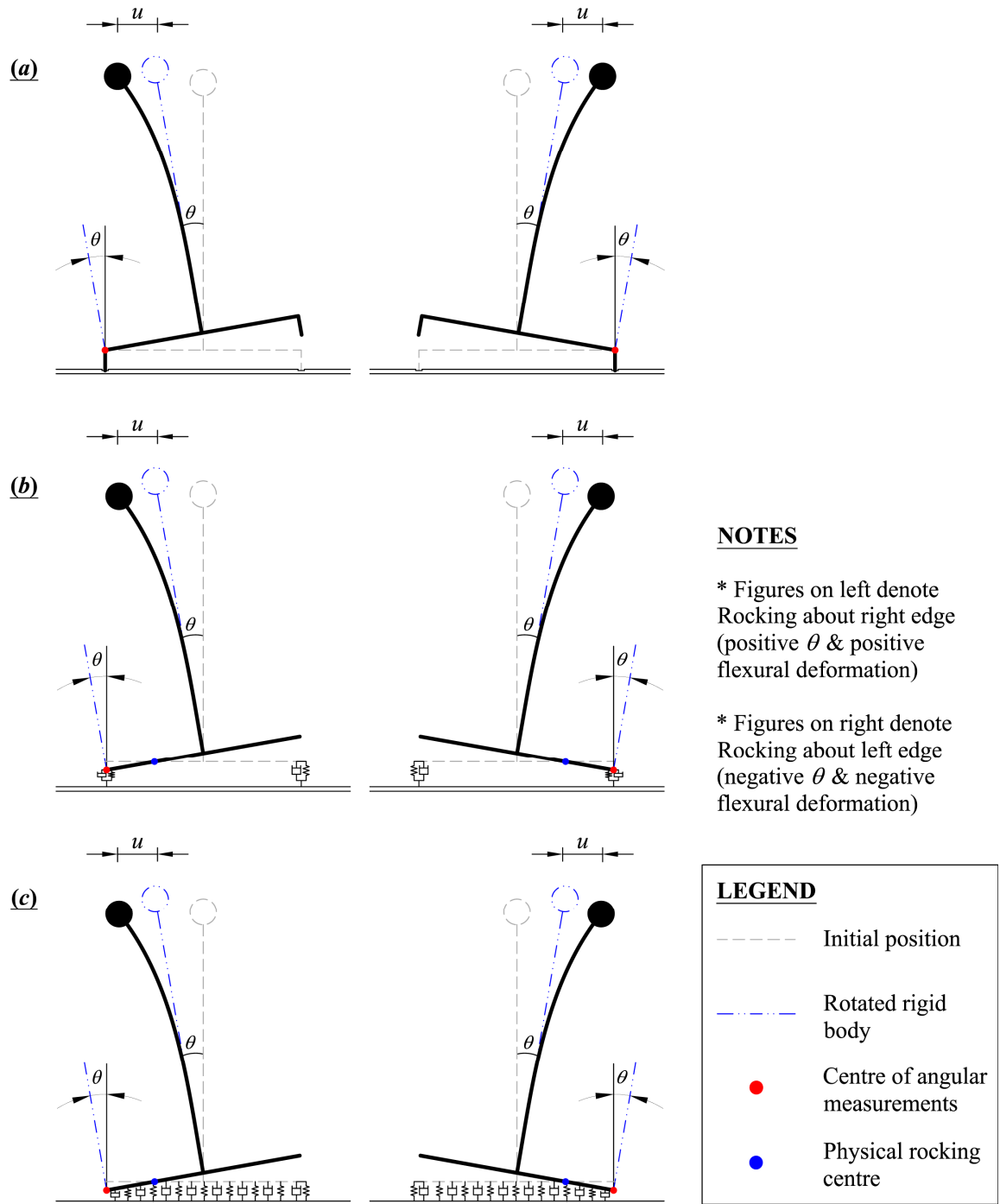
**Figure 1-5 – Reference frame for models with rigid block on bed of springs**

The aforementioned relative reference frames are also applied to models representing simple structural systems. Angular rotations are measured about the rocking edge for these models. The elastic flexural deformations are assumed to be small when compared to the overall rocking displacement, and are therefore recorded relative to a rotated rigid body independently. All the models in this thesis, except for that presented in Section 5.3.3, have assumed the rocking rotation is small and the structures are slender. This further permits the flexural deformations to be approximated as horizontal (Chopra and Yim 1985).

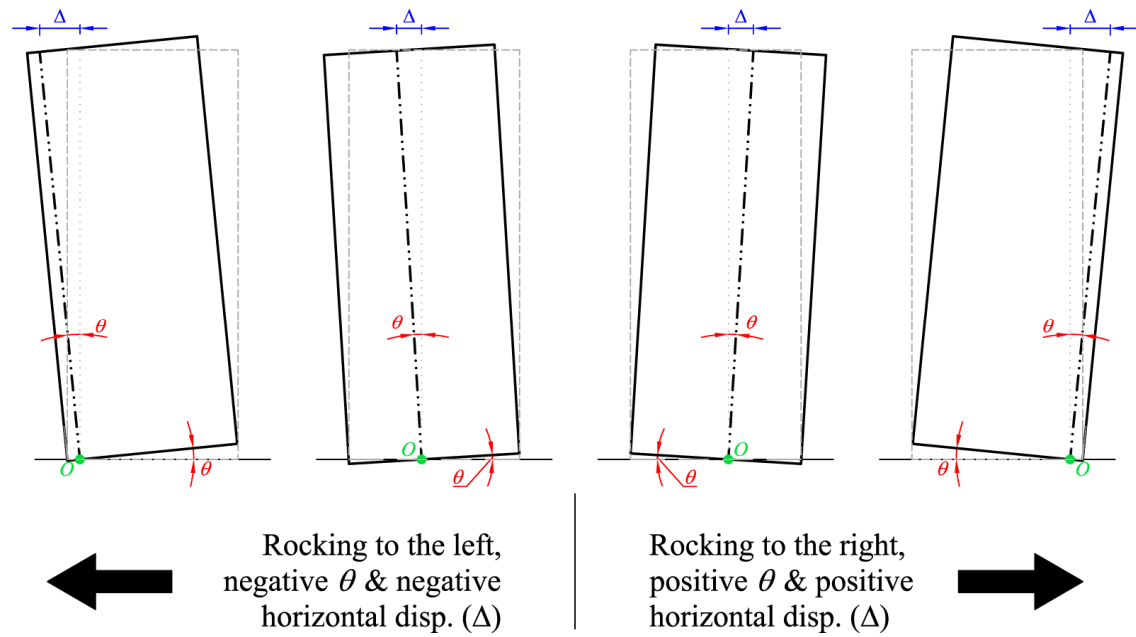
Illustrations of this reference frame applied to simple structures rocking on rigid ground, two-spring foundations and beds of springs are presented in Figure 1-6. More detailed descriptions of each of these models are given in later chapters.

The rocking model in Section 5.3.3 differs from the other models in this thesis, as it makes no assumption on the slenderness of the system or the relative magnitudes of rocking and flexural deflections. This rocking model approximates the flexural deformations as occurring perpendicular to a rocking rigid body at any given time. This leads to a more complex, geometrically nonlinear representation of the problem, but is applicable to all system configurations and is more consistent with reality. Rotations are measured about the rocking edge and flexural deformations are taken as the perpendicular distance between the deflected specimen from a rotated rigid body

about the rocking edge. An illustration of this is presented in Figure 5-37.



**Figure 1-6 – Reference frame for simple structural models rocking on a) rigid ground, b) Two-spring foundation and c) Tensionless-Winkler spring foundation**



**Figure 1-7 – Reference frame for the controlled rocking wall models**

Finally for the controlled rocking system analysed in Chapter 4, angular rotations are measured about the physical rotation centre. The physical rotation centre migrates smoothly from one extreme edge to another as the wall is displaced. Lateral displacement, often referred to as Top of Wall (ToW) displacement, is the horizontal displacement between the rotated wall and the initially upright wall. This is measured for a point, at the top of the wall and vertically above the instantaneous centre of rotation when the wall is upright. This arrangement is illustrated in Figure 1-7.



# Chapter 2

---

## LITERATURE REVIEW

---

An extensive literature review is presented herein with the aim of detailing the key developments in the understanding of the mechanics of rocking objects. The review focuses first on the development of the science, much of which originated from the study of a rigid rocking block, then moves to the study of flexible structural systems permitted to rock and the behaviour of controlled rocking systems.

### 2.1 THE DEVELOPMENT OF ROCKING SCIENCE

The modern scientific endeavours in the mechanics of rocking began in Japan in the late 1800s. John Milne published one of the earliest papers in 1881 attempting to quantitatively correlate the intensity of ground motion by studying the overturning of rectangular columns. He studied the overturning of traditional Japanese gravestones which were 1.5 m in height and about 0.6 m square (Milne 1881). Prior to this, earthquake magnitudes were estimated through individual felt intensity. Milne and his colleague C. D. West proposed that if the peak ground acceleration was greater than a value prescribed by Equation 2-1 below, then the column *may* overturn:

$$\ddot{u}_{g,peak} > g \frac{B}{H} \quad (2-1)$$

where  $\ddot{u}_{g,peak}$  is the peak horizontal component of acceleration,  $B$  and  $H$  are the width and height of the block respectively (Milne 1908). This model was derived by

considering static equilibrium of a rectangular block and equating the overturning moment from the gravitational restoring force about the block's corner. An implied result of this model is that the more slender an object is, the higher the likelihood that it will overturn. It should be noted that Milne concluded in his book that this approach was only at best approximate. In lieu of accurate seismographs, the overturning of rectangular blocks became widely used for measuring earthquake intensities in the first half of the 1900s.

The next major development came in the forms of papers by Ikegami and Kishinouye in 1946, 1947 and 1950 (Ikegami and Kishinouye 1946; 1947; 1950), which highlighted some of the shortcomings of Milne's simplistic rocking model. In their papers, Ikegami et al. investigated the phenomenon in which slender gravestones with low width to height ratio, seemingly likely to overturn in earthquakes, did not, while squat gravestones with high width to height ratio, deemed stable by Equation 2-1, overturned. This was later shown to be attributable to the dynamic interactions of the rocking motion and the ground motion, an important feature not considered in Milne's study. By considering only a static force, Milne's model at best correlated the magnitude of the peak acceleration required for initiating a rocking motion but not necessarily the acceleration which lead to a block overturning. Ikegami and Kishinouye concluded that the overturning and rocking response of rectangular columns in reality depended on the absolute magnitude of their height and width in addition to their ratios.

## **2.2 HOUSNER'S SIMPLE ROCKING MODEL**

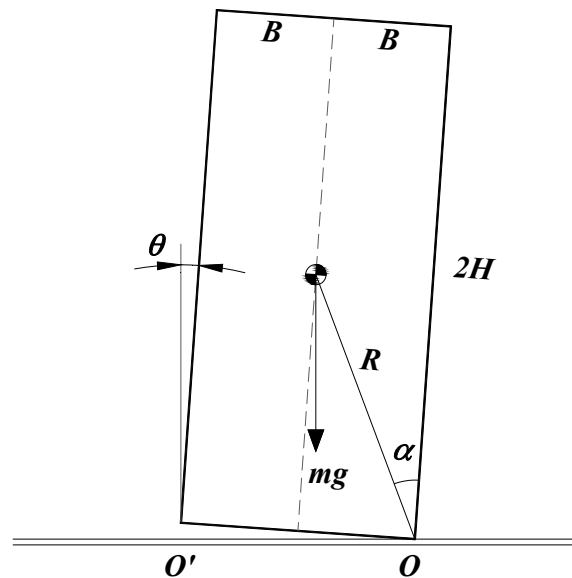
Whilst the previous section detailed some of the early developments in the field of rocking science, the modern study of the mechanics of rocking objects are typically attributed to Housner's seminal paper in 1963 (Housner 1963). In his paper, Housner investigated the same phenomenon of seemingly unstable structures, in this instance elevated water towers, surviving the devastating 1960 Chilean Earthquake essentially unscathed, while other more stable appearing structures were overturned and severely damaged. Housner first developed a piecewise differential equation of motion (Equation 2-2) by applying Newton's second law in the rotational direction for a rigid rocking block as shown in Figure 2-1.

$$I_o \ddot{\theta} = \begin{cases} -mgR \sin(\alpha - \theta) & \text{for } \theta > 0, \\ mgR \sin(\alpha + \theta) & \text{for } \theta < 0. \end{cases} \quad (2-2)$$

For tall, slender blocks with  $\alpha$  less than  $20^\circ$ , Equation 2-2 can be approximated as:

$$\text{for } \theta > 0 \quad I_o \ddot{\theta} - mgR\theta = -mgR\alpha \quad (2-3)$$

Housner then assumed that when a rocking block is set in motion, it rotates smoothly from one corner to the opposite corner as it rotates through its initial upright position. This led to two important assumptions in the Housner's simple rocking model, 1) angular momentum about the point of impending impact is assumed to be conserved, and 2) impacts are therefore inelastic point impacts. In other words, bouncing and sliding do not occur.



**Figure 2-1 – The Housner Rocking Block**

By solving the second order governing differential equation, Equation 2-3, for an initial rotation until the moment of impact, Housner developed a closed-form expression for the period of vibration for a quarter of a rocking cycle as a function of the peak rotation. Moreover, exploiting the conservation of angular momentum assumption, an expression for the apparent coefficient of restitution<sup>2</sup> (c.o.r.)  $r$  was developed. The  $r$  value in this context represents the ratio of kinetic energy

<sup>2</sup> The wording “apparent” is important and deliberate, as the term c.o.r. as used by Housner is defined for the system in a macro manner and not on a micro scale as in the “true” impact mechanics definition. The true c.o.r. for a Housner rocking block is zero, as the impacts are assumed to be plastic. In other words, the block rocks from corner to corner without bouncing.

immediately after and immediately before an impact and is widely used in rocking literature as a measure of the energy lost due to the impacts. The apparent c.o.r. is defined by Equation 2-4, as the square of the exiting angular speed divided by the entry angular speed of a rocking impact.

$$r = \left( \frac{\dot{\theta}_2}{\dot{\theta}_1} \right)^2 \quad (2-4)$$

Housner's expression for the rocking period and the apparent c.o.r. are presented as Equations 2-5 and 2-6 below respectively. Interestingly, Equation 2-5 together with an experimental verification were in fact presented three years prior, at the Second World Conference on Earthquake Engineering in Japan by Kiyoshi Muto (Muto et al. 1960).

$$T = \frac{4}{p} \cosh^{-1} \left( \frac{1}{1 - \theta_0 / \alpha} \right) \quad (2-5)$$

$$r = \left[ 1 - \frac{mR^2}{I_o} (1 - \cos 2\alpha) \right]^2 \quad (2-6)$$

Where

$$p = \sqrt{\frac{mgR}{I_o}}$$

Nevertheless, uniquely to Housner's paper, the overturning potential for a free standing rigid block subjected to a constant acceleration pulse, a simple half sine pulse and earthquake-like accelerations were theoretically evaluated based on energy principles. This led to the discovery that the vulnerability of a slender freestanding block to overturn is inversely proportional to the square root of its size. In other words, of two blocks of the same aspect ratios, the larger block will be more stable against overturning. Through this systematic and scientific approach, Housner concluded that the vibration characteristics of this type of structure are markedly different to those of linear elastic structures.

The conclusions of Housner's paper were the starting point for many subsequent investigations. His paper elegantly brought to light for the scientific and engineering community that rocking behaviour, a seemingly intuitive behaviour, is in fact a very complex nonlinear process, even when it is greatly simplified by idealistic assumptions and if the rocking object was only a simple rigid free standing block.

Over the years, several independent studies have validated the Housner rocking model through series of experiments. A frequently quoted study is the work by Aslam et. al, in which the displacement histories of a concrete block released from an initial tilt or alternatively subjected to harmonic ground motion via a shake table, were recorded (Aslam and Godden 1980). The block used in Aslam's experiment was 76.2 cm tall with a height to width ratio of 5. The block had an embedded concave aluminium base and rocked on a 25mm thick steel plate in an attempt to ensure reproduction of Housner's point impact boundary condition.

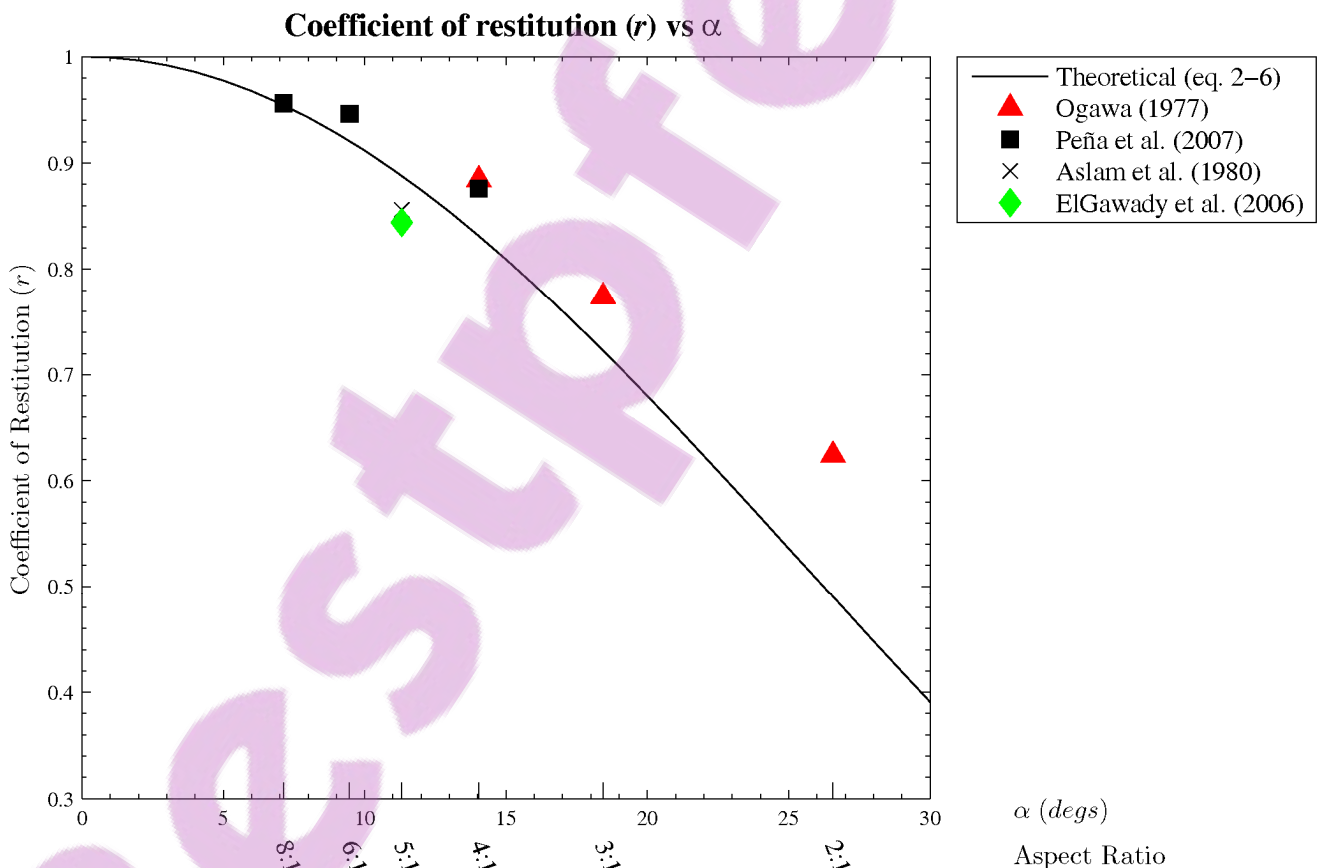
Aslam's experimental study in general confirmed the use of Housner's simple rocking model (SRM). By conducting a parametric study, Aslam also revealed that the SRM is extremely sensitive to small variations of boundary conditions. A minute change of the  $r$  value used in the SRM simulation produced large inconsistencies in predictions. Aslam's study also found that an  $r$  value different to that predicted by Equation 2-6 was generally required in the numerical simulation to match the experimentally measured response. Whilst this practice of establishing an  $r$  value retrospectively for the numerical simulations lacks a theoretical basis, it has been routinely adopted by other similar experimental studies (McManus 1980; Ogawa 1977; Priestley et al. 1978; Spanos and Koh 1984).

A survey of experimental studies on the restitution of rocking blocks as presented in Table 2-1 showed that, experimental  $r$  values in general exceed those predicted by Equation 2-6. It is also evident that the inconsistencies diminish as the slenderness of the block is increased.

**Table 2-1 – Comparison of experimental and theoretical apparent c.o.r. values**

Block Dimension			Apparent C.O.R. ( $r$ )	
H x B	H/B ratio	Material at the contact interface (model/sub-base)	Experimental	Theoretical (eq. 2-6)
200 x 100 mm <sup>a</sup>	2	Wood & steel	0.624	0.49
300 x 100 mm <sup>a</sup>	3	Wood & steel	0.774	0.723
400 x 100 mm <sup>a</sup>	4	Wood & steel	0.884	0.831
1000 x 250 mm <sup>b</sup>	4	Granite & granite	0.876	0.831
762 x 152 mm <sup>c</sup>	5	Aluminium & steel	0.856	0.888
950 x 190 mm <sup>d</sup>	5	Steel & concrete	0.844	0.888
1000 x 167mm <sup>b</sup>	6	Granite & granite	0.946	0.921
1000 x 125mm <sup>b</sup>	8	Granite & granite	0.956	0.954

<sup>a</sup>Ogawa (1977), <sup>b</sup>Peña et al. (2007), <sup>c</sup>Aslam et al. (1980), <sup>d</sup>ElGawady et al. (2006)



**Figure 2-2 – Theoretical prediction of coefficient of restitution of blocks of different aspect ratio compared with experimentally established values**

Ignoring the contributions from the varying materials on the contact interfaces, the phenomenon of decreasing error as slenderness increases can be rationalised by considering the  $r$  values as a measure of energy dissipation during an impact. Considering a series of blocks of different aspect ratios, conventional wisdom suggests the squatter a specimen, the higher the likelihood that it will bounce rather than rocking smoothly on impact when it is released from an initial lean. Interpreting this using the principles of conservation of energy, if a squat specimen bounces, much of the energy is returned to the specimen as kinetic energy instead of transferring to the sub-base material where it has a greater possibility of dissipation. This leads to less energy dissipation than Housner's inelastic impact assumption, a higher retention of kinetic energy in the rocking system, corresponding to a higher  $r$  value than Housner's prediction. Conversely, if the experimentally established  $r$  value is lower than that predicted by Equation 2-6, it represents a greater probability that an inelastic impact has occurred.

It is noteworthy that the previous rationalisation should not obscure the reality that if inelastic point impacts do not occur, the theoretical basis of using Housner's classical SRM or using an  $r$  value to simulate energy dissipation is fundamentally flawed. Important effects such as bouncing, sliding, free flight and elastic vibration may be masked.

### **2.3 OTHER ROCKING BLOCK MODELS**

Researchers have since proposed more complex mathematical models to allow for deviations from the inelastic impact assumption. Ishiyama presented a mathematical model assuming the possibility of planar impacts and separated the rocking response behaviour into six modes, namely, rest, slide, rotation, slide rotation, translation jump and rotation jump (Ishiyama 1982). Similarly, Shenton et al. presented a mathematical model assuming point impacts resulting in five modes of behaviour, namely, rest, slide, rock, slide-rock and free flight (Shenton and Jones 1991). Whilst these models are very interesting and challenging mathematical problems with very intriguing characteristics, because of the complexity and sensitivity to initial conditions of the system, they have not yet been verified experimentally to reflect actual rocking behaviour.

As hinted at in the previous discussions, the complexity involved in the dynamic evolution of the rocking problem is strongly affected by the impact assumptions adopted. The overarching problem statement associated with the impacts model of a rocking body is the prediction of initial conditions of the post-impact motion. Specifically, consider a rigid block under general rocking motion at the instant it impacts the ground as in Figure 2-3 overpage. The block has an instantaneous angular speed  $\dot{\theta}^+$  and a tangential velocity of  $\tilde{v}_G^+$  at the centre of gravity about some arbitrary centre of rotation  $C^+$ . The role of the impact model is to provide an estimation of the new instantaneous angular speed  $\dot{\theta}^-$ , tangential velocity  $\tilde{v}_G^-$  and the location of the new centre of rotation  $C^-$  after the impact.

The impact model simplifies the linkages between a relatively long duration event, the rocking motion, with the approximately infinitesimal duration action of the impact force. Typically, a closed form solution for the impact problem of a rocking rigid body cannot be achieved due to the uncertainties with the location of the new rotation centre and the area of the impending contact. Researchers have typically made assumptions on one or both of the above and consequently prescribed modes of behaviour. For instance, Housner's plastic impact assumption imposed the post-impact motion to be purely rotational about the point of application of the impulsive force which had an infinitesimal area.

Some researchers circumvented the impact problem altogether by enforcing continuity throughout the transition by the insertion of a compression only visco-elastic layer between the rigid block and the ground as in Figure 2-4 (Koh et al. 1986). Researchers rationalised this form of solution on the basis that real rocking structures rest on soils and foundations which have a finite stiffness. However, research in the field of soil-structure interaction showed that this simplified approach was critically flawed, as rocking and vertical vibrations are strongly coupled such that the spring stiffness value of the elastic layer can never model the dynamic behaviour of both effects precisely (Psycharis 2008). Nevertheless, this approach provided researchers with a valuable qualitative tool for the study of rocking objects.



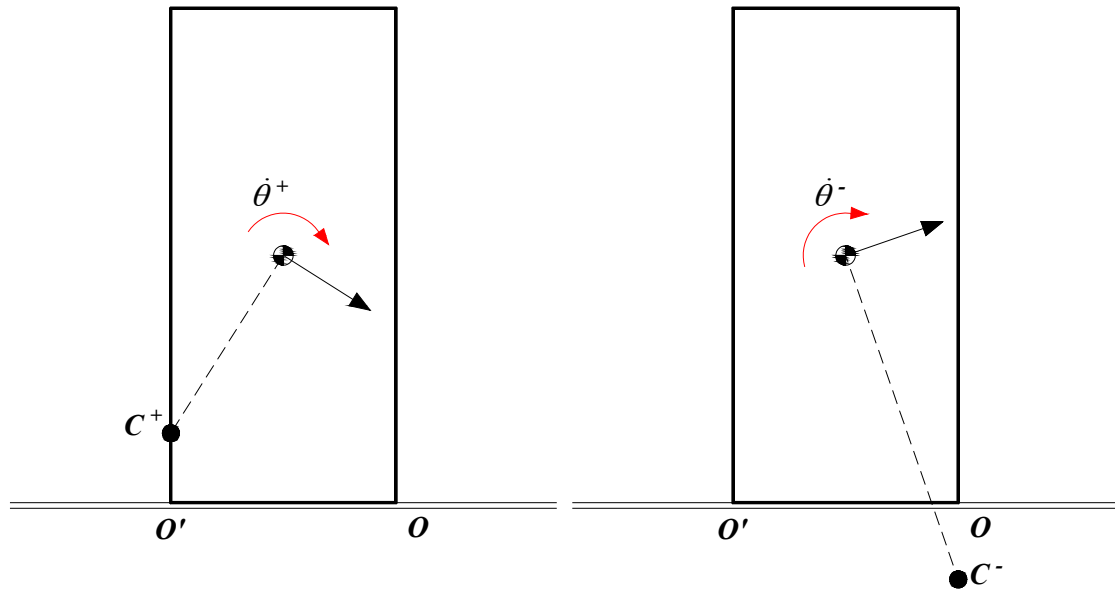


Figure 2-3 – Key parameters for an impacting rigid body

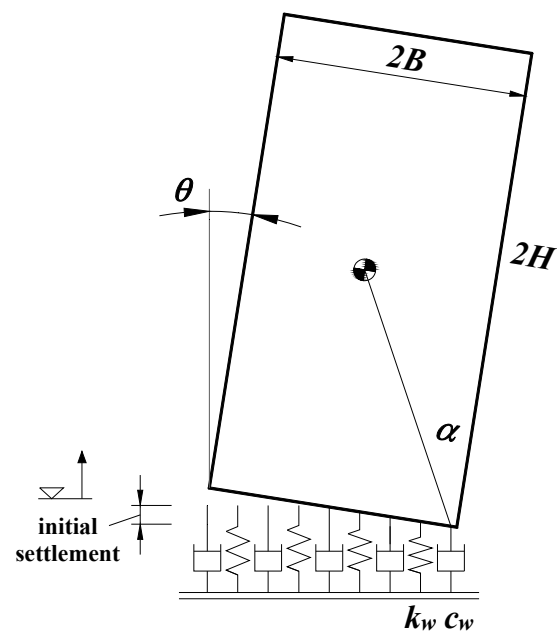


Figure 2-4 – Rocking block on tensionless, visco-elastic Winkler foundation

## 2.4 ROCKING STRUCTURAL SYSTEMS

In parallel with the aforementioned development of the models of rocking rigid blocks, researchers have also applied the same techniques to investigate the dynamic behaviour of flexible, structural systems with foundation uplift. The studies can be divided into three categories based on the assumptions of the properties of the rocking interface, namely

- A. Studies that assume the rocking interface is rigid, resulting in Housner's plastic impacts and fixed rocking pivots assumptions. (Ichinose 1986; Meek 1975; Psycharis 1991)
- B. Studies that assume the rocking interface is flexible but the locations of rocking pivots are fixed. (Huckelbridge and Clough 1978; McManus 1980; Psycharis 1991; Sharpe and Skinner 1983; Xu and Spyarakos 1996; Yim and Chopra 1984a; Yim and Chopra 1985)
- C. Studies that assume the rocking interface is a viscoelastic half-space, effectively assuming spatially varying rocking pivots, a continuous support force and the possibility of planar impacts. (Anderson 2003; Yim and Chopra 1984b)

The three approaches are illustrated diagrammatically in Figure 2-5.

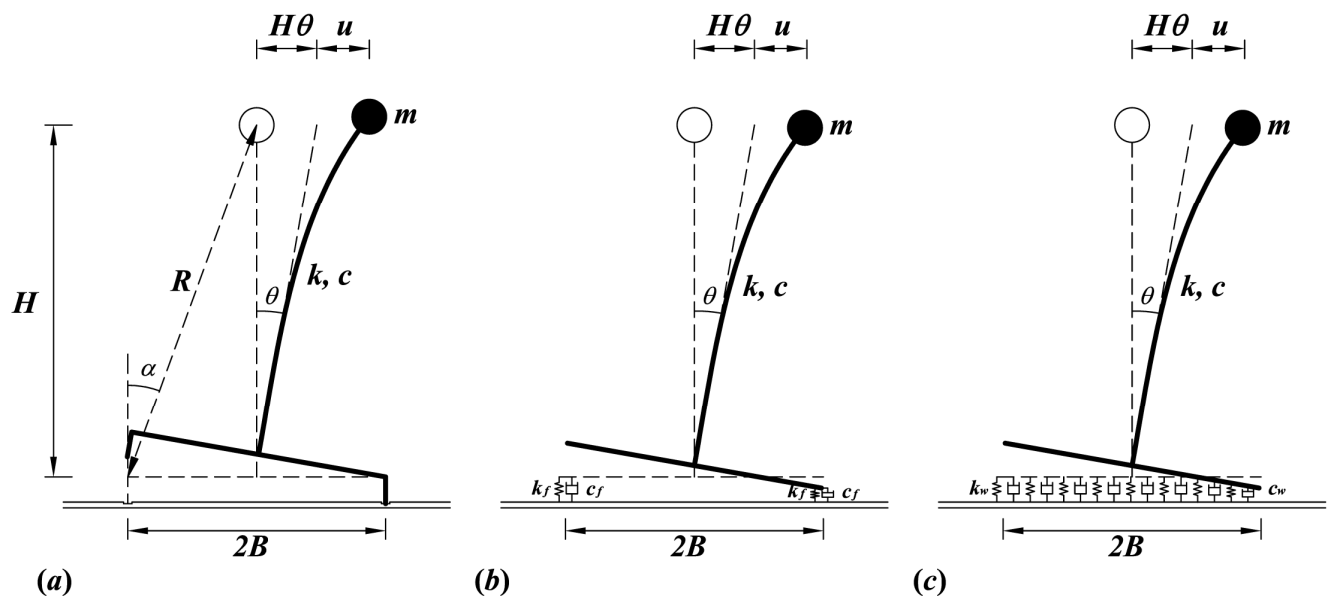


Figure 2-5 – Three categories of rocking interface assumption

### 2.4.1 RIGID INTERFACE SOLUTIONS

In the rigid rocking interface studies, solutions are typically based on the derivation of governing differential equations from first principles. Studies are often based on the response of an idealised single degree of freedom system as in Figure 2-5a. In the various published literature, as researchers have each made slightly different approximations, a number of expressions exist for the equation of motion for the rocking system. Assuming only horizontal ground excitation, small rotations and small elastic deformations compared to rotational displacements, these result in a decoupling of rotation and flexure displacements and leads to one of the simpler expressions presented as Equation 2-7 (Chopra and Yim 1985).

$$\ddot{u} + 2\zeta_r\lambda_r\dot{u} + \lambda_r^2u = -\left[\ddot{u}_g(t) \mp g\frac{H}{B}\right] \quad (2-7)$$

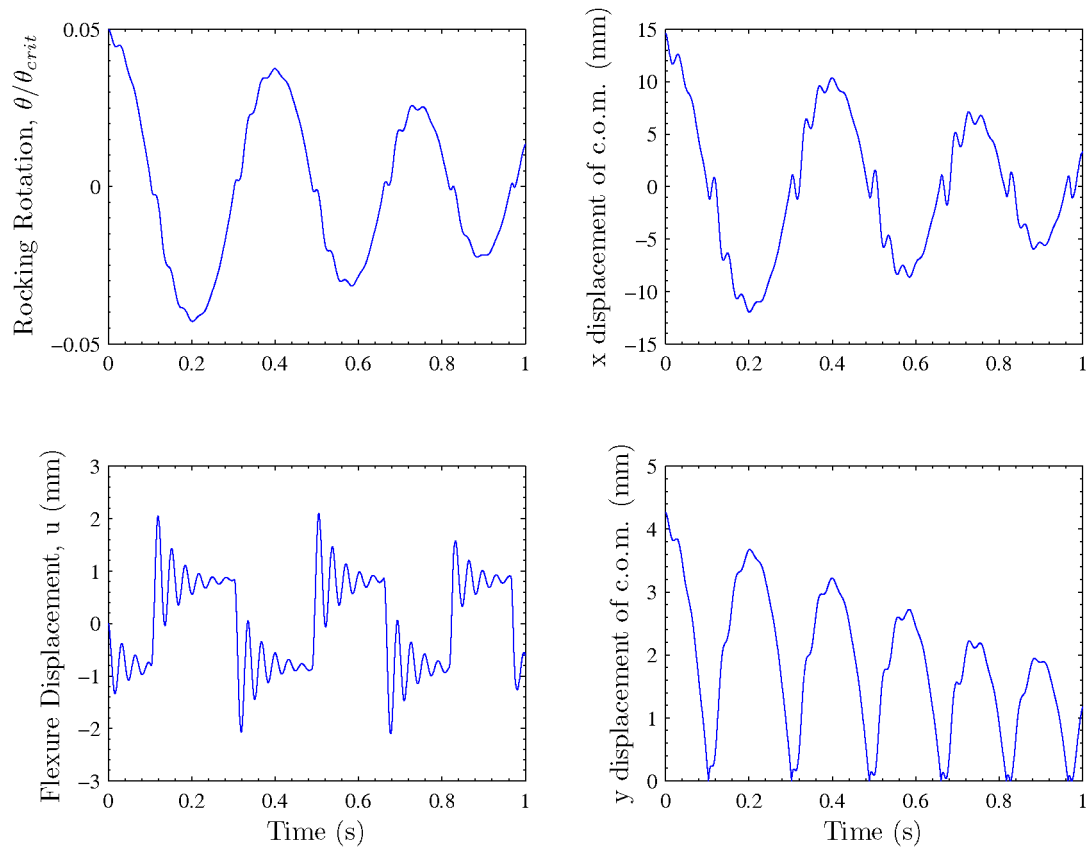
in which

$$\lambda_r = \omega\left(\frac{R}{B}\right) \quad (2-8a)$$

$$\zeta_r = \xi\left(\frac{R}{B}\right) \quad (2-8b)$$

and where Equations 2-8a and 2-8b denote the natural frequency and damping ratio of the uplifted system. Numerical simulations based on this approach showed that for such uplifting structures, the elastic deformation under a free rocking decay is a high frequency motion, superimposed on a longer period motion associated with the alternating rocking edge. The long period motion tends to alternate between the  $\pm u_c$ , the structural deformation which just initiates uplift or otherwise known as the critical static deformation.

A typical free vibration response time-history illustrating this is shown in Figure 2-6.



**Figure 2-6 – Free vibration time-history of a SDOF rocking system ( $H/B = 1/0.3$   
 $m$ ,  $\omega = 56.10 \text{ rads}^{-1}$ ,  $f = 8.9 \text{ Hz}$ ,  $\xi = 0.03$ ,  $\frac{\theta_0}{\theta_{crit}} = 0.05$ )**

Examining Equations 2-8a and 2-8b closely, it can be observed that the larger the rocking system, i.e. the higher the R/B ratio or implicitly the more slender the rocking system, the higher the post-rock frequency ( $\lambda_r$ ) and more importantly the greater the effect of damping for this oscillation ( $\zeta_r$ ). Consequently, for a large or slender uplifting system, the flexural motion typically simply alternates between the positive and negative flexure deformation which causes uplift, also defined as the critical static deformation ( $u_c$ ). Illustrating this numerically, for a system with a height over width ratio ( $H/B$ ) of 10 and a viscous damping ratio ( $\xi$ ) of 0.05, Equation 2-8b yields an effective damping ratio close to 0.5 for the post-rock oscillation, which renders the motion in the main rotational. The main practical implication of this is that the forces that a rocking structure experience are implicitly limited to those required for uplifting, or at  $u_c$ . Interestingly, although never identified and reported, this phenomenon was verified physically by a series of experiment of an uplifting flexible structure by McManus in 1980. Figure 2-7 shows a free rocking decay record from

McManus's report, where the trace representing the horizontal acceleration, i.e. proportional to flexural displacement, clearly illustrates this phenomenon.

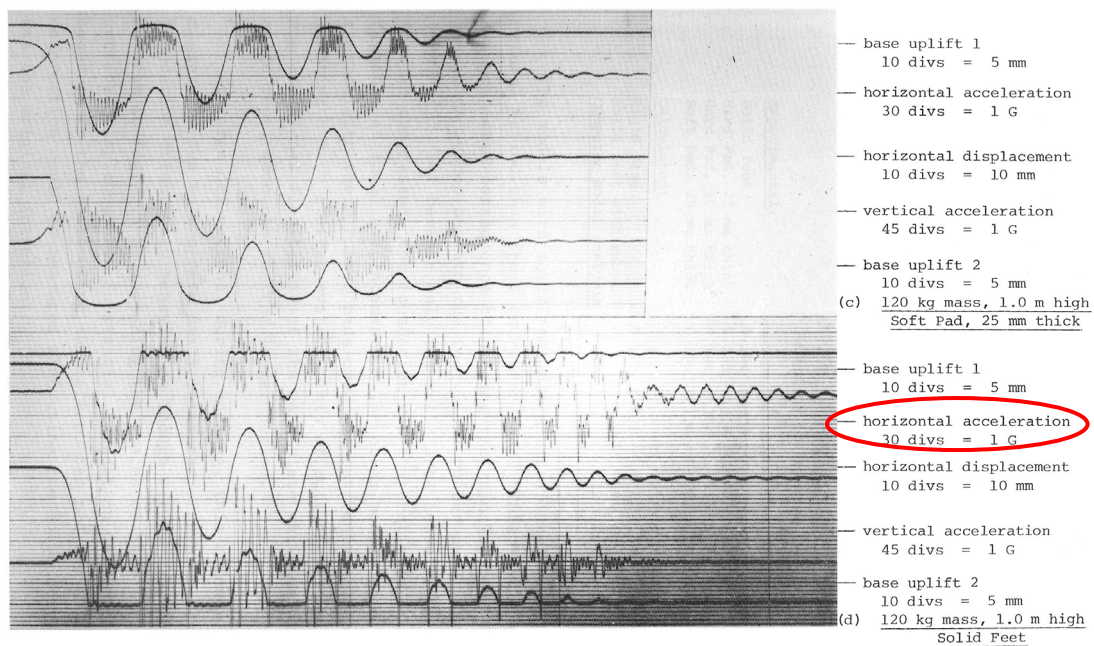


FIG. 3.1 Free Rocking Decay Records (continued)

**Figure 2-7 – Free rocking decay history of a SDOF rocking system ( $H/B = 1000/300$  mm) (Source: McManus 1980)**

#### 2.4.2 TWO-SPRING FOUNDATION SOLUTIONS

Following on from the category A studies, the rigid rocking interface constraints are incrementally relaxed in the category B investigations. In these studies, researchers permit a flexible rocking interface but have prescribed fixed locations for the rocking pivots as before. These assumptions lead researchers to the important use of “two-spring” foundations as shown in Figure 2-5b. Typically in these simulation models, sets of compression-only spring-damper elements are placed beneath the assumed fixed rocking pivots, where the springs represent the foundation compliance and dampers mimic the energy dissipation due to the impacts and conventional radiation damping.

One of the most important parameters in these studies is the selection of the spring stiffness,  $k_f$ . Strategies for selecting  $k_f$  values vary but typically involve the adoption of recognised soil stiffness formulae derived on the basis of a continuous elastic half-space, accompanied by a modification of the locations of the spring-damper elements. Additionally, researchers have also selected  $k_f$  values empirically

based on a backward substitution in numerical time-history analyses to match experimental data.

For information, the “two-spring” stiffness and damping coefficients for a corresponding circular and rectangular rigid foundation mat are presented in Table 2-2. These values were derived based on selecting stiffness and damping values to match the vertical and rotational equations of motion, developed in an elastic half space solution at the onset of rocking. (Yim and Chopra 1983a).

The advent of this simplified analysis technique permitted researchers to analyse significantly more complex rocking structural system than previously. Using the “two-spring” foundation, Xu and Spyrakos in their 1995 paper analysed the response of a rocking cylindrical tower including the effects of distributed mass. Yim and Psycharis independently analysed the responses of a rocking multi-storey shear building, and Huckelbridge in his 1978 study used multiple “two-spring” foundations to simulate the phenomenon of column uplift in a multi-bay moment resisting frame, the results were then verified against shake table data. It should be emphasized that the spring stiffness values in the Huckelbridge study were empirically chosen after the experiment to match the final result. Actual blind prediction of response using this approach, to the author’s knowledge, has not been achieved.

Despite the approximate nature of the “two-spring” foundations, three important findings that have emerged are that,

- 1) The response of the rocking system is nonlinear and the lengthening of fundamental period ( $T_1$ ) of the rocking system is a function of the uplift.
- 2) The increase in the fundamental period of the system has the effect of increasing the importance of higher vibration modes just as with a fixed base structure. This is simply due to the fact that the mode shapes and ratio of natural vibration modes do not change, and an increase in  $T_1$  increases the relative spectral ordinates of the higher modes.
- 3) While  $T_1$  is strongly affected by the foundation uplift, the second and higher modes are typically not affected at all by the interaction with the soil or the uplift.

**Table 2-2 – Spring-damper element parameters for a rocking circular and rectangular rigid foundation**

	<b>Circular</b> (Radius = $R_f$ )	<b>Rectangular</b> ( $B_f, L_f$ = Width and length of the foundation)
Elastic half-space vertical stiffness coefficient ( $K_z$ )	$\frac{4G_s R_f}{1 - \nu_s}$ (Timoshenko and Goodier 1951)	$\frac{G_s}{1 - \nu_s} \beta_z \sqrt{B_f L_f}$ (Barkan 1962)
Elastic half-space vertical damping coefficient ( $C_z$ ) (Richart et al. 1970)	$0.85 K_z R_f \sqrt{\frac{\rho_s}{G_s}}$	$\frac{13.6 B_f L_f}{\pi(1 - \nu_s)} \sqrt{\rho_s G_s}$
Two-spring stiffness coefficient ( $k_f$ )	$\frac{1}{2} K_z$	$K_z B_f$
Two-spring damping coefficient ( $c_f$ )	$\frac{1}{2} C_z$	$C_z B_f$
Location of spring-dampers from foundation centreline	$\sqrt{\frac{2}{3}} R_f$	$\frac{1}{\sqrt{3}} B_f$

### 2.4.3 TENSIONLESS WINKLER FOUNDATION SOLUTION

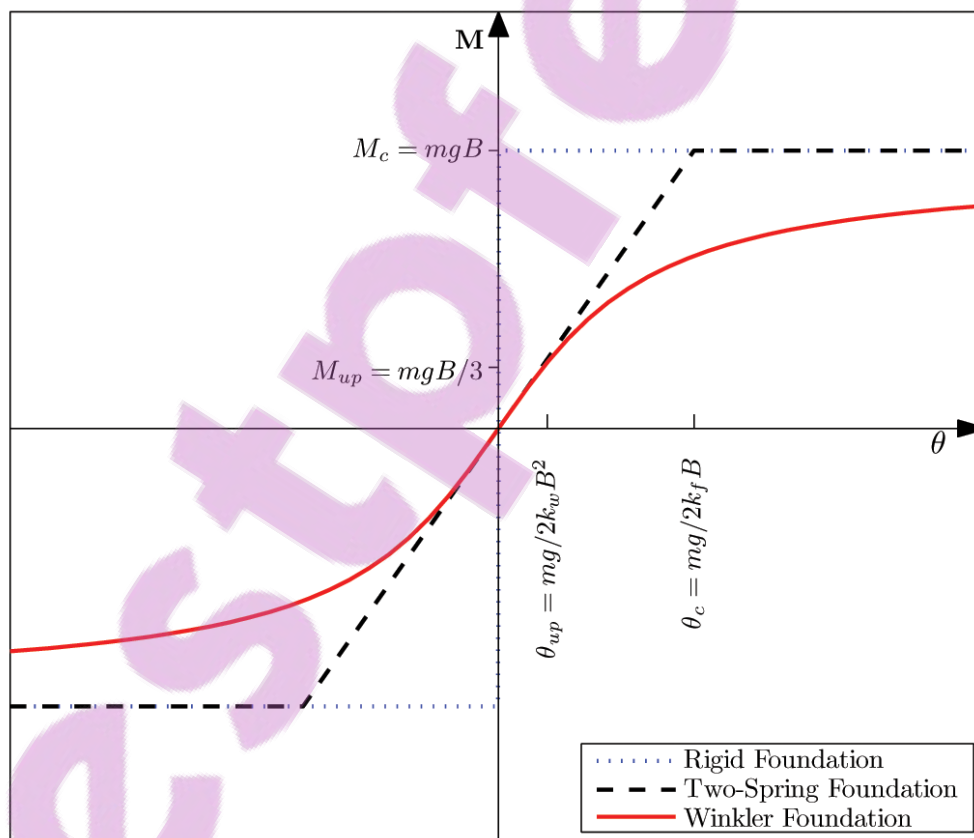
Seeking greater generality, researchers further relaxed the constraints assumption of the “two-spring” foundation and implemented a Tensionless Winkler (TW) foundation to approximately represent structural systems resting on an elastic half-space. The TW foundation eliminated the need for specifying the location of rocking pivots and the distribution of contact pressure. This permitted the possibility of a more accurate, varying soil reaction profile which was a function of the applied axial force, moment and foundation rotation.

It should be appreciated however that the use of TW foundation is still an approximation to reality. The TW foundation with constant stiffness and damping coefficients cannot replicate the excitation frequency and displacement amplitude-dependent nature of a more realistic viscoelastic soil model (Seed and Idriss 1970; Veletsos and Verbic 1973). The effects of 2D soil compliance for soil outside the immediate footprint of the foundation were also neglected, potentially lead to

unexpected bearing capacity failure and possible overturning for structures rocking on soft soils (Gazetas et al. 2003).

Additionally, it is impossible to select a single Winkler spring stiffness value,  $k_w$ , to model exactly the vertical and rotational stiffness simultaneously (Jennings and Bielak 1973). Nevertheless, the use of TW foundations represents a perceived improvement over the use of “two-spring” foundation in lieu of an exact viscoelastic half-space solution. Interestingly, the increased level of complexity in the TW models only offers refinements to conclusions reached with the “two-spring” foundations. The primary obstacle to more accurate results is still the selection of  $k_f$  or  $k_w$  which in practice depends on a number of factors such as shape, embedment of the foundation and the flexibility of the foundation mat.

Figure 2-8 presents a comparison of the moment rotational characteristics of the three rocking interface constraint assumptions.



**Figure 2-8 – The effective moment-rotation characteristics for unbounded foundation mats with three rocking interface constraint assumptions**

## 2.5 ROCKING SYSTEMS AS NONLINEAR DYNAMIC SYSTEMS

Rocking systems have also attracted much attention from a purely mathematical standpoint. The changing of boundary conditions associated with the different modes of motion (e.g. rest, slide, rock, slide-rock and free flight) results in a highly nonlinear dynamic system governed by sets of piecewise nonlinear differential equations. Even when the nonlinearity is restricted to just the effects of instantaneous impact, rocking systems' sensitivity to initial conditions and history dependency are apparent. Rocking systems have even been shown to exhibit phenomena of bifurcations, period-doubling cascades of asymmetric orbits and apparent chaotic behaviour when subjected to harmonic ground excitations.

It must be emphasized at this point that the review into this topic is only provided as it is academically interesting and for completeness. This sub-section merely aims to record intriguing properties of a rocking system that have been identified using basic nonlinear dynamic system theory. The results discussed in this section are mainly concerned with the response of a rocking system to an initial rotation or harmonic ground excitation.

Readers are advised not to directly apply the conclusions from these studies to a rocking system's response to earthquake type ground excitations. This is because many of the intriguing properties, such as the bifurcation phenomena to be shown later, are features which are rooted in the nature of the harmonic excitations. This is in contrast to properties and sensitivity which are consequences of actual intrinsic system properties. The sensitivity of this latter type do exist and are demonstrated by an example presented later in Figure 4-71a, but this is not within the scope of the literature review.

### 2.5.1 FREE STANDING BLOCK SUBJECTED TO HARMONIC GROUND MOTION

Examining the most basic rocking structure again, the Housner SRM of the rigid rocking block, the governing differential equation of the rigid block subjected to base excitations can be written as Equation 2-9 below.

$$I_o \frac{d^2\theta}{d\tau^2} \pm mgR \sin(\alpha \mp \theta) + m \frac{d^2u_g}{d\tau^2} R \cos(\alpha \pm \theta) = 0 \quad (2-9)$$

Assuming sinusoidal excitations,

$$\frac{d^2 u_g}{d\tau^2} = \alpha\beta g \cos(\Omega\tau)$$

Where

$\beta$  = non dimensional amplitude of the excitation

$\Omega$  = the excitation frequency (radians/sec)

$\tau$  = time (seconds)

Equation 2-9 can be rewritten non-dimensionally by the introduction of new non-dimensional parameters; non-dimensional rotation ( $x$ ), excitation frequency ( $\omega$ ) and time ( $t$ ) as outlined in Equations 2-10 to 2-12

$$x = \frac{\theta}{\alpha} \quad (2-10)$$

$$\omega = \Omega \times \sqrt{\frac{I_o}{mgR}} \quad (2-11)$$

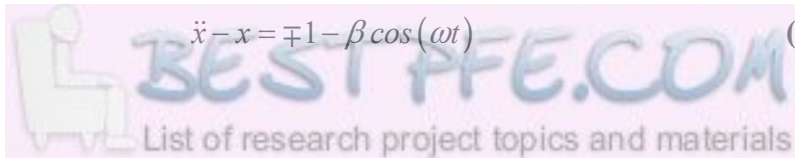
$$t = \sqrt{\frac{mgR}{I_o}} \times \tau \quad (2-12)$$

$$\alpha\ddot{x} = \alpha \frac{d^2 x}{dt^2} = \frac{I_o}{mgR} \times \frac{d^2 \theta}{d\tau^2}$$

Substitution of these into Equation 2-9 leads to the equation of motion in a non-dimensional format as presented in Equation 2-13 below. By rewriting the governing differential equation in this format, individual characteristics of any one system are removed. Hence, characteristics common to all rigid blocks of different aspect ratios can be easily investigated without the need to investigate the infinite sets of parameters individually. A detailed derivation of this can be found in a paper by Hogan (1989).

$$\alpha\ddot{x} \pm \sin(\alpha(1 \mp x)) = -\alpha\beta \cos(\omega t) \times \cos(\alpha(\alpha(1 \mp x))) \quad (2-13)$$

By further assuming the rigid block is slender ( $\alpha \ll 1$ ); Equation 2-13 is reduced to Equation 2-14.

$$\ddot{x} - x = \mp 1 - \beta \cos(\omega t) \quad (2-14)$$


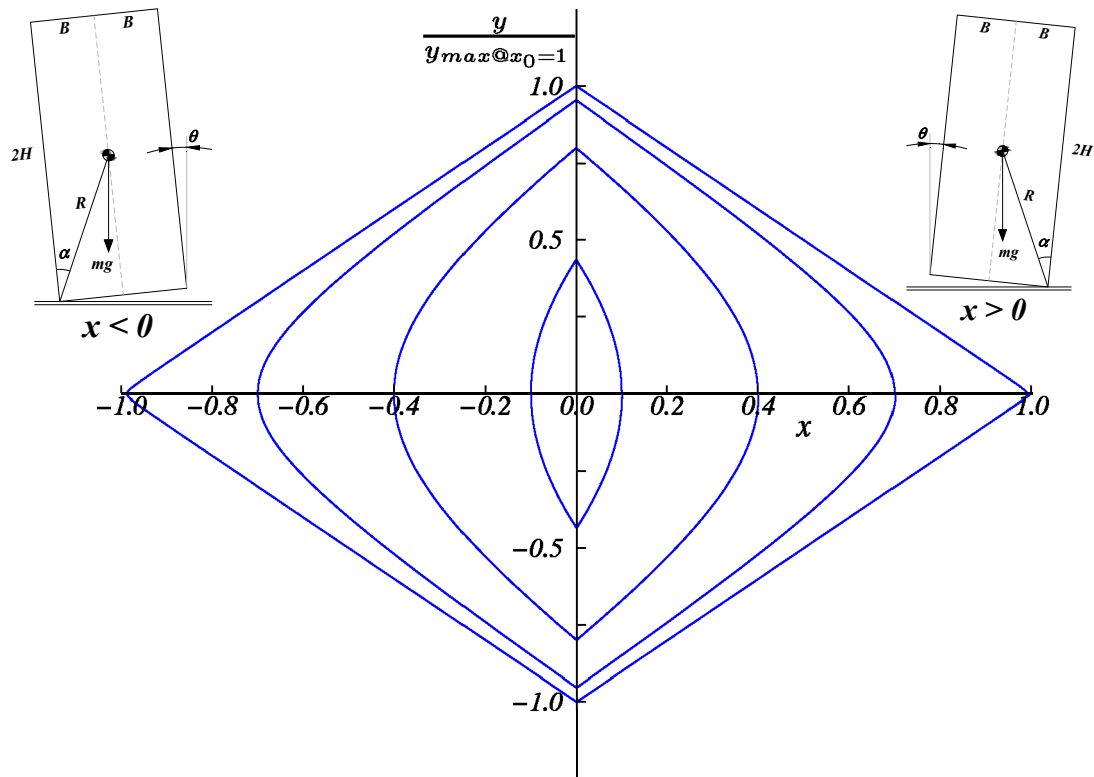
By numerically integrating the expression above, rotation time-histories of the rigid rocking block under free vibration and sinusoidal base excitation can be computed. Hogan in his 1989 paper then proceeded to plot the non-dimensional angular speed against the non-dimensional rotation of the rocking block. This resulted in a plot commonly known as a Phase Portrait or Phase Diagram in modern dynamical system theory.

The Phase Portrait is useful in identifying system behaviour as it consolidates the system response and removes the distracting effect of time. For instance, Figure 2-9 shows a range of orbits corresponding to the time-history results of a rigid block allowed to rock from a range of initial rotations. These time-histories are computed assuming zero energy dissipation. The motion begins on the positive x axis, an initial angular displacement with zero speed, then as time proceeds, the trace travels clockwise in the phase space until it reaches the upright position represented by the y axis, zero angular displacement with maximum speed. Subsequently the trace continues travelling clockwise until it reaches its starting point, signifying the completion of a conservative, free rocking cycle.

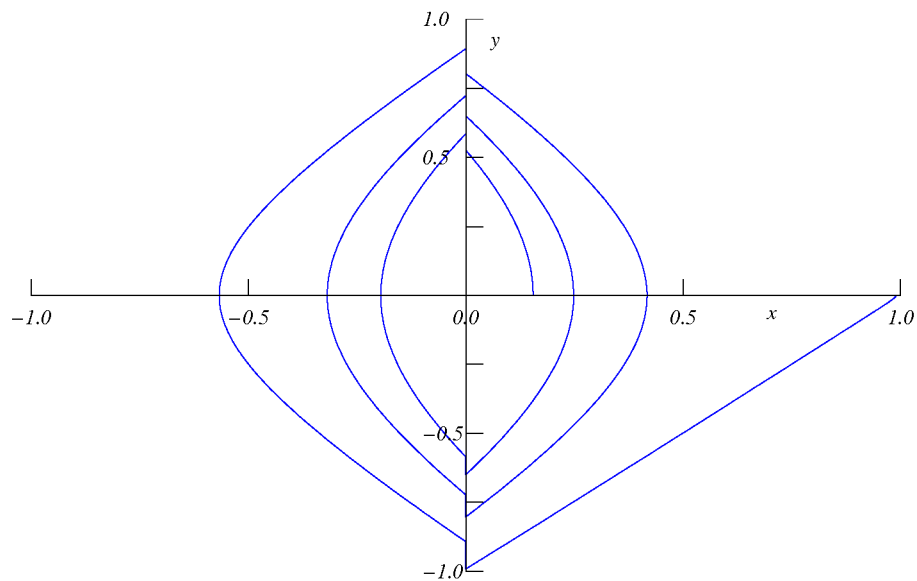
Similarly, Figure 2-10 shows the orbit of a rigid block simulated to rock freely, this time including the effects of energy dissipation by the use of a coefficient of restitution with a value of 0.9. In this analysis, the block is released just inside the angle of overturning, on the x axis. The trace, representing the passage of time in the time-history, travels clockwise as it did in the conservative case until the block reaches its upright position, the y axis. Here, the angular speed of the block is reduced instantaneously by the coefficient of restitution as described by Equation 2-4, corresponding to the effect of an impact. On the phase portrait, this is represented by an abrupt step towards the origin on every crossing of the y axis. Although not specifically depicted in Figure 2-10, the trace will eventually spiral towards the origin, illustrating that in the long term, the block will come to rest in its upright position with rotation and speed (x,y) equal to zero. This illustrates the use of a graphical technique in the prediction of long term behaviour of a system.

In addition to the prediction of the long term tendency of a free rocking block to come to rest, Hogan also identified other long term steady state behaviours under particular sinusoidal base excitations through the use of the phase portrait. Examples of these are illustrated in Figure 2-11. These orbits, although interesting, would not be

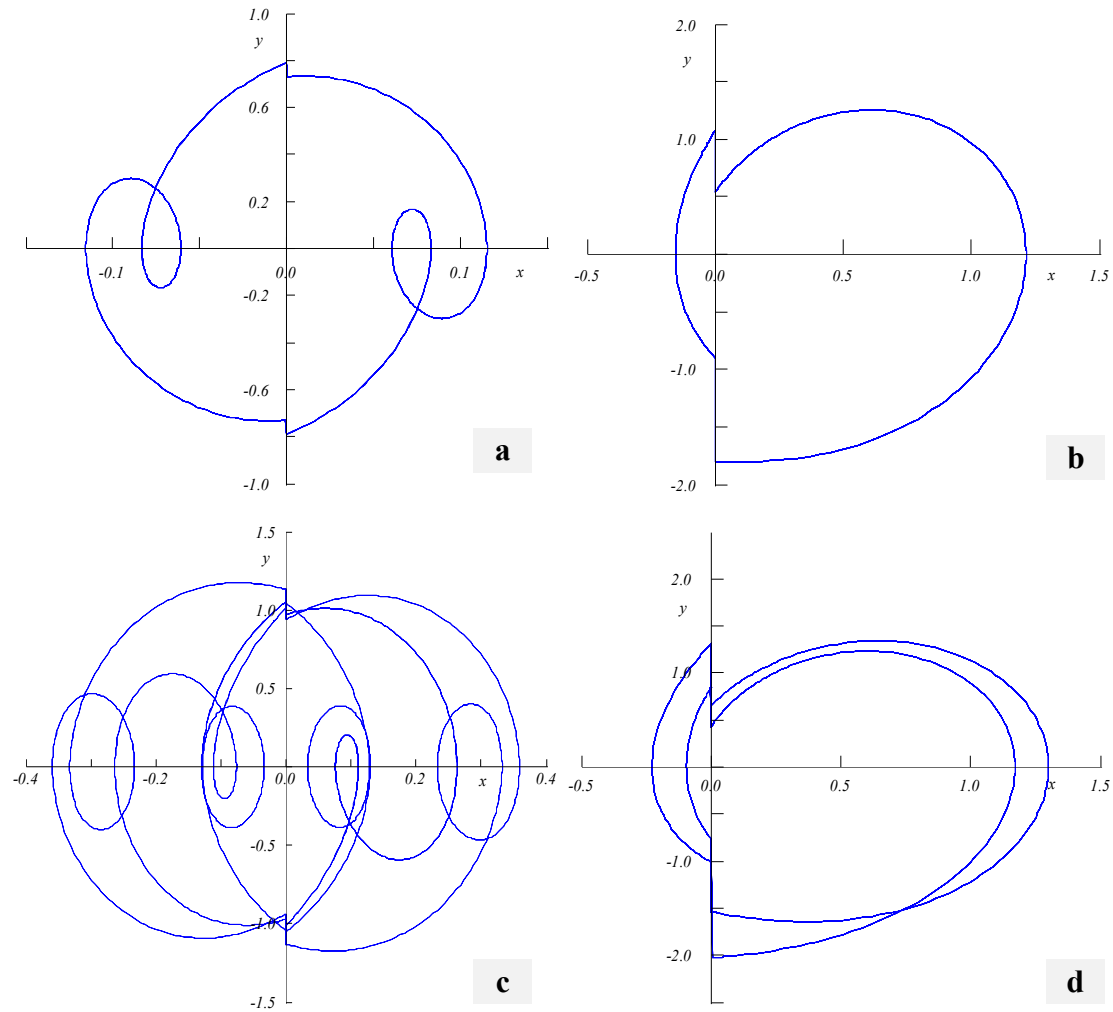
directly relevant to the response of rocking blocks to earthquake motions. This is because earthquake motions are never perfectly sinusoidal and typically are of too short duration for any steady state behaviour to develop.



**Figure 2-9 – Phase Portrait of a free rocking rigid block without energy dissipation**



**Figure 2-10 – Phase Portrait of a free rocking rigid block with  $r = 0.9$ .**



**Figure 2-11 – Examples of symmetric and asymmetric steady state orbits of a rocking block subjected to sinusoidal base excitation**

Another important discovery attributed to the analyses of the rocking block using modern dynamic system theory is the discovery of a rocking block's cascading, period-doubling route to deterministic chaos. Deterministic chaos in the context of this thesis refers to the apparent unpredictability of a deterministic system, a phenomenon in which special nonlinear systems whose future dynamics are fully defined without uncertainty given its current state, somehow results in indeterminable behaviour due to extreme sensitivity to initial conditions. Deterministic chaos has been found to occur in many natural systems in various disciplines, such as electrical engineering, fluid dynamics, quantum mechanics and celestial mechanics.

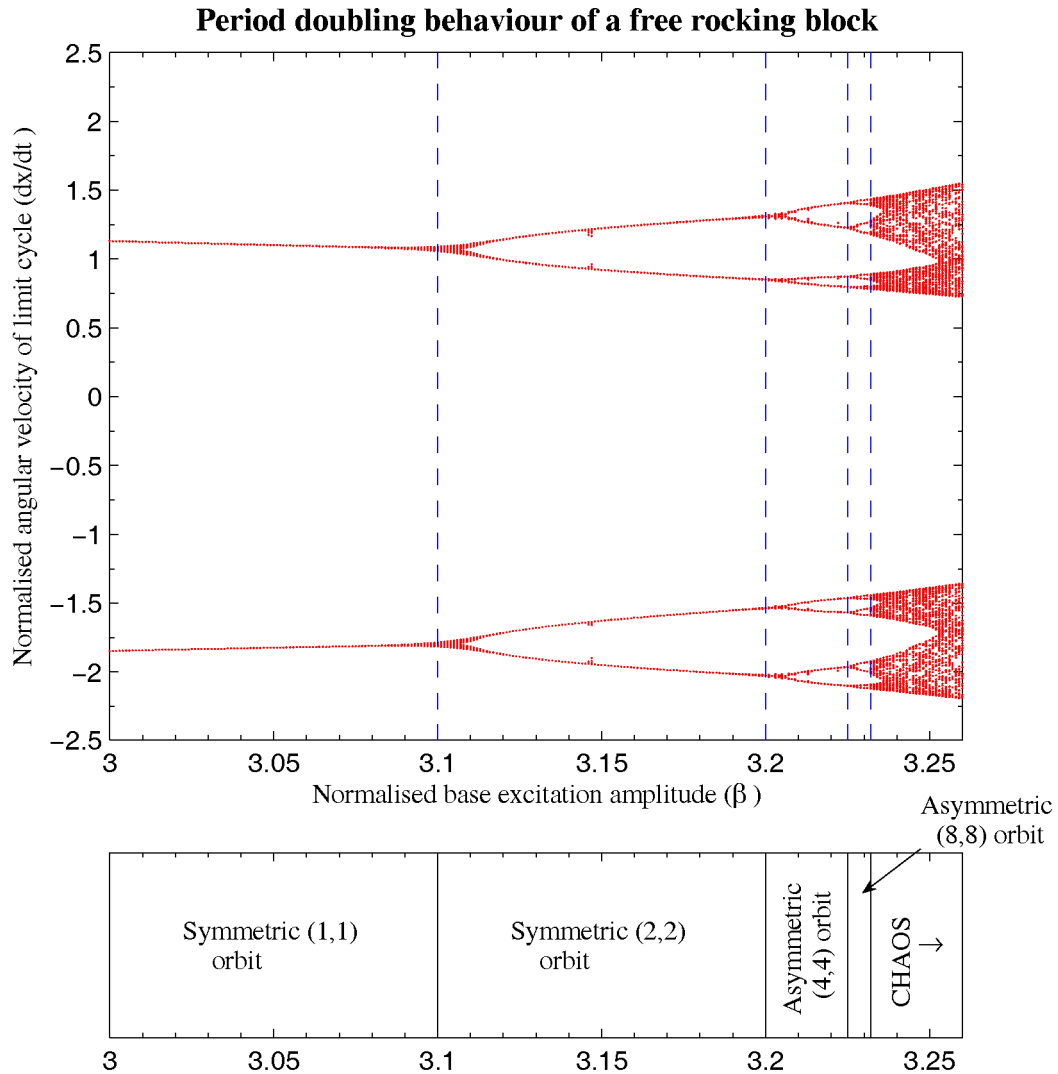
Cascading period-doubling route to chaos behaviour is a well documented universal property in a number of chaotic systems. It is characterised by a series of

sudden changes in steady state cyclical behaviour, doubling in period each instance when a control parameter is changed. This doubling in period occurs with increasing frequency until at a distinct point the behaviour is no longer cyclical and becomes unstable and chaotic. Figure 2-12 shows a bifurcation diagram which demonstrates this route to chaos for a free rocking block as a function of the amplitude of base excitations.

To produce Figure 2-12, numerical integration of Equation 2-13 was repeated thousands of times with  $\alpha = \arctan(0.5)$ ,  $r = 0.5$ ,  $\omega = \frac{2}{3}\pi$  and  $\beta$  from 3 to 3.26. In each cycle of the numerical integration conducted with a specific  $\beta$  value (amplitude of excitation), the integration is allowed to run for a sustained period to allow any cyclical behaviour to settle. Subsequently, the angular speeds of the rocking block at each occasion when it becomes upright are recorded as dots on the bifurcation diagram for a specific  $\beta$  value. The presence of overlapping dots indicates the rocking block returns to upright at the same angular speed at every cycle, and hence the motion of the block has reached a steady cyclical state or a limit cycle orbit. Two dots for a particular  $\beta$  value indicate the orbit is a simple (1,1) orbit and crosses the y axis twice in every cycle, while 4 and 8 dots corresponds with the period 2 and 4 cycles with 4 and 8 y axis crossings respectively. Failure of the dots to overlap or form distinct lines, for example in the smeared bands for  $\beta > 3.34$ , indicates stable cyclical behaviour no longer exists and the block instead roams *chaotically*<sup>3</sup> in the banded region.

---

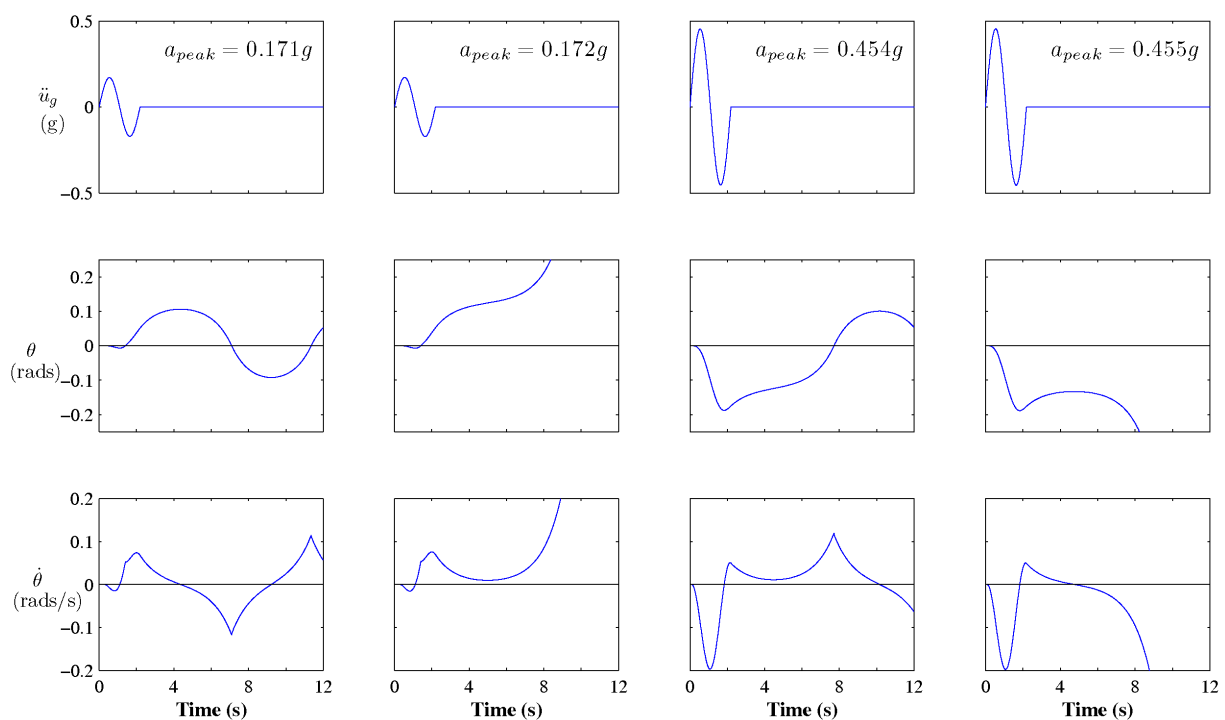
<sup>3</sup> The term chaotic is adopted liberally here. Strictly speaking, this result only attest to an aperiodic behaviour. More rigorous analyses in the true degree of chaos of a free standing rigid block subjected to sinusoidal ground excitations can be found in papers by Hogan (1989) and Lin and Yim (1996).



**Figure 2-12 – Bifurcation diagram for a free rocking block with  $\alpha = 0.464$ ,  $r = 0.5$ ,  $\omega = \frac{2}{3}\pi$  and  $\beta$  from 3 to 3.26**

The discovery of *chaotic* behaviour in the free rocking block is a significant crossroad in the research of rocking systems. This discovery suggests that a precise prediction of a rocking system's behaviour is impossible and hence stochastic or probabilistic based analyses are required for any significant advances (Lin and Yim 1996). The existence of chaotic or extreme sensitive behaviour in a free standing rocking block has been verified by a number of experimental studies (Aslam and Godden 1980; Wong and Tso 1989). The sensitivity of the problem was also highlighted in a numerical study by Zhang and Makris (2001), where similar ground acceleration pulses differing only by 0.1% in peak amplitudes, resulted in completely different displacement time-histories.

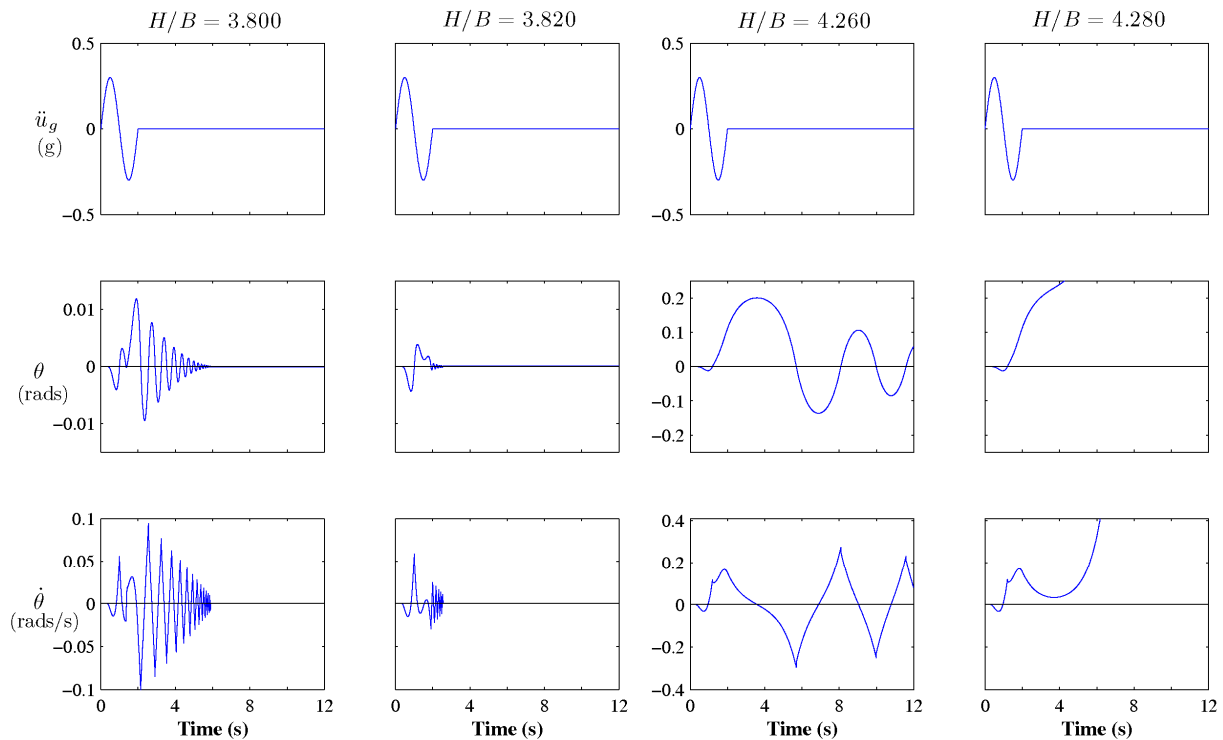
An analogous numerical simulation was repeated in this study by subjecting a 1 m wide by 8 m high rigid block to a series of sinusoidal ground acceleration pulses follow Equation 2-9. These acceleration pulses had a constant period of 2.192s and increasing peak acceleration amplitudes. Figure 2-13 below shows the block's rotational time-histories and it illustrates that 1) increasing peak ground acceleration may not necessarily lead to increased risk of overturning, as demonstrated by the fact that a pulse with a peak acceleration of 0.172 g results in overturning while a pulse of 0.454 g does not; and 2) even the slightest variation in the ground motion history can lead to a very different time-history response.



**Figure 2-13 – Time-history responses of a free rocking rigid block subjected to a single sine pulse increasing in peak acceleration ( $\alpha = 7.12^\circ$ ,  $r = 0.954$ )**

Furthermore, the response of a rigid rocking block is also extremely sensitive to the block geometry. Figure 2-14 presents the simulation results of 4 blocks with height to width ratios 3.8, 3.82, 4.26 and 4.28 subjected to an identical sine ground acceleration pulse. The results demonstrate that 1) a small change in aspect ratio of a block can lead to very different time-history response. This is evident from the widely varying responses amongst the two sets of blocks, differing only by 0.5% in aspect ratio; and 2) there is no clear correlation between peak responses and aspect ratios.

The example presented showed that rocking response can potentially decrease or increase for an increasing aspect ratio.



**Figure 2-14 – Time-history responses of 4 freestanding rigid blocks subjected to an identical single sine pulse ( $\ddot{u}_{g\max} = 0.3 \text{ g}$ ,  $T_{\text{pulse}} = 2 \text{ s}$ ,  $r$  is as per Equation 2-6)**

Interestingly, chaotic behaviour has not been verified analytically or experimentally for more realistic rocking structural systems. Anecdotally, researchers have postulated that chaotic behaviour is not applicable to the study of rocking structural systems. A common and unverified hypothesis is that the continuous nature of the effective moment rotation relationship and the presence of structural damping in a real rocking structural system significantly alter the mode of response, which prohibits the development of chaotic behaviour. This however may be optimistic as the continuous moment rotation relationship only exists prior to first uplift, and once uplift occurs, the system may well be dominated by its rocking motion or as a rigid block, as demonstrated by Chopra and Yim in their 1985 study. Moreover, a numerical study by Hogan in 1992 had shown that an unanchored rocking block with added viscous damping can still exhibit bifurcation, period and impact-doubling cascades and chaotic motion under sinusoidal forcing (Hogan 1992). This casts

further doubts on whether the sensitive and possibly chaotic characteristics of a rocking structural system can be ignored.

Researchers have also reasoned that the accurate prediction of structural response is irrelevant in any case, as it is impossible to predict the exact acceleration time-history of any impending earthquake motion. This argument although valid to an extent has led to the use of design response spectrum methods for conventional seismic resistant systems, but should not be used to dismiss the need for an accurate understanding of the behaviour of rocking systems.

This and other profound differences between a rocking system and a conventional system were highlighted in a paper by Makris and Konstantinidis (2003). The study compared existing rocking design methodology, FEMA 356 (2000), against benchmark results developed by the time integration of the governing differential equations of motion. The FEMA 365 procedure, based on an earlier experimental study by Priestley et. al. (1978) assumes:

- 1) An element will rock about the centre of a rectangular compression stress block at the corner of the element where it is in contact with the soil. The length of this stress block is  $mg/q_c$ , where  $q_c$  is the expected bearing capacity of the soil.
- 2) Rocking will only occur if the spectral acceleration,  $S_a$ , at the fundamental non rocking period is greater than  $\tan(\alpha)$ .
- 3) The maximum rotation of the rocking element can be estimated from the FEMA design spectra modified for an empirical equivalent viscous damping.

Makris reported that of all five simulations using five U.S. earthquake motions, “the FEMA procedure grossly overestimates the rotations to the extent that they are of no use”. The critical flaw of the FEMA procedure lies in the unsubstantiated assumption that a response spectrum technique can be applied to a rocking system. This assumption required that a rocking system be simplified to a SDOF oscillator with a constant period and constant viscous damping.

In the FEMA procedure, designers first construct a displacement spectrum by modifying the standard spectrum according to an empirical equivalent viscous damping ratio as given in Equation 2-15.

$$\xi_{eq} = 0.4(1 - \sqrt{r}) \quad (2-15)$$

where  $r$  is given by Equation 2-6.

Designers then estimate a peak rotation,  $\theta_i$ , which is translated into a rocking period ( $T_i$ ) according to Housner's Equation 2-5. The rocking period is used to look up a peak displacement estimate,  $\delta_{i+1}$  from the displacement spectrum. The peak displacement is in turn converted into a peak rotation following Equation 2-16, and the process is repeated until the peak rotation converges.

To make matters worse, in an attempt to be conservative the FEMA damping value in Equation 2-15 is up to 10% less than the more accurate approximation Equation 2-16 (Priestley et al. 1978).

$$\xi_{eq} = -0.34 \ln(r) \quad (2-16)$$

## 2.6 DIRAC- $\delta$ REPRESENTATION OF THE ROCKING IMPACT

A recent novel development in the mathematical treatment of rocking motion is the use of Dirac- $\delta$  interaction functions in the constructions of the governing differential equations of motion. In the context of a rocking rigid block, Prieto (2004) used a Dirac- $\delta$  function to replicate the discontinuous effects of a block rocking from one pivot to another. As a result, the classical piecewise nonlinear differential equations of motion are reduced to a single continuous differential equation. Moreover, the Dirac- $\delta$  formulation removed the need for an ad hoc inclusion of a coefficient of restitution. The Dirac- $\delta$  function has the effect of an impulsive force which will act on impact and simulates the energy lost through work done by the impulsive force.

This approach was trialled for modelling the behaviour of a rocking block under free vibration and harmonic forcing. It was shown that the Dirac- $\delta$  representation was able to match the result from a classical analysis. The Dirac- $\delta$  approach represented a more heuristic force-based formulation creating an opportunity for the effects of the impact interface to be better quantified.

The key to the Dirac- $\delta$  approach is the construction of an impulse force  $F_\delta$  which is introduced into the generalised governing differential equation of motion (Equation 2-14). Conducting the appropriate substitution, this leads to the new governing differential equation below:

$$\ddot{x} - x + \text{sign}(x) = F_\delta \quad (2-17)$$

In order to replicate the effect of the classical coefficient of restitution ( $r$ ),  $F_\delta$  must meet the three requirements below:

1. The force is concentrated in space and time,
2. The force produces a sudden change in rotational velocity at impact and has the effect of reducing the rotational velocity corresponding to the  $r$  value,
3. The force reduces the rotational velocity for both directions of motion.

Conceptually, as  $F_\delta$  is characterised by activating only at a particular rotation and has amplitudes that are related to the impact velocity, the most intuitive model is a product of two independent sub-functions in rotation and velocity as below.

$$F_\delta(x, \dot{x}) = f(x) \cdot g(\dot{x}) \quad (2-18)$$

Then in order to imitate a force which only acts at  $x = 0$ , the rotation sub-function,  $f(x)$  can be replaced by a Dirac- $\delta$  function,  $\delta(x)$ .

$$f(x) = \delta(x) \quad (2-19a)$$

where  $\delta(x) = 0$  when  $x \neq 0$  (2-19b)

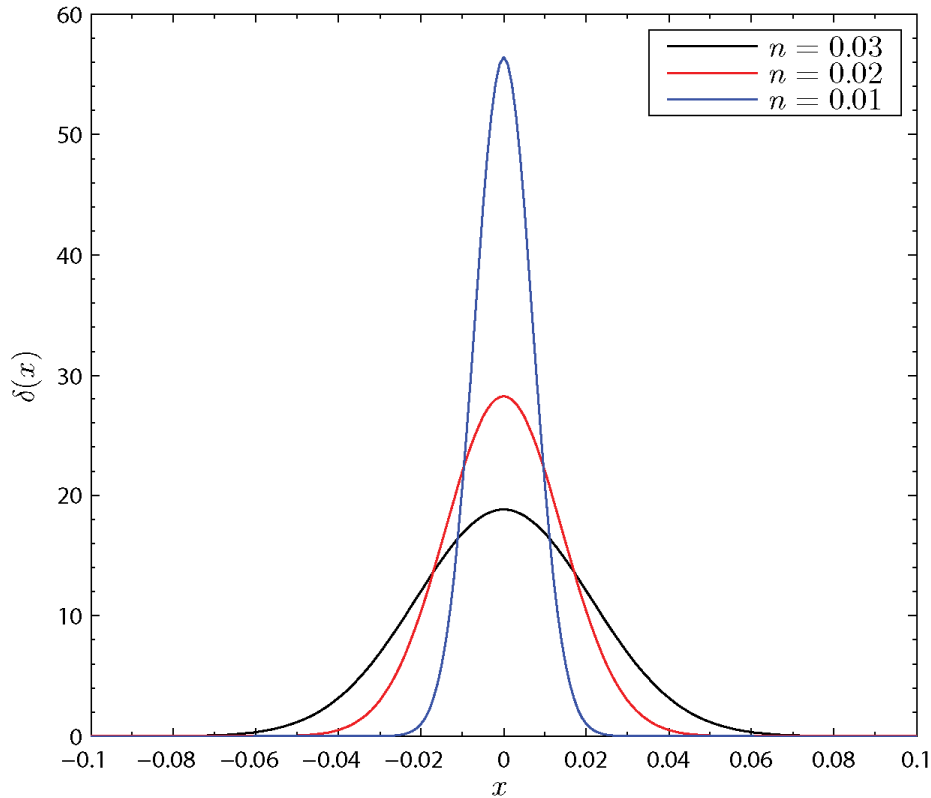
$$\int_a^b \delta(x) dx = 1 \quad (2-19c)$$

Now in order to avoid a piece-wise formulation, a continuous, normal distribution approximation of the Dirac- $\delta$  replaces the formal integral definition.

$$\delta_n(x) = \frac{1}{n\sqrt{\pi}} e^{-\frac{x^2}{n^2}} \quad (2-20)$$



where  $n$  can be interpreted as a penalty parameter which controls the abruptness of the contact force. Figure 2-15 shows the effect of a decreasing  $n$  value on the Dirac- $\delta$  function.



**Figure 2-15 – The effect of varying  $n$  on the Dirac- $\delta$  distribution approximation**

With the rotation dependent sub-function,  $f(x)$ , controlling when the impulse force is active, the velocity dependent sub-function,  $g(\dot{x})$  governs the amplitude of the force such that it reduces the entry velocity of the impact ( $\dot{x}_0$ ) to the desired exit velocity ( $\dot{x}_f$ ). To select a suitable functional form for  $g(\dot{x})$ , consider the momentary instant a rigid block is impacted by an impulse force when it returns to the upright position.

The system can be represented by a SDOF model, and as the impact occurs in a much shorter timescale compared to the rocking motion period, the gravity forces are ignored and this results in the equation of motion as in Equation 2-21a.

$$\frac{d^2x}{dt^2} = F_s(x, \dot{x}) \quad (2-21a)$$

It follows that:

$$\frac{d\dot{x}}{dt^2} = \delta(x) \cdot g(\dot{x}) \quad (2-21b)$$

$$\frac{1}{g(\dot{x})} d\dot{x} = \delta(x) dt \quad (2-21c)$$

$$\frac{\dot{x}}{g(\dot{x})} d\dot{x} = \delta(x) dx \quad (2-21d)$$

A definite integral carried out for the interval immediately before and after an impact leads to the requirement for a consistent velocity dependent sub-function, as in Equation 2-22.

$$\int_{\dot{x}_0}^{\dot{x}_f} \frac{\dot{x}}{g(\dot{x})} d\dot{x} = \int_{-x_0}^{x_f} \delta(x) dx$$

$$\int_{\dot{x}_0}^{\dot{x}_f} \frac{\dot{x}}{g(\dot{x})} d\dot{x} = 1 \quad (2-22)$$

Assuming a general power expression for  $g(\dot{x})$ ,

$$g(\dot{x}) = K \cdot \dot{x}^m \quad (2-23)$$

and importing it into Equation 2-22 by combining it with the concept of the coefficient of restitution yields:

$$\int_{\dot{x}_0}^{\sqrt{r} \cdot \dot{x}_0} \frac{1}{K \cdot \dot{x}^{m-1}} d\dot{x} = 1 \quad (2-24)$$

This leads to two possible scenarios for the form of Equation 2-23, 1) where  $m \neq 2$  and 2) where  $m = 2$ . It can be shown that only the second scenario produces a function that will achieve the correct reduction in angular velocity according to  $r$  yet is independent to the entry velocity ( $\dot{x}_0$ ). This is critically important as it is impractical to create a unique function at every impact where  $\dot{x}_0$  is different.

Substituting  $m = 2$  into Equation 2-24 yields:

$$\int_{\dot{x}_0}^{\sqrt{r} \cdot \dot{x}_0} \frac{1}{K \cdot \dot{x}} d\dot{x} = 1$$

$$[\ln(\dot{x})]_{\dot{x}_0}^{\sqrt{r} \cdot \dot{x}_0} = K$$

$$K = \ln(\sqrt{r}) \quad (2-25)$$

This amalgamates to:

$$g(\dot{x}, r) = -\ln(\sqrt{r}) \cdot \dot{x}^2 \quad (2-26)$$

The negative sign is introduced in Equation 2-26 to counteract the fact that the logarithm of  $r$  is always negative. Furthermore, Prieto proposed an inclusion of a signum function as below, in order for the impulse force to fulfil the third requirement of reducing the rotational velocity for both directions of motion.

$$g(\dot{x}, r) = -\ln(\sqrt{r}) \cdot \dot{x}^2 \cdot \text{sign}(\dot{x})$$

A hyperbolic tangent approximation can be introduced to remove the abruptness of the signum function,

$$g(\dot{x}, r, n) = -\ln(\sqrt{r}) \cdot \dot{x}^2 \cdot \tanh\left(\frac{\dot{x}}{n}\right) \quad (2-27)$$

Combining the results from Equations 2-18, 2-20 and 2-27 yields the complete expression for  $F_\delta$ :

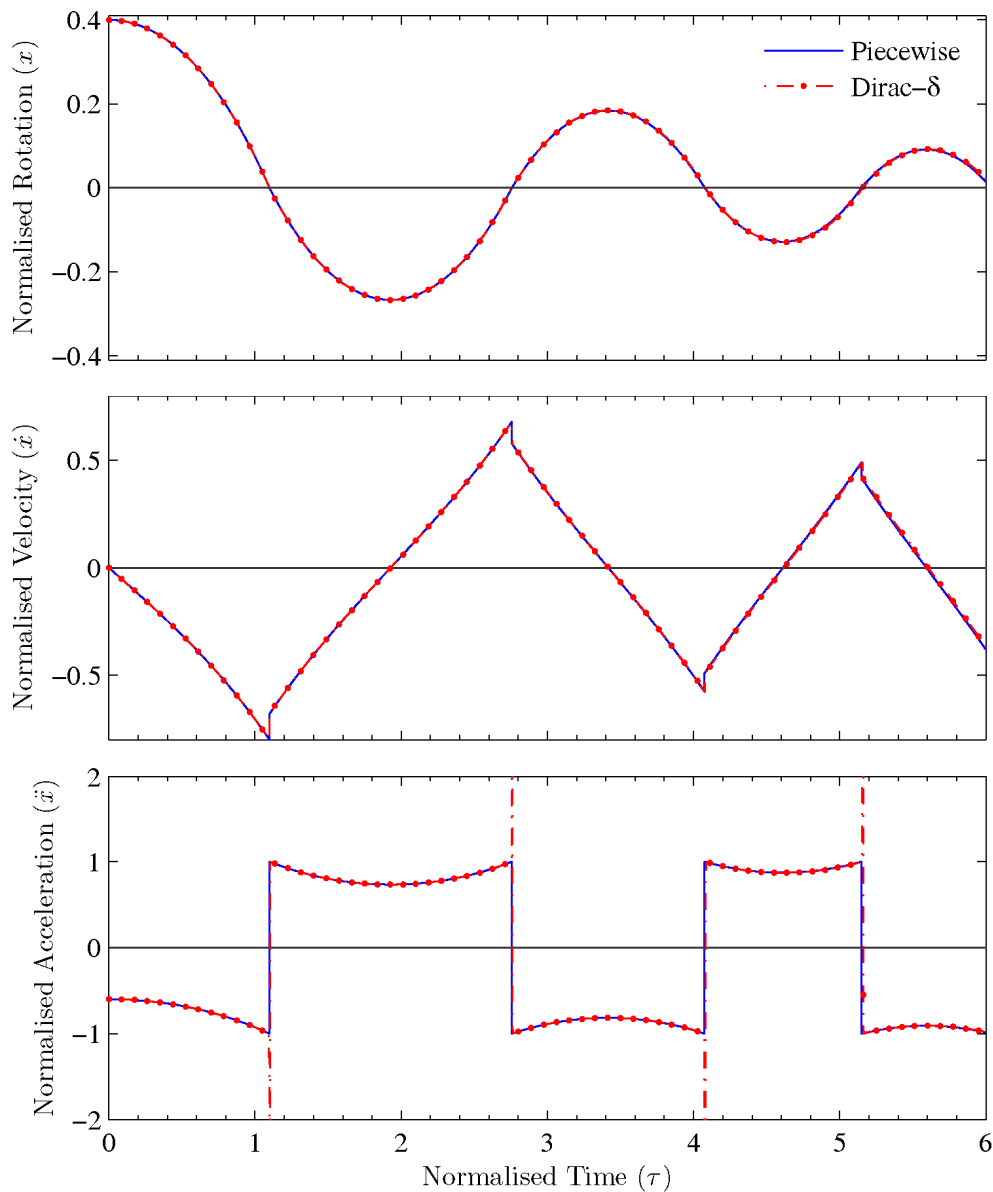
$$F_\delta(x, \dot{x}, r, n) = \frac{-\ln(\sqrt{r})}{n\sqrt{\pi}} \tanh\left(\frac{\dot{x}}{n}\right) \dot{x}^2 e^{-\frac{x^2}{n^2}} \quad (2-28)$$

Equation 2-28 can in turn be substituted into Equation 2-14 to form a continuous governing differential equation of motion for a rocking slender block as below:

$$\ddot{x} - x + \tanh\left(\frac{x}{n}\right) = \frac{-\ln(\sqrt{r})}{n\sqrt{\pi}} \tanh\left(\frac{\dot{x}}{n}\right) \dot{x}^2 e^{-\frac{x^2}{n^2}} \quad (2-29)$$

Equation 2-29 can subsequently be numerically integrated as per the classical piecewise formulation to calculate the time-history response of rocking rigid blocks. Figure 2-16 overpage presents the results of such a comparison of the two formulations. Simulations were conducted on two identical 1:3 freestanding rigid blocks set to rock from an initial rotation using the two formulations. It is clearly evident that the two formulations yield near identical results, with the exception of a much higher acceleration from the Dirac- $\delta$  formulation at the instant of an impact. The spikes in accelerations appear to have negligible effects on the overall rotation

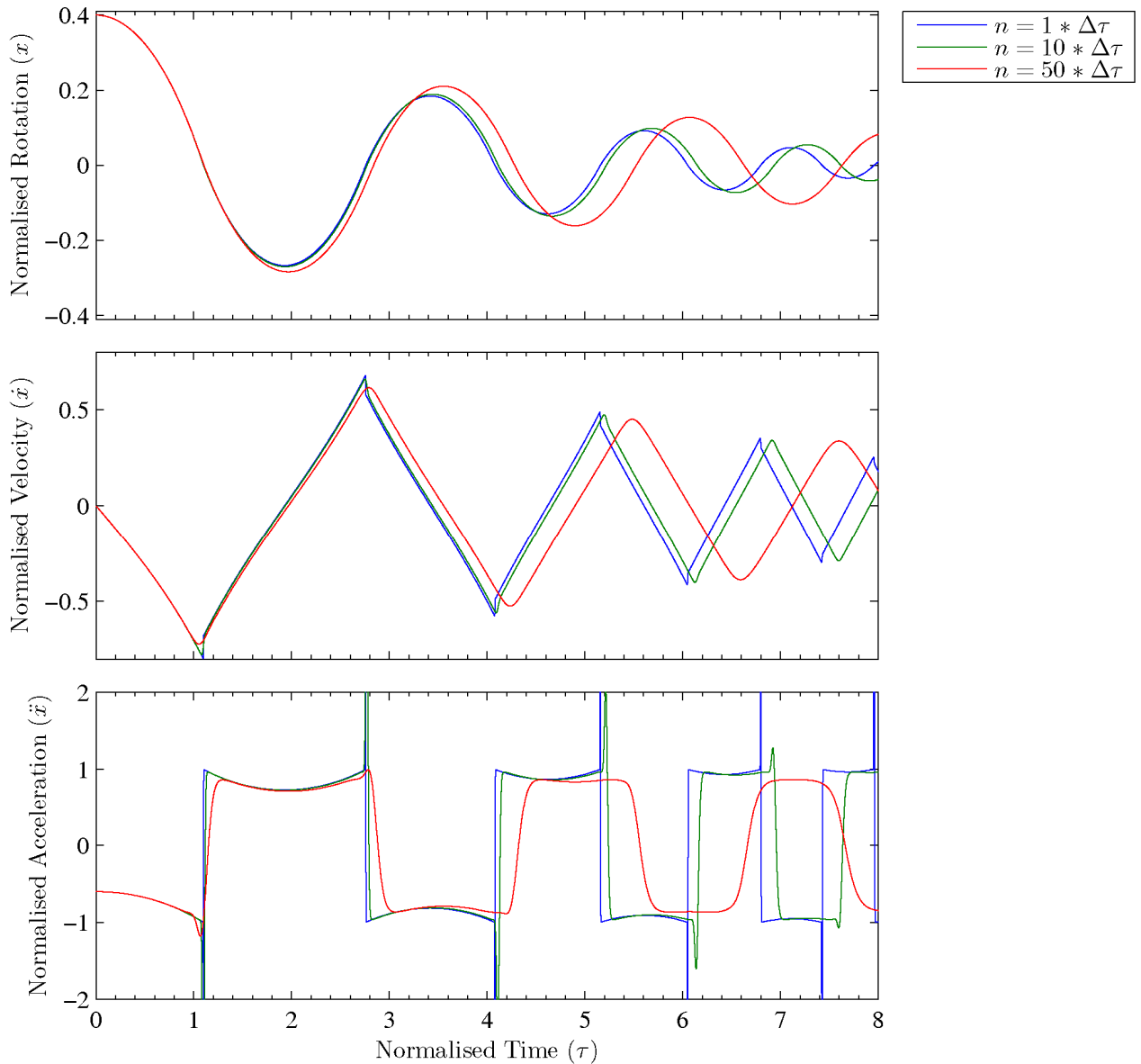
history of the block, moreover it is difficult to conclude which of the two formulations more closely reflects reality.



**Figure 2-16 – Time-history response of a 1:3 freestanding rigid block released from an initial rotation of  $x_0 = 0.4$  ( $r = 0.7225$ ,  $n = 10^{-3}$ ,  $\Delta\tau = 0.5 \times 10^{-3}$ )**

By introducing the penalty parameter,  $n$ , the Dirac- $\delta$  formulation can accurately control the amount of energy lost at an impact and also manipulate the rate at which the rocking pivot transfer occurs. The selection of the  $n$  values should be in conjunction with the integration time step,  $\Delta\tau$ . From the previous discussion, the smaller the  $n$  value, the higher and shorter duration the Dirac- $\delta$  force becomes. But as the solution is generally obtained through numerical integration with a fixed time step,

the minimum resolution in time that can be represented is  $\Delta\tau$ . This results in the  $n$  value having a functional lower bound limit equal to  $\Delta\tau$ , as any value lower than this is simply superfluous. Similarly,  $\Delta\tau$  should be kept sufficiently small to ensure impacts are detected. Figure 2-17 presents the results of three simulations demonstrating the overall effect of varying  $n$ .

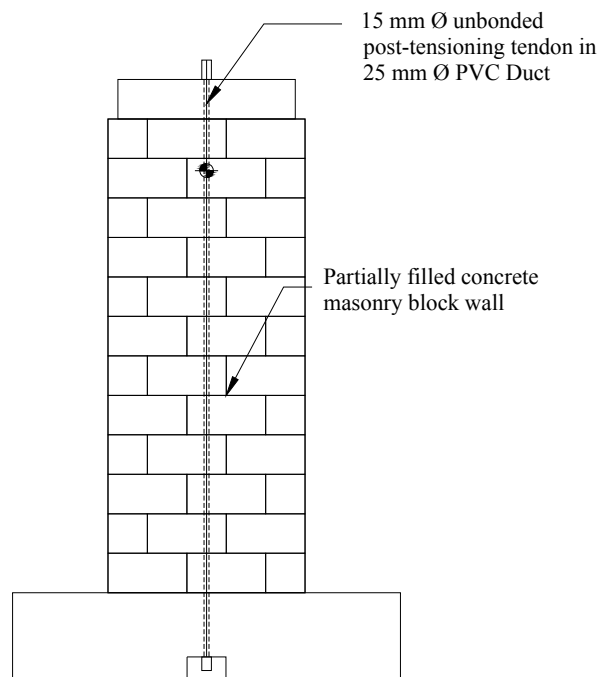


**Figure 2-17 – Time-history response of a 1:3 freestanding rigid block released from an initial rotation of  $x_0 = 0.4$  ( $r = 0.7225$ ,  $\Delta\tau = 0.5 \times 10^{-3}$ )**

## 2.7 CONTROLLED ROCKING MOTION

Another important area of recent research in the rocking field is the emergence of controlled rocking elements for seismic resistant design. Controlled rocking systems, sometimes referred to as self-centering systems, are systems typically comprised of a classical rocking system, with an additional elastic element to provide supplementary self-centering. Whilst the term controlled rocking is sometimes also used to describe the behaviour of special jointed ductile beam-column connections, this study will only investigate controlled rocking motions in which the supplementary self-centering is in the same direction as gravity.

An example of such a construction is the unbonded post-tensioned precast concrete walls found in the U.S. PRESSS programme as described previously in Chapter 1 (Priestley et al. 1999). Figure 2-18 below presents a typical schematic of such a system.

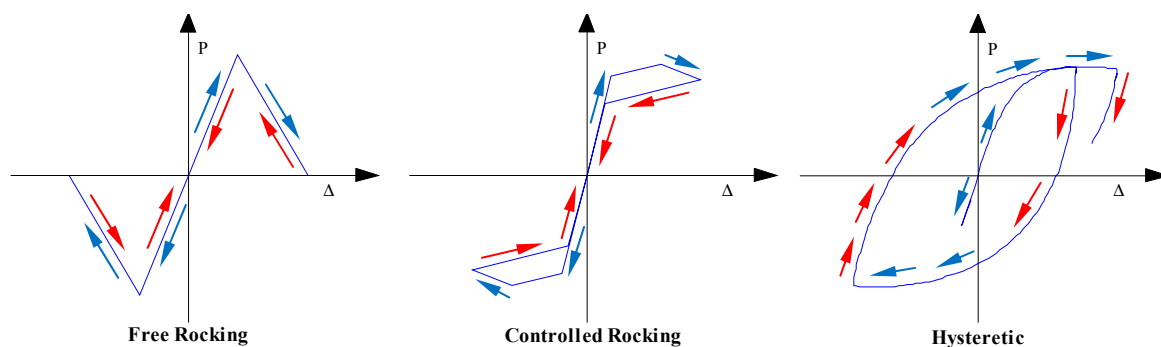


**Figure 2-18 – Typical schematic of an unbonded post-tensioned rocking wall**

Under low level lateral forces, a controlled rocking system behaves as a conventional fixed base structure with a high lateral stiffness due to the “clamping” from the added elastic element. When the system is subjected to high levels of lateral force, rocking is initiated as a gap opens at the base of the rocking interface. When gap opening occurs, controlled rocking systems rotate approximately about the same

centres of rotation as an unrestrained free rocking system, however the motion is much more stable because of the presence of the additional restoring force. Additionally, overturning is unlikely to occur and controlled rocking systems are generally immune from residual displacements effects. This is in contrast to free rocking systems where structures tend to “walk” away or when compared to fixed based systems where desirable ductile behaviour is at the expense of irreversible permanent displacements and damage.

The previously mentioned features can be explained by comparing the force-displacement responses of the three different systems in Figure 2-19 below.



**Figure 2-19 – Idealised nonlinear static force-displacement response (Blue arrows indicate the loading path and red arrows indicate the unloading path)**

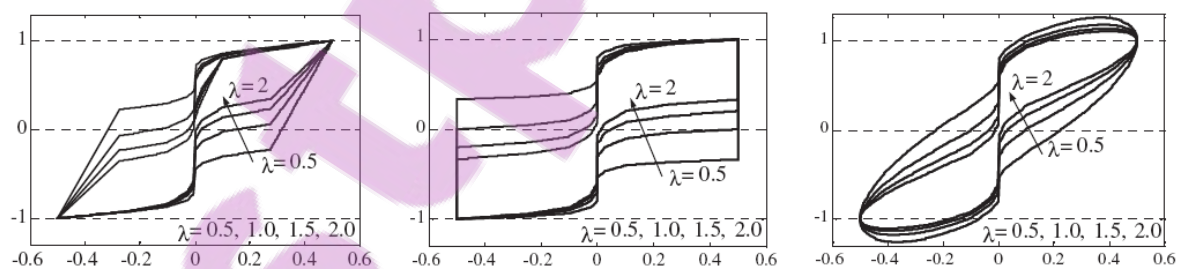
Firstly, the stability of the controlled rocking system against overturning is a result of the positive tangential stiffness after gap opening. The positive yet low tangential stiffness encourages the system to accommodate the lateral impulse by a mild drift into higher displacements, a process that could be likened to yielding in a ductile system. This extends the effective period of the system and detunes it from pending higher frequency impulses. This prolonged softening phase also provides extra time for impulses to reverse and hence aids self-centering. On the other hand, the negative tangential stiffness in the rocking phase of a rocking system results in a rapid loss of lateral strength much like the event of a brittle failure. Whilst the loss of strength would still isolate a free rocking system from succeeding high frequency impulses, the rocking motion would be boisterous, allowing little time for impulses to reverse and hence increasing the likelihood of overturning. In a dynamics system theory context, the negative tangential stiffness is associated with unstable

equilibrium states, whilst a positive tangential stiffness always leads to stable equilibrium states for a single degree of freedom system.

Figure 2-19 also highlights the fact that controlled rocking systems have a rather unique “flag-shape” hysteretic behaviour (Palermo et al. 2005). The uniqueness of the flag-shape hysteresis is that any inelastic deformations are typically fully recovered upon unloading. This is irrespective of whether the inelastic deformations result from the additional restoring element, the rocking element or additional energy dissipating devices. Consequently, satisfactory self-centering with little or no residual displacement is guaranteed provided a parameter  $\lambda$ , as defined by Palermo et al in Equation 2-30, is greater than 1.  $\lambda$  is the ratio of design moment contributions of a controlled rocking system from re-centering and dissipative parts.

$$\lambda = \frac{M_{AE} + M_N}{M_{ED}} \quad (2-30)$$

where  $M_{AE}$ ,  $M_N$  and  $M_{ED}$  are the moment contributions from the added restoring element, axial load and additional energy dissipaters respectively. Numerical modelling by Palermo showed that  $\lambda$  effectively defines the shape and zero crossings of the flag shape hysteresis. Figure 2-20 demonstrates that the greater the ratio of moment contribution from the additional energy dissipaters (irrespective of their types), the smaller the  $\lambda$  and the greater the flag area will be.



**Figure 2-20 – Illustrative non-dimensionalised Moment-Rotation plots for controlled rocking systems with added energy dissipating devices, i) Elastic-plastic, ii) Friction & iii) Viscous (Palermo et al. 2005)**

The flag shape hysteresis also highlights a lack of energy dissipating capacity of controlled rocking system through classical hysteretic mechanisms. Studies involving a large number of nonlinear inelastic time-history analyses showed that on average, a controlled rocking wall system will produce 40% larger peak

displacements than a comparable cast-in-place concrete construction (Kurama et al. 1999b; Kurama 2000). This result led to researchers asserting that additional damping devices be mandatory for controlled rocking systems to achieve adequate dynamic performance (Restrepo and Rahman 2007; Toranzo et al. 2001).

Putting the validity of the use of initial-stiffness proportional viscous damping to emulate radiation damping aside, it is noteworthy that Kurama's studies used a viscous damping ratio of 3%, which is a typically assumed value for controlled rocking systems and matches the value suggested by Equation 2-16. Recent free vibration decay test results by Wight et al (2004), summarised in Table 2-3, confirm that this is indeed reasonable. It may be argued however that this may be conservative in that it neglects the damping contributions from other structural and non-structural elements that may be expected in practice.

**Table 2-3 – Equivalent viscous damping ratios determined from free vibration tests of unbonded post-tensioned concrete masonry wall**

Wall ID	Length (mm)	Height (mm)	$\frac{f_p}{W}$	$\xi_{eq}$ (%)	Free rocking estimate	
					$r^{*1}$	$\xi_{eq}^{*2}$
UoA4	813	2438	3.82	2.61	0.944	1.96
UoA6	1016	2438	3.84	3.28	0.914	3.06

\*1 from Equation 2-6, \*2 from Equation 2-16

Another revealing technique for analysing the energy dissipating property of a controlled rocking system is through recent research on direct displacement-based design utilising a substitute structure. The substitute structure approach originally proposed by Jacobsen (1930) recast a nonlinear system into a substitute elastic SDOF system. Subsequently, an equivalent linear viscous damping ratio ( $\xi_{eq}$ ) simulates the effects of dissipative forces. In this approach, the stiffness of the substitute SDOF system is set at the initial stiffness of the nonlinear system, while the  $\xi_{eq}$  is calculated by equating the non-conservative work in the nonlinear system to that from linear viscous damping over one cycle at resonance. This approach, termed the Jacobsen Damping Initial Stiffness (JDIS) approach, implicitly assumes the equivalent linear viscous damping as a direct sum of the contributions from the elastic component ( $\xi_{el}$ ) and the hysteretic component ( $\xi_{hyst}$ ):

$$\xi_{eq} = \xi_{el} + \xi_{hyst} \quad (2-31)$$

For a particular hysteretic model, an equivalence equation can be derived to relate the hysteretic damping to the displacement ductility. Equations 2-32a - 2-32c present such equivalence equations for Bilinear, Takeda and Flag shape hysteretic models (Priestley and Grant 2005). Parameters appearing in the equations are explained in Figure 2-21. These equations are useful for displacement-based design, as they allow designers to estimate an equivalent viscous damping ratio based on a ductility parameter for the different hysteretic models.

$$\xi_{hyst,Bilinear} = \frac{2(\mu-1)\left(1-\frac{k_p}{k_i}\right)}{\pi\mu\left(1+\frac{k_p}{k_i}(\mu-1)\right)} \quad (2-32a)$$

$$\xi_{hyst,Takeda} = \frac{1}{\pi}\left(1-\left(1-\frac{k_p}{k_i}\right)\mu^{\alpha_r-1}-\frac{k_p}{k_i}\mu^{\alpha_r}\right) \quad (2-32b)$$

$$\xi_{hyst,FS} = \frac{\beta_{FS}(\mu-1)}{\pi\mu\left(1+\frac{k_p}{k_i}(\mu-1)\right)} \quad (2-32c)$$

Examining these equations closely, it demonstrates that a flag shape or controlled rocking system has consistently 2-3 times less energy dissipating capacity than the other systems sharing the same ductility. This is particularly obvious when the result is plotted as in Figure 2-22.

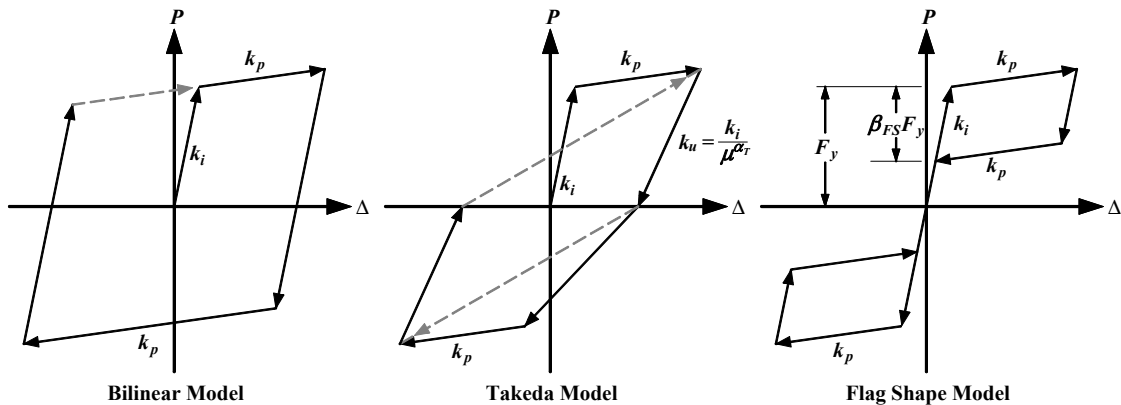
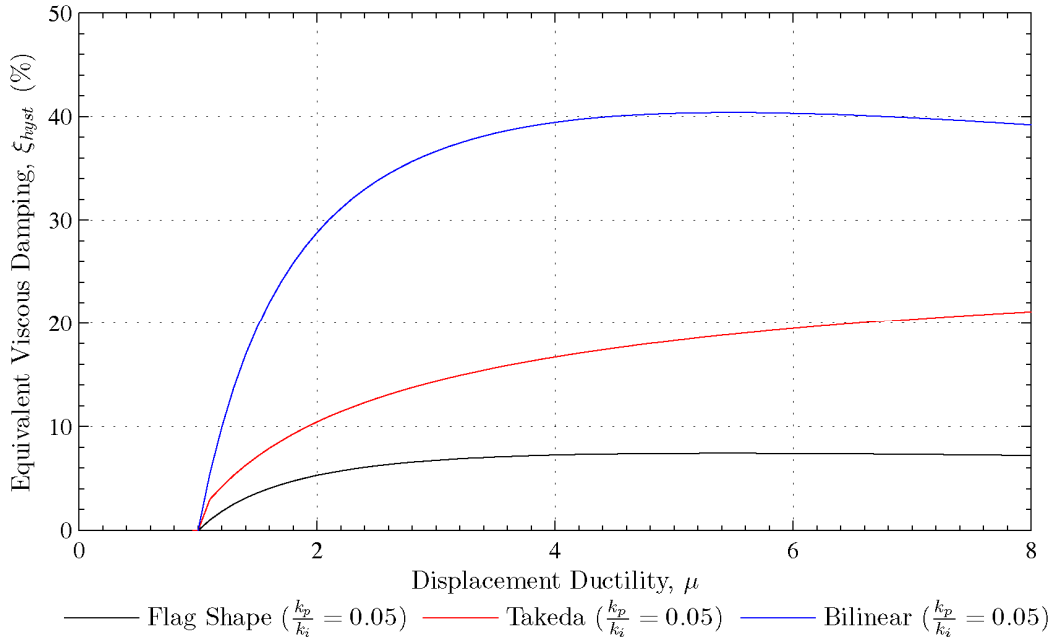


Figure 2-21 – Three typical hysteretic material models



**Figure 2-22 – Equivalent hysteretic damping against displacement ductility**

Over the years, researchers made improvements to the Jacobsen procedure to better predict the behaviour of structural systems. Rosenblueth and Herrera (1964) introduced the Jacobsen Damping Secant Stiffness (JDSS) approach where secant stiffness is used in place of initial stiffness to better simulate the phenomenon of period lengthening. This in turn led to the necessary corrections proposed by Grant et al (2005) to modify the previous expression for equivalent damping ratio ( $\xi_{eq}$ ), Equations 2-30.

Grant's expression presented in Equation 2-33 was a result of extensive time-history analyses with different hysteretic models subjected to a number of ground motion records. The correction factors ( $a - f$ ) in Equations 2-33 are calibrated by determining the best fit values in order to achieve the previous level of damping when a secant stiffness instead of an initial stiffness is used in the analysis. Table 2-4 presents the correction factors as published from Grant's study.

$$\xi_{eq} = a \left( 1 - \frac{1}{\mu^b} \right) \left( 1 + \frac{1}{(T_e + c)^d} \right) + \mu^e \xi_{el}^{const} + \mu^f \xi_{el}^{tang} \quad (2-33)$$

Dissecting the Grant empirical equation mathematically and relating it to the physical process, it can be shown that the correction factors  $a$  and  $b$  control the increase in equivalent hysteretic damping as a function of the displacement ductility,

while factors  $c$  and  $d$  control the period dependency. Examining Table 2-4, it can be seen that the flag shape and bilinear system have considerably different  $c$  and  $d$  factors compared to other hysteretic models.

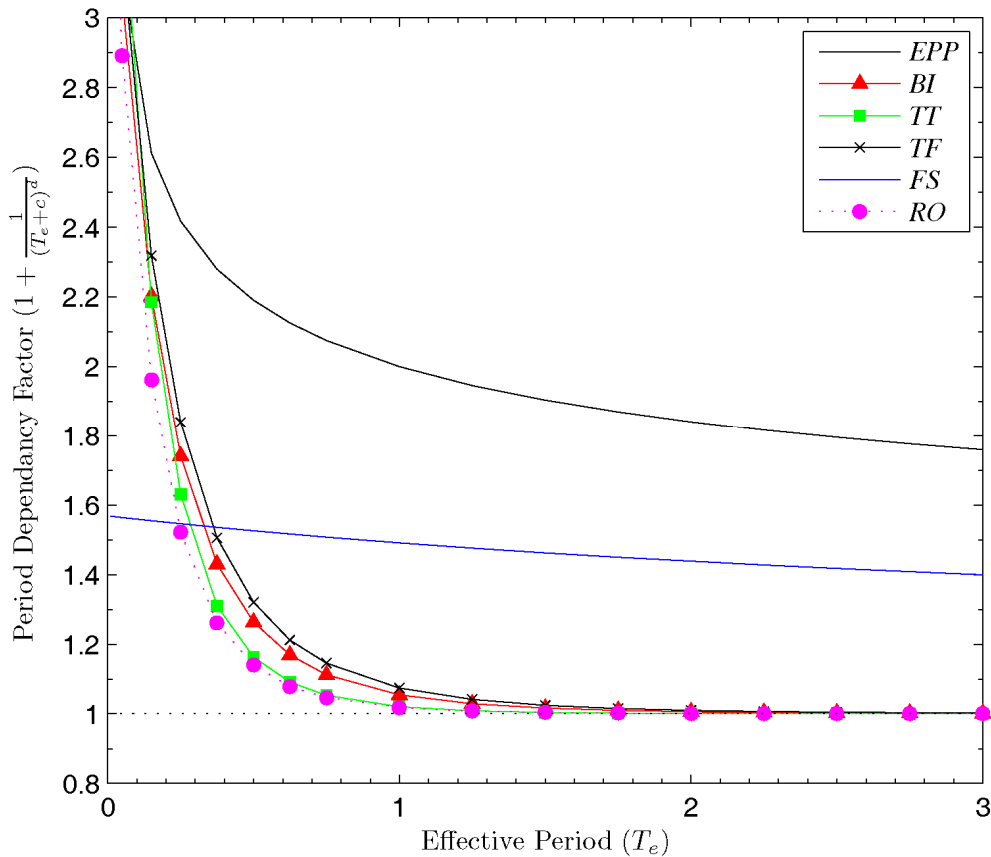
The effects of the abnormal  $c$  and  $d$  factors are best observed via a plot of the period dependency term in Equation 2-33 versus the effective period, as presented in Figure 2-23. The figure shows that for most systems, the period dependency term is within 10% of unity for effective periods ( $T_e$ ) over one second. In fact for  $T_e$  over two seconds, the period dependency factor is effectively one and the equivalent hysteretic damping in most systems can be deemed period independent. While the flag shape systems have a near constant period dependency factor of 1.5.

**Table 2-4 – Parameters for Equation 2-33 (Grant et al. 2005)**

Model	a	b	c	d	e	f
Elastic Perfectly Plastic (EPP)	0.224	0.336	-0.002	0.250	0.127	-0.341
Bilinear (BI) $\frac{k_p}{k_i} = 0.2$	0.262	0.655	0.813	4.890	0.193	-0.808
Takeda Thin (TT)	0.215	0.642	0.824	6.444	0.340	-0.378
Takeda Fat (TF)	0.305	0.492	0.790	4.463	0.312	-0.313
Flag Shape (FS) $\beta_{FS} = 0.35, \frac{k_p}{k_i} = 0.05$	0.251	0.148	3.015	0.511	0.387	-0.430
Ramberg-Osgood (RO)	0.289	0.622	0.856	6.460	-0.060	-0.647

**Table 2-5 – Parameters for “design” expression, Equation 2-35**

Model	a	b	c	d
Elastic Perfectly Plastic (EPP)	0.222	0.397	0.287	1.295
Bilinear (BI)	0.161	0.952	0.945	2.684
Takeda Thin (TT)	0.183	0.588	0.848	3.607
Takeda Fat (TF)	0.249	0.527	0.761	3.250
Flag (FS) $\beta_{FS} = 0.35, \frac{k_p}{k_i} = 0.05$	3566	6E-6	0.223	0.8405
Ramberg-Osgood (RO)	0.156	1.049	0.781	2.106



**Figure 2-23 – Equivalent hysteretic damping corrections as a function of Effective Period**

As a result of this finding, in cognizance of the fact that most building systems have  $T_e$  greater than one second and using a lower damping value would yield conservative results, researchers proposed new simplified versions of the Grant “analysis” equation dropping the period dependency term altogether (Dwairi et al. 2007; Priestley et al. 2007). The form of the simplified equation is presented below.

$$\xi_{eq} = \xi_v + C_i \left( \frac{\mu - 1}{\pi \mu} \right) \quad (2-34)$$

Where  $C_i$  is a constant calibrated based on individual hysteretic model.

However, as Figure 2-23 has demonstrated, the use of this approach for a flag shaped hysteretic system is potentially more inaccurate than for other systems.

For convenience, Grant et al also re-calibrated Equation 2-31 for “design” situations where the proportions of  $\xi_{el}$  and  $\xi_{hyst}$  contributions are unknown and designers often assume the total equivalent linear viscous damping is 5%. By

recalibrating the expression to have a total equivalent damping ratio equal to 5% and zero hysteretic damping at a ductility of one, this approach, termed the Empirical Damping Secant Stiffness (EDSS) approach, gives rise to Equation 2-35 and the correcting factors are presented in Table 2-5.

$$\xi_{eq} = 0.05 + a \left( 1 - \frac{1}{\mu^b} \right) \left( 1 + \frac{1}{(T_e + c)^d} \right) \quad (2-35)$$

Examining the table, the flag shape or controlled rocking hysteretic model is again proven to not conform well to a generalised model. A possible explanation for this is that the  $\xi_{el}$  of a flag shape system is strangely correlated with the displacement ductility. Grant's calibration exercise has shown that  $\xi_{el}$  tends to decrease with increasing ductility up to  $\mu = 5$ , after which it increases, unlike other systems which have a decreasing trend. Consequently, the correction factors  $a$  to  $d$  in Equation 2-35 are suitably varied to change the form of the design expression, to compensate for the constant  $\xi_{el}$  value in the "design" expression.

This analysis of the damping formulae in the core of displacement-based design also highlighted that these formulae are best-fit empirical relationships based on perfect numerical simulations of idealised system behaviours. Whilst they are without a doubt valid for revealing behaviour trends of different systems, care should be taken that the relationships are not blindly adopted as they are at present untested in earthquakes and are mere best fit formulae.

## 2.8 CONCLUSION

This chapter summarised some of the key research findings that have made significant contributions to the understanding of the behaviour of rocking objects. In the past one and a half centuries, researchers made many incremental improvements to the rocking science theories and provided insights into the dynamics of the most basic single two-dimensional rigid rocking block, extending to the dynamics of rocking structural systems.

The review focused on the development of techniques for predicting the time-history response of these systems, as this is regarded as the quintessential test of modelling and understanding the system behaviour. The current analysis demonstrated that one of the greatest challenges remaining is integrating two

problems of very different time scales, the very short duration (microseconds) impact or wave propagation problem and the ensuing geometrically nonlinear near rigid body motion problem. The review found that it was difficult to classify whether one model is better or worse than another. The models were rarely validated with dynamic experimental tests, or often the experimental data were used to adjust the models empirically such that the prediction matched the result (Huckelbridge and Clough 1978). It was also shown that more complex models did not equate to more accurate results. The substantially more complex models incorporating the effect of a flexible rocking interface often provided inconsequential change in the time history prediction.

The review found that the two-spring approach and the TW foundation approach are more commonly used for estimating the time history response of rocking systems. This is most likely because common design office software can be readily adapted to analyse these problems.

Amidst the level of uncertainty that surrounds the accuracy of the different models, specifying the correct system properties such as foundation stiffness and amount of energy dissipation will have a greater influence on the result than the selection of a particular rocking model.

The review investigated the intriguing effects of this from a mathematical, nonlinear system dynamics standpoint and has identified four key findings,

- 1) The rocking problem is a highly nonlinear and sensitive process which with the right conditions will lead to “chaotic” motion.
- 2) The idealised rigid rocking block problem can be non-dimensionalised into a single governing differential equation to represent blocks of all sizes.
- 3) A Dirac- $\delta$  function has been used with success to represent the impact problem for rigid rocking blocks, and
- 4) Little progress has been made in understanding the amount of energy dissipation beyond Housner’s apparent coefficient of restitution.

The review has examined the developing use of controlled rocking for seismic isolation. Controlled rocking systems share many similar characteristics with the free rocking system, such as the proven and desired ability to minimise seismic loadings onto structures via gap opening. Controlled rocking systems are further enhanced by

the additional restoring element which also prevents overturning. This combination of free rocking and the actions of the additional restoring element produces distinctive flag-shaped force-displacement behaviour.

Extensive research, much of it utilising the flag-shaped force-displacement behaviour, has yielded a general system level understanding on the behaviour of these system. This review has presented the contemporary treatment of energy dissipation in these systems through the displacement-based seismic design approach. This was particularly revealing as one can interpret the result to demonstrate that controlled rocking systems behave rather uniquely compared to more conventional systems, and do not conform well to a generalised model. Dynamic verifications of controlled rocking system models remain scarce.

# Chapter 3

---

## FREE ROCKING RIGID OBJECTS

---

This chapter presents an investigation of the behaviour of free rocking rigid objects under free vibration decay. The study scrutinizes the data from 430 free vibration tests on a rigid concrete block conducted at the University of Auckland. The intent of the study is to shed light on the dynamic processes that occur when a rigid object is in free rocking motion. Particular focus is placed on the variation of rocking periods, impact forces and energy dissipation.

The tests were jointly conducted by Dr. Mohamed Elgawady, a post-doctoral fellow of the university, and the author.

### 3.1 EXPERIMENTAL SETUP

In the experiments, a 900 mm high, 190 mm wide concrete block was set to rock from a range of initial rotations. A steel mechanism was cast into the base of the block to ensure point impacts and prevent sliding. The steel mechanism consisted of a 10 mm thick steel plate embedded into the base of the concrete block, two 15 mm diameter steel rods welded along the two side edges of the steel plates. One of these steel rods is connected to one end of a short steel bar through a freely rotating pin concentric with the centre of the steel rods, whilst the other end of this short steel bar is connected to a longer steel bar via another freely rotating pin. The longer steel bar is then welded to a steel angle which is bolted to the concrete base. Impacts occurred between the steel rods and the concrete base as the block alternated from rotating

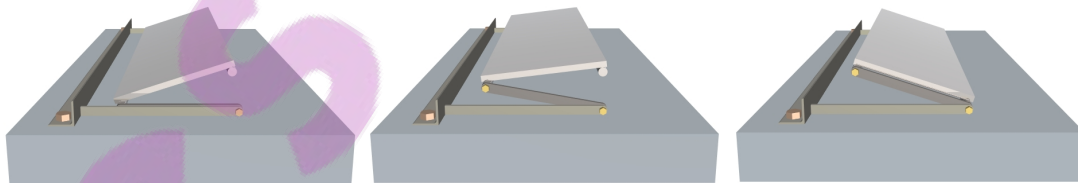
about one steel rod to the other. The short steel bar rotates with the block and prevents any sliding from occurring.

Including the steel mechanism, the specimen had an approximate ( $h/w$ ) aspect ratio of 4.9, a mass of 334.44 kg and a centroid 454.90 mm above the rocking surface. Figure 3-1 shows a drawing and a photo of the experimental setup and Figure 3-2 presents a schematic of the steel mechanism in action.

The specimen rested on a 75 mm thick concrete base simulating a perfectly rigid rocking interface. For each test run, the concrete block was tilted to a fixed horizontal displacement by hand, held still and released. Each test run was repeated 5 to 10 times at a particular displacement. In total, over 430 test runs were completed.



**Figure 3-1 – Rigid Rocking Block Experiment Setup**



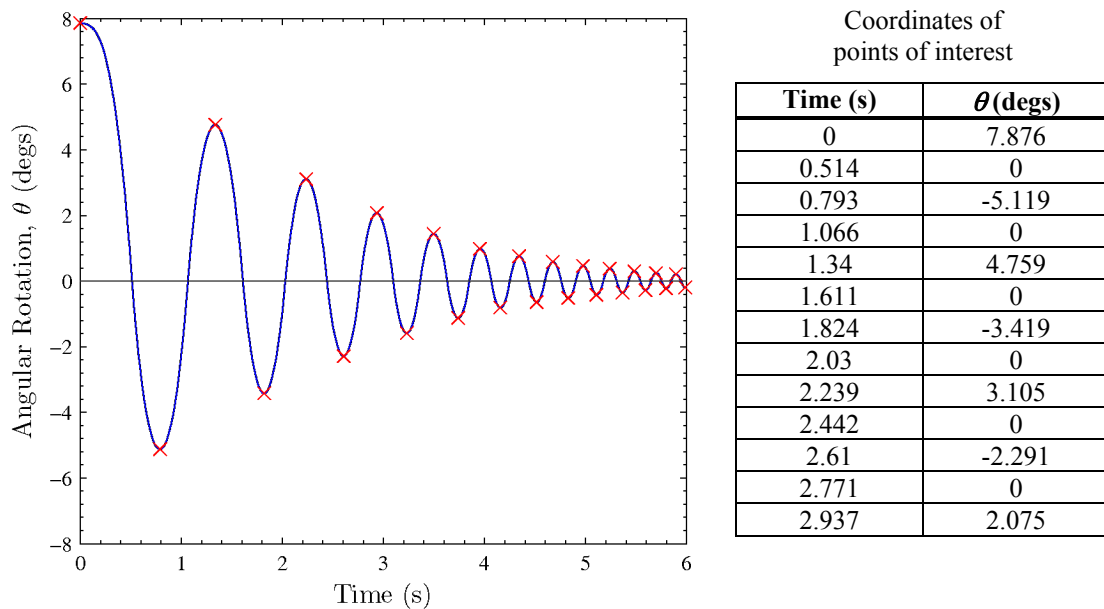
**Figure 3-2 – Schematic of the Steel Mechanism in action**

Two Linear Variable Differential Transformers (LVDTs) recorded the horizontal displacements of the concrete block. The LVDTs were free to pivot at both ends and applied negligible resistance to the motion of the block. The horizontal

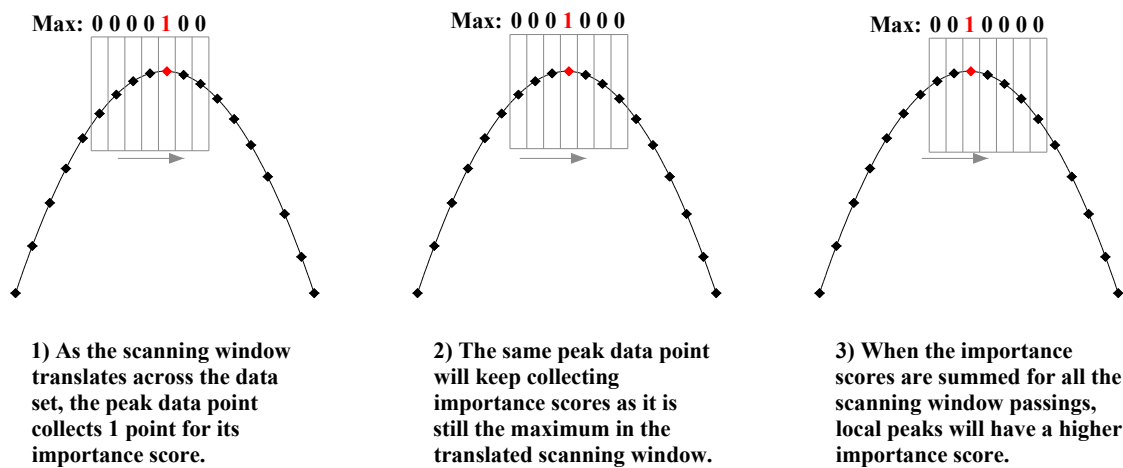
displacements were later converted to an angular rotation about the rocking pivot based on the geometry of the system.

### 3.2 RESULTS AND ANALYSIS

A typical displacement time-history of a test run is presented in Figure 3-3. In this figure, the block with an initial rotation appeared to come to rest as a typical viscously damped linear elastic system. On closer inspection, the system does not have a constant natural period, but instead, the period of vibration decreases as the peak amplitude of each quarter cycle is decreased, a hallmark characteristic of a nonlinear rocking system.



**Figure 3-3 – Typical angular rotation time-history of the concrete block released from an initial rotation**



**Figure 3-4 – Illustration of the peak finding algorithm**

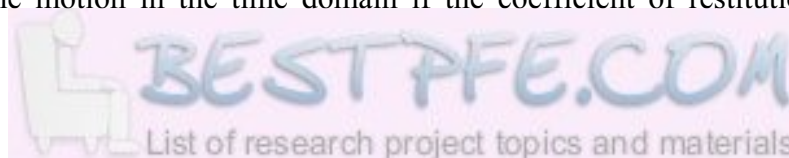
To confirm the amplitude dependency of the rocking motion, the periods of each quarter cycle were determined from the experiments using peaks and zero crossings in each test run. As there were over 430 test runs and each test run contained at least 20 peaks and zero crossings, a computer algorithm was developed to identify the points of interest.

The computer algorithm scanned across the time-history trace, approximately 500 sample points at a time, corresponding to 0.5 second of the record. An importance score of 1 was tallied against a particular data point if it was the largest or smallest number within the scanning window. The scanning window translated across the data set, moving forward one data point at a time. On a rising slope, data points took turns at being the maximum and acquired more or less the same importance score. The same occurred when the scanning window translated across a falling slope. When the scanning window translated across a peak, the peak data point collected a higher importance score than its neighbours as it was the maximum point for more scanning windows. The algorithm then compared the importance scores against a user selected threshold score, and any values greater than the threshold were considered as peaks. A simplified illustration of this process is summarised in Figure 3-4.

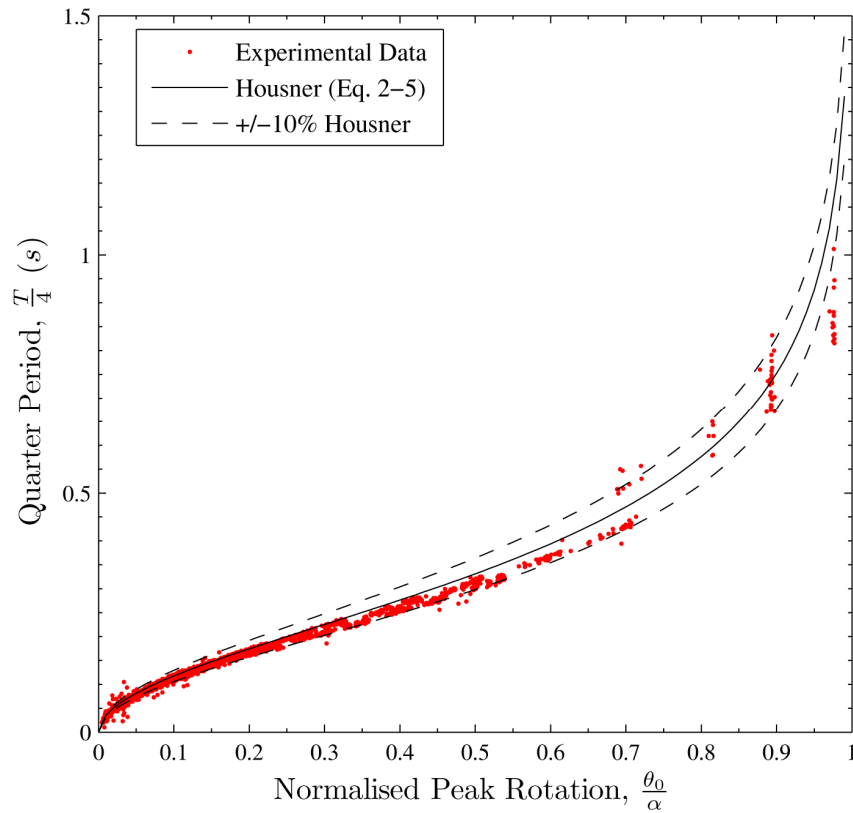
### 3.2.1 COMPARING EXPERIMENTAL RESULTS AGAINST HOUSNER'S SRM MODEL

After collating the results from all the test runs, the periods for a quarter of the free rocking cycle were plotted against the corresponding peak rotations at which each cycle began. This quarter cycle period is of interest as it corresponds to a continuous phase of the rocking cycle without the interference of the impacts. Figure 3-5 shows that the experimental data closely matched Housner and Muto's period prediction formula, Equation 2-5. It was also noted that the formula typically over-predicted the experimental periods but was generally accurate within 10%.

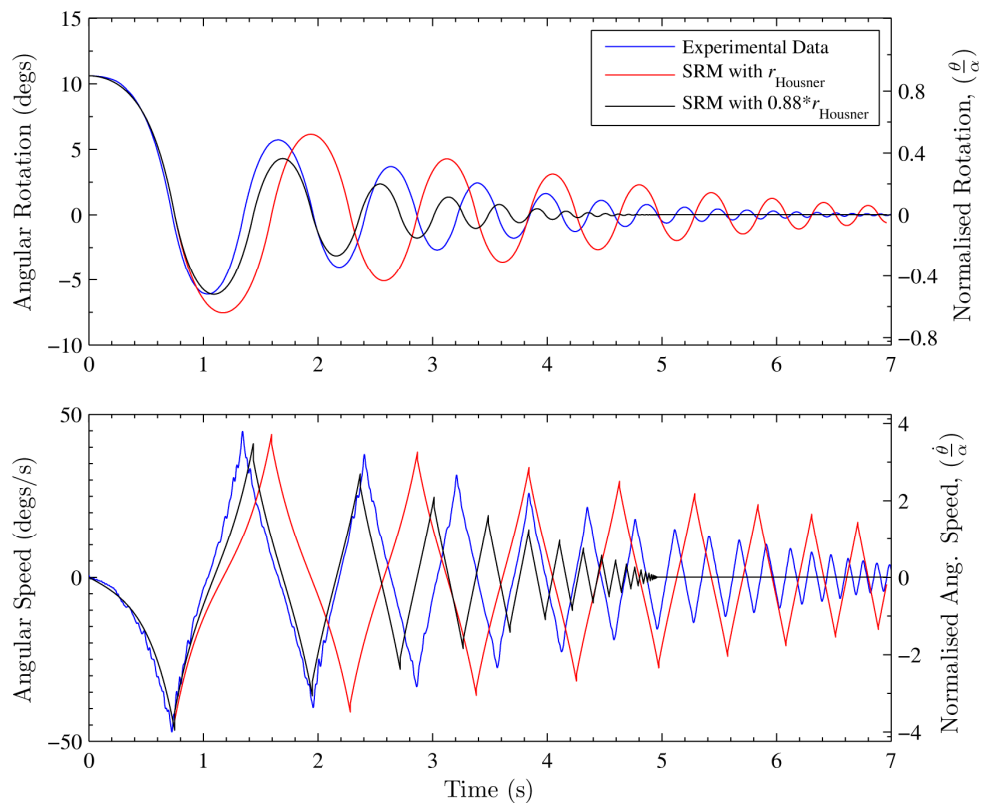
Comparing the test runs against the numerically simulated results based on Housner's simple rocking model (SRM) revealed a number of inconsistencies. Figure 3-6 shows the time-history comparison of the numerically simulated results against the experimental results for a typical test run. This plot highlights that the standard SRM only adequately simulated the motion. The matching is improved for the first few cycles of the motion in the time domain if the coefficient of restitution,  $r$ , is



decreased to 0.88 of the Housner value,  $r_{\text{Housner}}$  (Equation 2-6). However, this substitution predicts the motion to cease much earlier than expected.



**Figure 3-5 – Quarter periods versus normalised initial rotation**

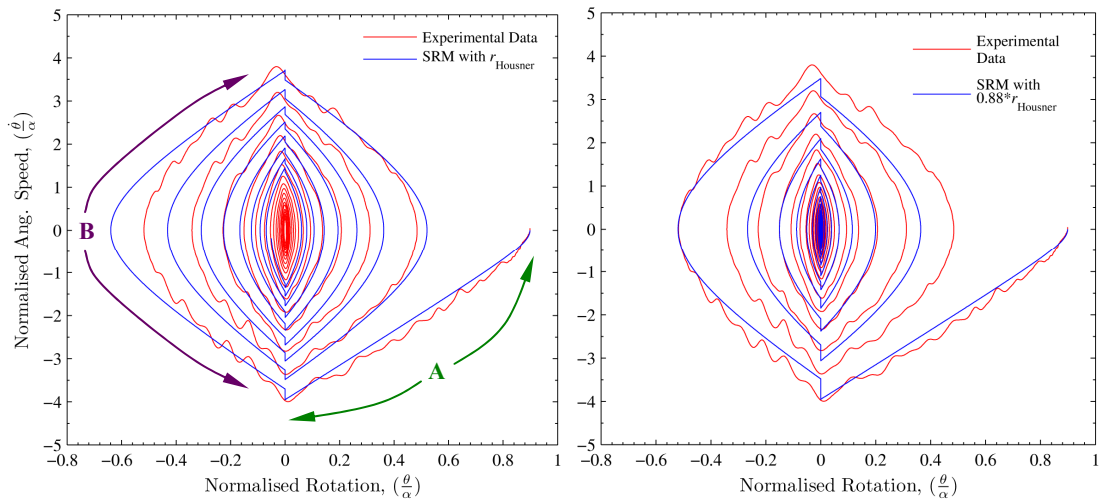


**Figure 3-6 – Typical experimental and numerically simulated results**

Figure 3-7 presents two phase diagrams of the same experimental test run and the two simulated results. In the phase diagrams, the angular speed is plotted against the angular rotation. This figure highlights that despite the unremarkable matching achieved by the standard SRM in the time domain, it simulated the angular velocity and rotation characteristics accurately, particularly during the smooth rocking phases<sup>4</sup> in the cycle.

The fact that the experimental data closely followed the simulated results during the first quarter cycle, confirms the governing differential equations of the SRM modelled the free rocking problem accurately prior to any impact. Then when the block returns to the upright position half a cycle later, at the predicted speed, it proves that energy is effectively conserved during any part of the cycle without impacts. These two regions are labelled A and B in the Figure 3-7 correspondingly.

However, it was intriguing to find that after the block was released, it did not reach the predicted peak rotation at the opposing side yet it attained the predicted speed by the next impact. This should have only been possible if the block reached the predicted peak rotation based on energy balance.



**Figure 3-7 – Phase diagram of the experimental and simulated time-history**

<sup>4</sup> The smooth rocking phase refers to the portion of the rocking cycle when the block is rocking smoothly about the same rocking pivot. It excludes the infinitesimal duration when the base of a rocking block is about to come into contact with the ground, the duration when the full base is in contact (i.e. when an impact is occurring), and the infinitesimal duration when the block returns to a rocking motion after an impact.

### 3.2.2 ENERGY CONTENT DURING A ROCKING CYCLE

In the SRM, a rigid block with an initial rotation begins to rock with a fixed gravitational potential energy,  $U^0$ . The energy is exchanged into kinetic energy,  $E_k$ , as the block rotates and accelerates. When the block reaches the upright position, an infinitesimal moment before an impact, it is said to have zero gravitation potential energy and maximum kinetic energy equalling to the potential energy it began with. Immediately after an impact, the kinetic energy is reduced to  $r \times U^0$  and the rocking motion begins again about a new rocking pivot, at a slightly reduced angular speed corresponding to the new energy content of the system,  $r \times U^0$ . The block then loses speed as it rocks further to the opposing peak, exchanging its kinetic energy with gravitational potential energy. When it reaches the peak rotation, the block again has maximum potential energy,  $U^1$ , and zero kinetic energy. Half of a rocking cycle is now complete at this point and the motion begins again as before but in the opposite direction. This is illustrated diagrammatically in Figure 3-8.

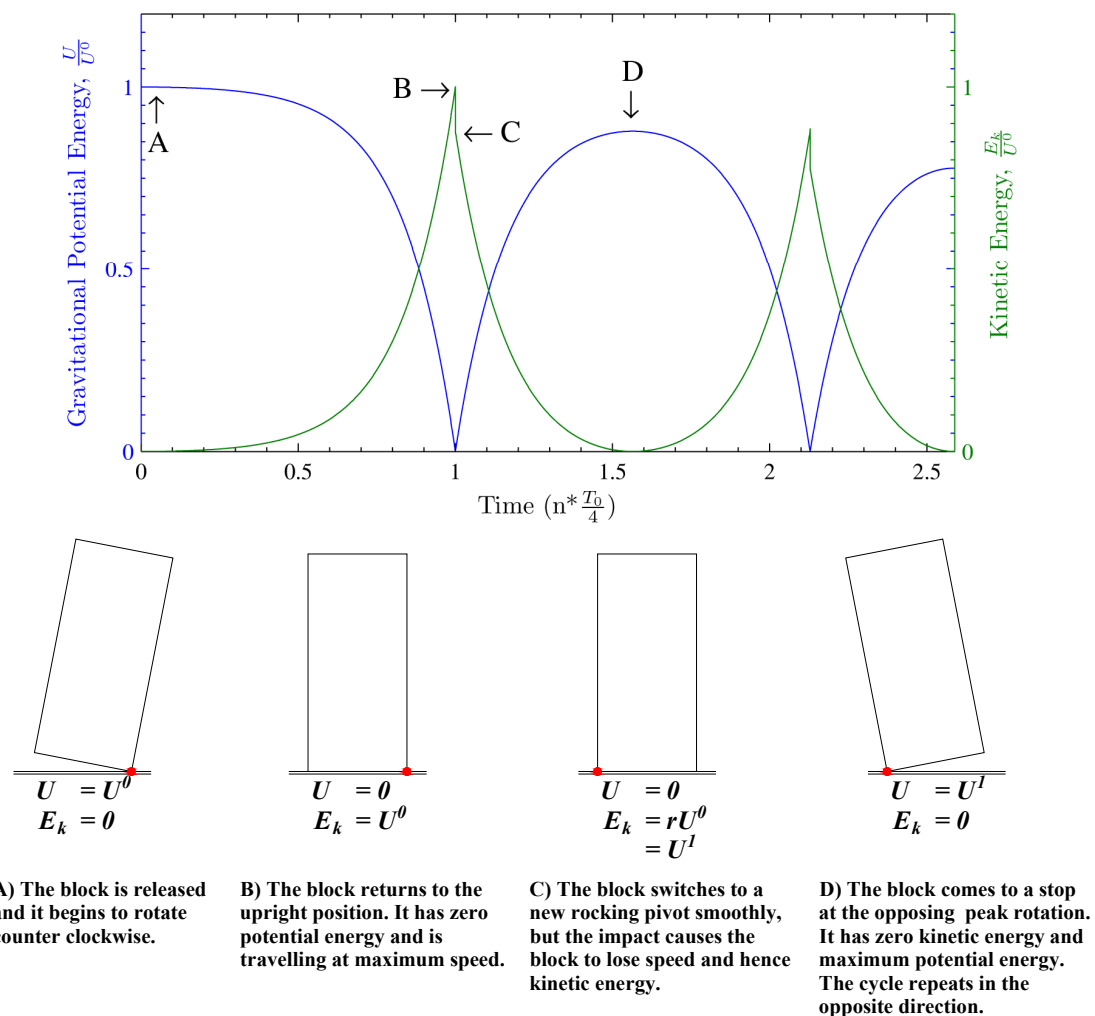


Figure 3-8 – Idealised energy content during a rocking cycle

Mathematically, the energy content of a rocking block can be evaluated by Equations 3-1 and 3-2 below.

$$E_k(t) = \frac{1}{2} I_o \dot{\theta}^2 \quad (3-1)$$

$$U(t) = mgR(\cos(\alpha - |\theta|) - \cos(\alpha)) \quad (3-2)$$

Moreover, if energy is conserved during the smooth phases of a rocking cycle, as assumed in SRM, the energy lost through an impact can be estimated by considering the energy of the system at the peak rotation of the cycle before and after the impact.

$$r = \frac{E_k^{i+1}}{E_k^i} = \frac{U^{i+1}}{U^i}$$

$$r = \frac{mgR(\cos(\alpha - |\theta_{peak}^{i+1}|) - \cos(\alpha))}{mgR(\cos(\alpha - |\theta_{peak}^i|) - \cos(\alpha))}$$

$$r = \frac{\cos(\alpha - |\theta_{peak}^{i+1}|) - \cos(\alpha)}{\cos(\alpha - |\theta_{peak}^i|) - \cos(\alpha)} \quad (3-3)$$

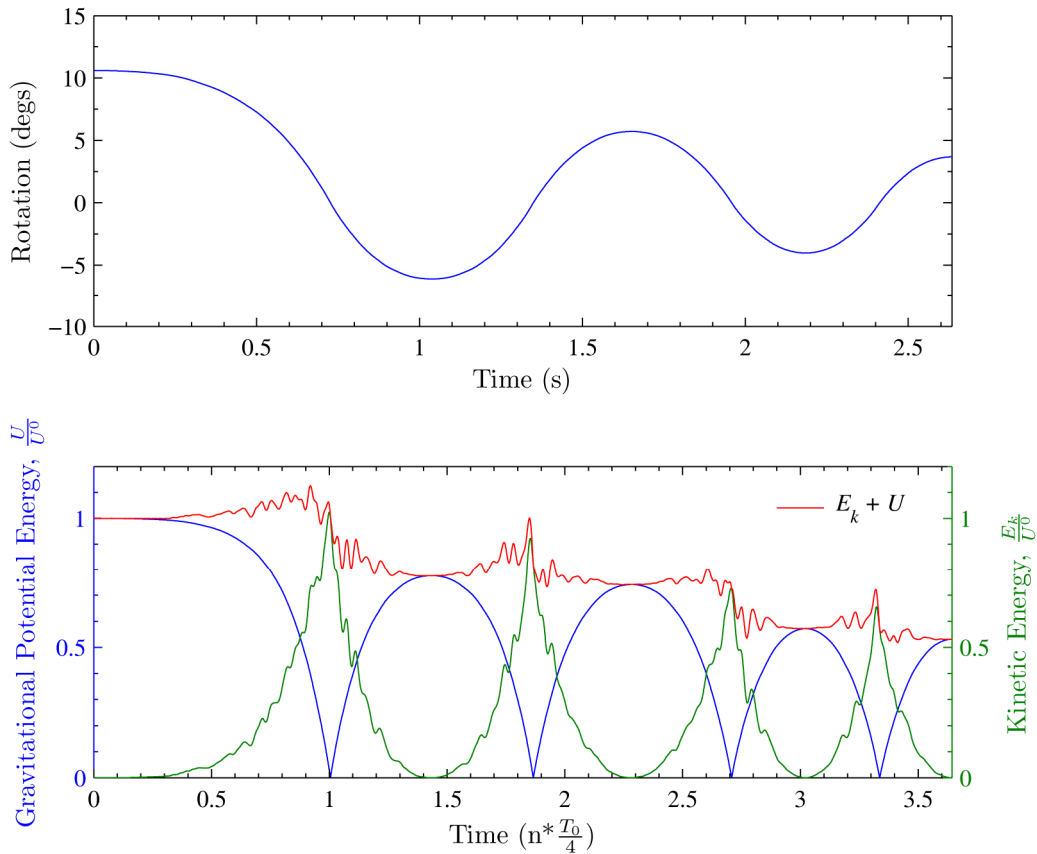
Where

$U^i$  = Potential energy content at the time of peak rotation before impact  $i$   
 $(\theta_{peak}^i)$  (A in Figure 3-8)

$E_k^i$  = Kinetic energy content just before impact  $i$  (B in Figure 3-8)

$E_k^{i+1}$  = Kinetic energy content just after impact  $i$  (C in Figure 3-8)

$U^{i+1}$  = Potential energy content at the time of peak rotation attained after  
 impact  $i$   $(\theta_{peak}^{i+1})$  (D in Figure 3-8)



**Figure 3-9 – Energy content of a rocking block during an experimental test run**

In contrast, the actual potential and kinetic energy content of the system for a typical test run is presented in Figure 3-9. Interestingly, it shows that the block at times possessed potential and kinetic energy greater than the theoretical maximum. Diagrammatically, the red line in Figure 3-9 should never have a positive gradient. A plausible explanation for this is the existence of experimental and data processing errors. This could include errors in establishing the properties of the block, sampling errors in the data acquisition and numerical processing errors in obtaining velocities from displacements.

The experimental data were re-examined carefully and the investigation subsequently ruled out experimental and numerical errors as the cause of the discrepancy. Key findings were that as the analyses examined the relative magnitudes of potential and kinetic energy, the effects of an error in the block properties were negligible. This was because such errors would be propagated consistently in the calculations of both quotients. Also many attempts were made to filter, up-sample and down-sample the displacement data to test whether there were errors in the numerical

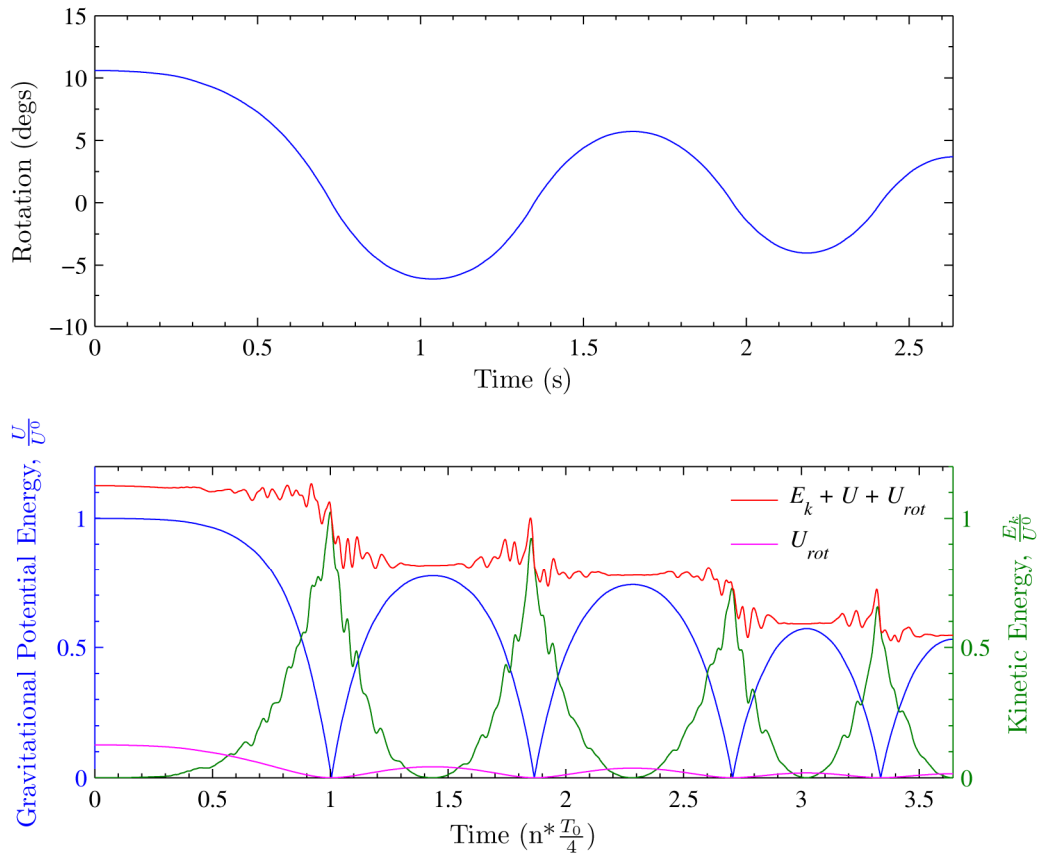
processing. These analyses all resulted in more or less the same velocity data and verified that the unexpected velocity data were results of actual physical processes.

This leaves us with the explanation that there are other energies in the system that are not yet accounted for. It is possible that the steel mechanism may have acted as a rotational spring to resist the motion of the rigid block. Accordingly, the energy in the spring would follow Equation 3-4 below:

$$U_{rot} = \frac{1}{2} k_{rot} \theta^2 \quad (3-4)$$

Assuming that the energy within the rotational spring is conserved, or in other words, energy is stored and released in the rotational spring without dissipation, the rotational spring constant can be approximated by substituting the peak excess energy and the rotation at which it occurs into Equation 3-4.

Figure 3-10 presents the amended results including the extra rotational spring potential energy. The figure shows that the “total” energy content has become noticeably more constant during the smooth rocking phase as expected theoretically. This did not eliminate the positive gradient of the “total” energy content, but this was probably because allowance was not made for the kinetic energy in the rotational spring system. Unaccounted kinetic energy from the rotational spring system may also explain the transient which exists in the energy content just before and after an impact.



**Figure 3-10 – Energy content of a rocking block including a hypothetical rotational spring**

### 3.2.3 SUPPORT AND IMPACT FORCES OF A ROCKING RIGID BLOCK

It is also possible to estimate the variation of support forces the rigid block experiences when it is in motion. Consider a rigid block in motion as shown in Figure 3-11. The centroid of the block moves in a circular motion about the rocking pivot. The centroidal acceleration ( $\ddot{u}_c$ ) is thus governed by rigid body motion mechanics, mathematically expressed in Equation 3-5.

$$\ddot{u}_c = \ddot{u}_g + \ddot{u}_{c/g} \quad (3-5)$$

Examining the expression above closely, the acceleration of the centroid with respect to the ground ( $\ddot{u}_{c/g}$ ) is the resultant of tangential and normal components of acceleration of the centroid in circular motion about the rocking pivot. This is summarised graphically in the vector diagram in Figure 3-11.

Making the substitution of  $\ddot{u}_{c/g}$  into Equation 3-5 and considering a horizontal ground acceleration, Equations 3-6 and 3-7 are derived to describe the centroidal accelerations in the  $x$  and  $y$  directions. These expressions for the resultant accelerations are then combined with Newton's second law of motion to form Equations 3-8 and 3-9.

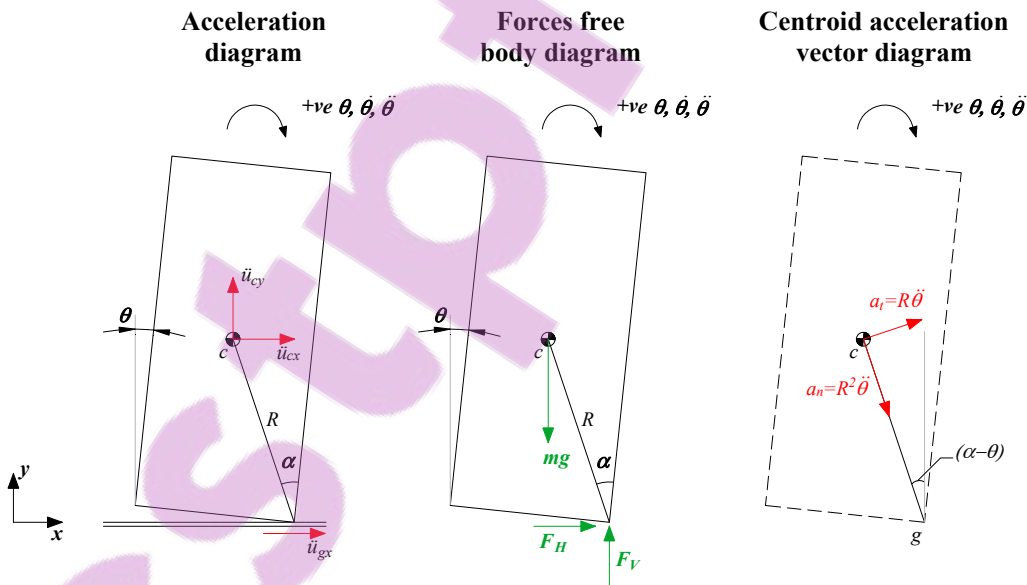
$$\ddot{u}_{cx} = \ddot{u}_{gx} + \text{sgn}(\theta) R \dot{\theta}^2 \sin(\alpha - |\theta|) + R \ddot{\theta} \cos(\alpha - |\theta|) \quad (3-6)$$

$$\ddot{u}_{cy} = -R \dot{\theta}^2 \cos(\alpha - |\theta|) + \text{sgn}(\theta) R \ddot{\theta} \sin(\alpha - |\theta|) \quad (3-7)$$

$$F_H = m(\ddot{u}_{gx} + \text{sgn}(\theta) R \dot{\theta}^2 \sin(\alpha - |\theta|) + R \ddot{\theta} \cos(\alpha - |\theta|)) \quad (3-8)$$

$$F_V = m(g - R \dot{\theta}^2 \cos(\alpha - |\theta|) + \text{sgn}(\theta) R \ddot{\theta} \sin(\alpha - |\theta|)) \quad (3-9)$$

These expressions enabled the calculation of the support force time-history using the angular rotation. Following this procedure, the horizontal and vertical support forces of a rigid rocking block were computed for a typical test run. The result is as shown in Figure 3-12 and provides a lower bound estimate of the impact force.

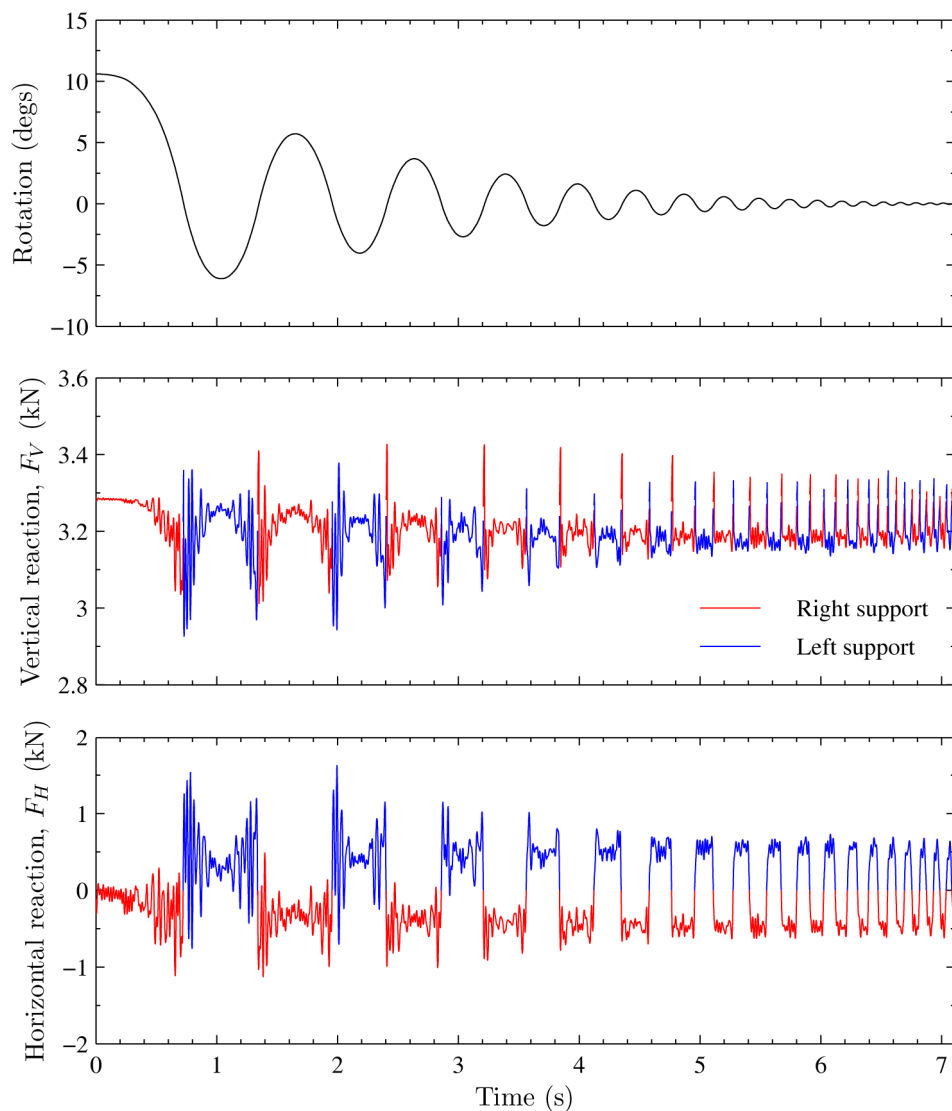


**Figure 3-11 – Accelerations and forces acting on a rigid rocking block; and the vector diagram of the centroidal accelerations**

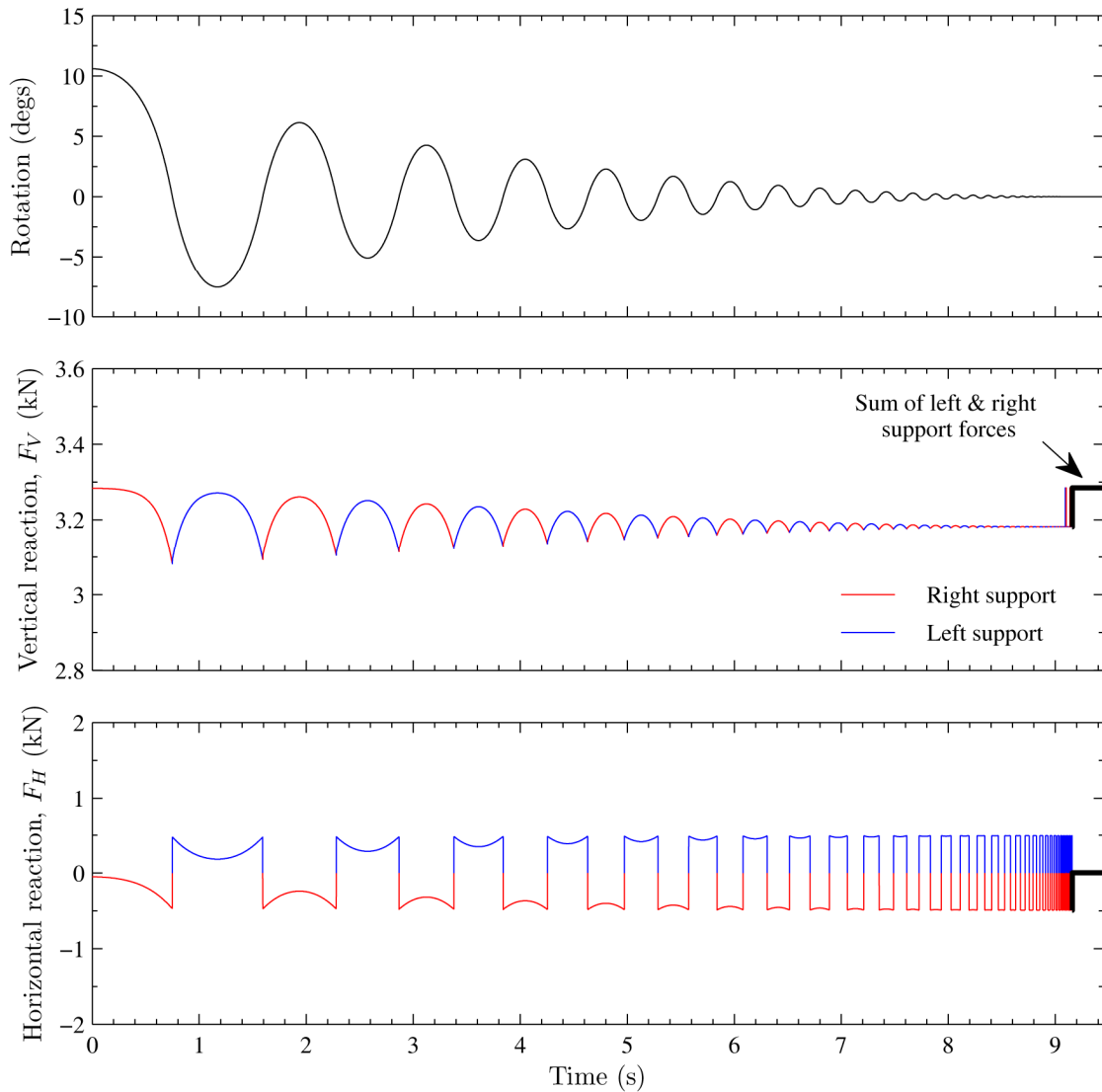
This procedure produced a lower bound estimate as the support forces were calculated using recorded displacements. The exact peak accelerations correlating to the effect of the impacts were not directly recorded. Even if accelerations were

directly measured, such sudden accelerations would be difficult to record accurately due to the limitations of data acquisition hardware and transducers. Further, in the current procedure, accelerations were estimated based on numerical differentiation, this had the effect of producing an average acceleration over a particular time step.

For comparison purposes, the theoretical support forces for a geometrically similar Housner rocking block were calculated in the same manner. The results are presented in Figure 3-13.



**Figure 3-12 – Support forces of a rocking block during an experimental test run**



**Figure 3-13 – Support forces of a simulated Housner rocking block**

It is clear from the figures that the experimentally derived forces resembled the numerically simulated results both in magnitude and form. The experimental results depicted in Figure 3-12 were noticeably more disorderly compared to the idealised numerically simulated results.

Considering the times when the rocking pivot changes from one corner to the other corner of the block, in Housner's SRM, angular momentum is conserved and the angular velocity is decreased in a stepwise fashion. This instantaneous change in angular velocity demands an infinite angular acceleration for an infinitesimal duration. This means that there must also be an infinitely large impact force to cause the infinite angular acceleration at every impact in Housner's SRM. If these were

included in Figure 3-13, they would be vertical lines in the horizontal and vertical support forces versus time plots.

In reality, the impact forces are finite and they act for a discrete duration. This allowed the forces to be detected as spikes in the experimental results as in Figure 3-12. The differences in the peak support forces for the presented test run is summarised in Table 3-1.

**Table 3-1 – Experimental and theoretical support forces for a typical test run**

Direction of support forces	Baseline peak value based on SRM (kN)	Experimental peak value (kN)	% Increase
Vertical	3.08	3.43	11.4
Horizontal	0.48	1.62	337.5

The baseline support force in Table 3-1 can be determined theoretically by substituting  $\theta = 0$  into the governing equation of motion (Equations 2-3) and the equations of the support forces (Equations 3-8 and 3-9).

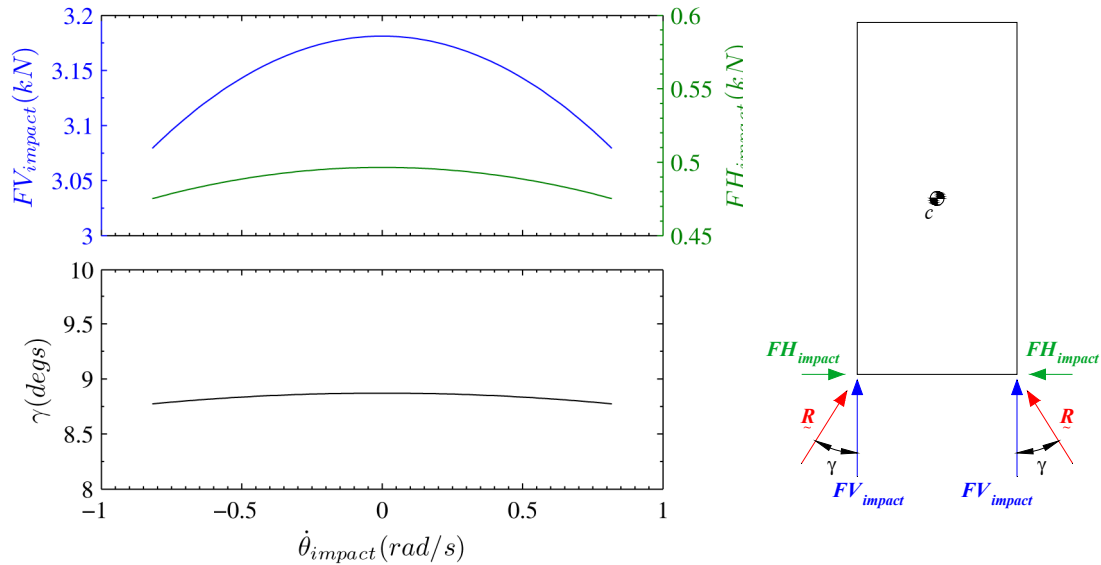
$$\ddot{\theta}_{impact} = -\text{sgn}(\theta) \frac{3g}{4R} \alpha \quad (3-10)$$

$$FH_{impact} = m \left( \text{sgn}(\theta) R \dot{\theta}_{impact}^2 \sin(\alpha) - \text{sgn}(\theta) \frac{3g}{4} \alpha \cos(\alpha) \right) \quad (3-11)$$

$$FV_{impact} = m \left( g - R \dot{\theta}_{impact}^2 \cos(\alpha) - \text{sgn}(\theta) \frac{3g}{4} \alpha \sin(\alpha) \right) \quad (3-12)$$

These equations stipulate that there is a direct relationship between the support forces (immediately before and after an impact) and the angular speed approaching the impact. These relationships, as presented graphically in Figure 3-14, illustrate that the support forces based on the SRM remain relatively constant for the probable range of angular impact speeds. It is also noted that the direction of the resultant support force is also effectively constant. The maximum foreseeable angular impact speed for this analysis is the speed which the block will attain when it is released just inside the static angle of instability,  $\alpha$ . The maximum impact speed is evaluated by assuming conservation of energy and is presented in Equation 3-13.

$$\dot{\theta}_{max,impact} = \pm \sqrt{\frac{3g}{2R} (1 - \cos(\alpha))} \quad (3-13)$$



**Figure 3-14 – Theoretical support forces just before and after an impact versus approaching angular speed**

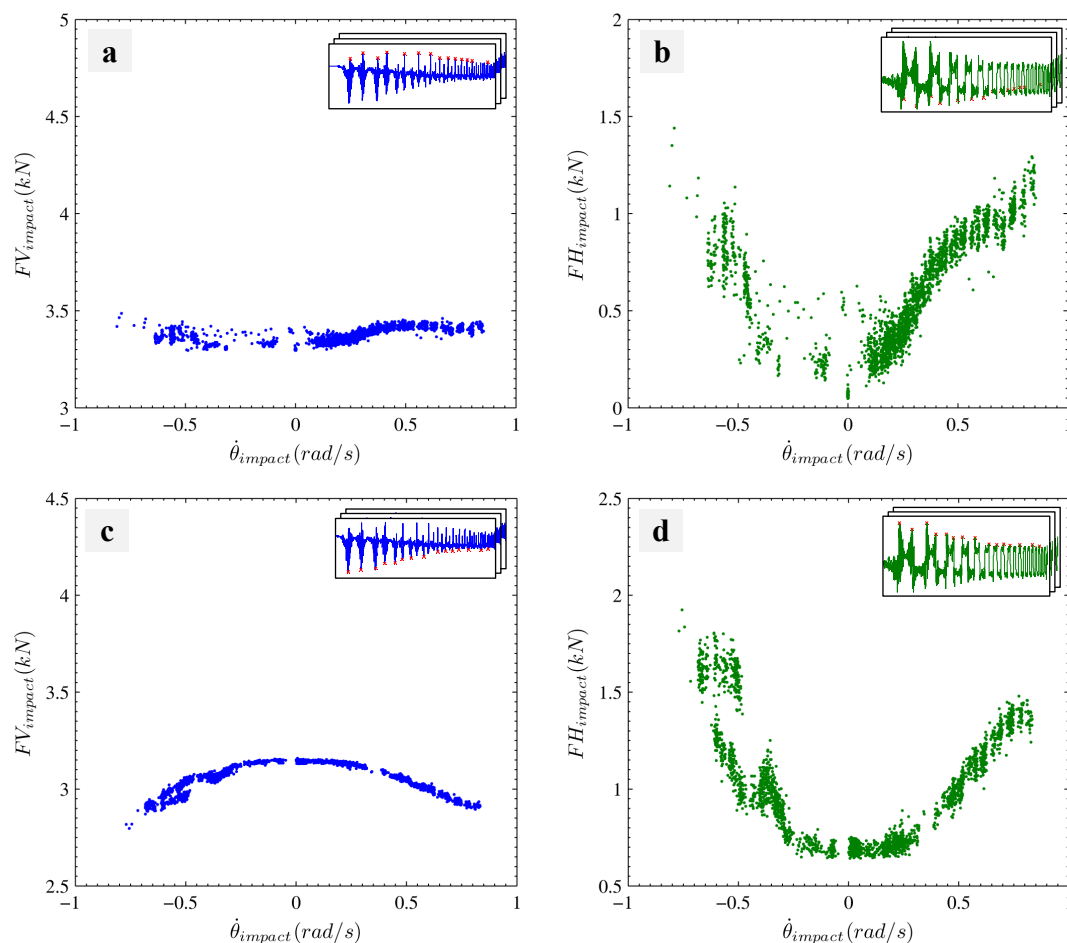
Figure 3-14 shows that the SRM requires the block experience a lower support force for a higher impact speed in order to preserve the smooth rocking assumption. This would be difficult to achieve as commonsense suggests that a higher impact speed leads to a larger impact force, which must then diminish to a lower force target to satisfy the theoretical relationship.

To investigate the relationship between the magnitude of the impact force and the approach velocity, the peak experimental support forces are collated from all the test runs. These peaks correspond to either the baseline values as predicted by the SRM or actual impact forces captured during the experiments. Figure 3-15 shows these forces plotted against their corresponding approach angular speeds. Figure 3-15 contains 4 sub-figures which are separate collections of the maximum and minimum peak values of the horizontal and vertical support forces across all test runs. A diagram in the top right corner of each sub-figure signals the force quantity which is collated in that particular sub-figure.

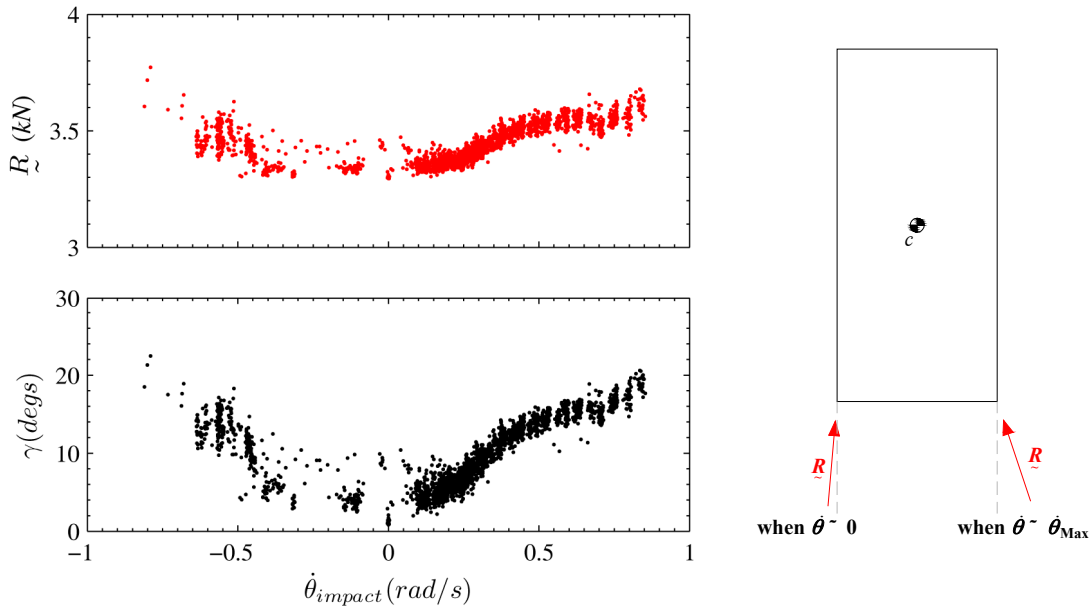
Figure 3-15c plots the lower peaks of the experimental vertical support force against their approaching angular speeds. These values correspond to the baseline theoretical values predicted by Equations 3-11 or as plotted in Figure 3-14. Figure 3-15c shows the experimental baseline vertical forces closely matched the theoretical values and thus confirms the block exhibited generally smooth rocking motion.

Figure 3-15a plots the upper peaks of the experimental vertical support forces against their approaching angular speeds. These values are rough measures of the vertical component of the peak impact forces during the experiments. The figure highlights that the vertical impact forces remain fairly constant and insensitive to impact speed. This is not the case for the horizontal component of the impact force which appears to remain constant for only small impact speed and then increases linearly with larger impact speed. This is illustrated in Figure 3-15b and Figure 3-15d.

Now if we consider the resultant of the impact force by combining the vertical and horizontal components from Figure 3-15a and Figure 3-15b, it shows that in general the resultant impact force increases only slightly with impact, but more importantly, the direction of the resultant becomes more horizontal as the impact speed is increased. This is shown in Figure 3-16.



**Figure 3-15 – Experimental support forces just prior and after an impact versus approaching angular speed**



**Figure 3-16 – Magnitude and direction of the impact force versus approaching angular speed**

Another interesting observation from the free rocking time-histories is that when a rocking block is about to come to a complete stop, the horizontal support force chatters between the positive and negative extreme values, while the vertical support force settles to a value less than the full weight of the system. This is apparent in Figures 3-12 and 3-13.

These force limits can be derived mathematically by computing the limits of Equations 3-11 and 3-12 as the angular speed tends to zero. The expressions for these force limits are presented as Equations 3-14 and 3-15 and they closely matched the experimental results.

$$FH_{impact} \Big|_{\lim \dot{\theta} \rightarrow 0} = \frac{3mg}{4} \alpha \cos(\alpha) \quad (3-14)$$

$$FV_{impact} \Big|_{\lim \dot{\theta} \rightarrow 0} = mg \left( 1 - \frac{3}{4} \alpha \sin(\alpha) \right) \quad (3-15)$$

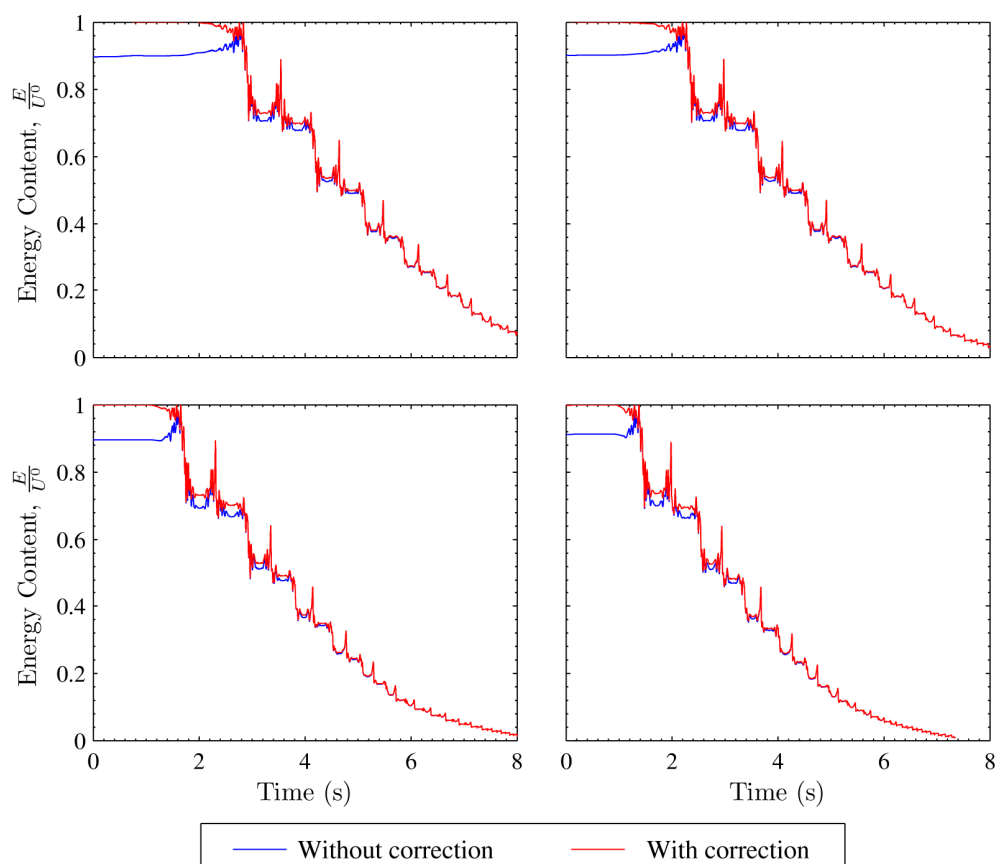
### 3.2.4 ENERGY DISSIPATION DUE TO IMPACTS

Having evaluated the magnitudes of the impact force during the experiments, it is also interesting to consider whether energy dissipation is a function of the magnitude of the impact force, the direction of the impact force and the speed of the impact. This analysis will adopt the use of the SRM's coefficient of restitution as a

measure of the energy dissipation rather than the absolute magnitude of energy before and after an impact.

In Figure 3-10, it is evident that the total energy content decreases noticeably only at the times of the impacts for a typical rocking cycle. This supports the SRM assumption which states that energy is conserved during the smooth rocking phases and is only dissipated at the time of impacts. Taking advantage of this assumption, the energy dissipation due to an impact can be evaluated by using the total energy content at points other than the time of impact as per Equation 3-3.

However, as discovered previously the experimental results required a rotational spring to correct for unexplained excess energies. For illustration, Figure 3-17 below shows the effects of this correction on the total energy content for four experimental test runs. This figure also highlights that the amount of energy dissipation for impacts on the left edge is markedly different to impacts on the right edge. It is also shown that the energy correction typically has little effect on the coefficient of restitution calculations except for the first cycle.



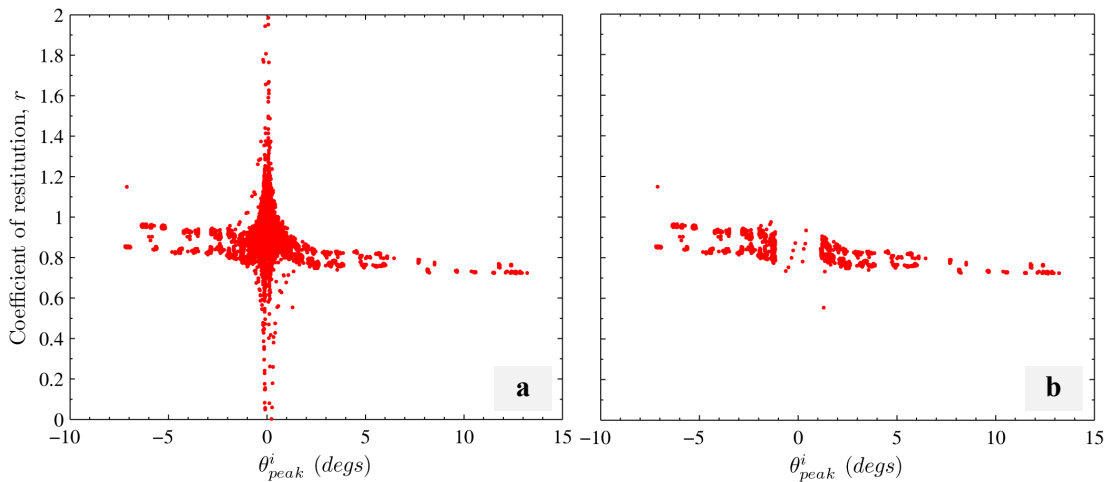
**Figure 3-17 – Effects of energy correction for four experimental test runs**

Despite the trivial nature of the energy correction, Equation 3-3 is modified to incorporate the effect of the hypothetical rotational spring for completeness. Combining Equation 3-3 and Equation 3-4, a new expression is derived below for the calculation of the coefficient of restitution from the experimental data.

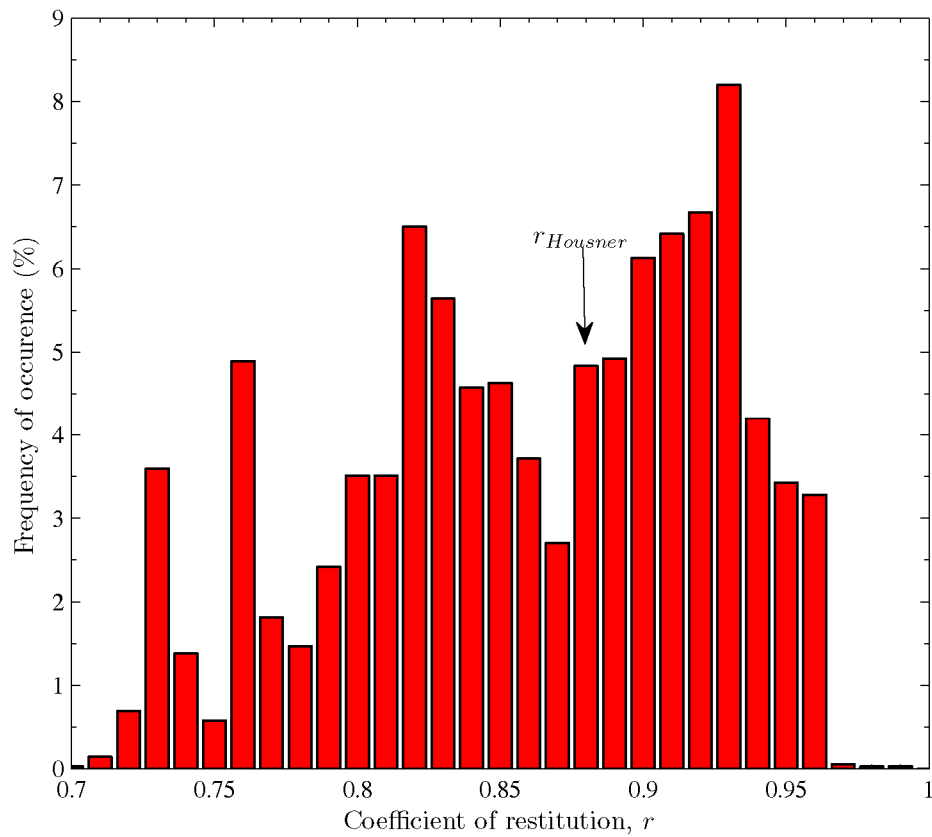
$$r = \frac{mgR \left( \cos(\alpha - |\theta_{peak}^{i+1}|) - \cos(\alpha) \right) + \frac{1}{2} k_{rot} (\theta_{peak}^{i+1})^2}{mgR \left( \cos(\alpha - |\theta_{peak}^i|) - \cos(\alpha) \right) + \frac{1}{2} k_{rot} (\theta_{peak}^i)^2} \quad (3-16)$$

The above expression, just as Housner's expression for  $r$ , is prone to hyperbolic error magnification as the divisor is reduced. Accordingly, experimental data points with energy content less than six joules are excluded in the subsequent analyses. Six joules is approximately the same energy content as the block being displaced by 1.1 degree off vertical or 10% of the  $\alpha$ . Figure 3-18 presents two plots of experimentally determined  $r$  values against the  $\theta_{peak}^i$  for the purpose of illustrating that trends are not affected by the filtering.

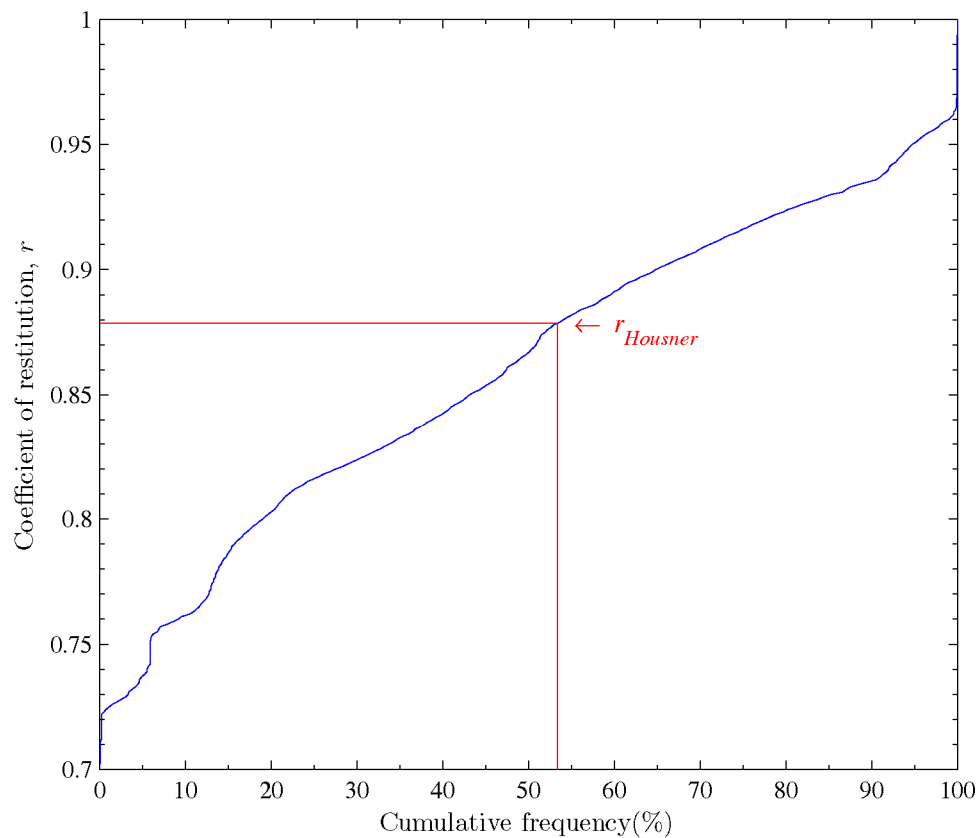
Closely examining Figure 3-18 which shows the  $r$  value against the peak rotation in the cycle preceding an impact, it appears that there are three distinct bunches of  $r$  values, two for impacts originating from negative rotations and another from a positive rotation origin. This is better illustrated in Figure 3-19 which plots the frequency distribution of the  $r$  values for the experimental test runs. Figure 3-20 plots the cumulative distribution frequency of the experimental  $r$  values and it reveals that the overall average experimental  $r$  value is fairly close to Housner's prediction.



**Figure 3-18 – Coefficient of restitution versus peak rotation before impact a) with all data points b) with small rotation data points omitted**

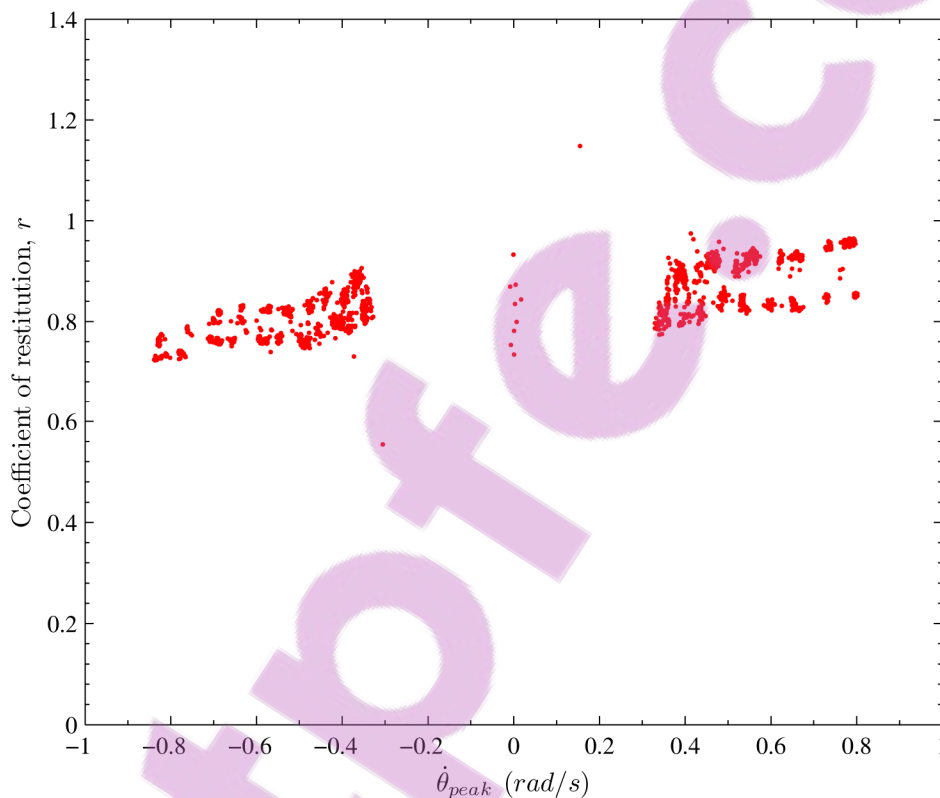


**Figure 3-19 – Frequency distribution of the coefficient of restitution**



**Figure 3-20 – Cumulative frequency distribution of the coefficient of restitution**

Following the statistical analyses, the experimentally determined  $r$  values are plotted against the approaching impact speed in Figure 3-21. The plot appears to show a linear relationship between the  $r$  values and the approach angular impact speed. This is highly unexpected as the SRM predicts  $r$  to be a constant value irrespective of the angular impact speed. In addition, one also expects the behaviour of the system to be symmetrical. It is peculiar that increasing angular impact speed in the negative direction results in higher energy dissipation while increasing angular impact speed in the positive direction yields lower energy dissipation.



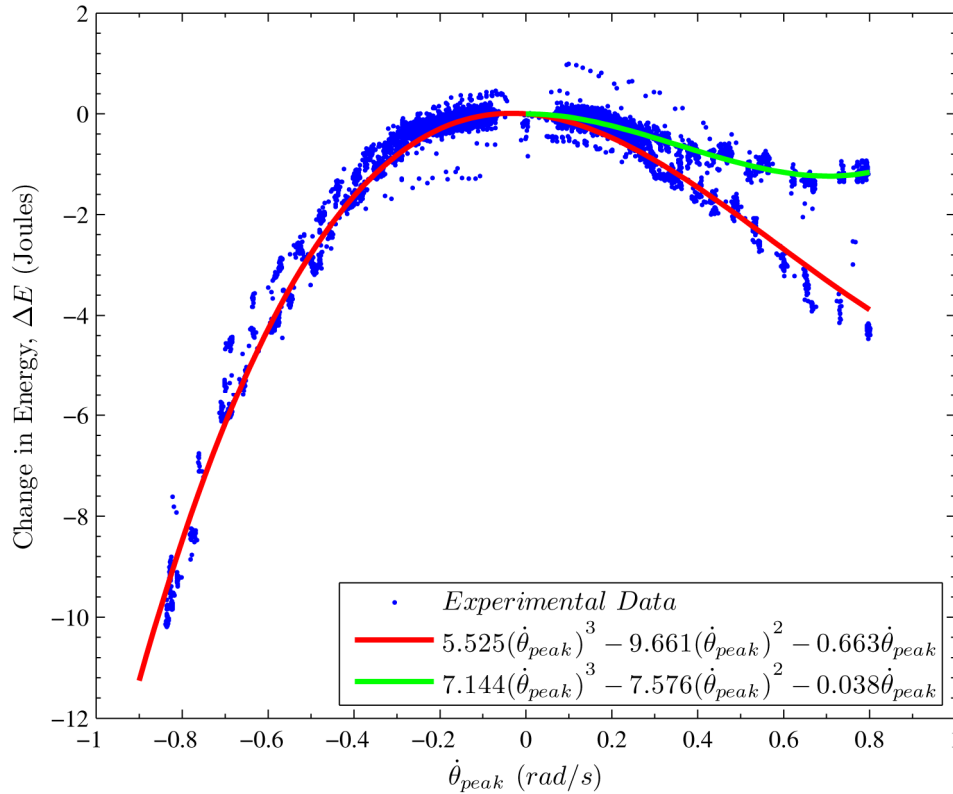
**Figure 3-21 – Experimental coefficient of restitution against impact speed**

To confirm the observations are not a result of data manipulations errors, the absolute energy reduction was plotted against the impact speed using all available data points in Figure 3-22.

This revealed two distinct energy loss trends against the angular impact speed, one which covered the entire impact velocity range and one for impacts on the “right” edge only (impacts with positive angular speed). Two equations have been fitted for these two trends and they are,

$$\Delta E = 5.525(\dot{\theta}_{peak})^3 - 9.661(\dot{\theta}_{peak})^2 - 0.6663(\dot{\theta}_{peak}) \quad (3-17)$$

$$\Delta E = 7.144(\dot{\theta}_{peak})^3 - 7.576(\dot{\theta}_{peak})^2 - 0.0381(\dot{\theta}_{peak}) \quad (3-18)$$



**Figure 3-22 – Absolute change in energy content against angular impact speed**

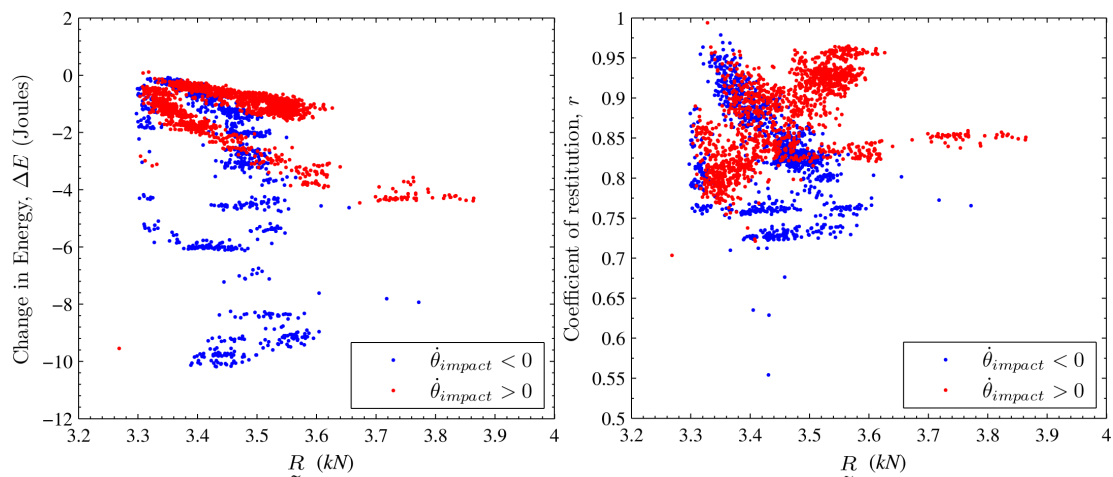
The two clear trends in Figure 3-22 confirm that the peculiar relationship in Figure 3-21 is no accident. Impacts on the left edge indeed dissipate more energy than impacts on the right edge. Further, energy dissipation for impacts on the right edge follows either Equations 3-17 or 3-18.

A plausible explanation for this asymmetrical behaviour is the asymmetrical design of the steel mechanism. This leads to a different impact characteristic for impacts on the left edge compared to impacts on the right edge. It should be noted that the asymmetrical behaviour cannot be attributed to frictional type losses in the mechanism, as a cycle for calculating the energy loss for both positive and negative impact speed undergoes the same rotations in the positive and negative domain.

Figure 3-23 presents the absolute and relative energy dissipation against the magnitude of the impact force. It appears no clear relationship can be inferred between energy dissipation and the impact force.

This is not surprising as energy dissipation of a free rocking block arises from the requirement of conservation of angular momentum of the system according to the SRM. There is never any consideration of the local impact force except that impacts are perfectly inelastic. Thus if perfectly inelastic impacts exist, in other words the rocking block does not bounce on impact, conventional impact mechanics knowledge is not directly applicable to the rocking problem.

This finding indicates that the steel mechanism may have affected the conservation of angular momentum at the point of pending impact, which has resulted in the asymmetrical energy dissipation characteristics in the current experiment.



**Figure 3-23 – Change in energy content against magnitude of the impact force**

### 3.3 SUMMARY OF FINDINGS

This study collated results from over 430 free rocking tests on a concrete block with an aspect ratio of 5. At first glance, the experimental results appeared to exhibit classic rocking traits. The rocking block pivoted from one rocking edge to another seemingly continuously, creating a smooth rotation time-history. The periods of vibration for a quarter of a rocking cycle were shown to be amplitude dependent and varied in close accord with Housner's and Muto's prediction formulas. The experimentally established periods were typically within 10% of the prediction. This study also attempted to simulate the experimental rotation time-history by numerically

integrating the governing differential equation of motion in the SRM. The matching was very accurate for the first quarter cycles for all test runs, or in other words, for the time between the block release from an initial rotation and just before the first impact. The matching deteriorated rapidly after the first impact and no single coefficient of restitution was able to achieve an overall satisfactory fit. This confirmed that the SRM's governing differential equation of motion approach would be suitable for modelling the smooth rocking phases of the free rocking motion, but would ultimately be let down by the modelling of the impacts using the coefficient of restitution approach. Accurate modelling of the behaviour during the impact was crucial to an accurate matching of results in the time domain as the free rocking problem is history dependent.

Phase diagram analyses of the experimental results revealed that the steel mechanism may have unintentionally participated in the rocking motion. A hypothetical rotational spring was introduced to account for the apparent excess energy available at the first impact of each test run. This led to ideologically consistent energy content and the corrections only had trivial effects on the later energy dissipation calculations.

This study also derived the differential equations of motion of a rocking block in Cartesian coordinates. This permitted the block's support forces to be back calculated from the recorded rotational time-history. These analyses again confirmed that the block conformed to the SRM during the smooth rocking phases. This was illustrated by the support forces resembling the theoretical predictions in form and magnitude during the smooth rocking phases. This agreement extended to how the vertical support force just before an impact varied against the angular impact speed. This study also derived expressions for the support forces as a block came to rest and these were shown to correspond well with the experimental results.

Through the back calculation approach, it was also possible to obtain an estimate of the impact force at each impact. Collating and analysing the forces from the thousands of impacts, showed that the impact force increased slightly as the angular impact speed increased and the direction of the impact force varied linearly with angular impact speed.

Statistical analyses revealed that the experimentally established coefficient of restitution varied between 0.72 and 0.97, with 53% of the impacts achieving an  $r$  value below that predicted by Housner's formula ( $r_{Housner} = 0.89$ ). The experimental  $r$  values mainly fell into three distinct bunches, namely 0.73-0.76, 0.8-0.86 and 0.90-0.95.

The analyses also showed that there was a convincing relationship between the energy dissipated by an impact and the angular impact speed. This relationship was much more evident when the energy dissipation was evaluated as absolute magnitudes rather than a ratio such as the coefficient of restitution,  $r$  parameter. There was also no apparent relationship between the impact force and the amount of energy dissipated. This was not surprising as the energy dissipation of a free rocking block originated from the requirement of conservation of angular momentum rather than conventional impact mechanics.

In conclusion, the experiments have demonstrated that despite the very simple appearance of free rocking motion, there exist many highly complex interactions. Even very slight departure from the assumptions of the SRM makes the exact time-history response of a simple block system unpredictable. The well-intended addition of a steel mechanism to prevent sliding has introduced a constraint that may have substantially altered the free rocking body system's behaviour. Nevertheless, this highlighted that it is easy to recreate SRM-like traits, but because of the sensitivity of the free rocking problem it raises doubt as to whether the conditions of SRM are ever satisfied. Also, despite the short duration of impacts when they are compared to the course of the rocking motion, the experiments have found them to have a significant effect on the overall predictability of the rocking systems. A number of features were identified for impacts during the analyses, but the understanding of many aspects of them remains incomplete.

# Chapter 4

---

## CONTROLLED ROCKING SYSTEMS

---

This chapter investigates the behaviour of controlled rocking objects under free vibration decay and when subjected to base excitation. The experimental data for this chapter originate from the work by Dr. Gavin Wight as part of his doctoral study (Wight 2006). Wight investigated the seismic performance of post-tensioned concrete masonry (PCM) walls, with a focus on developing a displacement-based design procedure for these walls in a high seismicity environment. The raw data have been post-processed for the purposes of this thesis work.

This chapter highlights the importance of the shift in rotation centre as a controlled rocking object displaces. It will be demonstrated that an accurate estimate of the rotation centre location is central to the understanding the dynamic characteristics of a controlled rocking system. The inability to model the energy dissipation of a controlled rocking system remains as the major obstacle to attaining an accurate time-history response prediction.

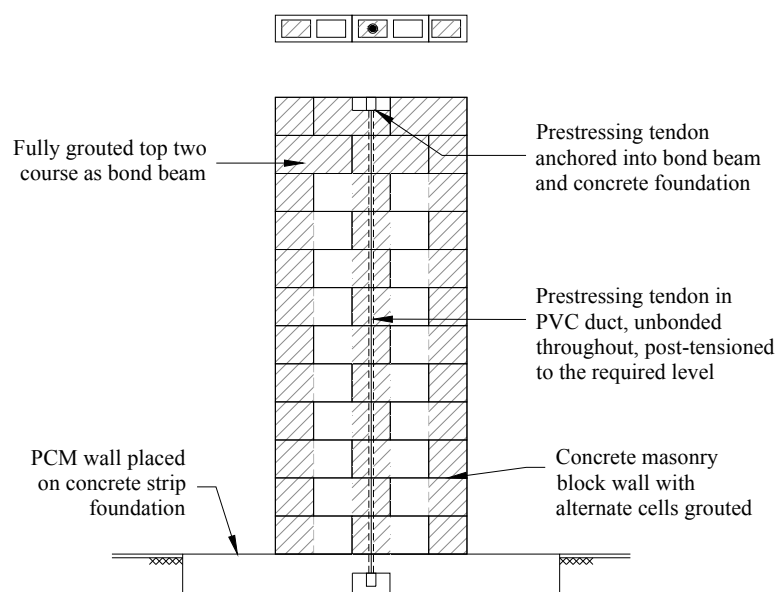
### 4.1 INTRODUCTION

The PCM wall is a relatively new type of construction which takes advantage of controlled rocking. As explained in Chapter 2, the concept of controlled rocking is material independent. It enhances the performance of a normally rocking system by increasing its self-centering capability by the addition of vertical prestress.

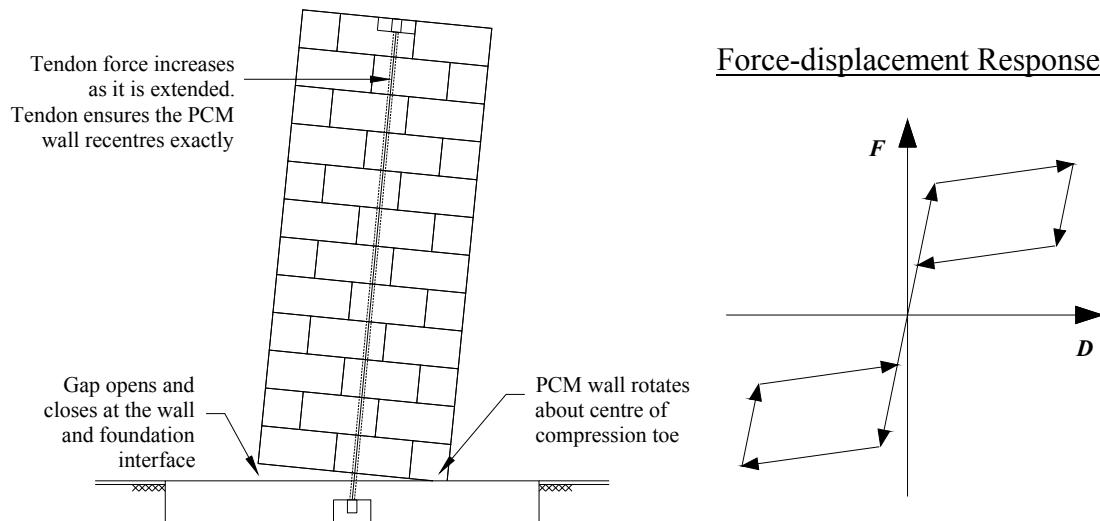
In a PCM wall, all or a selected number of masonry cells are grouted. Post-tensioned tendons are inserted into vertical ducts and are typically anchored into the foundation and the bond beam along the top of the wall. The ducts ensure the tendons remain unbonded throughout their entire length maximising their extension capability and preventing any stress transfer to the masonry units. A schematic of a typical PCM wall is presented in Figure 4-1.

Under low lateral in-plane loads, a PCM wall behaves as a fixed base shear wall (Kurama et al. 1999a). When the lateral load exceeds a critical value, a gap opens at the interface between the wall base and the foundation. The PCM wall then subsequently rocks non-destructively on this interface as per a free standing rocking wall. This mechanism is illustrated diagrammatically in Figure 4-2a.

As the PCM system uplifts or “rocks”, tensile stresses are isolated to the post-tensioned tendon and are not transferred to the concrete masonry wall due to the base opening. As a result the damage, if any, is typically confined to crushing of the rocking pivots and yielding of the prestressing tendon. Furthermore, the prestressing tendon forces the PCM wall to re-center to the origin, unlike a free standing rocking wall which has a tendency to “walk”, and thus minimises any residual displacements. The prestressing tendons also serve as a failsafe measure to prevent a controlled rocking element from overturning. A PCM wall exhibits the hallmark flag shaped, force versus displacement characteristics of controlled rocking as shown in Figure 4-2b.



**Figure 4-1 – A typical PCM wall construction**



**Figure 4-2 – a) An uplifting PCM wall, b) Distinctive force-displacement characteristics of a PCM wall**

## 4.2 EXPERIMENT DETAILS

The Wight study subjected 7 full-scale single storey PCM walls to a range of in-plane base excitations using the shake table at North Carolina State University. This was followed by a shake table test of a single storey PCM structure. Figure 4-3 presents photographs of an example single in-plane wall test and the test on the PCM structure. The current study focuses on the tests conducted on the wall depicted in Figure 4-3a.

The geometry of the PCM wall for the current study is summarised in Figure 4-4. The PCM wall was constructed from 6” concrete masonry units with alternate masonry cells grouted. The concrete masonry units had an approximate density of  $1600 \text{ kg/m}^3$ . Compression tests on prism specimens and mortar cylinders, 36 days after grouting, revealed an average masonry crushing strength of 20.8 MPa and a mortar compression strength of 12.1 MPa.

Two reinforcing steel bars were embedded horizontally into the top two courses of the fully grouted concrete masonry blocks to act as a bond beam. This was implemented to reflect typical construction and to maintain consistency with the other wall specimens. A nominally 15 mm diameter high strength post-tensioning tendon installed inside a centrally located PVC duct in the wall panel provided vertical prestress in the wall panel.



Figure 4-3 – a) Typical single PCM wall specimen and b) PCM structure on the shake table (Source: Wight 2006)

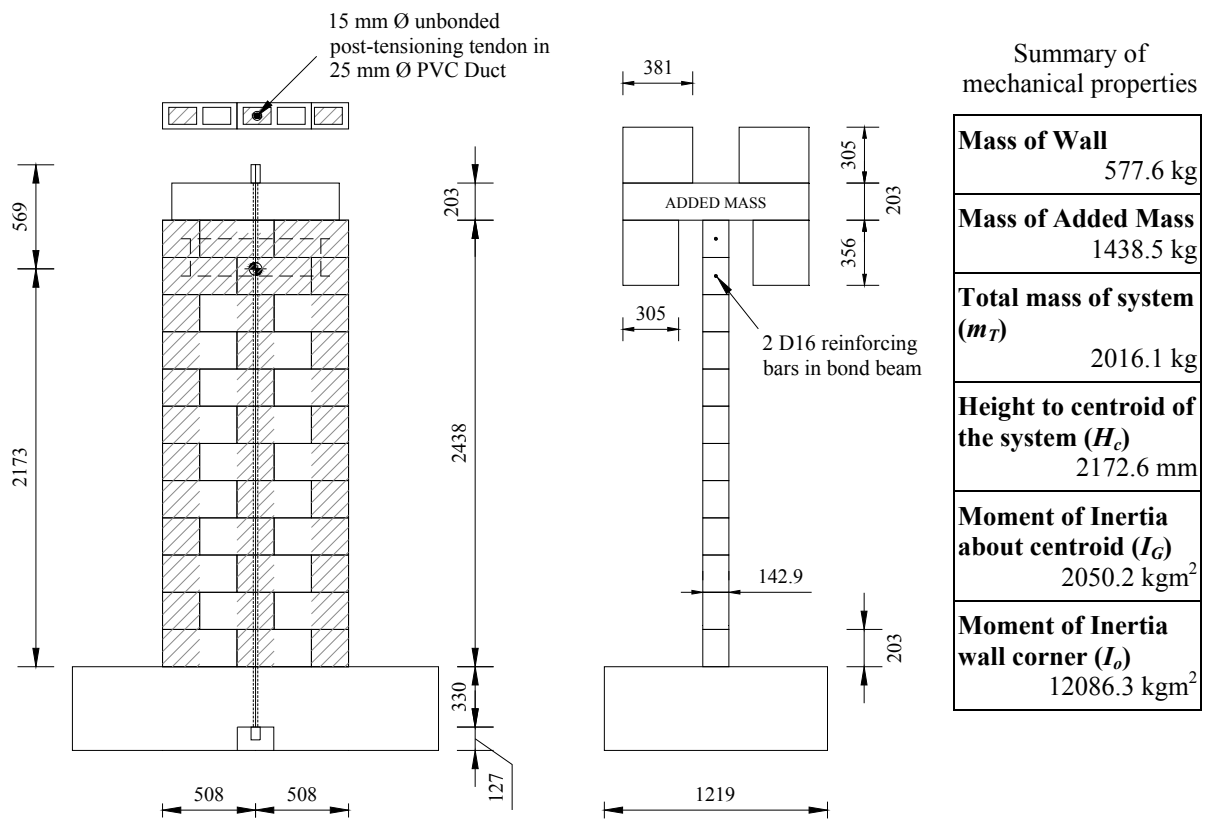


Figure 4-4 – Geometry of the PCM wall specimen

The masonry cell containing the PVC duct was grouted to provide lateral restraint to the tendon and increase the out-of-plane strength of the wall. The tendon itself remained unbonded throughout the entire height of the wall, between an anchor cast into the foundation block and an anchor near the top of the wall, 3100 mm apart.

The tendon had a specific rupture strength of 195 kN ( $f_{pu} = 1100$  MPa) and a yield strength of 160 kN ( $f_{py} = 900$  MPa). The tendon had an effective cross-sectional area of 177 mm<sup>2</sup> and was post-tensioned to 75 kN before the first shake table test. This was left unchanged for the first 6 tests and not readjusted until the final series of shake table tests when it was increased to 110 kN.

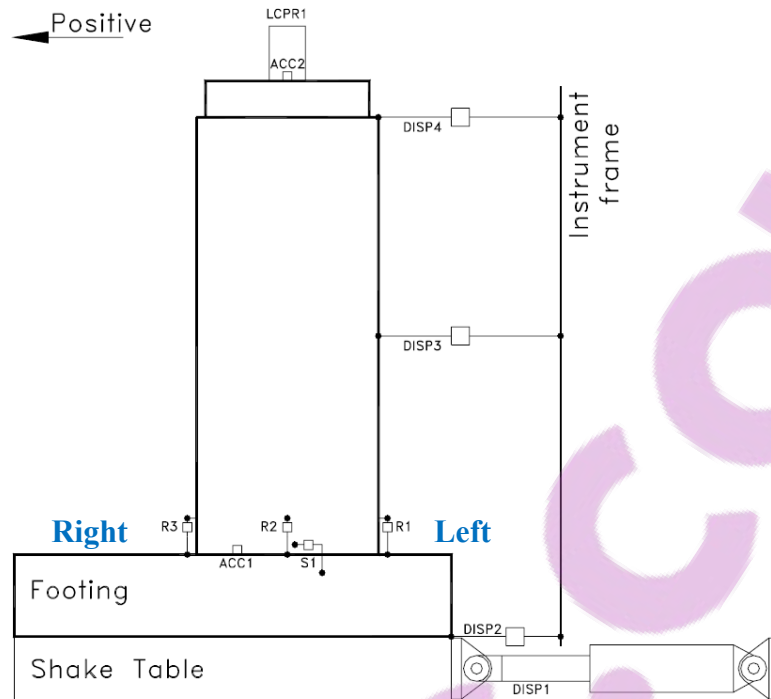
Finally, as the PCM walls would typically support a roof, additional mass in the form of custom concrete mass blocks were attached to the top of the wall to simulate a heavy residential roof with a tributary area of 9 m<sup>2</sup>. This ensured the PCM wall had a realistic seismic mass for the shake table test to simulate a wall in service. The added mass provided only small increase to the axial load of the wall as the post-tensioning tendon already provided a high level of prestress.

### **4.3 INSTRUMENTATION AND DATA ACQUISITION**

PCM wall systems are designed to endure large base excitations with damage isolated to the prestressing tendon with minimum effects to the walls themselves. Failures are defined by either 1) yielding of the prestressing tendon, 2) crushing of the compression rocking toe or 3) lateral displacement exceeding that permitted by design code or that can be accommodated by adjoining structural and non-structural components.

With the failure mechanisms in mind, the transducers were set up to focus on capturing the tendon stress variation, wall behaviour near the compression toe area and the overall drift of the system. This setup is also ideally suited for analysing the dynamic behaviour of the system.

A diagram of the instrumentation plan is presented in Figure 4-5. A variety of linear potentiometers and string potentiometers measured the local and overall displacements of the wall. Two accelerometers and a load cell measured the table and top of wall accelerations and tendon force respectively. A data acquisition system subsequently recorded the measurements digitally at a sampling rate of 200 Hz.



### Legend

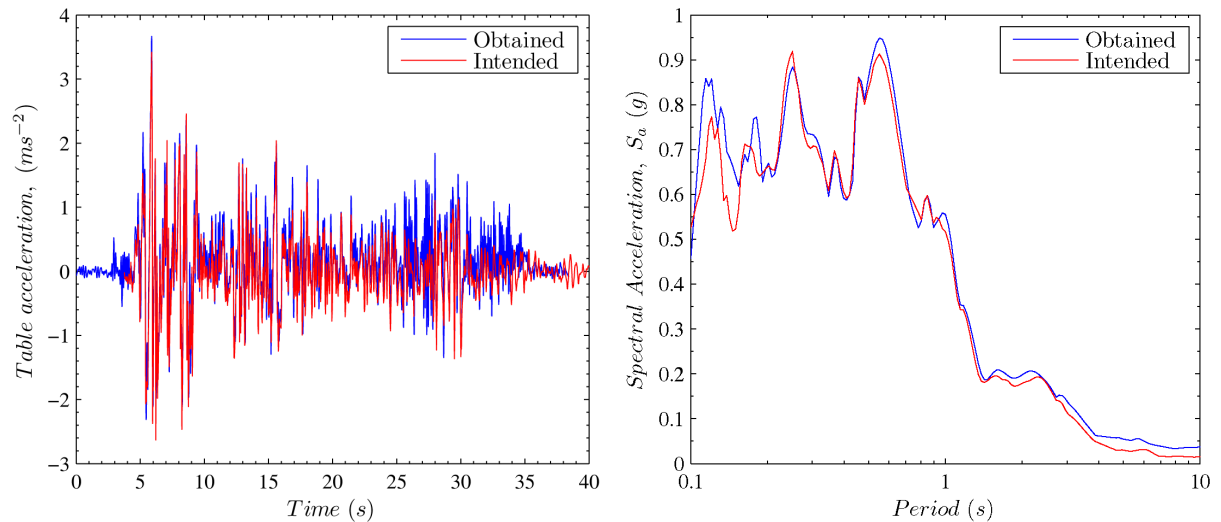
Prefix	Measurements	Type of transducer
DISP	Overall displacements	String potentiometers
ACC	Accelerations	Accelerometers
R	Rocking uplifts	Linear potentiometers
S	Sliding	Linear potentiometers
LCPR	Prestress force	Load cell

Figure 4-5 – Instrumentation plan for the shake table test (Source: Wight 2006)

## 4.4 SHAKE TABLE MOTION SELECTION

The input records were selected to cover a broad range of earthquake events. The records came from historic earthquake events which are familiar to the earthquake engineering community. Care was taken to ensure the input records covered a range of seismological signatures such as moment magnitudes, peak ground acceleration, frequency content, duration and the presence of forward directivity.

The amplitudes of selected records were scaled to represent a variety of shaking levels. Furthermore, the time ordinate for a number of the records were scaled down to ensure they fitted within the stroke limits of the shake table. In these instances, the walls were effectively subjected to new earthquake records. Thus, similitude requirements were not considered as the results were not designed to reflect the behaviour from the original earthquake record. The current study focuses on a subset of the full range of input records used in Wight's experiments. A summary of the shake table test runs considered and their input records is presented in Table 4-1.



**Figure 4-6 – A comparison of obtained and intended shake table motion for Run 2 (El Centro-A1-T1)**

**Table 4-1 – Summary of input motions**

Run	Source Earthquake	Date	PGA* (ms <sup>-2</sup> )	PGV* (ms <sup>-1</sup> )	Acc Scale	Time Scale	Prestress (kN)
1	El Centro – 180°	18/05/1940	2.364	0.167	0.5	1	75.7
2	El Centro – 180°	18/05/1940	3.668	0.324	1	1	75.9
3	Tabas – 344°	16/09/1978	5.354	0.412	1	0.38	75.8
4	Northridge – Sylmar 360°	17/01/1994	8.273	0.743	1	0.6	75.7
5	None (Free vibration)	---	0	0	1	1	75.6
6	Valparaiso – Lollole 10°	03/03/1985	6.987	0.408	1	1	75.3
7	El Centro – 180°	18/05/1940	3.659	0.324	1	1	110.8
8	Tabas – 344°	16/09/1978	5.568	0.422	1	0.38	110.9
9	Northridge – Sylmar 360°	17/01/1994	8.701	0.747	1	0.6	111.0

\* These values were measured on the shake table and differ from the intended values, PGA, PGV stands for peak ground acceleration and peak ground velocity respectively

A response spectrum analysis shows that although the accelerations reproduced on the shake table do not exactly mimic the intended accelerations in the time domain, the shake table runs in fact accurately reproduced the desired frequency response characteristics. This is illustrated in Figure 4-6 where the response spectral

accelerations calculated from the intended excitations are compared to the spectral accelerations calculated from the measured accelerations for a typical test run. This also explains the discrepancies in Table 4-1 where the peak ground accelerations (PGA) for the test runs are often inconsistent with the expected PGA for the known earthquake records.

The measured acceleration, displacement traces and the corresponding response spectrum for each of the shake table test runs are provided for reference in Figures A-1 through Figure A-10 in Appendix A. The same naming convention as in the Wight study is used to designate these tests. The designation contains the name of the original earthquake input, the acceleration scale and the time scale. For example, ‘El Centro–A0.5–T0.38’ identifies a shake table test using the El Centro acceleration record where the acceleration magnitudes is scaled down by 0.5 and the time scale is shortened by a factor of 0.38. The response spectra for the selected test runs are plotted against the elastic design spectrum in Figure 4-7 as a reference of the severity of the shake table input.

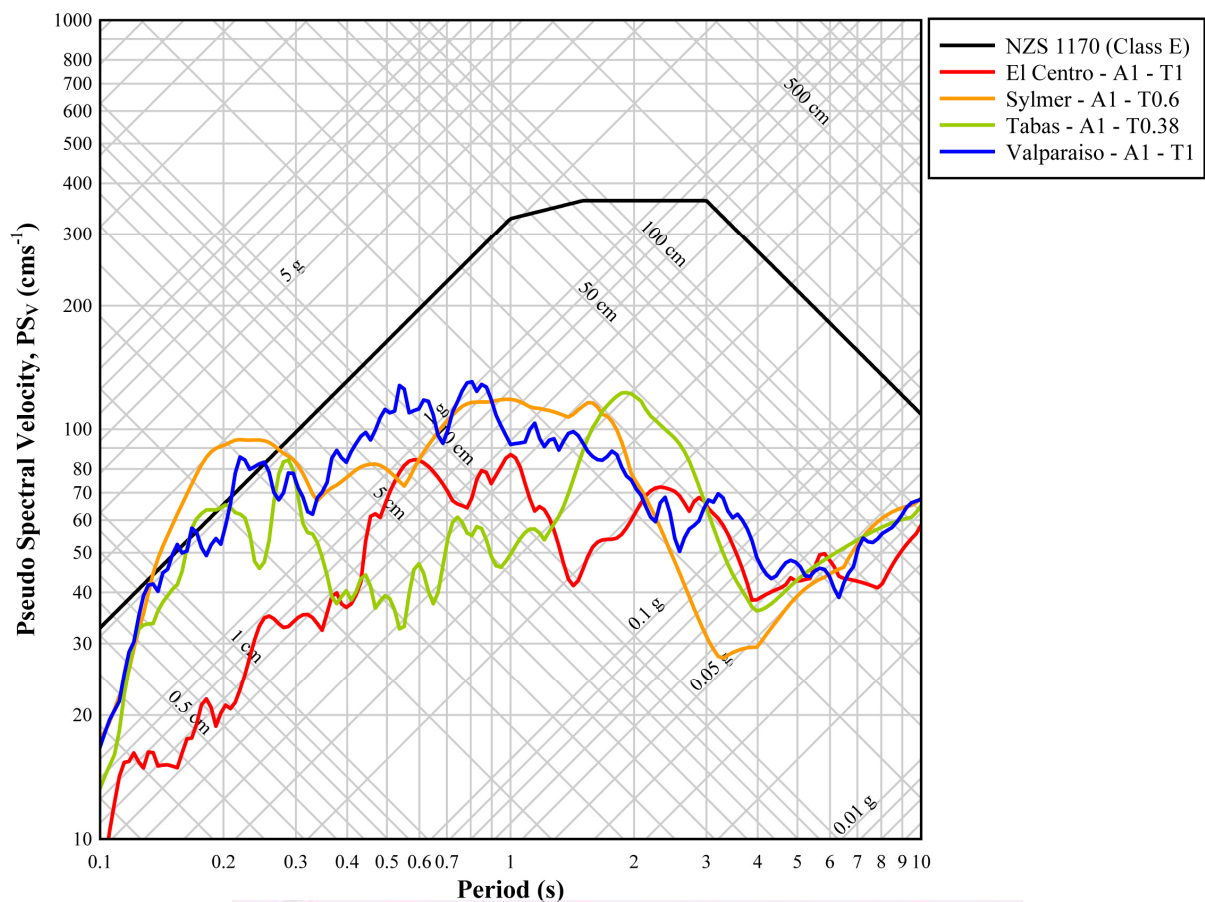
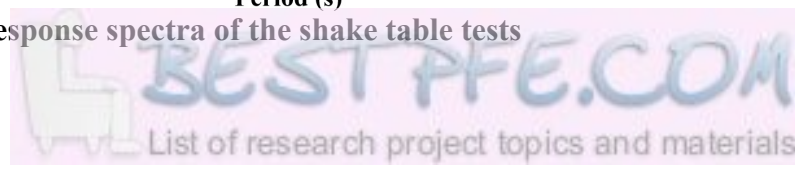


Figure 4-7 – Response spectra of the shake table tests



The elastic design spectrum represents the most detrimental design seismic actions specified by the New Zealand Loadings Standard (NZS 1170.5:2004) (Standards New Zealand. 2004), which is based on a very soft soil site experiencing the maximum considered motions in the highest seismicity area in New Zealand.

The response spectrum analysis shows that with the exception of the El Centro ground motion, the shaking in the selected test runs are near or in excess of the maximum design level of shaking for the rocking period of the wall specimen (between 0.10 and 0.24 seconds).

#### 4.5 EXPERIMENT RESULTS

As expected, the PCM wall accommodated the shake table tests with negligible damage. The post-tensioning tendon remained elastic throughout the tests despite the wall reaching a maximum displacement of 35.7 mm (1.5 % lateral drift). In all the test runs, the wall re-centered to within 0.8 mm of the in-plane alignment at the beginning of each run. The wall however did twist slightly about a vertical axis and resulted in a maximum residual out of plane displacement of 14 mm at one end of the wall when viewed in plan. After each test run, the tendon returned to approximately the same tension force.

**Table 4-2 – Summary of wall response**

Run ID	Max ToW* Disp. (mm)	Tendon Force Before (kN)	Max Tendon Force (kN)	Tendon Force After (kN)	$\Delta$ in Horiz. Alignment (mm)
1	-5.40	75.7	83.4	75.8	-0.37
2	-4.34	75.9	81.1	76.1	-0.19
3	8.65	75.8	89.1	75.8	-0.05
4	-23.91	75.7	119.5	75.7	-0.34
5	35.73	75.6	138.4	75.5	-0.24
6	9.44	75.3	90.5	76.0	-0.72
7	4.54	110.8	115.1	111.0	0.24
8	6.96	110.9	120.3	111.1	0.12
9	-4.63	111.0	115.8	111.3	-0.281

\*ToW – Top of Wall

The test data in the current study has been filtered by a 25 Hz digital low pass filter to remove the high frequency noise from the data acquisition system. This is the source of the slight discrepancies in the values from this study when they are compared to the results in the Wight study. Table 4-2 presents a summary of wall response for each shake table test run.

#### **4.5.1 FREE VIBRATION RESPONSE (TEST RUN 5)**

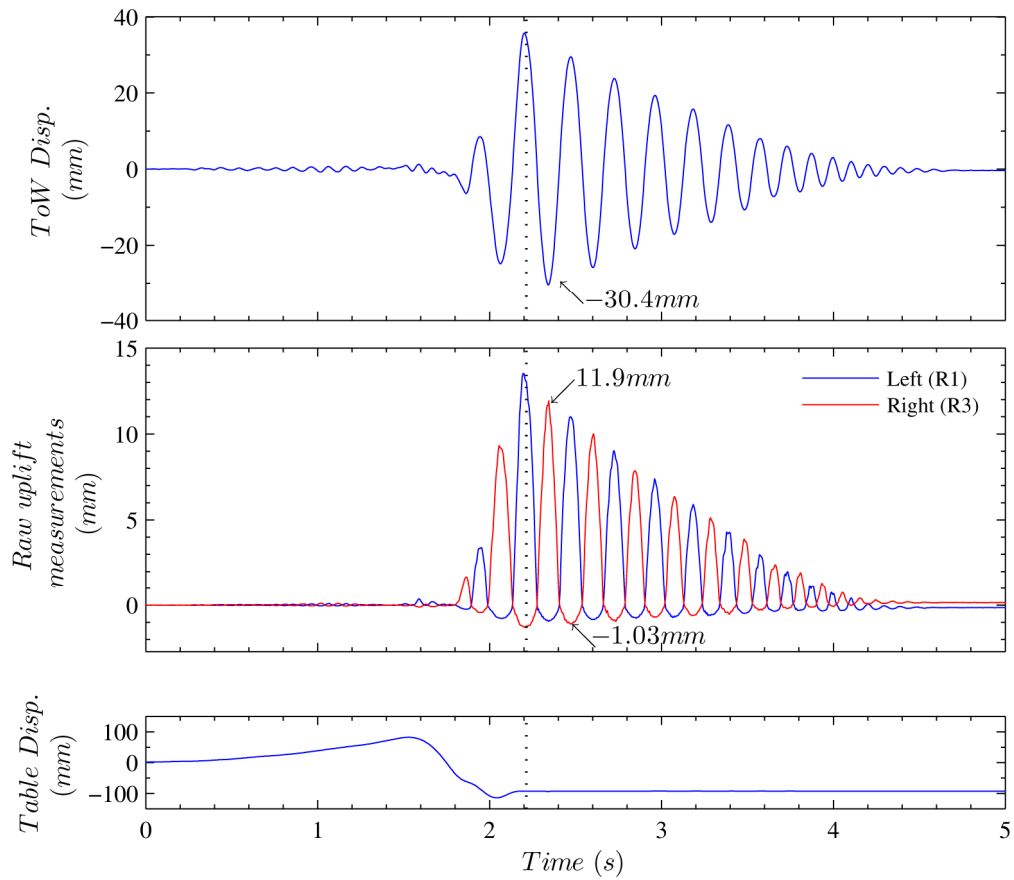
The free vibration response of the PCM wall is of particular interest to the current study. This free vibration test provides an opportunity to examine the dynamic characteristics of the PCM wall system without additional external excitations. It should be kept in mind that although the response of a particular PCM wall is investigated here, the intent is to catalogue knowledge on the behaviour of controlled rocking systems in general.

The free vibration test, test run 5, was initiated by applying the Sylmar ground motion record to the shake table until the time when the largest wall displacement was expected. The shake table was then stopped abruptly and the wall vibration was allowed to decay freely.

Figure 4-8 presents the lateral displacements at the top of wall, the uplifts at the left and right wall edges and the displacements of the shake table. The dotted line in the figure denotes the time when the shake table came to a complete stop. The beginning of the free vibration decay was subsequently taken as the time when the wall was at the next peak of its vibration cycle, when the ToW displacement was -30.4 mm.

Researchers observed virtually no damage to the PCM wall during the free vibration decay despite the large lateral displacement. The lateral movement of the wall was entirely due to rocking during the large displacement cycles. The wall rocked on a single continuous horizontal crack along the wall-foundation interface. This rocking motion can be observed from the displacement time-histories as generous uplifts on the alternate wall edges as the PCM wall rocked from one side to the other. Curiously, Figure 4-8 showed higher than expected negative uplift values at the wall edges. Negative uplift values correlate to the amount of crushing or compressive strains at the wall edge. This highlighted a shortcoming of the

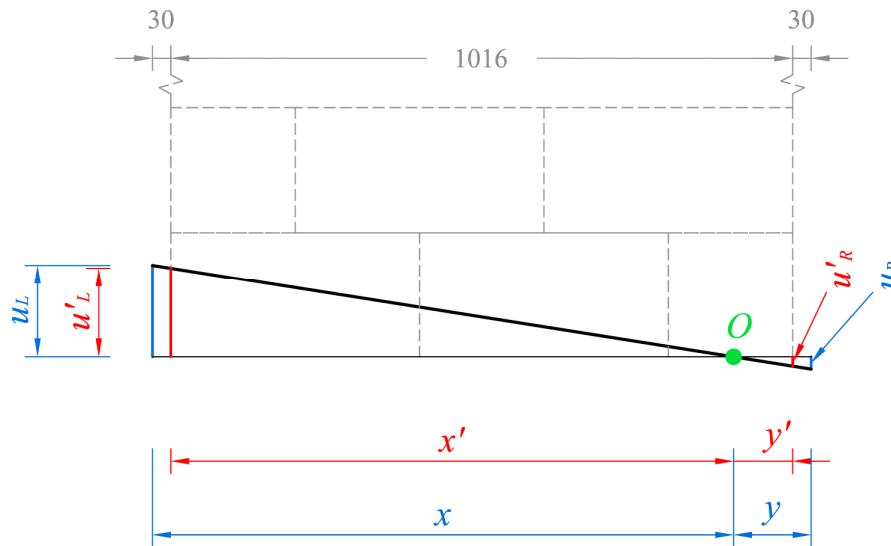
instrumentation system and was attributed to the uplift potentiometers being mounted slightly outside of the wall as illustrated in Figure 4-9.



**Figure 4-8 – Wall response and table motion during the free vibration test**



**Figure 4-9 – Mounting of an edge uplift potentiometer (Source: Wight 2006)**



**Figure 4-10 – Linear rotation profile assumption**

Consequently, the uplift readings were corrected based on a linear rotation profile assumption of the base as shown in Figure 4-10. Equations 4-1 through 4-4 evaluate the correct uplift readings and estimate the location of the centre of rotation,  $O$  in Figure 4-10.

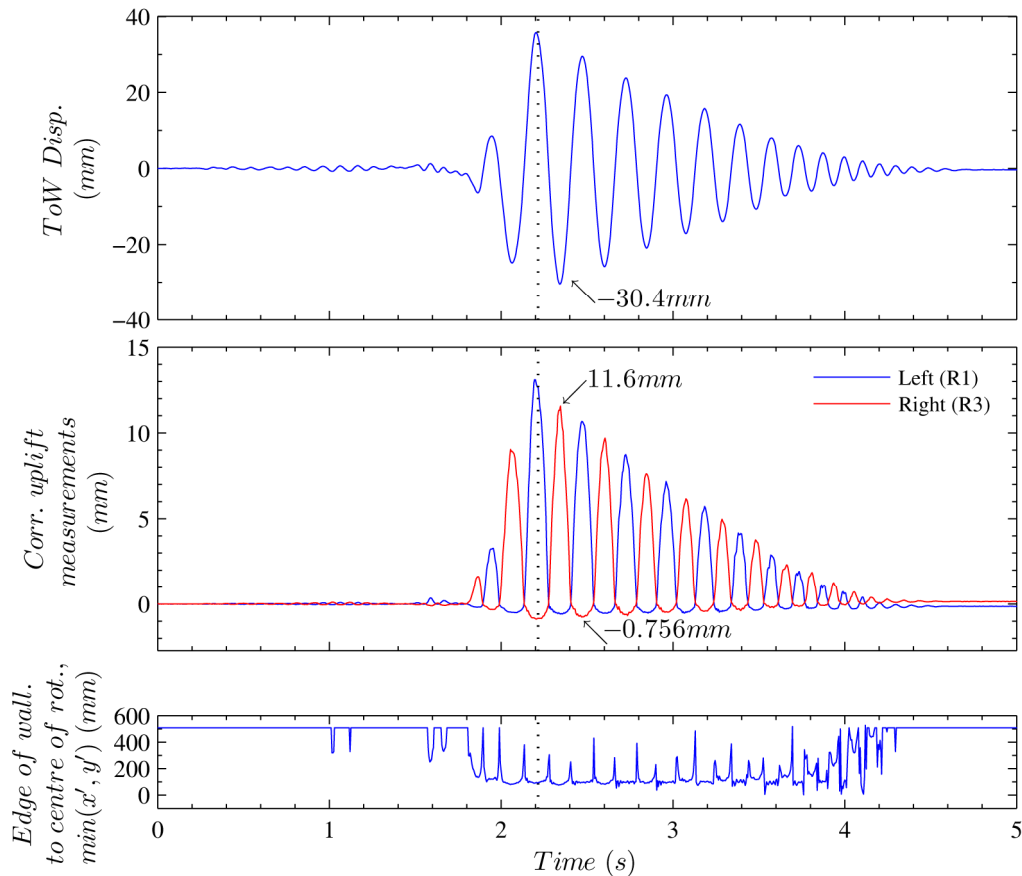
$$x = 1076 \times \frac{|u_L|}{|u_L| + |u_R|} \quad (4-1)$$

$$y = 1076 - x \quad (4-2)$$

$$u'_L = u_L \times \frac{x - 30}{x} \quad (4-3)$$

$$u'_R = u_R \times \frac{y - 30}{y} \quad (4-4)$$

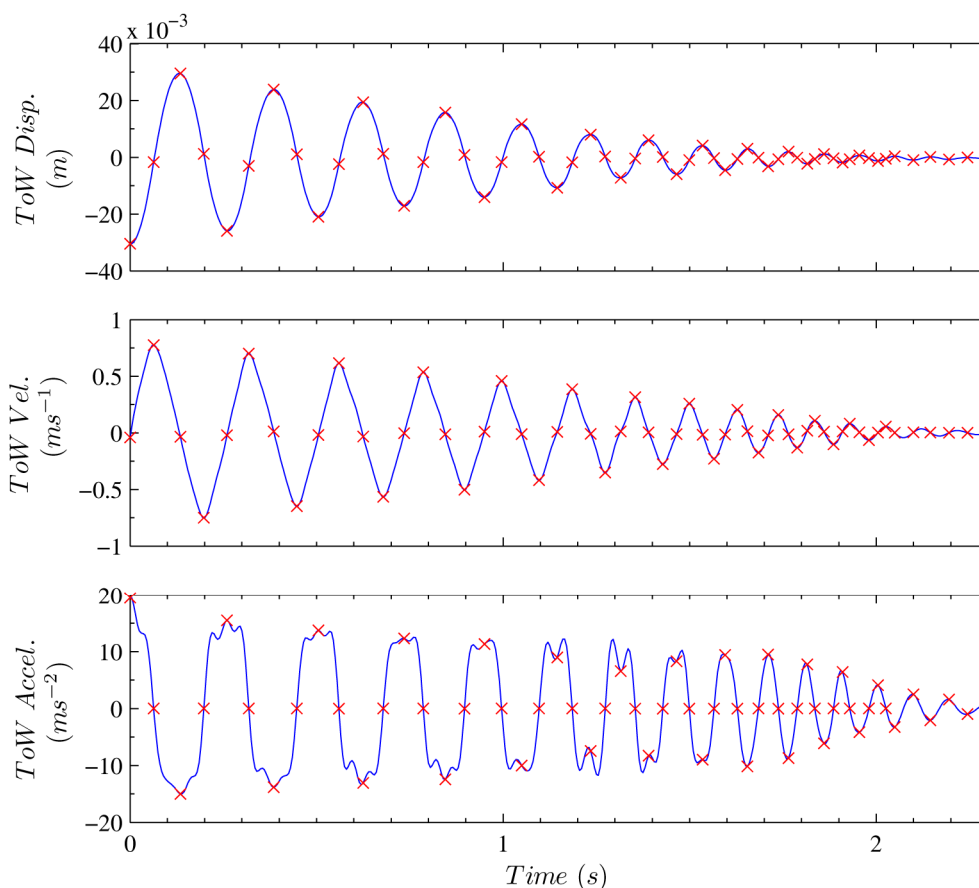
Figure 4-11 presents the modified response for the free vibration test. The correction has the effect of reducing the toe compression by up to 26%. It is also shown that the centre of rotation remains relatively stationary once rocking is initiated. It is noteworthy that as the wall comes to a stop, the centre of rotation gradually migrates from the outer edge back towards the centreline of the wall.



**Figure 4-11 – Corrected wall response and table motion for run 5**

The free vibration decay is further examined by the collation of data points at the peaks and zero crossings of the vibration cycle. The times of zero crossing are taken as the instances when the wall accelerations are zero. This is applicable because when the wall is truly upright, or at the precise time of zero crossing, there should be no unbalanced lateral forces and hence no more acceleration.

This proved to be a far more consistent method for determining the times of zero crossing, as it was difficult to ascertain the upright position from the horizontal displacement because the wall slid during the free vibration decay. Figure 4-12 presents a plot of the wall displacements with the points of interest highlighted. The full wall data at these times is tabulated in Table A-1.



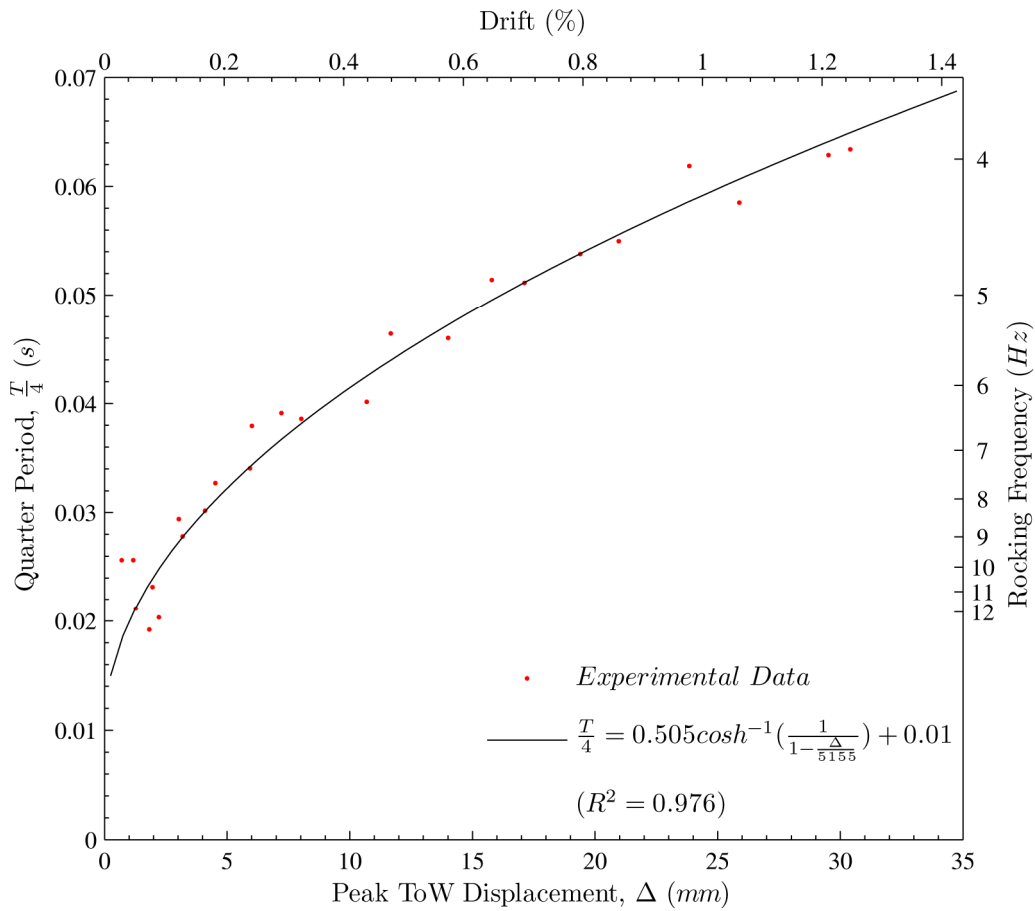
**Figure 4-12 – Free vibration decay with peaks and zero crossings highlighted**

As it was conducted previously for the free rocking block, the periods for a quarter of the vibration cycle are plotted against the peak displacement at which the cycle began. The results as shown in Figure 4-13 clearly illustrate that the rocking period of a controlled rocking structure is strongly amplitude dependent. For a 1.2% lateral drift of the PCM wall, the rocking frequency of the system decreased from approximately 11 Hz to 4 Hz.

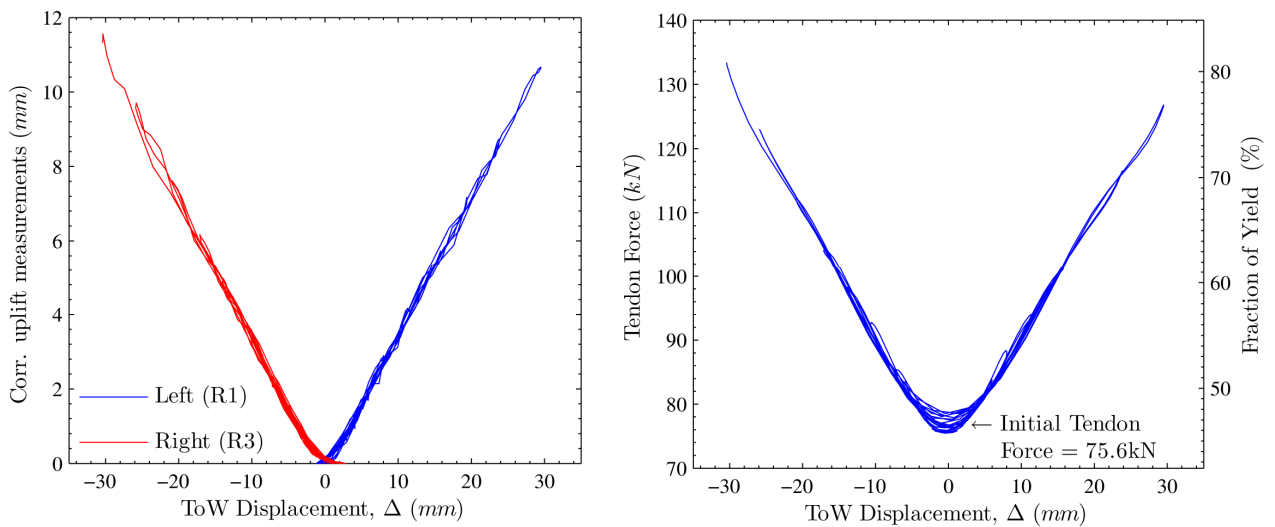
A line-of-best-fit has been fitted empirically to the experimental data and is also plotted in Figure 4-13. The line-of-best-fit expression, presented as Equation 4-5, has an algebraic form similar to Housner's expression for the quarter period of a free rocking block (Equation 2-5).

$$\frac{T}{4} = 0.505 \cosh^{-1} \left( \frac{1}{1 - \frac{\Delta}{5155}} \right) + 0.01 \quad (4-5)$$

This empirical formula shows a very good fit to the data with a  $R^2$  value of 0.976. This is remarkable as the experimental data was captured at 200 Hz which meant the quarter period readings have an inherent granularity of 0.005s.



**Figure 4-13 – Quarter periods of PCM wall versus peak ToW displacement**



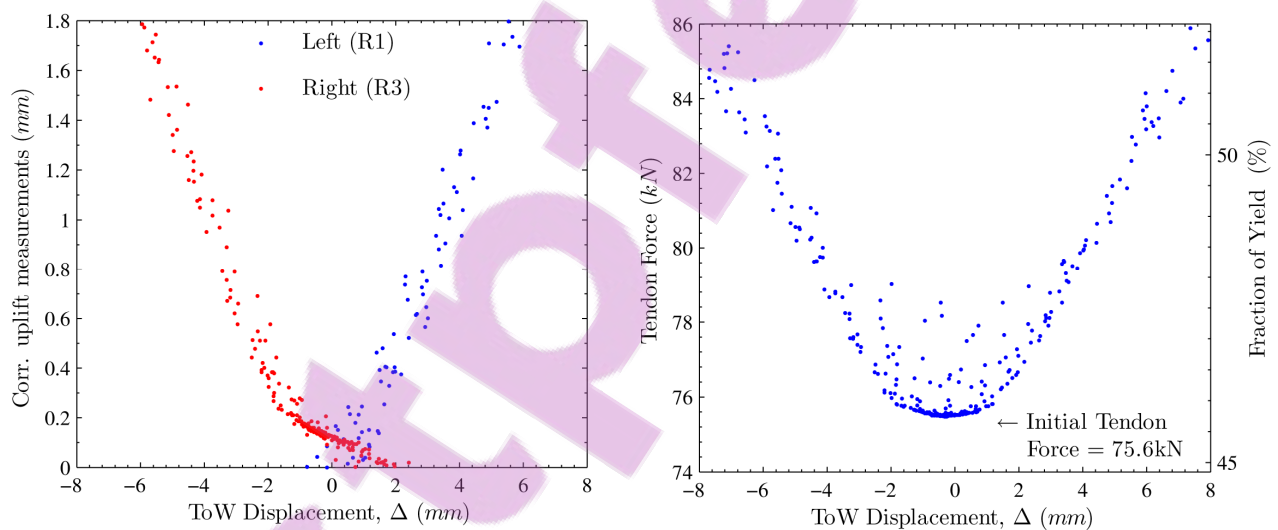
**Figure 4-14 – a) Wall uplifts and b) tendon force versus ToW displacements**

Figure 4-14 present two plots of the wall uplifts and the tendon force against the horizontal wall displacements. Figure 4-14a illustrates that the amount of vertical uplift is strongly correlated to the horizontal displacements. This suggests that the two

quantities are governed by some geometric constraints as would be expected from rigid body motion. This supports the previous observation that the motion of the PCM wall is predominately rocking.

Figure 4-14b shows that the tendon force is likewise correlated to the horizontal displacements. The correlation for tendon force at first glance appears much less defined near the origin when compared to the correlation between the uplifts and horizontal displacements. However on closer inspection, this is largely a misleading consequence of plotting consecutive data points with connected lines.

The problem stems from the fact that the wall shifts from rocking about one edge of the wall to the other over a very short period of time. The data acquisition system, which samples at 0.005s interval, typically only recorded data points either side of the exact instance of when the wall was upright. This led to the rounded off appearance of the curve in Figure 4-14b once a line was drawn between the two points either side of the steep minimum.



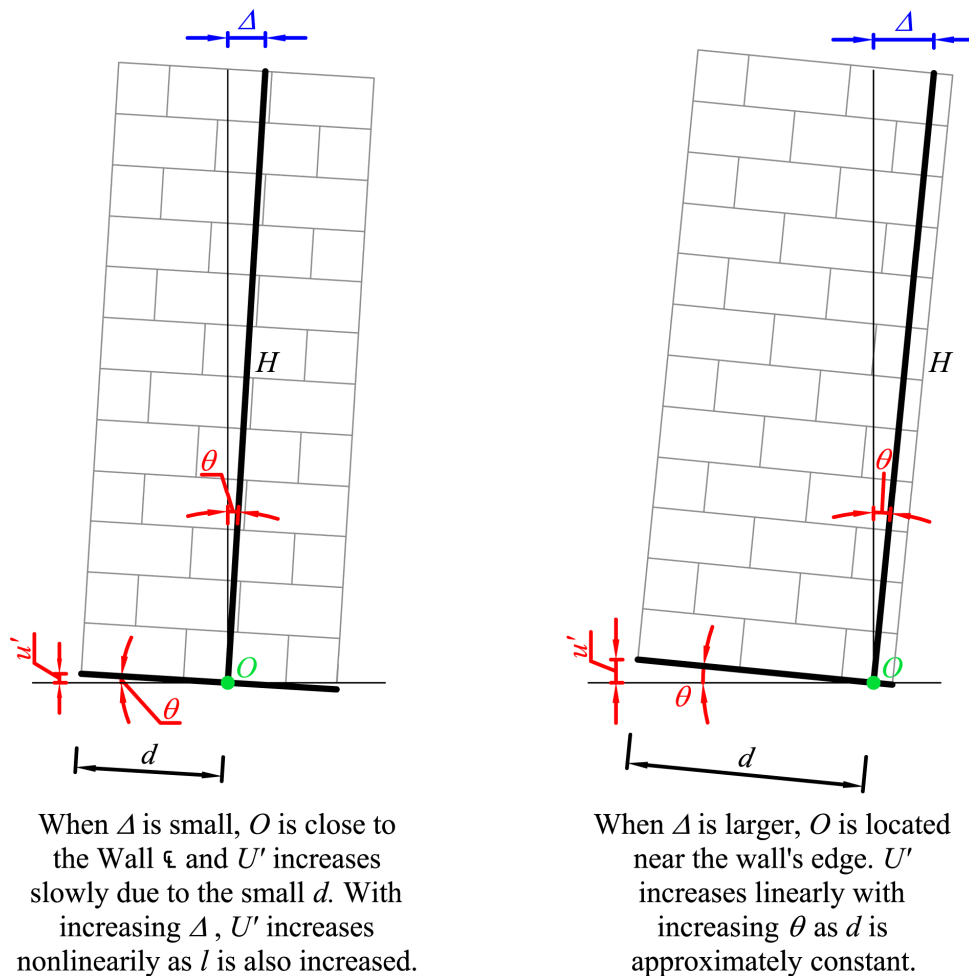
**Figure 4-15 – a) Wall uplifts and b) tendon force versus ToW displacements**

Figure 4-14 is re-plotted in Figure 4-15 with a focus in the origin region and with lines replaced by individual data markers. This exercise highlights that the tendon force has a distinct piecewise behaviour.

When the horizontal displacements are small, the tendon force increases slowly in a parabolic fashion in relations to increasing displacement. When the horizontal displacements are larger, beyond  $\pm 2$  mm say, the tendon force increases steeply and linearly in relation to increasing displacement.

Similarly, the uplift displacements vary differently under small and large horizontal displacements. However, this effect appears to be more isolated and leads to only a minor deviation from the overall linear trend when compared to the behaviour of the tendon force.

The piecewise behaviour in the tendon force and uplift relationships may be explained by the fact that under small displacements wall rocking is not properly initiated. As a result, the motion of the wall is governed by quite different geometric constraints under the two conditions. Under small lateral displacements, gap-opening occurs only along a small part of the wall base while under larger displacements, when rocking is properly initiated, the wall is detached along approximately the entire wall base. Figure 4-16 depicts graphically how the uplifts and the wall horizontal displacements are linked for the two extents of rocking.



**Figure 4-16 – The effect of a shifting centre of rotation on uplift**

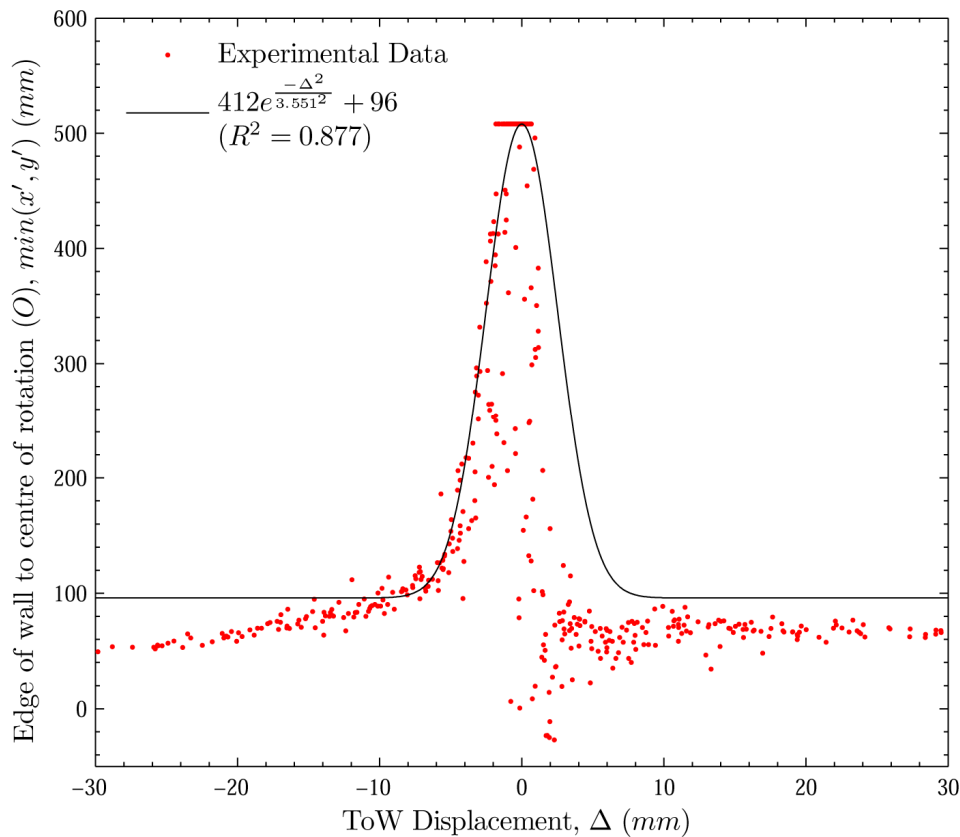
In a mathematical context, for a rotation of  $\theta$ , the uplift ( $u'$ ) and horizontal displacement ( $\Delta$ ) are approximately linked by Equation 4-6.

$$u' = |\Delta| \frac{d}{H} \quad (4-6)$$

Moreover, free vibration data presented in Figure 4-17 shows the location of the centre of rotation varies significantly when rocking is not properly initiated. This leads to the detached wall length ( $d$ ) becoming a nonlinear and sensitive function of  $\Delta$  under small lateral displacements. Incorporating this fact with Equation 4-6 reveals the reason for the complex piecewise behaviour between uplift and horizontal displacements.

Figure 4-17 shows the centre of rotation can be adequately predicted using an empirical expression with a Dirac- $\delta$  algebraic form, as Equation 4-7 below.

$$(1016 - d \cos \theta) = 412 e^{-\left(\frac{\Delta}{3.551}\right)^2} + 96 \quad (4-7)$$



**Figure 4-17 – Distance between the rotation centre and wall edge versus wall lateral displacement**

By selecting a Dirac- $\delta$  algebraic form for the empirical expression, a continuous function can be used to describe the behaviour of the system without the introduction of piecewise discontinuity. The empirical expression in a general sense is controlled by three parameters  $C_1$ ,  $C_2$  and  $\varepsilon$  as in Equation 4-8 below.

$$\text{Distance to centre of rotation} = C_1 e^{-\left(\frac{\Delta}{\varepsilon}\right)^2} + C_2 \quad (4-8)$$

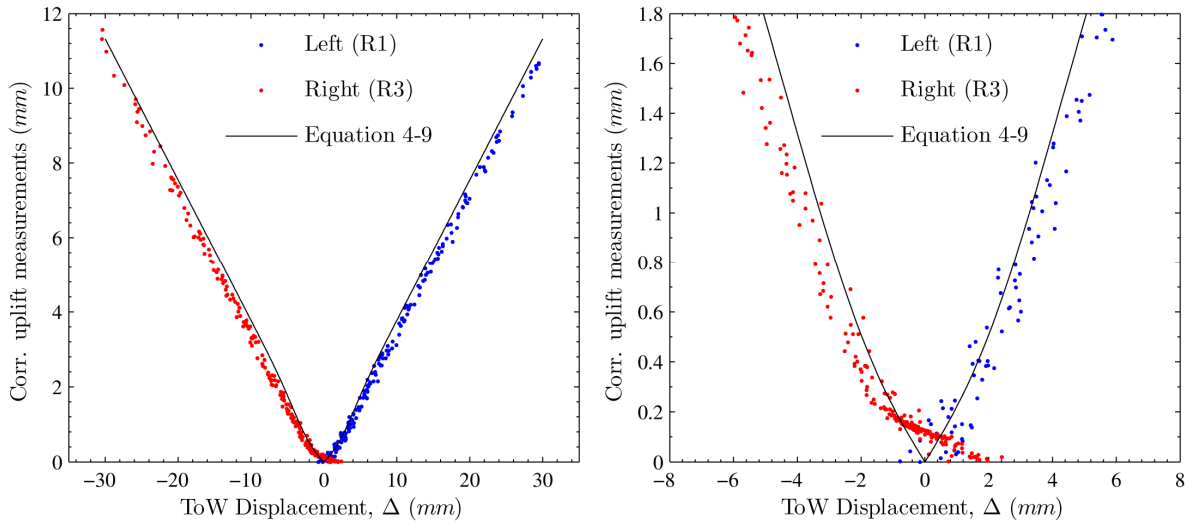
This format of the equation permits an engineer to conveniently prescribe two fixed points with direct physical relevance to the empirical fit.  $C_2$  prescribes the distance to the centre of rotation when rocking is fully developed. Then  $C_1 + C_2$  defines the location of centre of rotation at zero wall movement as the exponential term equals unity for  $\Delta = 0$ . Finally,  $\varepsilon$  is the empirical penalty parameter of the Dirac- $\delta$  function which controls sharpness of the peak in the empirical expression.

For illustration, in the current free vibration experiment  $C_2$  is selected as 96 mm which is the average distance to the centre of rotation in the positive  $\Delta$  range. Then, considering the instance when the wall is at an infinitesimal lateral displacement, the centre of the rotation is at the wall centreline. This means  $C_1 + C_2$  must equal half the width of the wall (508 mm) and leads to the selection of  $C_1$  as 412 mm. This leaves  $\varepsilon$  as the only parameter to adjust to obtain the curve of best fit.

As the penalty parameter essentially controls the rate at which the centre of rotation migrates with increasing horizontal displacement, it is possible that the selection of the penalty parameter is also controlled by some physical process. This could be the nature of the rocking surfaces. For instance, when both of the rocking interfaces are rigid, it may result in a low  $\varepsilon$  value as little sub-surface compliance is permitted and leads to an abrupt shift of rotation centre. Conversely, a soft wall base may lead to a gradual shift of the centre of rotation which may be modelled by a higher  $\varepsilon$  value.

The centre of rotation prediction formula, Equation 4-7 can be further combined with the geometric constraints outlined in Equation 4-6 for the rocking wall. This leads to a new expression, Equation 4-9, which describes the amount of uplift at the wall edge as a function of solely the horizontal displacement. This relationship is plotted against the experimental data in Figure 4-18, and shows a high level of fit with an  $R^2$  value of 0.99.

$$u' = \frac{|\Delta|}{\sqrt{H^2 - \Delta^2}} \left( 920 - 412 e^{-\left(\frac{\Delta}{3.551}\right)^2} \right) \quad (4-9)$$



**Figure 4-18 – a) Wall uplifts versus ToW displacements, b) close up of the origin**

#### 4.6 MODELLING THE TENDON EXTENSION

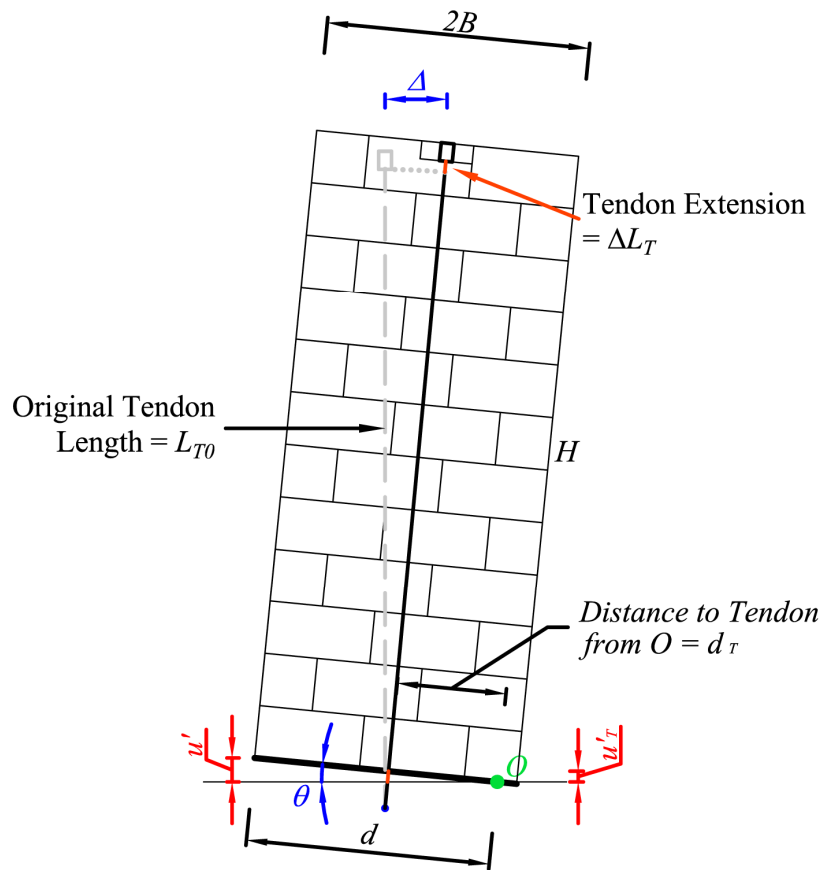
With an accurate prediction of the amount of uplift as a function of horizontal wall displacement now available, it is possible to extend this derivation theoretically to model the extension for the prestressing tendon in the PCM wall. Consider the PCM wall rocking about the centre ( $O$ ) as in Figure 4-19. Assuming small angle rotation about  $O$ , the extension of the tendon ( $\Delta L_T$ ) is approximately the length of the tendon exposed by the uplifted wall. This is because as the wall displaces, the tendon must pass through the entire height of the wall which offsets the length of the tendon by approximately the original length.

As a result, the tendon extension can be expressed as a function of the uplift at the location of the tendon ( $u'_T$ ).

$$\Delta L_T = \frac{u'_T}{\cos \theta} \quad (4-10)$$

Exploiting the proportionality in similar triangles, Equation 4-10 can be rewritten as a function of the uplift at the wall edge ( $u'$ ).

$$\Delta L_T = \frac{u'}{\cos \theta} \cdot \frac{d_T}{d} \quad (4-11)$$



**Figure 4-19 – Key variables controlling the tendon extension**

Equation 4-11 can be simplified by the introduction of the specific tendon location

$$\Delta L_T = \frac{u'}{\cos \theta} \cdot \frac{(d - B)}{d}$$

$$\Delta L_T = \frac{u'}{\cos \theta} \cdot \left(1 - \frac{B}{d}\right) \quad (4-12)$$

Substituting  $u' = d \sin \theta$ ,

$$\Delta L_T = \frac{d \sin \theta}{\cos \theta} \cdot \left(1 - \frac{B}{d}\right)$$

$$\Delta L_T = (d - B) \tan \theta \quad (4-13)$$

Substituting Equation 4-6,

$$\Delta L_T = \left( \frac{u' H}{|\Delta|} - B \right) \tan \theta$$

$$\Delta L_T = \left( \frac{u'H}{|\Delta|} - B \right) \frac{|\Delta|}{\sqrt{H^2 - \Delta^2}}$$

$$\Delta L_T = \frac{u'H}{\sqrt{H^2 - \Delta^2}} - \frac{B|\Delta|}{\sqrt{H^2 - \Delta^2}} \quad (4-14)$$

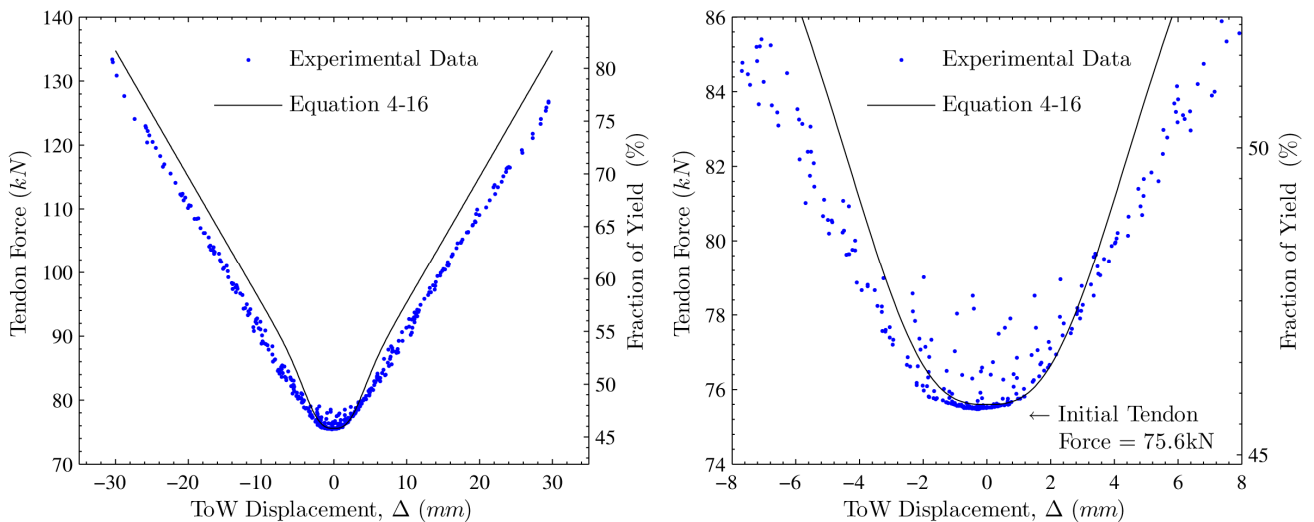
Finally substituting Equation 4-9 into 4-14 leads to the Equations 4-15 and 4-16 which describe the tendon extension and the tendon force as a function of the horizontal displacement only.

$$\Delta L_T = \frac{H|\Delta|}{H^2 - \Delta^2} \left( 920 - 412 e^{-\left(\frac{\Delta}{3.551}\right)^2} \right) - \frac{B|\Delta|}{\sqrt{H^2 - \Delta^2}} \quad (4-15)$$

$$P_{Tendon}(\Delta) = P_{Tendon}^0 + \frac{EA}{L_{T0}} \left( \frac{H|\Delta|}{H^2 - \Delta^2} \left( 920 - 412 e^{-\left(\frac{\Delta}{3.551}\right)^2} \right) - \frac{B|\Delta|}{\sqrt{H^2 - \Delta^2}} \right) \quad (4-16)$$

Where  $P_{Tendon}^0$  is the initial tendon force,  $EA$  is the axial property of the tendon and  $L_{T0}$  is the initial unbonded length of the tendon, 3106.6 mm in this instance.

Figure 4-20 presents a plot of the tendon force prediction formula against the experimental data. The prediction formula in this instance matches the experimental data adequately and achieves an  $R^2$  value of 0.927. However, the matching can be improved by a more accurate model for the transition area between the initiation of rocking and fully developed rocking.



**Figure 4-20 – a) Tendon force versus ToW displacements, b) close up of the origin**

It is noteworthy that this degree of fit is quite a remarkable achievement, particularly considering that each step of the derivation can be related back to a physical assumption or geometric constraint. Also, most of the variables in the formula are geometric or material properties of the PCM wall which are known prior to the experiment. The only empirical component of the derivation is the fitting of a Dirac- $\delta$  function in Equation 4-7, to model the shift of the physical rotation centre<sup>5</sup> as the wall displaces. This assumption of a rather abrupt but continuous shift of the physical rotation centre is central to the derivation of the relationships.

#### **4.7 DEVELOPING THE FORCE-DISPLACEMENT RELATIONSHIP OF A CONTROLLED ROCKING WALL**

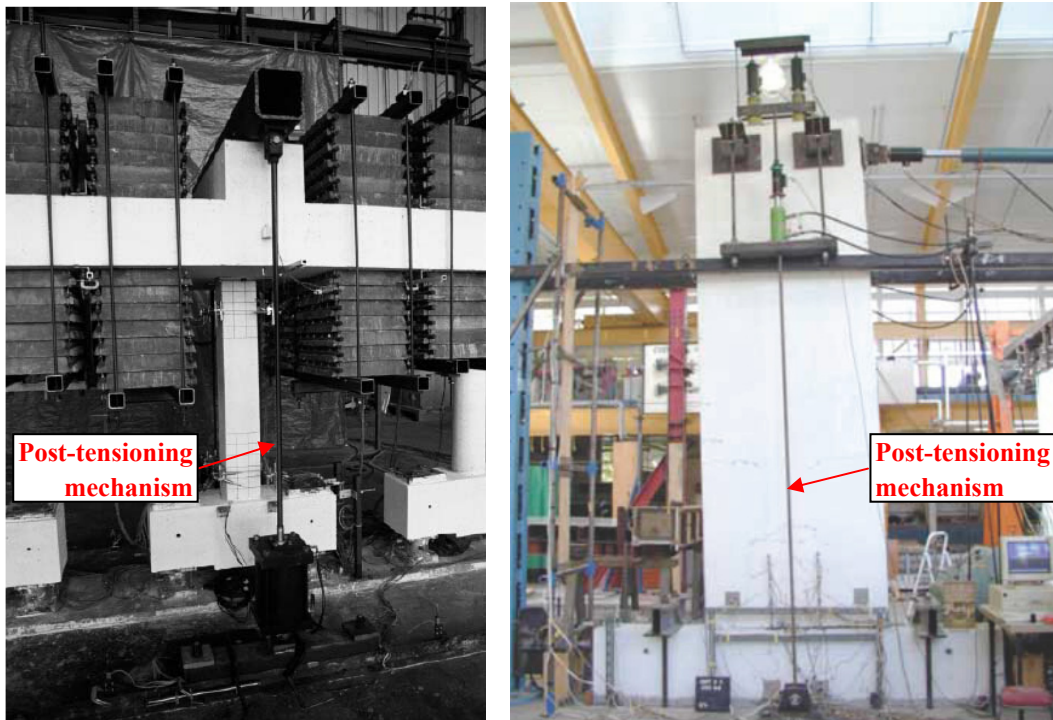
Encouraged by the ability to predict the tendon and uplift behaviour of the controlled rocking wall using mostly a theoretical approach, it is hypothesised that the dynamic characteristics of the wall can also be predicted by making use of the newly developed formulas. It is anticipated that there may be intelligent modifications to be made to the established formulas for a classical free rocking system.

One of the key differences between the controlled rocking system and a free rocking system is the presence of a large initial vertical force, applied by post-tensioning tendons. This enables a new mode of behaviour which is a mixture of the fixed base response and the free rocking response. This mode of behaviour is often short lived, occurring at a very restrictive domain, and is characterised by partial uplift of the wall base and a centre of wall rotation located well within the two wall corners.

It is interesting that the addition of the prestressing tendon in PCM construction bears significant resemblances to a laboratory testing technique that is regularly used to emulate superimposed dead load in a structural system. Figure 4-21 presents two tests illustrating how this is generally applied. Typically, a soft spring or a load control actuator maintains the tendon force to simulate a constant gravity load. This is very similar to the post-tensioning in the controlled rocking system with the exception that the tendon force increases with lateral displacement.

---

<sup>5</sup> The physical rotation centre is as explained on page 11. From here onwards, the physical rocking centre is interchangeably referred to as the centre of rotation.



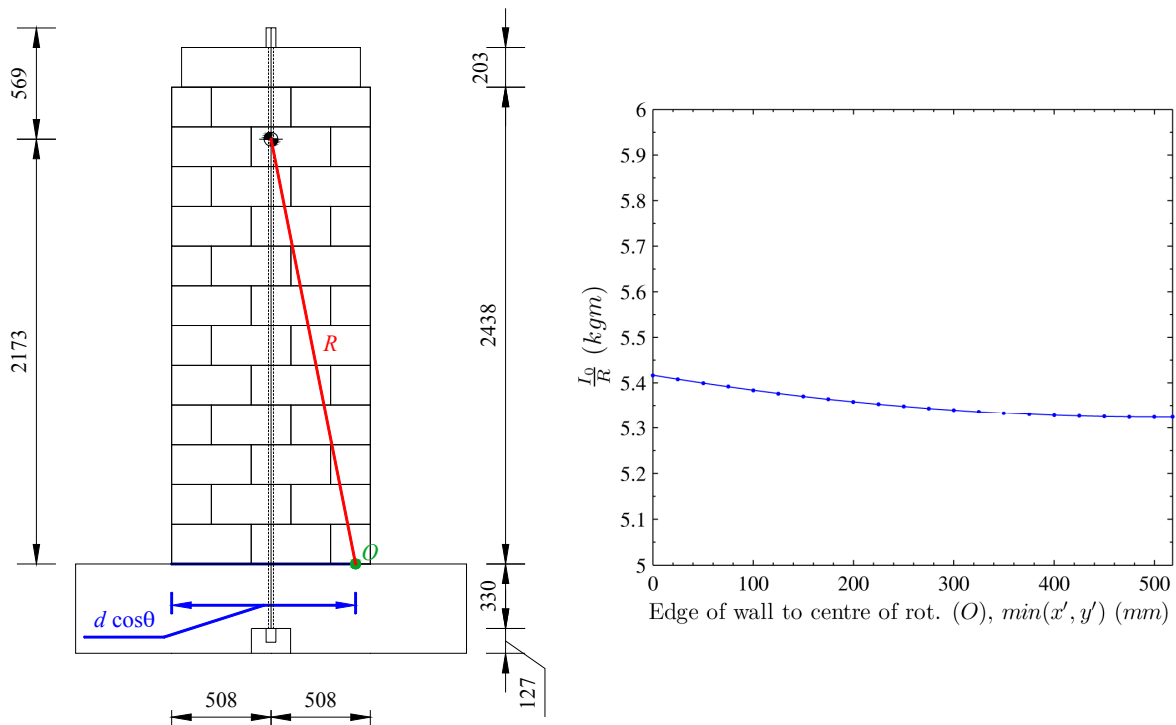
**Figure 4-21 – Two experiments where axial load is simulated through post-tensioning (Source: a)Elwood and Moehle 2003; b)Rahman and Restrepo 2000)**

With this in mind, it is postulated that the effect of the prestressing tendons in a controlled rocking system can be analysed as a free rocking system with an exaggerated gravity load. Additionally for simplicity, it is proposed that the new mixed elastic-rocking response can be approximately simulated by summing the fixed base response and the free rocking response.

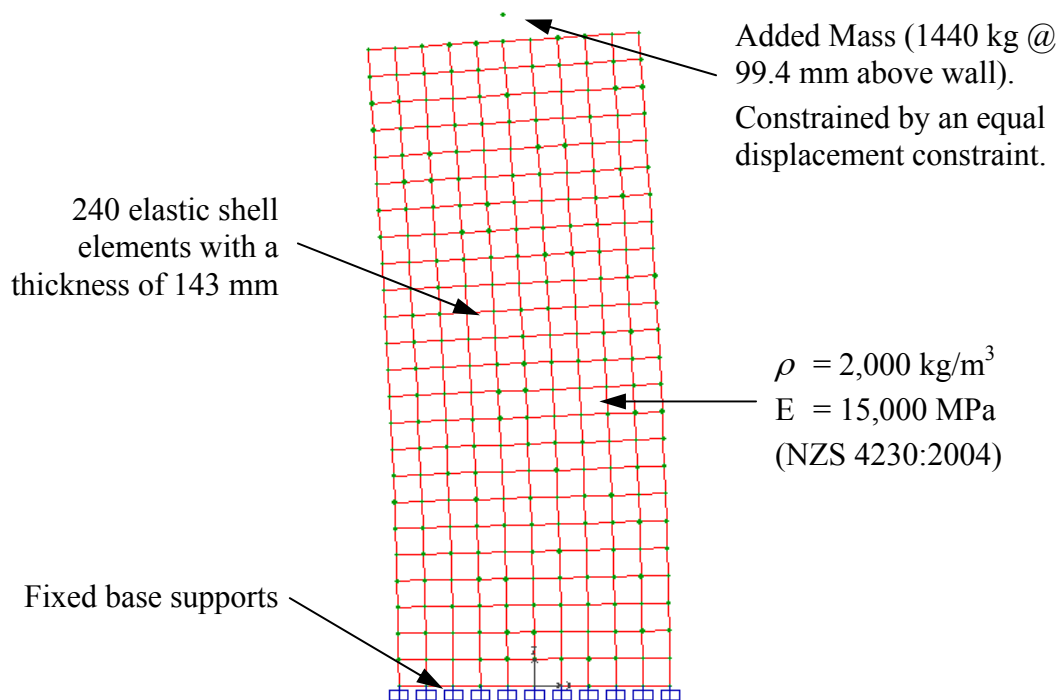
This concept is applied herein to estimate a controlled rocking system's quarter period, in conjunction with the recently developed equations for the properties of the PCM wall as it displaces.

Consider the PCM wall specimen presented in Figure 4-22. The wall's centre of mass of is located at the centreline of the wall, 2173 mm up from the wall base. As the wall displaces, the centre of rotation shifts from the wall centreline out towards the wall edge as illustrated previously in Figure 4-17. This leads to a changing moment of inertia about the rotation centre ( $I_0$ ) and a changing distance from the rotation centre to the mass centroid ( $R$ ). However, an analysis reveals that these values do not actually vary by much and the maximum deviation of  $I_0$  divided by  $R$  is less than 2%. Figure 4-22b illustrates this and it is subsequently justified to use constant  $I_0$  and  $R$

values, assuming rocking occurs about a wall corner for all lateral displacements as a simplification.



**Figure 4-22 – a) Key parameters for dynamic properties calculation, b)  $I_p/R$  versus the centre of rotation location**



**Figure 4-23 – Finite element model of the fixed based wall**

The elastic fixed base period of a controlled rocking system is another important property in estimating the rocking period. Observations suggest that under very small displacements, a controlled rocking wall behaves as an analogous fixed base wall without any prestressing. The natural period of such an analogous wall can be accurately estimated through the use of finite element analysis, with little or no testing data, using only typical material properties. For demonstration, an elastic finite element analysis is conducted on the PCM wall test specimen using code specified properties in SAP2000. The analysis predicted a natural period of 0.0428 second and Figure 4-23 presents the key input parameters of the analysis.

Now equipped with the necessary parameters, Housner's expression for the quarter period of a free rocking block, Equation 2-5 is modified to predict the quarter period for a controlled rocking wall. Recall that the two key assumptions are, 1) the effects of the prestress can be treated as an exaggerated gravity load, and 2) the new mixed elastic-rocking response can be represented by summing the fixed base response and the free rocking response.

$$\frac{T}{4} = \sqrt{\frac{I_o}{mgR}} \cosh^{-1} \left( \frac{1}{1 - \theta_0/\alpha} \right) \quad (2-5)$$

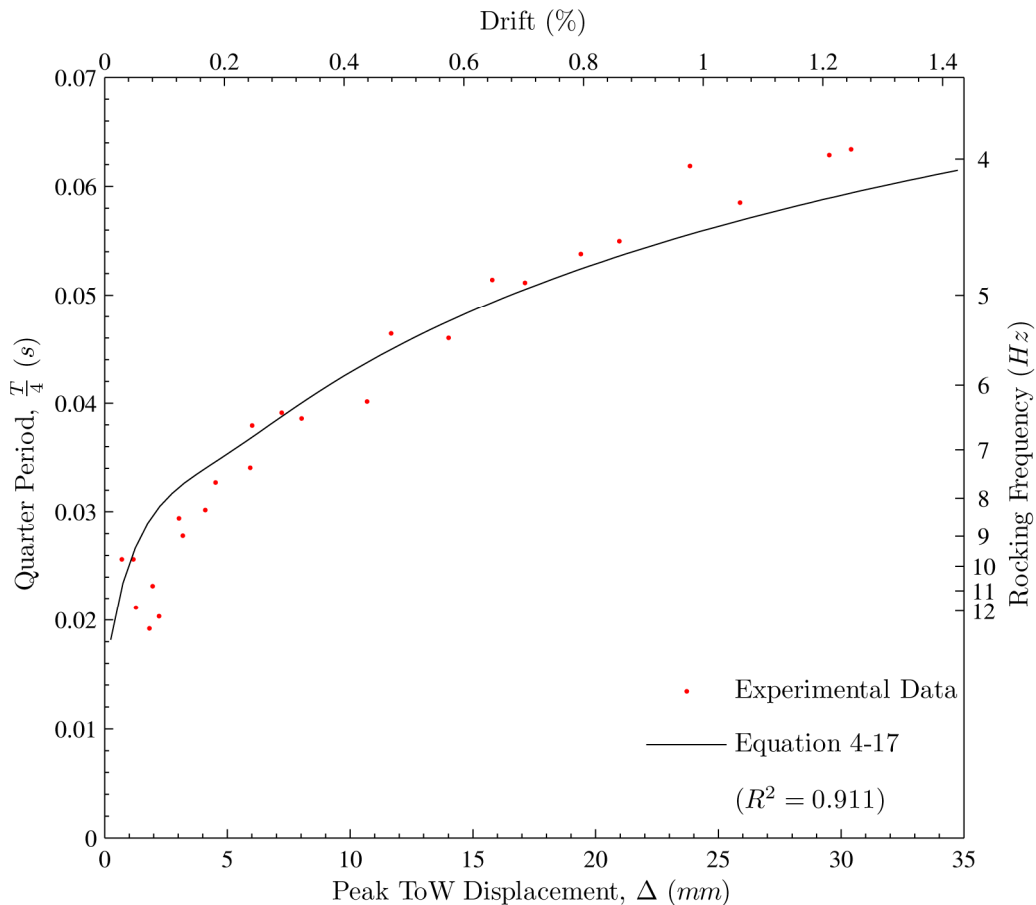
The modifications lead to Equation 4-17.

$$\frac{T}{4} = \sqrt{\frac{I_o}{R(mg + P_{tendon}(\Delta))}} \cosh^{-1} \left( \frac{1}{1 - \frac{\Delta}{d \cos(\theta)}} \right) + \frac{T_{Fixed Base}}{4} \quad (4-17)$$

A list of the modifications is as follows,

- The tendon force ( $P_{tendon}(\Delta)$ ) is added to the gravity force ( $mg$ ) in Equation 2-5 to represent an exaggerated restoring force.
- $I_o$  and  $R$  values are left alone as the ratio of the two is shown to remain relatively constant.
- The first mode period of the fixed base wall is added to Equation 2-5.
- The initial rotation divided by the static overturning angle for a free rocking block ( $\theta_0/\alpha$ ) is replaced with the initial lateral displacement divided by the horizontal projection of the detached wall base ( $\Delta/d\cos(\theta)$ ). This may appear to be an ad-hoc substitution and one might expect the

height to the centre of gravity to play a role. However this can be justified as the conventional point of overturning no longer exists in the controlled rocking system. A more appropriate limiting displacement would be when the edge of the wall is beyond the centre of rotation.

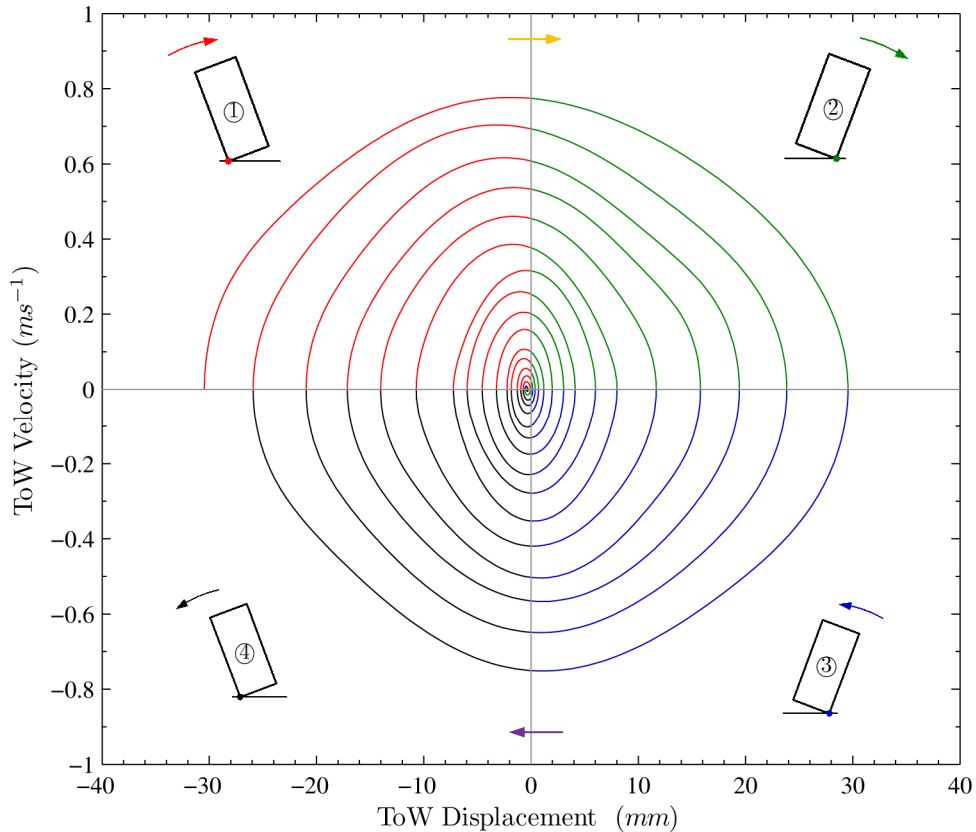


**Figure 4-24 – Quarter period predictions (Equation 4-17) against the test data**

Furthermore, Equations 4-7 and 4-16 can be substituted into Equation 4-17 to obtain a closed form prediction formula as a function of the peak ToW displacement. Figure 4-24 presents the prediction formula against the experimental data. It can be seen that the prediction formula tracks accurately to the experimental quarter periods and this is supported by an  $R^2$  value of 0.911 between the two data sets.

Another important aspect in understanding the dynamics of a controlled rocking system is understanding its energy dissipation mechanism. The free vibration decay data is used to examine the common use of an initial stiffness or tangent stiffness proportional viscous damping scheme to model the energy dissipation of a controlled rocking system.

To begin, the free vibration data is plotted on a phase diagram in Figure 4-25. The vibration data translates into a smooth near-elliptical trace without any noticeable abrupt changes. This is unlike the corresponding phase diagram for a free rocking system, such as Figure 3-7 on page 62, where there are abrupt drops in rotational speed whenever the wall returns to an upright position.



**Figure 4-25 – Free vibration decay displayed in a phase diagram**

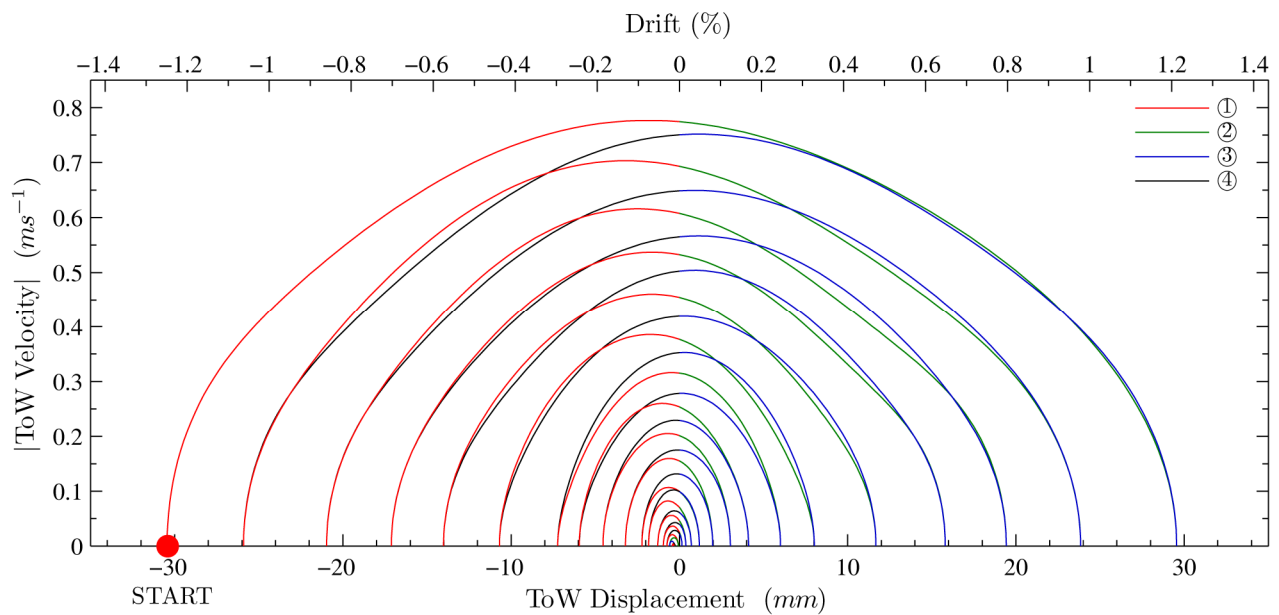
The absence of the abrupt changes in speed at the impacts initially suggests that energy dissipation may have occurred evenly throughout the vibration cycle. This is distinctively different to a free rocking system where energy is conserved during the rocking phases, and is only dissipated during the precise momentary impacts.

On a closer inspection of the phase diagram, it is revealed that energy dissipation for the PCM wall in fact also occurs only during a particular part of the vibration cycle. It is found that the PCM wall dissipates energy smoothly from a time slightly before to a time slightly after an impact. This is in contrast to a free rocking system which dissipates energy abruptly at the exact time of an impact.



This phenomenon is best observed in Figure 4-26 where the absolute speed of the PCM wall is plotted against the wall displacement. This ignores the direction of motion of the wall and is effectively mirroring the data points with negative velocities from Figure 4-25 about the horizontal axis.

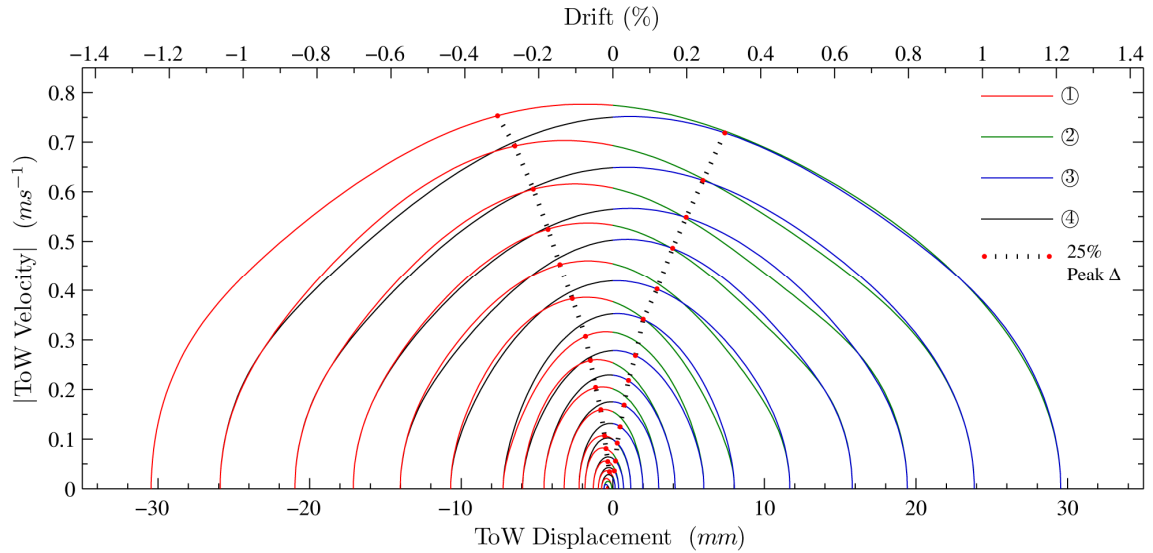
Figure 4-26 permits the phase diagram trajectory of the wall travelling towards a peak displacement to be compared against the reverse trajectory of the wall returning to the upright position from the same peak displacement.



**Figure 4-26 – ToW speed versus ToW displacement**

Focussing on the wall trajectory in Figure 4-26 for the first few cycles, starting from a negative ToW displacement, it demonstrates that once a wall reaches a peak displacement, it returns more or less along the same path. This is until it returns to approximately 25% of the peak displacement in each cycle, when it begins to deviate from the previous trajectory, decreasing in speed and energy content accordingly. This region of energy dissipation is highlighted by the dotted boundary in Figure 4-27.

This presents quite a modelling challenge as the exact energy dissipation mechanism is unknown, and the dissipation occurs and ends at a variable boundary which is a function of the velocity and displacement. For completeness, Figure 4-27 also suggests energy dissipation is activated for small displacements, less than 4 mm say, irrespective of the velocity.



**Figure 4-27 – Region of energy dissipation in the modified phase diagram**

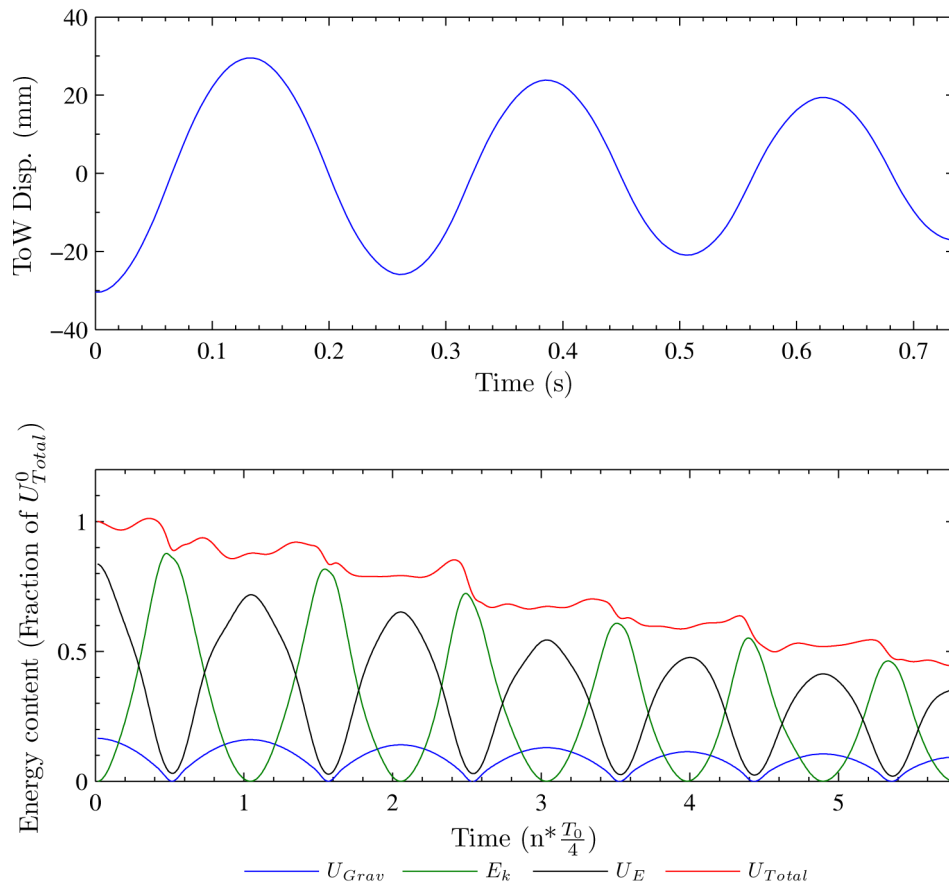
For a more thorough examination of the energy dissipation, the energy content of the PCM wall during the free vibration is separated into three components, gravitational potential energy ( $U$ ), kinetic energy ( $E_k$ ) and elastic potential energy ( $U_E$ ) from the stretching of the steel tendon.

Mathematically, the three quantities can be approximated from the ToW displacements and tendon force as per Equations 4-18, 4-19 and 4-20. The full derivations of these are available in Appendix B.

$$U(\Delta) = m_T g \left( \frac{|\Delta|}{\sqrt{H^2 - \Delta^2}} \left( 920 - 412 e^{-\left(\frac{\Delta}{3.551}\right)^2} \right) - \frac{B|\Delta|}{H} \right) \quad (4-18)$$

$$E_k(\dot{\Delta}) = \frac{1}{2H^2} I_o \dot{\Delta}^2 \quad (4-19)$$

$$U_E(\Delta) = \begin{cases} \frac{L_T}{2EA} [P_{Tendon}(\Delta)]^2 - 244.05 & \text{before tendon yield} \\ 159.03 \times \Delta L_T(\Delta) - 297.22 & \text{after tendon yield} \end{cases} \quad (4-20)$$



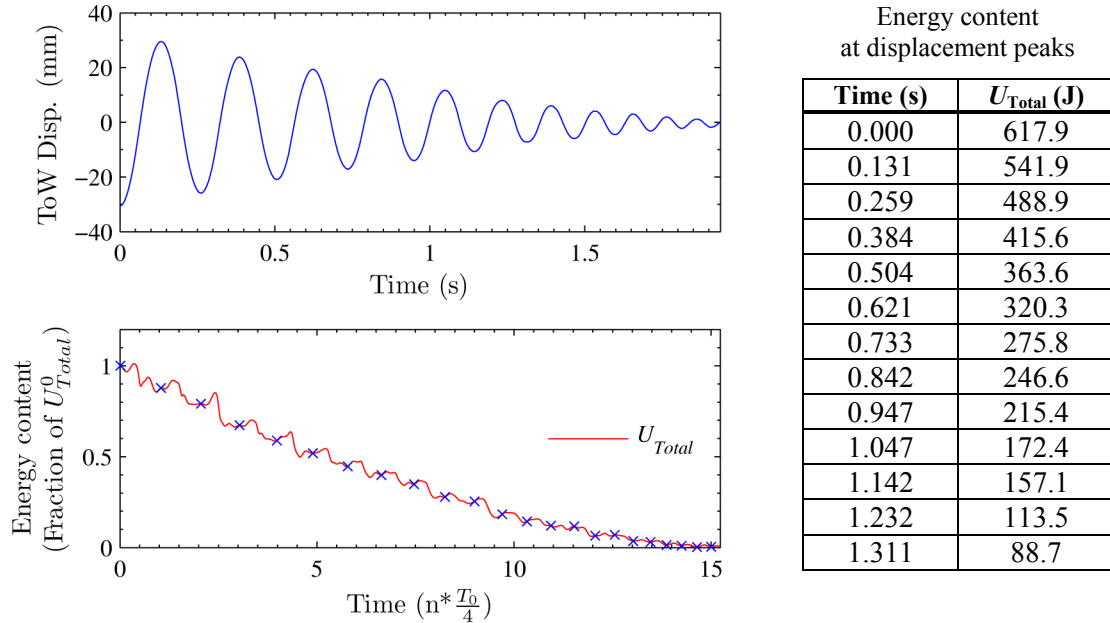
**Figure 4-28 – Energy content during the first three cycles of the FVD**

Figure 4-28 presents a plot of the three separate energy components for the first three cycles of the free vibration decay (FVD). The figure highlights that a majority of the energy exchange occurs between elastic potential energy in the prestressing tendon and kinetic energy of the wall. In fact, over 80% of the energy originates as elastic potential energy from the prestressing tendon. It is also noted that the total energy content have erroneously increased at times when the wall is upright, this is an effect of failures to locate the rotation centre location precisely at these times and has led to additional elastic potential energy.

Figure 4-28 also highlights that the total energy content during most of the rocking motion is effectively constant. This supports the previous phase diagram analyses finding, which suggests energy dissipation only occurs around the time of impact.

From the energy content data, it is also possible to investigate whether an apparent coefficient of restitution approach is suitable to characterise the energy dissipation of the system. Figure 4-29 presents the ToW displacement and the total

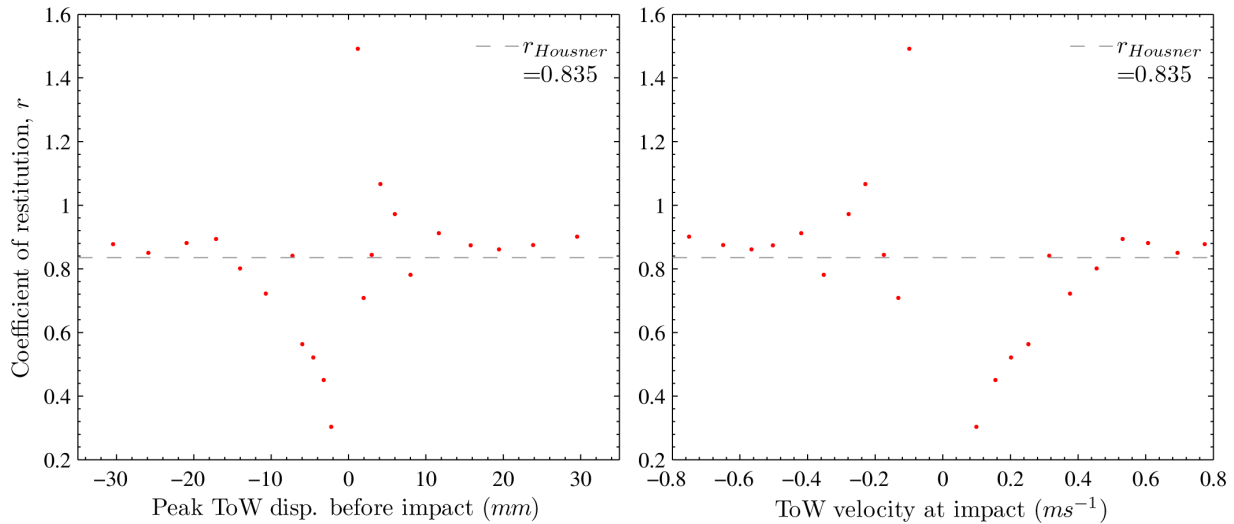
energy content for the entire free vibration decay. The accompanying table lists the total energy content at times when the wall is at the peak of its displacement cycle. Any two successive data points represent roughly the energy level before and after a passage through the upright position, or more simply before and after an impact.



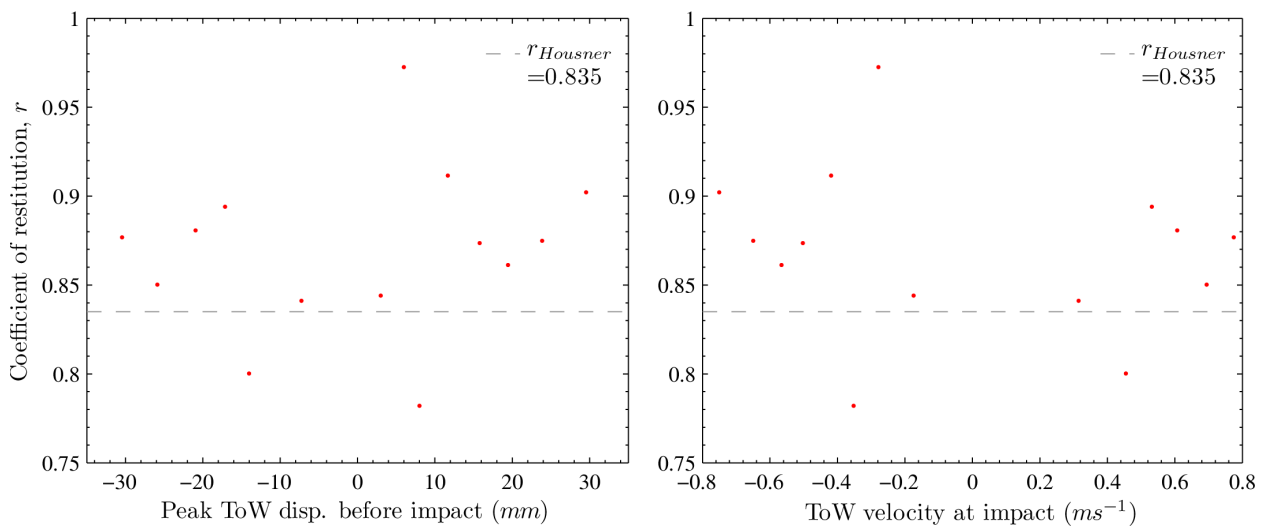
**Figure 4-29 – Total energy content at displacement peaks**

Apparent coefficients of restitution ( $r$ ) are calculated by obtaining a ratio of the successive total energy content. These are subsequently plotted against the peak displacement preceding the impact and the ToW speed at the time of impact in Figure 4-30. The figure appears to support the view that a constant  $r$  value describes the nature of energy dissipation adequately, except for small vibrations where the experimental  $r$  values are susceptible to hyperbolic error magnification.

However when the data are re-plotted with a focus on a smaller likely range of  $r$  values (0.7 - 1.0) in Figure 4-31, it highlights a high degree of variability. It is also evident from the two figures that there is no apparent relationship between the impact speed or the initial energy content with the experimental  $r$  values. It is noteworthy that the experimental  $r$  values are generally close to the theoretical Housner  $r$  value from Equation 2-6. In this instance  $R$  is taken as the distance from a bottom wall corner to the mass centroid and  $\alpha$  is taken as the angle between the vertical and a line connecting the bottom wall corner to the mass centroid.



**Figure 4-30 – Experimental coefficient of restitution versus Peak ToW displacement before impact and ToW velocity at impact**



**Figure 4-31 – Close up of Figure 4-30 with a focus on a range of realistic  $r$  values**

Enabled by the ability to evaluate the different components of energy as a function of the lateral displacements, it is now possible to theoretically predict the phase diagram trajectory of the controlled rocking wall in the no energy loss region, based on energy balance. Consider a PCM wall released from rest at an initial displacement,  $\Delta_0$ . The energy content of the wall at the start of motion  $U_{Total}^0$  is,

$$U_{Total}^0 = U(\Delta_0) + U_E(\Delta_0) \tag{4-21}$$

At a time  $t$  after the release, assuming zero energy dissipation, the total energy content remains the same as the total energy content at the time of release, except that

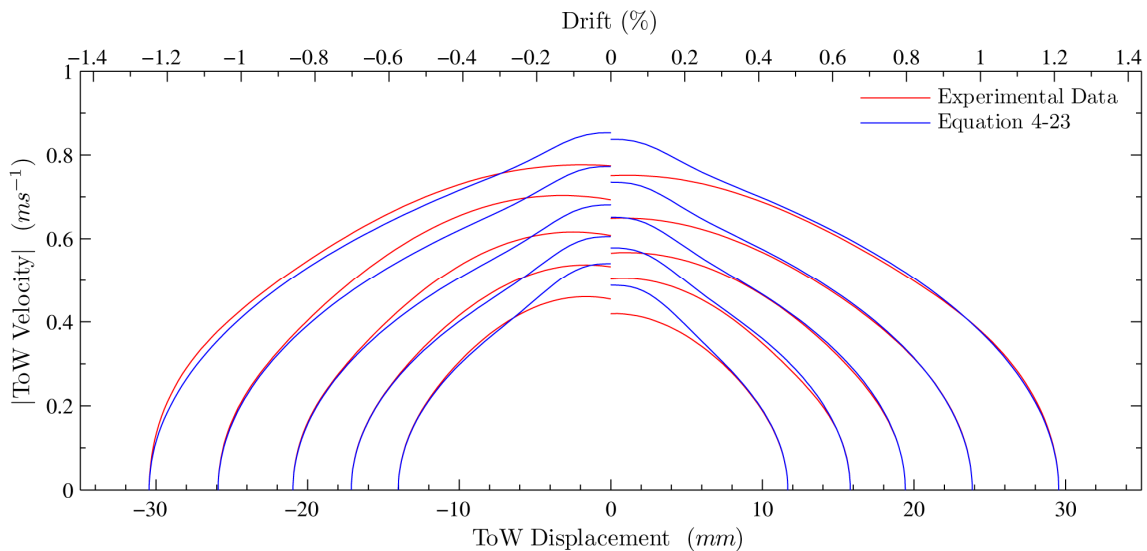
it is now the sum of gravitational potential, elastic potential and kinetic energies as described by Equation 4-22.

$$U_{\text{Total}} = U[\Delta(t)] + U_E[\Delta(t)] + E_k[\dot{\Delta}(t)] \quad (4-22)$$

Noting that time appears in Equation 4-22 as a parametric variable, Equation 4-21 is combined with Equations 4-19 and 4-22 to obtain Equation 4-23. This expression relates the ToW velocity as a function of the initial displacement ( $\Delta_0$ ) and the instantaneous ToW displacement ( $\Delta$ ). This equation can then predict the phase diagram trajectory of a conservative, controlled rocking wall from release to impact.

$$\dot{\Delta} = \sqrt{\frac{2H^2}{I_o} [U(\Delta_0) + U_E(\Delta_0) - U(\Delta) - U_E(\Delta)]} \quad (4-23)$$

Figure 4-32 presents a number of the theoretical trajectories predicted by Equation 4-23. They are plotted against the experimental trajectories originating from the same initial displacements for comparison. The matching of these two series for much of each trajectory reaffirms the previous finding that energy dissipation occurs only when the wall is near upright. Figure 4-32 also compares well with the previous observation that energy dissipation begins when the instantaneous displacement is less than 25% of the peak initial displacement.



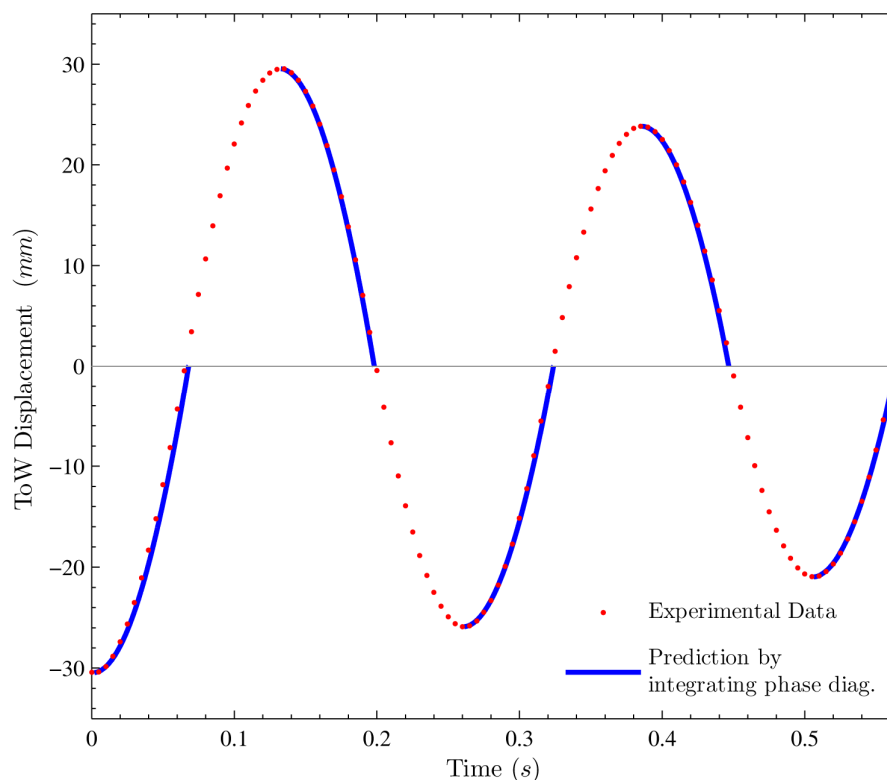
**Figure 4-32 – Experimental and conservative phase diagram trajectories**

For interest's sake, the phase diagram trajectories can be numerically integrated to achieve a response prediction in the time domain. The numerical integration process is summarised by,

$$\int_{\Delta_i}^{\Delta_{i+1}} \frac{1}{\dot{\Delta}} d\Delta = \delta t. \quad (4-24)$$

Where  $\delta t$  is the time interval required for the wall to displace from  $\Delta_i$  to  $\Delta_{i+1}$ . Examples of the application of this integral for five initial displacements are presented in Figure 4-33. It is clearly evident from this figure that an outstanding match is achieved in the time domain, which is a reflection of the accuracy of the theoretical phase diagram trajectory expression solely based on the assumption of the shift in rotation centre.

Accepting that the PCM wall travels more or less on the trajectory defined by Equation 4-23 until the instantaneous displacement is less than 25% of the peak initial displacement, Equations 4-25 and 4-26 were derived to represent the empirical boundary in Figure 4-27 which defines the energy dissipation region.

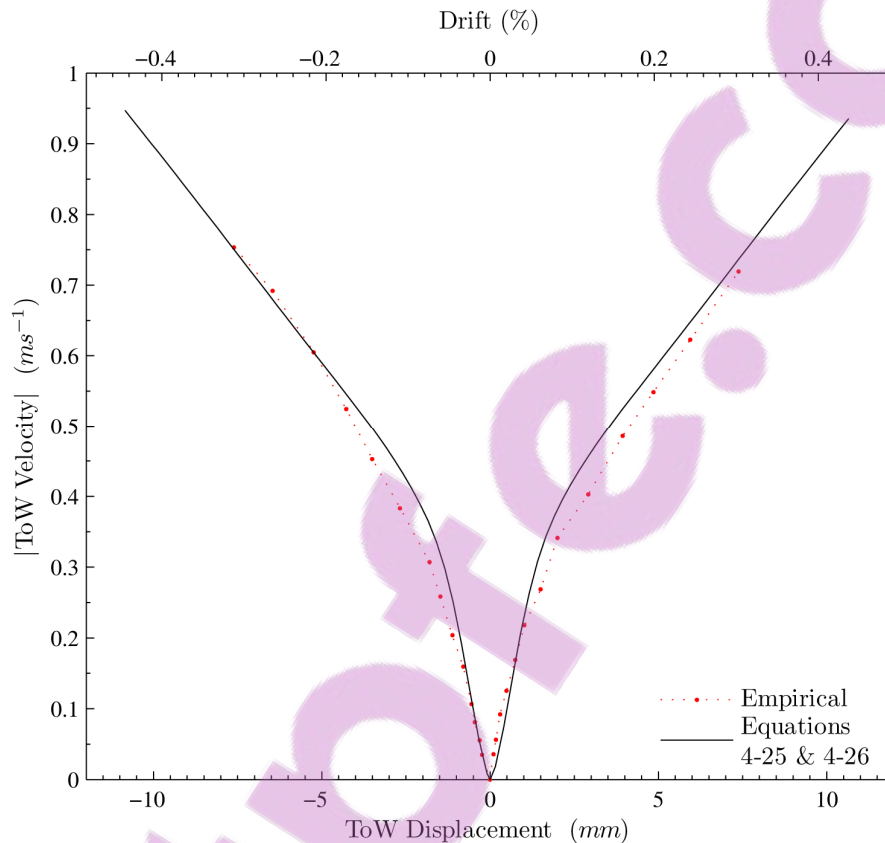


**Figure 4-33 – Time-history response by integrating the theoretical phase diagram trajectories**

Figure 4-34 shows the numerically calculated boundary closely matched the experimental boundary.

$$\Delta_{\text{limit}}(\Delta_0) = 0.25\Delta_0 \quad (4-25)$$

$$\dot{\Delta}_{\text{limit}}(\Delta_0) = \sqrt{\frac{2H^2}{I_o} [U(\Delta_0) + U_E(\Delta_0) - U(0.25\Delta_0) - U_E(0.25\Delta_0)]} \quad (4-26)$$



**Figure 4-34 – Empirical versus conjectural energy dissipation boundary**

#### 4.7.1 SUMMARY OF FINDINGS FROM THE FREE VIBRATION RESPONSE

Some of the key findings to this point include:

- 1) The centre of rotation shifts from the wall centreline out towards the wall corners as lateral displacement increases. The centre of rotation location can be approximated by a Dirac- $\delta$  type expression, Equation 4-7. The parameters in this equation have physical meanings and only the penalty parameter is empirically selected.
- 2) An expression for the uplift as a function of the lateral displacement can be derived based on the centre of rotation location. Taking advantage of the

geometric constraints, the uplift function can be extended to an expression for the tendon extension. This in turn leads to Equation 4-16 which prescribes the tendon force as a function of lateral displacement

- 3) The quarter period of controlled rocking PCM wall varies according to wall lateral displacements. The periods can be adequately predicted by making modification to the prediction formula for a free rocking system adopting the principle of equating the prestress as additional gravity load.
- 4) Phase diagram analyses have revealed that energy dissipation for a controlled rocking system is smooth and less abrupt than for a free rocking system. Energy dissipation occur slightly before and slightly after an impact, there is virtually no energy dissipation during the smooth rocking phases.
- 5) As there is little or no energy dissipation during the rocking phases, an accurate time-history response of the controlled rocking wall, from an initial displacement until impact can be computed by evaluating the line integral of the phase diagram. This is effectively tracing the transferral of energy from potential energy to kinetic energy. This approach works well when the wall displacements are large and not so well when the displacements are small.
- 6) There is no apparent trend in the variation of the coefficient of restitution.

#### **4.8 PREDICTING THE FREE VIBRATION TIME-HISTORY**

An interesting challenge now lies in combining the information gathered to this point, to accurately predict the time-history of the free vibration decay. Two possible techniques are examined herein; these are 1) by a nonlinearly elastic equivalent SDOF approximation, and 2) via solving the modified Housner type free rocking governing differential equations adopting the principle of equating the prestress as additional gravity load.

It is an aim of the study to create models that are familiar to structural engineers to simulate the two phases of the rocking response. The two phases of the rocking response being i) when rocking or full base uplift is not fully initiated, and ii) when full base uplift occurs during rocking.

#### 4.8.1 NONLINEARLY ELASTIC EQUIVALENT SDOF APPROXIMATION

In the equivalent SDOF approximation approach, the PCM wall is approximated as a nonlinearly elastic SDOF system in terms of its lateral displacement. The system has a generic second order governing differential equation of motion as per Equation 4-27, which is based on horizontal force equilibrium of an idealised one degree of freedom structure

$$M_e \ddot{\Delta} + F_k(\Delta) + F_{Damp}(r, \Delta, \dot{\Delta}, n) = P_e(t) \quad (4-27)$$

where  $M_e$  is the effective mass of the system,  $F_k(\Delta)$  is the nonlinear elastic restoring force,  $F_{Damp}(r, \Delta, \dot{\Delta}, n)$  is the Dirac- $\delta$  damping force which emulates the energy dissipation of the wall as it pass through the upright position and  $P_e(t)$  is the effective driving force of the system. The derivation of  $F_{Damp}$  is analogous to that presented on page 43 in Section 2 and the  $F_{Damp}$  expression is presented as Equation 4-28 below.

$$F_{Damp}(r, \Delta, \dot{\Delta}, n) = \frac{M_e \ln(\sqrt{r})}{n\sqrt{\pi}} \dot{\Delta}^2 e^{-\left(\frac{\Delta}{n}\right)^2} \cdot \text{sign}(\dot{\Delta}) \quad (4-28)$$

The nonlinear elastic restoring force,  $F_k(\Delta)$  represents the restoring force of the system due to the deformation or displacements alone excluding any dynamic effects. This is equivalent to a backbone curve from conducting a pseudo-static pushover experiment.

In such a pseudo-static pushover test, an increasing lateral force is applied slowly to the wall system. The force is applied slowly so that it does not induce any dynamic effects. The applied force is balanced by the restoring force associated with a particular strain level at any one time. The backbone curve is a plot of the applied force in this manner against the associated instantaneous displacement.

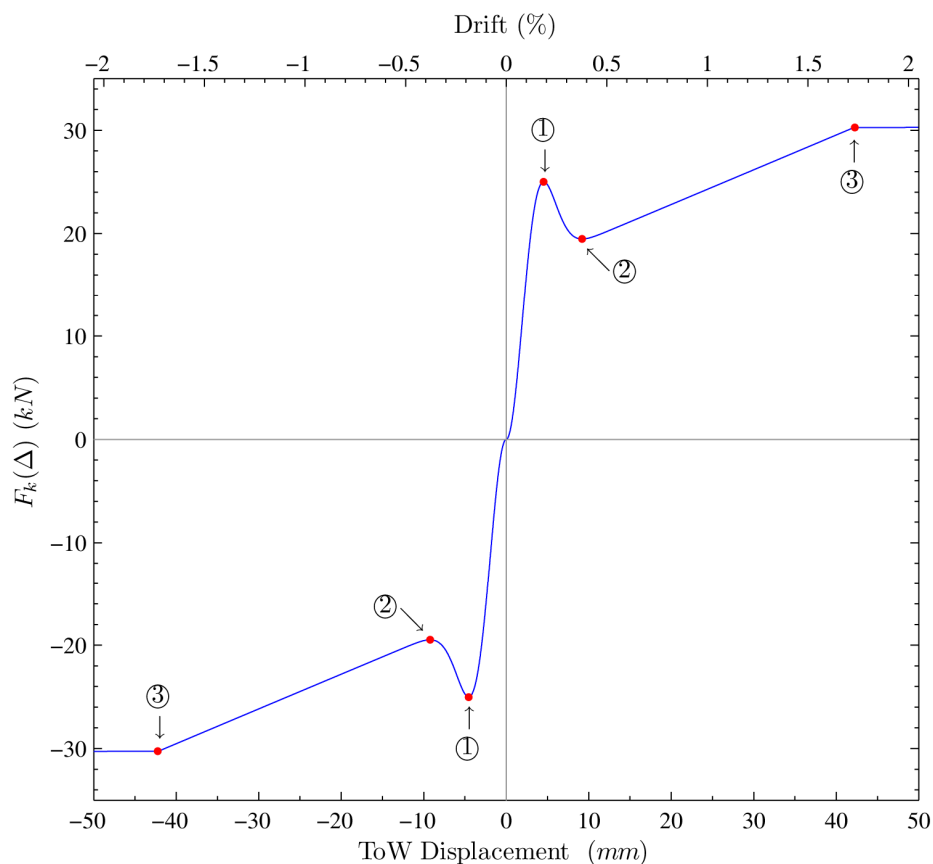
Consider the pushover test on a controlled rocking system using energy principles. Assuming that testing occurs in an idealised environment, there will be no energy dissipation in the system. As a result, the wall begins with a zero energy state, and then as the external force ( $F_k(\Delta)$ ) is applied, the work done by the external force over the incremental displacement ( $\delta\Delta$ ) is converted into gravitational potential energy ( $U$ ) and elastic potential energy ( $U_E$ ) which can be calculated by Equations 4-18 and 4-20. This energy balance is expressed mathematically by Equation 4-29.

$$\delta U_E + \delta U = F_k(\Delta) \cdot \delta \Delta \quad (4-29)$$

As the incremental displacement tends towards zero, the nonlinear elastic restoring force can be obtained by means of Equation 4-30. The calculation can be accomplished very simply by numerically differentiating Equations 4-18 and 4-20.

$$F_k(\Delta) = \frac{dU_E}{d\Delta} + \frac{dU}{d\Delta} \quad (4-30)$$

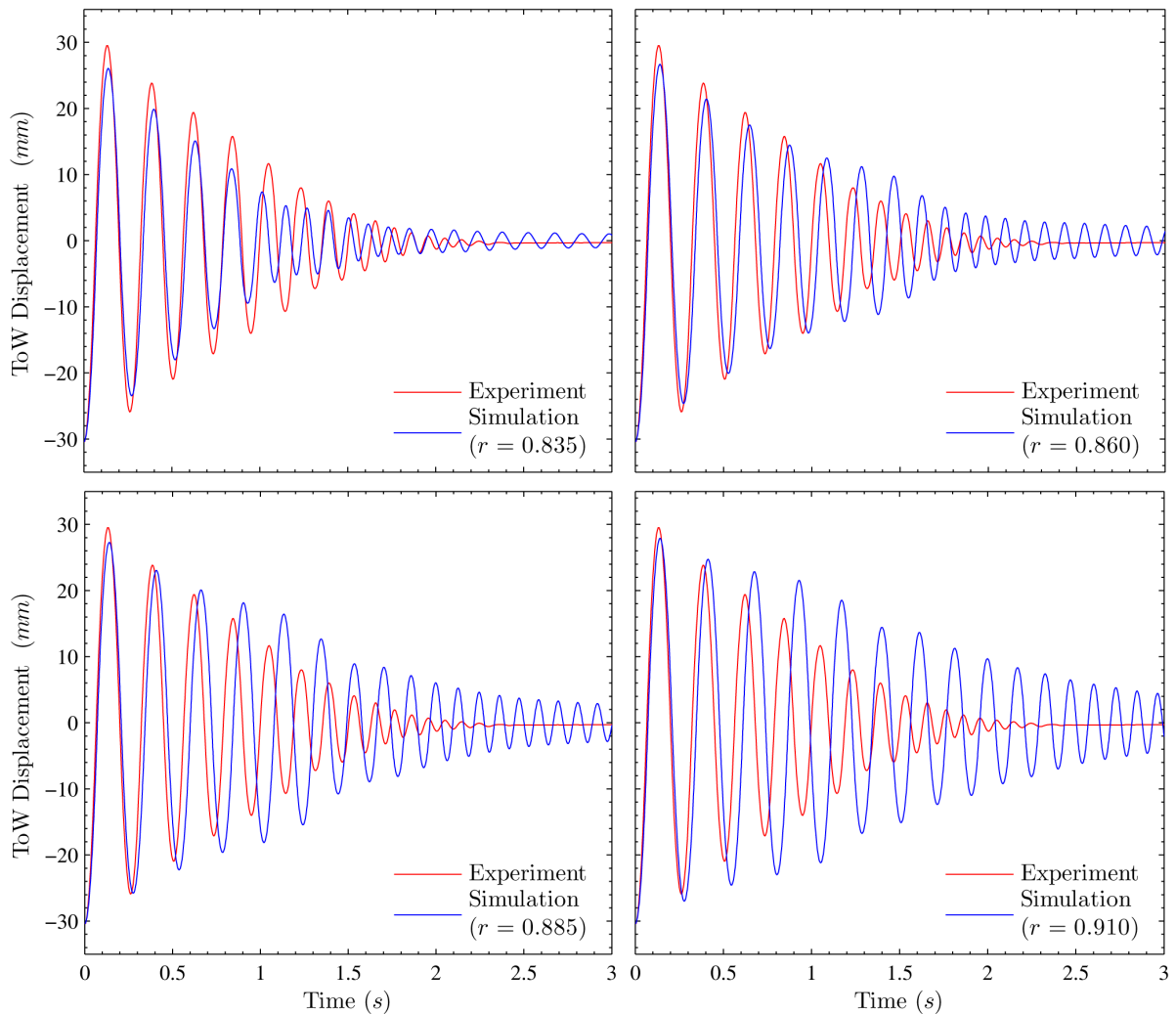
A plot of the nonlinear elastic restoring force as calculated using the theoretical energy gradients is presented in Figure 4-35. This plot compares well with previously published force-displacement data by Wight et al. (2006) which approximated the pseudo static response by using data points with zero velocity. Having obtained an expression for each of the components in Equation 4-27, the components are substituted into the equation and the equation solved numerically for the free vibration decay response using an ordinary differential equation solver.



Description	Coordinates
① - Centre of rotation migrates rapidly to the wall base corners	(4.55, 25.01)
② - Centre of rotation firmly fixed near the wall corner	(9.20, 19.48)
③ - Tendon begins to yield	(42.25, 30.27)

**Figure 4-35 – Theoretical nonlinear restoring force-displacement relationship**

In the following preliminary simulations,  $M_e$  is taken as the total mass of the wall and the penalty parameter ( $n$ ) is taken as 3.551, the same value as the penalty parameter in the rotation centre location equation, Equation 4-7. This is selected based on the observation that energy is only dissipated when the wall is near upright, coincidental to the shift of the rotation centre. Figure 4-36 presents a number of comparison plots of the time-history prediction against the experimental data, using a range of  $r$  values beginning from  $r_{Housner}$ .



**Figure 4-36 – Preliminary numerical simulation results with a range of  $r$  values**

Figure 4-36 highlights that there is not a single  $r$  value implemented using the current framework which can simulate the energy dissipation of the free vibration decay correctly. A high  $r$  value which works well for the early cycles with high displacements does not simulate sufficient energy dissipation for the later cycles with lower displacement. The final outcome is a poor prediction in the time domain.

The poor prediction is not unexpected as the experimental results show the  $r$  values vary considerably on each passage through the upright position. The Dirac- $\delta$  damping force would not emulate this as it merely smoothly distributes the fixed energy dissipation, which is controlled by a single  $r$  value over a fixed displacement region in turn controlled by the penalty parameter.

This result highlights the need to modify the damping force expression to permit different energy dissipations to be assigned for large and small displacement cycles. A sensible modification is to construct the  $r$  parameter as a function of the instantaneous velocity. This modification can exploit the fact that free vibration cycles originating from a larger displacement will pass through the upright position with higher velocity than cycles originating from lower displacements.

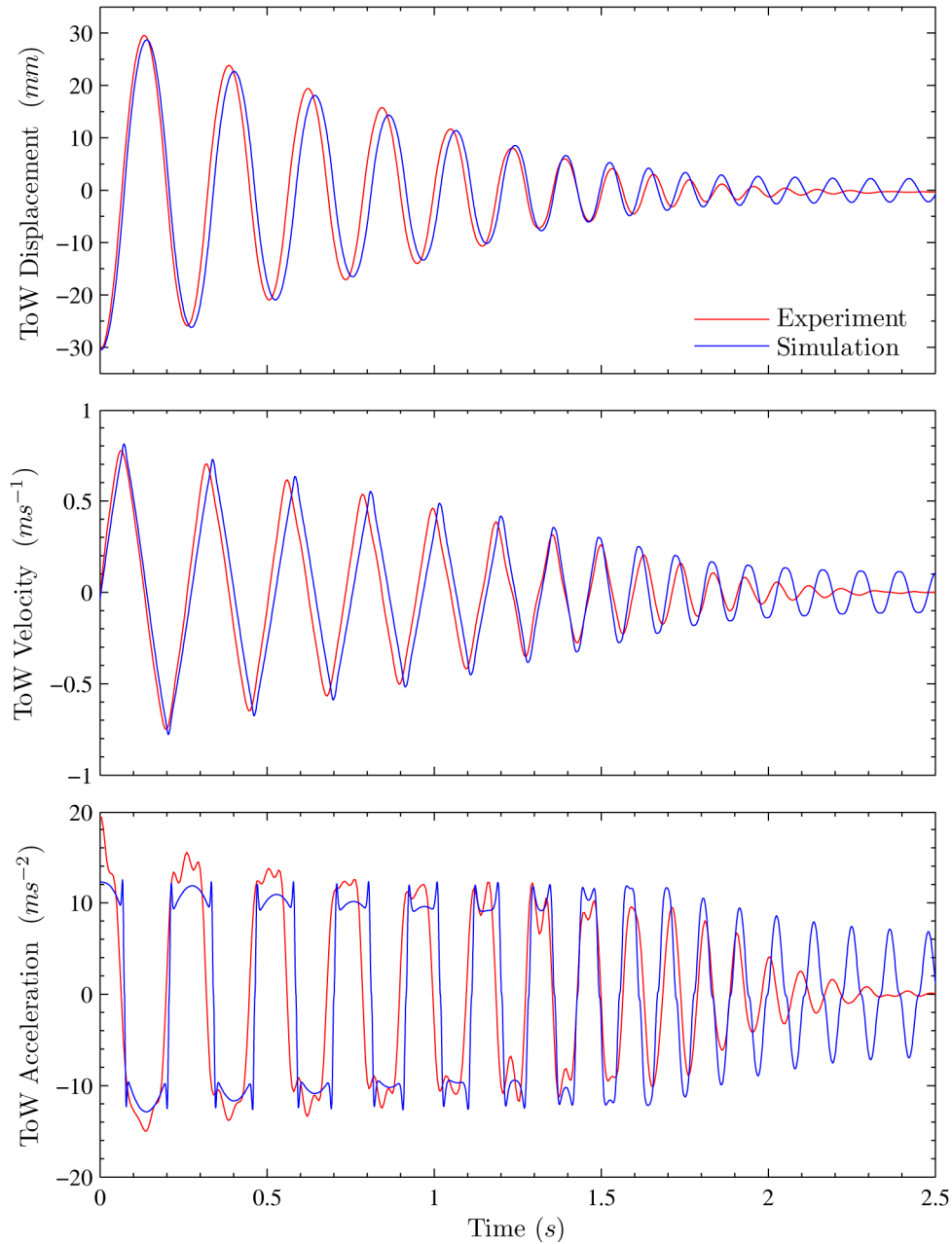
Through a trial and error approach, it was found that an accurate simulation of the free vibration response can be achieved by 1) increasing the theoretical elastic restoring force,  $F_k(\Delta)$  by 6%, and 2) allowing  $r$  to vary according to Equation 4-31.

$$r = \begin{cases} \frac{0.01}{0.45} \cdot |\dot{\Delta}| + 0.85 & \text{for } 0 < |\dot{\Delta}| < 0.3, \\ 0.81 & \text{for } 0.3 < |\dot{\Delta}| < 0.47, \\ 0.852 & \text{for } 0.47 < |\dot{\Delta}| < 0.78, \\ 0.95 & \text{for } |\dot{\Delta}| > 0.78. \end{cases} \quad (4-31)$$

The increase in nonlinear restoring force is driven by the observation that the first quarter cycle of the initial simulation lags the actual behaviour in the time domain. Increasing the restoring force increases the stiffness of the system and hastening the simulated response. This adjustment may be deemed reasonable as many physical factors could have attributed to the increased stiffness. Some possible factors include errors in the effective cross-sectional area of the prestressing tendon, variation of material properties, unaccounted elastic stiffness of the wall and unaccounted frictional resistance of the wall and the foundation.

Subsequent to attaining a correct system stiffness, the  $r$  value is adjusted from cycle to cycle to match the peak displacement decrements from the experimental results. Beginning from the first cycle,  $r$  values are substituted into the time-history solver and an optimum value is noted if it produces the best overall match for the cycle of interest. Velocity limits are introduced to activate a different  $r$  value for each

cycle with different peak displacements. The selection of these limits is guided by the equivalent velocity at which energy dissipation begins as described in Equation 4-26. Ultimately, they are refined by actual trials and engineering judgement to balance between accuracy and simplicity. The simulation result is compared against the experimental data in Figure 4-37.

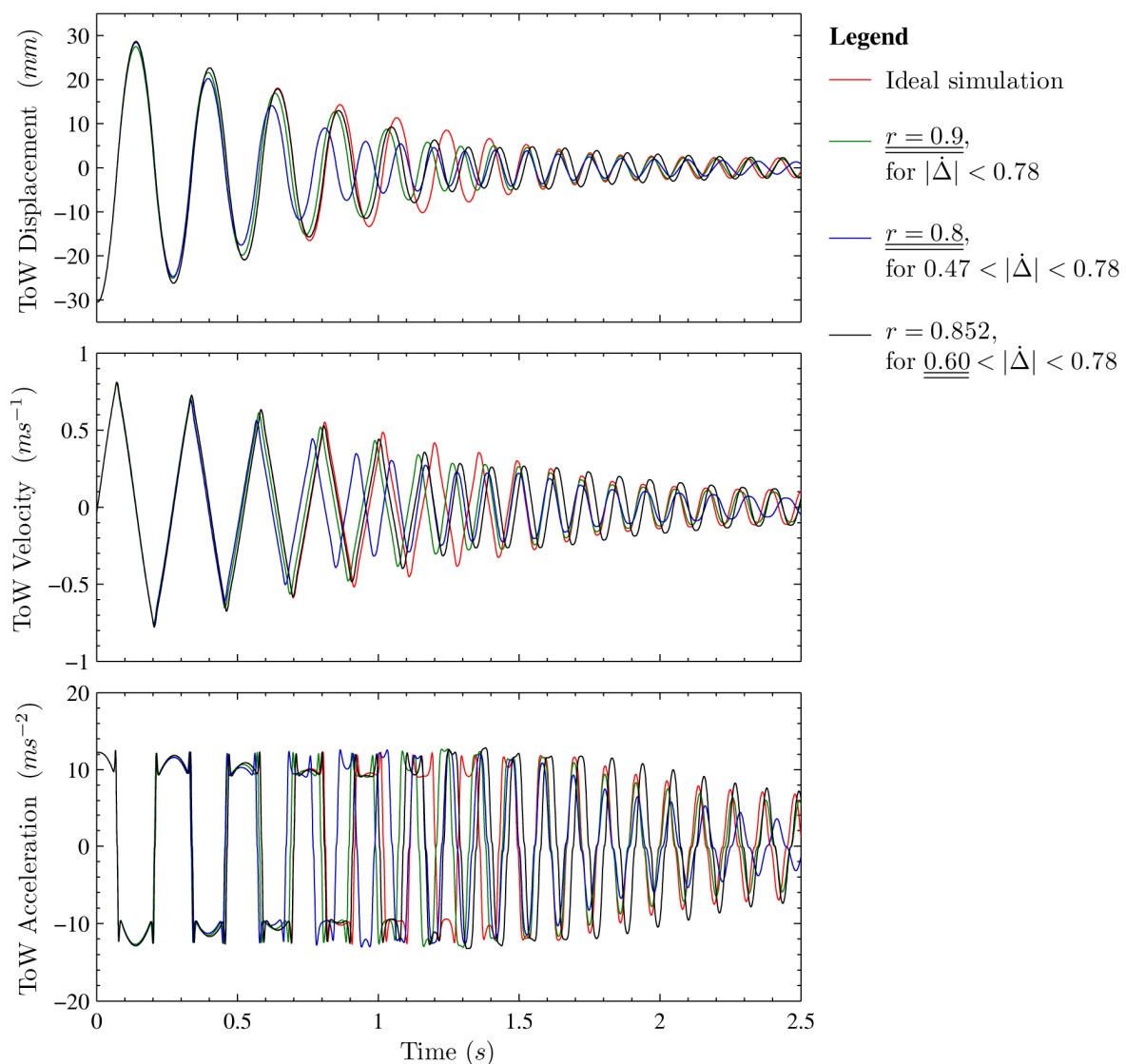


**Figure 4-37 – Final numerical simulation against experimental result**

Figure 4-37 highlights a good tracking between the actual response and the simulated results in terms of the displacement amplitudes and synchronicity in the time domain. The figure also illustrates that the theoretical elastic restoring force

adequately reproduces the distinctive velocity and acceleration behaviours when the wall is near upright, or in other words at times near impacts.

It may also be noted that the simulated response is moderately sensitive to variations of the  $r$  value. A minor deviation from the settings described in Equation 4-31, in the amplitudes or the velocity limits, results in a large change to the subsequent response. This is illustrated in Figure 4-38 where the simulated wall response for three scenarios with small deviations from Equation 4-31 is plotted against the ideal simulated response. The specific deviation is denoted by a double underscore in the legend.



**Figure 4-38 – Comparison of simulated response with small deviations in  $r$  value**

In closing, while this simulation procedure ultimately produced a successful matching of the free vibration result and is almost entirely justifiable by theory, it is

disappointing that there appears to be no physical foundation for the variation in the amount of energy dissipation, or in other words the  $r$  value. Because of the sensitivity of the problem to the energy dissipation, a best estimate of the energy dissipation relationship had to be backward manipulated from test data.

A key principle of the equivalent SDOF procedure is the development of the restoring force-displacement characteristics from potential energy gradients. This principle can be easily extended to predict the restoring force characteristics for other wall and tendon arrangements.

#### 4.8.2 MODIFIED HOUSNER - SUBSTITUTE GRAVITY APPROACH

The second approach for simulating the free vibration response considers the controlled rocking wall specimen as a free standing wall. The influence of the post-tensioning tendon is simulated as additional gravity load which increases as the wall is displaced according to the stress-strain relationship of the tendon. This effectively is solving the problem exactly in the rotational degree of freedom, ignoring the small rotations of the tendon force as the wall displaces. This approach has been adopted successfully in predicting of quarter periods of the controlled rocking wall as shown in Figure 4-24.

For the initial simplistic analyses, Equation 2-2 is applied to our wall specimen with the assumption that the centre of rotation is fixed at the wall corners. Accordingly,  $I_o$  would be the moment of inertia of the wall about a wall corner and  $R$  and  $\alpha$  would be measured from a wall corner to the mass centroid as similarly illustrated in Figure 4-22. The self weight term in Equation 2-2 is replaced with the self weight plus the instantaneous tendon force. This leads to Equation 4-32, the governing differential equation of the simplified, “modified Housner - substitute gravity” (MHSG) approach.

$$I_o \ddot{\theta} = -\text{sgn}(\theta) \cdot (mg + P_{tendon}(\Delta)) R \sin(\alpha - \text{sgn}(\theta) \cdot \theta) \quad (4-32)$$

It should be noted that  $P_{tendon}(\Delta)$  is defined previously in Equation 4-16 and the top of wall displacements ( $\Delta$ ) can be approximated in terms of  $\theta$  by Equation 4-33.

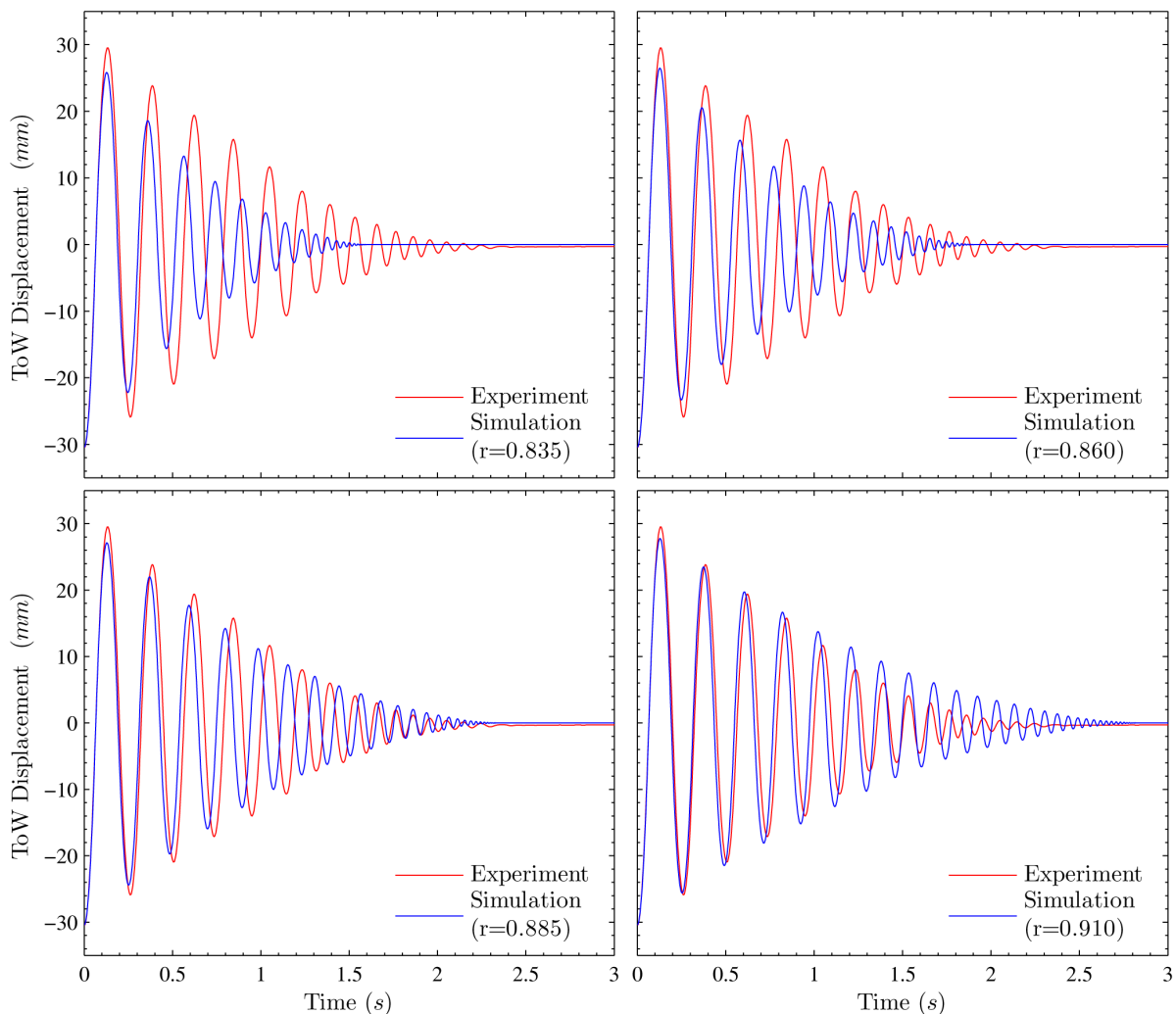
$$\Delta \approx H \sin(\theta) \quad (4-33)$$

Then, to simulate the response of the PCM wall specimen, Equation 4-32 is solved numerically in terms of rotation ( $\theta$ ) using an ordinary differential equation (ODE) solver, with the initial rotation of the free vibration experiment as the initial condition. The tendon force is constantly updated within the ODE solver.

During the analysis process, the ODE solver is set to terminate whenever the rotation is zero, or in other words when the wall passes through the upright position. The solver is then restarted with an initial angular velocity  $\sqrt{r}$  times the terminated angular velocity to simulate the energy dissipation at an impact. Once the analysis is complete, the angular response can be converted into rectilinear measurements using Equations 4-33, 4-34 and 4-35.

$$\dot{\Delta} = H \cos(\theta) \cdot \dot{\theta} \quad (4-34)$$

$$\ddot{\Delta} = H(\ddot{\theta} \cos(\theta) - \dot{\theta}^2 \sin(\theta)) \quad (4-35)$$

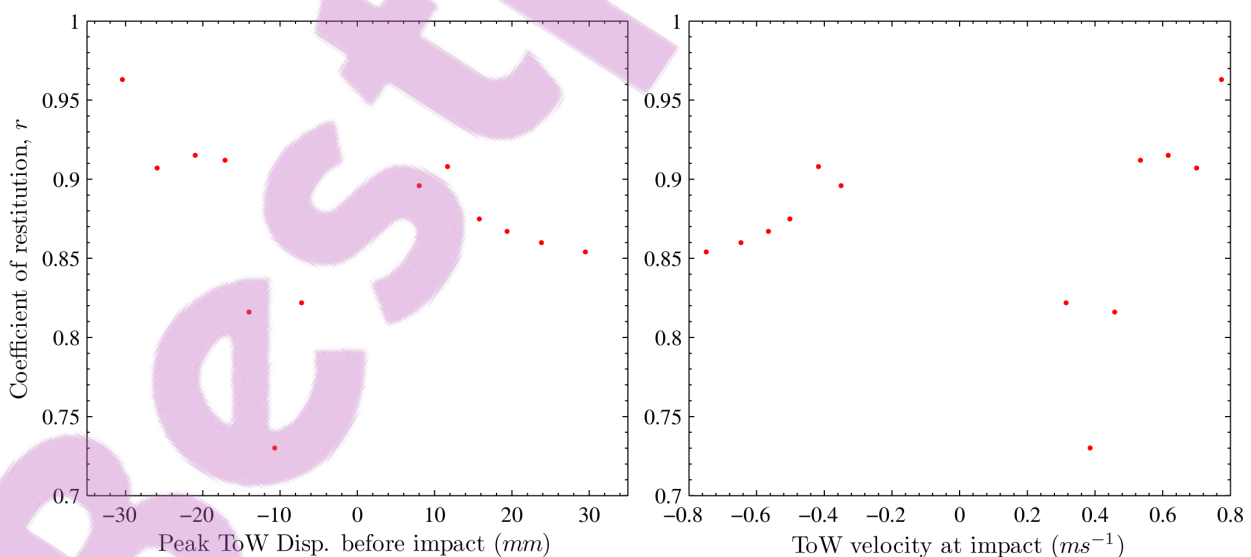


**Figure 4-39 – Simplified, MHSG simulation results with a range of  $r$  values**

Figure 4-39 presents a number of the simulated responses against the experimental data using this approach, adopting a range of  $r$  values from  $r_{Housner}$ . As shown, the simulation reproduced very similar behaviour to the actual experimental data. The matching is evident when simulated and actual cycles originating from comparable peak displacement amplitudes are overlaid. This exercise generally results in two lines following each other exactly for a short duration until the next peak of the cycle, at this time the simulated response deviates from the actual response as the simulation fails to simulate the correct energy dissipation.

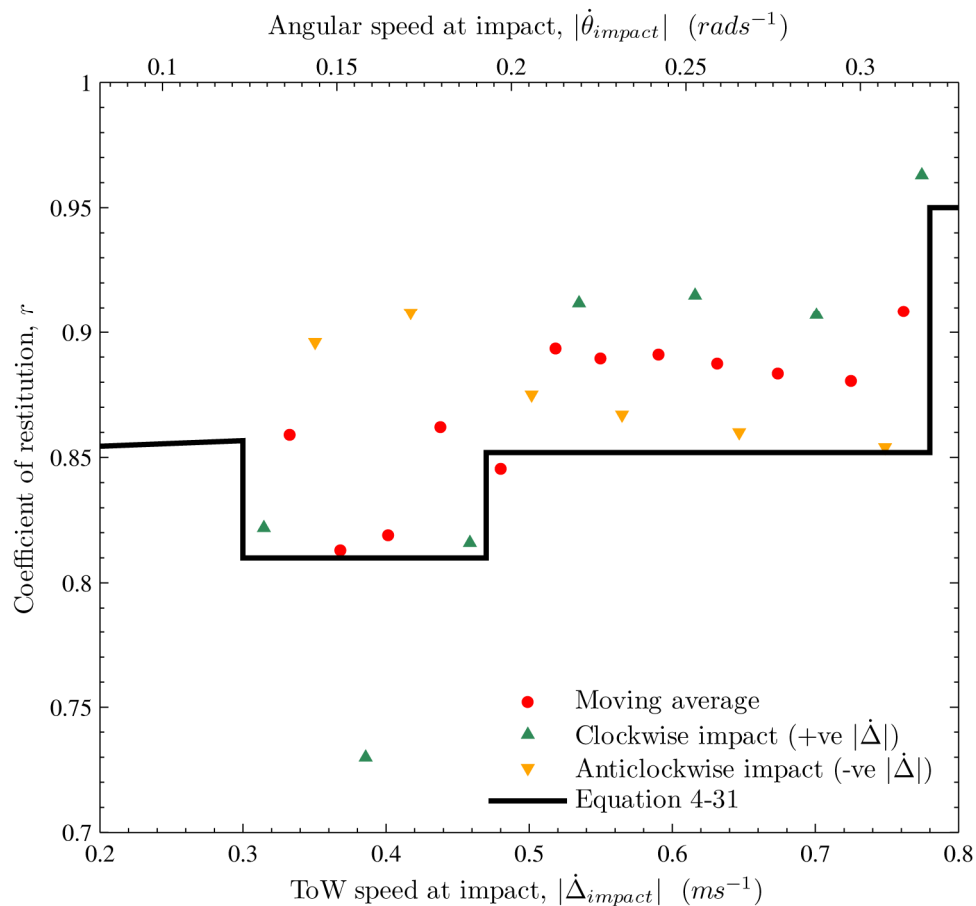
This comparison highlights the ability of the simulation procedure to produce the correct slope in the displacement time-history for the full range of displacements. This demonstrates the simulation is accurate in predicting the correct restoring stiffness of the system and in emulating the amplitude dependent rocking period.

Figure 4-39 also highlights that a single  $r$  value is more successful in replicating the energy dissipation in the simplified MHS procedure than the previous nonlinear elastic equivalent SDOF approximation approach. It is observed from Figure 4-49 that the “correct”  $r$  value appears to vary between 0.91 for the large displacement cycles to around 0.88 for the lower displacement cycles. A series of free vibration time-history simulations were subsequently conducted each beginning at an initial displacement corresponding to a peak displacement of the experimental results. Considering only the simulation results from one displacement peak to the opposing peak,  $r$  values were trialled until an accurate matching was achieved.



**Figure 4-40 –  $r$  values for each cycle for an accurate time-history simulation**

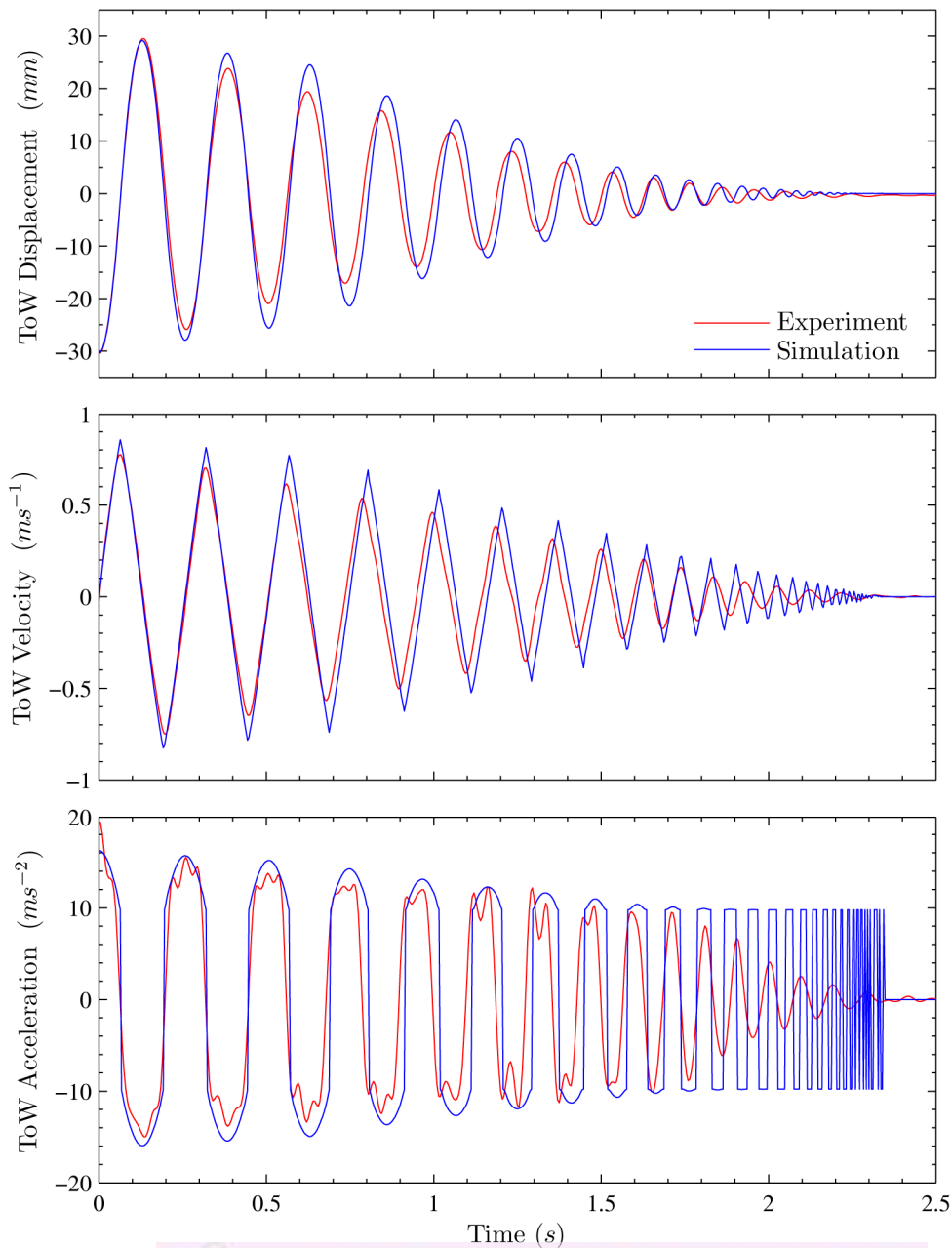
The ideal  $r$  values for each simulation are collated and plotted against the impact velocity and the peak displacement of each cycle in Figure 4-40. From Figure 4-40, no apparent relationship can be deduced to describe how the  $r$  value varies. It appears the  $r$  value or the required energy dissipation per impact for an accurate time-history simulation using this approach is seemingly random. To examine this hypothesis further, a moving average of the ideal simulation  $r$  values was calculated. Each moving average data point is the average of two data points sequential in time and is effectively the average  $r$  value from a clockwise and anticlockwise impact. The moving average  $r$  values were plotted against the average speed of each impact in Figure 4-41. Although there is still no apparent trend in the variation of  $r$ , it is encouraging that the moving average data resembles the empirical  $r$  expression derived previously for the equivalent SDOF approach.



**Figure 4-41 – Moving average of ideal  $r$  values for accurate time-history simulation against empirical expression for  $r$**

Upon noticing the similarity, the previously developed expression for  $r$ , Equation 4-31, was implemented into the ODE solving scheme and the free vibration response reanalysed. Figure 4-42 presents the resulting detailed response.

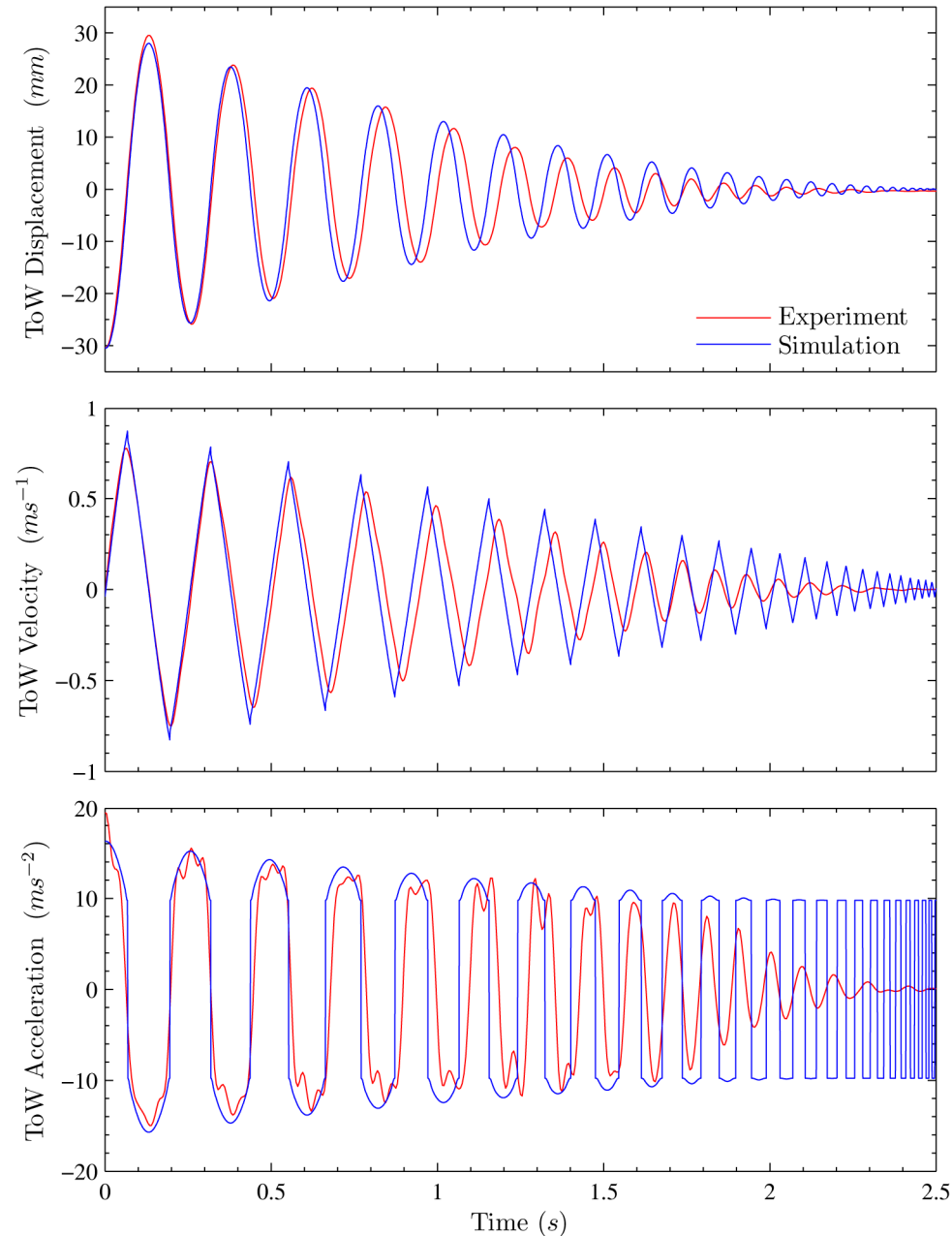
The figure shows that adopting the empirical  $r$  expression produces an adequate simulation of the system. However, it is not a dramatic improvement over the use of a single  $r$  value. In fact, an equally effective simulation can be achieved if  $r$  is varied linearly between 0.88 and 0.91 for large and small impact velocities as per initial observations.



**Figure 4-42 – Simplified MHSG simulation with  $r$  calculated using Equation 4-31**

The exact mathematical relationship for the simpler variation of  $r$  is provided as Equation 4-36 and the subsequent simulated response is presented in Figure 4-43.

$$r = 0.0441 \cdot |\dot{\Delta}| + 0.865 \quad (4-36)$$



**Figure 4-43 – Simplified MHS simulation with  $r$  calculated using Equation 4-36**

It is also interesting to note that the simplified MHS procedure is unable to emulate the distinctive velocity and acceleration behaviours of the controlled rocking free vibration. This is evident from the results of both presented simulations in Figures 4-42 and 4-43. The differences include,

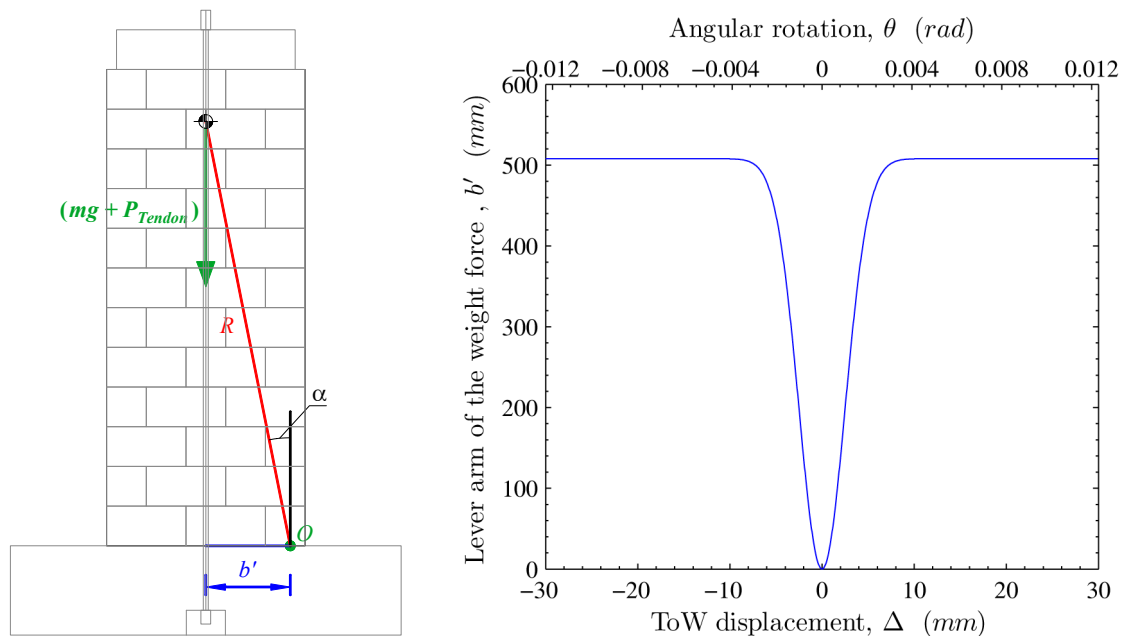
- 1) When the displacements are high, the simulated accelerations are rounded at the peaks while the experimental accelerations are jagged and appear as plateaus instead of peaks. This occurs because the simplified procedure assumes static rocking pivots whereas in reality the pivot migrates from the wall centre to the wall edge with increasing displacements. As this shift occurs, the wall experiences a momentary reduction in restoring moment and hence produces a plateau rather than a peak in the acceleration time-history. This is analogous to the transition of ① to ② in Figure 4-35.
- 2) The simplified MHSg procedure produces sharp changes from positive to negative accelerations, while the experimental results show the actual transition is slightly more gradual. This distinction is apparent from the vertical lines in the simulated acceleration time-history, in place of slightly sloped trace in the experimental results. This occurs as the simplified procedure shifts the rocking pivot from one corner to the other in a stepwise manner, whereas in reality, the rotation centre shifts gradually within a wall as the wall passes through the upright position. This is analogous to the transition from the positive ① to the negative ① and vice versa in Figure 4-35.
- 3) The simplified MHSg procedure is very poor at predicting the wall response when the wall displacement is small. The simulation produces a square acceleration waveform whereas the experimental result shows a more gentle decreasing sinusoidal trace. This phenomenon is again attributed to the inability of the simplified MHSg procedure to model the wall behaviour when the wall is near upright. The explanation of this is provided previously in 2) above.

The square waveform observed in 3) above highlights a more critical flaw of the simplified MHSg approach. The square wave form reveals that the procedure simulates a constant unreasonable restoring moment when the wall displacement is small. The effect of this may be small under free vibration decay, however if this procedure is extended to include base excitation, it would require an unreasonably large force just to initiate movement.

For illustration purpose, the wall in the current example has a self weight of 19.8 kN and an initial prestressing force of 75.6 kN. In the simplified MHSG approach, these two forces act vertically through the centroid, 508 mm away horizontally from the wall corner. When the wall is at rest, a ground acceleration pulse would generate a lateral force acting at the height of the centroid, 2173 mm above the ground level. Considering static moment equilibrium about a wall corner, in accordance with the static rotation centre assumption in the simplified MHSG approach, an acceleration greater than  $11.1 \text{ ms}^{-2}$  (1.1 g) would be required to initiate any motion. This would imply that none of the shake table runs in Table 4-1 would have resulted in any motion, which is clearly incorrect.

The simplified MHSG was subsequently improved by adopting the assumption that the centre of rotation migrates smoothly from the centre of the wall to the wall edge with increasing wall displacement. It was further assumed that the centre migrates following a Dirac- $\delta$  function as shown in Equation 4-37.

$$b' = 508 \left( 1 - e^{-\left(\frac{\Delta}{3.551}\right)^2} \right) \text{ mm} \quad (4-37)$$

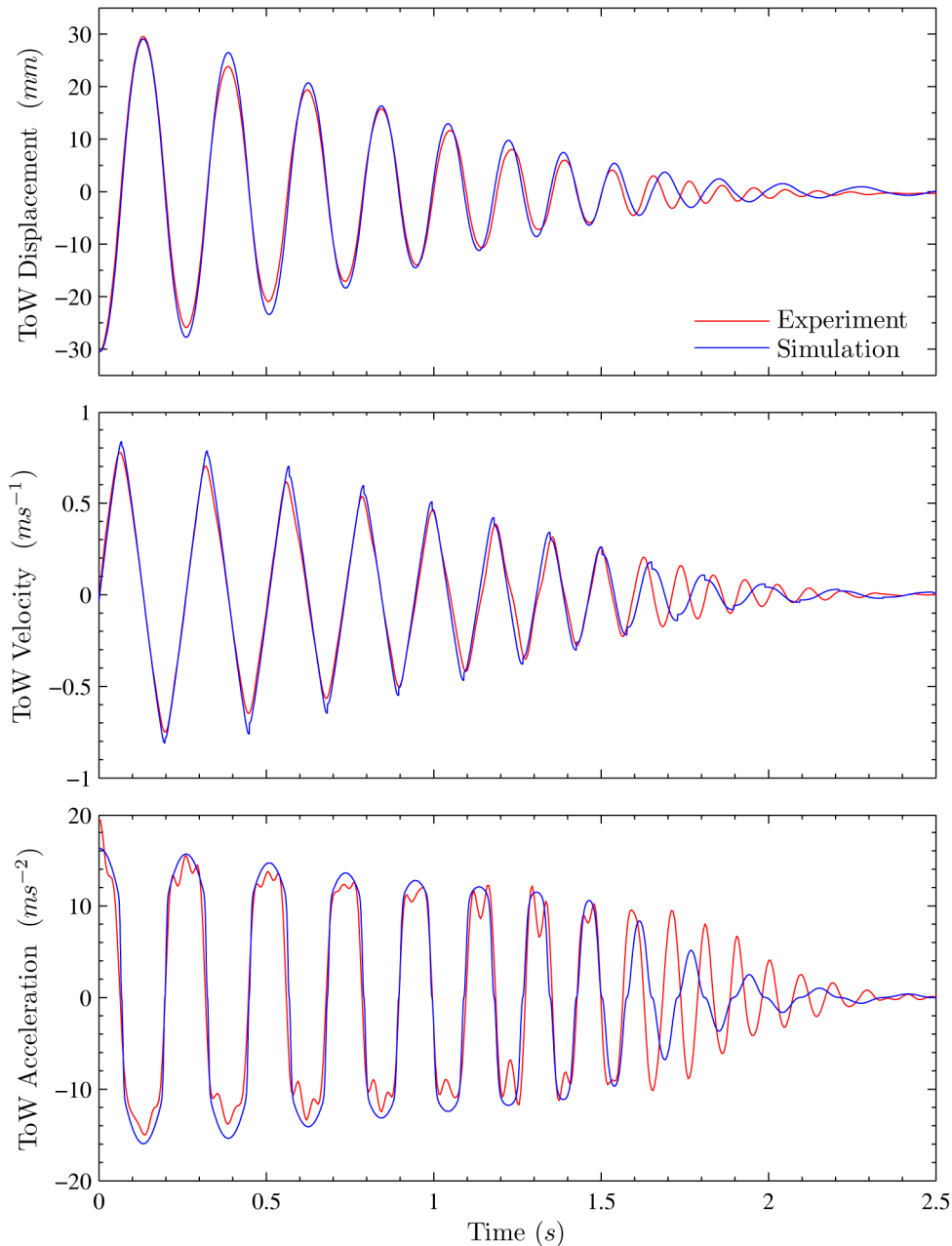


**Figure 4-44 – a) Parameters affected by the new assumption, b) centre of rotation migration relationship**

Equation 4-37 shares the same penalty parameter ( $n$ ) as Equation 4-7. This gives rise to a consistent centre migration rate as the assumption used in the equivalent SDOF procedure and the underlying assumption for the tendon force expression for this method. This new assumption means that  $\alpha$  and  $R$  must be constantly updated in the ODE solving scheme. The definitions of  $b'$ ,  $\alpha$  and  $R$  are shown again in Figure 4-44 alongside a plot of the Equation 4-37. The resulting new analysis method is termed the modified Housner - substitute gravity (MHSG) procedure.

The new MHSG procedure is applied to predict the free vibration time-history response. Energy dissipation is implemented by a stepwise reduction of wall velocity at every passage through the wall's upright position. The magnitude of the energy dissipation is controlled by an  $r$  value which follows an empirical Equation 4-38, a modified version of Equation 4-31 obtained via trial and error. The analysis result is presented in Figure 4-45.

$$r = \begin{cases} |\dot{\Delta}| + 0.445 & \text{for } 0 < |\dot{\Delta}| < 0.365, \\ 0.81 & \text{for } 0.365 < |\dot{\Delta}| < 0.47, \\ 0.85 & \text{for } 0.47 < |\dot{\Delta}| < 0.78, \\ 0.94 & \text{for } |\dot{\Delta}| > 0.78. \end{cases} \quad (4-38)$$



**Figure 4-45 – MHS simulation with  $r$  calculated using Equation 4-38**

It can be seen in Figure 4-45, the simulated response has greatly improved compared to the simplified MHS procedure results. In particular, the slope of the simulated acceleration time-history at times near zero crossings now matches the experimental result rather well. The simulated accelerations near the peaks also consistently capture the experimental results. This has led to a very good matching of the velocity and displacement time-histories.

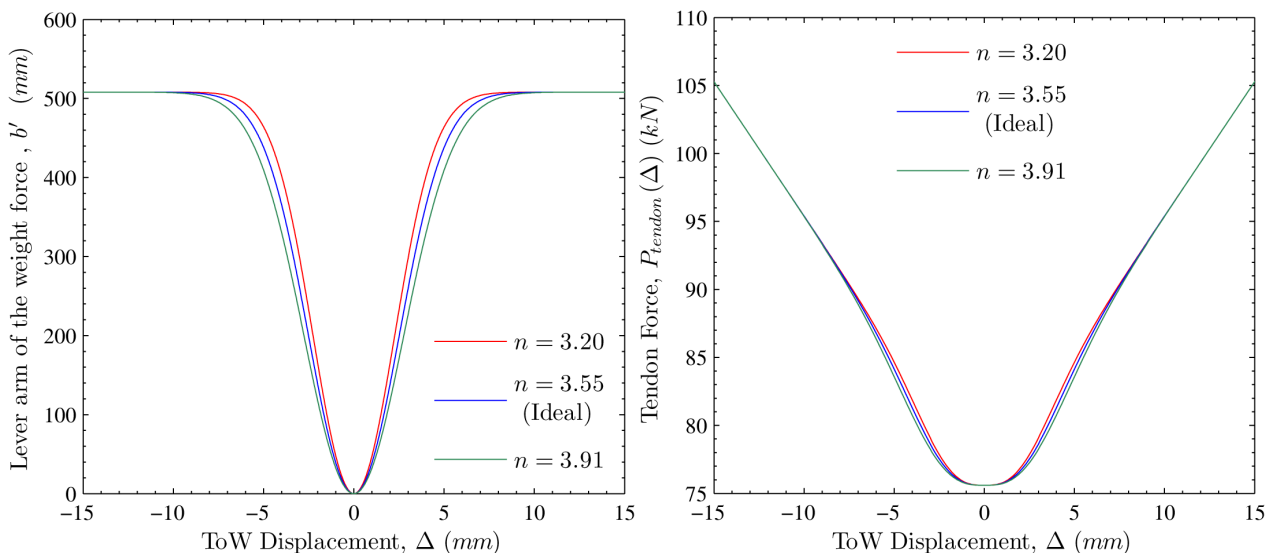
However, the MHS procedure is still poor at estimating the response of the controlled rocking wall when the vibration is small. This is not surprising as the

MHSG procedure assumes the wall motion is characterised by a governing differential equation based on the equilibrium in the rotational degree of freedom at all times. This assumption is invalid when the wall displacement is small and if rocking has not been properly initiated.

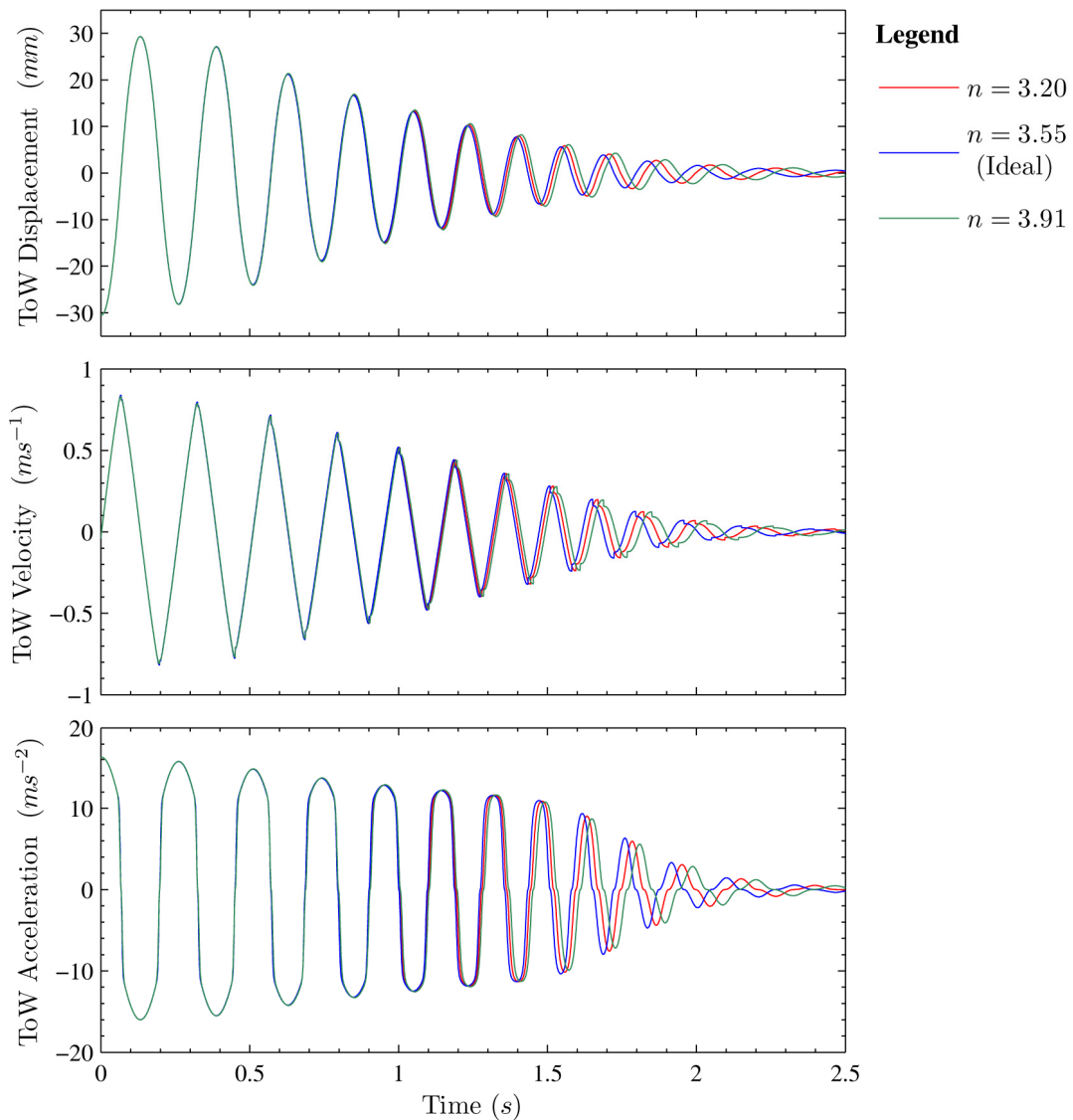
#### 4.8.3 SENSITIVITY OF THE MHSG METHOD TO INPUT PARAMETERS

Aside from the accuracy of the simulation procedure, the sensitivity of the analysis results as a function of the different input parameters is also of interest. Accordingly, the simulations were repeated with small deviations in the  $n$  value and the  $r$  value. These two parameters were deemed the principal input parameters upon which the MHSG simulation procedure is based. A variation of the  $n$  value controls the rotation centre migration rate. This affects the tendon force expression ( $P_{tendon}(\Delta)$ ) and the evaluation of the instantaneous wall properties ( $R$ ,  $\alpha$ ). A variation in the  $r$  value affects the energy dissipation of the system.

Figure 4-46 illustrates the effects of a 10% variation of  $n$  on the effective rocking half-width of the wall ( $b'$ ) and the simulated tendon force. As shown, the wall characteristics are relatively insensitive to variation of the  $n$  value. This suggests that it is quite easy to achieve a sufficiently accurate estimation of  $n$  to model the ideal rotation centre migration rate. The  $n$  value can be easily estimated by nominating the horizontal wall displacement at which rocking is properly initiated.

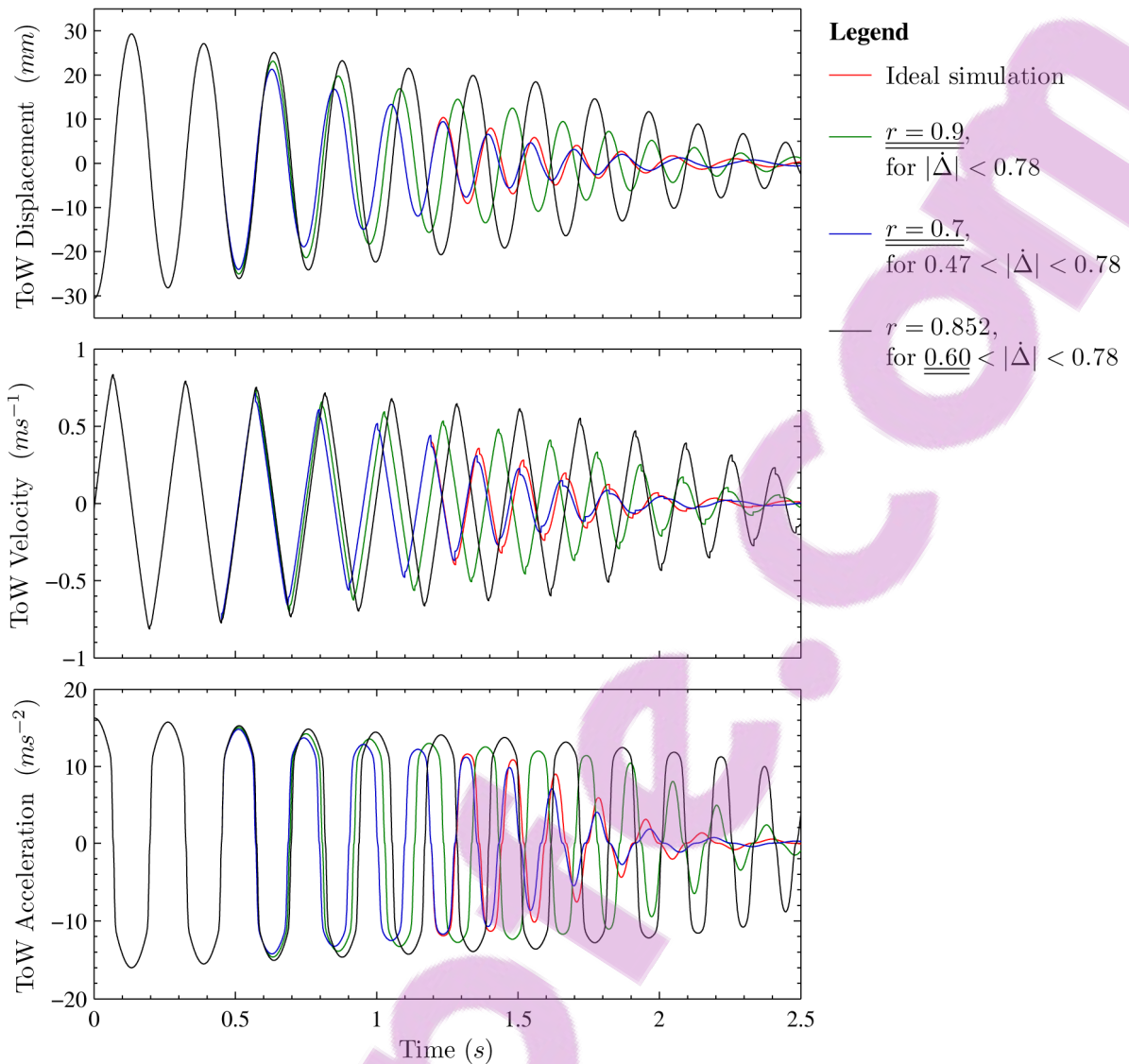


**Figure 4-46 – Effects of a variation in rotation centre migration rate ( $n$ )**



**Figure 4-47 – Comparison of simulated response with small deviations in  $n$  value**

The different  $n$  values were subsequently incorporated into the MHSG procedure and the resulting simulation results compared against the ideal MHSG simulation in Figure 4-47. As expected, the resulting simulated time-histories were effectively indifferent to the ideal settings. The larger the range of wall displacement where the rotation centre is permitted to be within the wall, or in other words, the slower the migration of the rotation centre, the more the response lags the ideal simulation and vice versa. This effect is only observed when the amplitude of vibration is small. Furthermore, it was shown that the  $n$  value does not affect the amplitudes of vibration.



**Figure 4-48 – Comparison of simulated response with small deviations in  $r$  value**

Next, a number of simulations were carried out with a small deviation in the  $r$  value. The results are presented in Figure 4-48 where the specific deviations are denoted by a double underscore in the legend. The figure demonstrates a moderate sensitivity to the selection of  $r$  similar to the equivalent SDOF procedure. A deviation which occurs earlier in the time-history creates a more obvious error as the simulation progress. This again highlights the strong history-dependent nature of the controlled rocking problem.

In closing, the MHS procedure has successfully simulated the free vibration response of the controlled rocking wall. This procedure is different to the equivalent SDOF approach as the governing differential equation is based on formulating an equation of motion in terms of rotation about the rocking pivot. The tendon force

increases are derived theoretically based on geometric constraints. The procedure assumes the tendon force acts vertically at the centroid as the wall displaces. This simplifies the governing differential equation greatly and it has since been demonstrated to be a reasonable and accurate assumption.

The development of the MHSg procedure has shown that the rotation centre for a controlled rocking wall migrates smoothly between the two extremes, particularly when the wall displacements are small. Failure to incorporate this assumption results in unrealistic step changes in the wall accelerations. This is identifiable as vertical lines in the acceleration time-history in Figures 4-42 and 4-43. A Dirac- $\delta$  type function has been shown to adequately model the smooth transition of the rotation centre and this leads to an improved overall simulation. This testing procedure has been found to be relatively insensitive to the selection of rotation centre migration rate but is moderately sensitive to the selection of the  $r$  value.

Whilst this procedure works well for a single centrally placed prestress tendon, it is doubtful that it could be applied directly for other more complex tendon arrangements.

## 4.9 PCM WALL RESPONSE SUBJECTED TO BASE EXCITATION

This section examines the response of the PCM wall specimen subjected to base excitations. A uniaxial shake table applied the base excitations which were scaled ground motion records from past earthquakes. Additional details on the shake table tests have been presented previously in Section 4.4. Summaries of the input ground motion and the wall response are found in Table 4-1 and Table 4-2. Of the eight shake table test runs considered by this study, five had a nominal initial tendon prestress force of 75 kN and the three remaining had a tendon force of 110 kN.

### 4.9.1 SHAKE TABLE TESTS WITH 75 kN INITIAL TENDON FORCE

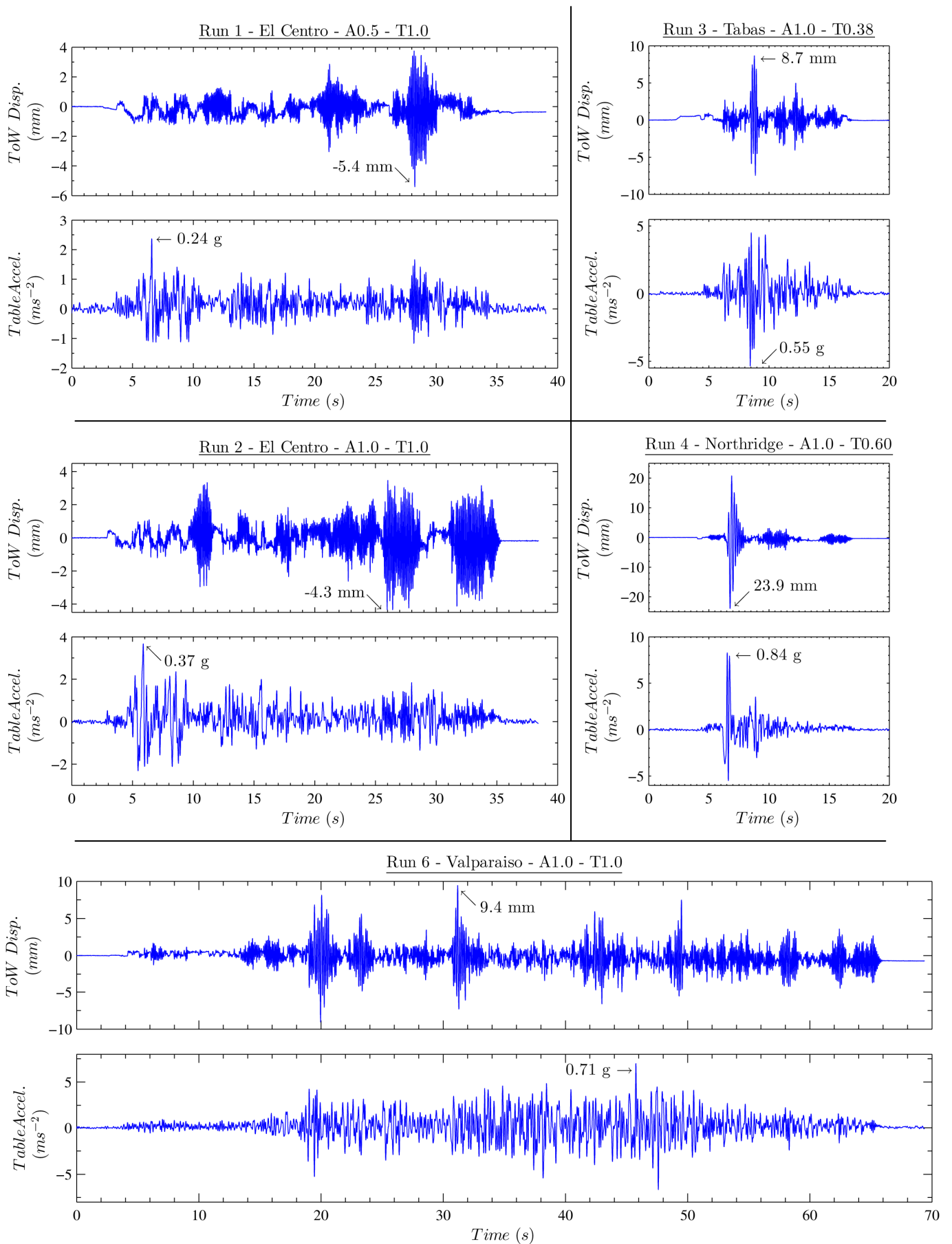
The five shake table tests that are examined initially are test runs 1 through 4 and 6 as they are designated in Table 4-1. The wall specimen in these tests nominally shares the same initial prestress with the previous free vibration decay study. There is a very slight variation (less than 0.04%) in initial tendon force amongst these shake table tests. This is because the steel prestressing tendon was post-tensioned to 75 kN before the first shake table test, and batches of shake table tests were conducted consecutively without readjustment of the tendon force between test runs.

The shake table motions for the selected tests had peak accelerations ranging from 0.24 g to 0.84 g, and they contained a range of seismological signatures. These shake table motions resulted in maximum top of wall (ToW) displacements ranging from 4.34 mm to 23.91 mm. These tests were selected specifically to ensure a wide range of responses resulting from a wide range of input motions were included.

Figure 4-49 presents the recorded wall displacements and their corresponding shake table motion for the five initially considered shake table tests. An immediately obvious feature of the results is the counter-intuitive nature of the PCM wall response brought about by the sensitivity and history dependency of the system.

Consider shake table tests 1 and 2; these two tests were subjected to essentially the same excitation, except the acceleration in test 2 is double that in test 1. Figure 4-49 shows that in fact the wall in test 1 has displaced more than test 2, despite it receiving a weaker but identical in nature shaking. Moreover, the two responses show no similarity.





**Figure 4-49 – Shake table tests with 75 kN initial tendon prestressing force**

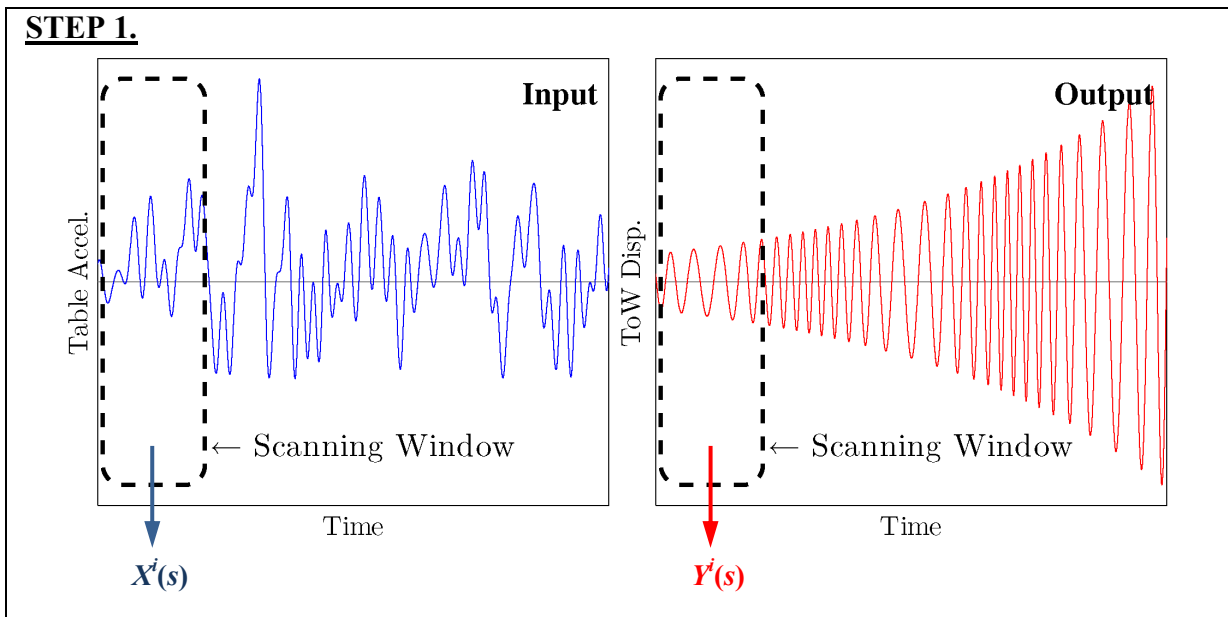
Another notable feature of the result is that maximum response does not necessarily occur at the same time with the maximum input acceleration amplitude. To analyse the data further, it is interesting to track the “natural frequency” of the controlled rocking wall as it displaces. The term “natural frequency” is used here in an imprecise sense to describe the dominant vibration frequencies which the structure is most responsive to.

The tracking of the dynamic characteristic of the PCM is achieved by conducting a moving window analysis of the system’s transfer function. This analysis is a slight variation of a signal analysis tool which is used to analyse the dynamic properties of nonlinear structures. A succinct mathematical description of the conventional moving window analysis method is presented in a paper by Nield et al. (2003).

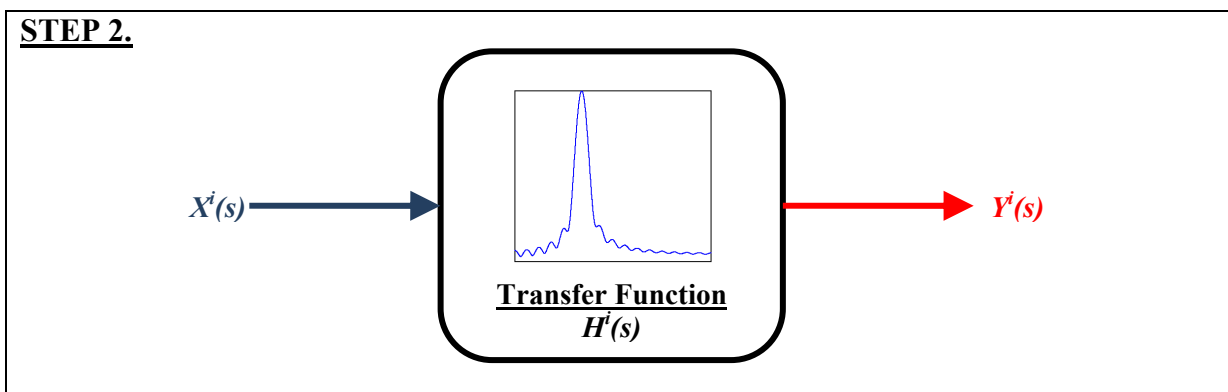
In brief, the method takes the base excitation and the ToW displacement time series during a fixed length in time (a window) from the start of the excitation. A transfer function is calculated by treating the base excitation as the input and ToW displacement as the output. This is achieved by dividing the cross power spectral densities of the two signals by the auto power spectral density of the input. The spectral densities are calculated using a Welch's periodogram ensemble averaging approach to reduce the noise content, and a Kaiser window is applied within the averaging process to minimise the spectral leakage due to the discretisation.

Once the transfer function is evaluated for a particular window, the window then scans forward in the time-history, with an overlap of the previous window. A transfer function is estimated again with the more recent data. Once the scanning window has traversed the entire record, the peaks of the transfer function in each window are collated and normalised. This then represents the approximate instantaneous “natural frequency” of the structure during the shake table test. The moving window analysis process is illustrated diagrammatically in Figure 4-50.

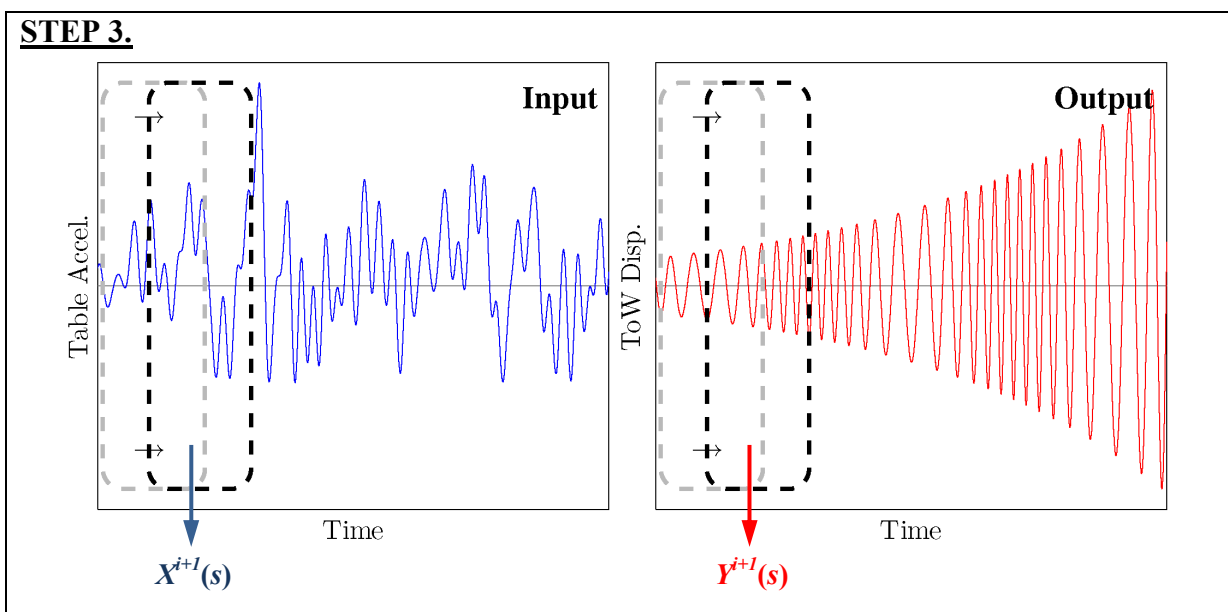
The moving window analysis procedure, like other spectrogram analysis tools, suffers from a trade off in accuracy between frequency and time. The frequency and time resolutions of the procedure are governed by the width of the moving window. A wider moving window contains more sample points per transfer function estimate, and thus provides a higher accuracy in the frequency prediction. However, this leads



Beginning from the start of the record, evaluate the power spectra using the table accelerations and ToW displacements occurring within the scanning window.

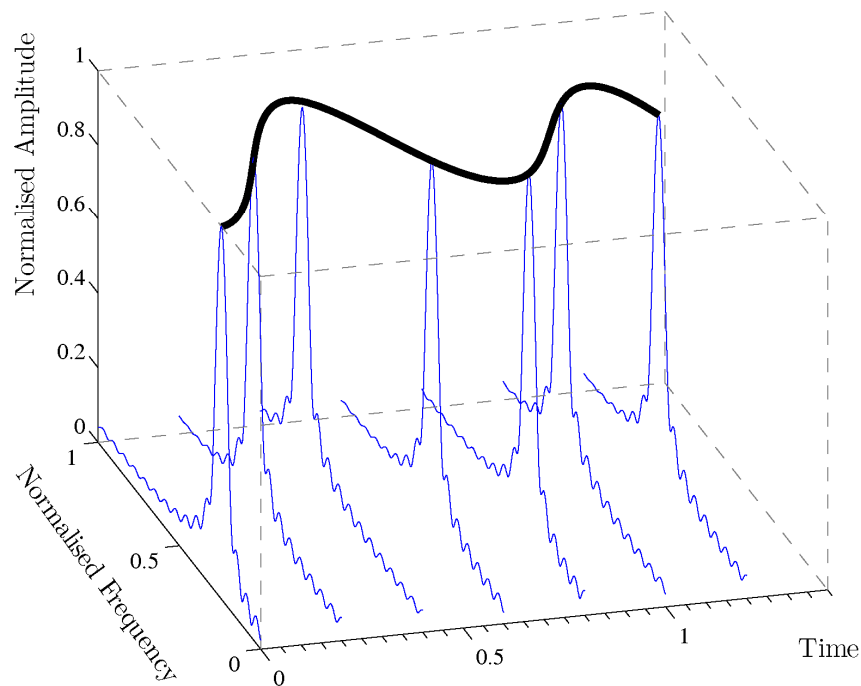


Estimate the transfer function of the system using the spectral densities of the input and the output.

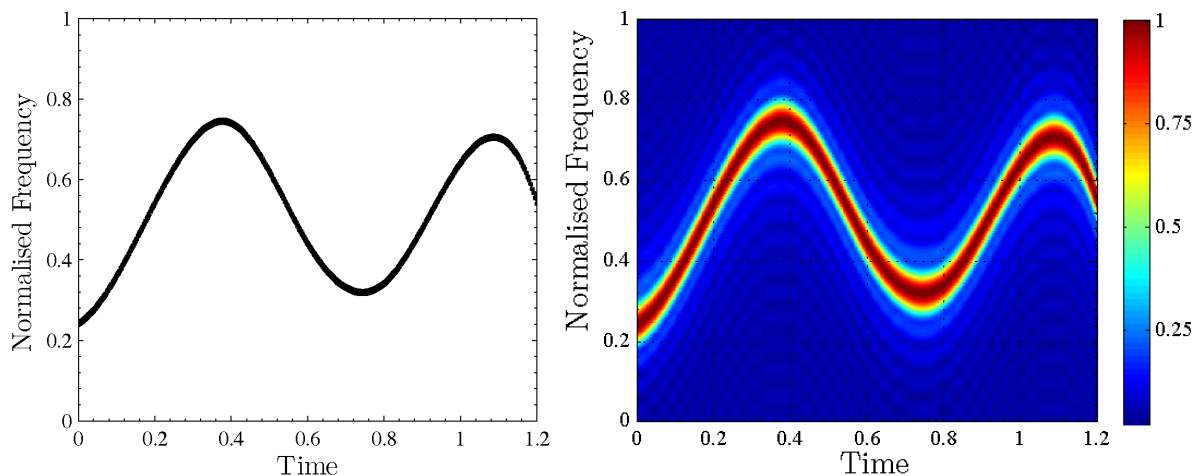


Move the scanning window forward, repeat step 1 to 3 using the new data until the entire record is processed.

**Figure 4-50 – Summary of the moving window transfer function analysis**

**STEP 4.**

Collate the transfer functions found in step 2. Normalise their amplitudes and plot the series in a three dimensional plot corresponding to the start time of each scanning window. The peaks in each series represent the instantaneous “natural frequency” of the system. The bold line joining the point of maximum frequency response represents the variation of principal natural frequency of the system.

**STEP 5.**

The plot in step 4 can be projected orthogonally onto a horizontal plane as a two dimensional graph to highlight the variation of natural frequencies of the system. This results in a contour plot or a Spectrogram.

**Figure 4-50 (cont.) – Summary of the moving window transfer function analysis**

to a lower responsiveness, immediacy or poor time resolution. Conversely, a narrower window width yields higher immediacy, which is important in tracking a fast changing nonlinear system response, but as it contains less sample points, it is less accurate in the actual frequency and response amplitude predictions.

The analyses of the shake table test results adopted a window width of 0.43 times the sampling rate. This provided an acceptable compromise between time and frequency resolutions. Moreover, the moving window translated across the time series at 2 sample points per step to give a smooth transition in the time axis.

A moving window analysis is conducted on the free vibration decay result for the purpose of illustrating how the spectrogram is interpreted for a simple data set. The result of this analysis is presented as Figure 4-51.

Three distinctive behaviour modes occurring at three frequency ranges are identified from Figure 4-51. These modes are labelled as regions in the greyscale spectrogram, and they occur when the following corresponding conditions are met,

- A) Rocking has fully developed and the wall is in the smooth rocking phase of the cycle. The dominant resonant frequency at these instances is approximately 3-5 Hz. It is noted that the resonant frequency increases slightly as the rocking amplitude decreases.
- B) The wall has been rocking about a wall corner and the wall base has now come into contact with the ground as it self-centers. As this occurs, conventional rocking is deactivated and the system stiffens rapidly. This is identified in the spectrogram by a step jump into region B from region A. The wall exhibits a dominant resonant frequency of approximately 9 Hz during these times. It is postulated that bouncing may have occurred momentarily during the impacts. This would lead to a minute extension of the steel tendon and explains the slightly higher resonant frequency in this region when compared to region C.
- C) Complete wall uplifts have now ceased. Flexural bending of the wall is now the main source of the measured ToW displacement. To a lesser extent, the ToW displacement may also result from a small amount of rigid body rotation with partial uplift of the wall base. The resonant frequency for this mode of behaviour is approximately 8-9 Hz.

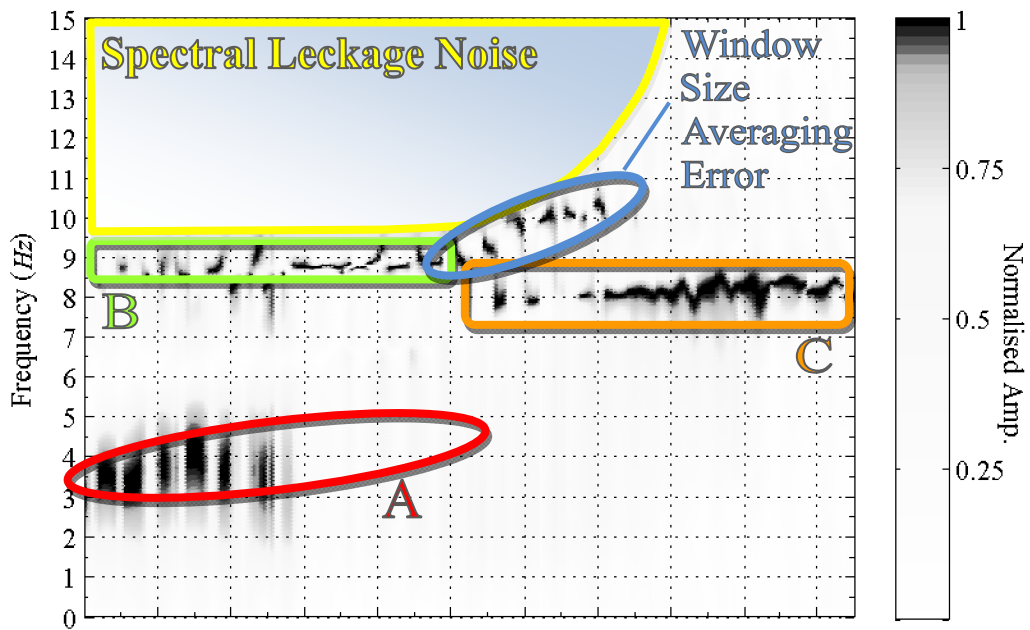
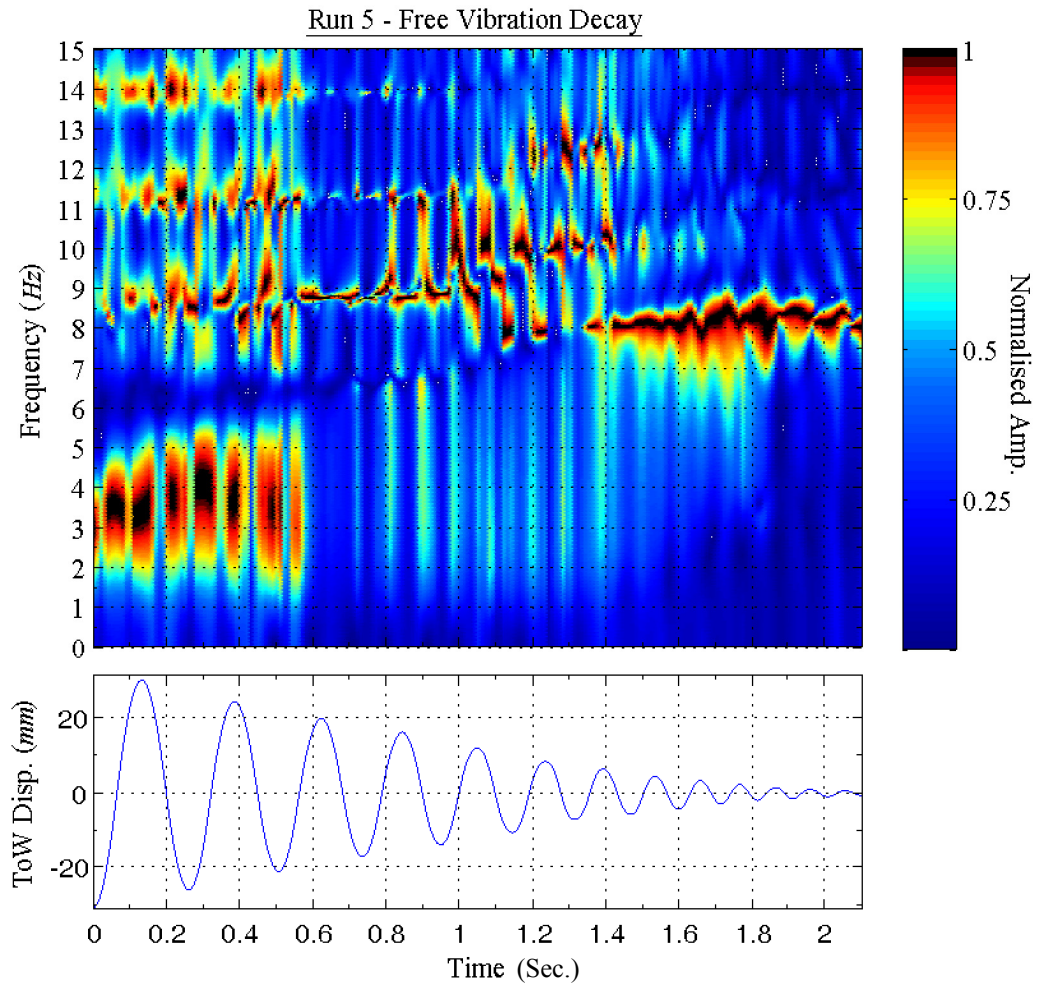


Figure 4-51 – Moving window transfer function analysis for the FV decay

Figure 4-61 also highlights the typical errors that are present in the moving window frequency domain analyses. These include spectral leakage noise and errors from the averaging effect of a moving window.

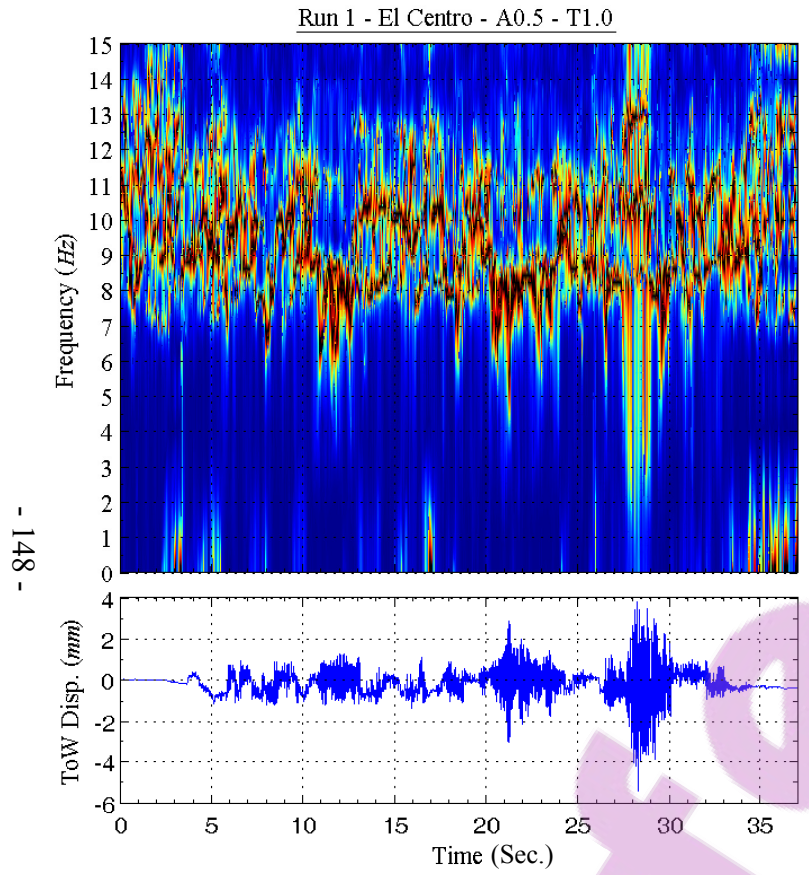
Spectral leakage describes the phenomenon where spectral energy is leaked to frequencies adjacent to the true source frequency. The noises typically appear as series of peaks, uniformly spaced in the frequency axis away from the true peak. They combine to appear as series of lines in the spectrogram as shown in Figure 4-51.

Spectral leakage is due to quantisation effects in the frequency analysis and the sampling processes. A discrete fourier frequency analysis transforms a signal with a continuous frequency content into spectral amplitudes in a number of discrete frequency sorting bins, governed by the number of sampling frequencies. When a signal's true frequency is in between the discrete frequency bins, a portion of the true frequency's energy is leaked into adjacent frequencies.

As the discrete fourier transform is designed for continuous, periodic signals, the windowed signal is looped continuously to emulate this for the frequency analysis. As our windowed signal is finite, typically aperiodic and begins and ends at different levels, when they are looped together they create step discontinuity which transforms as sinc functions and leads to the spectral leakage signature.

The moving window average errors are caused by the averaging effects of the moving window. A moving window contains finite sampling points to enable sufficient input for the frequency analysis. This has the effect of calculating average spectral amplitudes for the duration of the moving window. The distortion because of the averaging is generally small if the response is dominated by a single mode which varies slowly, however when the moving window traverses over a distinct bimodal change in frequency, the averaging process results in either of the dominant frequencies receiving the warranted emphasis. Moving average errors are usually quite apparent as they have exactly the same duration as the moving window.

The moving window transfer function analysis is further applied to the other five shake table tests with 75 kN initial tendon force. The corresponding spectrograms are presented in Figures 4-52 through 4-56.



- 148 -

Figure 4-52 – Transfer function variation for shake table test 1 (El Centro – A0.5 – T1.0)

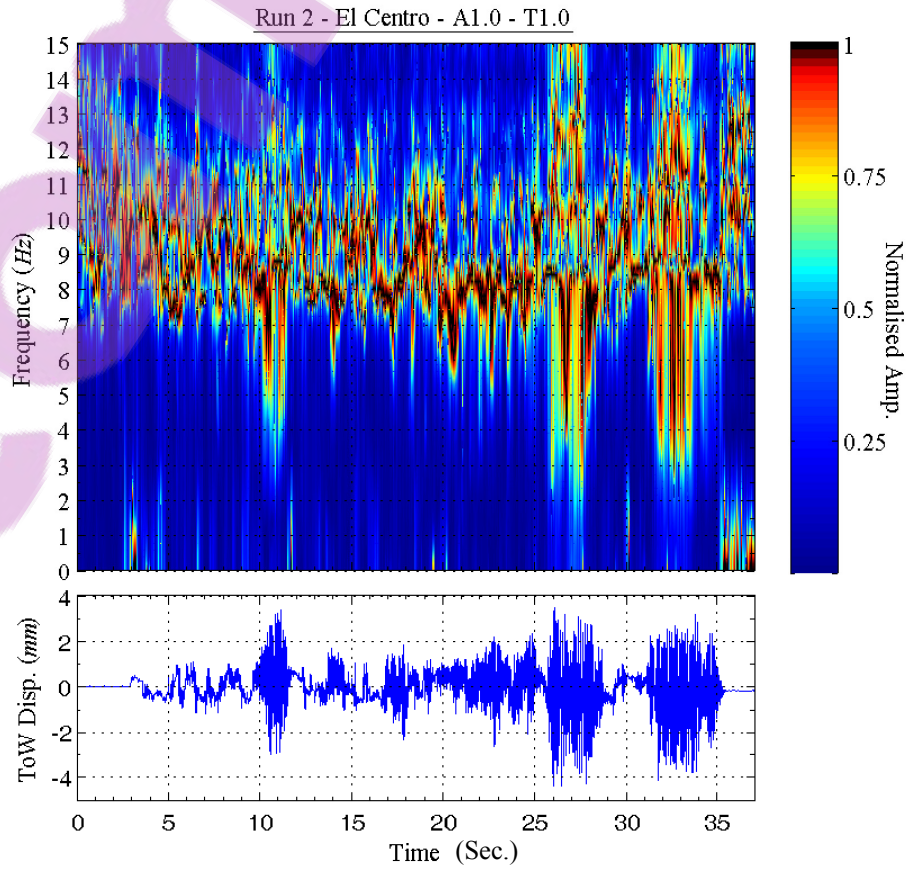


Figure 4-53 – Transfer function variation for shake table test 2 (El Centro – A1.0 – T1.0)

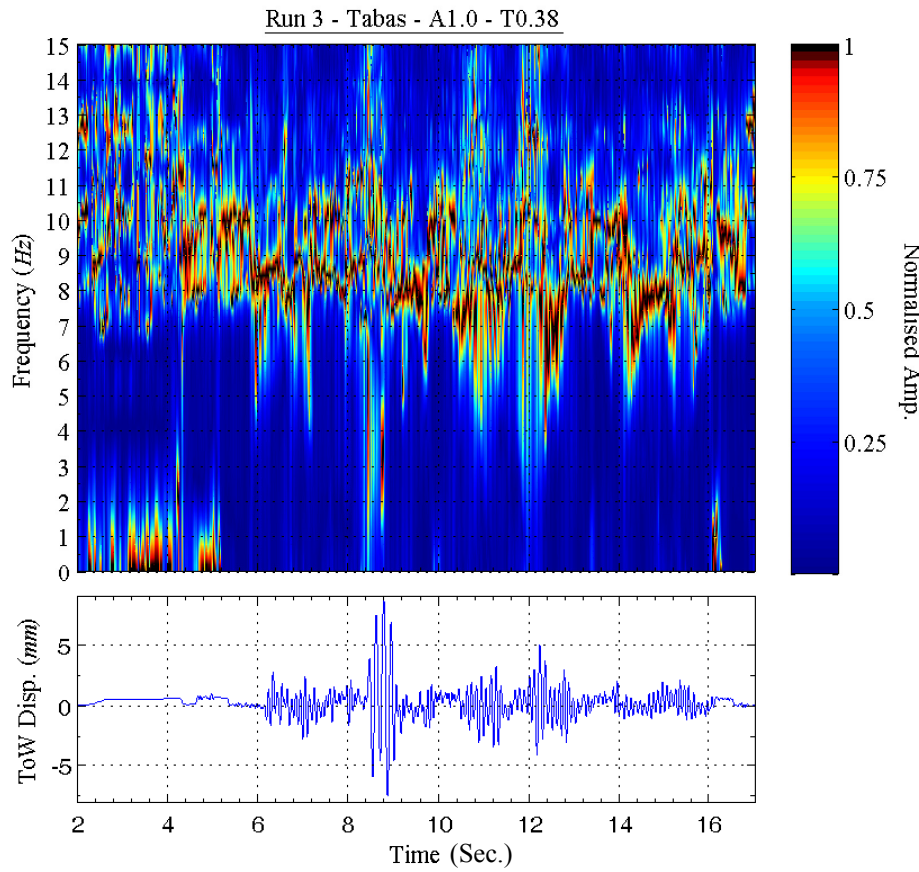


Figure 4-54 – Transfer function variation for shake table test 3 (Tabas – A1.0 – T0.38)

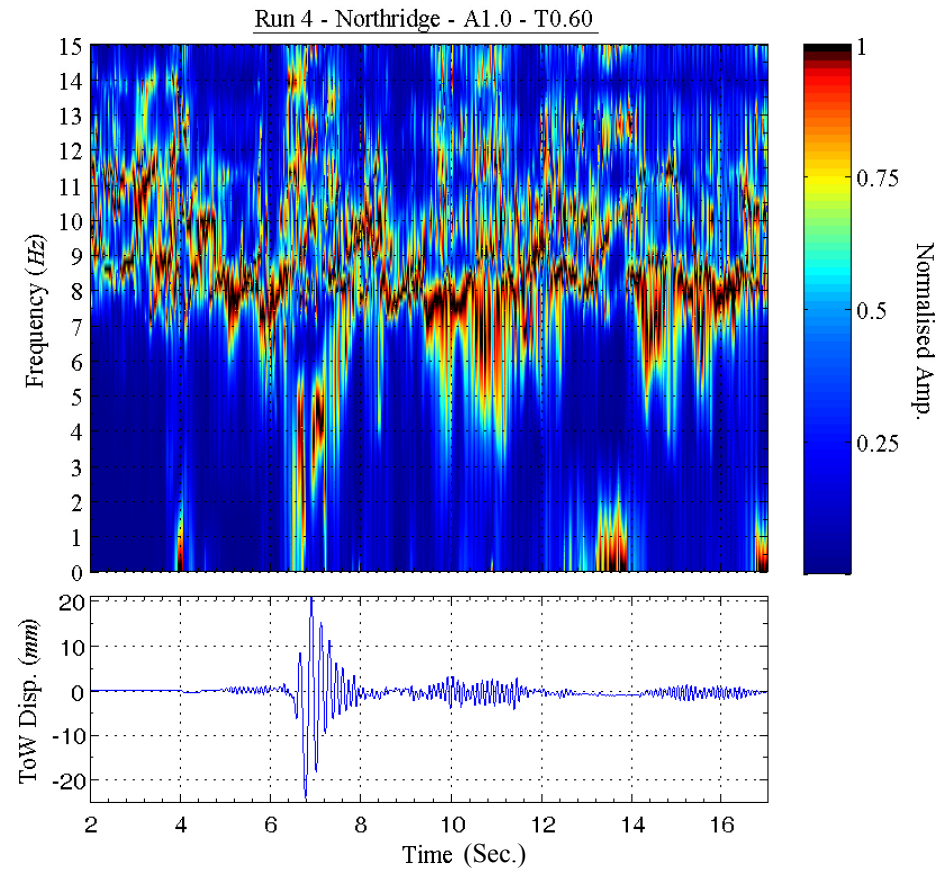
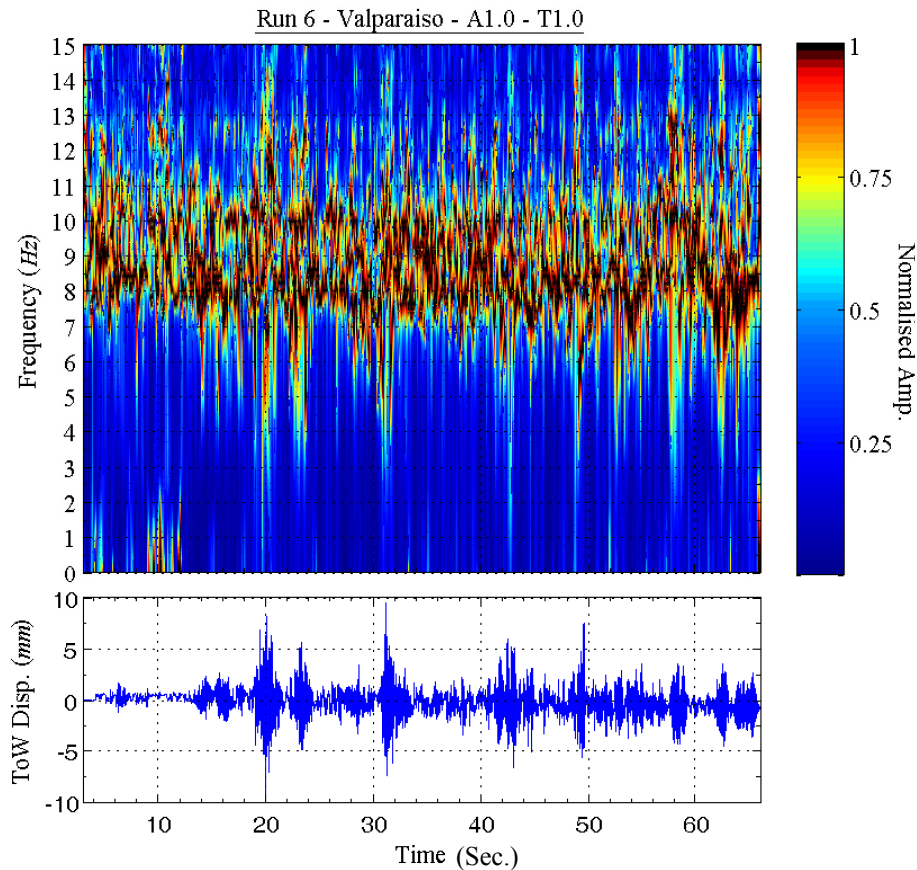


Figure 4-55 – Transfer function variation for shake table test 4 (Northridge – A1.0 – T0.6)



**Figure 4-56 – Transfer function variation for shake table test 6 (Valparaiso – A1.0 – T1.0)**

The spectrogram analyses show that well-defined smooth rocking was rarely initiated in the shake table tests. The wall specimen appears to have spent much of the shake table tests in a state of just uplifting and impacting or a pure flexural vibration state. These two states correspond to region B and region C behaviour from the free vibration analysis.

The El Centro and Valparaiso shake table tests illustrate that the natural frequency of the system under base excitation fluctuates widely despite the wall vibrations involving only flexural bending without base uplift. The natural frequency of the wall in these tests varied from 7-12 Hz compared to a corresponding stable 8 Hz obtained in the free vibration tests.

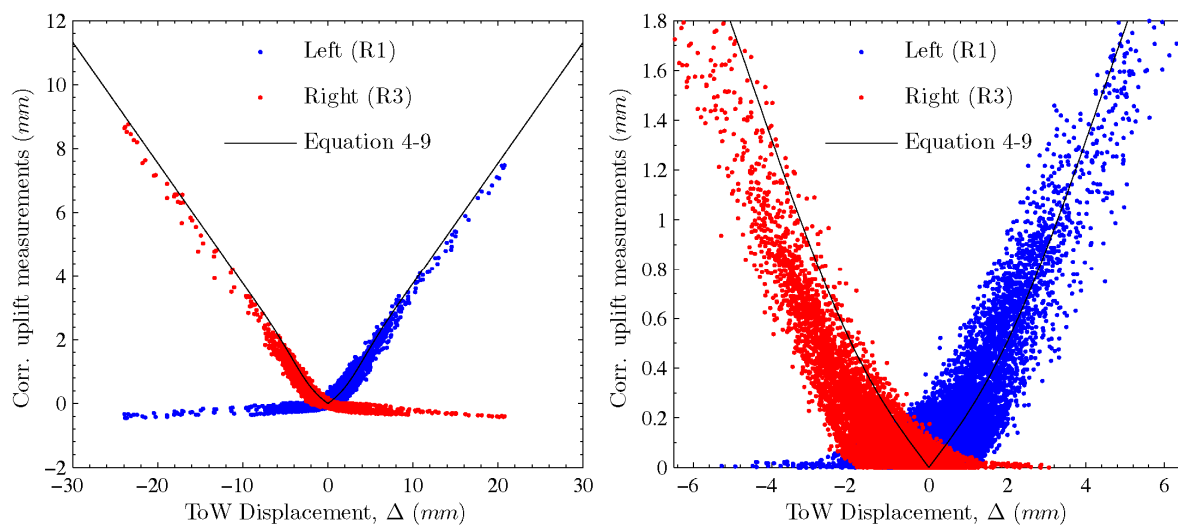
One plausible explanation for this is that the natural frequency is highly sensitive to the location of the resultant base reaction force. Under the free vibration decay, as the displacement is cyclical and varies approximately symmetrically in the positive and negative directions. This results in a stable average characteristic in a

moving window analysis. Under base excitation, when the wall undergoes frequent and rapid changes of direction, there is a higher likelihood that the moving window will capture a less central characteristic. This hypothesis is loosely supported by the observation that the transfer function estimate is more stable when the displacement is uniformly symmetrical. Examples of this occurred during 11-13s in run 1, 21-24s in run 2, 9-11s and 14-17s in run 4 and etc.

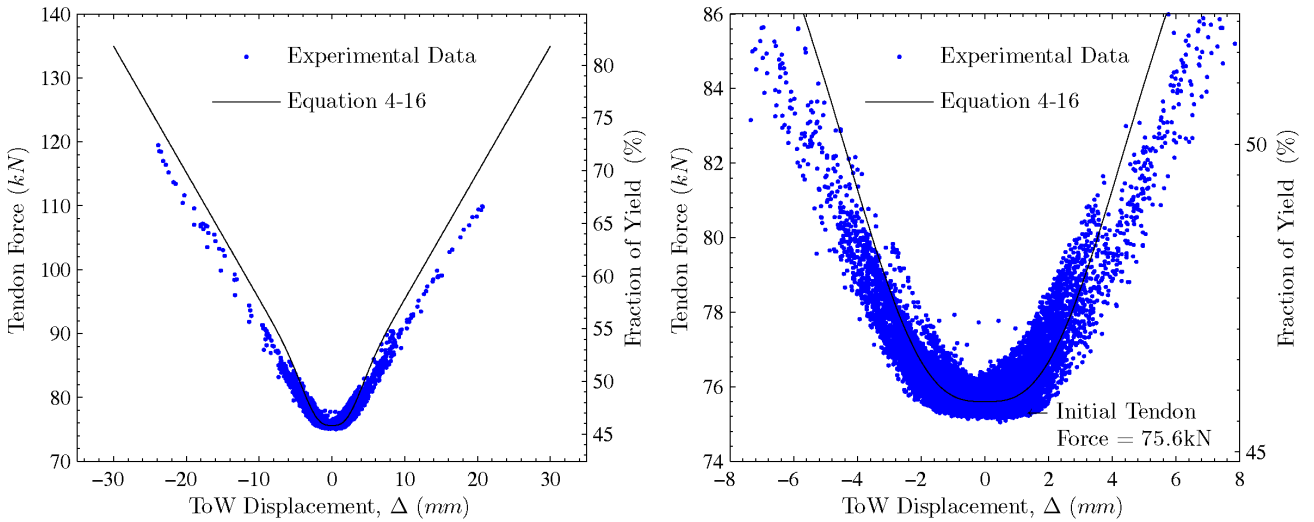
Finally the moving window analysis has detected clear rocking behaviour in the Northridge and Tabas shake table tests. This is apparent from the transfer function peaks occurring between 3-5 Hz. It is also noted that the transition between rocking and flexural behaviour is seemingly abrupt and is likely to be displacement amplitude dependent.

#### 4.9.1.1 Wall uplifts and tendon force increases

The wall-uplifts and tendon force increases under base excitation are examined in a search for similarities with the free vibration decay results. Figure 4-57 presents the wall uplifts at the left and right wall edges against the ToW displacement for the five shake table tests. As shown, the approximation equation established for the free vibration matches the experimental data well without any modification. However it is noted that there are significant variations in uplifts near the origin region. A plausible explanation for this is that sliding has occurred allowing data points to shift horizontally in Figure 4-57. If sliding is the source of variability then Figure 4-57 suggests the typical sliding displacement is approximately  $\pm 2.5$  mm.

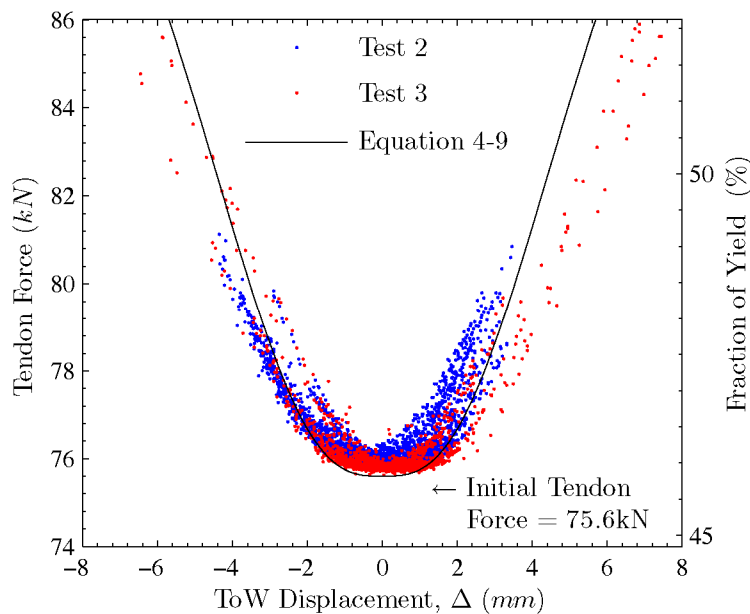


**Figure 4-57 – a) Wall uplifts versus ToW displacements, b) close up of the origin**



**Figure 4-58 – a) Tendon force versus ToW displacements, b) close up of the origin**

Subsequent to examining the uplifts, the tendon forces for the shake table tests were plotted against the ToW displacement in Figure 4-58. The figure highlights a reasonable prediction by the theoretical expression developed earlier from the free vibration results. Just as with the uplifts, there is an increased variability around the origin region with a spread of approximately 2.5 mm. The variability can again be explained by wall sliding. Figure 4-59 presents the tendon force variation from shake table tests 2 and 3. This figure shows a number of identical data series displaced horizontally from each other and supports the hypothesis that multiple sliding events occurred in each shake table test, with each sliding event causing a horizontal shift in the origin.



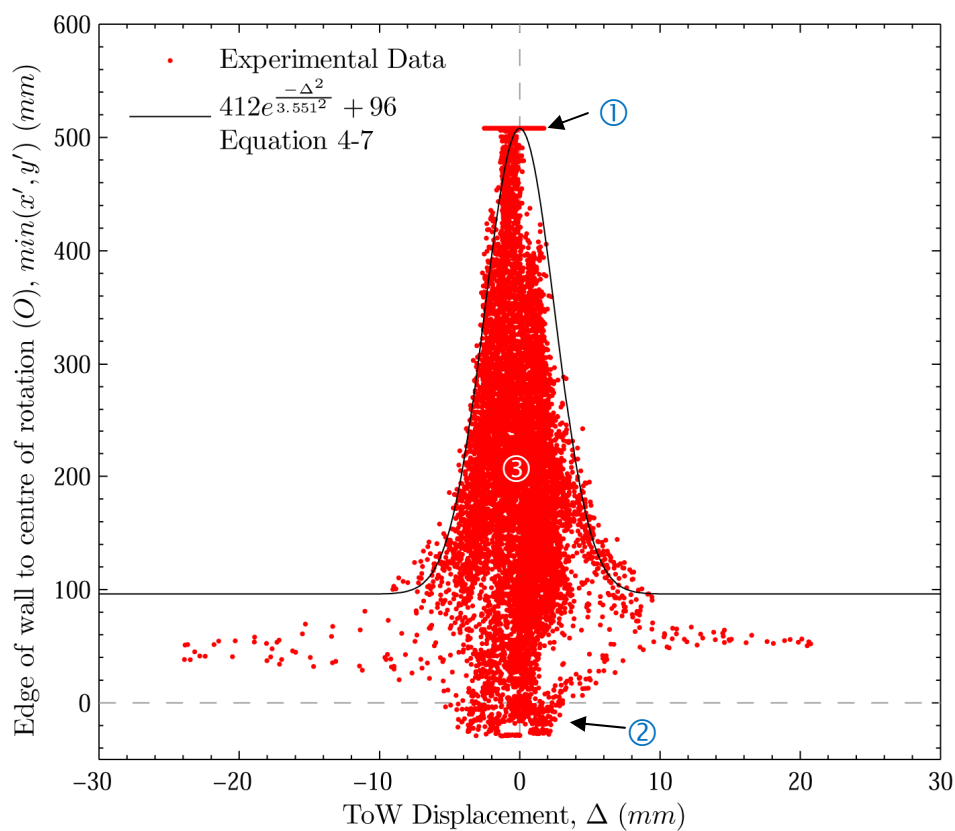
**Figure 4-59 – a) Tendon force versus ToW displacements for test run 2 and 3**

#### 4.9.1.2 Location of rotation centre

It was found previously in the free vibration decay motion analysis that the rotation centre location is crucial in predicting the dynamics of a controlled rocking wall. An accurate rotation centre prediction leads to an accurate uplift prediction, which in turn leads to a correct prediction of the tendon force increase. Consequently, these provide a basis for evaluating the potential energy of the system which is used to derive an accurate pushover characteristic.

Continuing from the free vibration analysis, the rotation centre locations from the shake table tests are plotted against the ToW displacements in Figure 4-60. The figure presents a much less distinct relationship than a similar plot for the free vibration results in Figure 4-17. Figure 4-60 also demonstrates that Equation 4-7 from the free vibration analysis appears to envelope the experimental results well.

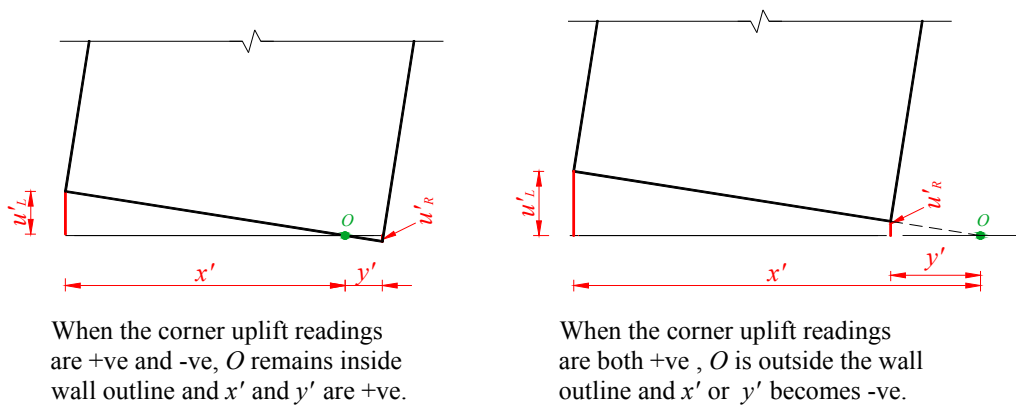
Three interesting features of the results are the presence of 1) a flat top near zero ToW displacements, 2) “negative” edge of wall to rotation centre distances and 3) a general scatter of the results within the free rocking empirical expression.



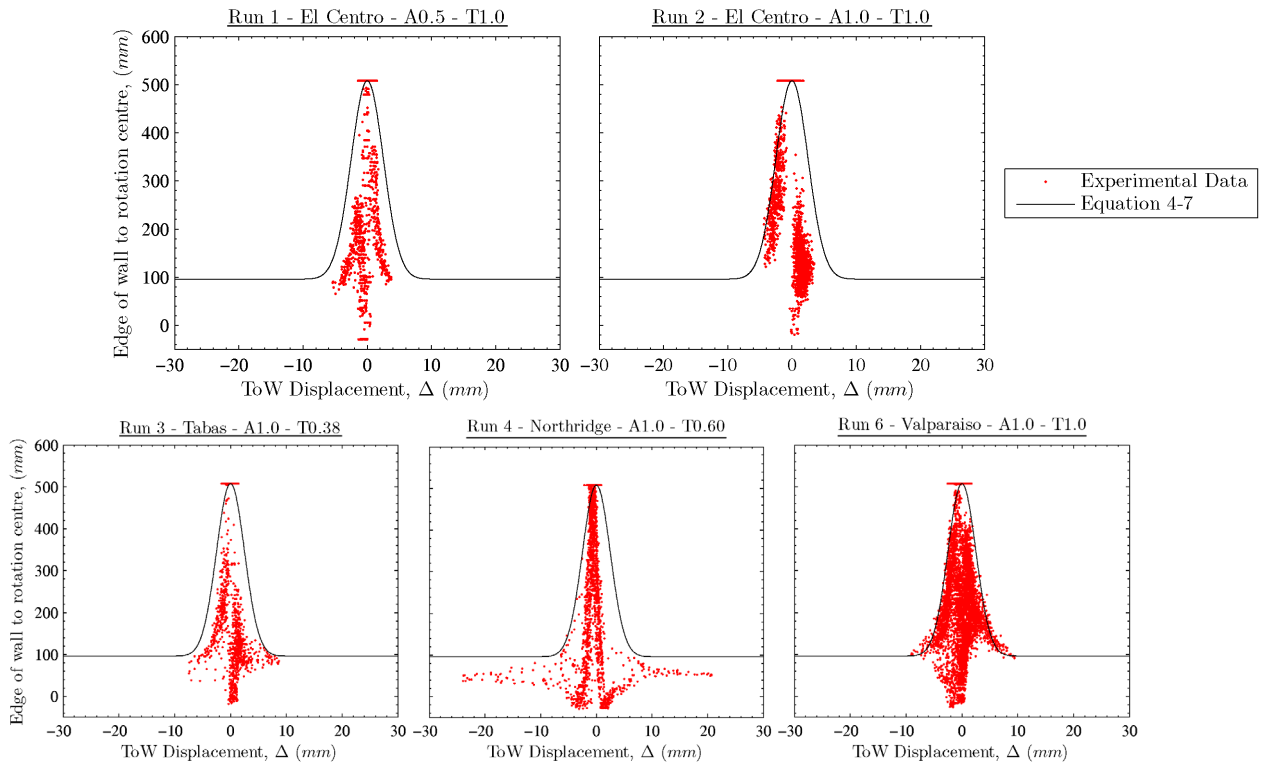
**Figure 4-60 – Distance between the rotation centre and wall edge versus wall lateral displacement for the 75 kN shake table tests**

The three distinctive features in Figure 4-60 can be explained as follows:

- ① The horizontal line at the top of the graph indicates the wall has displaced horizontally while the centre of rotation is firmly fixed at the wall centreline. This suggests that the wall has displaced without any rotation or rocking. This definitively shows that sliding must have occurred during the shake table tests. The width of the horizontal line shows that the typical sliding displacement is between -2.5 and 1.7 mm.
- ② The negative readings in Figure 4-60 may be explained by free flight of the wall or “wall bouncing”. Since the rotation centre is estimated through readings of uplift gauges that are mounted on the outside of the wall, when the wall is in free flight, both uplift readings are positive and the interpolation algorithm leads to a rotation centre beyond the wall edges. This is illustrated diagrammatically in Figure 4-61.
- ③ The scattering of the data points within the free rocking behaviour boundary can be attributed to the interactions of flexural behaviour and rigid body motion. The scattering is less apparent in the free vibration test, as flexural behaviour is kept to a minimum by the release condition. However this is not the case for the shake table tests. Since the wall starts from an at-rest state, a significant threshold has to be overcome before rocking motion can occur. This is particularly difficult to achieve with a constantly reversing load like that from earthquake excitations. As a result, the wall spends much of the time in a transitory state, in which the flexural characteristics dominate the response and leading to significant deviations from the rocking motion assumption.



**Figure 4-61 – Negative rotation centre distances and PCM wall in free flight**



**Figure 4-62 – Distance between the rotation centre and wall edge versus ToW displacement for the 75 kN shake table tests plotted individually**

The rotation centre migration also provides clues to understanding the wall base pressure, as the wall develops a rocking motion from rest and during rocking motion. Figure 4-62 presents the distances between the rotation centre and wall edge for each shake table test individually. The figure highlights distinct patterns of rotation centre location for test runs with small or large displacements, with or without rocking.

For tests with small ToW displacements and no definitive rocking, like test run 1 and 2, the rotation centre distances form a narrow column of data points in the central lobe of the free rocking boundary in Figure 4-62. Then as the wall behaviour becomes more rocking-like, as in test runs 3 and 6, the column of data points spreads to meet the free rocking boundary. Finally when definitive rocking takes place, the data points spread away from the central lobe and the rotation centre tends towards a stable position.

The causes of these patterns are explained through the interpretation of base pressure in Figure 4-63 and Figure 4-64. Two pathways are presented to represent the idealised behaviour of the rotation centre as the wall develops a rocking motion from

rest, and simply rocking from one edge to another. Figure 4-63 highlights a greater opportunity for flexure bending interactions along one of the pathways, and it explains the significant scattering in the central lobe, along this path.

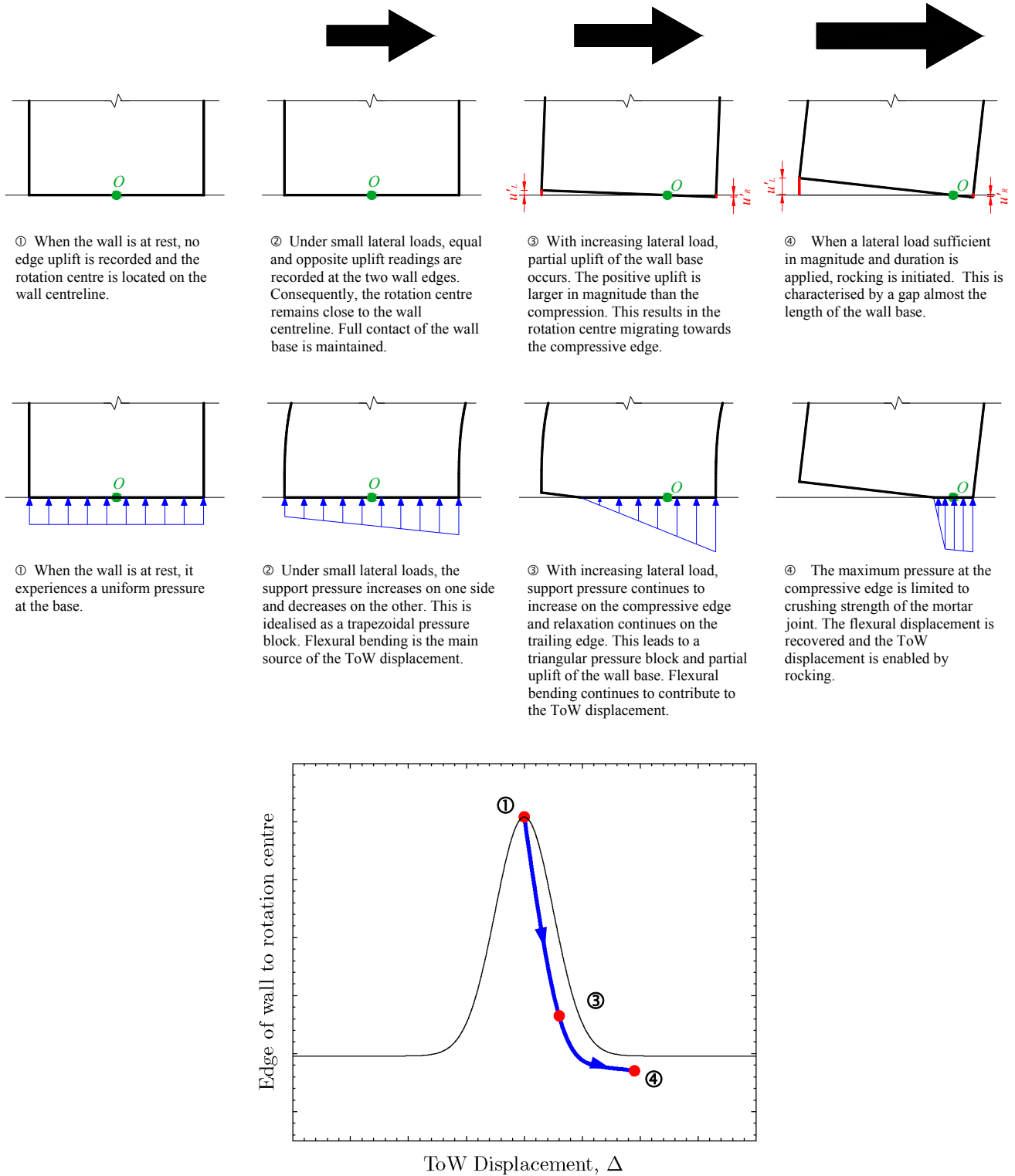
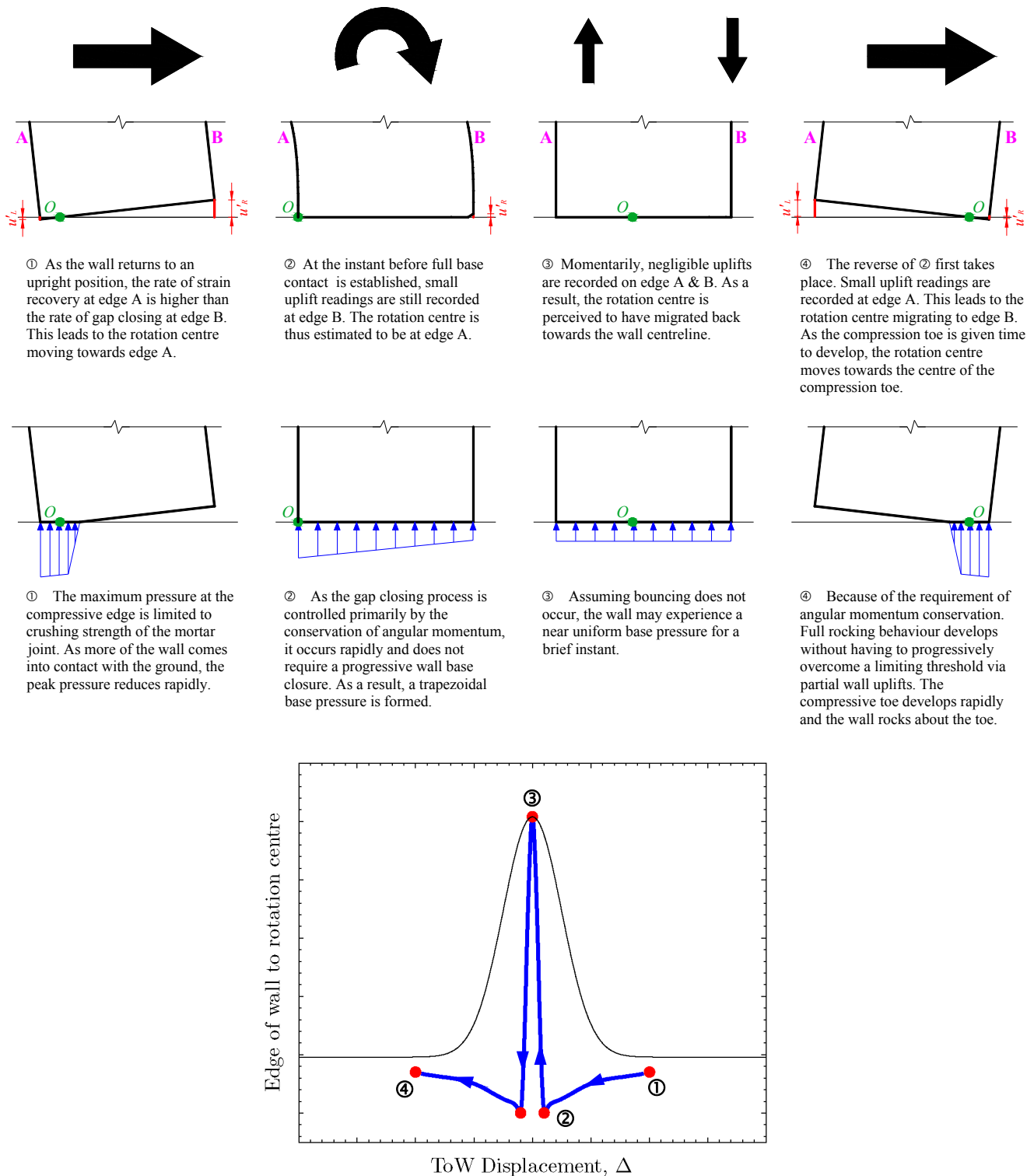


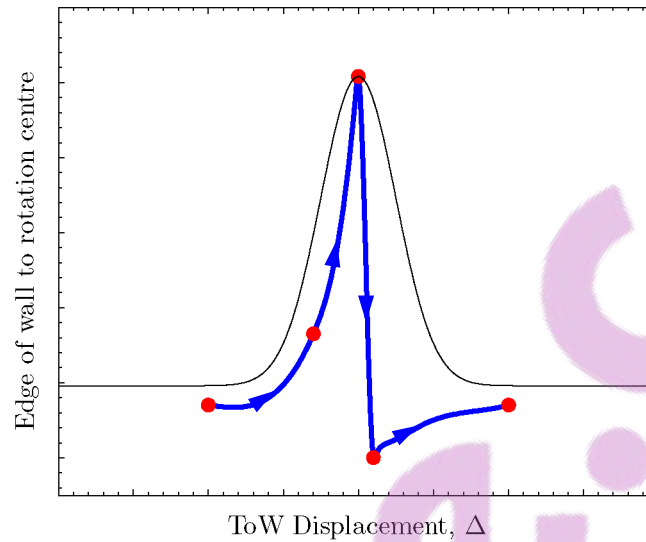
Figure 4-63 – The migration of rotation centre from rest to rocking



**Figure 4-64 – The migration of rotation centre during developed rocking**

Moreover, it is sometimes observed that the rotation centre motion is a mixture of behaviours found in Figures 4-63 and 4-64. The free vibration results plotted in Figure 4-17 are a good example of where the rocking occurred slowly enough to allow the base opening to close progressively and the rotation centre unloads on a

reverse rest-to-rocking as illustrated in Figure 4-63. When impact occurs, the conservation of angular momentum causes the wall to rock immediately about the opposing corner and thus follows a loading path found in Figure 4-64. An illustration of this pathway is presented in Figure 4-65 below.



**Figure 4-65 – The migration of rotation centre during developed rocking**

This presents an additional challenge for modelling the behaviour of PCM walls subjected to base excitation, as it is impossible to predict which path the rotation centre will follow. It appears there is an angular momentum threshold which controls the path of the rotation centre migration.

Irrespective of path, Equation 4-7 from the free vibration analysis remains an acceptable estimate of the rotation centre in lieu of a more sophisticated model.

### 4.9.1.3 Predicting the time-history response to base excitation

The two previously established techniques for modelling the free vibration response are extended here to simulate the wall's response to base excitations. Recall the two techniques are 1) modelling the rocking wall as a nonlinearly elastic equivalent SDOF system and 2) a modified Housner – substitute gravity (MHSB) approach.

The key to the nonlinearly elastic equivalent SDOF approach is the integration of the governing differential equation of an idealised SDOF structure. The equation has been presented as Equation 4-27 and is repeated below.

$$M_e \ddot{\Delta} + F_k(\Delta) + F_{Damp}(r, \Delta, \dot{\Delta}, n) = P_e(t) \quad (4-27)$$

Under base excitation, the effective equivalent driving force of the system,  $P_e(t)$  is simply the effective mass multiplied by the ground excitation, as in Equation 4-39 below,

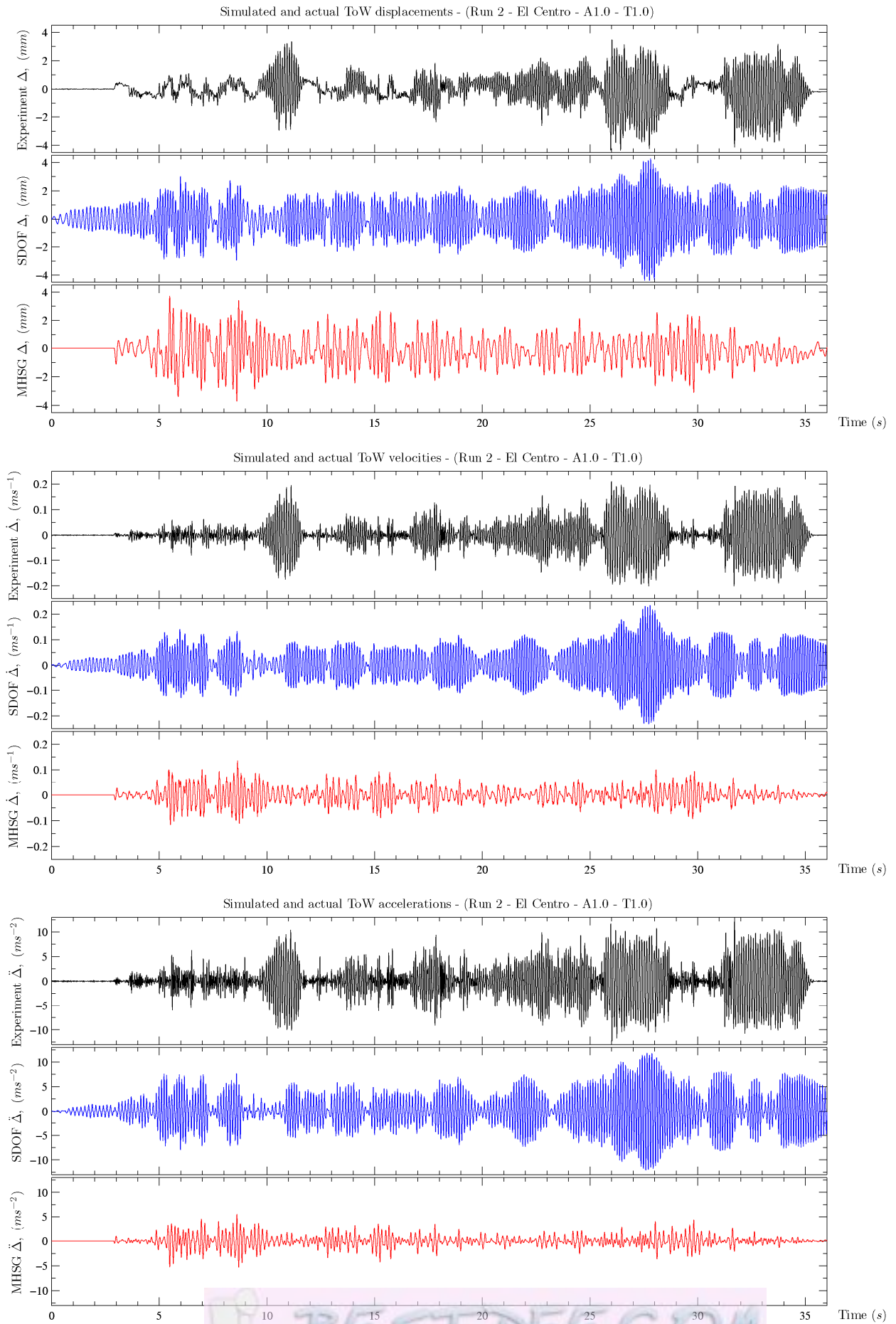
$$P_e(t) = -M_e \ddot{u}_g(t). \quad (4-39)$$

When applying the MHSB approach, a forcing term is added to the previously developed governing differential equation, Equation 4-32. As the equation is effectively an equilibrium equation in the rotational direction, the forcing term is simply the inertial force multiplied by the instantaneous lever arm to the rotation centre as shown in Equation 4-40.

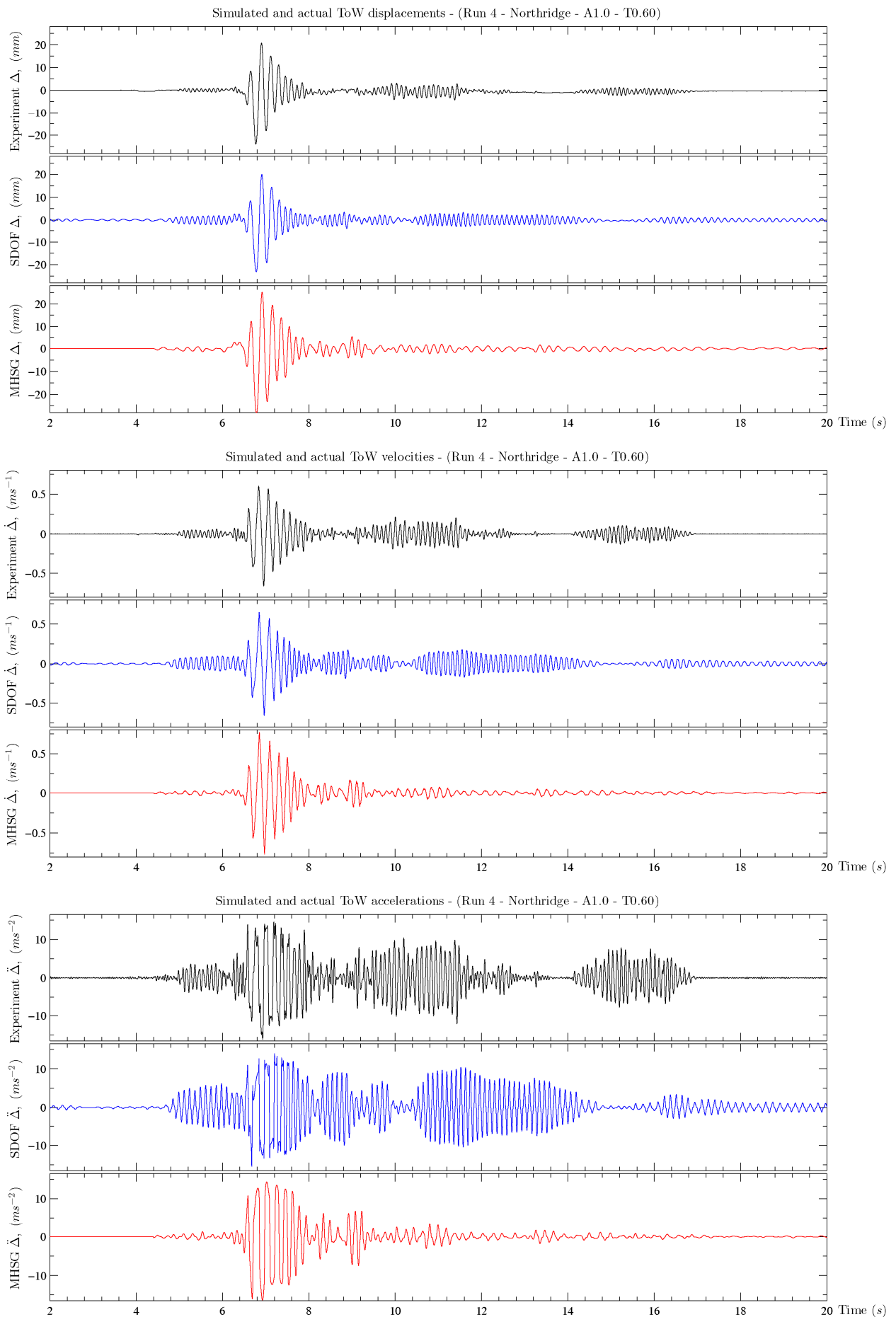
$$I_o \ddot{\theta} = -\text{sgn}(\theta) \cdot (mg + P_{tendon}(\Delta)) \cdot R(\theta) \cdot \sin[\alpha - \text{sgn}(\theta) \cdot \theta] - \tau(t), \quad (4-40)$$

where  $\tau(t) = M_e \ddot{u}_g(t) \cdot R(\theta) \cdot \cos[\alpha - \text{sgn}(\theta) \cdot \theta]$ .

The two approaches are applied to simulate the five shake table tests employing the same parameters from the free vibration analysis. Table 4-3 presents a summary of the key results and Figures 4-66 and 4-67 present the simulated time-histories for shake table tests 2 and 4. These two shake table tests are presented specifically to highlight the ability of the procedures to simulate small amplitude, non-rocking response like that in test 2, and moderate amplitude, rocking response like that in test 4. The simulation outputs for the other test runs are presented as Figures C-1 through C-5 in Appendix C for completeness.



**Figure 4-66 – Simulated and actual time-histories (Run 2 – El Centro – A1.0 – T1.0)**

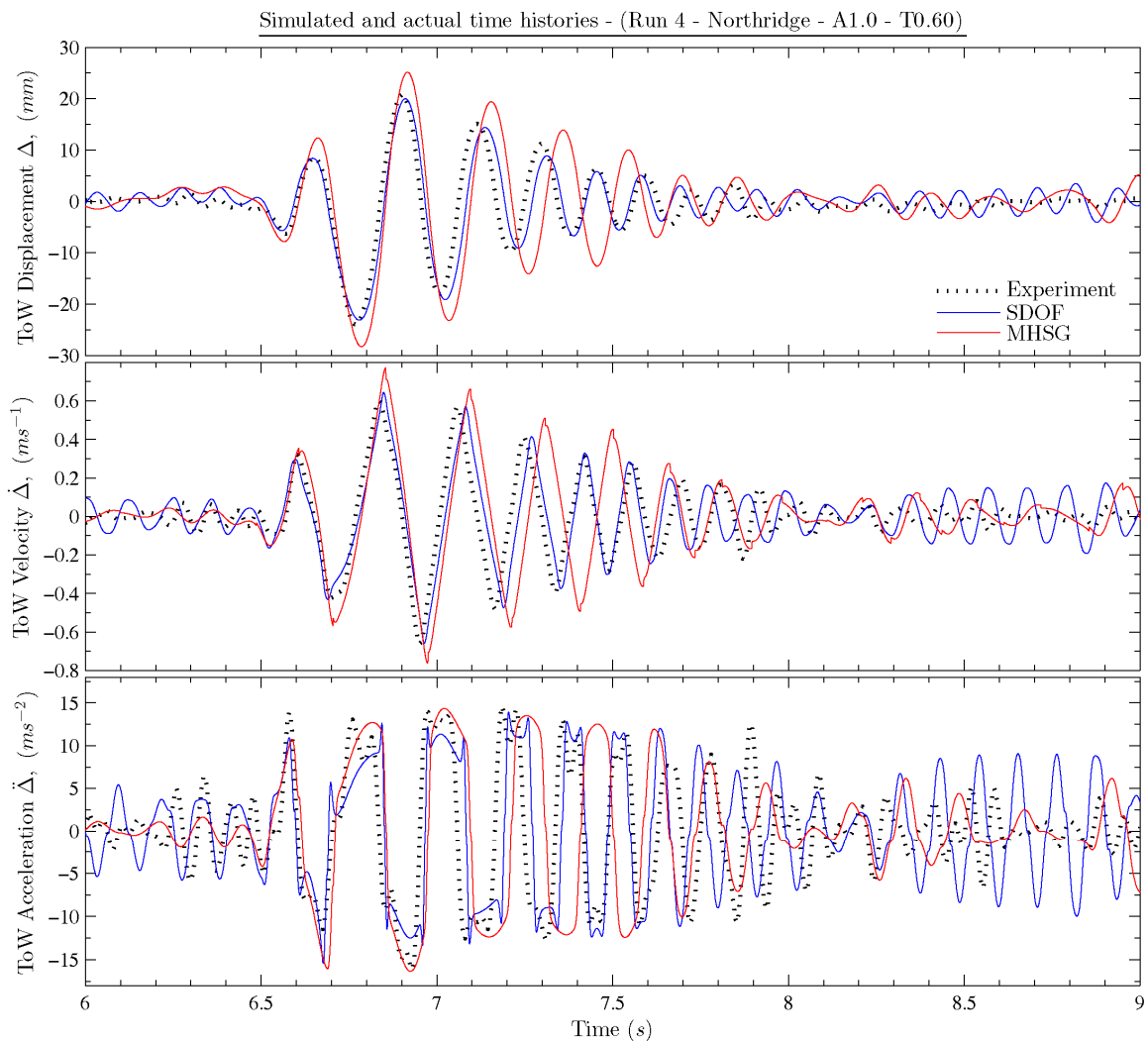


**Figure 4-67 – Simulated and actual time-histories (Run 4 – Northridge – A1.0 – T0.6)**

**Table 4-3 – Summary of simulation results**

Run ID	Peak ToW Disp. (mm)			Peak ToW Vel. (ms <sup>-1</sup> )			Peak ToW Accel. (ms <sup>-2</sup> )		
	Actual	SDOF	MHSG	Actual	SDOF	MHSG	Actual	SDOF	MHSG
1	-5.40	-3.39	3.12	-0.26	-0.17	0.11	-11.50	-9.74	-4.87
2	-4.34	-4.37	3.72	0.21	0.23	0.14	12.89	-12.06	5.50
3	8.65	-4.03	12.11	-0.36	0.20	-0.46	14.61	-10.78	-14.73
4	-23.91	-23.13	-28.29	-0.66	-0.66	0.77	-16.10	-15.41	-16.35
6	9.44	-6.60	-18.71	0.37	-0.32	0.55	17.97	-14.21	-15.12

\*Absolute magnitudes within 0 – 25 %, 25 – 50 %, 50 – 100% of actual data.



**Figure 4-68 – A close up comparison of simulated time-history during rocking**

An examination of the table of results and Figure 4-66 and Figure 4-67 quickly points out significant shortcomings in the performance of the SDOF and MHSG approaches.

In terms of peak predictions, both the SDOF and MHSG procedures predicted meaningful peak acceleration values in most cases. These values at times led to acceptable peak displacement predictions. However, the time-history plots revealed that the successes appeared to be mostly coincidental. It was only in the simulation of shake table test 4, that there was evidence of the simulated time-history tracking the actual response. In all the other cases, particularly when the displacements were small and rocking was not clearly initiated, there was little or no correlation between the simulated results and the actual shake table data. It was also discovered that both procedures were very sensitive to the input parameters. In particular, a small deviation in the rotation centre migration assumption or the energy dissipation per impact, results in wildly different time-histories. The sensitivity of the SDOF method and the controlled rocking system in general is addressed in greater detail in the next section.

Encouragingly though, as shown in a close up comparison of the simulated results of shake table tests 4 in Figure 4-68, the tracking in the simulation of this case, during moderate rocking motion is excellent. This suggests that both the SDOF and MGSG procedures would be very acceptable if rocking was guaranteed and only the peak amplitude motion was of interest.

This exercise has shown that the nonlinearly elastic equivalent SDOF procedure in unchanged form is superior and more reliable than the unchanged MHSG procedure.

#### **4.9.1.4 Attempts to improve the equivalent SDOF procedure**

It was decided from the previous investigation that the equivalent SDOF procedure was more promising in modelling a controlled rocking system's response to base excitation. The failings of the SDOF approach appeared to lie in the ability of the procedure to model the system response under small and non-rocking amplitudes.

Recall that the two key components of the SDOF approach are i) the elastic restoring force relationship,  $F_k(\Delta)$  and ii) the energy dissipation controlled by an  $r$  value. The shake table test results are now used to back calculate these two components and check whether they can be improved.

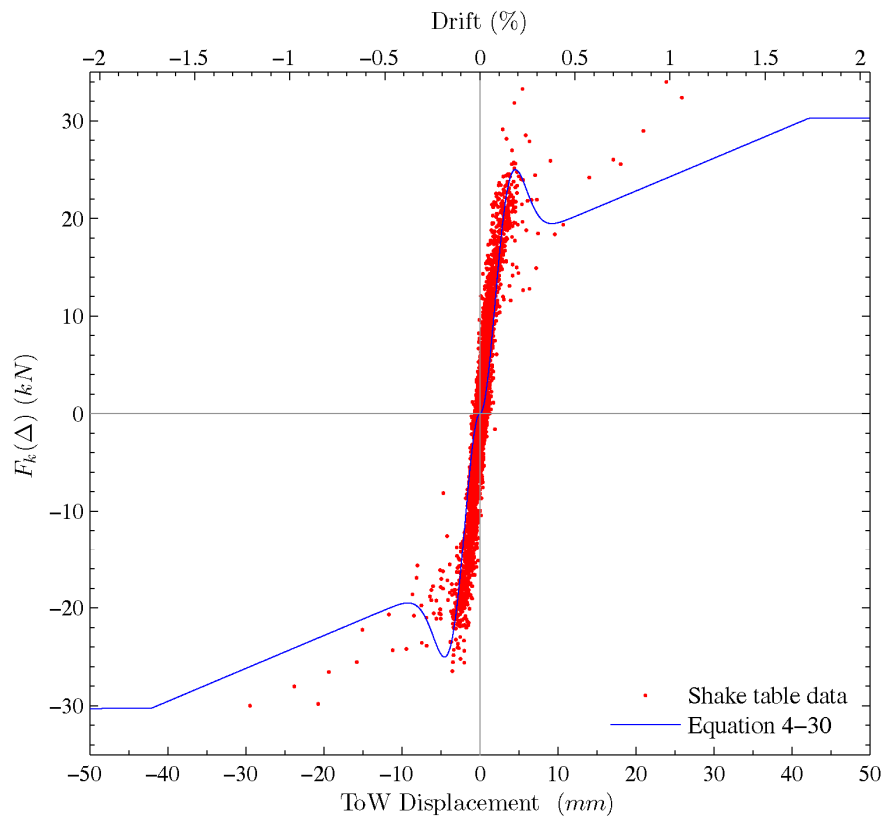
In order to check the restoring force relationship using the dynamic data, it is first assumed that there may well be velocity dependent damping forces in the system. As a result, the governing differential equation of the system can be approximated as Equation 4-41.

$$M_e \ddot{\Delta} + F_k(\Delta) + F_D(\dot{\Delta}) = -M_e \ddot{u}_g \quad (4-41)$$

Then at instances when the wall velocities are zero, differential Equation 4-41 prescribes that the elastic restoring force is the effective mass time the total acceleration of the system, as per Equation 4-42.

$$\text{Base Shear, } F_k(\Delta) = -M_e (\ddot{u}_g + \ddot{\Delta}) \quad \text{when } \dot{\Delta} = 0 \quad (4-42)$$

Since the wall is likely to be at some displacement at the instant when the wall velocity is zero, or in other words when the wall changes direction of travel, this permits  $F_k(\Delta)$ , the pseudo-static pushover force-displacement relationship, to be approximately mapped using the dynamic data. The data from the five shake table tests were subsequently processed and the result is plotted against the theoretical relationship in Figure 4-69.



**Figure 4-69 – Theoretical pushover characteristics versus dynamic data**

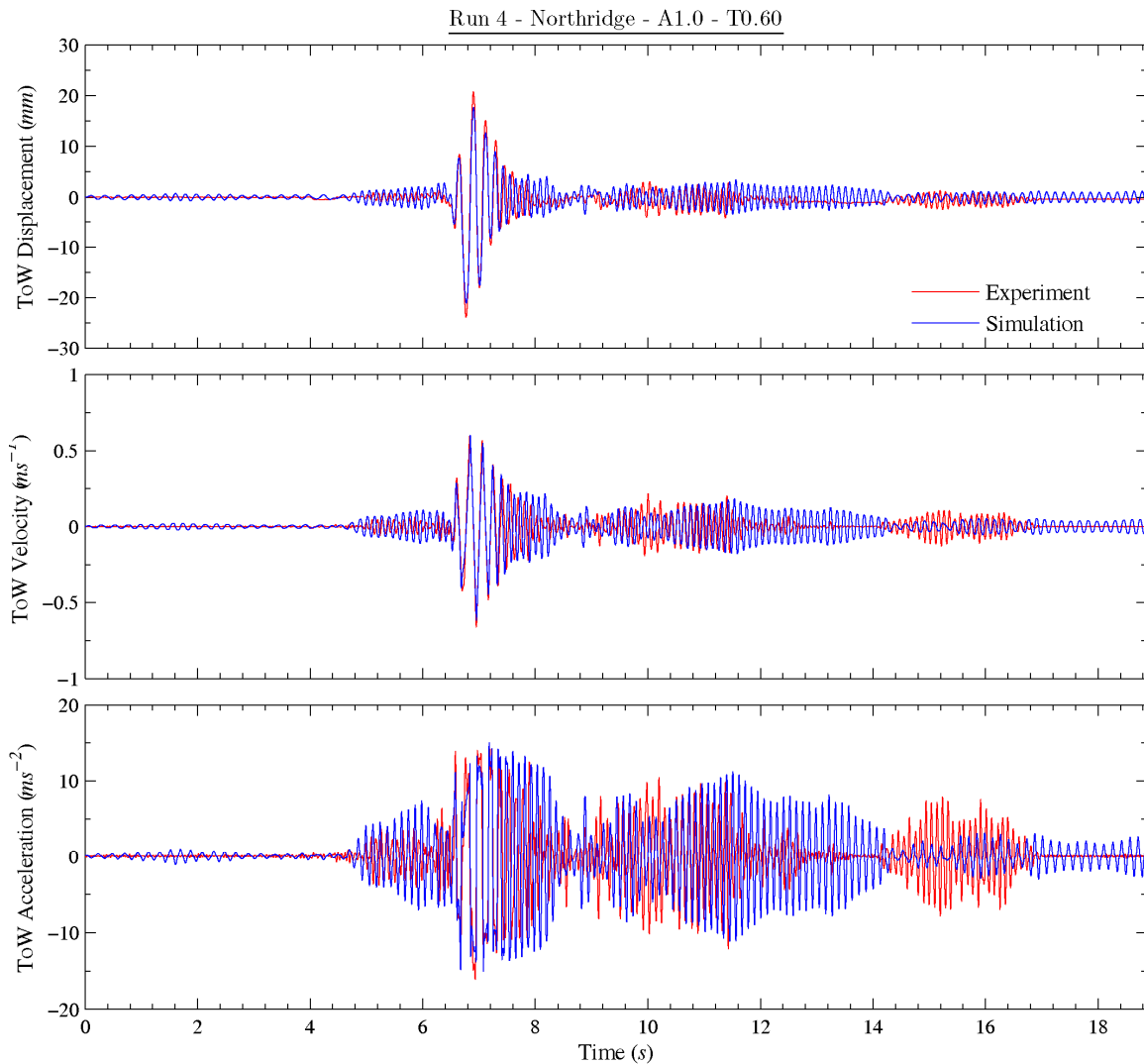
Figure 4-69 demonstrates that the theoretical relationship based on rotation centre migration in fact adequately characterises the overall dynamic response. A number of modifications to the pushover relationship were subsequently trialled but none improved the response prediction, either for the lower intensity shake table tests without rocking behaviour or the higher intensity shake table test with rocking observed. The modifications trialled included,

- 1) Fitting a linear relationship for the initial part of the  $F_k(\Delta)$ , in an attempt to stiffen the system to emulate the flexural interactions.
- 2) Updating the rotation centre migration relationships based on shake table rotation centre migration data in Figure 4-60.
- 3) Approximating  $F_k(\Delta)$  as a bilinear relationship.

In conjunction with the modifications in the restoring force relationship, a large number of modifications to the energy dissipation scheme were also trialled to improve the time-history prediction. Again, no combinations were sufficiently successful to justify a change. A few of the modifications trialled included,

- 1) Varying the  $r$  values from the settings described in Equation 4-31. The different configurations trialled included changing the displacement limits at which different  $r$  values are activated, changing the  $r$  values at the different threshold levels and using a single  $r$  value for all impacts.
- 2) Adding viscous damping for displacements less than a particular threshold.
- 3) Replacing the energy dissipation scheme with pure viscous damping.
- 4) Replacing the energy dissipation with a tangent stiffness proportional damping scheme.

This exercise illustrated a strong sensitivity of the results to the energy dissipation mechanism. Particularly noteworthy is that a single  $r$  value for all displacement and velocity ranges at times produced satisfactory time-history predictions. An example of this occurrence is when  $r$  is selected as 0.852 ( $r_{\text{Housner}}$ ), the resulting time-history prediction is presented in Figure 4-70 for illustration.

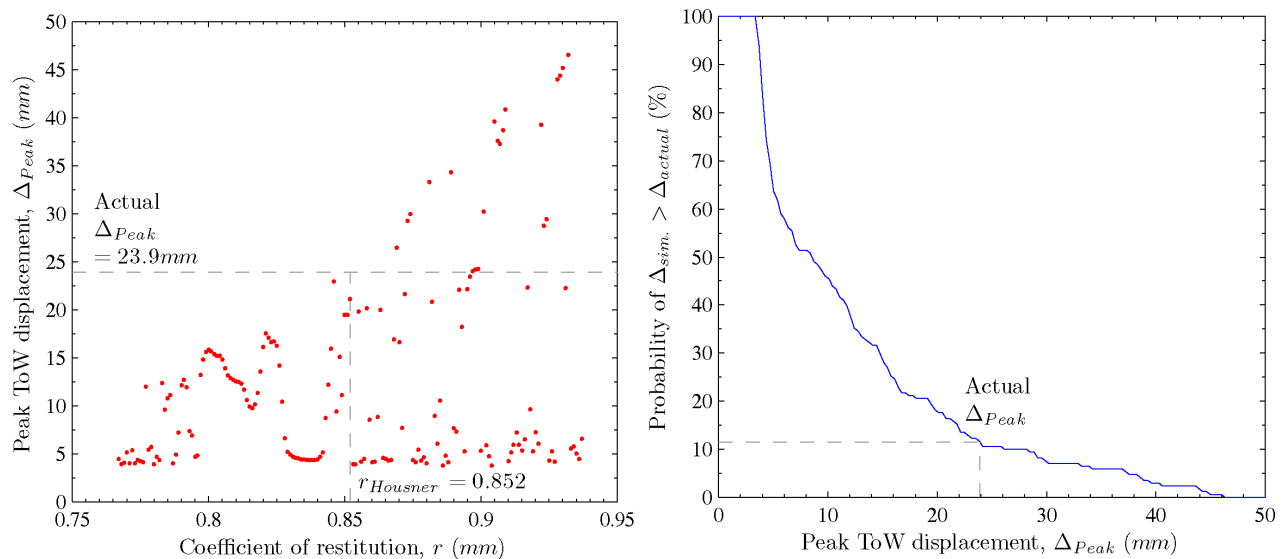


**Figure 4-70 – A time-history simulation using a constant  $r$  value ( $r = 0.852$ )**

Given this glimpse of success, an attempt was made to devise a prediction procedure using single  $r$  value analyses. Analyses using a single  $r$  value would be useful in design situations as it is unlikely that users would have free vibration data to enable calibration for the ideal energy dissipation settings.

For design purposes, users are typically only interested in a conservative estimate of the maximum response. A possible design procedure would be to simply conduct a large number of time-history analyses using a range of  $r$  values, and subsequently selecting a maximum response from these analyses. This brute force approach assumes that a single  $r$  value within the range of trial values would activate the correct response, or at least produce a response greater than the actual behaviour. This procedure be somewhat justifiable if it could be demonstrated that the peak response is a slowly varying function of  $r$ , and consequently, analyses conducted with

$r$  values further away from the ideal  $r$  value would be progressively more optimistic or conservative. Regrettably, this condition is not met as demonstrated by a series of time-history simulations on shake table test 4, using  $r$  values 10% above and below the ideal setting (0.852). The peak displacements from these analyses are collated and are presented in Figure 4-71. Notably from Figure 4-71b, only 11% of the analyses resulted in conservative peak displacement predictions.



**Figure 4-71 – a) Simulated peak ToW displacements versus the  $r$  value, b) probability of a time-history analysis resulting in a conservative estimate**

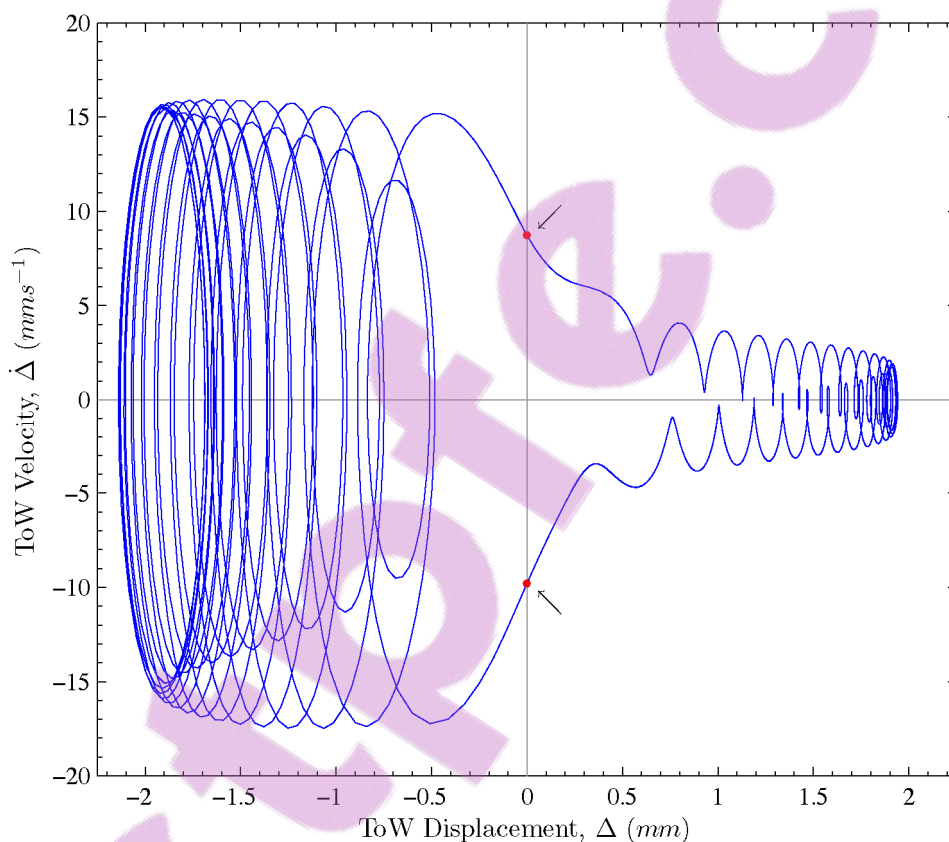
Figure 4-71 also shows that the time-history prediction is very sensitive to the selection of  $r$ . And not only is the solution sensitive, but there does not appear to be any trend in the variation.

#### 4.9.1.5 Sensitivity of controlled rocking system

Of side interest, the SDOF model representation of the controlled rocking problem appears to be similarly sensitive to initial conditions such as those which occur for a rocking rigid block as discussed in Section 2.5. To demonstrate this, additional series of time-history simulations were conducted on the controlled rocking wall subjected to harmonic ground excitations. In each time-history simulation, the  $r$  value was set as 0.852 and a varying amplitude sinusoidal base excitation applied to the wall. The governing differential equation of the system becomes,

$$M_e \ddot{\Delta} + F_k(\Delta) + F_{Damp} = -M_e Z \sin(16\pi t) \quad (4-43)$$

Each simulation initially runs for a sustained period to allow the transient behaviour to vanish and any possible cyclical behaviour to settle. The time-history algorithm then continues for some time, while it records every instance when the wall returns to the upright position. These instances represent the times when the motion of the wall, expressed as a trajectory in a phase diagram, crosses the y axis. These y intercepts or wall velocities when the wall returns to an upright position are subsequently collated for each time-history simulation with a fixed amplitude of forcing, ( $Z_i$ ). An example of a phase diagram trajectory from a typical time-history simulation is as shown in Figure 4-72.

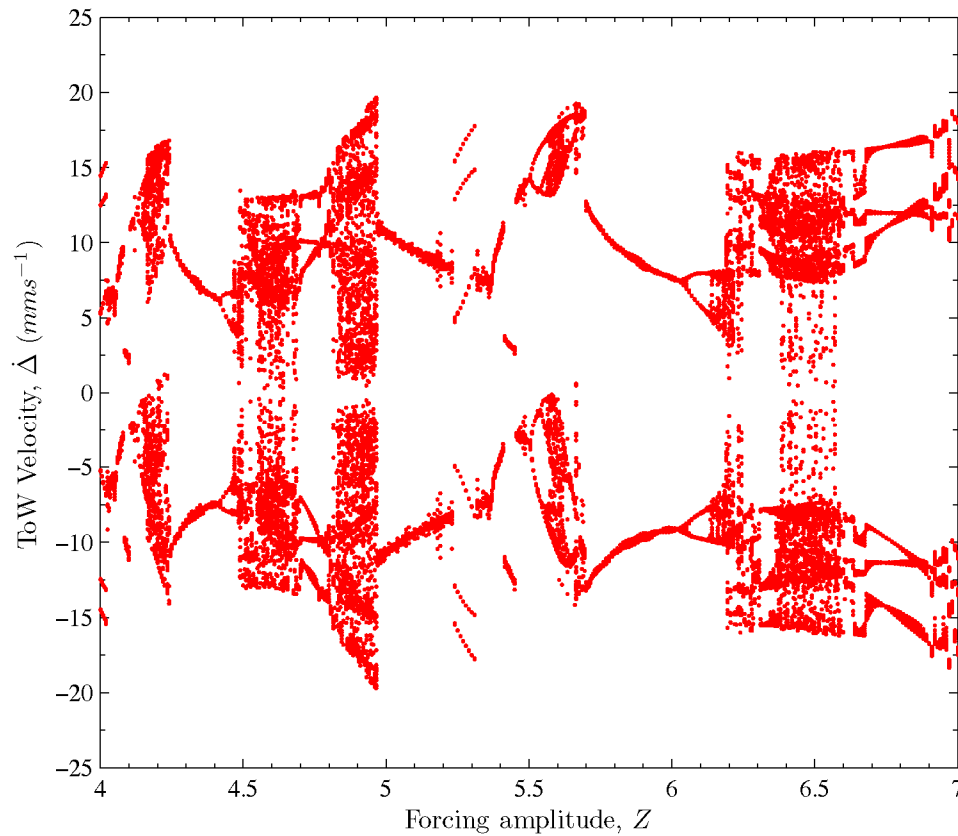


**Figure 4-72 – A typical time-history simulation expressed on a phase diagram ( $P_e(t) = 5.88 \sin(16\pi t)$ )**

When the time-history analyses over the range of forcing amplitudes are completed, the y intercepts are plotted against the forcing amplitudes as dots in a bifurcation diagram, as shown in Figure 4-73.

The presence of overlapping dots for a particular forcing amplitude indicates the wall reaches the upright position at the same velocity on every return. This indicates the wall has developed a steady periodic response or has reached a *limit*

cycle in nonlinear system dynamic theory. If these overlapping dots form a line as the forcing amplitude is varied, it indicates the long term system behaviour changes steadily as the forcing is modified. An example of this can be observed in Figure 4-73 when  $Z$  is between 5.7 and 6.0.



**Figure 4-73 – Bifurcation diagram of controlled rocking wall response subjected to varying sinusoidal base excitation**

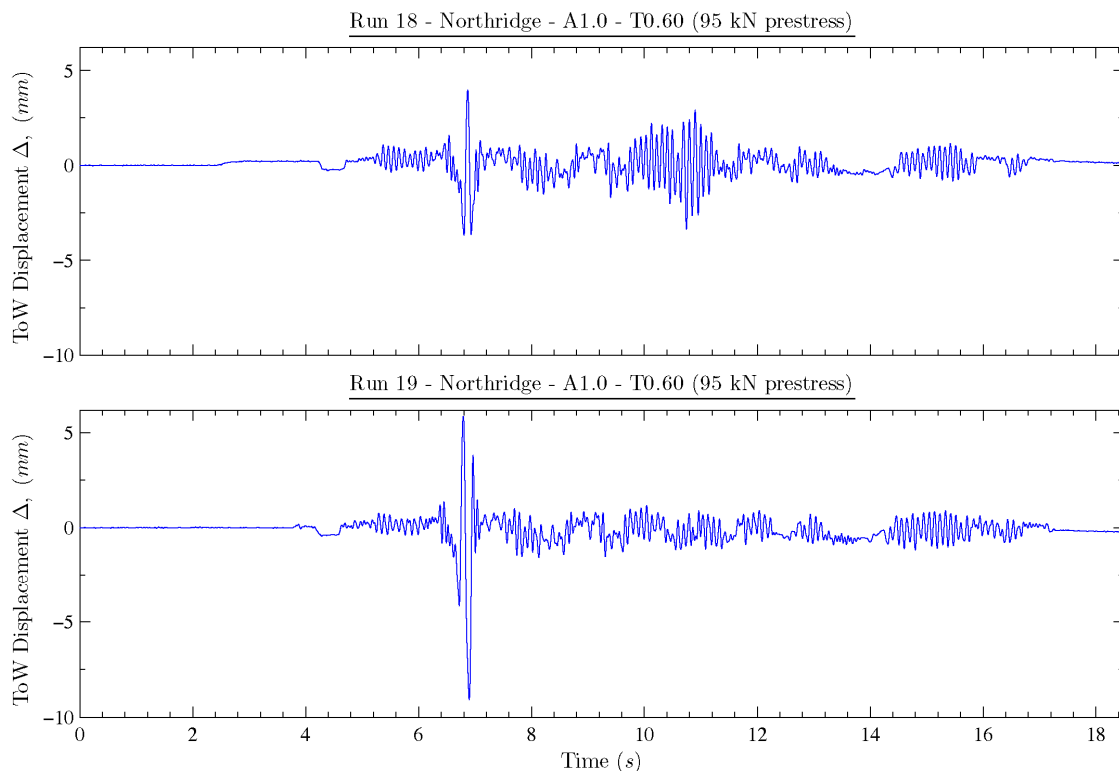
When a line splits to form two separate branches, like the case when  $Z = 6.03 \text{ ms}^{-2}$ , this indicates the normal periodic motion which crosses the  $y$  axis twice in one cycle, now crosses the  $y$  axis four times before it has the exact same dynamic state or in other words returns to the same location on the phase diagram. This period doubling phenomenon is common amongst many other nonlinear dynamic systems found in other branches of science (Hilborn 1994).

When the forcing amplitude is increased further from 6.2, the well defined lines now disappear into a smear band. This indicates the long term motion of the wall is no longer periodic and there is significant divergence of nearby trajectories, resulting in an unpredictable or aperiodic response. the discovery of unpredictable

response shows much similarity to the chaotic motion demonstrated by a rigid rocking block subjected to sinusoidal excitations.

Accepting that the proposed analysis procedure provides an acceptable representation of a controlled rocking system's behaviour, this exercise has demonstrated by example the extreme sensitivity of the system. Whilst the exercise has not shown comprehensively the source of this unpredictability, and perhaps cannot through the use of periodic excitations alone, it is more than likely that the source of the unpredictability is a sensitivity to initial conditions which is exacerbated by the history dependent nature of the problem.

To further illustrate that this sensitivity is not just a feature of the mathematical model, Figure 4-74 presents the shake table time-histories from two shake table tests with identical shake table motions and prestress levels. These tests previously reported as Run 18 and 19 from the original Wight study (2004), demonstrate that extreme sensitivity also occurs in the experimental results.



**Figure 4-74 – Displacement time-histories from two identical shake table tests**

In summary, this controlled rocking system appears to suffer from extreme sensitivity much like that which defines a free standing rigid rocking block. Thus it is not surprising that a precise time-history prediction of a controlled rocking system's response is difficult to obtain, and it explains why the time-history predictions are at times completely unrecognisable from the experimental results.

#### 4.9.2 SHAKE TABLE TESTS WITH 110 kN INITIAL TENDON FORCE

This next section examines the wall response from shake table tests 7, 8 and 9 as they are designated in Table 4-1. As it has been shown in the previous section that a precise time-history simulation of the response is virtually impossible, this section will focus on validating the proposed theoretical formula which predicts the tendon force, uplifts and pushover characteristics in relations to the ToW displacements.

While this section will not focus on the exact time-history simulation of the shake table tests, the results will be compared in an overview manner with corresponding tests conducted with 75kN initial tendon force. The shake table tests to be examined in this section are selected specifically as they each received effectively identical base excitations as one of the tests in the earlier series of shake table test.

These test results provide a unique opportunity to validate the ability of the theoretical model to predict a controlled rocking system's properties at a different prestress level. To begin, Table 4-4 presents a comparison of the key wall responses for the three shake table tests. The results show in cases where definitive rocking is expected, like the shake table tests with the Tabas and Northridge record, an increase of wall prestress generally decreases the maximum wall displacements and brings about higher wall accelerations for the same drift level. When uplift is not expected, there is insufficient data to show any definitive trend.

**Table 4-4 – Shake table tests results with 75kN and 110kN prestress**

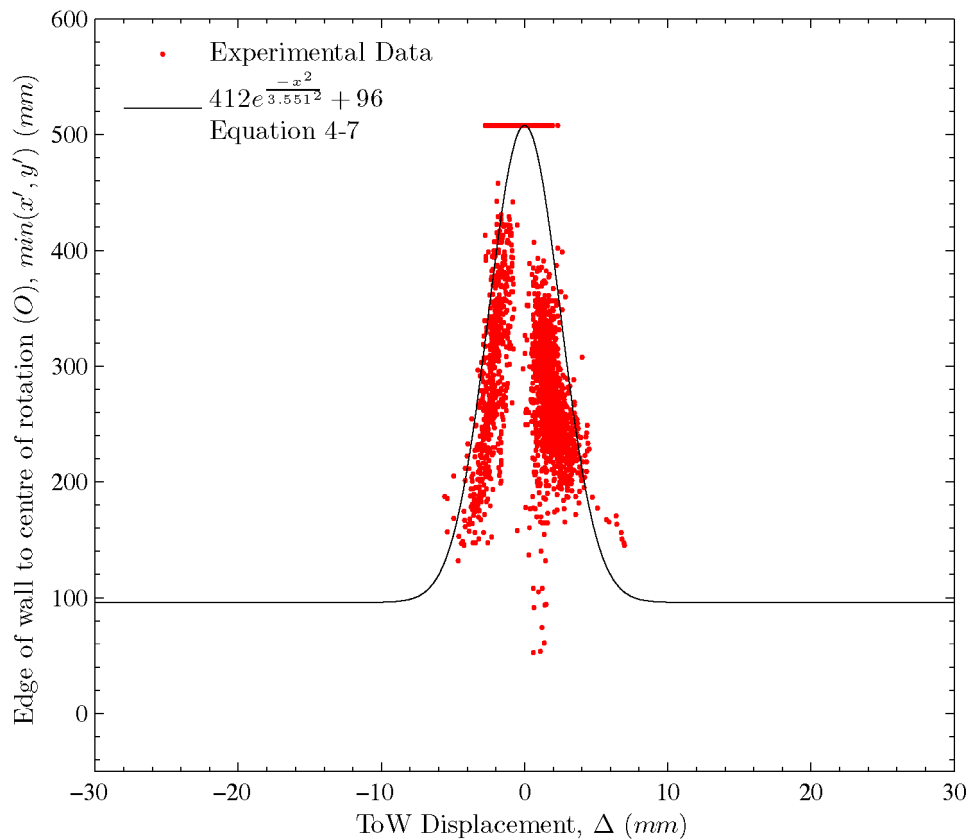
EQ Record	Peak ToW Disp. (mm)		Peak ToW Vel. (ms <sup>-1</sup> )		Peak ToW Accel. (ms <sup>-2</sup> )	
	75 kN	110kN	75 kN	110 kN	75 kN	110 kN
El Centro – A1 – T1	-4.34	4.54	0.21	0.25	12.89	15.74
Tabas – A1 – T0.38	8.65	6.96	-0.36	-0.33	14.61	17.17
Northridge – A1 – T0.6	-23.91	-4.63	-0.66	-0.24	-16.10	15.06

\*Absolute magnitude decreased / increased

Next, the locations of the wall rotation centre during the shake table tests with higher prestress are plotted against the ToW displacement in Figure 4-75. Figure 4-75 shows the rotation centre migration behaviour appears relatively unchanged by the prestress level and it is still adequately predicted by Equation 4-9. Though this cannot be confirmed entirely as the shake table tests did not generate sufficient data points in the larger ToW displacement ranges.

With consideration of the stress-strain properties of the wall and previous observations of the compression toe formation, it is postulated that if definitive rocking is developed under a higher level of prestress, the compression toe region must expand to accommodate the increased compression force through the toe. As a result, this would lead to the centre of rotation being closer to the wall centreline when definitive rocking is developed. The rotation centre migration under low displacement would be unaffected.

It may also be noted from Figure 4-75 that a similar level of sliding has occurred during this series of shake table tests.



**Figure 4-75 – Distance between the rotation centre and wall edge versus wall lateral displacement for the 110 kN shake table tests**

For the remainder of this section, the rotation centre is assumed to migrate similarly to the previous tests and can be described by Equation 4-7. Consequently, the uplift prediction formula remains as per Equation 4-9.

$$(1016 - d \cos \theta) = 412 e^{-\left(\frac{\Delta}{3.551}\right)^2} + 96 \quad (4-7)$$

$$u' = \frac{|\Delta|}{\sqrt{H^2 - \Delta^2}} \left( 920 - 412 e^{-\left(\frac{\Delta}{3.551}\right)^2} \right) \quad (4-9)$$

Equipped with these equations, the tendon force is predicted by Equation 4-16 with  $P_{Tendon}^0$  updated to 111 kN.

$$P_{Tendon}(\Delta) = P_{Tendon}^0 + \frac{EA}{L_{T0}} \left( \frac{H|\Delta|}{H^2 - \Delta^2} \left( 920 - 412 e^{-\left(\frac{\Delta}{3.551}\right)^2} \right) - \frac{B|\Delta|}{\sqrt{H^2 - \Delta^2}} \right) \quad (4-16)$$

This leads to the three equations below for the potential energy of the systems. As the rotation centre migration remains the same as before, the only expression requiring updating is the expression for the elastic potential energy of the tendon,  $U_E(\Delta)$ , and this is presented as Equation 4-44 below.

$$U(\Delta) = m_T g \left( \frac{|\Delta|}{\sqrt{H^2 - \Delta^2}} \left( 920 - 412 e^{-\left(\frac{\Delta}{3.551}\right)^2} \right) - \frac{B|\Delta|}{H} \right) \quad (4-18)$$

$$E_k(\dot{\Delta}) = \frac{1}{2H^2} I_o \dot{\Delta}^2 \quad (4-19)$$

$$U_E(\Delta) = \begin{cases} \frac{L_T}{2EA} [P_{Tendon}(\Delta)]^2 - 526.12 & \text{before tendon yield} \\ 159.03 \times \Delta L_T(\Delta) - 98.506 & \text{after tendon yield} \end{cases} \quad (4-44)$$

These energy expressions are then numerically differentiated following Equation 4-30 to arrive at a pseudo-static pushover force-displacement relationship of the wall with nominally 110 kN tendon prestress.

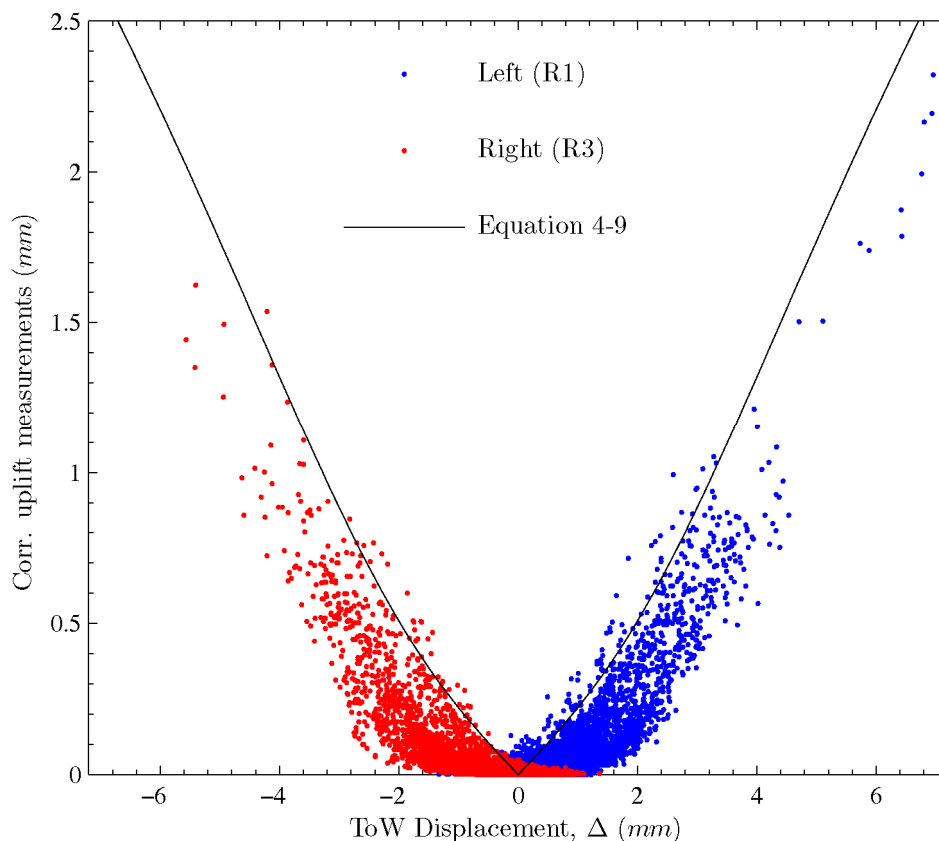
$$F_k(\Delta) = \frac{dU_E}{d\Delta} + \frac{dU}{d\Delta} \quad (4-30)$$

To examine the validity of the updated prediction formulas, each of the predicted quantities is plotted against actual shake table test results. Figure 4-76

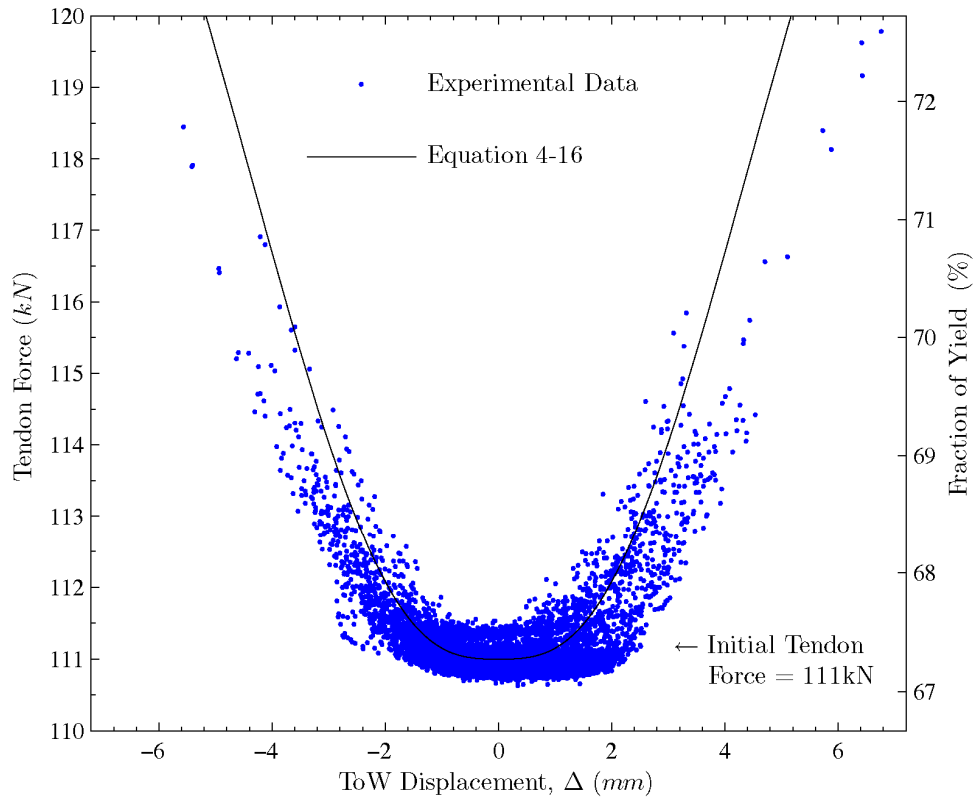
presents the wall corner uplifts as a function of the ToW displacement from the three shake table tests, alongside the predicted relationship by Equation 4-9. As shown, the updated Equation 4-9 has adequately modelled the uplift characteristics as a function of the ToW displacement. The deviations from the prediction formula are not perceptibly higher than before.

Figure 4-77 presents the tendon force as a function of the ToW displacement. Again, the prediction formula is shown to model the shake table results well.

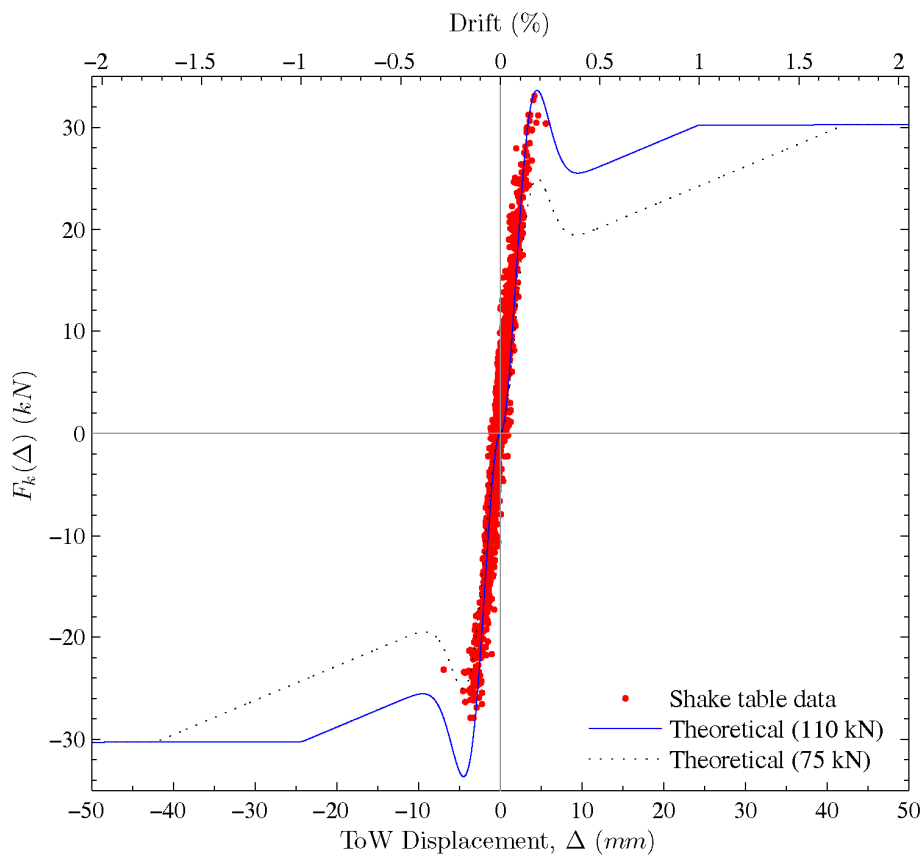
Finally, the updated force-displacement relationship is plotted alongside the experimental data in Figure 4-78. It is clear from this figure that the pseudo-static properties of the wall at a different level of prestress can be estimated using the same extension of the rotation centre migration assumption. It is disappointing that the shake table could not generate a greater ToW displacement to confirm this with a greater level of certainty.



**Figure 4-76 – Wall uplifts versus ToW displacements for tests with 110 kN tendon prestress**



**Figure 4-77 – Tendon force versus ToW displacements for 110 kN prestress**

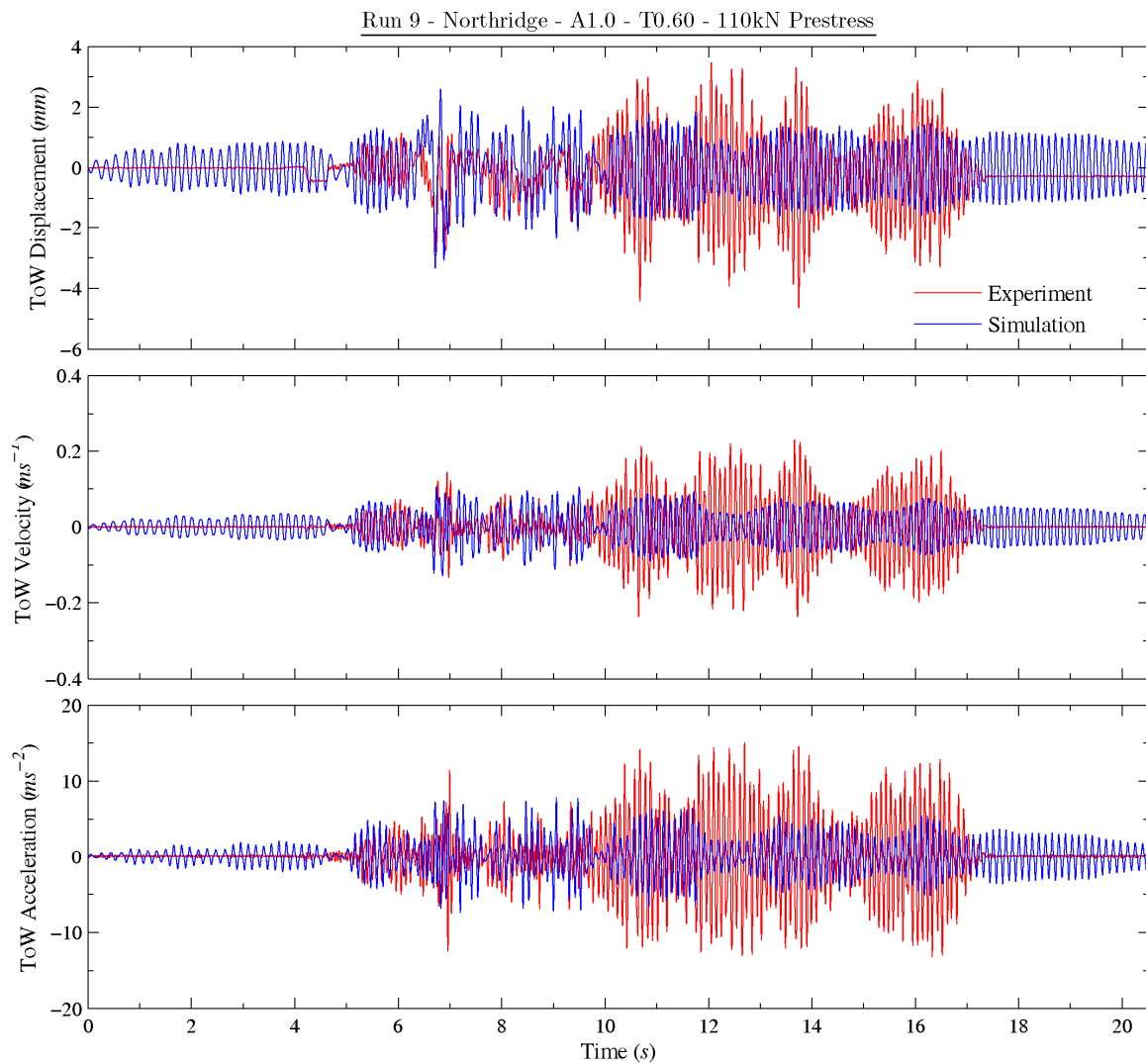


**Figure 4-78 – Theoretical pushover characteristics versus dynamic data**

Figure 4-78 also sensibly demonstrates that an increase in wall prestress leads to a higher force threshold required for rocking or rotation centre migration to initiate. Furthermore, an increase of wall prestress also reduces the lateral displacement at which tendon yielding begins.

#### 4.9.2.1 Predicting the time-history response subjected to base excitation

For the sake of completeness, the nonlinearly elastic equivalent SDOF procedure is applied in an attempt to simulate the 110 kN prestress shake table tests. Two series of simulations are conducted, one using the  $r$  value settings derived from the free vibration decay analysis and the other using a constant  $r$  value of 0.835. A summary of the key results is presented in Table 4-5 overpage and a typical simulated time-history is compared against the shake table results in Figure 4-79



**Figure 4-79 – Typical time-history simulation using a constant  $r$  value ( $r = 0.852$ )**

**Table 4-5 – Summary of simulation results**

Run ID	Peak ToW Disp. (mm)			Peak ToW Vel. (ms <sup>-1</sup> )			Peak ToW Accel. (ms <sup>-2</sup> )		
	Actual	<i>r</i> (FV)	<i>r</i> = 0.852	Actual	<i>r</i> (FV)	<i>r</i> = 0.852	Actual	<i>r</i> (FV)	<i>r</i> = 0.852
7	4.54	2.26	-2.10	0.25	-0.11	0.10	15.74	-7.83	7.92
8	6.96	-2.47	-2.45	-0.33	-0.12	-0.12	17.17	8.48	9.05
9	-4.63	-3.33	-3.32	-0.24	-0.13	-0.13	15.06	7.14	7.80

\*Absolute magnitudes within 0 – 25 %, 25 – 50 %, 50 – 100% of actual data.

The table of results shows the simulations with the two *r* settings produced very similar and poor predictions. They all underestimated the peak response by a large margin. As observed in the typical time-history plot, the simulated time-histories do not resemble the actual shake table results. The simulated time-histories for the other shake table test runs are available in Appendix C.

These simulations also demonstrate that because of the history dependency of the problem, it is important to accurately simulate the behaviour of a controlled rocking wall at all drift levels. As it is shown in Table 4-5, a failure to model some part of the force-displacement behaviour will lead not only to poor time history prediction but also poor peak response prediction. This further illustrates the importance of modelling the continuous migration of the rotation centre.

#### 4.10 CONCLUSION

This chapter describes a thorough investigation of the dynamic characteristics of controlled rocking objects. The investigations first studied the free vibration decay response of a controlled rocking wall specimen. Then new findings from this analysis were applied to predict the wall specimen behaviour subjected to base excitations at two prestress levels.

The study has found a novel approach to predict key mechanical properties of a controlled rocking wall based on the migration of the rotation centre. It was found that by fitting an empirical formula with a Dirac- $\delta$  form to describe the rotation centre migration behaviour, it was possible to accurately predict the uplift and post-tensioning tendon extension as a function of the wall displacements. Once these are obtained, they can be manipulated to predict the pseudo-static force-displacement relationship, a property that is well understood by structural engineers for modelling

nonlinear structures. It should be emphasized however, that despite this new ability to predict the pseudo-static force-displacement relationship of a controlled rocking wall. There is insufficient evidence at the present time to support the use of a secant stiffness equivalent linear modal analysis for the prediction of time history or peak response behaviour.

The concept of a continuous migration of rotation centre is significant, as it provided a logical basis to explain the behaviour of controlled rocking walls when rocking is partially and fully initiated. This is in contrast to having separate assumptions and models for different phases during rocking, which would be too cumbersome to apply. The rotation centre migration approach was first validated against the free vibration decay response to predict the rocking period variations as a function of displacement amplitude. The approach was then extended into two procedures to predict the time-history response of the controlled rocking wall specimen. The two procedures are the equivalent SDOF approximation and the MHSG procedures.

It was shown in this chapter that both the equivalent SDOF and MHSG procedure adequately simulated the free vibration decay motion. However, it was the equivalent SDOF procedure which was more successful and reliable in simulating the controlled rocking wall subjected to base excitations. It was pointed out in the investigations that the time-history simulations are very sensitive to a small change in input parameters. Particularly, a small change in the  $r$  value or the energy dissipation parameter results in dramatically different time-histories.

When the sensitivity of the system is coupled with unavoidable effects from sliding, bouncing and flexural interactions, which cannot be precisely accounted for, it led to the conclusion that a reliable and accurate time-history prediction of a controlled rocking wall subjected to base excitations is unattainable.

In the process of illustrating the unpredictability of the controlled rocking system, the controlled rocking system was found to be so sensitive that it exhibited classical chaotic system traits. This extreme sensitivity was also shown to occur in reality by two shake table tests on the same wall specimen with identical base excitations. These two effectively identical tests resulted in very different time-history responses.

It was also illustrated that the rotation centre migration approach can be applied to walls at different levels of prestress. Finally, it should be noted that this approach can be easily extended to accommodate walls with different tendon arrangements by simply considering the geometry of the system.



# Chapter 5

---

## SIMPLIFIED ROCKING STRUCTURAL SYSTEMS

---

This chapter presents an investigation of the behaviour of simplified structural systems permitted to rock on their foundation. As discussed in the literature review in Chapter 2, many researchers have explored this topic using SDOF idealisations. However the models are rarely validated by an experimental study.

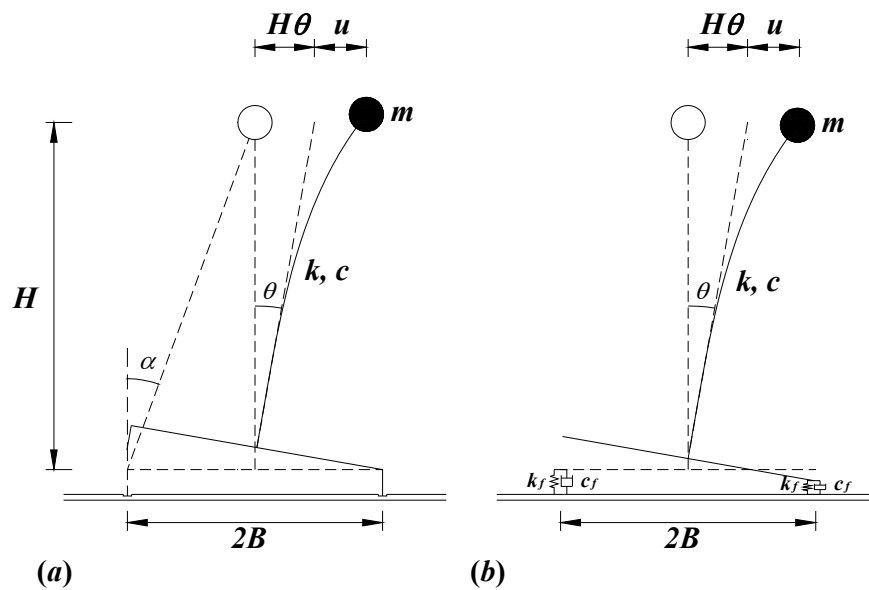
One of the key assumptions in the models for predicting the dynamic response of rocking SDOF structures lies in the treatment of the rocking interface. This section explores the accuracy of a range of these assumptions, by comparing the predicted time-history response against experimental results reported previously by McManus (1980). This chapter also presents three new procedures for predicting the response of rocking structures subjected to base excitation.

### 5.1 INTRODUCTION

One of the simplest rocking structural systems is the uplifting SDOF ‘lollipop’ structure as shown in Figure 5-1. In this model, the structural system is idealised as a SDOF system with an equivalent mass  $m$ , a linear stiffness  $k$  and an equivalent viscous damping  $c$ . This SDOF system is assumed to rest on rigid ground and when subjected to lateral forcing is permitted to detach from the ground and rock from side to side. This study will develop new formulations of the problem from first principles and the proposed formulations will be validated using published experimental data.

The rocking structural models in this chapter will adopt one of the following rocking interface assumptions,

- A. The rocking interface is rigid. This leads to Housner's plastic impacts and fixed rocking pivots assumptions.
- B. The rocking interface is flexible but the locations of rocking pivots are fixed. Consequently, the interface can be adequately represented by two compression-only springs.



**Figure 5-1 – Two rocking interface assumptions examined in this chapter**

## 5.2 EXPERIMENTAL VALIDATION DATA

The experimental validation data for this chapter came from a set of experiments by McManus (1980). In these experiments, McManus constructed a simple steel column structure as shown in Figures 5-2 and 5-3. The steel column was designed to allow additional steel masses to be attached at different heights to emulate systems with different aspect ratios. Aspect ratio here refers to the ratio of the height to the centre of mass divided by the base width. Key mechanical properties of the column model are listed in Figure 5-2. The column model had removable steel feet which were removed to simulate different base conditions. When the steel feet were removed, a 25 mm thick soft rubber layer was placed beneath the base plate to emulate a flexible foundation. The soft rubber layer behaved elastically and it had a nonlinear force-deformation characteristic as shown in Figure 5-4.

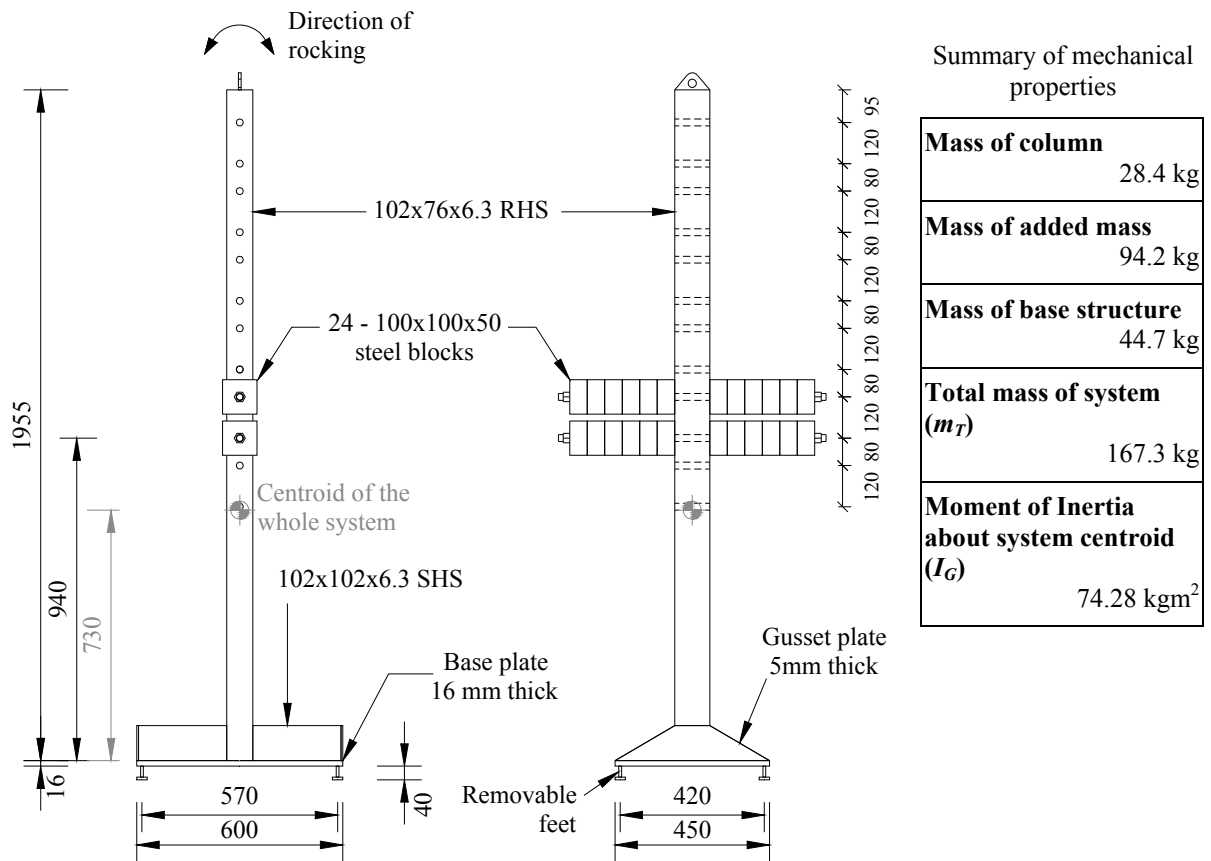


Figure 5-2 – Geometry of the steel column specimen

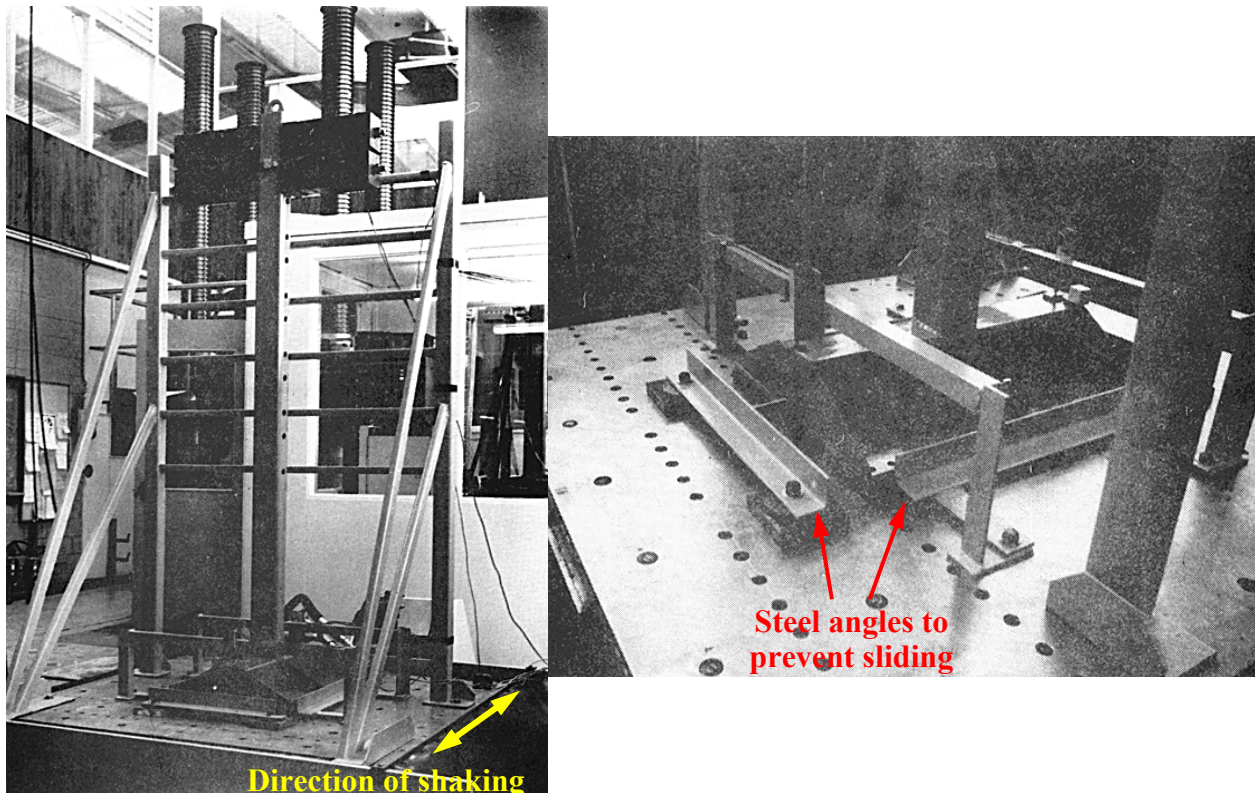
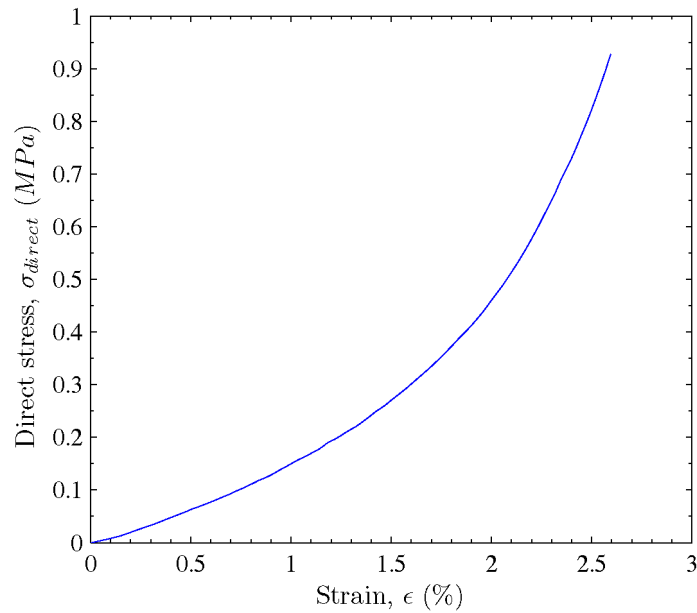


Figure 5-3 – Photographs of the experimental rig (Source: McManus 1980)



**Figure 5-4 – Stress-strain property of the soft rubber pad (Source: McManus 1980)**

Series of tests were conducted on each mass/height configuration and base interface condition. Each series of tests included a snap back test, where the specimen was given an initial displacement, held still, then released and the motion allowed to decay freely. This was followed by series of shake table tests where modified earthquake ground accelerations were applied to the specimen.

The validation data for this study was obtained by digitizing the plots reproduced in the McManus report. As a result, only a selection of the shake table tests results was available as time-history traces. Furthermore, as the recordings were made by a chart recorder, some of the plots were unclear and could not be processed this way. For these reasons, this study will focus on four tests with the additional masses attached at 1 m from the base as shown in Figure 5-2. A brief description of the four tests is included in Table 5-1 below.

**Table 5-1 – Summary of dynamic test data**

Run	Description	Max horiz. disp. (mm)	Max uplift (mm)
1	Snap back test, free rocking decay, solid steel feet	28.1	16.5
2	Snap back test, free rocking decay, soft rubber pad	28.6	13.2
3	Shake table test, steel feet, El Centro-NS record	18.6	10.8
4	Shake table test, soft rubber pad, Pacoima Dam N76°W record	37.7	22.6

In addition to the dynamic tests listed in Table 5-1, a number of small amplitude dynamic tests were conducted to find the flexural properties of the steel column. In these tests, the model was struck firmly at approximately the centre of gravity. This generated a small transient vibration in the column without uplift which was recorded by an accelerometer. These tests showed the flexural period of the column ( $T_{fixed}$ ) is 0.112 s and 0.092 s for the solid feet arrangement and the soft rubber foundation arrangement respectively. It may at first appear strange that the solid feet arrangement produced a longer natural period than the system with the soft rubber foundation. This was because when the specimen had solid feet, the base plate was free to bend and introduced additional flexibility to the steel column, whereas the soft rubber foundation provided a continuous support and minimised the base plate flexibility.

Idealising the steel column specimen as a SDOF lollipop structure fixed at the base plate, an equivalent lateral stiffness was estimated using the natural period from the small transient vibration experiment. This was achieved simply by substituting a period of 0.092 s and the equivalent mass of the system into Equation 5-1. The mass of the base structure was excluded from the calculation as it was assumed that it did not participate in the flexural vibration.

$$k = \frac{4\pi^2}{T_{fixed}^2} m_e = 571.8 \text{ kN/m} \quad (5-1)$$

### 5.2.1 FREE ROCKING DECAYS (FRD) – SOLID FEET

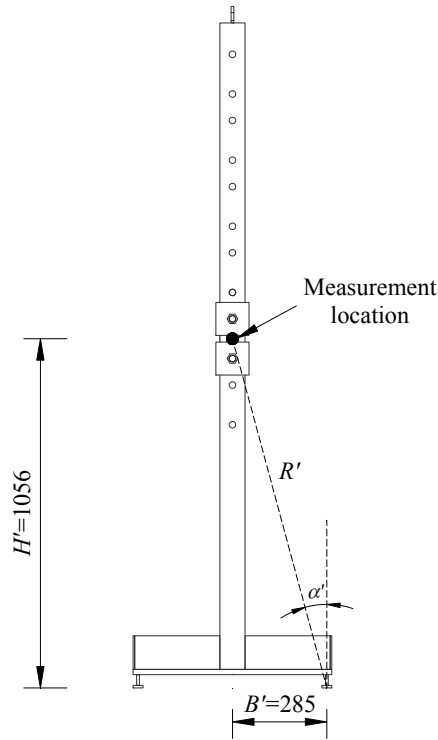
The displacement time-history of the snap back test with the solid feet arrangement is presented in Figure 5-6. The horizontal deflection time-history shows a smooth cyclical response, while the uplift trace is slightly undulated presumably from the flexing of the base plate.

The displacements were recorded at the centre of the additional masses and they are converted into rotations according to Equation 5-2.

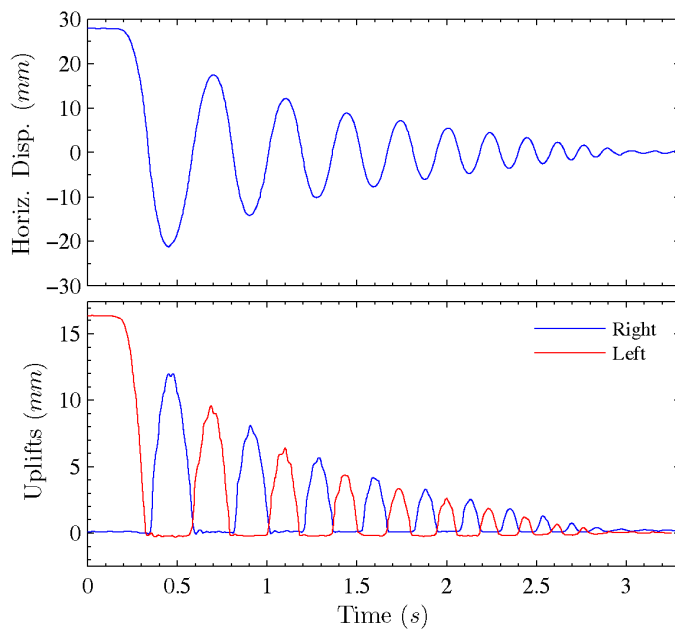
$$\theta = \begin{cases} \alpha' - \sin^{-1}\left(\frac{B' - \Delta}{R'}\right) & \text{for } \Delta > 0, \\ \sin^{-1}\left(\frac{B' + \Delta}{R'}\right) - \alpha' & \text{for } \Delta < 0, \end{cases} \quad (5-2)$$

where 
$$\alpha' = \tan^{-1}\left(\frac{B'}{H'}\right).$$

$B'$ ,  $H'$  and  $R'$  are distances from the base of the steel foot to the point of measurement and are as shown in Figure 5-5. These are 285 mm, 1056 mm and 1093.8 mm respectively.



**Figure 5-5 – Measurement location (dimensions shown in mm)**



Points of interest

Time (s)	$\Delta$ (mm)	$\Phi = \theta/\alpha_e$
0.138	27.93	0.099
0.339	0	0
0.453	-21.30	-0.076
0.585	0	0
0.695	17.42	0.062
0.809	0	0
0.901	-14.18	-0.051
1.008	0	0
1.106	12.16	0.043
1.194	0	0
1.274	-10.17	-0.036
1.364	0	0
1.443	8.88	0.032
1.522	0	0
1.590	-7.77	-0.028
1.669	0	0

**Figure 5-6 – Displacement time-history of run 1, FRD – solid feet**

The peaks and zero crossings of the displacement time-history were identified and details from the first few cycles are listed in Figure 5-6. These were used to calculate the quarter periods of the free rocking vibration and are plotted against the corresponding peak displacement in Figure 5-7.

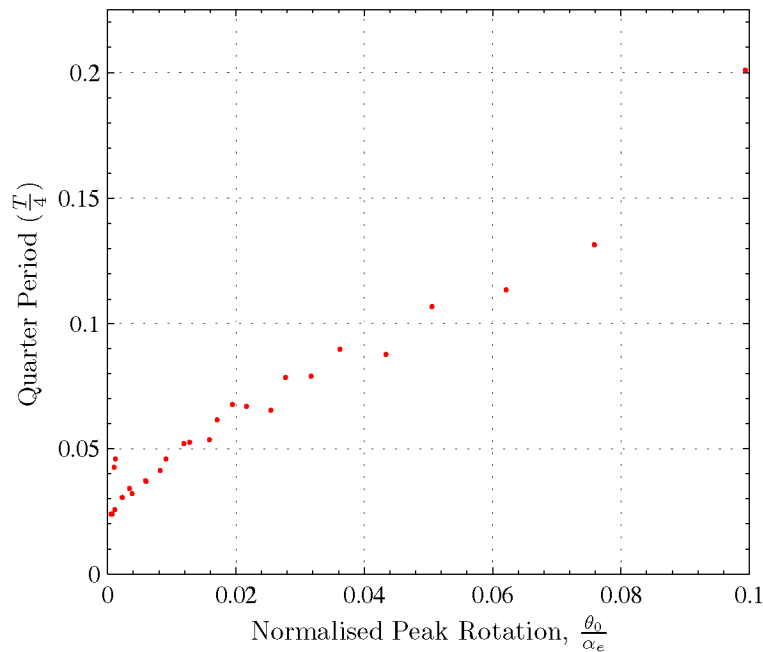


Figure 5-7 – Quarter periods versus norm. peak rotation (run 1, FRD – solid feet)

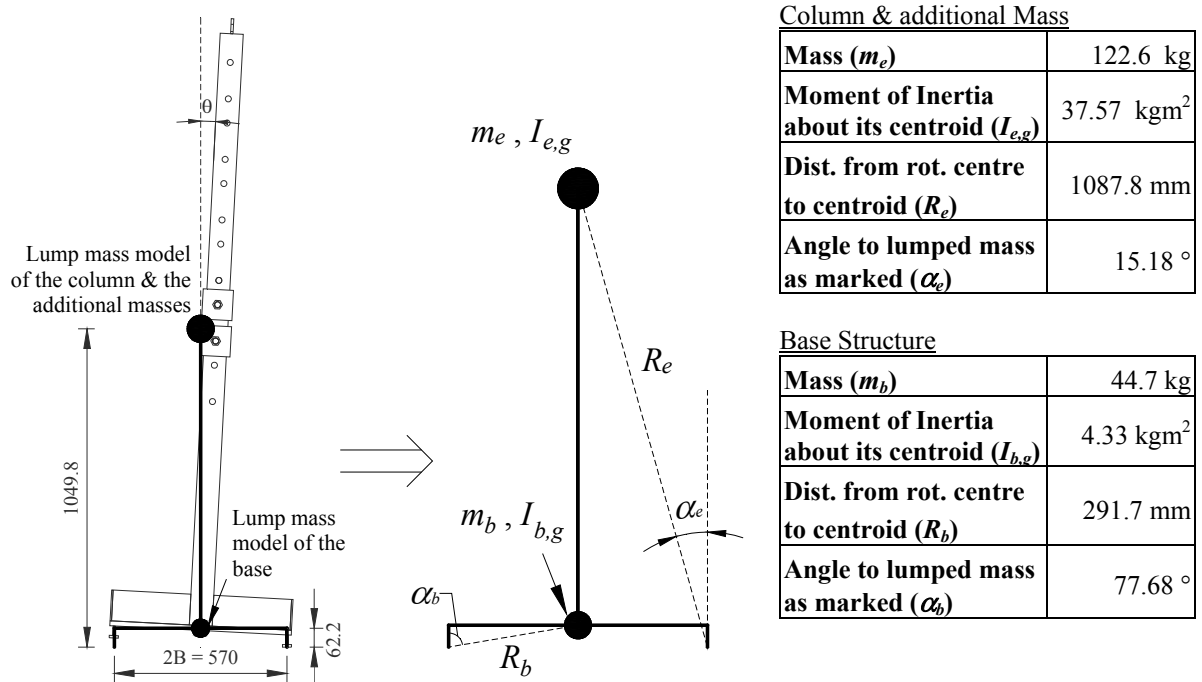


Figure 5-8 – The equivalent lumped mass model of the system

It should be noted that Figure 5-7 differed slightly from a corresponding plot from the McManus report as quarter periods from peak to zero crossing are measured here instead of half cycle periods. Furthermore the definitions of the equivalent lumped mass models are different and this led to different  $\Phi$  values. The definition of the lumped mass model for this study is as shown in Figure 5-8.

Next the energy dissipation in the experiment can be quantified by a coefficient of restitution,  $r$ , associated with each impact. This was evaluated from the experimental result by examining the ratios of successive peaks in the displacement time-history.

Idealising the steel column specimen as a lumped mass model as shown in Figure 5-8, the gravitation potential energy of the system can be expressed as a function of the rotation, Equation 5-3.

$$U_{Grav}(\theta) = m_e g R_e [\cos(\alpha_e - |\theta|) - \cos(\alpha_e)] + m_b g R_b [\cos(\alpha_b - |\theta|) - \cos(\alpha_b)] \quad (5-3)$$

Assuming the flexural deflections are insignificant in the free rocking experiments and energy is conserved in the smooth rocking phases between impacts, the kinetic energy content just before an impact is the same as the gravitational potential energy content when the specimen is at a peak displacement in the preceding cycle. Similarly, the kinetic energy content immediately after an impact is the same as the gravitational potential energy content when the specimen is at the next displacement peak. As a result, the coefficient of restitution for the  $i$ -th impact can be evaluated by Equation 5-4.

$$r^i = \frac{E_k^{i+1}}{E_k^i} = \frac{U^{i+1}}{U^i}$$

$$r^i = \frac{m_e R_e [\cos(\alpha_e - |\theta_{peak}^{i+1}|) - \cos(\alpha_e)] + m_b R_b [\cos(\alpha_b - |\theta_{peak}^{i+1}|) - \cos(\alpha_b)]}{m_e R_e [\cos(\alpha_e - |\theta_{peak}^i|) - \cos(\alpha_e)] + m_b R_b [\cos(\alpha_b - |\theta_{peak}^i|) - \cos(\alpha_b)]} \quad (5-4)$$

Where

$U^i$  = Potential energy content at the time of peak rotation before the  $i$ -th impact

$E_k^i$  = Kinetic energy content just before the  $i$ -th impact

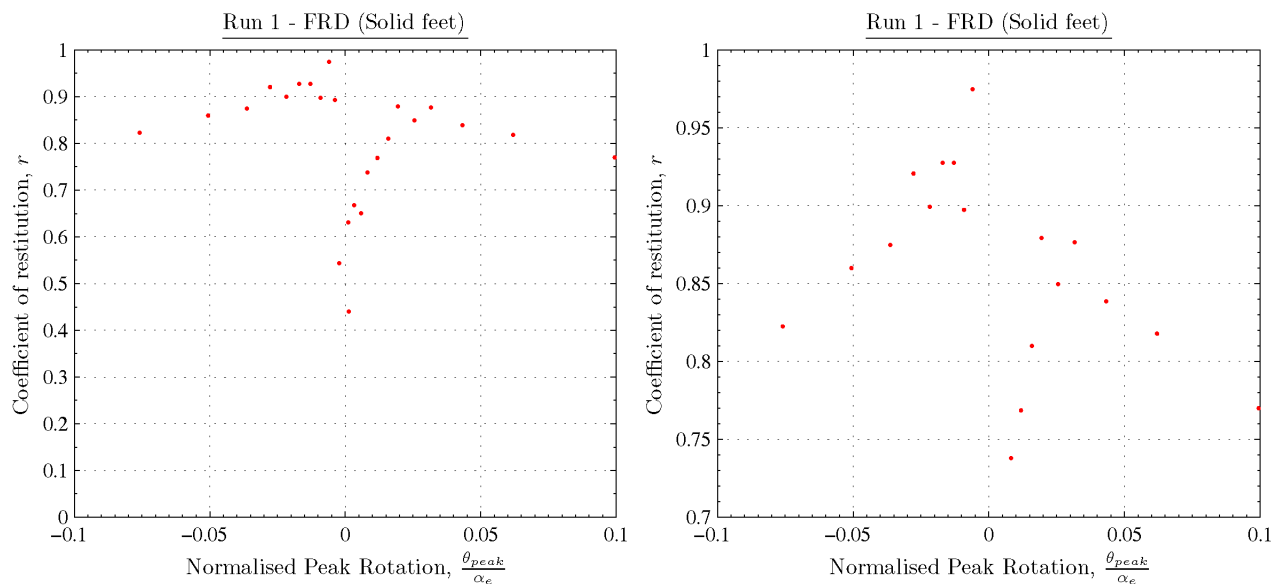
$E_k^{i+1}$  = Kinetic energy content just after the  $i$ -th impact

$U^{i+1}$  = Potential energy content at the time of peak rotation after the  $i$ -th impact

$m_e, m_b$  = Mass of the column structure and the base structure respectively

$R_e, \alpha_e, R_e, \alpha_e$  = As shown in Figure 5-8.

The experimentally determined  $r$  values are plotted against the peak rotations in Figure 5-9. This figure highlights a considerable variation in the experimental  $r$  value from impact to impact. The  $r$  value in this experiment varied between 0.75 and 0.95. It was also observed that the  $r$  value increased as the vibration diminished, perhaps because flexure displacement became relatively more important and the energy stored in flexural vibration is not dissipated by the impacts.

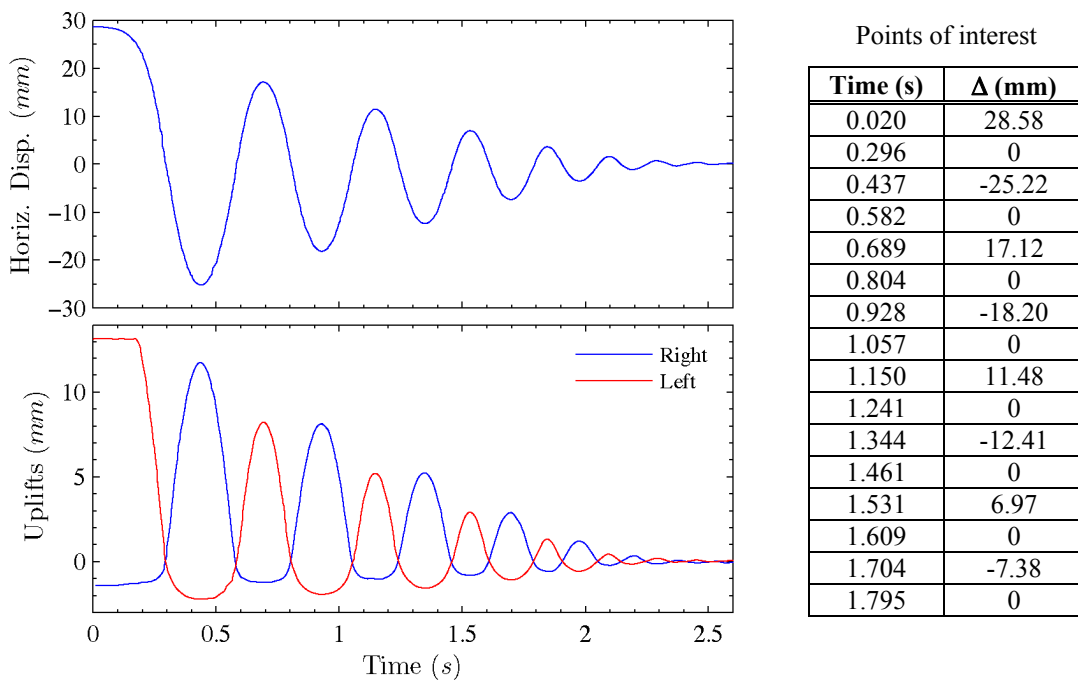


**Figure 5-9 – a) coefficient of restitution versus  $\theta_{peak}/\alpha_e$ , b) A close up of a) with data points from small vibrations removed**

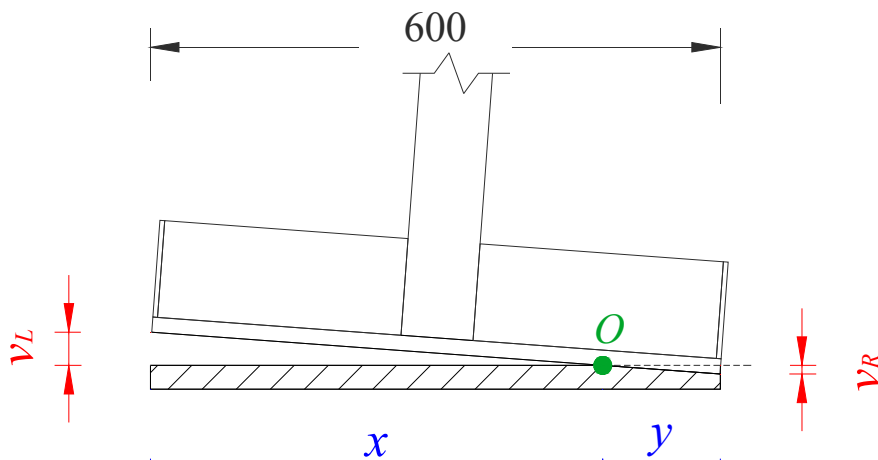
**5.2.2 FREE ROCKING DECAYS (FRD) – SOFT RUBBER PAD**

The displacement time-history of the snap back test on the specimen situated over a soft rubber pad is presented in Figure 5-10. As shown, the vibration decayed much more rapidly than the corresponding experiment with the solid steel feet.

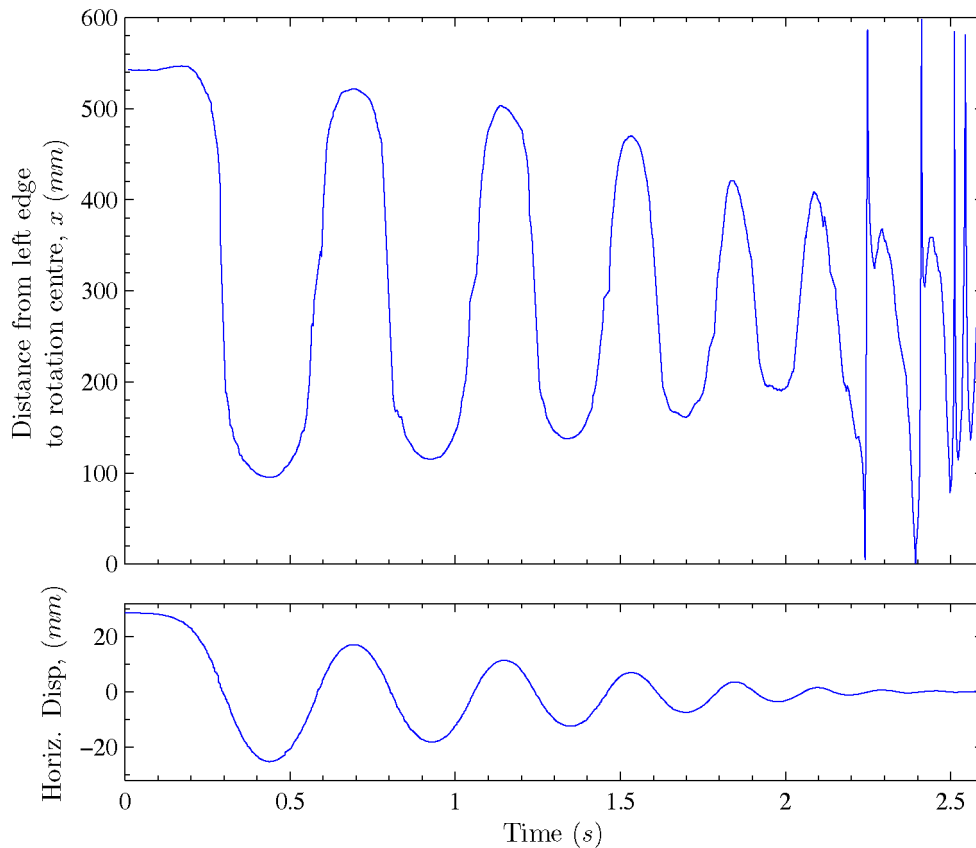
The data highlighted the ability of the specimen to compress into the soft rubber layer below the at-rest position. This feature is observed as “negative uplifts” in Figure 5-10. An implicit result of the negative uplifts is that the rocking pivot is no longer fixed at the edge of the base plate.



**Figure 5-10 – Displacement time-history of run 2, FRD – soft rubber pad**



**Figure 5-11 – Relationship between uplifts and centre of rotation**



**Figure 5-12 – Location of rotation centre versus time (run 2, FRD – rubber pad)**

The location of the rotation centre can be approximated using the uplift readings assuming a linear rotation profile as shown in Figure 5-11. Figure 5-12 presents the location of the rotation centre for the duration of the free vibration decay. This figure shows the rotation centre migrated smoothly from one edge of the base plate to the other as the specimen rocked from side to side.

The analysis also detected a relationship between the location of the rotation centre and the horizontal displacement during the free vibration decay. Figure 5-13 presents the location of the rotation centre as the wall displaces. The rotation centre locations during the times when the block is rotating clockwise are plotted separately from when the block is rotating counter-clockwise. It appears the relationship is sensitive to the direction of motion and can be approximated by Equation 5-5.

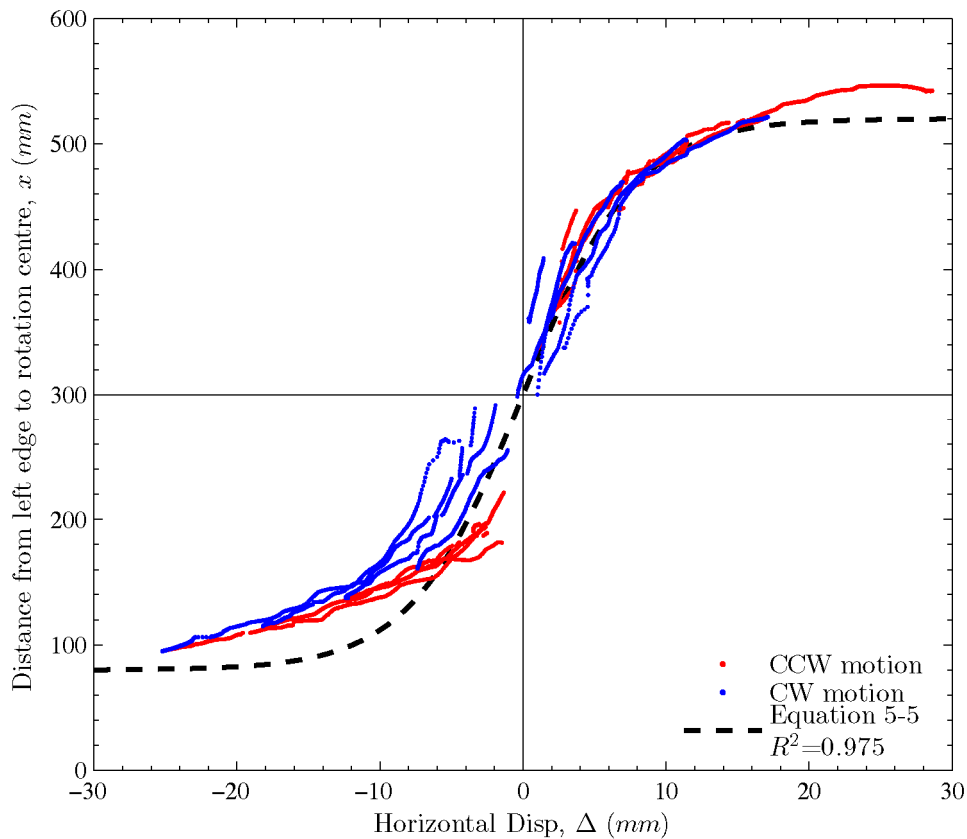
$$x = 220.1 \times \tanh(0.1276\Delta) + 300 \quad (5-5)$$

Next, as the rotation centre shifts during the free vibration, the rotation of the specimen becomes a function of the horizontal displacement and the location of the

rotation centre. An accurate rotation of the specimen can be evaluated following Equation 5-6, although the modification was found to be relatively insignificant.

$$\theta = \begin{cases} \alpha'(x, y) - \sin^{-1}\left(\frac{B'(x, y) - \Delta}{R'(x, y)}\right) & \text{for } \Delta > 0, \\ \sin^{-1}\left(\frac{B'(x, y) + \Delta}{R'(x, y)}\right) - \alpha'(x, y) & \text{for } \Delta < 0. \end{cases} \quad (5-6)$$

where  $B'(x, y) = 300 - \min(x, y)$ ,  $H = 1056$  mm and  $\alpha'(x, y) = \tan^{-1}\left(\frac{B'(x, y)}{H'}\right)$

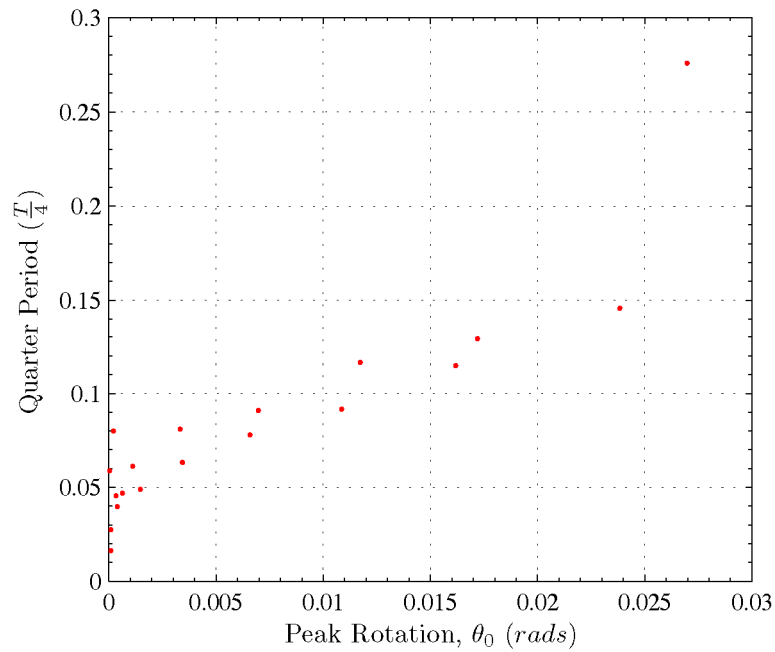


**Figure 5-13 – Location of rotation centre versus horizontal displacement**

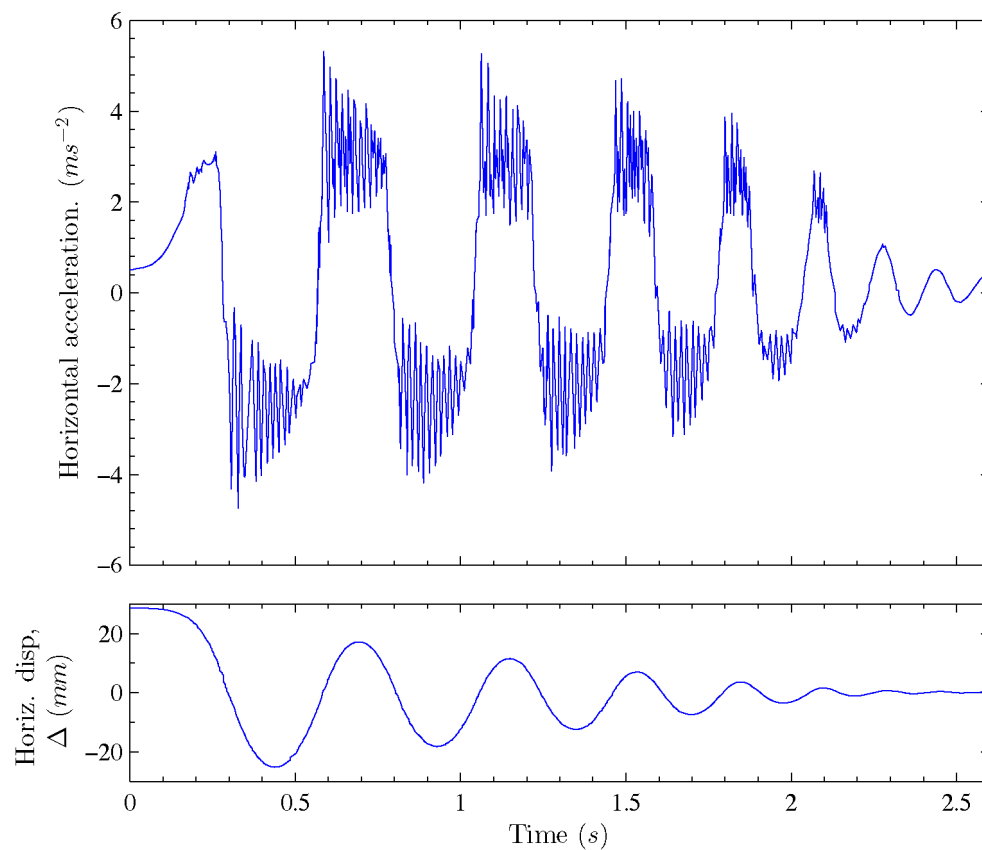
The quarter periods of the free vibration decay were evaluated and are plotted against the rotation in Figure 5-14. The plot highlights a similar nonlinear increase in the quarter period to the specimen with solid feet as rotation is increased.

Another noteworthy data set available from this experiment is the lateral accelerations measured at the additional steel masses during the free vibration decay. The acceleration time-history is plotted in Figure 5-15 and it exposes the activation of an elastic mode which is masked by the rocking motion in the displacement plots. A

power spectrum analysis on the accelerations shows the elastic mode had a frequency of approximately 56 Hz. This is much higher than the expected natural frequency of the flexural response and suggests the motion was a higher mode response.



**Figure 5-14 – Quarter periods versus rotation peak (run 2, FRD – rubber pad)**



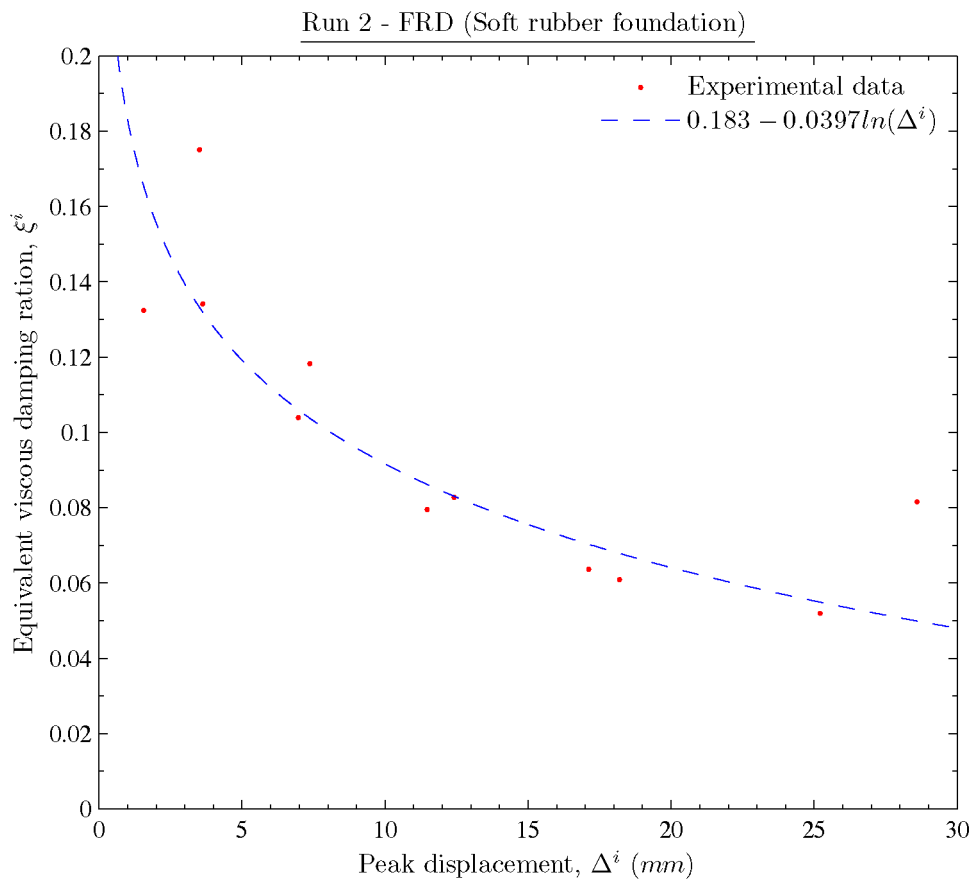
**Figure 5-15 – Horizontal accelerations versus time (run 2, FRD – rubber pad)**

Finally, as the model on the rubber foundation did not have distinctive impacts but rather rolled from one side to the other, it was decided that the coefficient of restitution will not be used to characterise the energy dissipation. Instead an equivalent viscous damping ratio for each cycle,  $\xi^i$ , was estimated using the logarithmic decay formula for a SDOF system, Equation 5-7. These are plotted against the peak rotations of their corresponding cycle in Figure 5-16, and it shows that energy dissipation, as represented by  $\xi^i$ , increased as the motion decayed. The average viscous damping ratio over the entire record was 0.104.

$$\xi^i = \frac{1}{2\pi} \ln\left(\frac{\Delta^i}{\Delta^{i+1}}\right) \quad (5-7)$$

Where

$\Delta^i$  = Peak horizontal displacement for the  $i$ -th cycle



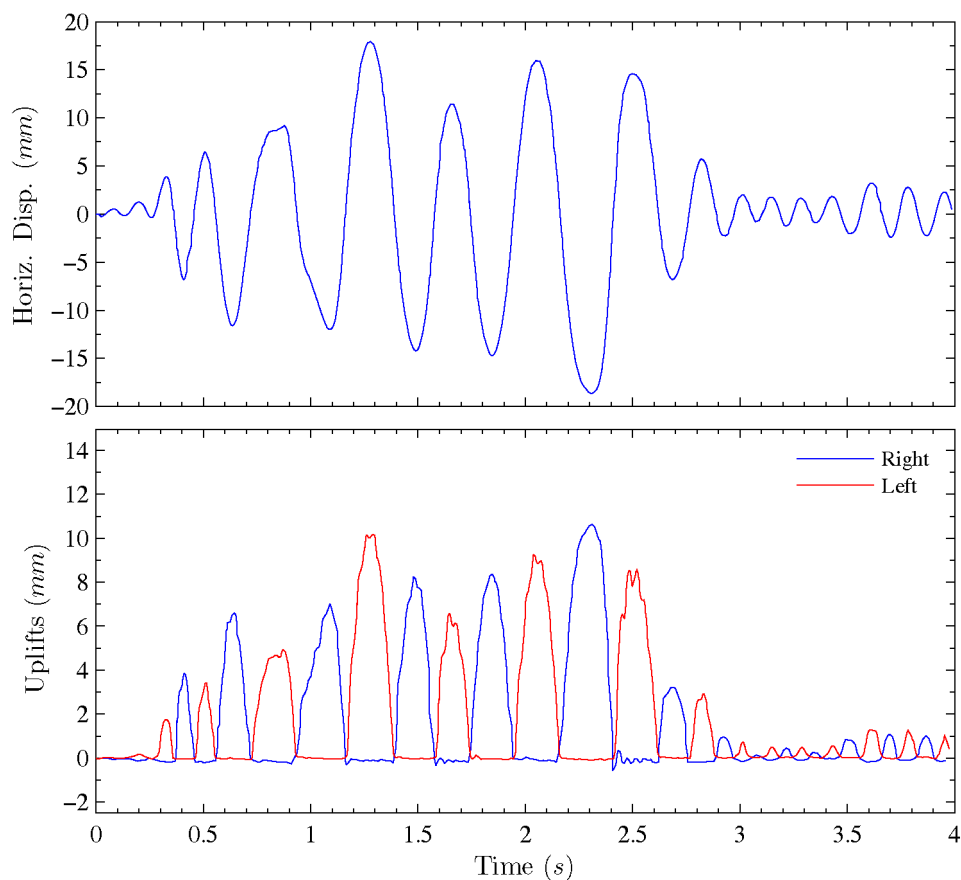
**Figure 5-16 – Equivalent viscous damping ratio versus peak displacement**

### 5.2.3 SHAKE TABLE TESTS

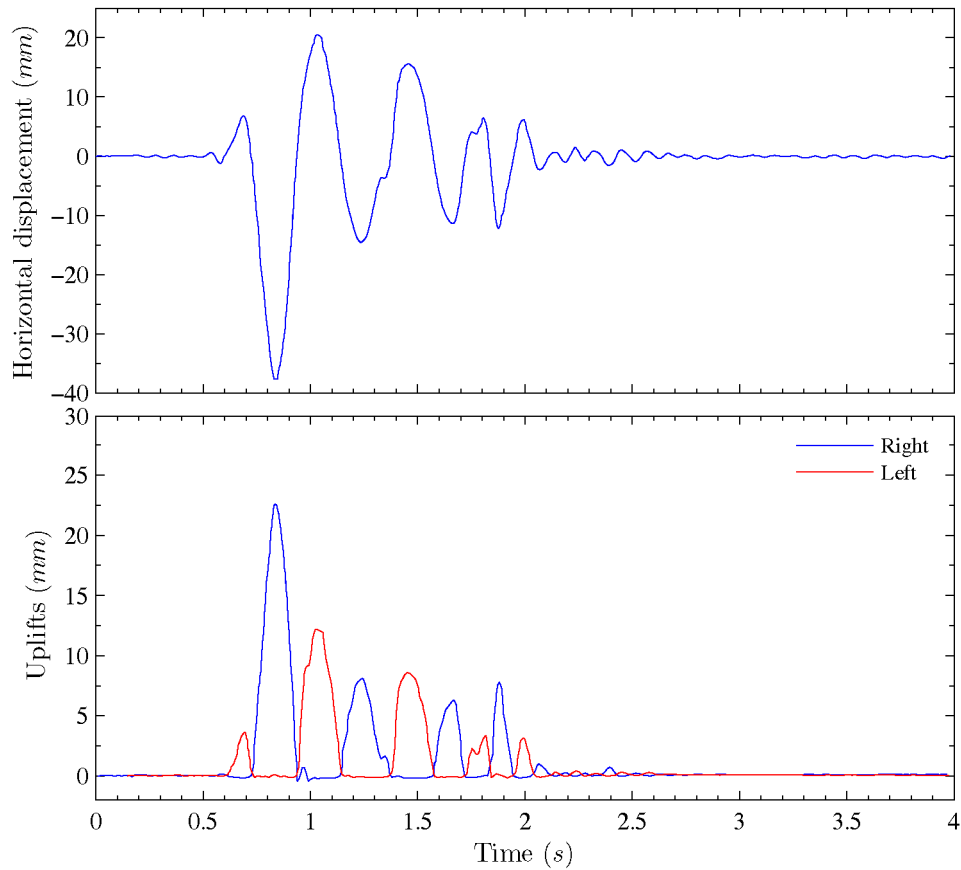
Two shake table tests from the McManus report are examined here. One of the tests was conducted with the column specimen resting on solid steel feet and the other was with the specimen resting on a soft rubber foundation.

The base excitation records for the tests are described in Table 5-1 and they consisted of scaled acceleration histories from past earthquake events. The time scales in the records were reduced to 1/5 of the original scale. This was done to ensure the shake table test results would emulate qualitatively the seismic response of an actual size prototype bridge pier. For this project, no attempts were made to scale up the shake table test results to infer the behaviour of a larger structure during a particular earthquake event. Instead, the shake table test results are interpreted as the actual response of a simple steel column model, with the exact properties as built, subjected to a new acceleration record as provided by the shake table.

Figure 5-17 presents the displacement time-history of the specimen for test run 3. The overall motion of the specimen was stable and rocking was clearly initiated.



**Figure 5-17 – Displacement time-history of test run 3 (El Centro NS – Solid feet)**



**Figure 5-18 – Displacement time-history of test run 4 (Pacoima Dam N76°W – rubber pad)**

The displacement time-history of test run 4 is presented in Figure 5-18. In this test, the column specimen rested on a soft rubber pad and was subjected to scaled motions from Pacoima Dam during the 1971 San Fernando Earthquake. The base excitation record in this case had a number of unusually large and sharp acceleration pulses within the first 2 seconds, which was followed by a series of very small accelerations in the next 5 seconds.

Examining Figure 5-18 closely, it shows the specimen response was again stable and smooth. Rocking was clearly detected as shown by the characteristic alternate edge uplifts. It is intriguing however that the specimen did not compress into the soft rubber layer as it did in the free vibration decay with the soft rubber foundation. It appears the specimen in this test had rocked about approximately stationary pivots at the edges of the base plate, just as the tests conducted with the steel feet.

This may be explained by the fact that rubber is a highly viscous material which becomes stiffer with an increased rate of loading. As a result, when the specimen was subjected to rapid impulsive loads, such as that resulting from earthquake type acceleration, the “soft” rubber layer became stiff and incompressible, leading to the model rocking about the edge of the base plate.

It would have been desirable to have another shake table test result to confirm whether this always occurs or if this behaviour is characteristic of a pulse type earthquake. Unfortunately, this was the only time-history trace available from the McManus report.

### **5.3 THEORETICAL MODELS OF ROCKING STRUCTURAL SYSTEMS**

In this section, a number of mathematical models are presented for a range of simple idealised rocking structures. The mathematical models were developed from first principles with the intention that they will be used to predict the time-history response of rocking structures subjected to base excitations. The three rocking models investigated in this study are,

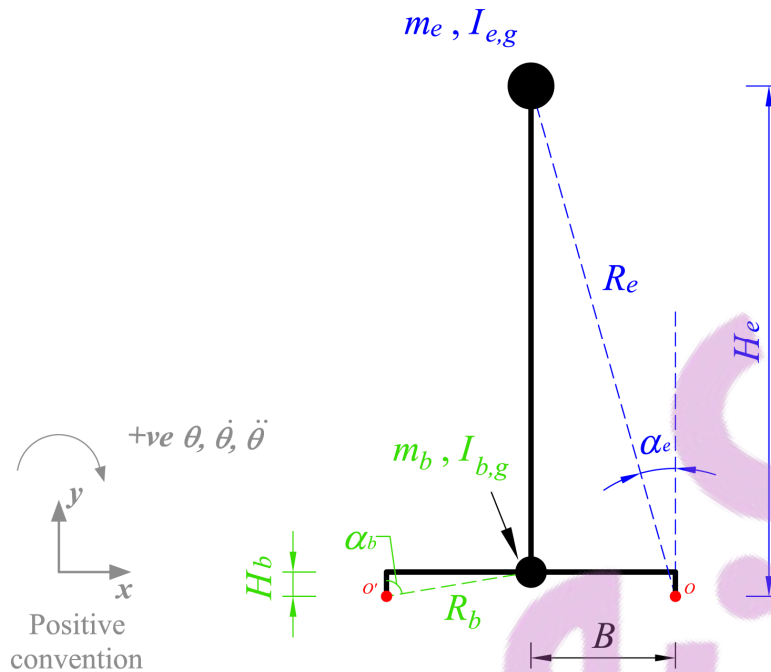
- A. A rigid lumped-mass structure rocking about fixed pivots on a rigid foundation
- B. A rigid lumped-mass rocking structure resting on two compression-only springs
- C. A flexible 2 DOF structure rocking about fixed pivots on a rigid foundation

Each of the mathematical models will be compared against the relevant experimental data set presented earlier in Section 5.2.

#### **5.3.1 RIGID LUMPED-MASS STRUCTURE ROCKING ABOUT FIXED PIVOTS ON A RIGID FOUNDATION**

One of the simplest idealisation of a structural system is a lumped mass model. The model to be discussed in this section has a lumped mass at the superstructure’s centre of gravity and a lumped mass at the centre of gravity of the base structure. The structure is also assumed to be completely rigid. An illustration of the model is as shown in Figure 5-19. It is assumed that the model rests on rigid ground at two fixed points and the model is restricted from sliding. This model also assumes that the sole

source of energy dissipation is through the impacts. The impacts are assumed to be plastic and no bouncing is permitted.



**Figure 5-19 – Idealised rigid lumped-mass structure rocking about fixed pivots**

The governing differential equation of motion for the system can be derived by considering dynamic moment equilibrium about the rocking pivots. The derivations are as follows.

To begin, the moment of inertia of the system about the pivot,  $O$  or  $O'$ , can be calculated following Equation 5-8.

$$I_O = I_{O'} = (I_{e,g} + m_e R_e^2) + (I_{b,g} + m_b R_b^2) \quad (5-8)$$

Now consider the model at a positive angular displacement  $\theta$ , experiencing a positive ground acceleration  $\ddot{u}_g$ . The active forces are as shown in the free body diagram in Figure 5-20b.

By D'Alembert's principle, the system is in a static equilibrium. A summation of the moments about pivot  $O$  ( $\sum M_O - I_O \ddot{\theta} = 0$ ) yields, the governing differential equation (GDE) of motion for the system when  $\theta$  is greater than zero;

$$\ddot{\theta} = \frac{-M_e R_e g}{I_o} \left[ \frac{\ddot{u}_g}{g} \cos(\alpha_e - \theta) + \sin(\alpha_e - \theta) \right] - \frac{M_b R_b g}{I_o} \left[ \frac{\ddot{u}_g}{g} \cos(\alpha_b - \theta) + \sin(\alpha_b - \theta) \right] \quad (5-9)$$

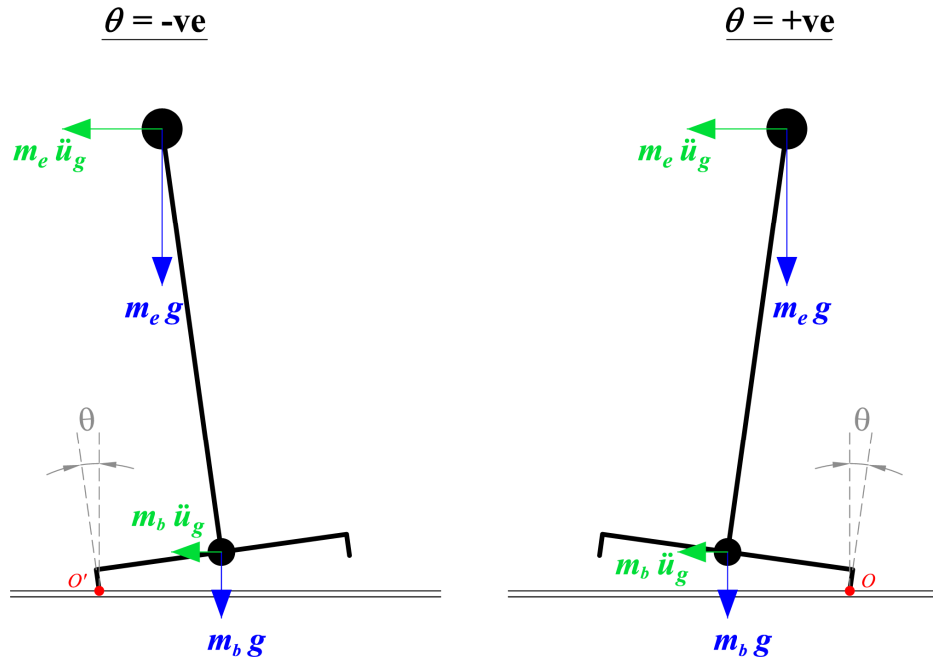


Figure 5-20 – Free body diagram of the rocking rigid lumped-mass structure

Similarly, consider the case when the structure is at a negative angular displacement, a summation of moments about  $O'$  yields the GDE of motion for the system when  $\theta$  is less than zero;

$$\ddot{\theta} = \frac{-M_e R_e g}{I_{o'}} \left[ \frac{\ddot{u}_g}{g} \cos(\alpha_e + \theta) - \sin(\alpha_e + \theta) \right] - \frac{M_b R_b g}{I_{o'}} \left[ \frac{\ddot{u}_g}{g} \cos(\alpha_b + \theta) - \sin(\alpha_b + \theta) \right] \quad (5-10)$$

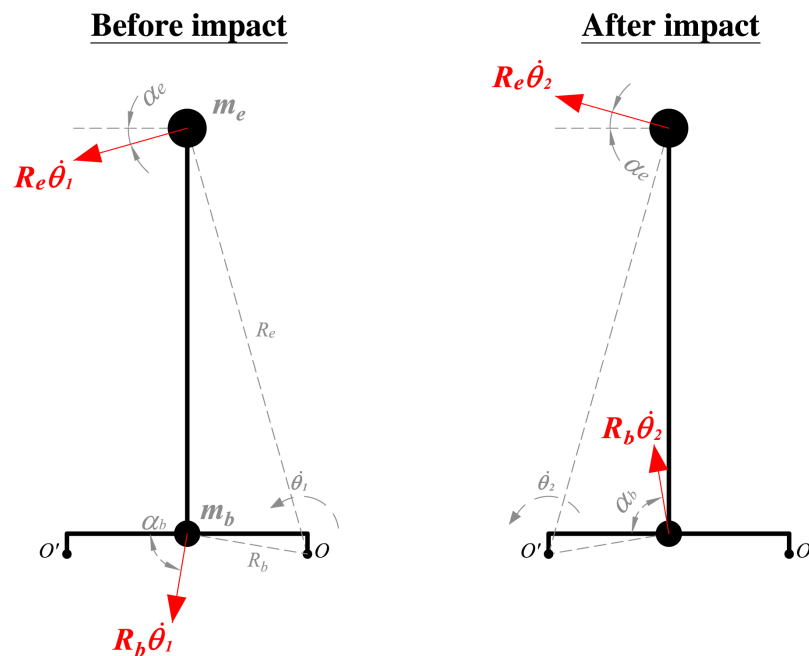
Combining Equations 5-9 and 5-10 leads to the complete equation of motion for a rocking rigid lumped-mass structure with fixed pivot as below.

$$\ddot{\theta} = \frac{-M_e R_e g}{I_o} \left[ \frac{\ddot{u}_g}{g} \cos(\alpha_e + \text{sgn}(\theta) \cdot \theta) + \text{sgn}(\theta) \sin(\alpha_e + \text{sgn}(\theta) \cdot \theta) \right] - \frac{M_b R_b g}{I_o} \left[ \frac{\ddot{u}_g}{g} \cos(\alpha_b + \text{sgn}(\theta) \cdot \theta) + \text{sgn}(\theta) \sin(\alpha_b + \text{sgn}(\theta) \cdot \theta) \right] \quad (5-11)$$

Next, the energy dissipation of the system from impacts can be estimated by adopting the same assumptions as Housner for the simple rocking block. The assumptions are i) the impacts are inelastic, in other words, bouncing does not occur and the system continues to rotate smoothly as it switches from rocking about  $O$  to  $O'$  and vice versa; and ii) the impact force acts through the new rocking pivot.

Consequently, the impact force does not apply any additional torque to the system during the infinitesimal duration of an impact, and leads to a conservation of momentum about the impending point of impact.

For illustration, consider the system rocking from  $O$  to  $O'$ . The motion of the system is as shown on a velocity diagram in Figure 5-21.



**Figure 5-21 – Velocity diagram of the lumped-mass model before and after impact**

Applying König's theorem to angular momentum, the total angular momentum ( $L$ ) of the system about the impending point of impact  $O'$  is the sum of the orbital and spin components of angular momentum about  $O'$  for the two lumped masses. The orbital angular momentum of a body about any axis  $Z$  parallel to its centroidal axis, is the angular momentum of a particle moving coincidentally with the body's mass centre about  $Z$ , and the spin angular momentum is the angular momentum of the body about its centroidal axis.



Accordingly, the angular momentum of the rocking system about O' immediately before and after a counter-clockwise impact is described in Equations 5-12 and 5-13.

$$\begin{aligned}
 L_{O',\text{before}} &= (L_{\text{orbital},e} + L_{\text{spin},e}) + (L_{\text{orbital},b} + L_{\text{spin},b}) \\
 L_{O',\text{before}} &= m_e R_e \dot{\theta}_1 \cos \alpha_e \times H_e - m_e R_e \dot{\theta}_1 \sin \alpha_e \times B + I_{e,g} \dot{\theta}_1 \\
 &\quad + m_b R_b \dot{\theta}_1 \cos \alpha_b \times H_b - m_b R_b \dot{\theta}_1 \sin \alpha_b \times B + I_{b,g} \dot{\theta}_1 \\
 L_{O',\text{before}} &= \left\{ \left[ m_e (H_e^2 - B^2) + I_{e,g} \right] + \left[ m_b (H_b^2 - B^2) + I_{b,g} \right] \right\} \dot{\theta}_1 \quad (5-12)
 \end{aligned}$$

Similarly,

$$\begin{aligned}
 L_{O',\text{after}} &= (L_{\text{orbital},e} + L_{\text{spin},e}) + (L_{\text{orbital},b} + L_{\text{spin},b}) \\
 L_{O',\text{after}} &= m_e R_e \dot{\theta}_2 \cos \alpha_e \times H_e + m_e R_e \dot{\theta}_2 \sin \alpha_e \times B + I_{e,g} \dot{\theta}_2 \\
 &\quad + m_b R_b \dot{\theta}_2 \cos \alpha_b \times H_b + m_b R_b \dot{\theta}_2 \sin \alpha_b \times B + I_{b,g} \dot{\theta}_2 \\
 L_{O',\text{after}} &= \left\{ \left[ m_e (H_e^2 + B^2) + I_{e,g} \right] + \left[ m_b (H_b^2 + B^2) + I_{b,g} \right] \right\} \dot{\theta}_2 \\
 &= (I_{e,O'} + I_{b,O'}) \dot{\theta}_2 \quad (5-13)
 \end{aligned}$$

Now equating the angular momentum from before and after an impact,

$$\frac{\dot{\theta}_2}{\dot{\theta}_1} = \frac{\left[ m_e (H_e^2 - B^2) + I_{e,g} \right] + \left[ m_b (H_b^2 - B^2) + I_{b,g} \right]}{\left[ m_e (H_e^2 + B^2) + I_{e,g} \right] + \left[ m_b (H_b^2 + B^2) + I_{b,g} \right]}$$

Substitute: 
$$r = \left( \frac{\dot{\theta}_2}{\dot{\theta}_1} \right)^2$$

$$r = \left( \frac{\left[ m_e (H_e^2 - B^2) + I_{e,g} \right] + \left[ m_b (H_b^2 - B^2) + I_{b,g} \right]}{\left[ m_e (H_e^2 + B^2) + I_{e,g} \right] + \left[ m_b (H_b^2 + B^2) + I_{b,g} \right]} \right)^2 \quad (5-14)$$

Equation 5-14 represents a theoretical estimate of the reduction of kinetic energy due to an inelastic impact for the rocking structural system, expressed as a coefficient of restitution. Substituting the properties of the experimental test rig presented earlier in Figure 5-8 yields a theoretical  $r$  value of 0.74 for the specimen which is approximately 12% below the average  $r$  value from the free rocking decay of the test specimen with solid steel feet.

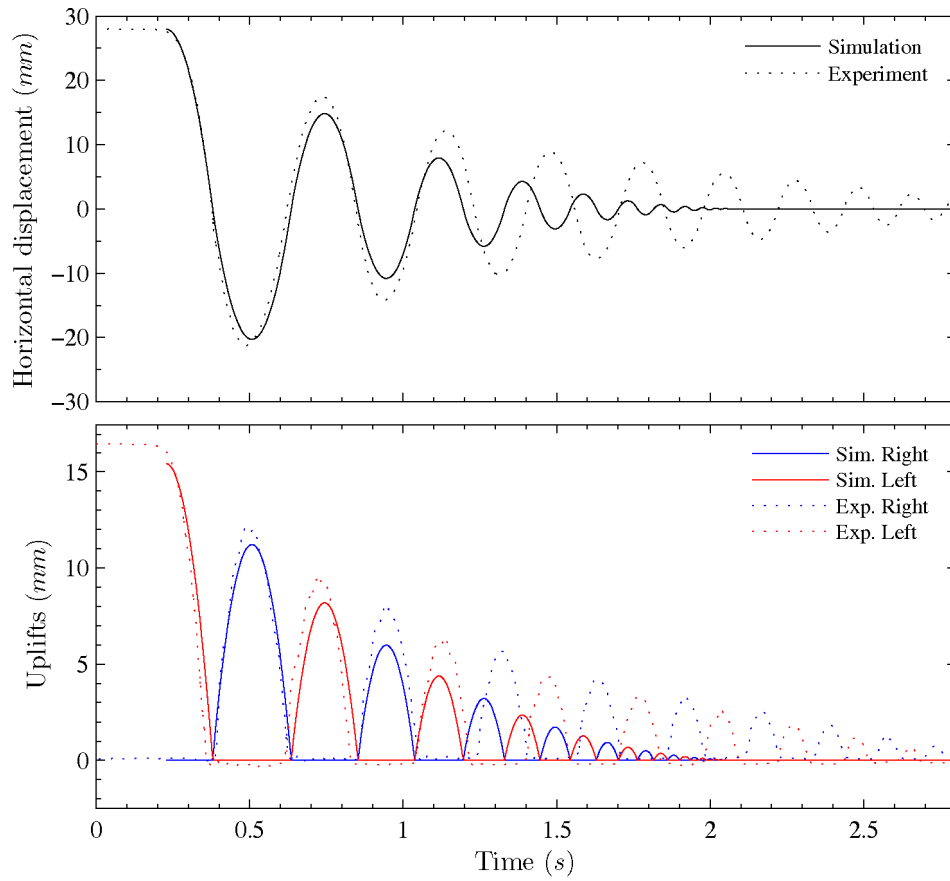
### 5.3.1.1 Validating the analytical model

Having established the two key components of the analytical model, namely the GDE described by Equation 5-11 and the energy dissipation characteristics described by Equation 5-14, these are implemented into a numerical time integration scheme to predict the response of a rocking system subjected to base excitation.

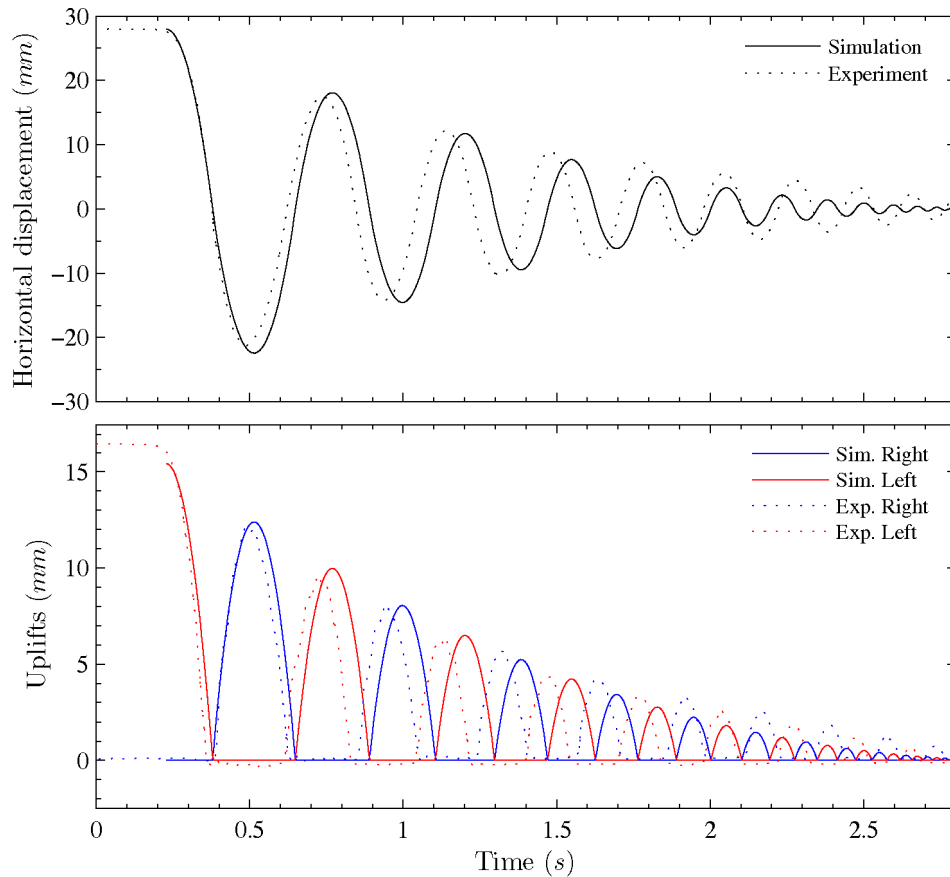
To examine the validity of the analytical model, an attempt is first made to simulate the free rocking decay of the McManus test specimen with solid steel feet, as per the experiment described in Section 5.2.1. The analytical model is first set to decay freely from the same initial rotation as the experiment. Then, on every occasion when the angular displacement is zero, or in other words whenever an impact is detected, the angular velocity is reduced to  $r_{theory}$  (0.74) times the angular velocity before the impact.

Figure 5-22 presents the simulated displacement time-history alongside the experimental results. As can be seen, the simulation was very successful with the analytical model predicting the first quarter cycle of the motion very accurately. This confirms the derived GDE is valid for simulating the smooth rocking phases of the motion. The deterioration of simulation results as the simulation progressed is clearly due to errors in estimating the true coefficient of restitution. This is not surprising as it was shown earlier that the experimental coefficient of restitution varied considerably.

The simulation was repeated with an  $r$  value matching the average  $r$  value from the experiment. This improved the overall matching of the results and the resulting displacement time-history is presented in Figure 5-23.



**Figure 5-22 – Simulated versus actual displacement time-history of run 1 ( $r_{sim}=0.74$ )**

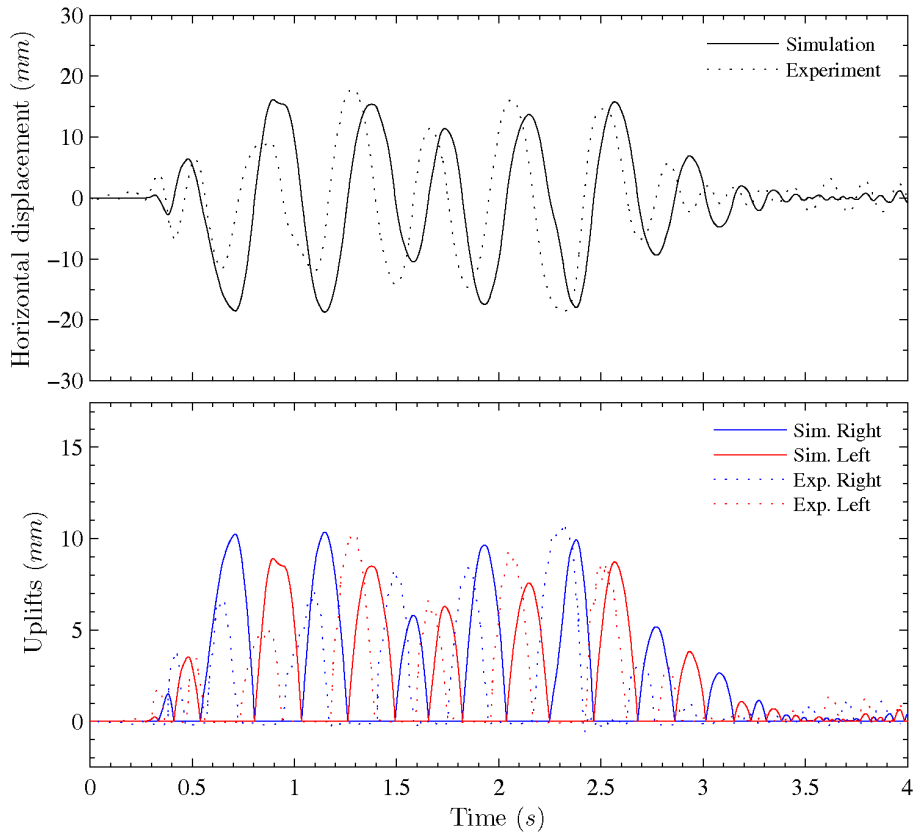


**Figure 5-23 – Simulated versus actual displacement time-history of run 1 ( $r_{sim}=0.81$ )**

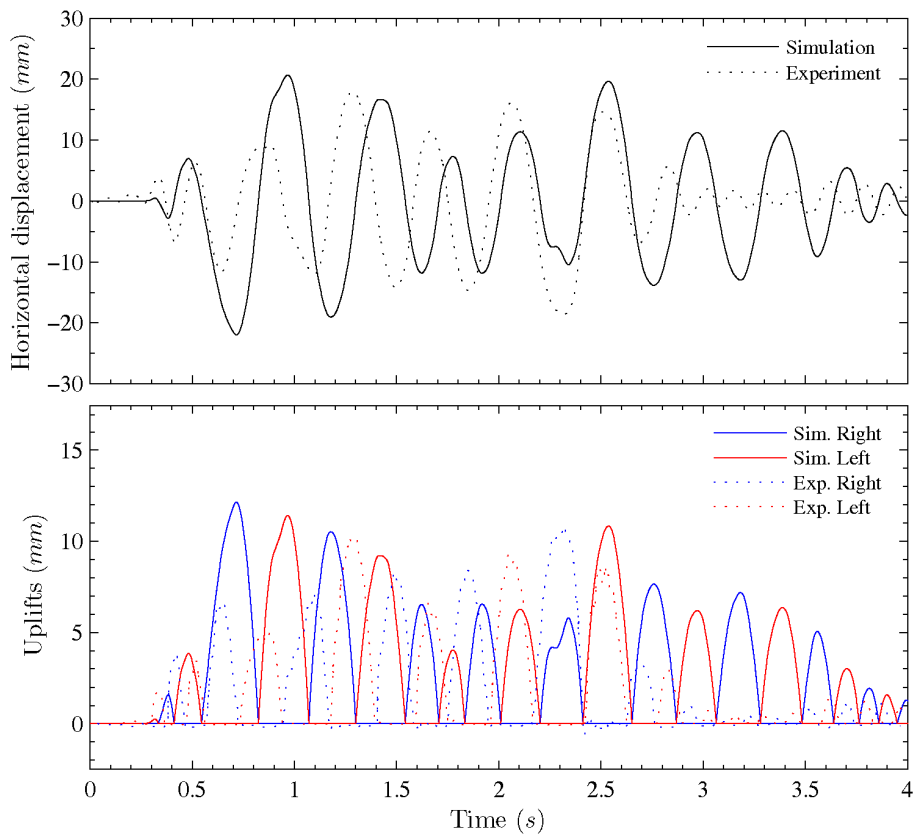
Following the successful simulation of the free rocking decay, another simulation was conducted to assess whether the analytical model could predict the rocking response due to base excitations. The best available experimental data set for this is test run 3, where the column specimen on steel feet was subjected to base excitations from the shake table.

Unfortunately, as the actual acceleration time-history reproduced on the shake table was not available, the input acceleration for the simulation was taken as the original El Centro NS record with the time ordinates scaled to 1/5 and the accelerations scaled by a constant factor such that the peak acceleration equalled 0.8 g.

The decision to scale the peak acceleration to 0.8 g was based on the fact that a similar shake table test on a steel feet specimen using the table motion had recorded a peak acceleration of 0.8 g. This was the best available information on the exact shake table motion.



**Figure 5-24 – Simulated versus actual displacement time-history of run 3 ( $r_{sim}=0.74$ )**



**Figure 5-25 – Simulated versus actual displacement time-history of run 3 ( $r_{sim}=0.81$ )**

The initial simulation adopted a theoretical  $r$  value of 0.74. The ensuing displacement time-history prediction is presented alongside the experimental result in Figure 5-24. As shown, the prediction resembled the experimental results remarkably well, despite the uncertainty in the input acceleration record and the exact energy dissipation.

The simulation was repeated with the best fit  $r$  value from the free rocking decay and the ensuing displacement time-history is presented in Figure 5-25. This simulation was less successful. However, it would be impossible to distinguish whether this was the fault of poor input acceleration data or an error in estimating the energy dissipation of the system.

### **5.3.2 RIGID LUMPED-MASS ROCKING STRUCTURE RESTING ON TWO COMPRESSION-ONLY SPRINGS**

The next idealisation of a rocking structural system is a rigid lumped-mass structure resting on two compression-only springs. The two springs are fixed at the edge of the foundation and an illustration of this model is provided in Figure 5-26.

This model, herein referred to as the two-spring model, is an improvement over the previous idealisation as it incorporates the elasticity of the supporting ground into the rocking problem. This permits a gradual transfer of support forces from one support to the other prior to the initiation of uplift. This in effect assumes the rigid structure rotates about its centreline until complete liftoff occurs in one of the compression-only springs. After liftoff occurs, the structure rotates about the spring which is still in contact.

While it would be relatively simple to analyse a specific problem adopting the two-spring model using finite element techniques, for this section we will examine the behaviour of the rocking system using only basic mechanics and establishing a simplified nonlinear SDOF system. This would provide a framework which can be used to study the behaviour of rocking systems generally, rather than on a case by case basis using finite element techniques.

The assumptions of the two-spring model are similar to the previous model. The model is restricted from sliding at the point of contact with the ground. The sole source of energy dissipation is through impacts. The impacts are assumed to be plastic and no bouncing is permitted.

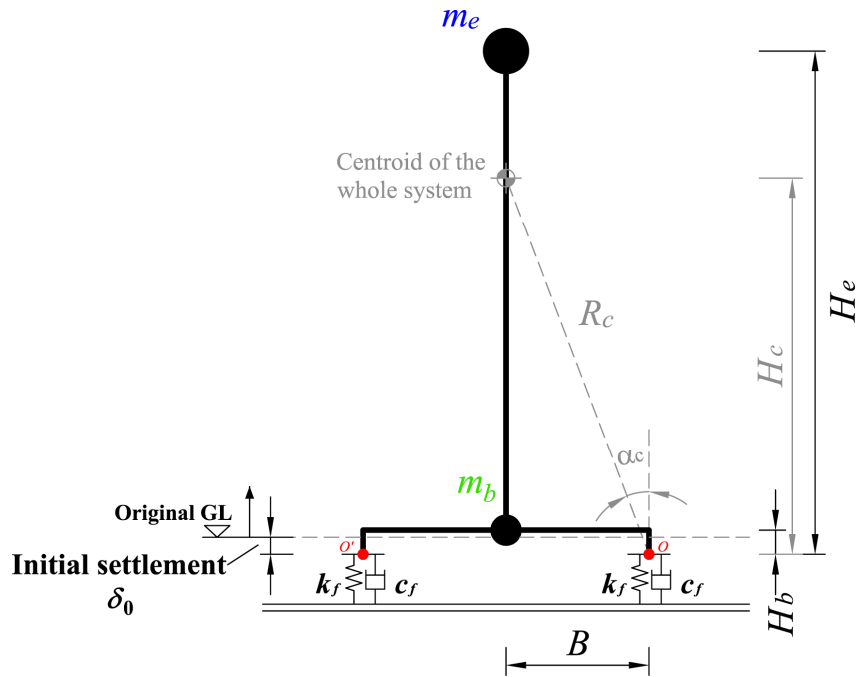


Figure 5-26 – Rigid lumped-mass rocking structure on two compression only springs

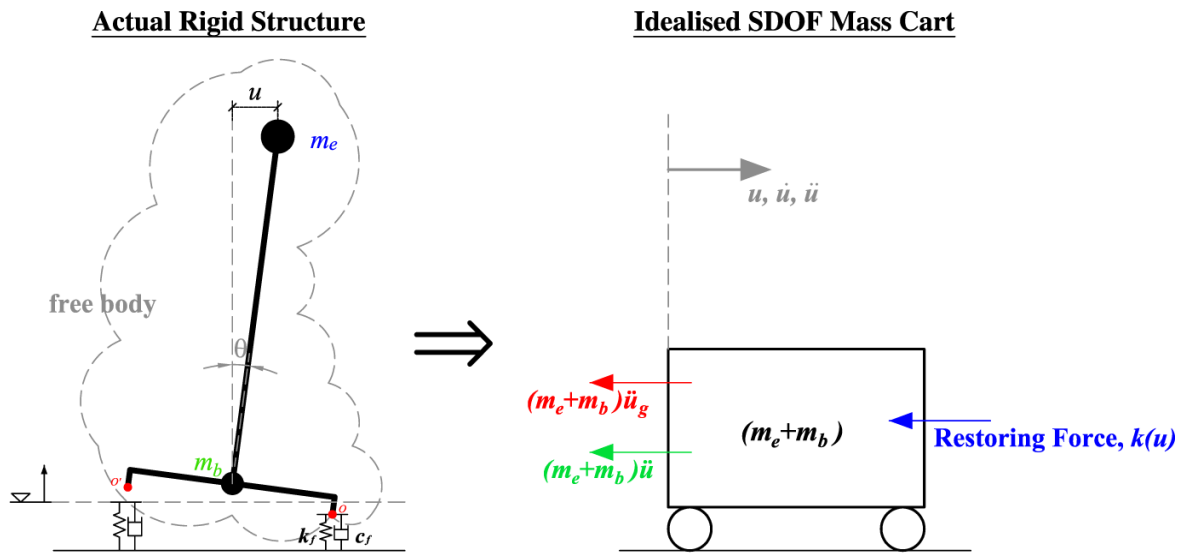


Figure 5-27 – The idealised SDOF mass cart

Taking advantage of the rigid body assumption, the rocking system is simplified as a SDOF system with the displacement of the top mass ( $u$ ) as the only active degree of freedom. An analogy is considering the rocking system as a SDOF mass cart as shown in Figure 5-27.

Applying D'Alembert's principle, the equivalent system is in static equilibrium. A summation of forces in the direction of  $u$  gives rise to the GDE of motion in Equation 5-15.

$$(m_e + m_b)\ddot{u} + k(u) = P(t) \quad (5-15)$$

Where

- $k(u)$  = Restoring force-displacement characteristics of the rocking system  
 $P(t)$  = Driving force of the system, equals  $-(m_e + m_b)\ddot{u}_g$  when the forcing is a result of ground acceleration  $\ddot{u}_g$ .

It is noteworthy that the inertial term of the system is taken as  $(m_e + m_b)$  even when the two lumped masses appear to experience different accelerations. This is justified as the system is simplified as an effective free body, and the rigid body geometric nonlinearity is represented in the nonlinear restoring force-displacement relationship. The role of the inertial term is to ensure it gives rise to a correct base shear under unit acceleration.

Next, to obtain an expression for the equivalent restoring force-displacement relationship of the rocking system  $k(u)$ , imagine a varying pseudo-static lateral force applied at the top lumped mass of the actual rigid structure. If the lateral force is applied slowly enough, it will not generate any dynamic effects. Consequently the inertial term in Equation 5-15 is deactivated and the restoring force  $k(u)$  is the pseudo-static lateral force required to satisfy equilibrium. Typically, the pseudo-static lateral force would be increasing, however it may also decrease so long as  $u$  is increased smoothly. This is analogous to a displacement controlled pushover analysis.

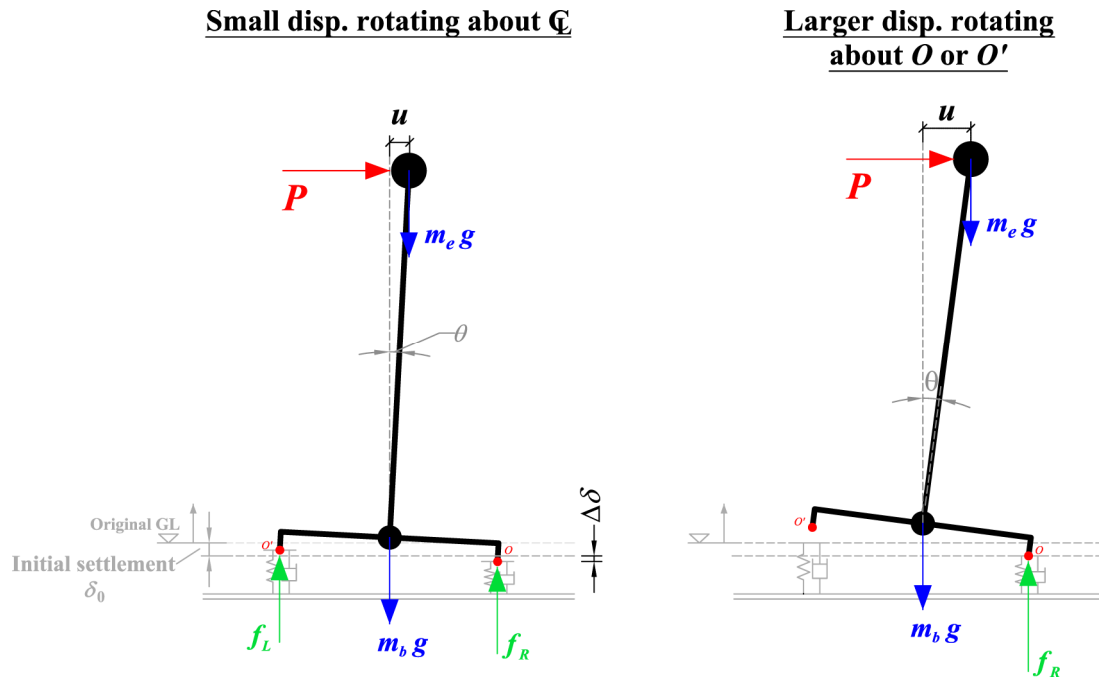
Prior to the lateral load ( $P$ ) being applied, the initial settlement of the rocking system on the two springs can be evaluated by Equation 5-16.

$$\delta_0 = \frac{W}{2k_f} \quad (5-16)$$

where

$$W = (m_e + m_b)g \quad (5-17)$$

If a small lateral load is applied, the rigid structure rotates by an angle  $\theta$  and both ground springs remain in contact. The rigid structure rotates about its centreline and the support force is transferred from one spring to the other as illustrated in the force diagram in Figure 5-28a.



**Figure 5-28 – Force diagrams of the rocking structure subjected to increasing displacement**

During this time, the horizontal displacement is related to the rotation by Equation 5-18, and the change in spring length is approximated by Equation 5-19.

$$u = H_e \sin(\theta) \quad (5-18)$$

$$\Delta\delta \approx B \times \theta \quad (5-19)$$

Accordingly, the spring forces at the two supports in the scenario depicted in Figure 5-28a are expressed as Equations 5-20 and 5-21.

$$f_L = \frac{W}{2} - k_f B \theta \quad (5-20)$$

$$f_R = \frac{W}{2} + k_f B \theta \quad (5-21)$$

The transfer of support force continues as the lateral load is increased. This continues until the support force on the left spring reaches zero, when liftoff occurs. The rotation at which liftoff occurs, herein known as the critical rotation  $\theta_{crit}$ , can be estimated by substituting  $f_L$  equal to zero in Equation 5-20. An estimate of critical rotation and the horizontal displacement associated with the critical rotation can be achieved by evaluating Equations 5-22 and 5-23.

$$\theta_{crit} = \frac{W}{2k_f B} \quad (5-22)$$

Assuming  $\theta_{crit}$  is small:

$$u_{crit} = \frac{WH_e}{2k_f B} \quad (5-23)$$

The lateral force to cause a particular rotation when both springs are in contact can be evaluated by considering moment equilibrium about the rotation centre. This yields,

$$\Sigma M_{rot. cen} = 0$$

$$PH_e \cos \theta + m_e g H_e \sin \theta + m_b g H_b \sin \theta + f_L B = f_R B$$

Assuming  $\theta_{crit}$  is small  $\rightarrow \cos \theta = 1$  and  $\sin \theta = \theta$ ,

$$PH_e + m_e g H_e \theta + m_b g H_b \theta + \left( \frac{W}{2} - k_f B \theta \right) B = \left( \frac{W}{2} + k_f B \theta \right) B$$

$$P = \left[ \frac{2k_f B^2}{H_e} - g \left( m_e + m_b \frac{H_b}{H_e} \right) \right] \theta \quad (5-24)$$

or

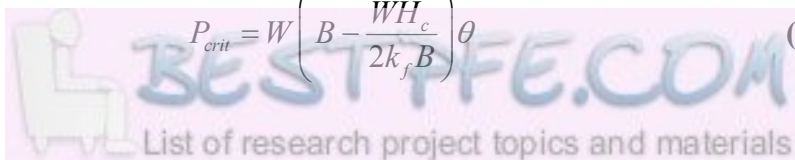
$$P = \left[ \frac{2k_f B^2 - m_e g H_e - m_b g H_b}{H_e^2} \right] u \quad (5-25)$$

Equation 5-25 illustrates that the lateral restoring force increases linearly with increasing horizontal displacement when both springs are in contact. Furthermore the lateral force causing liftoff can be found by substituting  $\theta_{crit}$  into Equation 5-24.

$$P_{crit} = \left[ \frac{WB}{H_e} - g \left( m_e + m_b \frac{H_b}{H_e} \right) \frac{W}{2k_f B} \right] \quad (5-26)$$

It can be shown that Equations 5-24 through 5-26 can be simplified by treating the two-mass system as a single lumped mass at the system centroid. This results in the following simplified formulae,

$$P = \left[ \frac{2k_f B^2 - WH_c}{H_e^2} \right] u \quad (5-27)$$

$$P_{crit} = W \left( B - \frac{WH_c}{2k_f B} \right) \theta \quad (5-28)$$


$$P_{crit} = \frac{W}{H_e} \left( B - \frac{WH_c}{2k_f B} \right) u \quad (5-29)$$

where

$$H_c = \frac{m_e H_e + m_b H_b}{m_e + m_b}, \quad \alpha_c = \frac{B}{H_c} \quad \& \quad R_c = \sqrt{B^2 + H_c^2} \quad (5-30)$$

Now considering the case after liftoff has occurred, the rotation centre shifts to the compression spring that is in contact with the structure. From this point onwards, geometric nonlinearity becomes important and there is no further change in spring forces because of vertical equilibrium.

Adopting the representation of the system with a single lumped mass at the centroid, the restoring force of the rocking system can be evaluated by considering moment equilibrium about the rocking pivot. This leads to Equation 5-31 which prescribes the restoring force of the system as a function of the rotation.

Assuming a positive  $\theta$ ,

$$\Sigma M_o = 0$$

$$PR_e \cos(\alpha_e - \theta) = WR_c \sin(\alpha_c - \theta)$$

$$P = W \frac{R_c \sin(\alpha_c - \theta)}{R_e \cos(\alpha_e - \theta)} \quad (5-31)$$

A closer examination of Equation 5-31 reveals the trigonometric term in the equation is effectively linear in  $\theta$  for a slender structure. This is convenient as there are two readily available fixed points on this curve which can be used to fit a linear approximation. The two points are i) the instant when uplift is initiated, and ii) the instant when the centroid of the system is directly above the pivot and the restoring force diminishes to zero.

Consider fixed point i) when uplift is just initiated. The critical rotation and displacement are described by Equations 5-22 and 5-23 respectively. Substituting the critical rotation into Equation 5-31 yields the restoring force when uplift is just initiated. This is presented as Equation 5-32 below.

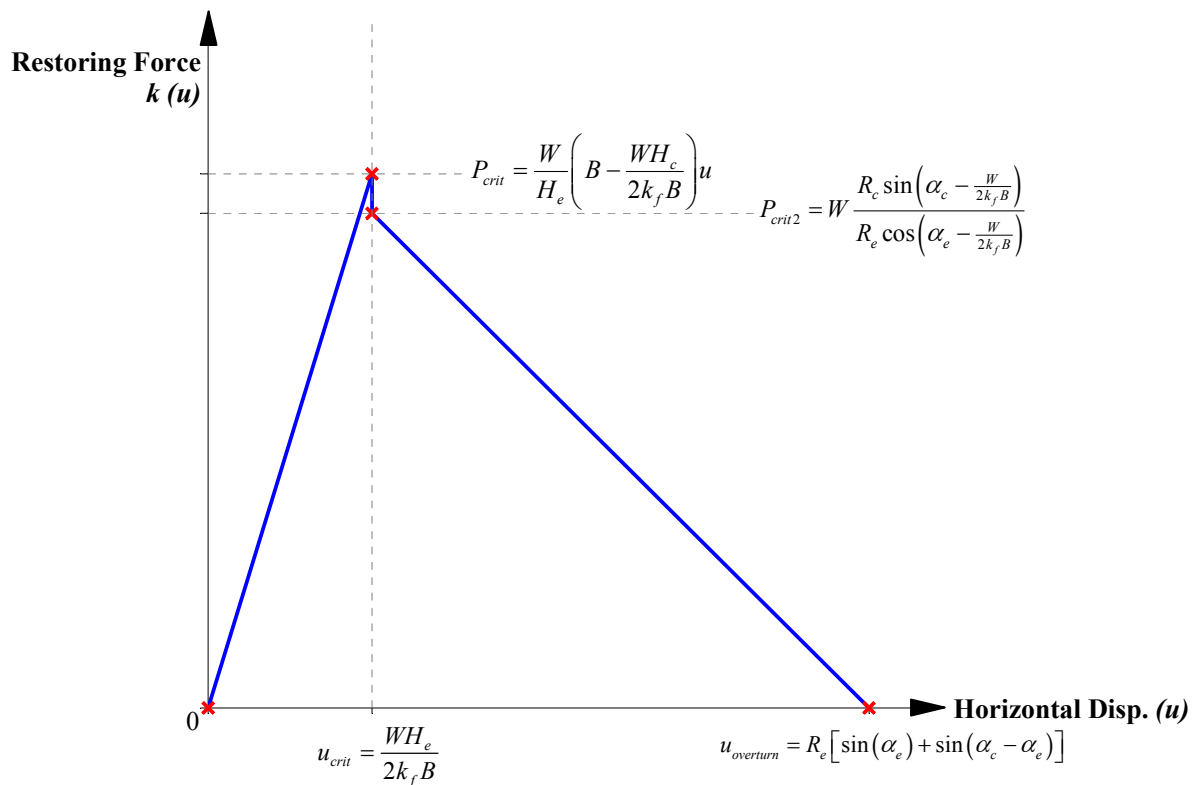
$$P_{crit2} = W \frac{R_c \sin\left(\alpha_c - \frac{W}{2k_f B}\right)}{R_e \cos\left(\alpha_e - \frac{W}{2k_f B}\right)} \quad (5-32)$$

Now consider fixed point ii) when  $\theta = \alpha_c$ , the restoring force reduces to zero and this occurs at a displacement of  $u_{\text{overturn}} = R_e [\sin(\alpha_e) + \sin(\alpha_c - \alpha_e)]$ .

By combining the results of the two cases, a linear approximation of the restoring force-displacements relationship for displacements after the onset of rocking can be fitted. This is presented as Equation 5-33 below.

$$P(u) = \frac{P_{\text{crit}2} (u - u_{\text{overturn}})}{u_{\text{crit}} - u_{\text{overturn}}} \quad (5-33)$$

The results to this point have now effectively mapped the restoring force-displacement characteristics of the rocking system  $k(u)$  using a number of closed form formulae. The relationships are summarised graphically in Figure 5-29.



**Figure 5-29 – Simplified restoring force-displacement characteristic of a rigid rocking structure on two compression only springs**

Next a computer simulation of a pseudo-static pushover test was conducted in Working Model 2D (Design Simulation Technologies 2003), to test the validity of the simplified restoring force-displacement relationship. Working Model 2D is a rigid body dynamic simulation program which makes use of a Newtonian physics engine.

For illustration, an annotated screenshot of the Working Model 2D analysis adopting the properties of the steel column model is presented in Figure 5-30.

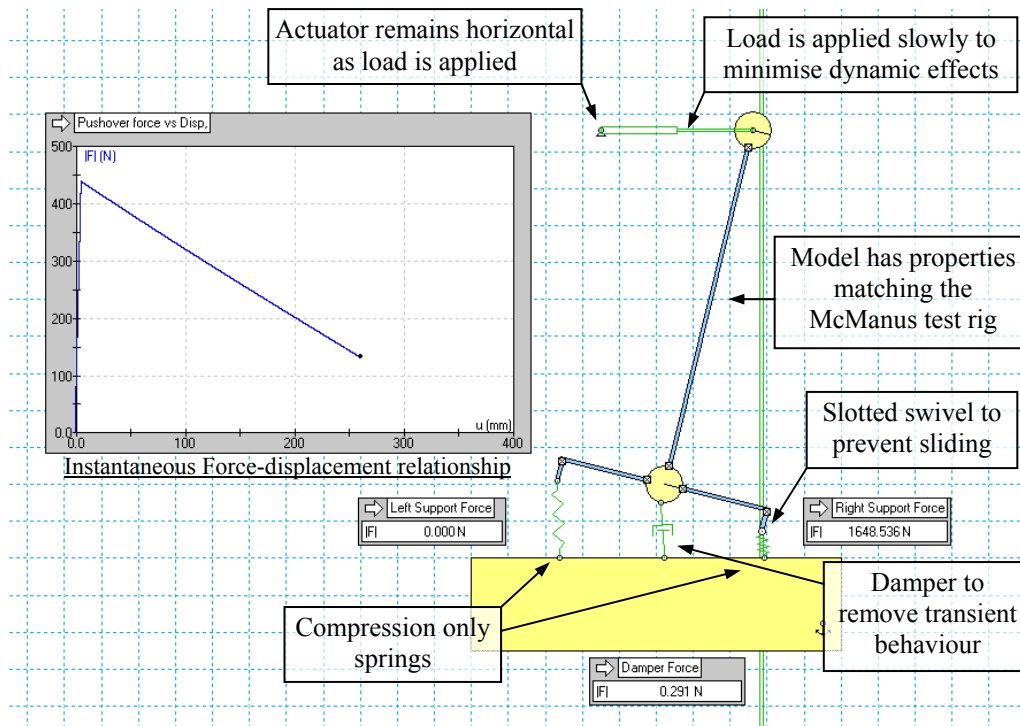


Figure 5-30 – Annotated screenshot of the Working Model analysis

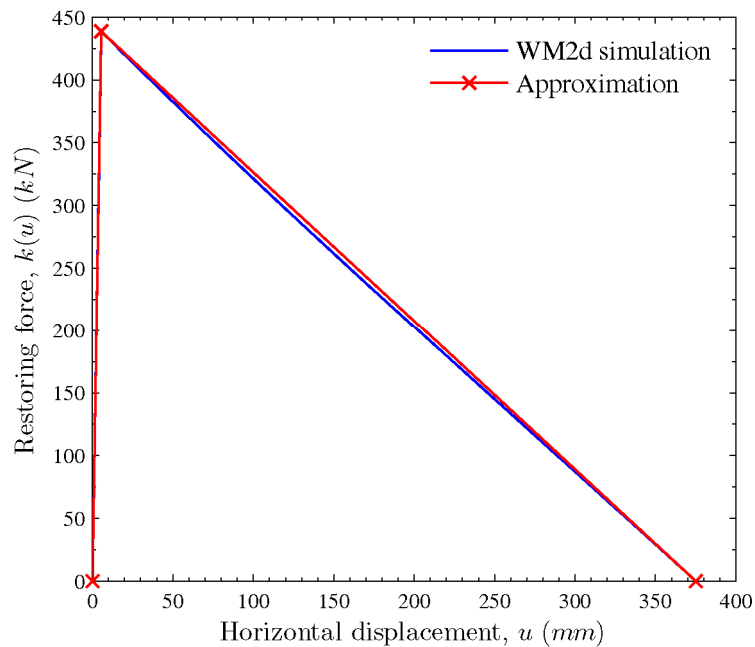


Figure 5-31 – Force-displacement characteristics from Working Model simulation and the approximation formulae

For this simulation, the individual stiffness of the springs ( $k_f$ ) was set at 550 kN/m, this is a value derived from the observation that the compression toe was depressed by approximately 1.5 mm under an additional loading of  $W/2$ .

Figure 5-31 presents a comparison plot of the force-displacement relationship obtained via the Working Model 2D pushover analysis and the approximation formulae. As shown, the linear approximation formulae are very accurate across the full range of lateral displacements. Many additional analyses not presented here confirm the approximation formulae are accurate for a wide range of other structural configurations. Finally, Equation 5-23, shows that the lateral displacement at which complete uplift begins ( $u_{crit}$ ) is inversely proportional to the spring stiffness ( $k_f$ ). This presents another valuable fixed point with physical relevance which can be exploited to estimate a key parameter of the rocking problem.

### 5.3.2.1 Validating the analytical model

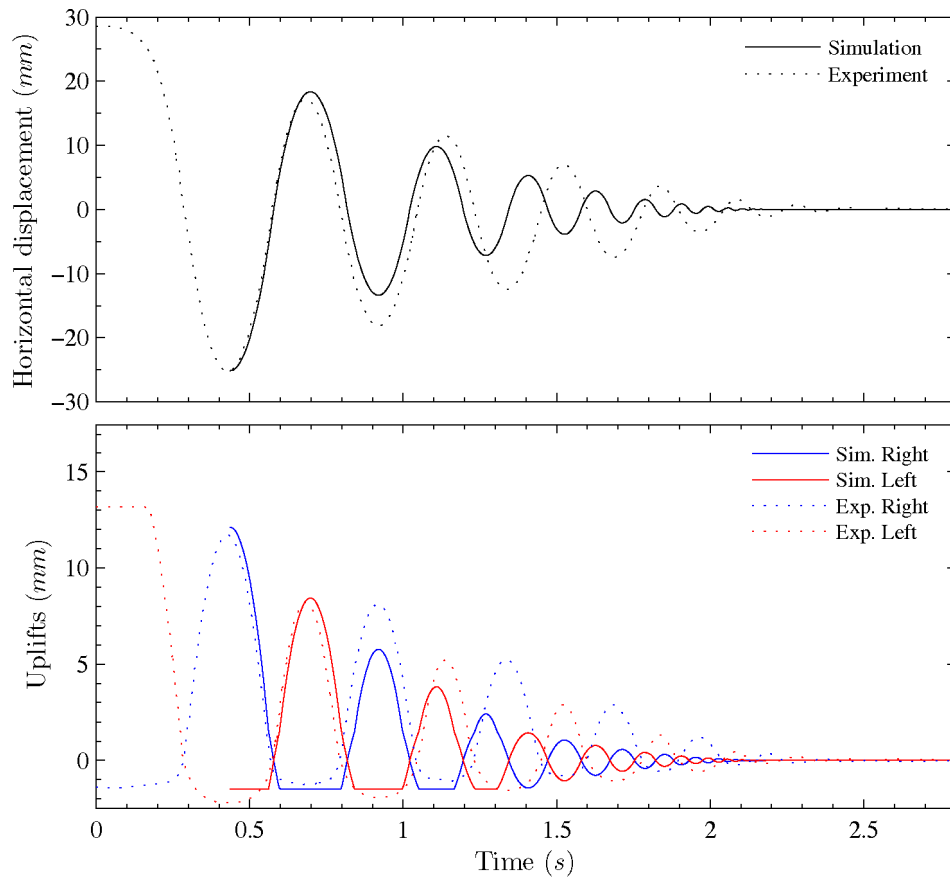
Following the mapping of the force-displacement behaviour, the time-history response of a rocking structure can be estimated by numerically integrating the GDE of motion, Equation 5-15. Suppose plastic impacts take place, then the energy dissipation of the system can be simulated using the coefficient of restitution approach. The two-spring model will use the same  $r$  value derived previously in Equation 5-14. This presumes the conservation of angular momentum about the fixed pivots.

Figure 5-32 presents the simulated displacement time-history using this approach plotted against the actual free rocking decay results from test run 2. In this test run, the steel column specimen rested on a soft rubber pad, it was given an initial displacement, then released suddenly and allowed to rock freely.

The comparison plot shows the simplified procedure produced a near perfect displacement prediction from the moment of release until the first impact. This is encouraging as it confirms that it is acceptable to model the rocking problem using the nonlinear SDOF approach based on the two-spring model, and that the proposed approximation equations are accurate.

The deterioration of the simulation results after the first impact is again attributed to poor emulation of energy dissipation of the system. If the analysis used an empirical  $r$  value higher than  $r_{theory}$ , it would improve the overall prediction of the

displacement time-history. However this practice would have the consequences of violating the conservation of angular momentum assumption.



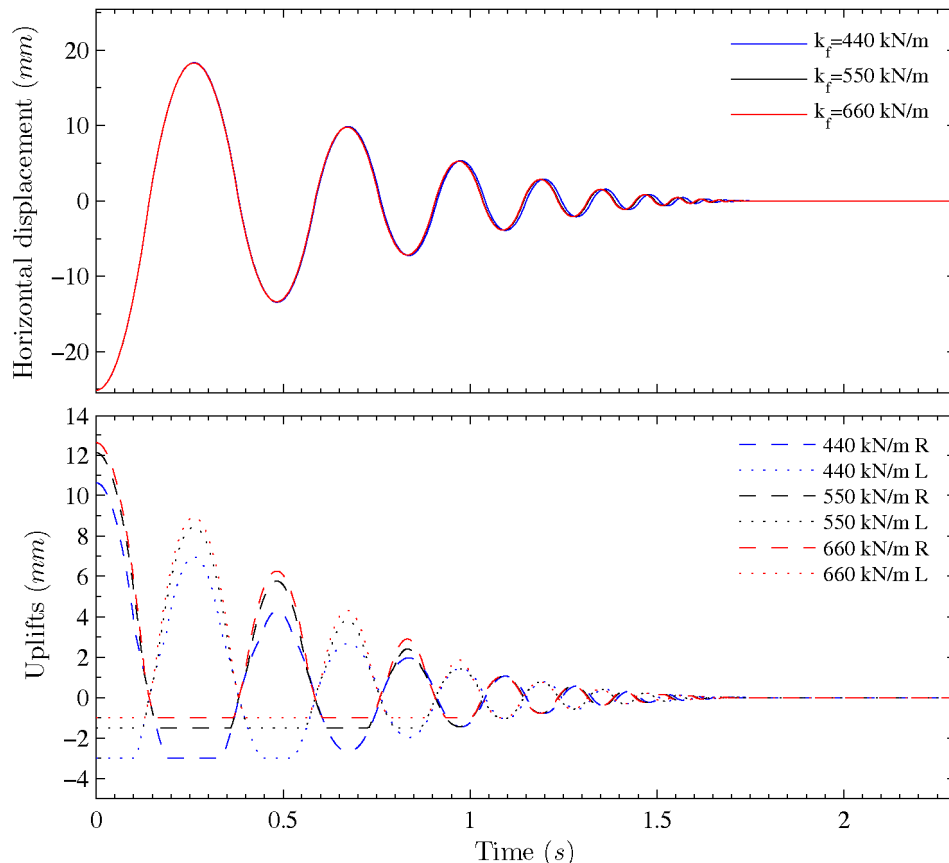
**Figure 5-32 – Simulated versus actual displacement time-history of run 2 ( $r_{sim}=0.74$ )**

It is also of note that the uplift predictions corresponded very well with the experimental uplifts. The simulated uplifts are calculated by converting the horizontal displacements into angular rotations, then by considering rigid body rotation of the structure about the centreline or about the spring in contact, for cases before and after the onset of uplift respectively.

The close match of the predicted and actual uplifts validates the ability of the two-spring model to replicate the smooth rotation centre migration behaviour as shown earlier in Figure 5-13 for free rocking decay on a flexible foundation.

Next, the free rocking decay simulation was repeated with foundation spring stiffness values ( $k_f$ ) 50% above and below the theoretical value used previously. The purpose of these simulations were to examine the influence of the  $k_f$  value on the overall result.

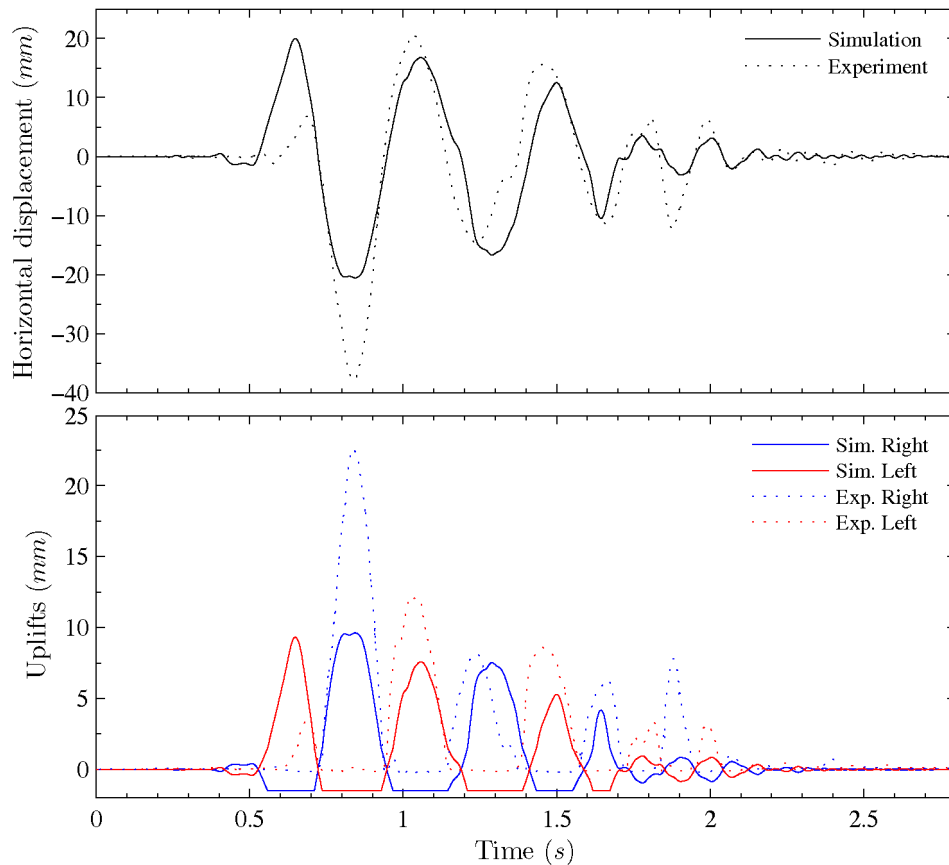
Figure 5-33 presents the results of the simulations, it illustrates that the horizontal displacement predictions using this simulation procedure are rather insensitive to the selection of  $k_f$ . This is not to say that the selection of  $k_f$  has no effects on the simulation result, but rather that an erroneous selection of the  $k_f$  value, even by 50%, would still produce reasonable predictions.



**Figure 5-33 – Displacement from FRD simulations with different  $k_f$  values**

For completeness, a number of simulations were conducted to examine the ability of the two-spring model to predict the displacement response subjected to base excitation. As the two-spring model was designed to model cases where the rocking structure may compress into the foundation, test run 4 was deemed as the most suitable experimental data set for the validation.

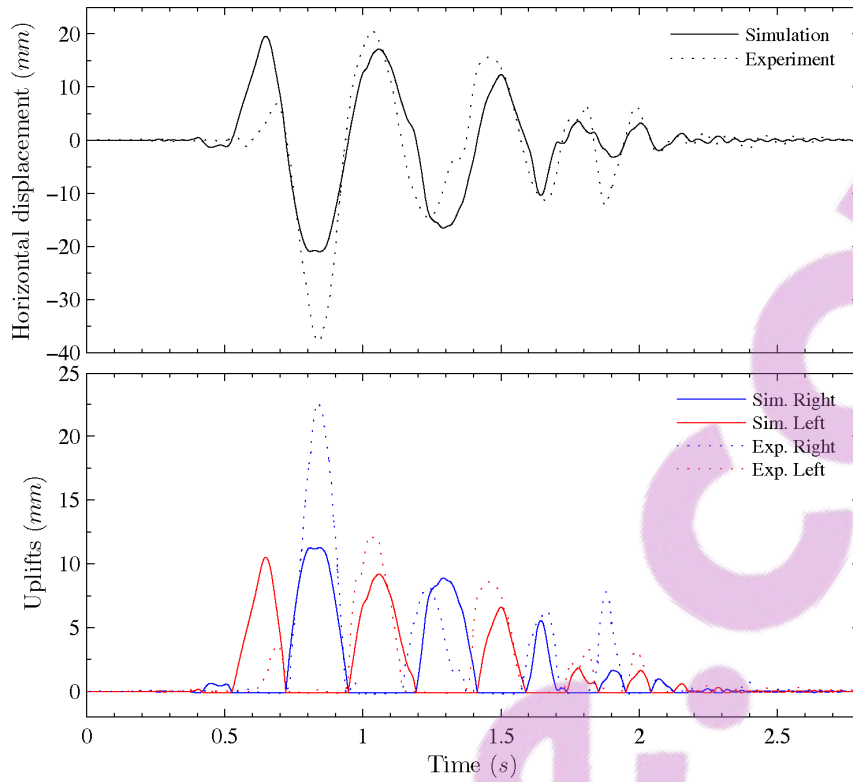
Unfortunately, as with the previous case with the rigid structure rocking on rigid ground, the actual acceleration time-history reproduced on the shake table is not available. As a result, the input acceleration for the current simulation was taken as the original Pacoima record with the time ordinates scaled to 1/5 and the accelerations scaled by a constant factor such that the peak acceleration equalled 2.4 g.



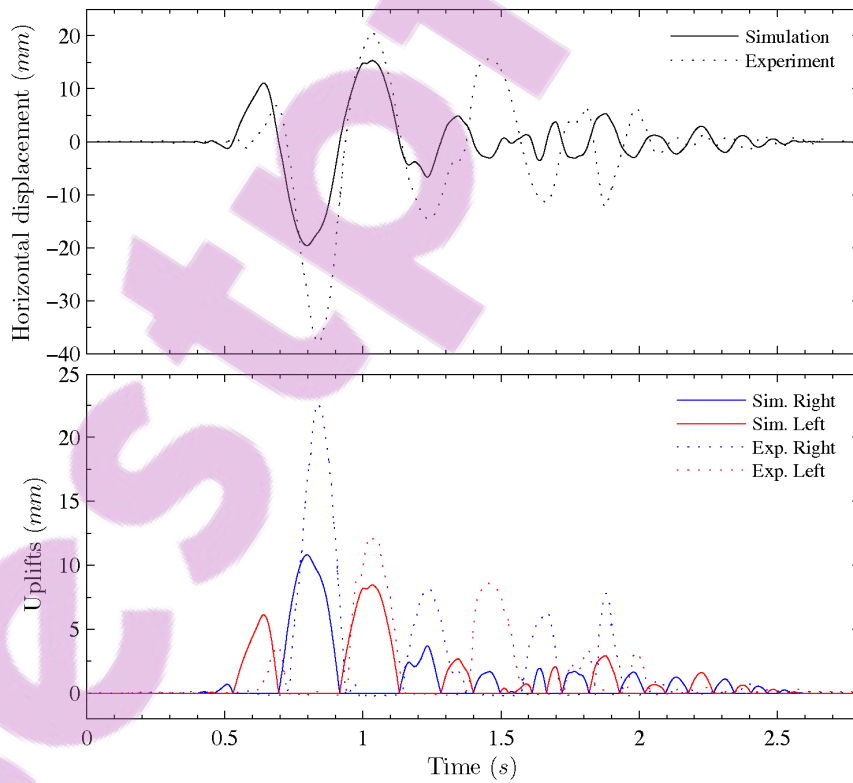
**Figure 5-34 – Simulated versus actual displacement time-history of run 4**  
 ( $r_{sim}=0.74$ ,  $k_f=550$  kN/m)

The simulated displacement time-history was subsequently plotted against the actual results from test run 4 in Figure 5-34. The simulated response appears to track the measured response. However this matching alone is insufficient to validate the model with certainty, nor is it possible to improve on the prediction without having the exact input accelerations. It is noteworthy that the two-spring model predicted compression into the rubber layer, however this did not occur in the experiment.

Upon this observation, the simulation was repeated with a much higher foundation stiffness ( $k_f=10$  MN/m) to reflect the effective stiffness of the foundation to impulsive loads. The displacement time-history from this simulation is presented in Figure 5-35. It shows that although the higher  $k_f$  value had prevented compression into the foundation and resulted in uplift behaviour which is closer to reality, the change had negligible effects on the horizontal displacement prediction.



**Figure 5-35 – Simulated versus actual displacement time-history of run 4 ( $r_{sim}=0.74$ ,  $k_f=10$  MN/m)**



**Figure 5-36 – Simulated time-history of run 4 assuming a rigid foundation adopting Model A from Section 5.3.1 ( $r_{sim}=0.74$ )**

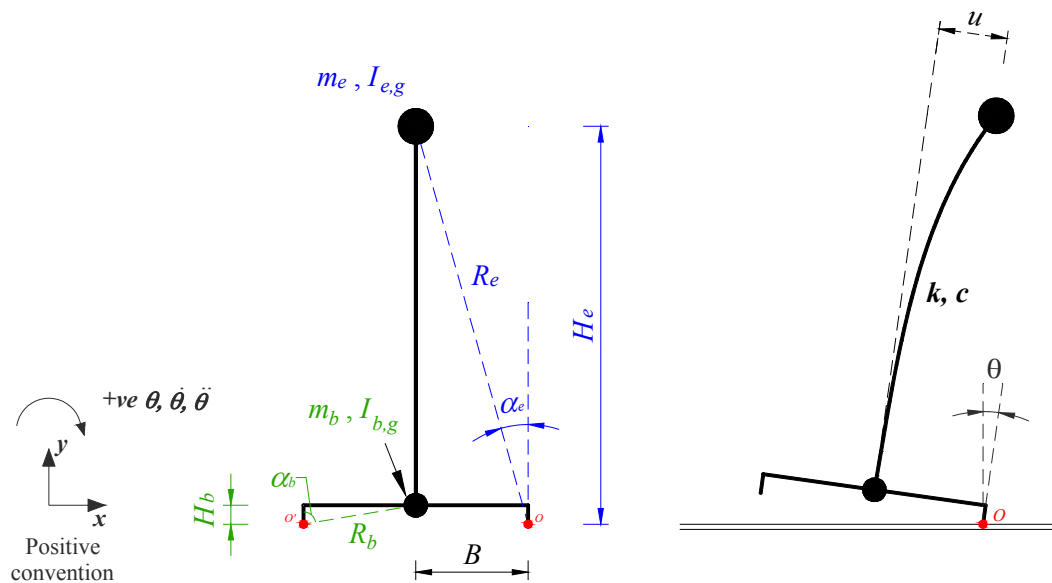
Finally, noting that the use of a high  $k_f$  value had effectively emulated a very stiff foundation, it was interesting to check whether this practice in fact converges to a solution developed using Model A which directly assumed a rigid foundation. Figure 5-36 presents the simulated displacement time-history of test run 4 developed using Model A. A comparison of this figure with Figure 5-35 shows that in fact the two-spring model with the linear approximation will not achieve the exact result from model A, which contains no simplifications, addresses the accelerations of the two masses individually and explicitly prescribes a rigid foundation.

### **5.3.3 ELASTIC 2 DOF STRUCTURE ROCKING ABOUT FIXED PIVOTS ON A RIGID FOUNDATION**

The mathematical models developed for rocking structures thus far have assumed only rigid structures. This assumption significantly reduces the complexity of the problem and allows the dynamics of rocking structures to be approximately explored. The rigid structure assumption is justified by observations that the rocking mode is typically the primary source of displacements in a rocking structure. Any structural deformations are usually orders of magnitude smaller and are consequently assumed to not greatly affect the overall dynamics greatly.

Now whilst the rigid structure analyses are useful for estimating maximum drifts or assessing systems stability against overturning, they do not provide an accurate estimation of the induced actions on the structure. To overcome this limitation, a mathematical model is developed in this section incorporating the elastic and viscous properties of the structure. Moreover, this would result in a more complete analysis and reveal the interactions between the elastic vibration mode and the rocking mode. Of particular interest is whether the intrinsic energy dissipation of the structure is an important source of energy dissipation.

The mathematical model proposed in this section is based on a 2DOF lumped mass structure, rocking about two fixed pivots on a rigid ground. The two masses represent the base structure and the superstructure. The superstructure is assumed to be flexible with elastic and viscous properties, while the base structure is rigid. An illustration of this idealisation is provided in Figure 5-37. As per the two previous models, the structure is restricted from sliding, energy is dissipated instantaneously when impact occurs, the impacts are plastic and no bouncing is permitted.



**Figure 5-37 – Flexible 2 DOF rocking structure on rigid ground**

It is noteworthy that a mathematical model has been developed previously for a structural idealisation similar to the one studied here (Yim and Chopra 1983b). However the development of Yim's model involved a number of simplifications, linearization and assumed modal uncoupling which will not be used here, in the spirit of keeping the derivation as free of assumptions as possible.

The first step in the analysis of a flexible rocking system is the derivation of the governing differential equation (GDE) of motion. It was found that the most systematic method to achieve this is via an energy approach using Lagrange's equation. This is in contrast to the usual technique of forming the GDE by equilibrium equations which involves complex geometry. The Lagrange's equation is presented as D-5 in Appendix D.

The full derivation of the GDE is so complex and tedious that in the interests of preserving some readability in this section, only the key results are presented here. The full derivation is available in Appendix D.

Lagrange's equation leads to the two governing second order differential equations of motion for the system presented as Equations 5-34 and 5-35. These equations are subsequently transformed into a system of single order differential equations and are implemented into a time integration scheme using MATLAB's ordinary differential equation solver function, ODE45. The full details of the transformation are also available in Appendix D.

$$\begin{aligned}
& (m_e R_e^2 + m_e u^2 - \text{sgn}(\theta) \times 2m_e u R_e \sin \alpha_e + I_{e,g} + m_b R_b^2 + I_{b,g}) \ddot{\theta} \\
& + (2m_e u \dot{u} - \text{sgn}(\theta) \times 2m_e \dot{u} R_e \sin \alpha_e) \dot{\theta} + m_e \ddot{u} R_e \cos \alpha_e \\
& + \text{sgn}(\theta) \times m_e g \left[ R_e \sin(\alpha_e - \text{sgn}(\theta) \cdot \theta) - \text{sgn}(\theta) \times u \cos \theta \right] \\
& + \text{sgn}(\theta) \times m_b g R_b \sin(\alpha_b - \text{sgn}(\theta) \cdot \theta) = \\
& -m_e \ddot{u}_g \left[ R_e \cos(\alpha_e - \text{sgn}(\theta) \cdot \theta) - u \sin \theta \right] - m_b \ddot{u}_g R_b \cos(\alpha_b - \text{sgn}(\theta) \cdot \theta)
\end{aligned} \tag{5-34}$$

$$\begin{aligned}
& m_e \ddot{u} + m_e R_e \cos \alpha_e \ddot{\theta} - (m_e u - \text{sgn}(\theta) \times m_e R_e \sin \alpha_e) \dot{\theta}^2 \\
& -m_e g \sin \theta + ku + c\dot{u} = -m_e \ddot{u}_g \cos \theta
\end{aligned} \tag{5-35}$$

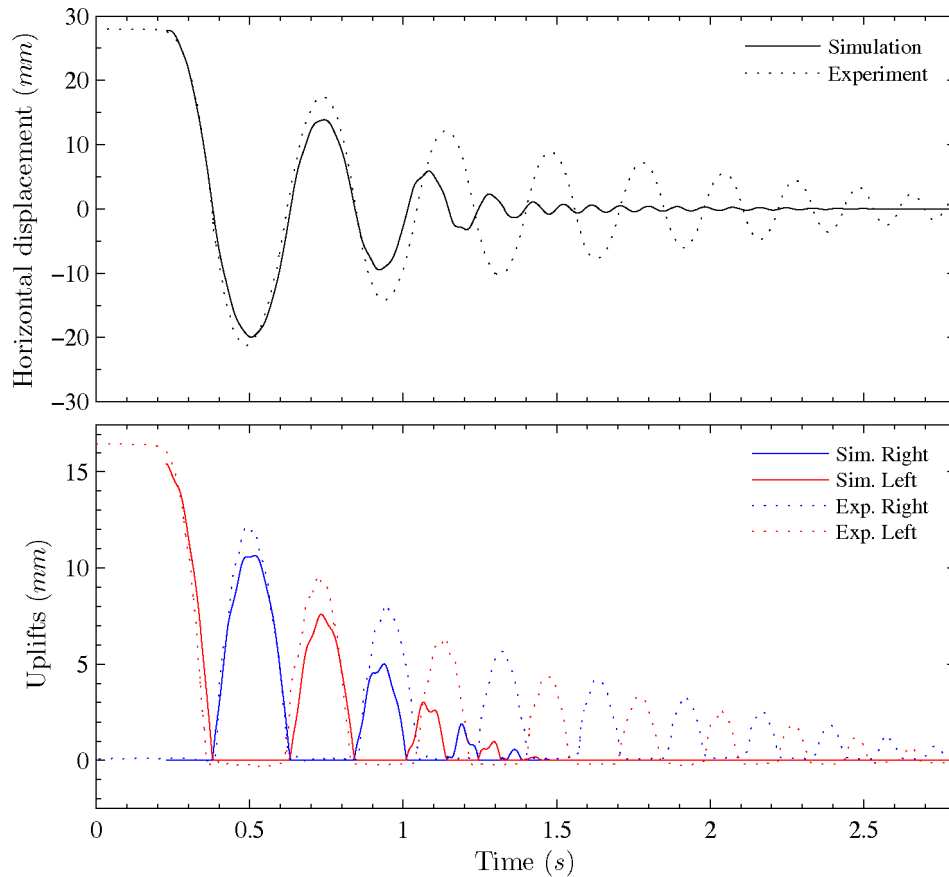
In this simulation procedure, there are two sources of energy dissipation. These involve energy loss through impacts and energy loss through the inherent damping of the flexible structure. A coefficient of restitution approach is adopted to emulate the energy loss through impacts. The  $r$  value predicted by theory, assuming plastic impacts and conservation of angular momentum, is the same as that from Model A. This is as specified previously by Equation 5-14. The inherent damping of the structure is modelled as equivalent viscous damping which relates to the structural deformation of the system. The amount of viscous damping in the model is controlled by a viscous damping coefficient,  $c$ .

### 5.3.3.1 Validating the analytical model

To assess the performance of the proposed analytical model, the simulation procedure is used to estimate the specimen's free rocking decay from test run 1 and the specimen response subjected to scaled El Centro accelerations in test run 3. For these simulations, the flexural stiffness of the model ( $k$ ) is taken as 571.8 kN/m as calculated in Equation 5-1. The viscous damping coefficient ( $c$ ) associated with the structural deformation is assumed to be 3% of the critical viscous damping coefficient. This works out to be 502.4 Ns/m as shown in Equation 5-36 below.

$$c = 0.03 \times 2\sqrt{m_e k} = 502.4 \text{ Ns/m} \tag{5-36}$$

A numerical simulation is conducted using an initial rotation matching the initial rotation from test run 1. All other initial conditions, namely the initial deformation, initial flexural velocity and angular velocity are set as zero.



**Figure 5-38 – Simulated versus actual displacement time-history of run 1 ( $r_{sim}=0.74$ )**

The overall simulated time-history of the free rocking decay is presented in Figure 5-38 alongside the experimental result. The simulated displacements in Figure 5-38 incorporated the rotation time-history  $\theta(t)$  and the flexural displacement time-history  $u(t)$ . These were combined by following Equation 5-37 below.

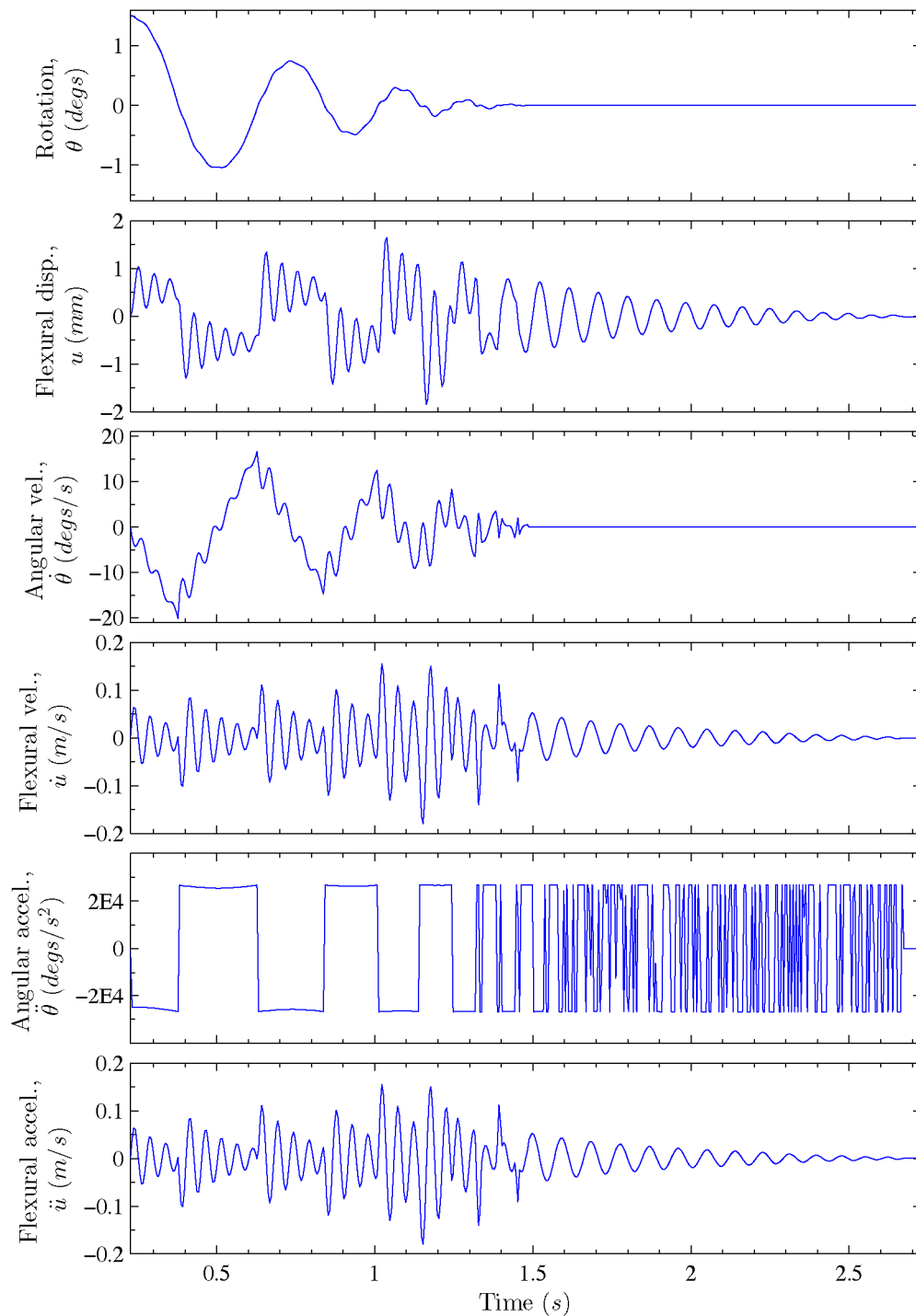
$$\begin{aligned} \text{Displacement} = & \left\{ \text{sgn}(\theta) R_e \left[ \sin \alpha_e - \sin(\alpha_e - \text{sgn}(\theta) \cdot \theta) \right] + u \cos \theta \right\} \underline{\hat{i}} \\ & + \left\{ R_e \left[ \cos(\alpha_e - \text{sgn}(\theta) \cdot \theta) - \cos \alpha_e \right] - u \sin \theta \right\} \underline{\hat{j}} \end{aligned} \quad (5-37)$$

As shown, the simulated displacement time-history matched the experimental result perfectly for the first quarter cycle of the free rocking decay. This is expected as the modelling of free rocking motion prior to any impacts contains little uncertainty.

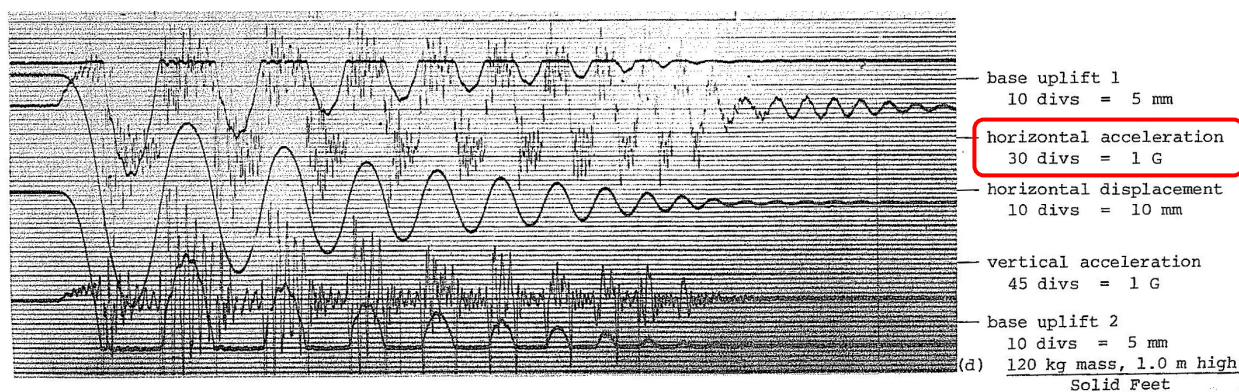
It is also observed that the inclusion of structural flexibility has caused the rocking component of the motion to cease about 0.5 second earlier. This is evident by comparing the uplifts in Figure 5-38 against the result from a corresponding simulation assuming a rigid structure in Figure 5-22. This can be explained by the fact that while the systems in both simulations began with the same potential energy from

the initial rotation, in the analysis with the flexible structure, some of the energy is shared to sustain the elastic vibration. This led to less energy being available to sustain the rocking motion and resulted in fewer rocking cycles.

Also, whilst the structure stopped rocking earlier in the current simulation, Figure 5-39 shows that flexural vibrations continued long after rocking had stopped, and resulted in the overall motion actually taking longer to completely cease.



**Figure 5-39 – Individual simulated response time-histories for run 1 ( $r_{sim}=0.74$ )**

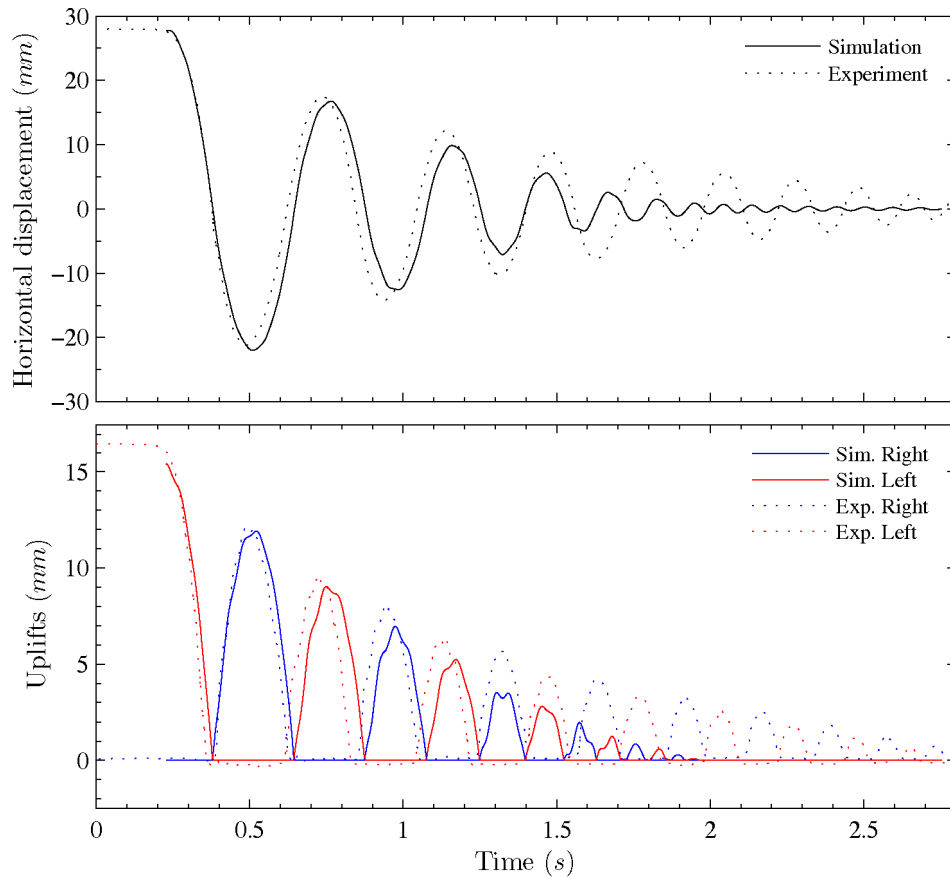


**Figure 5-40 – Experimental time-history traces from run 1 (Source: McManus 1980)**

Another notable feature of the result is the coupling of the rocking and flexural motion. This is evident by the way that flexural vibrations were set off when the model was given an initial rotation only. The effects of the coupling are also observable as a number of noticeable kinks in the previously smooth sinusoidal variations of the horizontal displacements and uplifts. For information, the rotation and flexural responses are plotted separately in Figure 5-39.

For an approximate comparison, the experimental lateral acceleration time-history of the free rocking decay is reproduced from the McManus report in Figure 5-40. The experimental lateral accelerations showed a high frequency sinusoid superimposed onto a longer period square waveform. This is similar to the result of summing the simulated angular acceleration and flexural acceleration time-histories. The comparison also highlighted that the transition from rocking and flexing to simply flexing was modelled remarkably well.

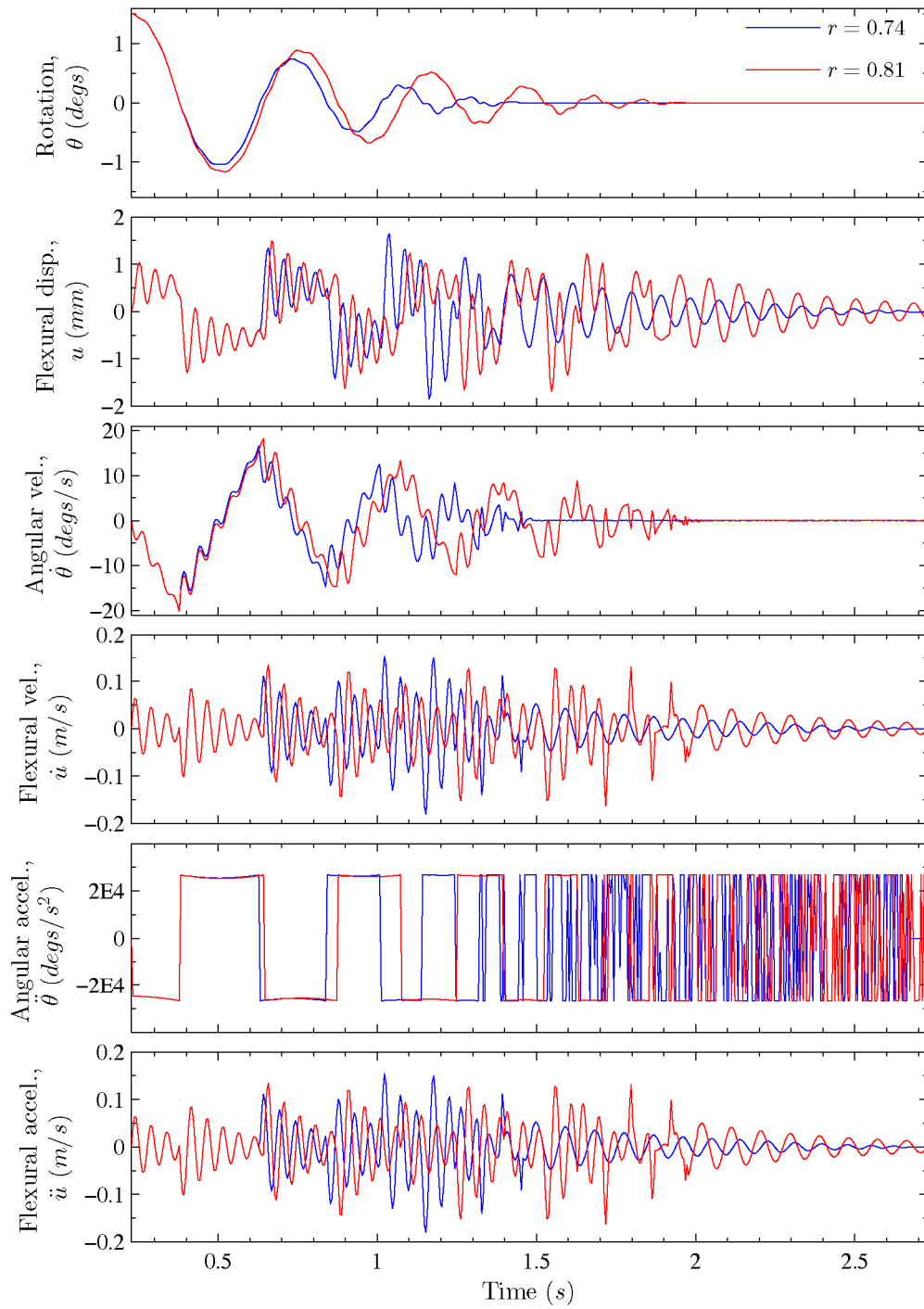
It was also noted that the theoretical  $r$  value based on plastic impacts led to excessive energy dissipation, just as it did in the rigid model simulation. Accordingly, the simulation was repeated with an  $r$  value matching the average  $r$  value from the experiment. This improved the overall matching of the results for several more cycles (Figure 5-41). However, the improvement ultimately dissipates, since the true energy dissipation per impact cannot be represented by a single  $r$  value. It is worth noting that most errors appear to stem from inadequate modelling of the energy dissipation at impacts.



**Figure 5-41 – Simulated versus actual displacement time-history of run 1 ( $r_{sim}=0.81$ )**

Another notable feature revealed by the improved simulation shown in Figure 5-41 is the oddly shaped uplift time-history traces. The oddly shaped traces were noted previously in the experimental results, but they were presumed to be due to flexing of the base plate, measurement errors or errors from the digitizing process. However, as the distinctive traces are closely simulated by the current procedure, these must in fact be features of the flexural interaction of the column specimen and the rocking motion.

Figure 5-42 presents a comparison of the time-history traces from the simulations with the two different  $r$  value settings. The figure highlights the departure of the two predictions as more impacts occurred during the simulation.

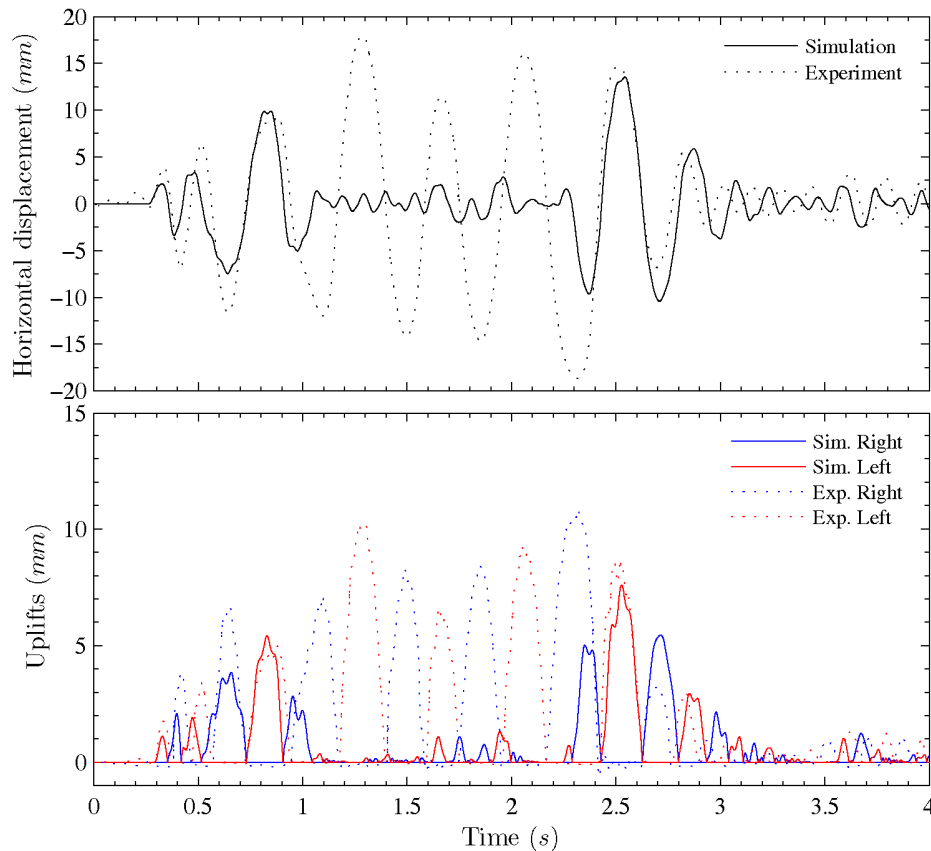


**Figure 5-42 – Simulated time-history traces of the FVD with two different  $r$  values**

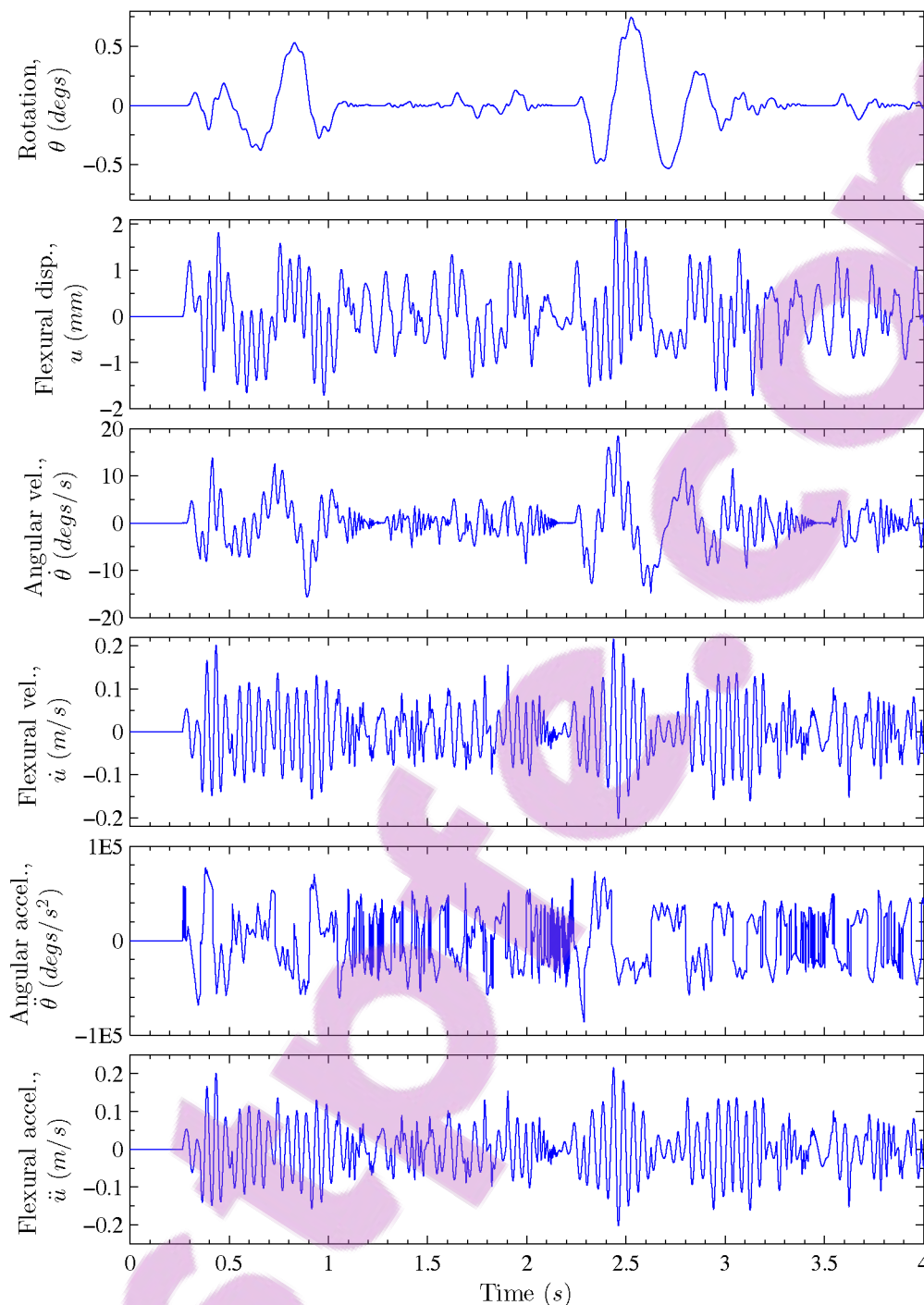
Following the successful free rocking decay simulations, the analytical procedure was applied to the modelling of a flexible rocking structure subjected to base excitations. Test run 3 was chosen as the benchmark verification data. And as discussed previously, the simulations adopted the ideal base accelerations rather than the actual motion replicated by the shake table, as the latter was not available.

A simulation was first conducted with the theoretical  $r$  value based on the conservation of angular momentum, the ideal structural stiffness ( $k = 571.8$  kN/m) and 3% critical viscous damping. The result of this simulation is plotted against the experimental results in Figure 5-43.

As can be seen, there is some resemblance between the features of the simulation and those of the actual response, however it is difficult to gauge whether the simulation was successful without the actual base excitation input. It can be concluded however that the flexibility of the structure has substantially altered the predicted response. This is evident from comparing Figure 5-43 with Figure 5-24 which depicts the displacement prediction for a rigid structure subjected to the same excitation record.



**Figure 5-43 – Simulated versus actual displacement time-history of run 3 ( $r_{sim}=0.74$ )**



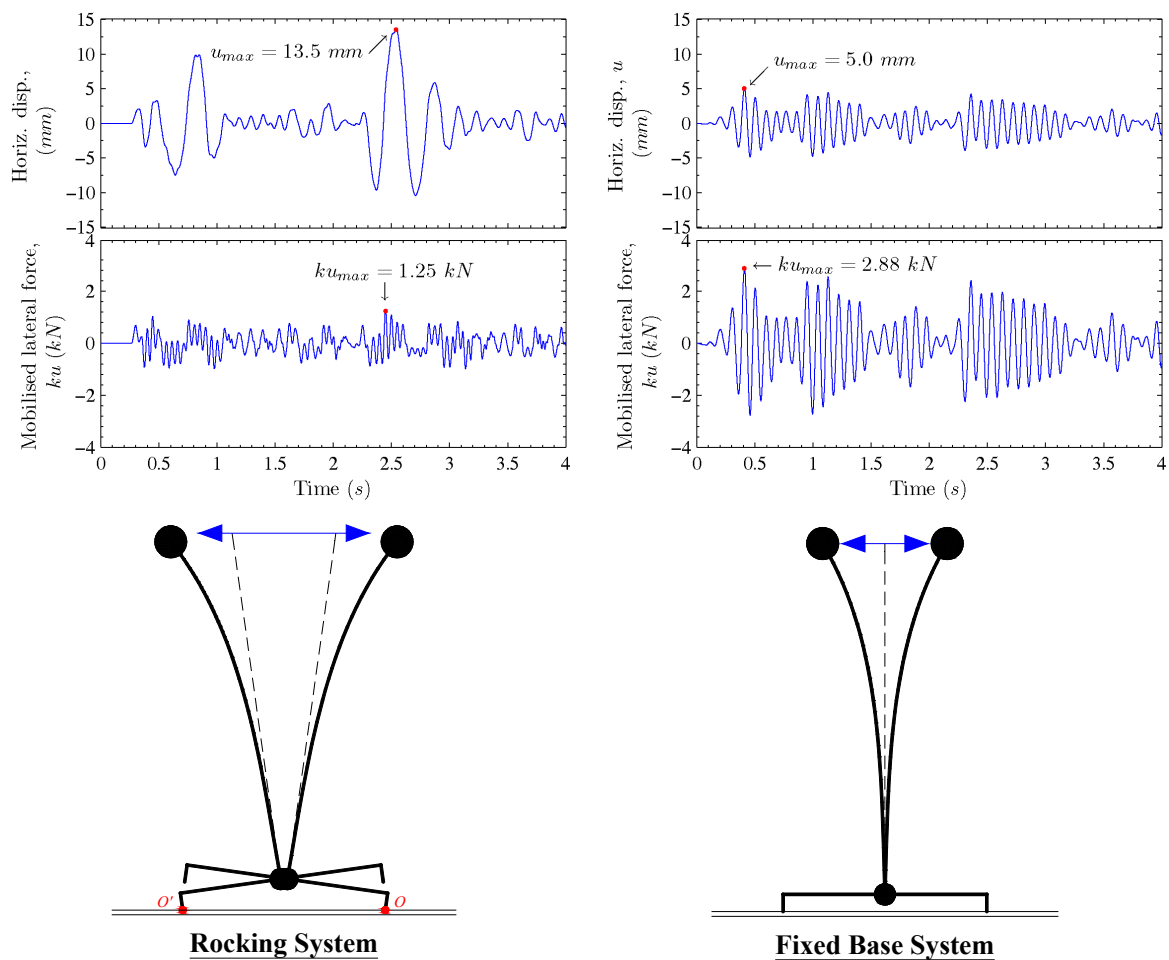
**Figure 5-44 – Individual simulated response time-histories for run 3 ( $r_{sim}=0.74$ )**

For completeness, the simulated rocking and the flexural response time-histories are presented individually in Figure 5-44. This figure illustrates the strong coupling of flexural and rocking motion especially when a rocking structure is subjected to earthquake-like loadings.

A very useful outcome of the proposed simulation procedure is the ability to accurately predict the structural demand on the rocking system. This permits

engineers and researchers to quantitatively assess the isolation properties of rocking structures. For illustration, Figure 5-45 presents the lateral force demand and the displacement response for a fixed base flexible structure against its rocking counterpart subjected to the base excitation from test run 3.

The proposed analysis procedure provides researchers with clearer than ever quantitative data to assess the tradeoffs between increases in drift and decreases in design actions by implementing a rocking isolation solution.



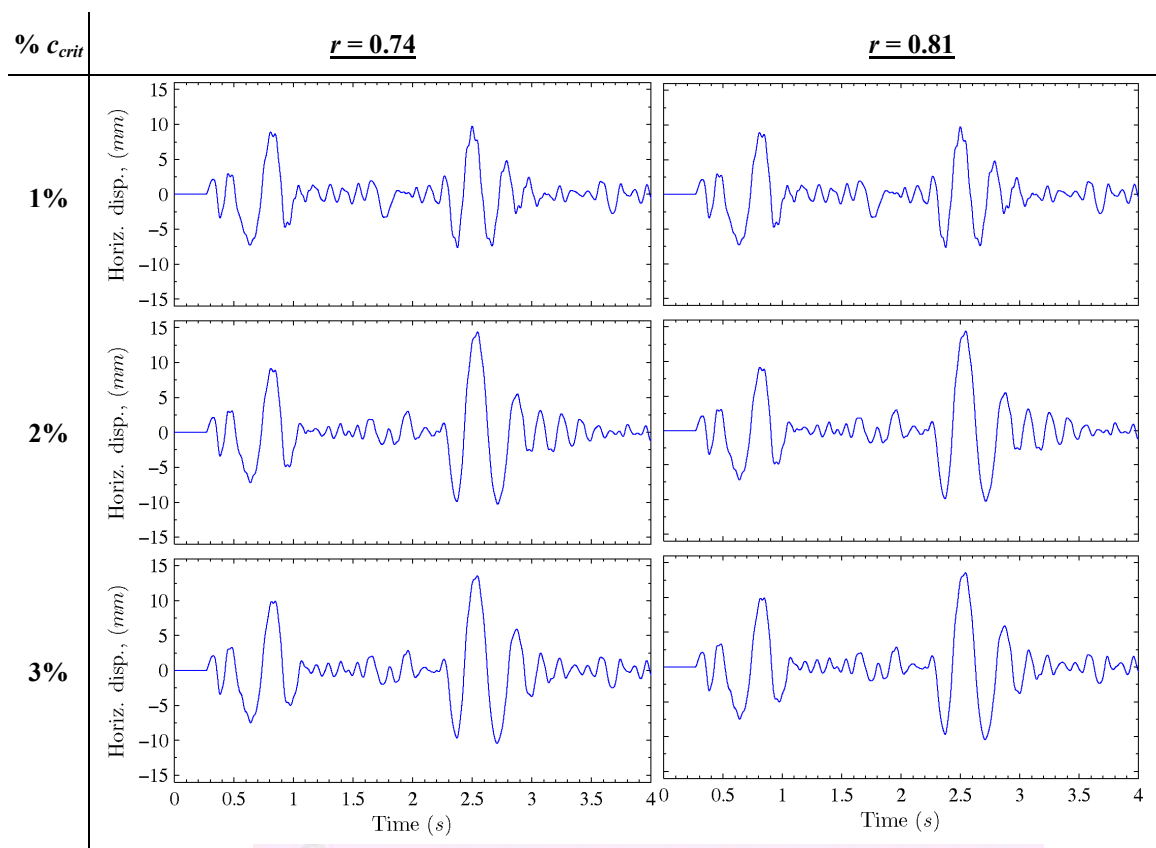
**Figure 5-45 – Rocking system response versus fixed base response ( $r_{sim}=0.74$ ,  $k = 571.8$  kN/m and  $c = 502.4$  Ns/m)**

Next, accepting that the proposed modelling procedure in this section is an accurate technique to predict the response of flexible rocking structures to base excitations, it is of interest to examine: 1) whether inherent structural damping has a significant effect on the overall behaviour, and 2) whether the response of the system

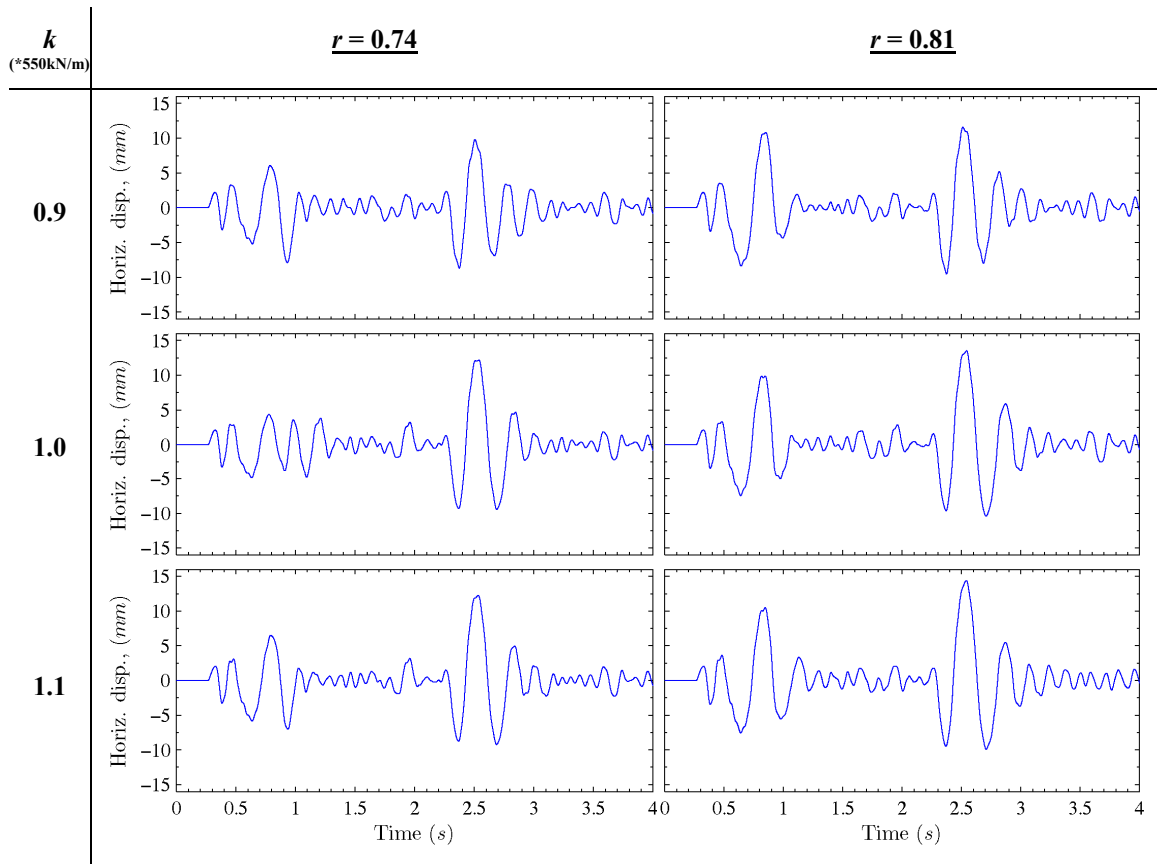
or the analysis procedure is sensitive to a change in structure properties and the assumed coefficient of restitution.

To address these queries, a number of additional simulations were conducted with systematic variations in  $k$ ,  $c$  and  $r$  values. The response time-histories of these simulations are presented in Figures 5-46 and 5-47. From this particular example, it is observed that,

- the rocking response is insensitive to small variations of the coefficient of restitution ( $r$ ).
- Inherent damping from the flexural vibration of the structure does contribute to the damping of the system and affects the overall response of the structure. However the effects are seemingly minor.
- The overall response is relatively insensitive to a small change in the structure's flexural stiffness. However small deviations could lead to large change of the time-history as rocking is a history dependent phenomenon.



**Figure 5-46 – Simulated response time-histories with a range of  $k$  values**  
( $c = 502.4$  Ns/m)



**Figure 5-47 – Simulated response time-histories with a range of  $c$  values**  
( $k = 571.8$  kN/m)

## 5.4 CONCLUSION

This chapter proposed three analytical models for predicting the response of simplified rocking structures subjected to base excitations. The assumptions in each successive model were relaxed slightly and led to an increase in complexity in each subsequent model.

The first proposed model, Model A presented in Section 5.3.1, assumed a structural system can be represented by a two-mass rigid structure resting on rigid ground. The structure made contact with the ground at two fixed points. The structure did not slide and horizontal displacements could occur only during rocking. As the structure rocked, the two fixed points became the rocking pivots. Impacts occurred whenever the structure returned to the upright position, at which time, the structure would switch from rotating about one rocking pivot to the other. The impacts were assumed to be inelastic or in other words bouncing was not permitted. Impacts were the sole source of energy dissipation in this model, and the energy loss per impact was

estimated by assuming conservation of angular momentum about the new rotation centre.

The second proposed model, Model B presented in Section 5.3.2, extended Model A by the introduction of a flexible foundation. Apart from the flexible foundation, this model shared the same assumptions of Model A. In Model B, the effects of the flexible foundation were implemented by assuming the structure rested on two compression-only springs. Instead of deriving the GDE of motion in the usual manner, the system was treated as an equivalent nonlinear SDOF system with uncoupled dynamic and static restoring properties. This resulted in a number of simple, closed form approximation formulae which predicted the nonlinear static response of the rocking system. This was then integrated into a time integration algorithm and led to a simple and effective technique to predict the response of rocking rigid structures subjected to base excitation.

Finally, the third proposed model, Model C presented in Section 5.3.3, shared the same assumptions as the first model, with the exception that the rigid structure was replaced by a flexible structure. The flexible structure in this model had elastic and viscous properties. An energy approach was used to evaluate the GDEs of motion of the system. The GDEs were then implemented in a time integration algorithm to predict the response of flexible rocking structures subjected to base excitation. This procedure was found to be very accurate and predicted distinctive features from recorded response time-histories from a shake table test. The model was effective in emulating the coupling of flexural and rocking behaviour.

Model C also provides users with a valuable tool to estimate the structural design actions on a rocking structure. This procedure facilitates a quantitative assessment of the benefits of implementing a rocking isolation solution.

# Chapter 6

---

## CONCLUSIONS AND FUTURE WORK

---

A principal objective of this research was to make a contribution to the current understanding of the behaviours of rocking objects subjected to base excitation. As discussed in the literature review, this topic has been a focus of many studies for the past one and half centuries. Despite this long period of study, it became evident in the course of this research that there are still many complex and unexplained phenomena beneath the simple appearance of rocking systems.

The present work thoroughly examined the behaviour of three simple rocking systems. The three systems included, i) a freestanding rigid block, ii) a controlled rocking rigid wall, and iii) three idealised rocking structural systems. The investigation systematically examined the available experimental data before conducting an extensive number of numerical analyses to either predict or explain the findings. A focus was placed on predicting the time-history response of the three systems, as this was regarded as the quintessential test of modelling and understanding the system behaviour.

Whenever possible, the study attempted to address the rocking problem from a first principles stance, making as few assumptions as possible and maintaining an approach that was as 'ideologically' consistent as possible. This often meant that each analysis and proposed numerical model began as a variation of Housner's simple rocking model (SRM).

## 6.1 BEHAVIOUR OF RIGID, ROCKING BLOCKS

For the study on the behaviour of rocking rigid blocks, a freestanding concrete block was set to rock from a range of initial rotations in a series of more than 430 experiments. The concrete block was cast into a steel mechanism which precluded sliding. The displacement time-histories from these experiments were collated and were used to show that Housner's SRM is generally satisfactory for modelling slender rigid blocks rocking on stiff ground. This was evident by inspecting the experimental and simulated rotation time histories plotted on the same phase diagram, as in Figure 3-7. This showed Housner's SRM performed well in modelling the smooth rocking phase<sup>6</sup> of the rocking cycle, when it is given the correct initial conditions. The only real failing of the SRM was the inability to explain and predict the energy dissipation which occurs during impacts. This led to departures in subsequent time-history predictions and highlighted the history dependency of rocking.

Formulae to estimate the support force variation were developed by rewriting the governing equation of motion in Cartesian coordinates. These were validated by the experimental results and were later used to estimate the impact forces that had occurred during the experiments.

The experimental data showed impact forces tended to increase slightly as angular impact speed was increased. There was clear evidence that the energy loss during an impact was related to the angular impact speed. It was also clear that the amount of energy loss was not related to the magnitude of the impact force. This was not surprising as the energy dissipation of a free rocking block originated from the requirement of conservation of angular momentum rather than conventional impact mechanics. It was also shown that the addition of a steel mechanism to prevent slip and satisfy the conditions of Housner's SRM, had side effects which slightly altered the system's behaviour. The fact that a rocking system, carefully detailed to satisfy Housner's SRM assumptions still failed to fully achieve this objective, suggests that the SRM assumptions are very unlikely to be fully satisfied in practice.

Despite this, the author still recommends the use of Housner's SRM to model rigid rocking blocks as it is easy to implement, free of assumptions that cannot be explained by simple mechanics and provides an acceptable prediction.

---

<sup>6</sup> Ibid. 4., on page 62.

## 6.2 DYNAMICS OF CONTROLLED ROCKING SYSTEMS

A thorough investigation was conducted on the dynamics of controlled rocking systems. Controlled rocking systems are normally rocking objects with the addition of vertical prestress. The vertical prestress is usually applied through vertical unbonded post-tensioning tendons, and these enhance the lateral resistance of a normally rocking system by increasing its self-centering capability.

This study first analysed the results from free vibration decay and shake table tests conducted on a 2.4 m high, post-tensioned concrete masonry wall. The study identified that the migration of the rotation centre during rocking is central to understanding the dynamic characteristics of a controlled rocking system.

It was shown that unlike a free rocking system which only rocks about its corners, the rotation centre of a controlled rocking system typically migrates continuously from one wall corner to the next through the wall centre. By fitting an empirical formula to describe the rotation centre migration behaviour, it was possible to accurately predict the uplift and post-tensioning tendon extension as a function of the wall displacement. From these, the energy content of the system could be estimated as a function of wall displacement. By differentiating the energy expressions it was possible to predict the pseudo-static force-displacement behaviour of the controlled rocking system.

The rotation centre migration approach was extended into two procedures to predict the time-history response of controlled rocking systems. Both of these procedures simulated the free vibration decay successfully. They also simulated the shake table tests accurately when rocking was clearly initiated. When rocking was not clearly initiated, typically in cases where the lateral displacements were small, they produced rather inaccurate predictions.

It was clear from the investigations that time-history simulations were very sensitive to a small change in input parameters. In particular, small changes in the  $r$  value or the energy dissipation parameter resulted in dramatically different time-histories. The controlled rocking system was found to be so sensitive that it exhibited classical chaotic system traits under sinusoidal excitations. This sensitivity to initial conditions casts doubt on whether a reliable and accurate time-history prediction of a

controlled rocking system subjected to base excitation is attainable, as conjectured by Hogan in his 1989 paper. This extreme sensitivity was also practically demonstrated by two shake table tests on the same wall specimen with identical base excitations. These two effectively identical tests resulted in substantially different time-history responses. It was also noted that the proposed rotation centre migration approach can be extended and applied to walls of different tendon configurations and different level of prestress, simply by reconsidering the geometry of the system.

### **6.3 SIMPLIFIED ROCKING SYSTEMS**

The final section of research addressed the behaviour of simple structural systems permitted to rock when subjected to base excitations. Three analytical models were developed using three simple structural idealisations. Each successive model contained a less restrictive assumption in the boundary condition or the structural properties. The outputs of the models were compared against experimental results from a published report. The comparisons demonstrated that each model emulated particular traits which they had been designed to handle, and they all satisfactorily emulated the overall rocking response.

The first proposed model led to the development of a new expression for the coefficient of restitution for a rocking structural system, based on the assumptions of plastic impacts and conservation of angular momentum. The second proposed model presented a set of simplified closed form formulae which precisely predicted the nonlinear static force-displacement relationship of a rocking structural system. The third proposed model developed governing differential equations of motion for a flexible structure permitted to rock on rigid ground. These governing differential equations were implemented in a time integration algorithm. The resulting time-history prediction was an improvement over the other two methods and explained distinctive features from the shake table tests which had originally been considered to be experimental errors.

This third analytical procedure provided a practical quantitative tool to enable assessment of the benefits of implementing a rocking isolation solution, as it outputs the elastic force demand on the structure as well as the displacement time history. This procedure is recommended by the author when maximum accuracy in the displacement time history is desired, in lieu of an even more advanced model.

## 6.4 FUTURE WORK

This research has highlighted that there are still many challenges remaining in the journey towards a complete comprehension of the underlying mechanics of rocking objects. A common obstacle which was encountered during many parts of this research was the modelling of energy loss due to impacts.

Despite the short duration of the impacts when they are compared to the period of the rocking motion, they have a significant effect on the overall behaviour and predictability of rocking systems, particularly free rocking and controlled rocking systems.

The current study trialled two different techniques to emulate the energy dissipation due to impacts. The two techniques were namely 1) by directly modifying the exiting angular velocity from an impact, and 2) by developing a non-conservative force which activates when a rocking object is near upright, as specified in Equation 4-28. The second of these techniques offered new parameters to specify how energy was dissipated, and it reproduced the results of a seemingly instantaneous dissipation consistent with experimental observation. However neither of these techniques could say exactly how much energy was dissipated. This question remains unanswered, but what is known from the experimental data studied is that the amount of energy dissipation at times varies significantly from that predicted on the basis of conservation of angular momentum. This was highlighted by Figures 3-19, 4-40 and 5-9.

Additional research examining the exact mechanical interactions at the moments of impact could yield exponential improvement in the modelling of rocking objects. Along the same line, investigations into the influence of the material on the rocking interfaces and the statistical characteristics of rocking impacts would also contribute greatly to the understanding of rocking mechanics.

One of the major impediments encountered in this study was the lack of dynamic test data on rocking systems. It would be desirable if more shake table tests were conducted on rocking systems to provide validation data for the research community.

Finally, it was noted earlier the model of a flexible structure rocking on rigid ground proposed in Chapter 5 produced high restoring moments under small rotations. This phenomenon was also encountered during the modelling of controlled rocking objects. It was concluded that it stemmed from the fact that the rocking pivots were fixed at the two edges. This was corrected in the modelling of controlled rocking objects in Chapter 4 by assuming a smooth migration of the rotation centre. The same can be easily achieved for the flexible structure model by extending it to rock on flexible ground. Additionally, such a model may be simplified using an equivalent nonlinear single degree of freedom system with uncoupled dynamic and static restoring properties, similar to that proposed for the rigid structure rocking on flexible ground in this thesis. This could provide a possible tool to accurately model a structure with rocking and non-rocking elements, or perhaps a structure with a system of rocking elements.

## REFERENCES

Anderson, D. L. (2003). "Effect of foundation rocking on the seismic response of shear walls." *Canadian Journal of Civil Engineering*, 30(2), 360-365.

Arze, E. (1993). "Seismic design of industrial facilities." *Tectonophysics*, 218(1-3), 23-41.

Aslam, M., and Godden, W. G. (1980). "Earthquake Rocking Response of rigid bodies." *Journal of the Structural Division*, 106(ST2), 377-392.

Barkan, D. D. (1962). *Dynamics of bases and foundations*, translated from Russian by L. Drashevskaya, McGraw-Hill, New York.

Beck, J. L., and Skinner, R. I. (1974). "Seismic Response of a Reinforced Concrete Bridge Pier Designed to Step." *Earthquake Engineering & Structural Dynamics*, 2(4), 343-358.

Chopra, A. K., and Yim, S. C. S. (1985). "Simplified Earthquake Analysis of Structures with Foundation Uplift." *Journal of Structural Engineering*, 111(4), 906-930.

Cloud, W. K. (1963). "Period Measurements of Structures in Chile." *Bulletin of the Seismological Society of America*, 53(2), 20.

Davison, C. (1921). "On Scales of Seismic Intensity and on the Construction and Use of Isoseismal Lines." *Bulletin of the Seismological Society of America*, 11(2), 95-130.

Design Simulation Technologies, Inc. (2003). Working Model 2D (6.0.0). Available Distributor: Design Simulation Technologies, Inc., Canton, MI 48187 <<http://www.workingmodel.com>>

Dwairi, H. M., Kowalsky, M. J., and Nau, J. M. (2007). "Equivalent Damping in Support of Direct Displacement-Based Design." *Journal of Earthquake Engineering*, 11, 19.

ElGawady, M. A., Ma, Q. T., Butterworth, J. W., and Ingham, J. M. (2006). "Effects of interface material on the dynamic behaviour of rigid blocks." *19th Australasian Conference on the Mechanics of Structures and Materials*, Christchurch, New Zealand, 7.

Elwood, K. J., and Moehle, J. P. (2003). "Shake table tests and analytical studies on the gravity load collapse of reinforced concrete frames." *PEER-2003/01*, Pacific Earthquake Engineering Research Center, University of California Berkeley.

Englekirk, R. E. (1990). "Seismic design considerations for precast concrete multistory buildings." *PCI Journal*, 35(3), 40-51.

FEMA 356. (2000). "Prestandard and Commentary for the Seismic Rehabilitation of Buildings." Prepared by the American Society of Civil Engineers for the Federal Emergency Management Agency. FEMA, Washington, D.C.

Gazetas, G., Apostolou, M., and Anastasopoulos, J. (2003). "Seismic uplifting of foundations on soft soil, with examples from Adapazari (Izmit 1999 earthquake)." *BGA International Conference on Foundations, Innovations, Observations, Design and Practice, Sep 2-5 2003*, Dundee, United Kingdom, 37-49.

Grant, D. N., Blandon, C. A., and Priestley, M. J. N. (2005). "Modelling Inelastic Response in Direct Displacement-Based Design." *European School of Advanced Studies in Reduction of Seismic Risk*, Pavia, Italy.

Hanson, R. D. (1973). "Behavior of liquid-storage tanks, the Great Alaska earthquake of 1964." *Proceedings of the National Academy of Science*, 7, 331-339.

Hilborn, R. C. (1994). *Chaos and nonlinear dynamics : an introduction for scientists and engineers*, Oxford University Press, New York.

Hogan, S. J. (1989). "On the dynamics of rigid-block motion under harmonic forcing." *Proceedings of the Royal Society of London, Series A, Mathematical and Physical Sciences*, 425(1869), 441-476.

Hogan, S. J. (1992). "The Effect of Damping on Rigid Block Motion under Harmonic Forcing." *Proceedings: Mathematical and Physical Science*, 437(1899), 97-108.

Housner, G. W. (1963). "The behaviour of Inverted pendulum structures during earthquakes." *Bulletin of the Seismological Society of America*, 53(2), 403-417.

Huckelbridge, A. A., and Clough, R. W. (1978). "Seismic Response of Uplifting Building Frame." *ASCE J Struct Div*, 104(8), 1211-1229.

Ichinose, T. (1986). "Rocking Motion of Slender Elastic Body on Rigid Floor." *Bulletin of the New Zealand National Society for Earthquake Engineering*, 19(1), 18-27.

Ikegami, R., and Kishinouye, F. (1946). "A Study on the Overturning of Rectangular Columns in the case of the Nankai Earthquake on December 21, 1946." *Bulletin of Earthquake Research Institute*, 24, 49-55.

Ikegami, R., and Kishinouye, F. (1947). "A Study on the Overturning of a Rectangular Column." *Bulletin of Earthquake Research Institute*, 25, 11-18.

Ikegami, R., and Kishinouye, F. (1950). "The Acceleration of Earthquake Motion Deduced from Overturning of the Gravestones in Case of the Imaichi Earthquake on Dec. 26 1949." *Bulletin of Earthquake Research Institute*, 28, 121-127.

Ishiyama, Y. (1982). "Motions of Rigid Bodies and Criteria for Overturning by Earthquake Excitations." *Earthquake Engineering & Structural Dynamics*, 10, 630-650.

Jacobsen, L. S. (1930). "Steady forced vibration as influenced by damping." *Transactions of the American Society of Mechanical Engineers*, 52(1), 169-181.

Jennings, P. C., and Bielak, J. (1973). "Dynamics of building-soil interaction." *Bulletin of the Seismological Society of America*, 63(1), 9-48.

- Kelly, J. M. (1986). "Aseismic base isolation: review and bibliography." *Soil Dynamics and Earthquake Engineering*, 5(4), 202-216.
- Klohn Crippen. (2002). "North Viaduct to Lions Gate Bridge." *Canadian Consulting Engineer*, 43(7), 34-35.
- Koh, A. S., Spanos, P. D., and Roesset, J. M. (1986). "Harmonic rocking of rigid block on flexible foundation." *Journal of Engineering Mechanics*, 112(11), 1165-1180.
- Kurama, Y., Sause, R., Pessiki, S., and Lu, L.-W. (1999a). "Lateral load behavior and seismic design of unbonded post-tensioned precast concrete walls." *ACI Structural Journal*, 96(4), 622-632.
- Kurama, Y., Sause, R., Pessiki, S., and Lu, L.-W. (1999b). "Lateral load behavior and seismic design of unbonded post-tensioned precast concrete walls." *ACI Structural Journal*, 96(4), 622-632.
- Kurama, Y. C. (2000). "Seismic design of unbonded post-tensioned precast concrete walls with supplemental viscous damping." *ACI Structural Journal*, 97(4), 648-658.
- Lin, H., and Yim, S. C. S. (1996). "Nonlinear rocking motions. I: Chaos under noisy periodic excitations." *Journal of Engineering Mechanics*, 122(8), 719-727.
- Makris, N., and Konstantinidis, D. (2003). "The rocking spectrum and the limitations of practical design methodologies." *Earthquake Engineering and Structural Dynamics*, 32(2), 265-289.
- McConnel, R. E. (1970). "Seismic response of a proposed railway viaduct," A report submitted in partial fulfilment of the requirements for the degree of Master of Engineering at the University of Canterbury, Christchurch, New Zealand, University of Canterbury, Christchurch, N.Z.
- McManus, K. J. (1980). "The seismic response of bridge structures free to rock on their foundations," A report submitted in partial fulfilment of the requirements for the degree of Master of Engineering at the University of Canterbury, Christchurch, New Zealand, University of Canterbury, Christchurch, N.Z.
- Meek, J. W. (1975). "Effects of Foundation Tipping on Dynamic Response." *Journal of the Structural Division, ASCE*, 101(7), 1297-1311.
- Milne, J. (1881). "Experiments in observational seismology." *Transactions of the Seismological Society of Japan*, 3, 12-64.
- Milne, J. (1908). *Seismology*, Kegan Paul, Trench, Trubner, & Co. Ltd., London.
- Milne, J., and Omori, F. (1893). "On the Overturning and fracturing of Brick and Other Columns by Horizontally Applied Motion." *Seismological Journal of Japan*, 17, 59-86.

- Muto, K., Umemura, H., and Sonobe, Y. (1960). "Study of overturning vibration of slender structures." *2nd World Conference on Earthquake Engineering*, Tokyo, Japan, 1239.
- Neild, S. A., McFadden, P. D., and Williams, M. S. (2003). "A review of time-frequency methods for structural vibration analysis." *Engineering Structures*, 25(6), 713-728.
- Ogawa, N. (1977). "A study on Rocking and Overturning of Rectangular Column." *Report of the National Research Center for disaster Prevention*(18), 14.
- Omori, F. (1900). "Note on the Great Mino-Owari Earthquake of Oct. 28th 1911." *Publications of the Earthquake Investigation Committee in foreign language*, 4(2), 13-24.
- Omori, F. (1902). "On the Overturning and Sliding of Columns." *Publications of the Earthquake Investigation Committee in foreign language*, 12(2), 8-27.
- Palermo, A., Pampanin, S., and Calvi, G. M. (2005). "Concept and development of hybrid solutions for seismic resistant bridge systems." *Journal of Earthquake Engineering*, 9(6), 899-921.
- Pampanin, S. (2006). "Controversial aspects in seismic assessment and retrofit of structures in modern times: Understanding and implementing lessons from ancient heritage." *Bulletin of the New Zealand Society for Earthquake Engineering*, 39(2), 120-134.
- Park, R., and Paulay, T. (1975). *Reinforced concrete structures*, John Wiley & Sons, New York.
- Peña, F., Prieto, F., Lourenço, P. B., Campos Costa, A., and Lemos, J. V. (2007). "On the dynamics of rocking motion of single rigid-block structures." *Earthquake Engineering and Structural Dynamics*, 36(15), 2383-2399.
- Priestley, M. J. N. (1991). "Overview of PRESSS research program." *PCI Journal*, 36(4), 50-57.
- Priestley, M. J. N., Calvi, G. M., and Kowalsky, M. J. (2007). *Displacement-based seismic design of structures*, IUSS Press : Fondazione Eucentre, Pavia.
- Priestley, M. J. N., Evison, R. J., and Carr, A. J. (1978). "Seismic Response of Structures Free to Rock on their Foundations." *Bulletin of the New Zealand National Society for Earthquake Engineering*, 11(3), 10.
- Priestley, M. J. N., and Grant, D. N. (2005). "Viscous Damping in Seismic Design and Analysis." *Journal of Earthquake Engineering*, 9(Special Issue 2), 27.
- Priestley, M. J. N., Sritharan, S., Conley, J. R., and Pampanin, S. (1999). "Preliminary results and conclusions from the PRESSS five-story precast concrete test building." *PCI Journal*, 44(6), 42-67.

Psycharis, I. N. (1991). "Effect of base uplift on dynamic response of SDOF structures." *Journal of Structural Engineering*, 117(3), 733-754.

Psycharis, I. N. (2008). "Investigation of the dynamic response of rigid footings on tensionless Winkler foundation." *Soil Dynamics and Earthquake Engineering*, 28(7), 577-591.

Psycharis, I. N., Papastamatiou, D. Y., and Alexandris, A. P. (2000). "Parametric investigation of the stability of classical columns under harmonic and earthquake excitations." *Earthquake Engineering & Structural Dynamics*, 29, 1093-1109.

Rahman, A., and Restrepo, J. I. (2000). "Earthquake Resistant Precast Concrete Buildings: Seismic Performance of Cantilever Walls Prestressed using Unbonded Tendons." *Research Report 2000-5*, Department of Civil Engineering, University of Canterbury, Christchurch, New Zealand.

Restrepo, J. I., and Rahman, A. (2007). "Seismic performance of self-centering structural walls incorporating energy dissipators." *Journal of Structural Engineering*, 133(11), 1560-1570.

Richart, F. E., Hall, J. R., and Woods, R. D. (1970). *Vibrations of soils and foundations*, Prentice-Hall, Englewood Cliffs, N.J.

Seed, H. B., and Idriss, I. M. (1970). "Soil Moduli and Damping Factors for Dynamic Response Analyses." *EERC 70-10*, Earthquake Engineering Research Center, University of California, Berkeley.

Sharpe, R. D., and Skinner, R. I. (1983). "The Seismic Design of an Industrial Chimney with Rocking Base." *Bulletin of the New Zealand Society for Earthquake Engineering*, 16(2), 98-106.

Shenton, H. W., and Jones, N. P. (1991). "Base excitation of rigid bodies. I. Formulation." *Journal of Engineering Mechanics*, 117(10), 2286-2306.

Spanos, P. D., and Koh, A.-S. (1984). "Rocking of rigid blocks due to harmonic shaking." *Journal of Engineering Mechanics*, 110(11), 1627-1642.

Standards New Zealand. (2004). *NZS 4230:2004, Design of Reinforced Concrete Masonry Structures*, Standards New Zealand, Wellington.

Standards New Zealand. (2004). *NZS 1170.5:2004, Structural design actions - Part 5: Earthquake actions New Zealand*, Standards New Zealand, Wellington.

Timoshenko, S., and Goodier, J. N. (1951). *Theory of Elasticity*, McGraw-Hill, New York.

Toranzo, L. A., Carr, A. J., and Restrepo, J. I. (2001). "Displacement Based Design of Rocking Walls Incorporating Hysteretic Energy Dissipators." *7th International Seminar on Seismic Isolation, Passive Energy Dissipation and Active Control of Vibrations of Structures*, Assisi, Italy, 10.

Veletsos, A. S., and Verbic, B. (1973). "Vibration of Viscoelastic Foundations." *Earthquake Engineering and Structural Dynamics*, 2(1), 87-102.

Wight, G. D. (2006). "Seismic performance of a post-tensioned concrete masonry wall system," A report submitted in partial fulfilment of the requirements for the degree of Doctor of Philosophy at the University of Auckland, University of Auckland, Auckland, N.Z.

Wight, G. D., Ingham, J. M., and Kowalsky, M. J. (2006). "Shaketable testing of rectangular post-tensioned concrete masonry walls." *ACI Structural Journal*, 103(4), 587-595.

Wight, G. D., Kowalsky, M. J., and Ingham, J. M. (2004). "Shake Table Testing Of Post-Tensioned Concrete Masonry Walls." *RD-04-04*, North Carolina State University, Raleigh, NC, USA.

Wong, C. M., and Tso, W. K. (1989). "Steady state rocking response of rigid blocks part 2: experiment." *Earthquake Engineering & Structural Dynamics*, 18(1), 107-120.

Xu, C., and Spyarakos, C. C. (1996). "Seismic analysis of towers including foundation uplift." *Engineering Structures*, 18(4), 271-278.

Yim, C.-S., and Chopra, A. K. (1983a). "Effects of Transient Foundation Uplift on Earthquake Response of Structures." *UCB/EERC-83/09*, Earthquake Engineering Research Center, University of California, Berkeley.

Yim, C.-S., and Chopra, A. K. (1983b). "Effects of transient foundation uplift on earthquake response of structures." *UCB/EERC-83/09*, University of California, Berkeley.

Yim, S. C. S., and Chopra, A. K. (1984a). "Dynamics Of Structures On Two-Spring Foundation Allowed To Uplift." *Journal of Engineering Mechanics, ASCE*, 110(7), 1124-1146.

Yim, S. C. S., and Chopra, A. K. (1984b). "Earthquake Response of Structures with Partial Uplift on Winkler Foundation." *Earthquake Engineering & Structural Dynamics*, 12, 263-281.

Yim, S. C. S., and Chopra, A. K. (1985). "Simplified Earthquake Analysis Of Multistory Structures With Foundation Uplift." *Journal of Structural Engineering*, 111(12), 2708-2731.

Yim, S. C. S., Chopra, A. K., and Penzien, J. (1980). "Rocking Response of Rigid Blocks to Earthquakes." *Earthquake Engineering & Structural Dynamics*, 8, 565-587.

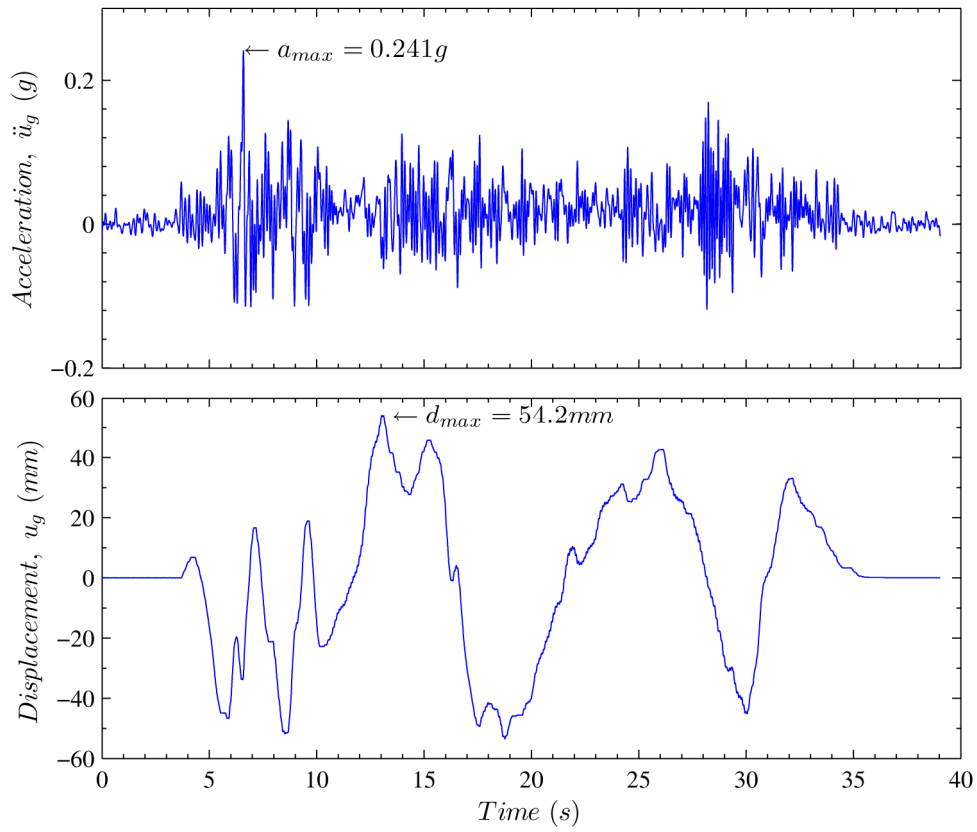
Zhang, J., and Makris, N. (2001). "Rocking response of free-standing blocks under cycloidal pulses." *Journal of Engineering Mechanics*, 127(5), 473-483.

# Appendix A

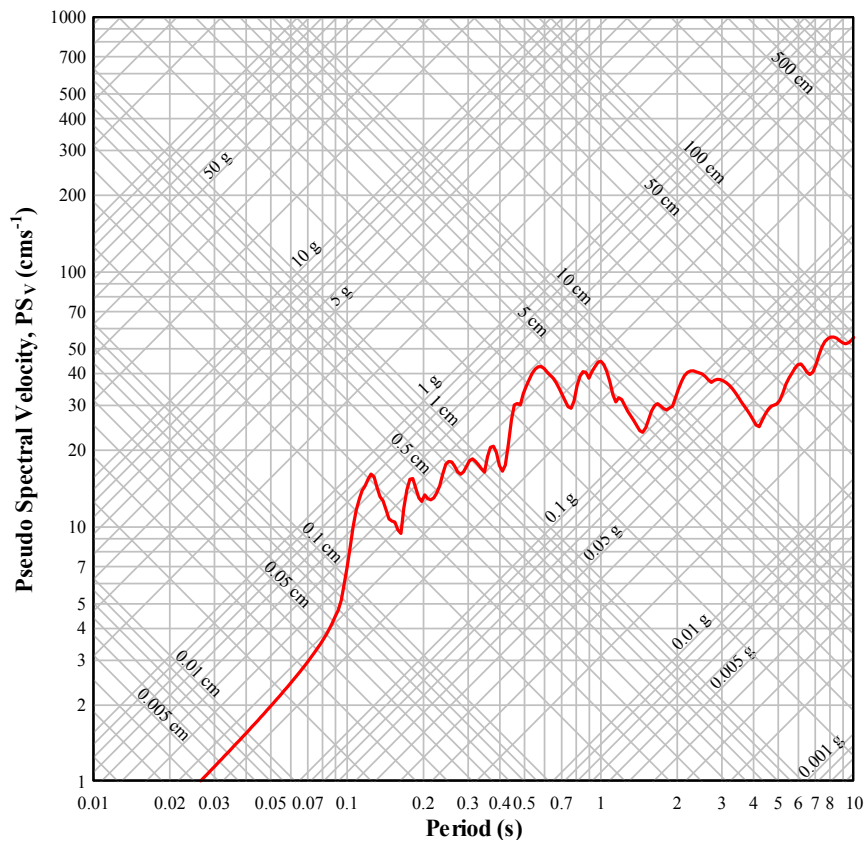
---

## **DETAILED RESULTS FOR THE ANALYSES OF CONTROLLED ROCKING SYSTEMS**

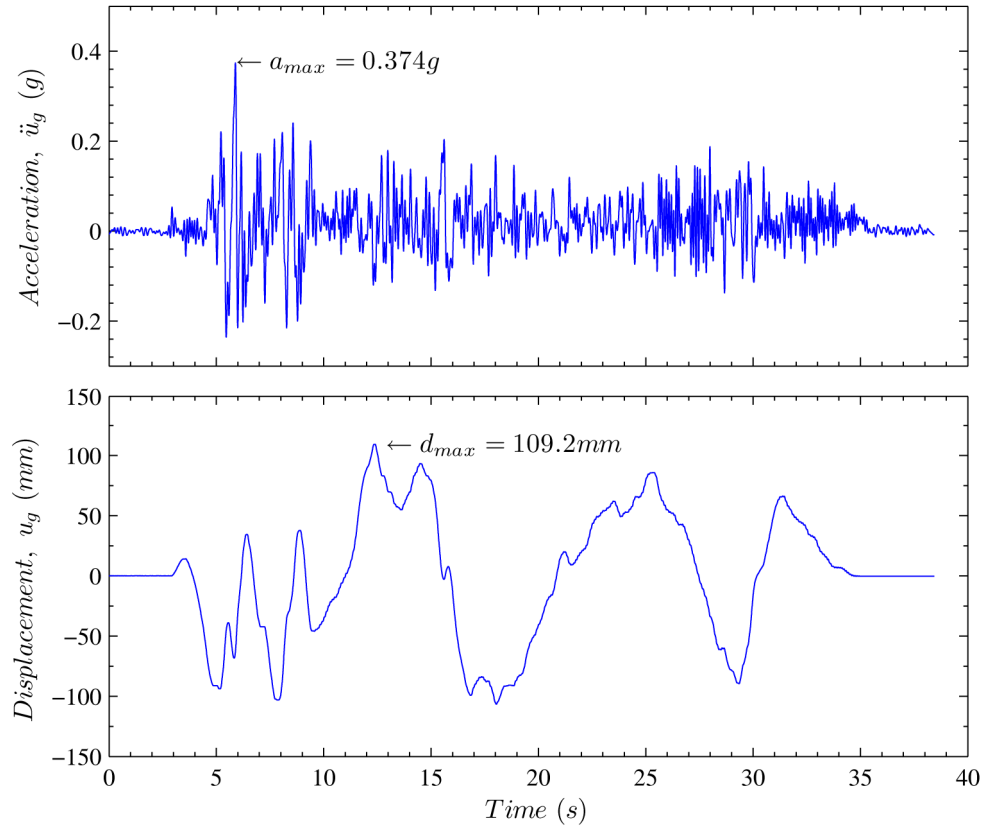
---



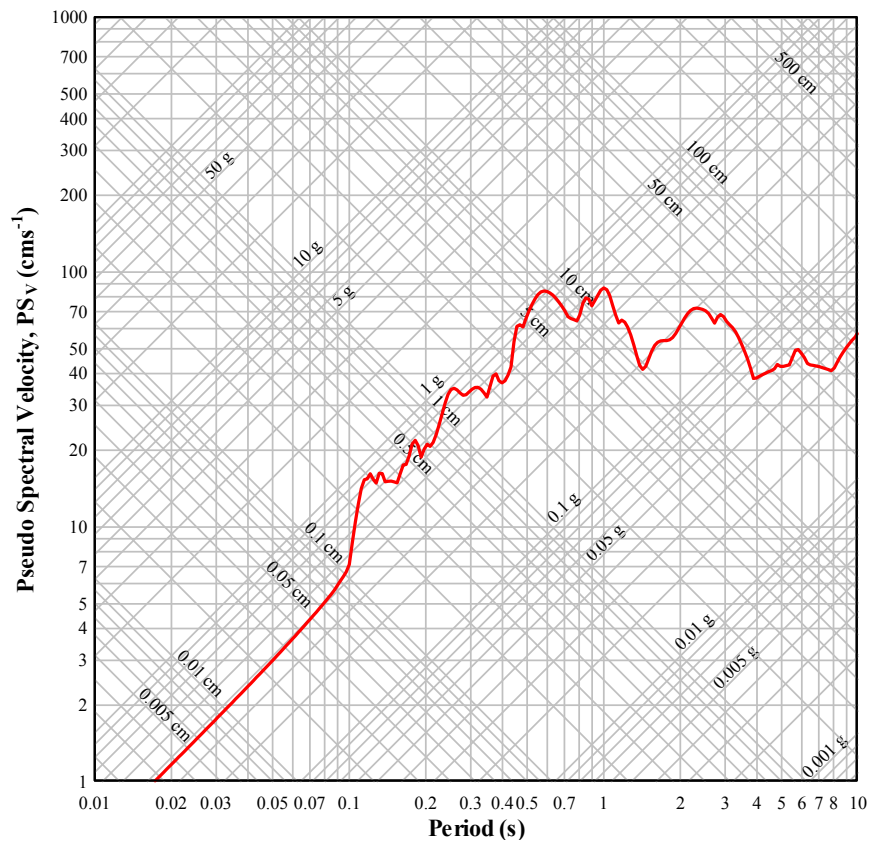
**Figure A-1 – Acceleration and Displacement traces of Run 1 (El Centro-A0.5-T1)**



**Figure A-2 – Response spectrum of Run 2 (El Centro-A0.5-T1), (5% damping)**



**Figure A-3 – Acceleration and Displacement traces of Run 2 (El Centro-A1-T1)**



**Figure A-4 – Response spectrum of Run 2 (El Centro-A1-T1), (5% damping)**

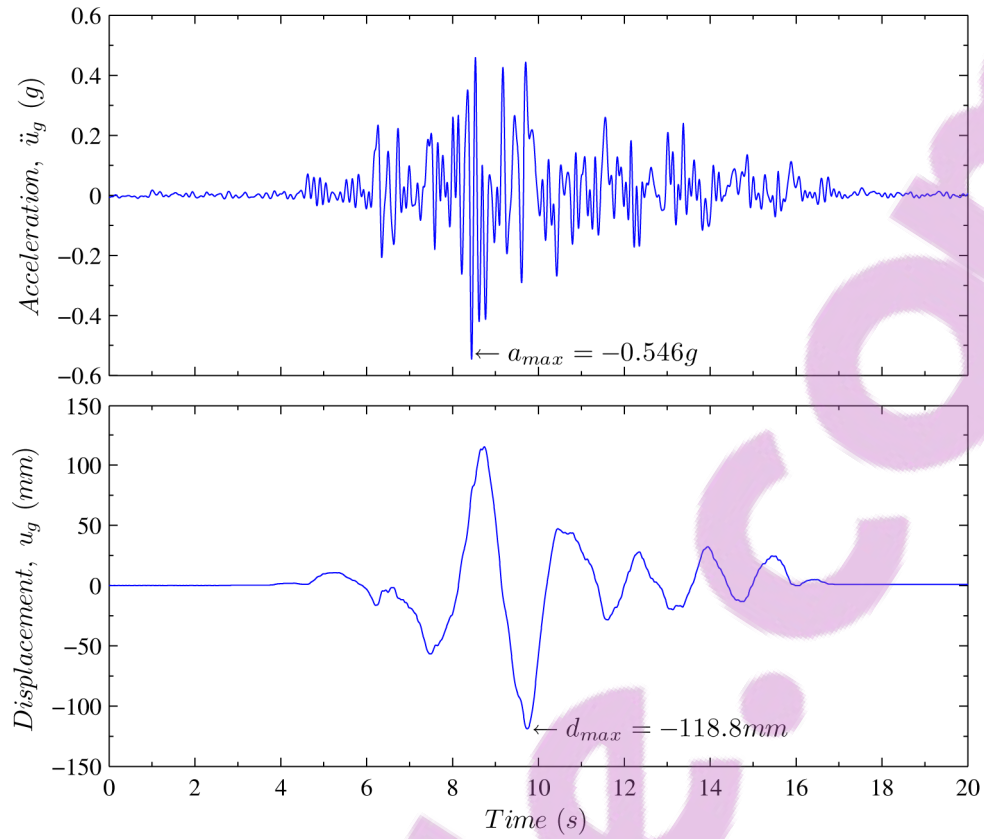


Figure A-5 – Acceleration and Displacement traces of Run 3 (Tabas-A1-T0.38)

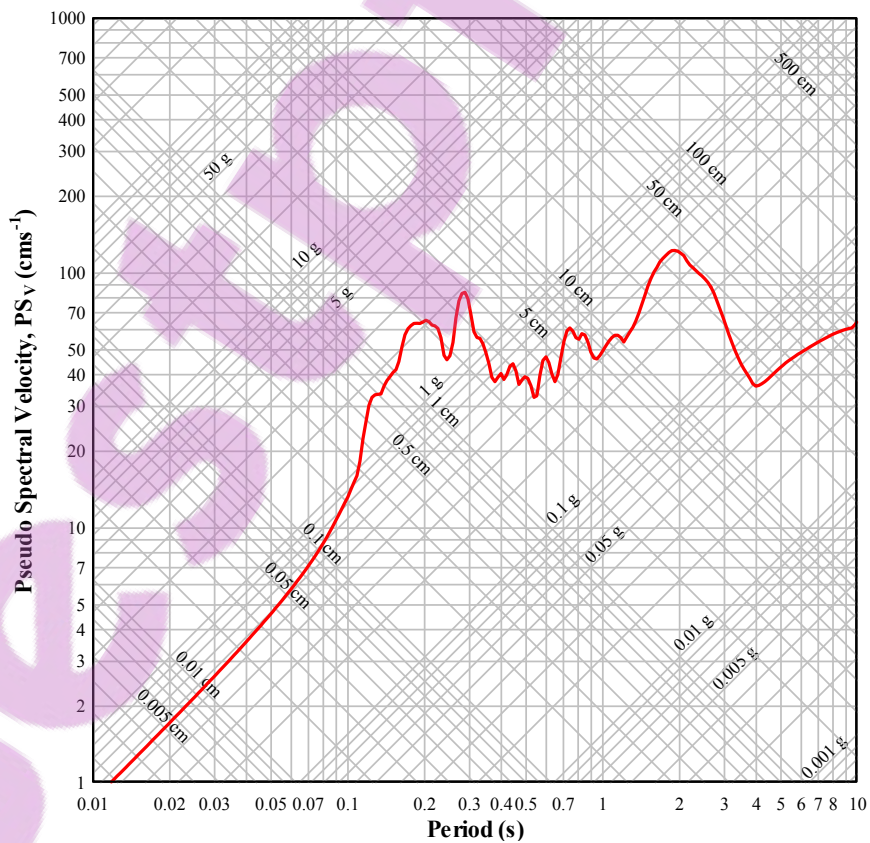


Figure A-6 – Response spectrum of Run 3 (Tabas-A1-T0.38), (5% damping)

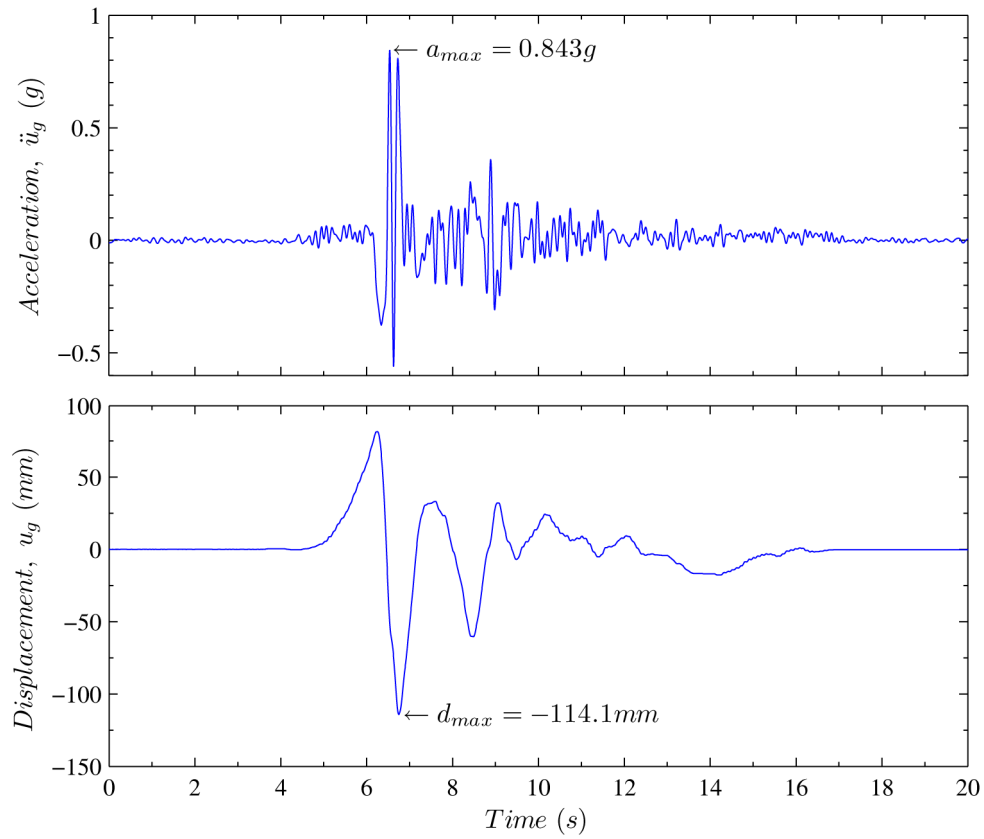


Figure A-7 – Acceleration and Displacement traces of Run 4 (Sylmer-A1-T0.6)

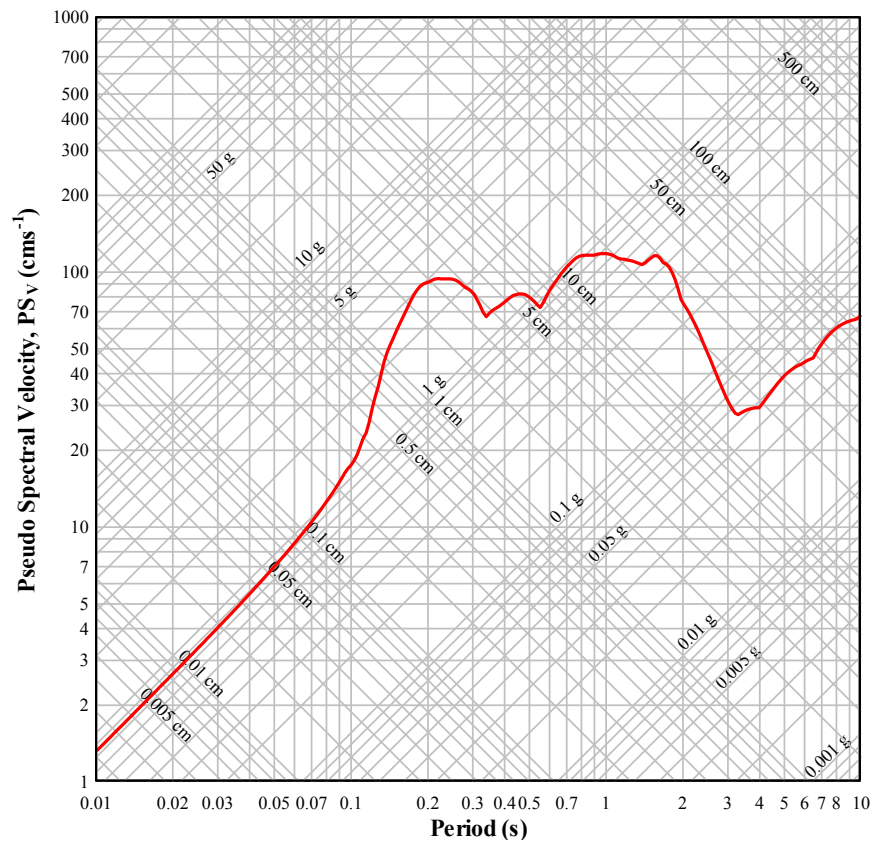


Figure A-8 – Response spectrum of Run 4 (Sylmer-A1-T0.6), (5% damping)

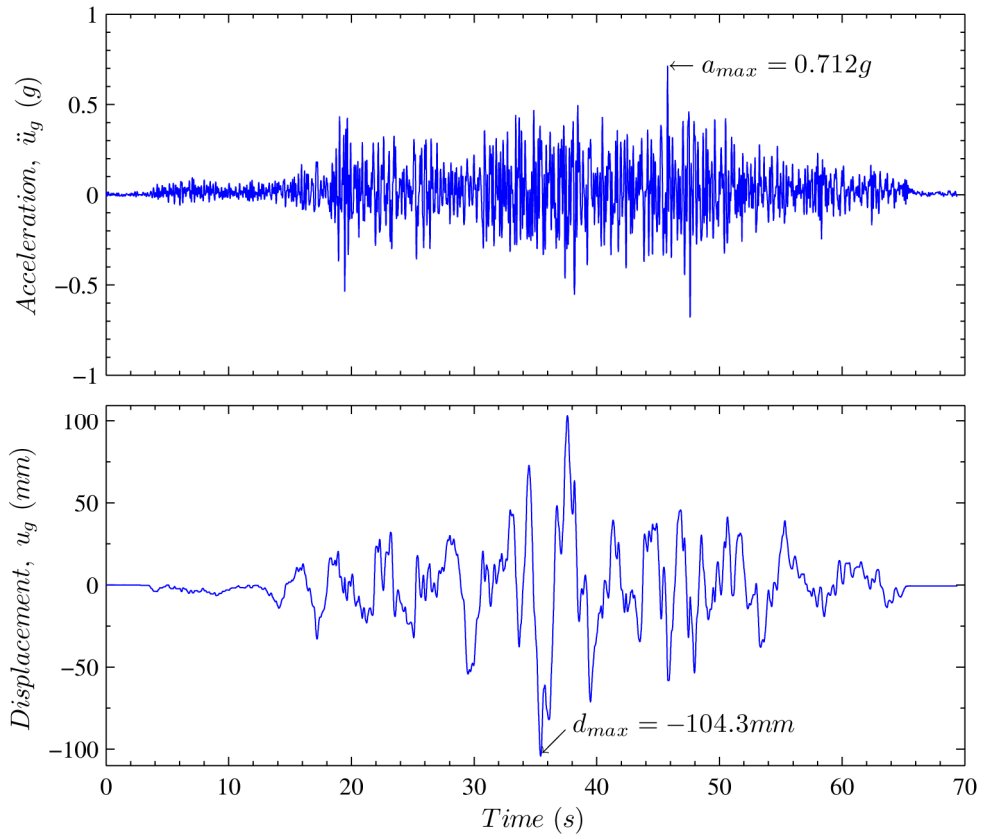


Figure A-9–Acceleration and Displacement traces of Run 6 (Valparaiso-A1-T1)

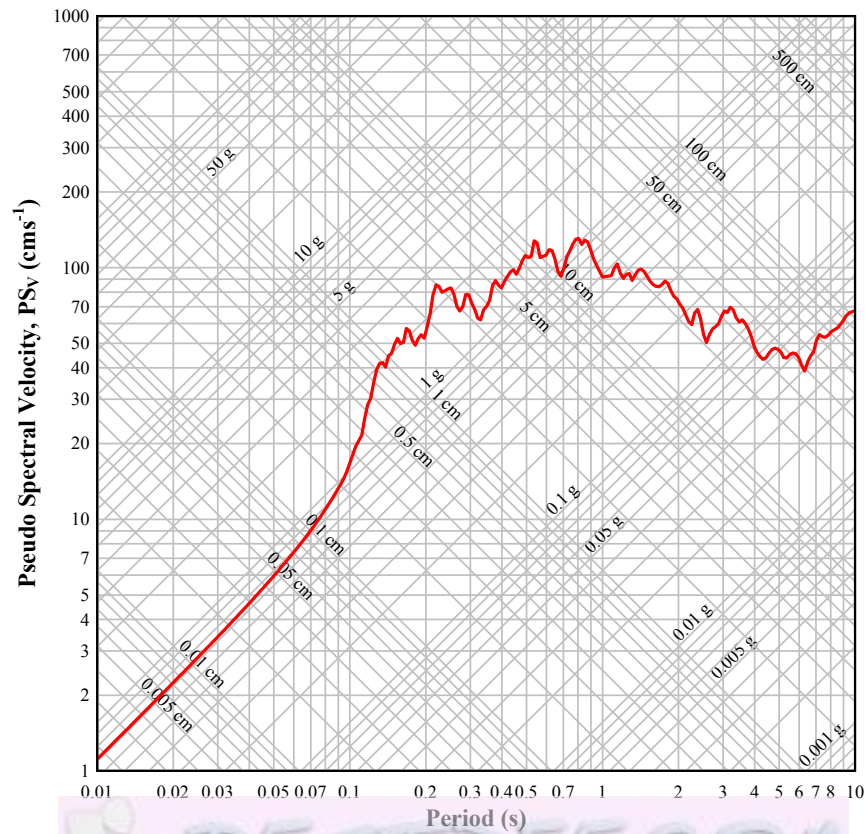


Figure A-10–Response spectrum of Run 6 (Valparaiso-A1-T1), (5% damping)

**Table A-1 – Wall response at peak displacements and zero crossings**

Time (s)	ToW Disp. (mm)	ToW Vel. (ms <sup>-1</sup> )	ToW Accel. (ms <sup>-2</sup> )	Tendon Force (kN)	Uplift Left, $u'_L$ (mm)	Uplift Right, $u'_R$ (mm)	Dist. to O' from wall edge (mm)
0	-30.41	-0.04	19.52	133.39	-0.56	11.32	78.20
0.0634	-1.68	0.77	0.02	79.29	-0.11	0.52	230.98
0.1350	29.51	-0.03	-14.99	126.81	10.64	-0.74	95.92
0.1979	1.20	-0.75	0.03	78.77	0.32	0.05	299.11
0.2600	-25.89	-0.02	15.52	122.99	-0.53	9.58	83.29
0.3185	-3.04	0.70	0.02	80.02	-0.15	0.77	243.80
0.3850	23.84	0.01	-13.82	116.51	8.74	-0.60	95.08
0.4469	1.09	-0.65	0.01	78.61	0.43	0.06	210.91
0.5050	-20.96	-0.02	13.75	112.10	-0.49	7.62	91.27
0.5600	-2.36	0.62	0.00	78.60	-0.17	0.70	229.93
0.6250	19.39	-0.03	-13.07	108.08	7.01	-0.47	94.16
0.6788	1.23	-0.56	0.00	78.13	0.41	0.03	237.43
0.7350	-17.12	0.00	12.32	104.07	-0.45	6.17	98.77
0.7861	-1.72	0.53	0.03	77.96	-0.12	0.44	337.35
0.8450	15.79	-0.01	-12.44	101.27	5.73	-0.42	98.87
0.8964	0.81	-0.50	-0.01	77.48	0.23	0.09	127.87
0.9500	-14.02	0.01	11.35	98.32	-0.39	4.87	105.80
0.9960	-1.65	0.46	0.01	77.24	-0.08	0.34	313.24
1.0500	11.67	-0.01	-10.02	94.05	4.09	-0.35	109.69
1.0965	0.23	-0.42	0.02	76.43	0.13	0.10	169.69
1.1450	-10.70	0.01	8.99	92.59	-0.35	3.71	116.83
1.1851	-1.76	0.39	0.00	76.86	-0.11	0.37	277.13
1.2350	8.01	-0.01	-7.45	88.16	2.85	-0.15	81.37
1.2736	0.31	-0.35	0.02	76.65	0.12	0.15	98.47
1.3150	-7.22	0.01	6.58	85.20	-0.28	2.16	148.21
1.3541	-0.44	0.31	-0.02	76.72	0.05	0.15	474.77
1.3900	6.01	0.00	-8.28	83.80	1.87	-0.13	97.95
1.4280	0.11	-0.28	0.00	76.52	0.08	0.11	300.94
1.4650	-5.94	-0.01	8.32	83.54	-0.25	1.79	156.60
1.4991	-1.02	0.26	0.00	76.51	-0.02	0.20	73.91
1.5350	4.10	-0.02	-9.00	80.21	1.04	-0.08	101.97
1.5652	-0.24	-0.23	0.00	75.92	-0.02	0.15	131.38
1.5950	-4.53	-0.01	9.41	80.23	-0.29	1.26	219.28
1.6277	-0.62	0.20	-0.02	75.85	-0.06	0.17	220.09
1.6550	3.02	0.01	-10.15	78.26	0.60	-0.04	94.75
1.6844	-0.11	-0.17	0.01	75.57	-0.05	0.11	494.24
1.7100	-3.19	-0.02	9.48	77.55	-0.28	0.68	326.11
1.7378	-0.64	0.16	0.00	75.77	-0.16	0.19	494.59
1.7650	1.97	-0.01	-8.69	76.65	0.40	0.00	18.84
1.7882	-0.12	-0.13	0.01	75.56	-0.10	0.13	392.90
1.8150	-2.21	0.02	7.74	76.17	-0.26	0.39	436.44
1.8353	-0.61	0.11	0.01	75.63	-0.18	0.18	508.00
1.8600	1.18	0.01	-6.09	75.81	0.08	0.04	343.86
1.8856	-0.36	-0.10	0.00	75.57	-0.14	0.13	508.00
1.9100	-1.82	0.01	6.42	75.81	-0.24	0.29	508.00

# Appendix B

---

## DERIVATION OF THE INDIVIDUAL ENERGY COMPONENTS OF A PCM WALL

---

### B.1 GRAVITATIONAL POTENTIAL ENERGY

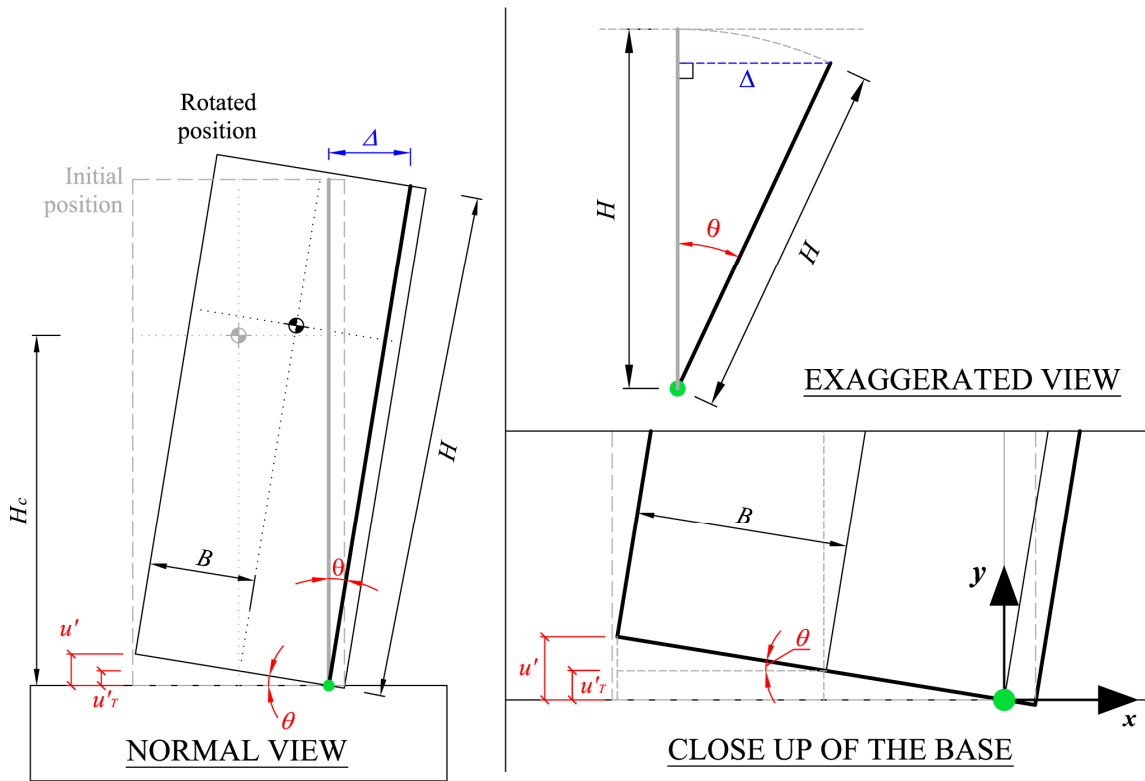
The gravitational potential energy for the PCM wall is a function of the vertical displacement of the mass centroid. As the wall does not fall below the initial upright position, it is convenient to adopt that position as the reference level at which other energies are calculated.

Since the mass centroid of the PCM wall lies on the centreline and the centre of rotation shifts as the wall is displaced (see Figure 4-16), the vertical displacement of the mass centroid is in fact approximately the uplift at the tendon location ( $u'_T$ ).

This can be shown by considering a rotated wall as shown in Figure B-1. Assuming a near rigid body system, the original y co-ordinate of the centroid is  $H_c$ , and the new y co-ordinate of the rotated wall is,  $u'_T + H_c \cos \theta$ . In other words, the vertical displacement is  $u'_T + H_c (\cos \theta - 1)$ . Now assuming small angle rotations,  $\cos \theta \approx 1$ , the vertical displacement of the mass centroid is hence simply  $u'_T$ .

Next inspecting the close-up view of the base in Figure B-1, it can be readily seen that the uplift at the tendon location is,

$$u'_T = u' - B \sin \theta \quad (\text{B-1})$$



**Figure B-1 – Geometric relationships of a rotating PCM wall**

Substituting  $\sin \theta = \frac{\Delta}{H}$  into Equation B-1, a geometric relationship that is evident upon inspection of exaggerated view in Figure B-1, this leads to the following expression for the uplift at the tendon location

$$u'_T = u' - \frac{B|\Delta|}{H} \tag{B-2}$$

Substituting the approximation formula for the wall edge uplift (Equation 4-9):

$$u'_T = \frac{|\Delta|}{\sqrt{H^2 - \Delta^2}} \left( 920 - 412 e^{-\left(\frac{\Delta}{3.551}\right)^2} \right) - \frac{B|\Delta|}{H} \tag{B-3}$$

This leads to the expression for the gravitational potential energy ( $U$ ).

$$U(\Delta) = m_T g \left( \frac{|\Delta|}{\sqrt{H^2 - \Delta^2}} \left( 920 - 412 e^{-\left(\frac{\Delta}{3.551}\right)^2} \right) - \frac{B|\Delta|}{H} \right) \tag{B-4}$$

## B.2 KINETIC ENERGY

The kinetic energy content of the PCM wall can be shown to be simply the rotational energy about the centre of rotation. This may appear to have neglected the translational kinetic energy. However this is not the case and can be shown to give the same results compared to calculations using centre of mass properties. This is because the calculation of moment of inertia about the rotational centre captures the translational motion of the individual mass particles. Consequently, the approximate expression for the kinetic energy of the PCM wall is derived as follows.

Consider a PCM wall displaced by a lateral displacement  $\Delta$  as in Figure 4-19. The rotation and the lateral displacement can be related by Equation B-5.

$$\sin(\theta) = \frac{\Delta}{H} \quad (\text{B-5})$$

Taking the time derivative of Equation B-5,

$$\dot{\theta} = \frac{\dot{\Delta}}{H \cos(\theta)} = \frac{\dot{\Delta}}{\sqrt{H^2 - \Delta^2}} \quad (\text{B-6})$$

Adopting small angle approximations again, in other words  $\sin \theta \approx \theta$  and  $\cos \theta \approx 1$ ,

$$\dot{\theta} \approx \frac{\dot{\Delta}}{H} \quad (\text{B-7})$$

Accordingly, the kinetic energy of the PCM wall can be estimated by Equation B-8.

$$E_k(\dot{\Delta}) = \frac{1}{2H^2} I_o \dot{\Delta}^2 \quad (\text{B-8})$$

Now as the centre of rotation shifts, a portion of the wall on the compression side of the rotation centre is in contact with the ground and is assumed not to rotate. This leads to a variable reduction of  $I_o$ . Although the maximum effect of this is only a 3% reduction, this must be included in the energy calculation as the maximum reduction coincides with maximum velocity and consequently greatly amplifies the error. An approximate expression for  $I_o$  as a function of the detached wall length ( $d$ ) is presented in Equation B-9.

$$I_o = \underbrace{\left[ 686 + \frac{577.56}{3} (H^2 + d^2) \right]}_{\text{Contribution from wall mass}} + \underbrace{\left[ 442 + 1438.5 (2.537^2 + d^2) \right]}_{\text{Contribution from added mass}} \text{ kgm}^2 \quad (\text{B-9})$$

### B.3 ELASTIC POTENTIAL ENERGY

The elastic potential energy of the PCM wall is stored and released through the elongation and contraction of the prestressing tendon as the wall displaces. Since the experiment recorded the tendon force, the elastic potential energy would be most accurately evaluated using the change in tendon force directly. The general formula for the change in elastic potential energy is listed in Equation B-10. Where  $x$  is the extension of the tendon referenced against the length with zero force, and  $x_1$  and  $x_2$  are the two tendon lengths at which the change in potential energy is sought.

$$\Delta U_E = \int_{x_1}^{x_2} kx \, dx \quad (\text{B-10})$$

Now as the PCM wall is post-tensioned, the tendon is already at some force level, the application of Equation B-10 requires knowledge of the extension at this state, as any increase or decrease in force results in a trapezoidal area under the force-displacement diagram.

Subsequent calculations show that in order to attain a tendon tension of 75.6 kN between two anchors 3100 mm apart, the initial length of the tendon ( $L_T$ ) is 3093.5 mm or  $x_1 = 6.4564$  mm.

Assuming the prestressing tendon remains elastic, the axial stiffness of the system is  $EA/L_T$ . Consequently, elongation for a particular tendon force can be calculated by Equation B-11 below.

$$x_2 = \frac{[P_{Tendon}(\Delta)]L_T}{EA} \quad (\text{B-11})$$

Accordingly, if the tendon remains elastic, an expression for the elastic potential energy of the PCM wall is found by substituting Equation B-11 and  $x_1 = 6.4564$  mm into Equation B-10. The result is presented as Equation B-12 which has origin  $U_E = 0$  at the initial post-tensioned, zero displacement state.

$$U_E = \int_{6.4564}^{\frac{P_{Tendon}(\Delta)L_T}{EA}} \frac{EA}{L_T} x \, dx$$

$$U_E(\Delta) = \frac{L_T}{2EA} [P_{Tendon}(\Delta)]^2 - \frac{EA}{2L_T} (6.4564 \text{E-}03)^2$$

$$U_E(\Delta) = \frac{L_T}{2EA} [P_{tendon}(\Delta)]^2 - 244.050 \quad (\text{Joules}) \quad (\text{B-12})$$

If the PCM wall is displaced beyond the displacement which causes yielding of the post-tensioning tendon, Equation B-12 is no longer valid as the elastic potential energy is no longer simply the trapezoidal area between two points under a straight line.

Assuming the behaviour of the post-tensioning tendon is elasto-plastic, the elastic potential energy at the post yield displacements would be a function of the extension beyond the yield extension.

Substituting the tendon yield stress of 900 MPa and the tendon yield extension of 13.58 mm from the current experiment, the elastic potential energy content of the system post tendon yield is thus,

$$U_E(\Delta) = \int_{6.4564}^{13.5814} \frac{EA}{L_T} x \, dx + 159.03 \times [\Delta L_T(\Delta) - (13.5814 - 6.4564)]$$

$$U_E(\Delta) = 159.03 \times \Delta L_T(\Delta) - 297.22 \quad (\text{Joules}) \quad (\text{B-13})$$

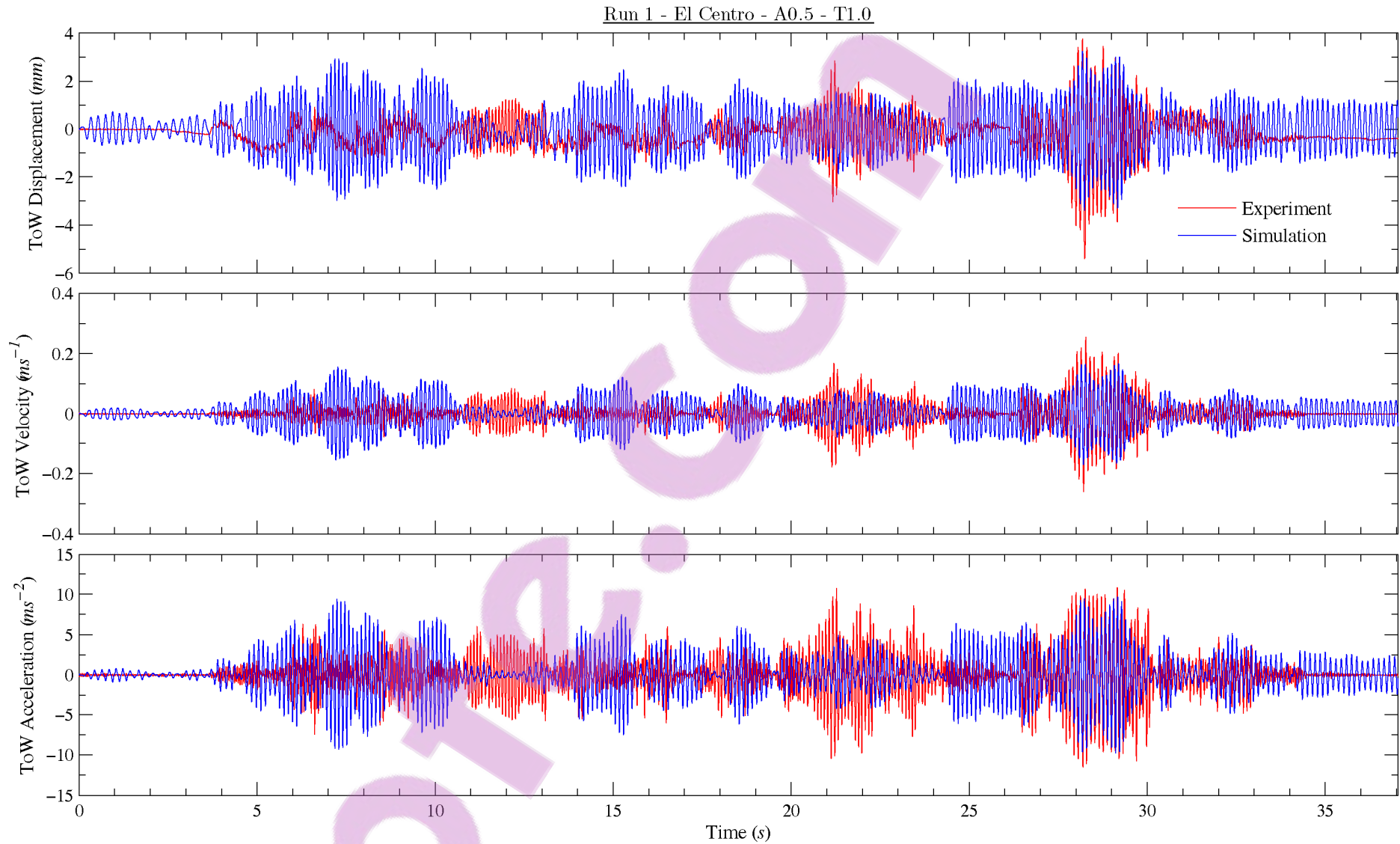
where the extension of the tendon,  $\Delta L_T(\Delta)$ , is still governed by the geometric constraints which can be calculated from Equation 4-15.

# Appendix C

---

## **SIMULATED TIME-HISTORIES OF THE SHAKE TABLE TESTS**

---



**Figure C-1 – Simulation Results using the unmodified nonlinearly elastic equivalent SDOF approach (Run 1 – El Centro A-0.5 T-1.0)**

Run 2 - El Centro - A1.0 - T1.0

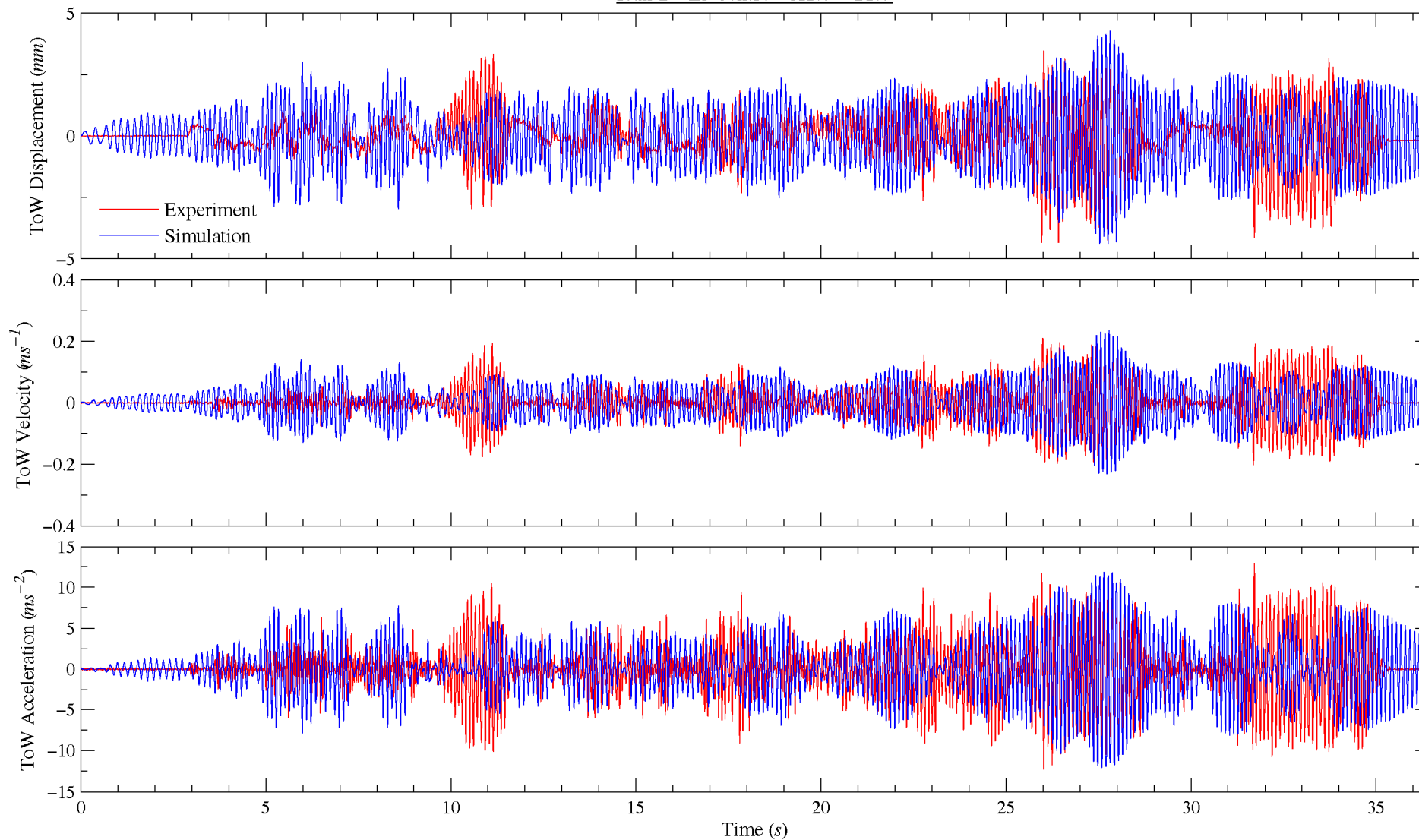
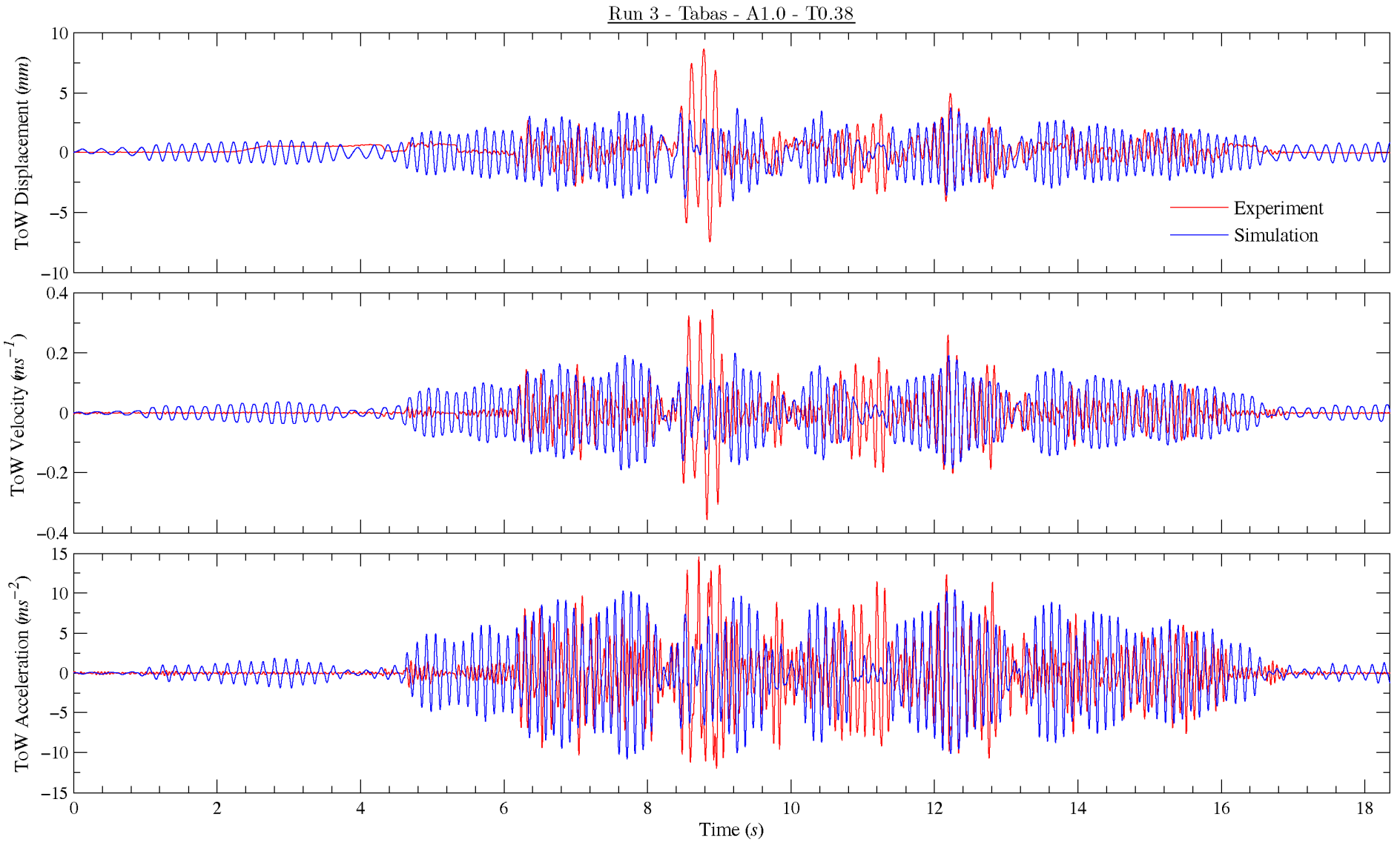
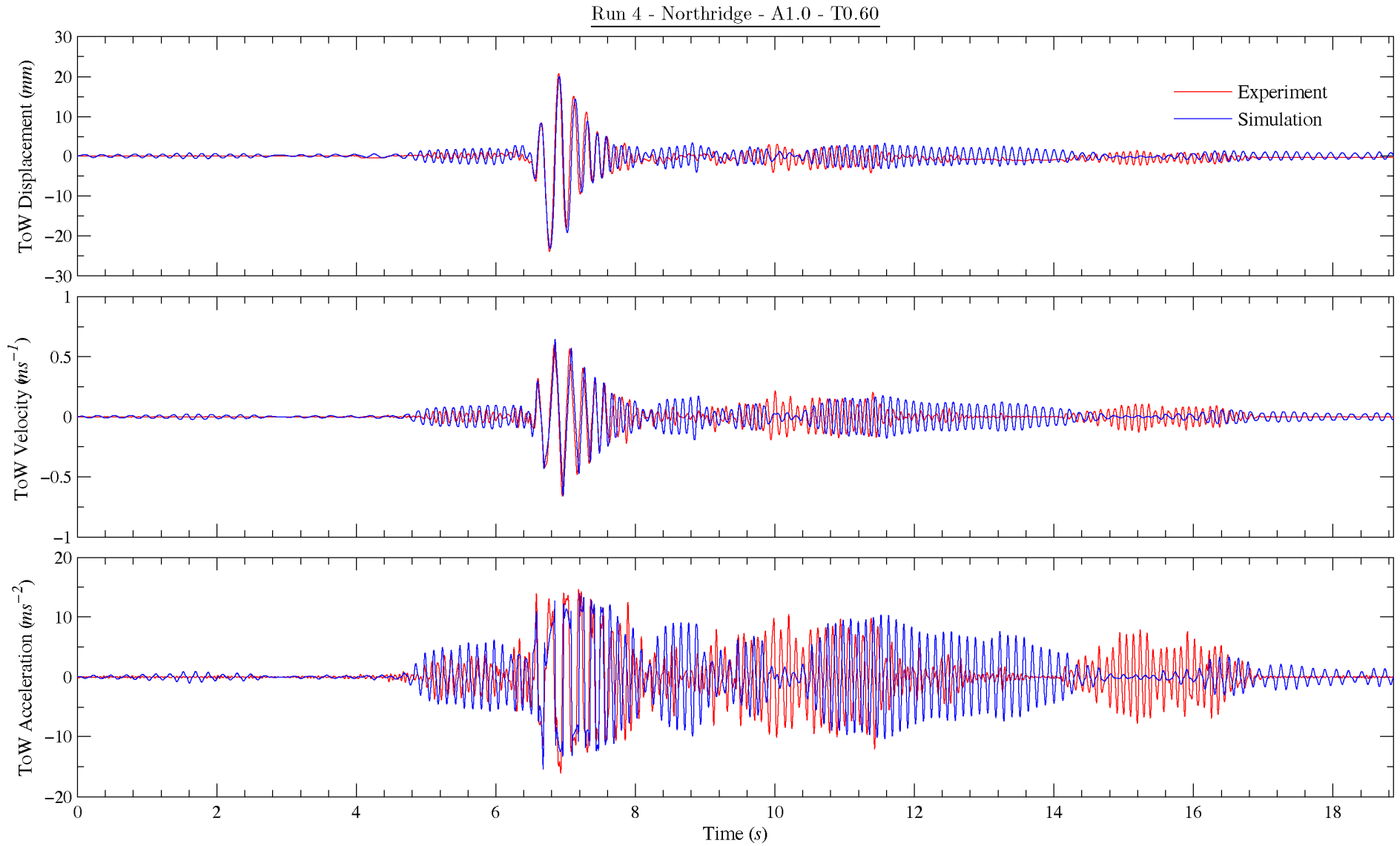


Figure C-2 – Simulated results using the unmodified nonlinearly elastic equivalent SDOF approach (Run 2 – El Centro A-1.0 T-1.0)



**Figure C-3 – Simulated results using the unmodified nonlinearly elastic equivalent SDOF approach (Run 3 – Tabas A-1.0 T-0.38)**



**Figure C-4 – Simulated results using the unmodified nonlinearly elastic equivalent SDOF approach (Run 4 – Northridge A-1.0 T-0.6)**

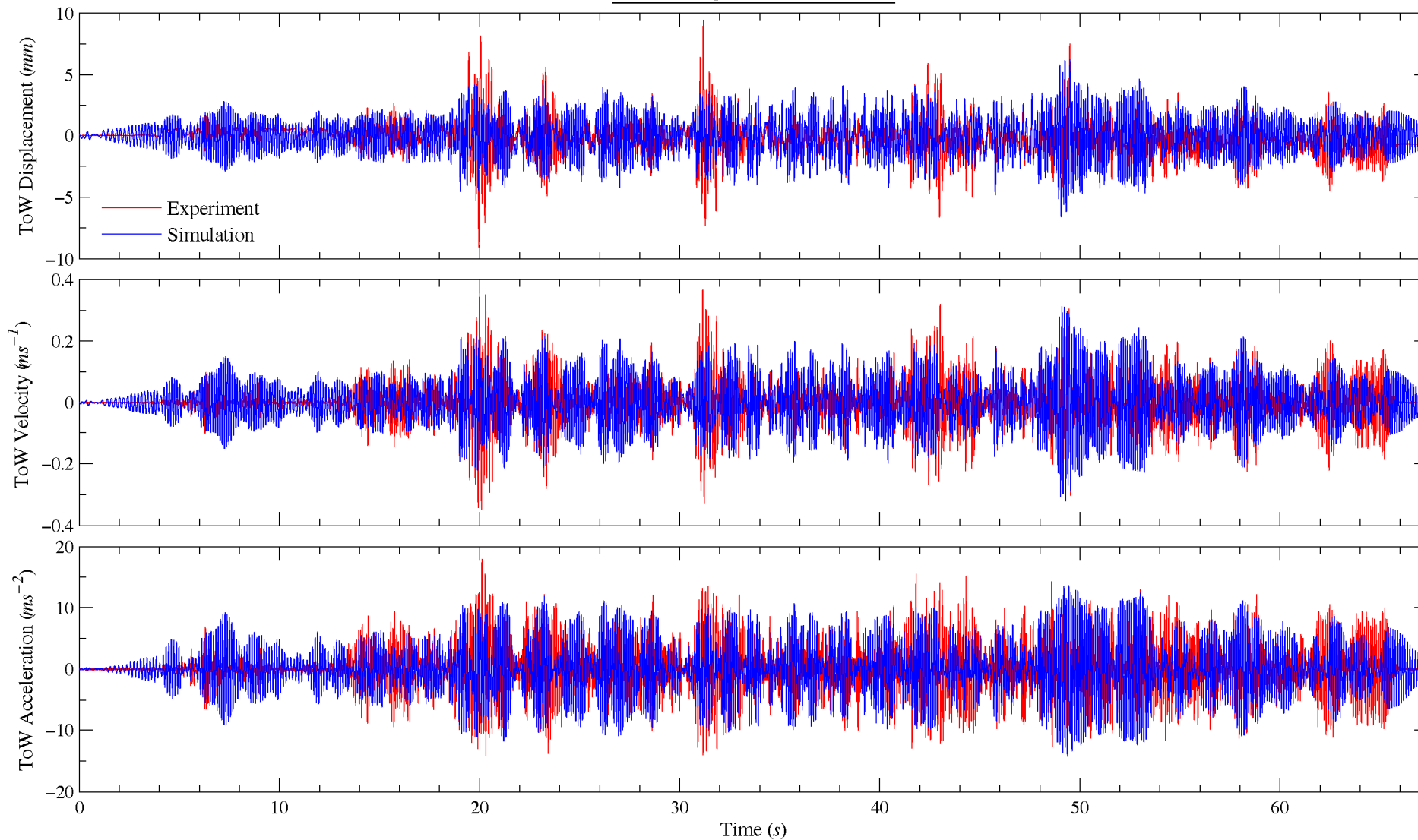
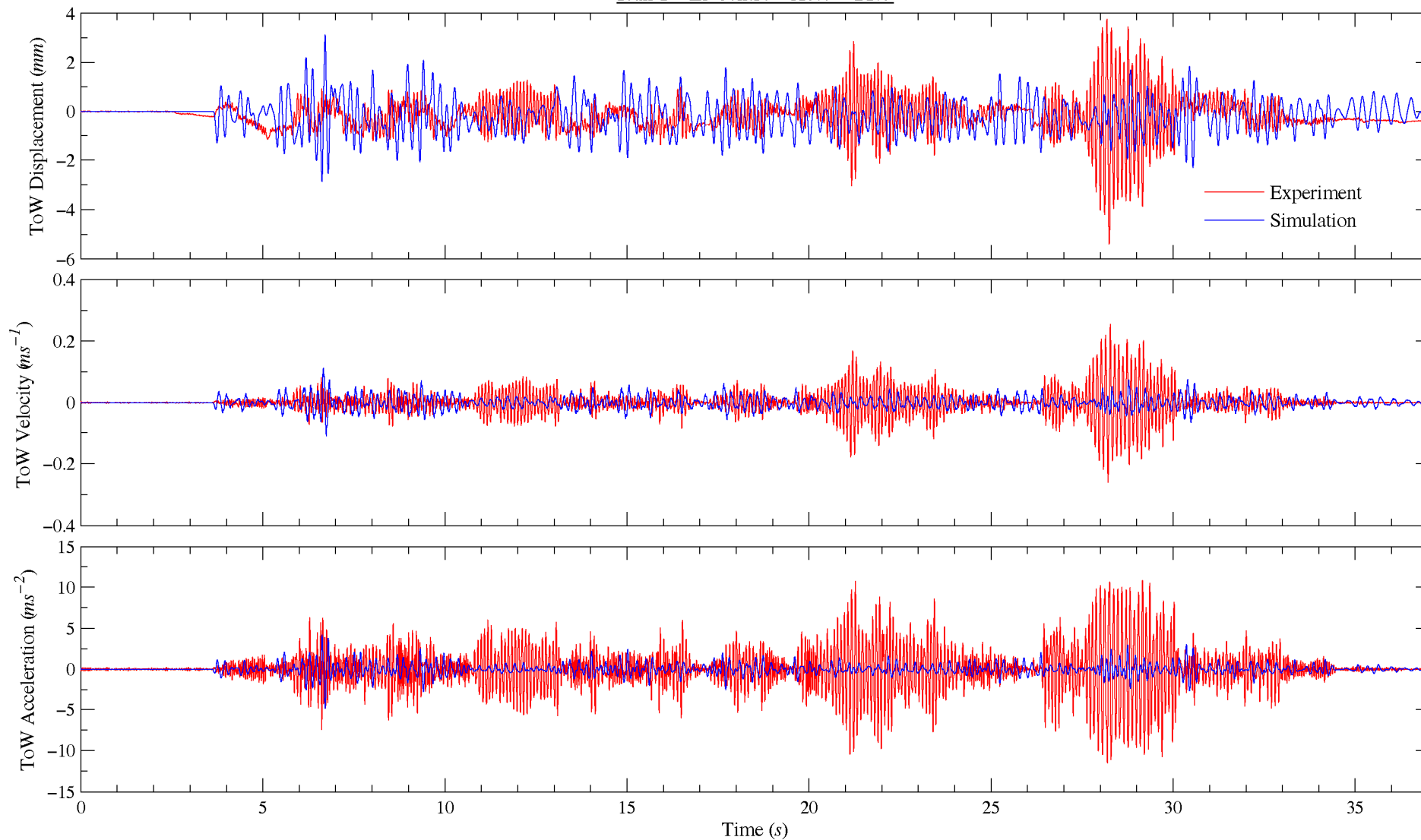


Figure C-5 – Simulated results using the unmodified nonlinearly elastic equivalent SDOF approach (Run 6 – Valparaiso A-1.0 T-1.0)

Run 1 - El Centro - A0.5 - T1.0



- 263 -

Figure C-6– Simulated results using the MHSg approach from free vibration analysis (Run 1 – El Centro A-0.5 T-1.0)

Run 2 - El Centro - A1.0 - T1.0

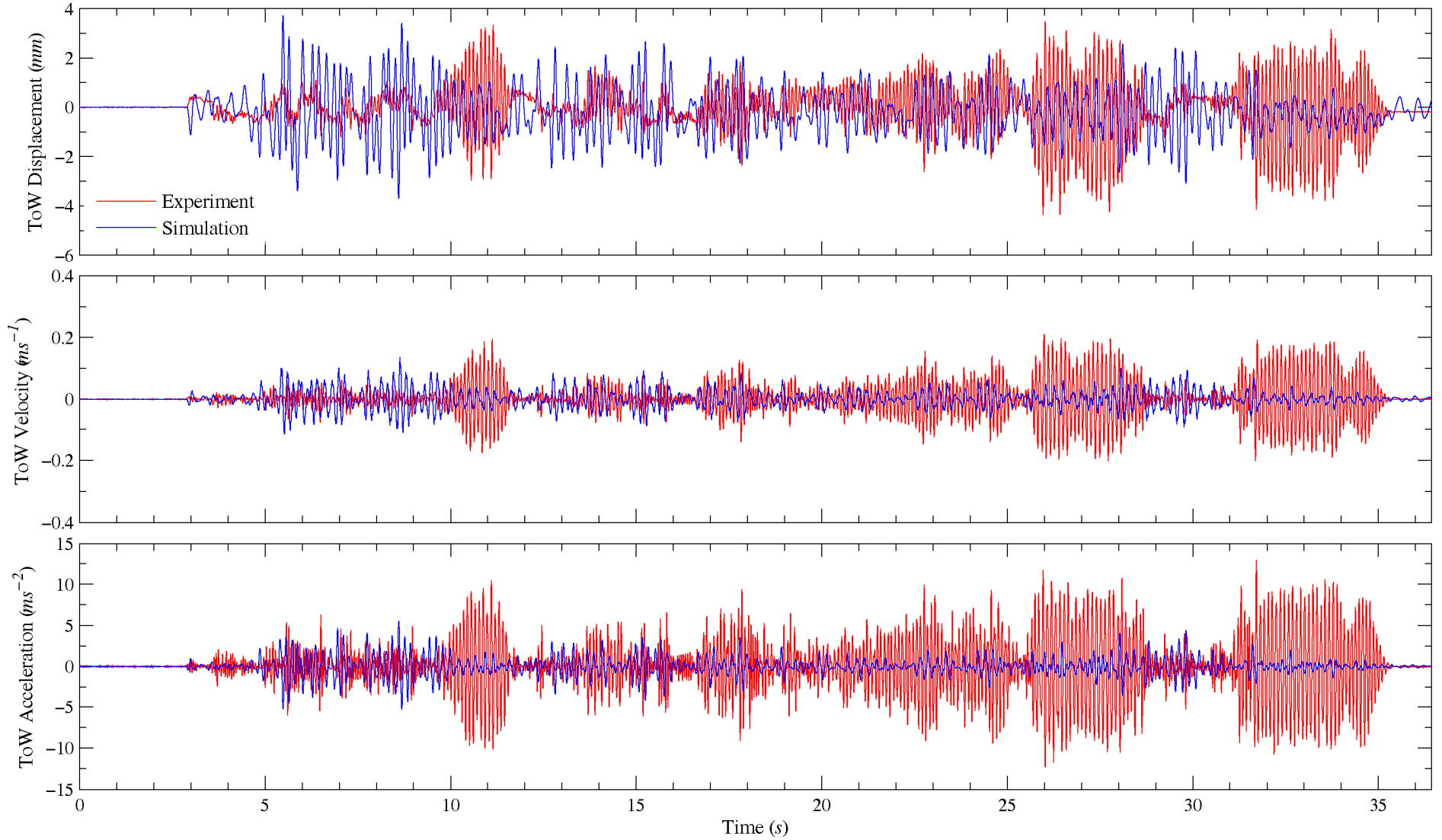
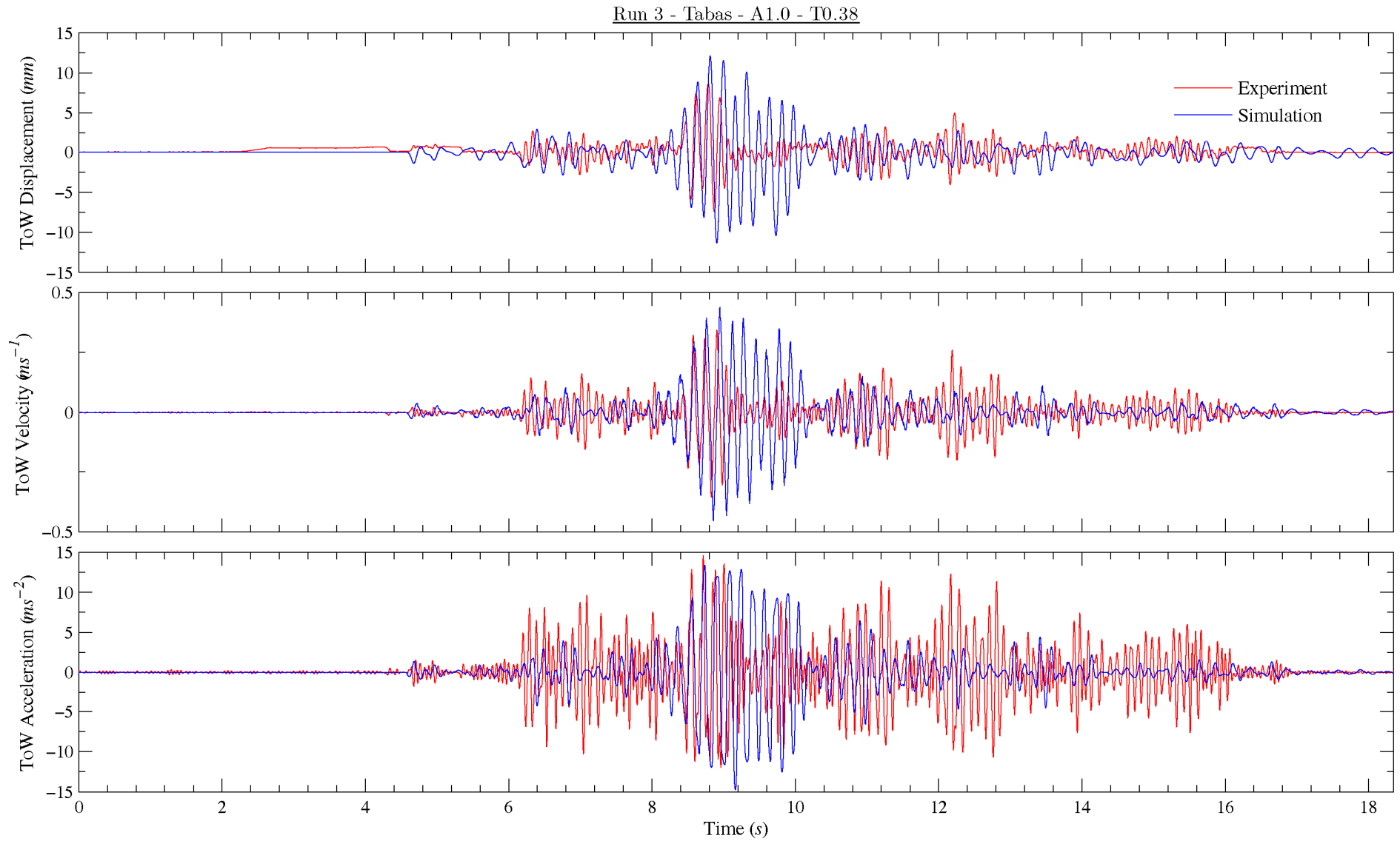
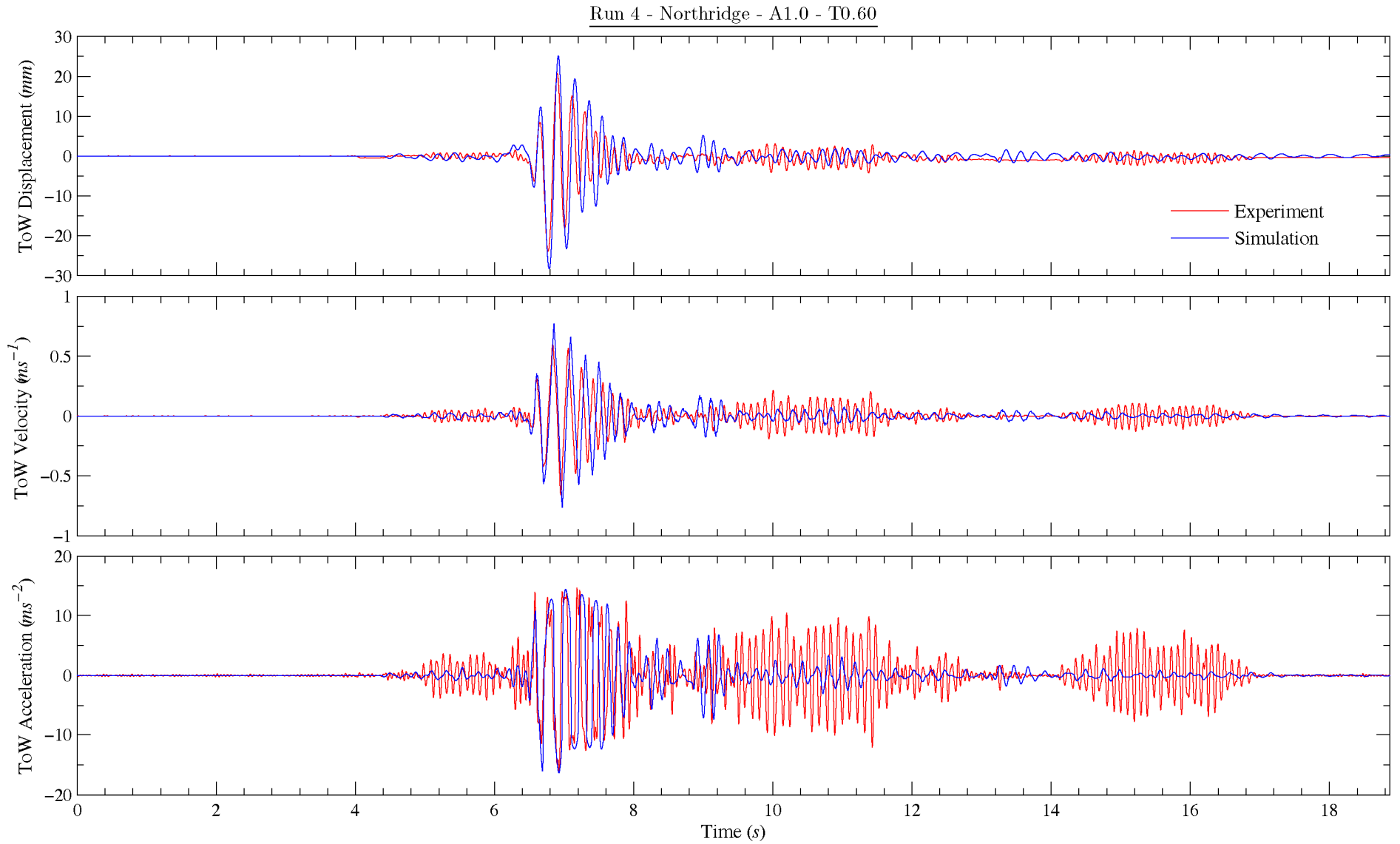


Figure C-7– Simulated results using the MHSg approach from free vibration analysis (Run 2 – El Centro A-1.0 T-1.0)

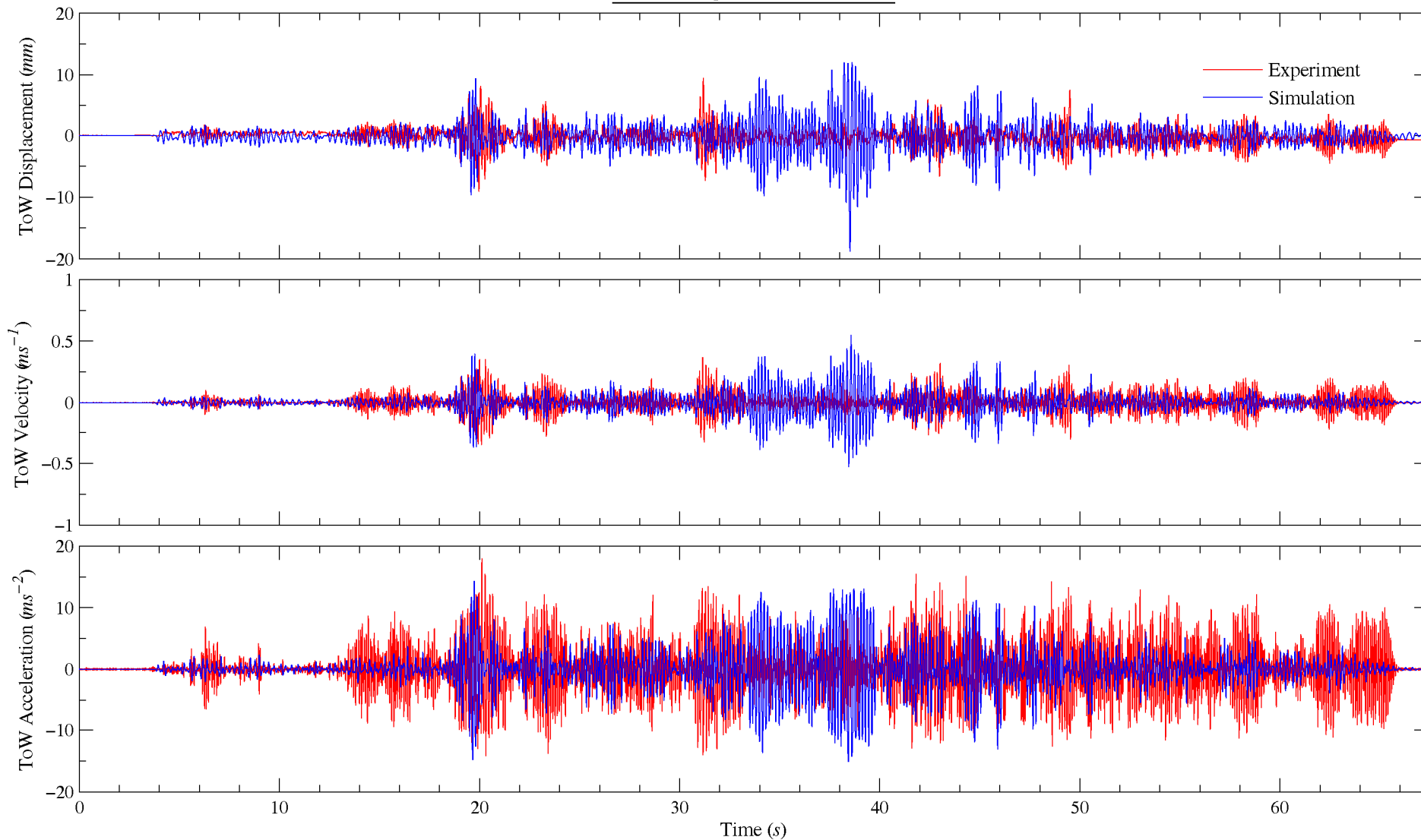


**Figure C-8 – Simulated results using the MHS approach from free vibration analysis (Run 3 – Tabas A-1.0 T-0.38)**



**Figure C-9 – Simulated results using the MHSg approach from free vibration analysis (Run 4 – Northridge A-1.0 T-0.6)**

Run 6 - Valparaiso - A1.0 - T1.0



- 267 -

Figure C-10 – Simulated results using the MHS approach from free vibration analysis (Run 6 – Valparaiso A-1.0 T-1.0)

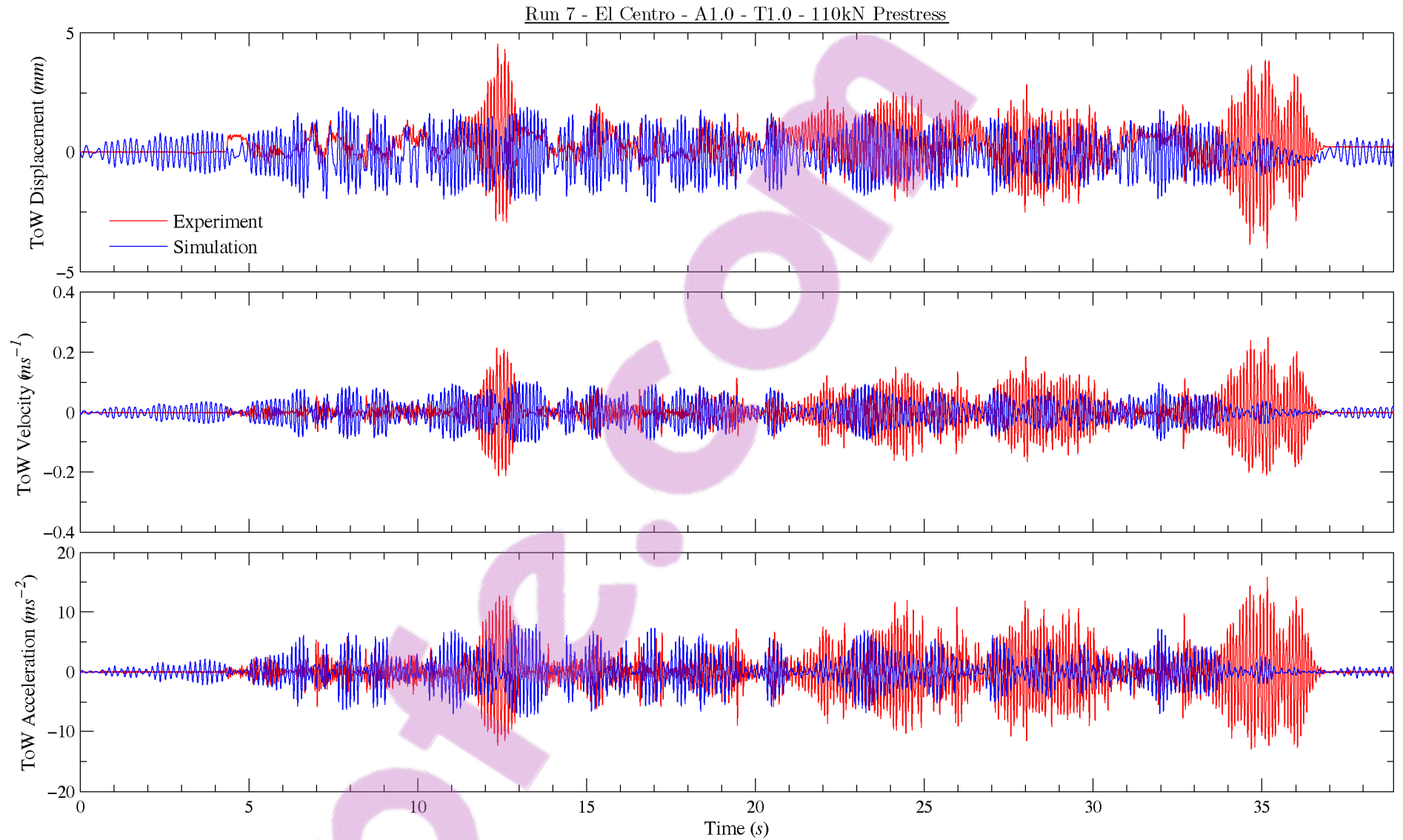


Figure C-11 – Simulated results using the SDOF approach with a constant  $r = 0.835$  (Run 7 – El Centro A-1.0 T-1.0, 110kN prestress)

Run 8 - Tabas - A1.0 - T0.38 - 110kN Prestress

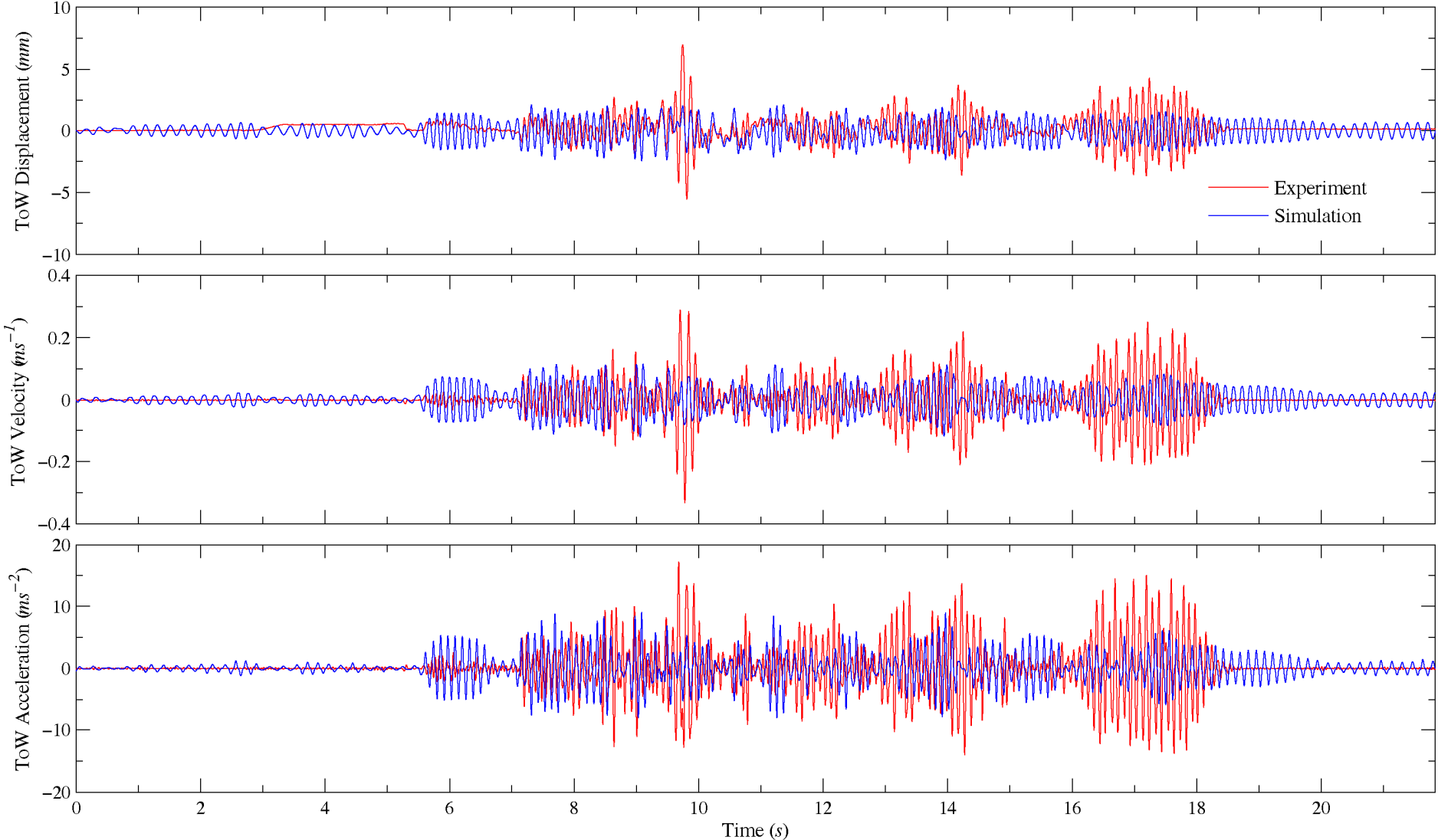
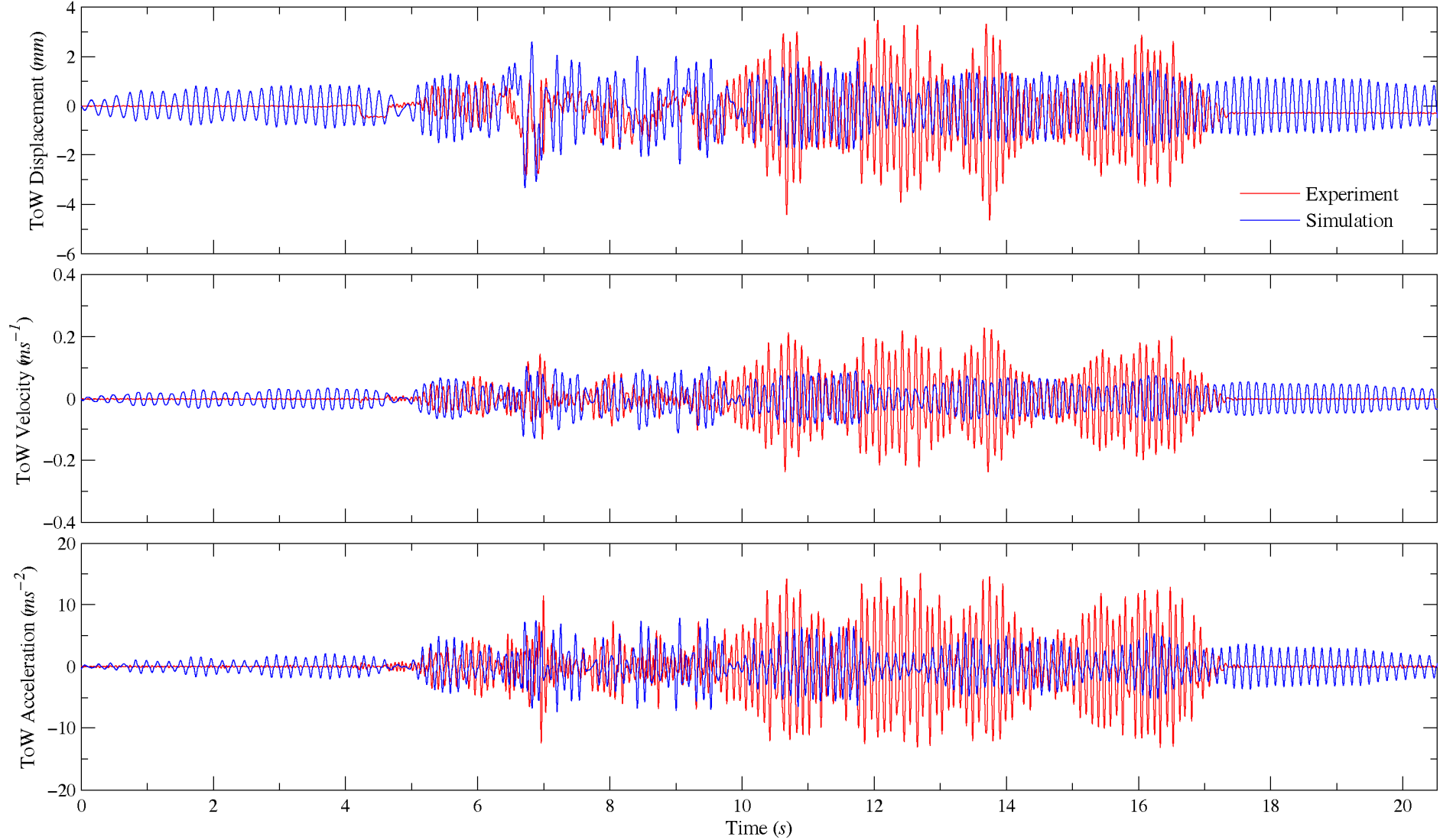


Figure C-12 – Simulated results using the SDOF approach with a constant  $r = 0.835$  (Run 8 Tabas A-1.0 T-0.38, 110kN prestress)

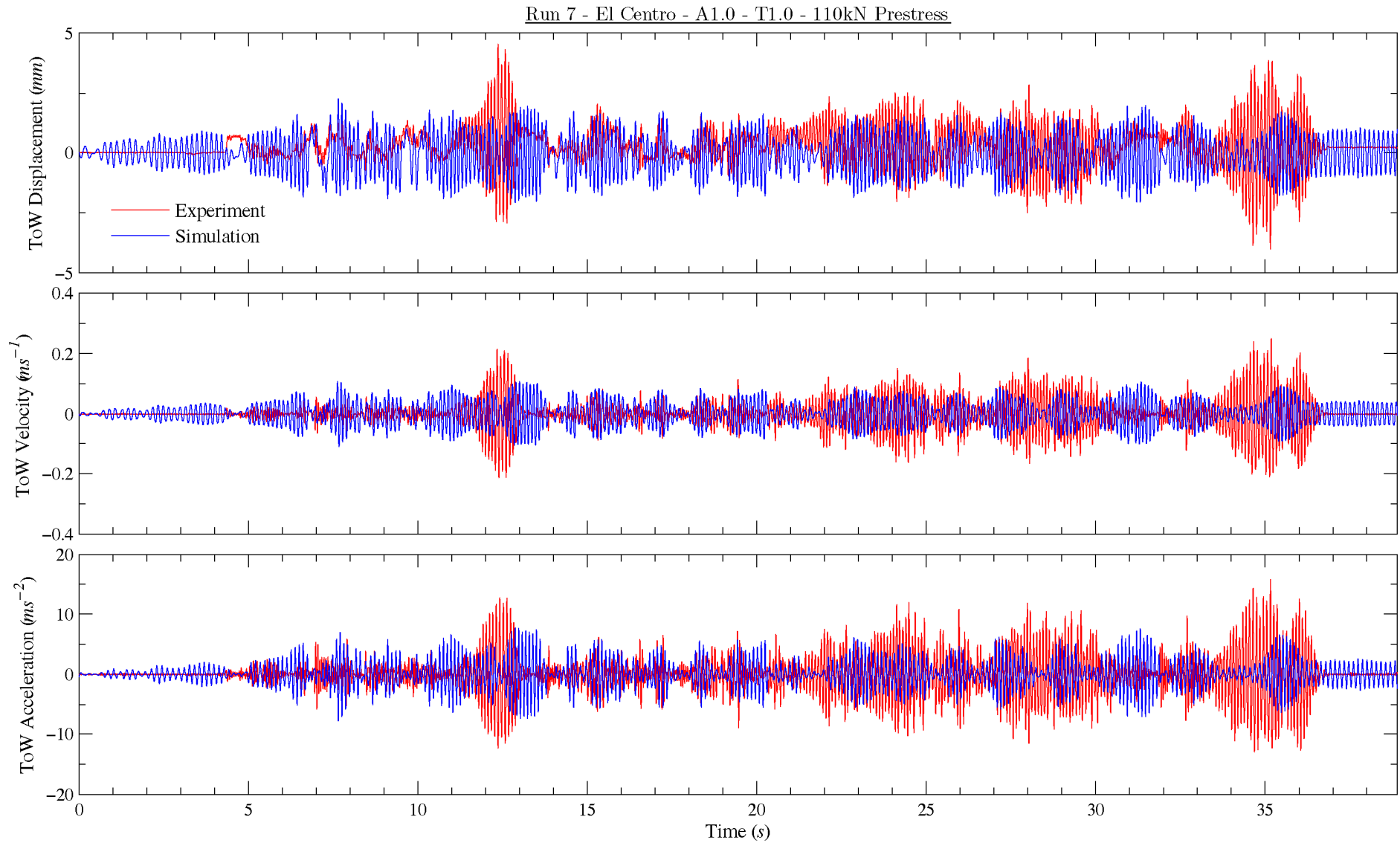
Run 9 - Northridge - A1.0 - T0.60 - 110kN Prestress



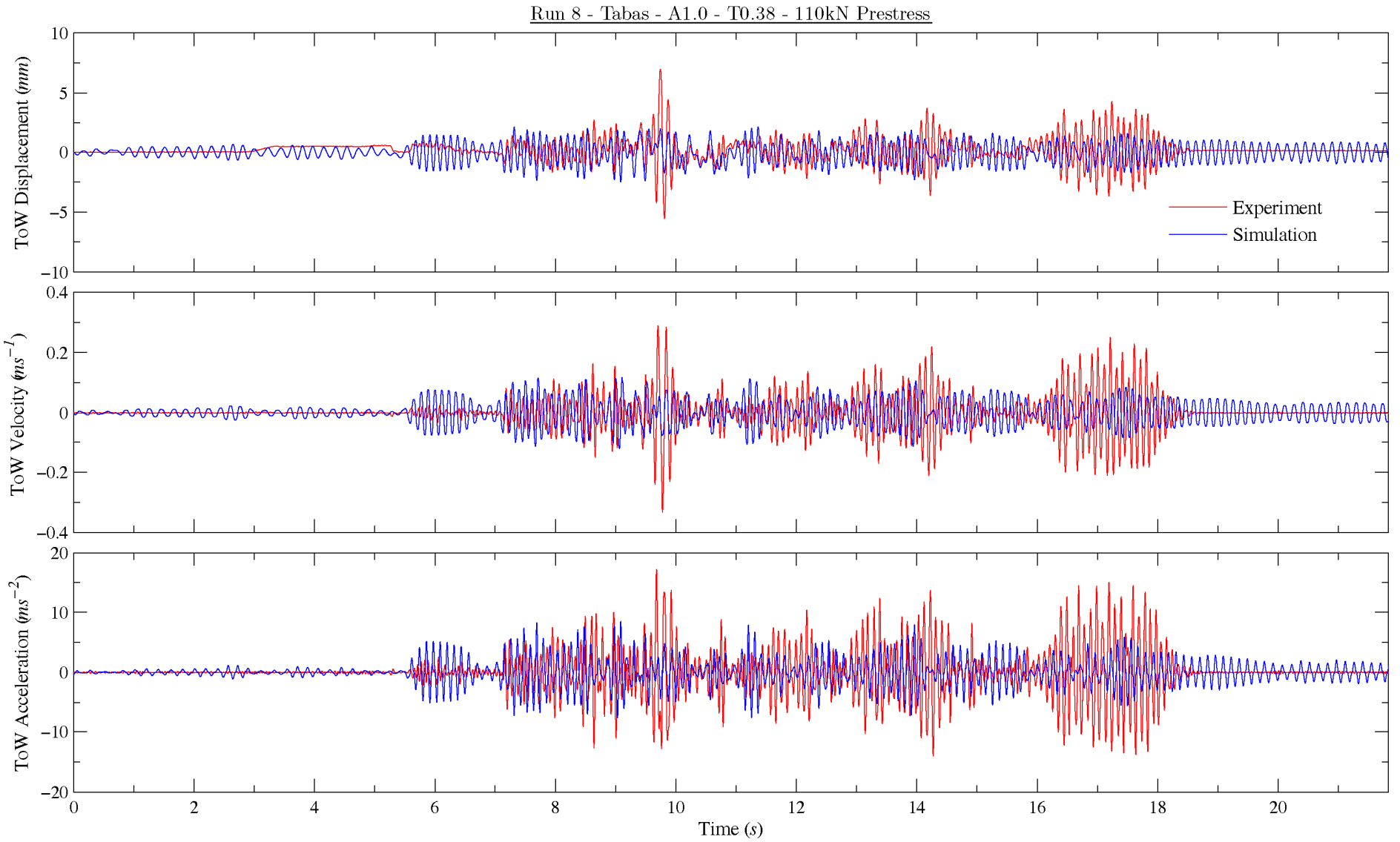
- 270 -

270

Figure C-13 – Simulated results using the SDOF approach with a constant  $r = 0.835$  (Run 9 Northridge A-1.0 T-0.6, 110kN prestress)

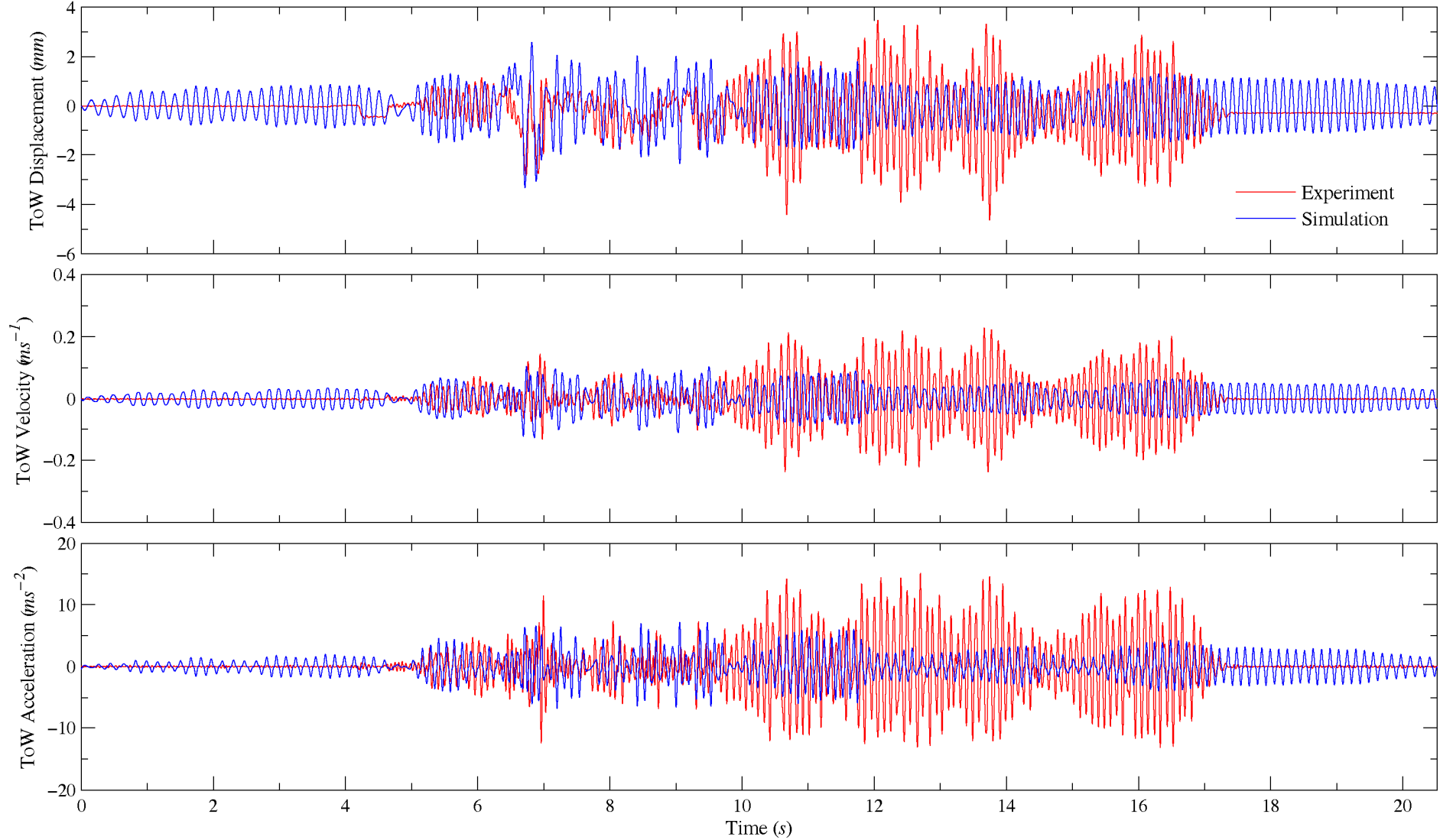


**Figure C-14 – Simulated results using the SDOF approach  $r$  from FV analysis (Run 7 – El Centro A-1.0 T-1.0, 110kN prestress)**



**Figure C-15 – Simulated results using the SDOF approach  $r$  from FV analysis (Run 8 Tabas A-1.0 T-0.38, 110kN prestress)**

Run 9 - Northridge - A1.0 - T0.60 - 110kN Prestress



- 273 -

Figure C-16 – Simulated results using the SDOF approach  $r$  from FV analysis (Run 9 Northridge A-1.0 T-0.6, 110kN prestress)

# Appendix D

---

## MATHEMATICAL DESCRIPTION OF THE FLEXIBLE ROCKING STRUCTURE ON RIGID GROUND

---

Consider the rocking structure at a positive rotation ( $\theta$ ) and positive lateral deformation ( $u$ ). A displacement and velocity diagram of the system at this instant are presented as Figure D-1. The position vectors of the two lumped-masses with respect to  $O$ ,  $r_e$  and  $r_b$  can be expressed by Equations D-1 and D-2 below.

$$r_e = [-R_e \sin(\alpha_e - \theta) + u \cos \theta] \underline{i} + [R_e \cos(\alpha_e - \theta) - u \sin \theta] \underline{j} \quad (\text{D-1})$$

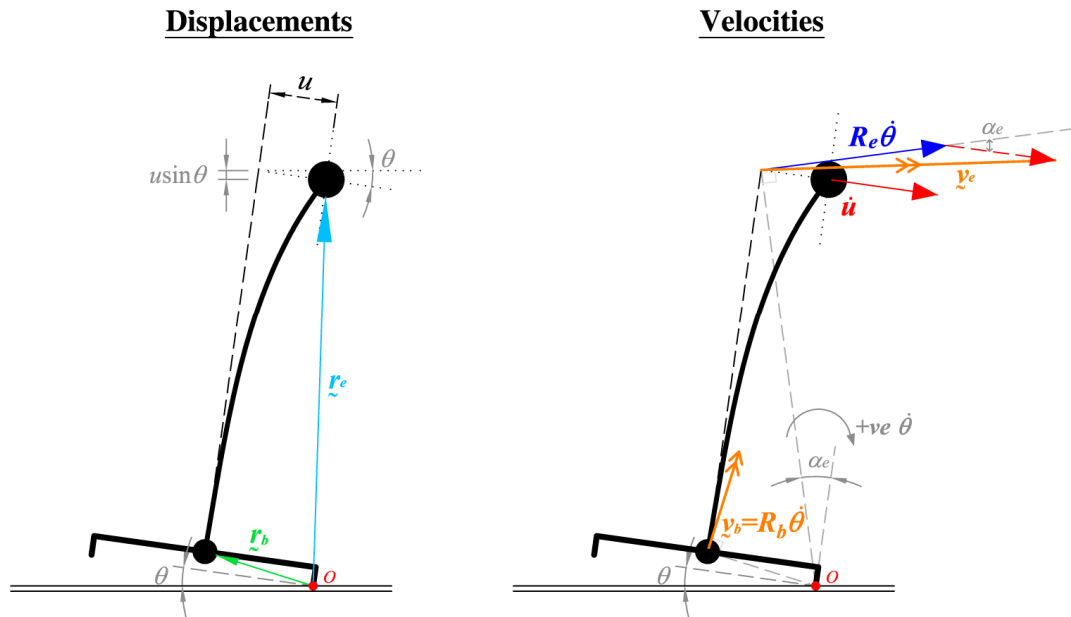
$$r_b = [-R_b \sin(\alpha_e - \theta)] \underline{i} + [R_b \cos(\alpha_e - \theta)] \underline{j} \quad (\text{D-2})$$

Where  $\underline{i}$  and  $\underline{j}$  are versors in the  $i$  and  $j$  (or  $x, y$ ) directions respectively.

The velocities of the two lumped-masses can be determined subsequently by differentiating Equations D-1 and D-2 with respect to time. Note that this can be achieved only approximately by adopting a vector addition approach making use of the cosine rule. Equations D-3 and D-4 below present the algebraic expressions for the velocity vectors of the two lumped-masses.

$$v_e = [\dot{\theta} R_e \cos(\alpha_e - \theta) - \dot{\theta} u \sin \theta + \dot{u} \cos \theta] \underline{i} + [\dot{\theta} R_e \sin(\alpha_e - \theta) - \dot{\theta} u \cos \theta - \dot{u} \sin \theta] \underline{j} \quad (\text{D-3})$$

$$v_b = [\dot{\theta} R_b \cos(\alpha_e - \theta)] \underline{i} + [\dot{\theta} R_b \sin(\alpha_e - \theta)] \underline{j} \quad (\text{D-4})$$



**Figure D-1 – Displacement and velocity diagram of the flexible rocking structure (Positive Rotation)**

Inspecting Equations D-1 through D-4, it is clear that the rocking system can be defined using two generalised coordinates,  $q_1 = \theta$  and  $q_2 = u$ . Consequently, the Lagrange's equation for the system is,

$$\frac{d}{dt} \left( \frac{\partial \mathcal{L}}{\partial \dot{q}_i} \right) - \frac{\partial \mathcal{L}}{\partial q_i} + \frac{\partial F_{nc}}{\partial \dot{q}_i} = Q_i \quad (\text{D-5})$$

Where

$q_i$  = Generalised coordinate ( $i = \theta$  or  $u$ )

$\mathcal{L}$  = The Lagrangian

$F_{nc}$  = Velocity dependent non-conservative generalised forces  
(e.g. viscous damping type forces)

$Q_i$  = Other displacement and velocity independent generalised forces

In order to make use of Equation D-5 the following definition of the Lagrangian is required.

$$\mathcal{L} = T - V \quad (\text{D-6})$$

Where

$T$  = Kinetic energy of the system

$V$  = Potential energy of the system

Now the total kinetic energy of the system is the sum of kinetic energies for the two lumped-masses. Mathematically,

$$T = T_e + T_b \quad (\text{D-7})$$

Where the kinetic energy of the top mass is,

$$\begin{aligned} T_e &= \frac{1}{2} m_e \mathbf{v}_e \cdot \mathbf{v}_e + \frac{1}{2} I_{e,g} \dot{\theta}^2 \\ T_e &= \frac{1}{2} m_e \left\{ \left[ R_e \dot{\theta} \cos(\alpha_e - \theta) - \dot{\theta} u \sin \theta + \dot{u} \cos \theta \right]^2 \right. \\ &\quad \left. + \left[ R_e \dot{\theta} \sin(\alpha_e - \theta) - \dot{\theta} u \cos \theta + \dot{u} \sin \theta \right]^2 \right\} + \frac{1}{2} I_{e,g} \dot{\theta}^2 \\ T_e &= \frac{1}{2} m_e \left\{ R_e^2 \dot{\theta}^2 \cos^2(\alpha_e - \theta) - 2R_e u \dot{\theta}^2 \sin \theta \cos(\alpha_e - \theta) + 2\dot{u} R_e \dot{\theta} \cos(\alpha_e - \theta) \cos \theta \right. \\ &\quad \left. + u^2 \dot{\theta}^2 \sin^2 \theta - 2u\dot{u} \sin \theta \cos \theta + \dot{u}^2 \cos^2 \theta \right. \\ &\quad \left. + R_e^2 \dot{\theta}^2 \sin^2(\alpha_e - \theta) - 2R_e u \dot{\theta}^2 \cos \theta \sin(\alpha_e - \theta) - 2\dot{u} R_e \dot{\theta} \sin(\alpha_e - \theta) \sin \theta \right. \\ &\quad \left. + u^2 \dot{\theta}^2 \cos^2 \theta + 2u\dot{u} \sin \theta \cos \theta + \dot{u}^2 \cos^2 \theta \right\} + \frac{1}{2} I_{e,g} \dot{\theta}^2 \end{aligned} \quad (\text{D-8})$$

Taking advantage of the following trigonometric identities:

$$\sin(A \pm B) = \sin A \cos B \pm \cos A \sin B \quad (\text{D-9})$$

$$\cos(A \pm B) = \cos A \cos B \mp \sin A \sin B \quad (\text{D-10})$$

Equation D-8 becomes,

$$T_e = \frac{1}{2} m_e \left[ R_e^2 \dot{\theta}^2 + u^2 \dot{\theta}^2 + \dot{u}^2 - 2R_e u \dot{\theta}^2 \sin \alpha_e + 2\dot{u} R_e \dot{\theta} \cos \alpha_e \right] + \frac{1}{2} I_{e,g} \dot{\theta}^2 \quad (\text{D-11})$$

Accordingly, the kinetic energy of the bottom mass is,

$$\begin{aligned} T_b &= \frac{1}{2} m_b \mathbf{v}_b \cdot \mathbf{v}_b + \frac{1}{2} I_{b,g} \dot{\theta}^2 \\ T_b &= \frac{1}{2} m_b \left\{ \left[ R_b \dot{\theta} \cos(\alpha_b - \theta) \right]^2 + \left[ R_b \dot{\theta} \sin(\alpha_b - \theta) \right]^2 \right\} + \frac{1}{2} I_{b,g} \dot{\theta}^2 \\ T_b &= \frac{1}{2} m_b R_b^2 \dot{\theta}^2 + \frac{1}{2} I_{b,g} \dot{\theta}^2 \end{aligned} \quad (\text{D-12})$$

Following this, the potential energy of the system ( $V$ ) is the sum of the gravitational potential energy of the two masses and the elastic potential energy of the system.

Mathematically,

$$V = [0, \quad m_e g] \cdot \underline{r}_e + [0, \quad m_b g] \cdot \underline{r}_b + \frac{1}{2} k u^2$$

$$V = m_e g [R_e \cos(\alpha_e - \theta) - u \sin \theta] + m_b g [R_b \cos(\alpha_b - \theta)] + \frac{1}{2} k u^2 \quad (\text{D-13})$$

Combining Equations D-6, D-7, D-11, D-12 and D-13, yields the expression for the Lagrangian as below.

$$\begin{aligned} \mathcal{L} = & \frac{1}{2} m_e [R_e^2 \dot{\theta}^2 + u^2 \dot{\theta}^2 + \dot{u}^2 - 2R_e u \dot{\theta}^2 \sin \alpha_e + 2\dot{u} R_e \dot{\theta} \cos \alpha_e] + \frac{1}{2} I_{e,g} \dot{\theta}^2 \\ & + \frac{1}{2} m_b R_b \dot{\theta}^2 + \frac{1}{2} I_{b,g} \dot{\theta}^2 \\ & - m_e g [R_e \cos(\alpha_e - \theta) - u \sin \theta] - m_b g [R_b \cos(\alpha_b - \theta)] - \frac{1}{2} k u^2 \end{aligned} \quad (\text{D-14})$$

Continuing to evaluate each term in the Lagrange's equation, the non-conservative generalised force ( $F_{nc}$ ) of the system arises from the idealised viscous dissipative force of the flexible structure only. The expression for  $F_{nc}$  is thus,

$$F_{nc} = \frac{1}{2} c \dot{u}^2 \quad (\text{D-15})$$

Next, the generalised forces on the system arise from the forcing on the system. In this study, the forcing is a result of base excitation ( $\ddot{u}_g$ ), which can be idealised as D'Alembert forces acting at the lumped-mass centres as shown in Figure D-2. Mathematically, the definition of the generalised forces is,

$$Q_i = f_e \frac{\partial r_e}{\partial q_i} + f_b \frac{\partial r_b}{\partial q_i} \quad (\text{D-16})$$

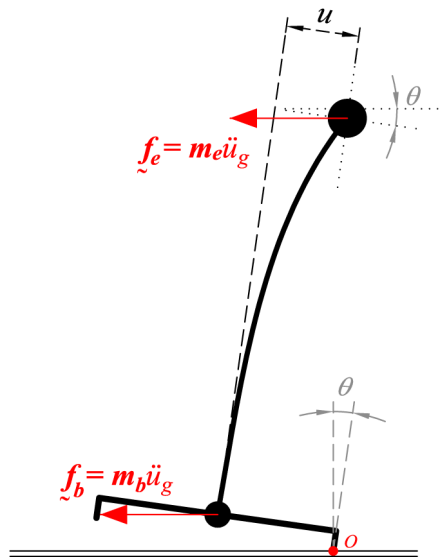


Figure D-2 – D'Alembert forces as a result of a base excitation ( $\ddot{u}_g$ )

Evaluating Equation D-16 for  $q_1 = \theta$ ,

$$Q_\theta = -m_e \ddot{u}_g [R_e \cos(\alpha_e - \theta) - u \sin \theta] - m_b \ddot{u}_g R_b \cos(\alpha_b - \theta) \quad (\text{D-17})$$

Similarly for  $q_2 = u$ ,

$$Q_u = -m_e \ddot{u}_g \cos \theta \quad (\text{D-18})$$

Now substituting all the require terms into the Lagrange's equation, carrying out the differentiations and rearranging, it yields two equation of motion, Equations D-19 and D-20 below.

$$\begin{aligned} & (m_e R_e^2 + m_e u^2 - 2m_e u R_e \sin \alpha_e + I_{e,g} + m_b R_b^2 + I_{b,g}) \ddot{\theta} \\ & + (2m_e u \dot{u} - 2m_e \dot{u} R_e \sin \alpha_e) \dot{\theta} + m_e \ddot{u} R_e \cos \alpha_e \\ & + m_e g [R_e \sin(\alpha_e - \theta) - u \cos \theta] + m_b g R_b \sin(\alpha_b - \theta) = \end{aligned} \quad (\text{D-19})$$

$$\begin{aligned} & -m_e \ddot{u}_g [R_e \cos(\alpha_e - \theta) - u \sin \theta] - m_b \ddot{u}_g R_b \cos(\alpha_b - \theta) \\ & m_e \ddot{u} + m_e R_e \cos \alpha_e \ddot{\theta} - (m_e u - m_e R_e \sin \alpha_e) \dot{\theta}^2 \\ & - m_e g \sin \theta + k u + c \dot{u} = -m_e \ddot{u}_g \cos \theta \end{aligned} \quad (\text{D-20})$$

Now repeat the exercise for rocking about the other edge, in other words when the rocking structure is at a negative rotation ( $\theta$ ) and a positive lateral deformation ( $u$ ). The position vectors measured from  $O'$  for the two lumped-masses are,

$$\underline{r}_e = [R_e \sin(\alpha_e + \theta) + u \cos \theta] \underline{i} + [R_e \cos(\alpha_e + \theta) - u \sin \theta] \underline{j} \quad (\text{D-21})$$

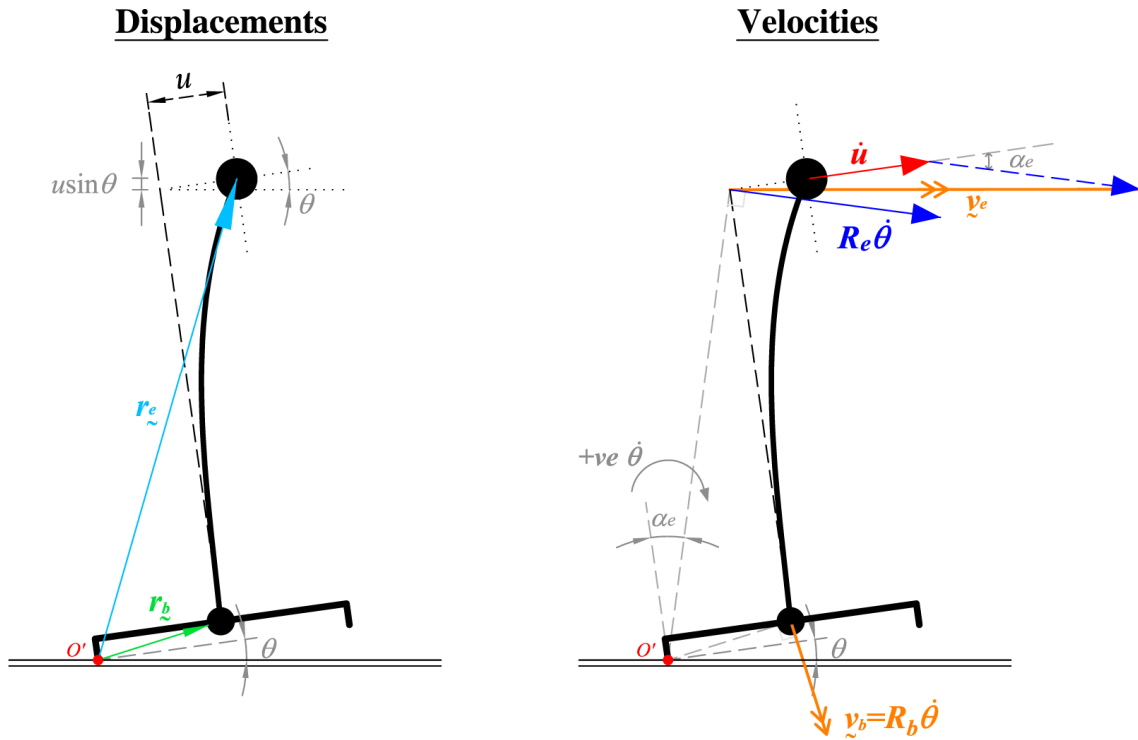
$$\underline{r}_b = [R_b \sin(\alpha_e + \theta)] \underline{i} + [R_b \cos(\alpha_e + \theta)] \underline{j} \quad (\text{D-22})$$

These are also illustrated graphically in Figure D-3. Repeating the derivations with the new position vectors yields the following GDE for the structure at negative rotations.

$$\begin{aligned} & (m_e R_e^2 + m_e u^2 + 2m_e u R_e \sin \alpha_e + I_{e,g} + m_b R_b^2 + I_{b,g}) \ddot{\theta} \\ & + (2m_e u \dot{u} + 2m_e \dot{u} R_e \sin \alpha_e) \dot{\theta} + m_e \ddot{u} R_e \cos \alpha_e \\ & - m_e g [R_e \sin(\alpha_e + \theta) - u \cos \theta] - m_b g R_b \sin(\alpha_b + \theta) = \end{aligned} \quad (\text{D-23})$$

$$\begin{aligned} & -m_e \ddot{u}_g [R_e \cos(\alpha_e + \theta) - u \sin \theta] - m_b \ddot{u}_g R_b \cos(\alpha_b + \theta) \end{aligned}$$

$$\begin{aligned}
& m_e \ddot{u} + m_e R_e \cos \alpha_e \ddot{\theta} - (m_e u + m_e R_e \sin \alpha_e) \dot{\theta}^2 \\
& - m_e g \sin \theta + ku + c\dot{u} = -m_e \ddot{u}_g \cos \theta
\end{aligned}
\tag{D-24}$$



**Figure D-3 – Displacement and velocity diagram of the flexible rocking structure (Negative Rotation)**

Combining Equations D-19, D-20, D-23 and D-24 yields the GDEs of motion for the rocking flexible structure across the positive and negative rotations. These are presented as Equations D-25 and D-26 below.

$$\begin{aligned}
& (m_e R_e^2 + m_e u^2 - \text{sgn}(\theta) \times 2m_e u R_e \sin \alpha_e + I_{e,g} + m_b R_b^2 + I_{b,g}) \ddot{\theta} \\
& + (2m_e u \dot{u} - \text{sgn}(\theta) \times 2m_e \dot{u} R_e \sin \alpha_e) \dot{\theta} + m_e \ddot{u} R_e \cos \alpha_e \\
& + \text{sgn}(\theta) \times m_e g [R_e \sin(\alpha_e - \text{sgn}(\theta) \cdot \theta) - \text{sgn}(\theta) \times u \cos \theta] \\
& + \text{sgn}(\theta) \times m_b g R_b \sin(\alpha_b - \text{sgn}(\theta) \cdot \theta) = \\
& -m_e \ddot{u}_g [R_e \cos(\alpha_e - \text{sgn}(\theta) \cdot \theta) - u \sin \theta] - m_b \ddot{u}_g R_b \cos(\alpha_b - \text{sgn}(\theta) \cdot \theta)
\end{aligned}
\tag{D-25}$$

$$\begin{aligned}
& m_e \ddot{u} + m_e R_e \cos \alpha_e \ddot{\theta} - (m_e u - \text{sgn}(\theta) \times m_e R_e \sin \alpha_e) \dot{\theta}^2 \\
& - m_e g \sin \theta + ku + c\dot{u} = -m_e \ddot{u}_g \cos \theta
\end{aligned}
\tag{D-26}$$

Next, to enable numerical integration of the above GDEs, the equations are rearranged into a system of single order differential equations as in Equation D-27.

$$[M]\dot{y} = f(t, y) \quad (\text{D-27})$$

Let  $y_1 = u$ ,  $y_2 = \dot{u}$ ,  $y_3 = \theta$  and  $y_4 = \dot{\theta}$ . The GDEs becomes,

$$\begin{aligned} \dot{y}_1 &= y_2 \\ m_e \dot{y}_2 + (m_e R_e \cos \alpha_e) \dot{y}_4 &= [m_e y_1 - \text{sgn}(y_3) \times m_e R_e \sin \alpha_e] y_4^2 \\ &\quad + m_e g \sin(y_3) - k y_1 - c y_2 - m_e \ddot{u}_g \cos(y_3) \\ \dot{y}_3 &= y_4 \\ (f_1) \dot{y}_2 + (f_2) \dot{y}_4 &= [\text{sgn}(y_3) \times 2m_e \dot{u} R_e \sin \alpha_e - 2m_e u \ddot{u}] y_4 \\ &\quad - \text{sgn}(y_3) \times m_e g [R_e \sin(\alpha_e - \text{sgn}(y_3) \cdot y_3) - \text{sgn}(y_3) \times y_1 \cos y_3] \\ &\quad - \text{sgn}(y_3) \times m_b g R_b \sin(\alpha_b - \text{sgn}(y_3) \cdot y_3) \\ &\quad - m_e \ddot{u}_g [R_e \cos(\alpha_e - \text{sgn}(y_3) \cdot y_3) - y_1 \sin y_3] \\ &\quad - m_b \ddot{u}_g R_b \cos(\alpha_b - \text{sgn}(y_3) \cdot y_3) \end{aligned} \quad (\text{D-28})$$

Where

$$\begin{aligned} f_1 &= m_e R_e \cos \alpha_e \\ f_2 &= m_e R_e^2 + m_e y_1^2 - \text{sgn}(y_3) \times 2m_e (y_1) R_e \sin \alpha_e + I_{e,g} + m_b R_b^2 + I_{b,g} \end{aligned} \quad (\text{D-29})$$